

**University of Alberta**

Computational Fluid Dynamics Modeling of Deposition of Oil Sand Slurry into  
Mature Fine Tailings

by

Junwen Yang

A thesis submitted to the Faculty of Graduate Studies and Research  
in partial fulfillment of the requirements for the degree of

Doctor of Philosophy

in

Geotechnical Engineering

Department of Civil and Environmental Engineering

©Junwen Yang

Fall 2009

Edmonton, Alberta

Permission is hereby granted to the University of Alberta Libraries to reproduce single copies of this thesis and to lend or sell such copies for private, scholarly or scientific research purposes only. Where the thesis is converted to, or otherwise made available in digital form, the University of Alberta will advise potential users of the thesis of these terms.

The author reserves all other publication and other rights in association with the copyright in the thesis and, except as herein before provided, neither the thesis nor any substantial portion thereof may be printed or otherwise reproduced in any material form whatsoever without the author's prior written permission.

## **Examining Committee**

Dr. Rick Chalaturnyk, Supervisor, Civil & Environmental Engineering

Dr. Dave Segó, Civil & Environmental Engineering

Dr. Nallamuthu Rajaratnam, Civil & Environmental Engineering

Dr. Vivek Bindiganavile, Civil & Environmental Engineering

Dr. Carlos Lange, Mechanical Engineering

Dr. Dirk van Zyl, External Examiner, University of British Columbia

## ABSTRACT

The objective of this research program is to study the feasibility of using computational fluid dynamics (CFD) approach to the modeling of dense slurry flow with a special emphasis on oil sand slurry inflow into oil sands mature fine tailings (MFT).

An experimental program is established to measure the viscosity and the yield stress of the slurry with various solids and fines contents. The viscosity and yield stress of the slurry are curve fitted using Power Law model and Herschel-Bulkley model. Then the flow curve for pure MFT is applied in the CFD simulation of the viscosity and yield stress measurements using the single phase model in CFX-10. The simulated torques reasonably agree with those from experiments.

Sedimentation process for bidisperse and polydisperse suspension from literature are simulated using MFIX and FLUENT. Simulation results indicate that the Euler-Euler Model in those two CFD packages is capable of modeling the sedimentation process of the bidisperse and polydisperse suspension. Then the settling process of the segregating and non-segregating oil sand tailing slurry is selected to test the capability of MFIX, FLUENT-6 and CFX-10. The results show that the transient process of the sedimentation, therefore the segregation, of the tailing slurry can not be captured by those models if the viscosity of the water phase is not changed to reflect the interaction between clay particles and the water phase.

The flume test conducted by Scott et al. (1993) is simulated using the Free Surface Model and the Particle Model in CFX-10. It is found that the traveling speed of the slurry is significantly faster than was measured in the laboratory tests. The solids and fines content profiles in the simulation do not match those in the laboratory deposit.

The flow of sand slurry into the simplified MFT ponds is simulated. Segregation always occurs for non-segregation mixture using the Particle Model if a viscosity of 0.001 Pa.s is assigned to water phase. Considering MFT to be composed of sand particles and clay-water suspension results in more realistic sand particle distribution in the tailing pond using both Mixture Model and two phase Particle Model.

## ACKNOWLEDGEMENTS

I am very grateful to my supervisor, Dr. Chalaturnyk, for his guidance, encouragement and technical and financial support throughout conducting research at the University of Alberta.

I would like to thank Suncor Energy Ltd. for the financial and technical support through the Oil Sands Tailings Research Facility (OSTRF). The individual support provided by Dr. Don Sheeran and Mr. Mike Agnew in establishing this research effort is also very much appreciated.

I would like to thank all the faculty and staff at the Department of Civil and Environmental Engineering and especially those at the Geotechnical and Geoenvironmental group. I would like to thank Steve Gamble for their laboratory support.

I would like to express my gratitude to Dr. Scott, for his guidance and technical support.

I would like to thank my doctoral committee members for the valuable comments and recommendations.

I am indebted to my parents who gave me an education and constantly support.

Finally, I would like to extend my deepest thanks to my wife, Zhi, and my daughter, Carolyn, for their love and support.

## Table of Content

<b>Chapter 1 Introduction.....</b>	<b>1</b>
1.1 Backgrounds.....	1
1.1.1 Overview of Bitumen Extraction and Production of Tailings .....	1
1.1.2 Reclamation of Tailing Ponds.....	4
1.1.3 Brief Discussion of Suncor Pond 1 Issues .....	5
1.1.4 Challenges .....	5
1.2 Objectives of Research Program.....	6
1.3 Scope of This Work.....	7
1.4 Organization of Thesis.....	7
Reference.....	9
<b>Chapter 2 Literature Review .....</b>	<b>10</b>
2.1 Introduction to Oil Sand Tailings .....	10
2.1.1 Oil Sands and Origin of Oil Sand Tailings .....	10
2.1.2 Tailings Composition.....	14
2.2 Oil Sands Tailing Properties.....	17
2.2.1 Uniqueness of Oil Sands Mature Fine Tailings .....	17
2.2.2 Geotechnical Properties of Oil Sand Mature Fine Tailings (MFT) .....	18
2.2.3 Non-Segregating Tailings (NST) .....	18
2.3 Management of Tailings.....	19
2.3.1 Management of Tailings.....	19
2.3.2 Reclamation of Tailing Ponds.....	23
2.3.2.1 Dry Landscape Options .....	24
2.3.2.2 Wet Landscape Options.....	25
2.4 Rheological Properties of Natural Clay-Water Mixture and Clay-Sand- Water Mixture .....	25
2.4.1 Rheological Properties of Clay-Sand-Water Mixture.....	25
2.4.1.1 Rheological Properties of Clay-Water Mixture.....	25
2.4.2 Rheological Properties of Clay-Sand-Water Mixture.....	29
2.4.2.1 Rheology of Clay-Sand-Water Mixture .....	29
2.4.3 Measurement of Viscosity .....	32
2.5 Sedimentation and Segregation of Mixture.....	32
2.5.1 Sedimentation of a Sphere in an Infinite Fluid.....	32
2.5.1.1 Laminar Flow .....	33
2.5.1.2 Transitional and Turbulent Flow .....	34
2.5.2 Nonspherical Particles in an Infinite Fluid.....	35
2.5.3 Settling in the Presence of Other Particles .....	36
2.5.3.1 Suspension of Uniform Particle .....	37
2.5.3.2 Suspensions Consisting of a Range of Particle Sizes, Shapes, and Densities.....	37
2.5.3.3 Concentrated Solid-Fluid System .....	38



3.1.3.8 Test 8: Slurry with Solids Content of 49% and Fines Content of 68% .....	123
3.1.3.9 Test 9: Slurry with Solids Content of 51% and Fines Content of 78% .....	124
3.1.3.10 Test 10: Slurry with Solids Content of 49% and Fines Content of 86% .....	126
3.1.3.11 Test 11: Slurry with Solids Content of 41% and Fines Content of 95% .....	128
3.1.3.12 Test 12: Slurry with Solids Content of 19% and Fines Content of 24% .....	130
3.1.3.13 Test 13: Slurry with Solids Content of 25% and Fines Content of 49% .....	130
3.1.3.14 Test 14: Slurry with Solids Content of 27% and Fines Content of 94% .....	131
3.1.4 Analysis and Discussion of the Results .....	131
3.1.4.1 Analysis of the Results of Vane Shear Tests .....	131
3.1.4.2 Analysis of the Viscometer Tests .....	135
3.2 Verification of CFD Model Using Rheological Model Obtained from Experiments .....	146
3.2.1 Simulation of Viscosity Measurements Using DV-II Viscometer by Single-Phase Model .....	146
3.2.2 Simulation of Vane Shear Tests Using R/S Solid Rheometer by Single-Phase Model .....	152
3.3 Summary and Conclusions .....	161
Reference .....	163
<b>Chapter 4 CFD Simulation of Oil Sand Slurry Segregation' .....</b>	<b>166</b>
4.1 Introduction .....	166
4.2 Verification of the CFD Simulation of Sedimentation .....	166
4.2.1 Bidisperse Suspension .....	166
4.2.2 Polydisperse Suspension .....	171
4.2.2.1 MFIX Simulation .....	171
4.2.2.2 FUENT Simulation .....	176
4.2.2.3 Comparison .....	180
4.3 Simulation of Segregation of Oil Sand Tailing Slurry .....	180
4.3.1 Unique Properties of Oil Sand Tailing Slurry .....	181
4.3.2 Segregation Tests in Laboratory .....	181
4.3.3 CFD Simulation of Segregation Tests .....	183
4.3.3.1 CFX-5 Simulation .....	184
4.3.3.2 FLUENT-6 Simulation .....	195
4.3.3.3 MFIX Simulation .....	221
4.3.3.4 Comparison of Simulation Results .....	241
4.3.4 Proposed Solution to Oil Sand Slurry Segregation Simulation .....	243
4.3.4.1 Modification of Solid-Solid Exchange Coefficient .....	243
4.3.4.2 Modification of the viscosity of water phase .....	245

4.3.4.3 Two-Phase Simulation.....	245
4.4 Summary and Conclusions.....	246
Reference.....	248
<b>Chapter 5 CFD Simulation of Laboratory Flume Tests .....</b>	<b>250</b>
5.1 Introduction .....	250
5.2 Laboratory Scale Flume Tests.....	250
5.2.1 Objectives of the Flume Tests.....	250
5.2.2 Set-Up of the Tests .....	250
5.2.3 Test Procedure.....	254
5.2.4 Test Results .....	254
5.3 CFD Simulation of Flume Tests .....	260
5.3.1 Free-Surface Model.....	260
5.3.1.1 Model Set-Up.....	260
5.3.1.2 Simulation Results.....	261
5.3.2 Particle Model Using Water Viscosity .....	268
5.3.2.1 Model Set-Up.....	268
5.3.2.2 Simulation Results.....	269
5.3.3 Particle Model Using MFT Viscosity .....	276
5.3.3.1 Model Set-Up.....	276
5.3.3.2 Simulation Results.....	276
5.4 Summary and Conclusion.....	283
Reference.....	284
<b>Chapter 6 CFD Simulation of Suncor’s Pond 1 Trial Tests.....</b>	<b>285</b>
6.1 Introduction .....	285
6.2 Suncor Pond 1 and Sand Infilling Trial in 2002.....	285
6.3 Computational Fluid Dynamics Simulation.....	293
6.3.1 Three Phases for MFT .....	293
6.3.1.1 Particle Model .....	294
6.3.1.2 Mixture Model .....	301
6.3.2 Two Phases for MFT Using Particle Model .....	308
6.4 Conclusions .....	313
Reference.....	314
<b>Chapter 7 Summaries, Conclusions and recommendations .....</b>	<b>315</b>
7.1 Summaries and Conclusions .....	315
7.1.1 Rheological Properties of Oil Sand Tailings .....	315
7.1.2 CFD Simulation of Oil Sand Tailing Slurry Segregation .....	316
7.1.3 CFD Simulation of Flume Tests .....	318
7.1.4 CFD Simulation of Oil Sand Deposition into MFT Pond .....	318
7.2 Recommendations .....	320

Reference.....	321
<b>Appendix A: Raw Data for Viscosity Measurement for Tailing Slurry.....</b>	<b>322</b>

## List of Tables

Table 2.1 Composition of Syncrude and Suncor MFT (from FTFC, 1995).....	15
Table 2.2 Equations relating viscosity to solid concentration (from Ferraris, 2001).....	29
Table 2.3 Summaries of Models and Parameters in CFX 5 and Fluent 6 .....	71
Table 3.1 The Source Materials and Corresponding Solids and Fines Contents .....	102
Table 3.2 Matrix of Samples for Viscosity and Yield Stress Measurements .....	103
Table 3.3 Calculated Shear Stress and Apparent Viscosity for Slurry with s%=66 and f%=37 .....	110
Table 3.4 Calculated Shear Stress and Apparent Viscosity for Slurry with s%=65 and f%=32 .....	112
Table 3.5 Calculated Shear Stress and Apparent Viscosity for Slurry with s%=43 and f%=75 .....	114
Table 3.6 Calculated Shear Stress and Apparent Viscosity for Slurry with s%=52 and f%=60 .....	116
Table 3.7 Calculated Shear Stress and Apparent Viscosity for Slurry with s%=40 and f%=94 .....	118
Table 3.8 Calculated Shear Stress and Apparent Viscosity for Slurry with s%=61 and f%=95 .....	120
Table 3.9 Calculated Shear Stress and Apparent Viscosity for Slurry with s%=50 and f%=95 .....	121
Table 3.10 Calculated Shear Stress and Apparent Viscosity for Slurry with s%=49 and f%=68.....	123
Table 3.11 Calculated Shear Stress and Apparent Viscosity for Slurry with s%=51 and f%=78.....	125
Table 3.12 Calculated Shear Stress and Apparent Viscosity for Slurry with s%=49 and f%=86.....	127
Table 3.13 Calculated Shear Stress and Apparent Viscosity for Slurry with s%=41 and f%=95.....	129
Table 3.14 Static Yield Stress for Mixture with Various Solids and Fines Contents .....	133
Table 3.15 Comparison of Static Yield Stress for Mixture with Similar Solids Content and Different Fines Content .....	134
Table 3.16 Comparison of Static Yield Stress for Mixture with Similar Solids Content and Different Fines Content .....	134
Table 3.17 Static Yield Stress for MFT with Various Solids Contents .....	135
Table 3.18 Parameters for Viscosity Regression Equations.....	141

Table 3.19 Richardson Extrapolation for Simulated Torque.....	151
Table 3.20 Richardson Extrapolation for Simulated Torque.....	157
Table 4.1 The Properties of the Composition of Polydisperse System .....	171
Table 4.2 Comparison of three Standpipe Tests for Determining Segregation Boundary .....	183
Table 4.3 Material Properties for Each Phase.....	185
Table 4.4 Initial Volume Fractions for SB1 and SB3 .....	185
Table 4.5 Parameters Used in CFX Particle Models for SB1 and SB3 .....	186
Table 4.6 Sensitivity Analysis for SB1 using Fluent-6.....	197
Table 4.7 Calculated Effective size D31 in mm for CT, coarse and fine particles based on number Probability Distribution Function using different fine-coarse particle divisions.....	204
Table 4.8 Calculated Effective size D31 in mm for CT, coarse and fine particles based on mass Probability Distribution Function using different fine- coarse particle divisions.....	205
Table 4.9 Calculated Effective size D50 in mm for coarse and fine particles based on 50% mass using different fine-coarse particle divisions .....	206
Table 4.10 Common Settings for MFIX Simulation Cases.....	223
Table 4.11 Segregation Slope Values for MFIX Simulation Cases .....	223
Table 5.1 Summary of Flume Tests (from Scott et al. 1993) .....	254

## List of Figures

Figure 1.1 Current and Predicted MFT Volume in Fort McMurray (after Houlihan et al, 2008).....	4
Figure 2.1 Alberta’s Oil Sand Deposit in Peace River, Fort McMurray and Cold Lake areas (NEB, 2004) .....	12
Figure 2.2 Illustration of the depth of the overburden and surface mining area (from AMEC, 2007).....	12
Figure 2.4 Generalized scheme for surface mining (based on Alberta Chamber of Resources, 2004.).....	14
Figure 2.5 Typical Range of Grain size distribution of Oil Sand Tailings (Modified from Fair, 2008).....	16
Figure 2.6 Typical Grain Size Distribution of Oil Sand Fine Tailings (after FTFC, 1995) .....	17
Figure 2.7 Tailings management (based on Alberta Chamber of Resources, 2004.) .....	20
Figure 2.8 Rheological Classification of Water-debris Mixture (after Coussot 1997). The total solid volume fraction is defined as the total volume of the solids divided by the sum of the solid volume and liquid volume in percent.....	31
Figure 2.10 Drag coefficient versus Reynolds number for different shape factors (after Albertson, 1953).....	36
Figure 2.11 Finite Volume Grid .....	48
Figure 2.12 Multiphase Description of a Fluid-Solid Mixture (after Syamlal et al., 1993).....	52
Figure 2.13 Lagrangian Description of Fluid Motion(after Kundu and Cohen, 2002).....	53
Figure 2.14 Concepts of Interpenetrating Continua and Volume Fractions for a Fluid-Solid Mixture .....	55
Figure 2.15 Slowly and Rapidly Shearing Granular Flow (after Syamlal et al., 1993).....	61
Figure 3.1 Shear stress – shear rate curves for typical time independent Non-Newtonian fluids (after Wasp et al., 1977).....	98
Figure 3.2 Shear diagrams for thixotropic and rheopectic fluids (after Wasp et al., 1977) .....	98
Figure 3.3 Brookfield DV-II+ Programmable Viscometer.....	101
Figure 3.4 Brookfield R/S Soft Solid Rheometer .....	101
Figure 3.5 Sample Matrix on Tailing Properties Diagram (based on Chalaturnyk and Scott, 2001; Azam & Scott, 2005).....	104

Figure 3.6 Grain size distribution of MFT from Syncrude .....	108
Figure 3.7 Grain size distribution of Cyclone Underflow Sand from Syncrude .....	108
Figure 3.8 Illustration for typical plot of torque vs. time and the data points used to obtain averaged torque .....	109
Figure 3.9 Shear Stress vs. Strain for Mixture with $s\% = 66$ and $f\% = 37$ in the Vane Shear Tests (Vane 80-40, Constant Strain Rate= $0.03 \text{ s}^{-1}$ ).....	110
Figure 3.10 Plot of Shear Stress vs. Shear Rate in Semi-Log Scale for Slurry with $s\%=66$ and $f\%=37$ .....	111
Figure 3.11 Plot of Apparent Viscosity vs. Shear Rate in Log-Log Scale for Slurry with $s\%=66$ and $f\%=37$ .....	111
Figure 3.12 Shear Stress vs. Strain for Mixture with $s\% = 65$ and $f\% = 32$ (Vane 80-40, Constant Strain Rate= $0.03 \text{ s}^{-1}$ ).....	112
Figure 3.13 Plot of Shear Stress vs. Shear Rate in Semi-Log Scale for Slurry with $s\%=65$ and $f\%=32$ .....	113
Figure 3.14 Plot of Apparent Viscosity vs. Shear Rate in Log-Log Scale for Slurry with $s\%=65$ and $f\%=32$ .....	113
Figure 3.15 Comparison of Averaged Shear Stress vs. Strain for Mixture with $s\% = 43$ and $f\% = 75$ (Vane 80-40, Constant Strain Rate= $0.05$ and $0.1 \text{ s}^{-1}$ ).....	114
Figure 3.16 Plot of Shear Stress vs. Shear Rate in Semi-log Scale for Slurry with $s\% = 43\%$ and $f\% = 75\%$ .....	115
Figure 3.17 Plot of Apparent Viscosity vs. Shear Rate in Log-Log Scale for Slurry with $s\% = 43\%$ and $f\% = 75\%$ .....	115
Figure 3.18 Comparison of Averaged Shear Stress vs. Strain for Mixture with $s\% = 52$ and $f\% = 60$ (Vane 80-40, Constant Strain Rate= $0.05$ and $0.1 \text{ s}^{-1}$ ).....	116
Figure 3.19 Plot of Shear Stress vs. Shear Rate in Semi-Log Scale for Slurry with $s\%=52$ and $f\%=60$ .....	117
Figure 3.20 Plot of Apparent Viscosity vs. Shear Rate in Log-Log Scale for Slurry with $s\%=52$ and $f\%=60$ .....	117
Figure 3.21 Comparison of Averaged Shear Stress vs. Strain for Mixture with $s\% = 40$ and $f\% = 94$ (Vane 80-40, Constant Strain Rate= $0.03 \text{ s}^{-1}$ ) .....	118
Figure 3.22 Plot of Shear Stress vs. Shear Rate in Semi-Log Scale for Slurry with $s\%=40$ and $f\%=94$ .....	119
Figure 3.23 Plot of Apparent Viscosity vs. Shear Rate in Log-Log Scale for Slurry with $s\%=40$ and $f\%=94$ .....	119
Figure 3.24 Shear Stress vs. Strain for Mixture with $s\% = 61$ and $f\% = 95$ (Vane 40-20, Constant Strain Rate= $0.05 \text{ s}^{-1}$ ).....	120

Figure 3.25 Plot of Shear Stress vs. Shear Rate in Semi-Log Scale for Slurry with $s\%=61$ and $f\%=95$ .....	120
Figure 3.26 Plot of Apparent Viscosity vs. Shear Rate in Log-Log Scale for Slurry with $s\%=61$ and $f\%=95$ .....	121
Figure 3.27 Shear Stress vs. Strain for Mixture with $s\% = 50$ and $f\% = 94.5$ (Vane 40-20, Constant Strain Rate= $0.05 \text{ s}^{-1}$ ).....	122
Figure 3.28 Plot of Shear Stress vs. Shear Rate in Semi-Log Scale for Slurry with $s\%=50$ and $f\%=95$ .....	122
Figure 3.29 Plot of Apparent Viscosity vs. Shear Rate in Log-Log Scale for Slurry with $s\%=50$ and $f\%=95$ .....	122
Figure 3.30 Shear Stress vs. Strain for Mixture with $s\% = 49$ and $f\% = 68$ (Vane 40-20, Constant Strain Rate= $0.05 \text{ s}^{-1}$ ).....	123
Figure 3.31 Plot of Shear Stress vs. Shear Rate in Semi-Log Scale for Slurry with $s\%=49$ and $f\%=68$ .....	124
Figure 3.32 Plot of Apparent Viscosity vs. Shear Rate in Log-Log Scale for Slurry with $s\%=49$ and $f\%=68$ .....	124
Figure 3.33 Shear Stress vs. Strain for Mixture with $s\% = 44$ and $f\% = 79$ (Vane 40-20, Constant Strain Rate= $0.05 \text{ s}^{-1}$ ).....	125
Figure 3.34 Plot of Shear Stress vs. Shear Rate in Semi-Log Scale for Slurry with $s\%=51$ and $f\%=78$ .....	126
Figure 3.35 Plot of Apparent Viscosity vs. Shear Rate in Log-Log Scale for Slurry with $s\%=51$ and $f\%=78$ .....	126
Figure 3.36 Shear Stress vs. Strain for Mixture with $s\% = 49$ and $f\% = 86$ (Vane 40-20, Constant Strain Rate= $0.05 \text{ s}^{-1}$ ).....	127
Figure 3.37 Plot of Shear Stress vs. Shear Rate in Semi-Log Scale for Slurry with $s\%=49$ and $f\%=86$ .....	128
Figure 3.38 Plot of Apparent Viscosity vs. Shear Rate in Log-Log Scale for Slurry with $s\%=49$ and $f\%=86$ .....	128
Figure 3.39 Diagram of Averaged Shear Stress vs. Strain for Mixture with $s\% = 41$ and $f\% = 95$ (Vane 40-20, Constant Strain Rate= $0.05 \text{ s}^{-1}$ ).....	129
Figure 3.40 Plot of Shear Stress vs. Shear Rate in Log-Log Scale for Slurry with $s\%=41$ and $f\%=95$ .....	129
Figure 3.41 Plot of Apparent Viscosity vs. Shear Rate in Log-Log Scale for Slurry with $s\%=41$ and $f\%=95$ .....	130
Figure 3.42 Diagram of Averaged Shear Stress vs. Strain for Mixture with $s\% = 19$ and $f\% = 24$ (Vane 80-40, Constant Strain Rate= $0.05 \text{ s}^{-1}$ ).....	130
Figure 3.43 Diagram of Averaged Shear Stress vs. Strain for Mixture with $s\% = 25$ and $f\% = 49$ (Vane 80-40, Constant Strain Rate= $0.05 \text{ s}^{-1}$ ).....	131

Figure 3.44 Diagram of Averaged Shear Stress vs. Strain for Mixture with $s\% = 27$ and $f\% = 94$ (Vane 80-40, Constant Strain Rate= $0.05 \text{ s}^{-1}$ ) .....	131
Figure 3.45 Diagram of Variation of Static Yield Stress with Solid sand Fines Contents .....	132
Figure 3.46 Diagram of Variation of Static Yield Stress with Solids Content .....	132
Figure 3.47 Comparison of Measured and Predicted Yield Stress Using Exponential Equation.....	135
Figure 3.48 Shear stress vs. shear strain rate curves for various solids and fines contents .....	136
Figure 3.49 Apparent viscosity for mixture with various solids and fines contents ....	136
Figure 3.50 Effects of solids contents on apparent viscosity.....	137
Figure 3.51 Effects of fines contents on apparent viscosity .....	138
Figure 3.52 Variation of the dimensionless torque as a function of $\Gamma$ .....	139
Figure 3.53 Effects of addition of coarse sand into MFT .....	140
Figure 3.54 Herschel-Bulkley Model and Power Law Model Fitting of Relationship between Shear Stress and Strain Rate for Test 1 .....	141
Figure 3.55 Herschel-Bulkley Model and Power Law Model Fitting of Relationship between Shear Stress and Strain Rate for Test 2 .....	142
Figure 3.56 Herschel-Bulkley Model and Power Law Model Fitting of Relationship between Shear Stress and Strain Rate for Test 3 .....	142
Figure 3.57 Herschel-Bulkley Model and Power Law Model Fitting of Relationship between Shear Stress and Strain Rate for Test 4 .....	143
Figure 3.58 Herschel-Bulkley Model and Power Law Model Fitting of Relationship between Shear Stress and Strain Rate for Test 5 .....	143
Figure 3.59 Herschel-Bulkley Model and Power Law Model Fitting of Relationship between Shear Stress and Strain Rate for Test 7 .....	144
Figure 3.60 Herschel-Bulkley Model and Power Law Model Fitting of Relationship between Shear Stress and Strain Rate for Test 8 .....	144
Figure 3.61 Herschel-Bulkley Model and Power Law Model Fitting of Relationship between Shear Stress and Strain Rate for Test 9 .....	145
Figure 3.62 Herschel-Bulkley Model and Power Law Model Fitting of Relationship between Shear Stress and Strain Rate for Test 10 .....	145
Figure 3.63 Herschel-Bulkley Model and Power Law Model Fitting of Relationship between Shear Stress and Strain Rate for Test 11 .....	146
Figure 3.64 Geometry of DV-II Viscometer Model .....	146
Figure 3.65 Coarse Mesh of DV-II Viscometer Model (3,791 nodes).....	147
Figure 3.66 Medium Mesh of DV-II Viscometer Model (24,294 nodes).....	148

Figure 3.67 Fine Mesh of DV-II Viscometer Model (185,464 nodes).....	149
Figure 3.68 Geometry of Brookfield R/S Soft Solid Rheometer Model.....	154
Figure 3.69 Coarse mesh of Brookfield R/S Soft Solid Rheometer model (27,320 nodes) .....	155
Figure 3.70 Medium mesh of Brookfield R/S Soft Solid Rheometer model (28,212 nodes) .....	156
Figure 3.71 Fine mesh of Brookfield R/S Soft Solid Rheometer model (41,597 nodes).....	157
Figure 3.72 Shear strain rate for MFT yield stress measuring.....	158
Figure 3.73 Shear strain rate for MFT along a curve with radius of 0.010 m on the horizontal mid-plane passing through the blade.....	159
Figure 3.74 Location of the curve for shear rate plot.....	159
Figure 3.75 Shear strain rate surface plot for MFT slurry over the plane passing through the middle of the vane .....	160
Figure 3.76 Vector of velocity on the plane passing through the middle of the vane blades for MFT.....	161
Figure 4.1 The grid independence tests for the bidisperse mixture.....	167
Figure 4.2 Comparison of volume fraction of coarse and fine particles at time = 51.9 seconds.....	168
Figure 4.3 Comparison of volume fraction of coarse and fine particles at time = 299.8 seconds .....	169
Figure 4.4 Comparison of fine particle volume fraction at time = 599.7 seconds .....	170
Figure 4.5 Grid Used in Dispersed Simulation (MFI).....	172
Figure 4.6 The Volume Fraction Profile for Four Solid Phases ( Particle Size Decrease from Left to Right) at the Time of 150 s.....	173
Figure 4.7 The Volume Fraction Profile for Four Solid Phases ( Particle Size Decrease from Left to Right) at the Time of 600 s.....	174
Figure 4.8 The Volume Fraction Profile for Four Solid Phases ( Particle Size Decrease from Left to Right) at the Time of 1000 s .....	175
Figure 4.9 Comparison of volume fraction profiles from MFI simulation and Burger's data at Time = 615.07s.....	176
Figure 4.10 Volume Fraction Profile for Largest and Large Particle Sizes at Time = 500s (FLUENT) .....	177
Figure 4.11 Volume Fraction Profile for Largest and Large Particle Sizes at Time = 750s (FLUENT) .....	178
Figure 4.13 Volume Fraction Profile for Four Particle Sizes at Time = 500s (FLUENT).....	179

Figure 4.14 Volume Fraction Profile for Four Particle Sizes at Time = 750s (FLUENT).....	179
Figure 4.15 Volume Fraction Profile for Four Particle Sizes at Time = 1200s (FLUENT).....	180
Figure 4.16 Measurement of Segregation and Fines Capture (after Chalaturnyk et al., 2001) .....	181
Figure 4.17 Size Distribution of Solid Particles Used in Segregation Tests .....	183
Figure 4.18 Solids and fines content for SB1 at Time = 300s for CFX-Case1 .....	187
Figure 4.19 Solids and fines contents for SB1 at Time = 300 s for CFX-Case1.....	187
Figure 4.20 Comparison of Interface Development for SB1 .....	188
Figure 4.21 Solids and fines contents for SB3 at Time = 344 s .....	188
Figure 4.22 Solids and fines contents for SB3 at Time = 344 s for CFX-Case1.....	189
Figure 4.23 Comparison of Interface Development for SB3 .....	189
Figure 4.24 Solids and fines contents using fine particle dynamic viscosity of 150 kg/m.s for SB1 at 147 s.....	190
Figure 4.25 Slurry Properties Diagram for Suncor's Pond 1 tailings (SFR<0.5) (From McMurray Resources (Research & Testing) Ltd.'s report, 2002) .....	192
Figure 4.26 Slurry Properties Diagram for Suncor's Pond 1 tailings (SFR>0.5) (From McMurray Resources (Research & Testing) Ltd.'s report, 2002) .....	193
Figure 4.27 Comparison of solids and fines contents using default settings and user segregation boundary for SB1 at 30 second .....	194
Figure 4.28 The mesh used for all the sensitivity analysis in FLUENT-6.....	198
Figure 4.29 Effects of granular temperature model and solid pressure on solids and fines contents.....	199
Figure 4.30 Effects of bulk viscosity on solids and fines contents .....	199
Figure 4.31 Effects of frictional viscosity on solids and fines contents.....	200
Figure 4.32 Effects of Packed Bed on solids and fines contents .....	200
Figure 4.33 Effects of granular viscosity on solids and fines contents .....	201
Figure 4.34 Effects of frictional angle on solids and fines contents.....	201
Figure 4.35 Effects of particle diameter on solids and fines contents.....	202
Figure 4.36 Effects of particle density on solids and fines contents.....	202
Figure 4.37 Grain size distribution for the mixture of coarse tailing sands and MFT. Here the mixture is referred to as CT. The grain size distribution for the coarse tailings and MDT is shown in Figure 3.6	

and Figure 3.7. The grain size distribution of the mixture is calculated based on its solids and fines contents.....	206
Figure 4.38 Effective particle sizes D31 for CT, coarse and fine particles for SB1 using number PDF, mass PDF and 50 percent mass .....	207
Figure 4.39 Effective particle sizes D31 for CT, coarse and fine particles for SB3 using number PDF, mass PDF and 50 percent mass .....	207
Figure 4.40 Comparison of effective particle sizes D31 for SB3 calculated using number PDF with that calculated using mass PDF.....	208
Figure 4.41 Solids and fines content profiles at 200s, 1000s and 2000s for simulation of SB1. D31 is calculated using 44 micron as coarse-fine division based on mass PDF.....	209
Figure 4.42 Solids and fines content profiles at 200s, 1000s and 2000s for simulation of SB1. D31 is calculated using 22 micron as coarse-fine division based on mass PDF.....	209
Figure 4.43 Solids and fines content profiles at 200s, 1000s and 2000s for simulation of SB1. D31 is calculated using 5.5 micron as coarse-fine division based on mass PDF.....	210
Figure 4.44 Effects of coarse-fine division on solids and fines content profiles at 200s for SB1. D31 is calculated based on mass PDF.....	210
Figure 4.45 Effects of coarse-fine division on solids and fines content profiles at 2000s for SB1. D31 is calculated based on mass PDF.....	211
Figure 4.46 Solids and fines content profiles at 200, 1000 and 2000 second for simulation of SB3. D31 is calculated using 44 micron as coarse-fine division based on mass PDF.....	212
Figure 4.47 Solids and fines content profiles at 200, 1000 and 2000 second for simulation of SB3. D31 is calculated using 22 micron as coarse-fine division based on mass PDF.....	212
Figure 4.48 Solids and fines content profiles at 200, 1000 and 2000 second for simulation of SB3. D31 is calculated using 5.5 micron as coarse-fine division based on mass PDF.....	213
Figure 4.49 Effects of coarse-fine division on the solids and fines content profiles at 200 second for simulation of SB3. D31 is calculated based on mass PDF.....	213
Figure 4.50 Effects of coarse-fine division on the solids and fines content profiles at 2000 second for simulation of SB3. D31 is calculated based on mass PDF.....	214
Figure 4.51 Solids and fines content profiles at 200, 1000 and 2000 second for simulation of SB3. D31 is calculated using 44 micron as coarse-fine division based on number PDF.....	215

Figure 4.52 Solids and fines content profiles at 200, 1000 and 2000 second for simulation of SB3. D31 is calculated using 22 micron as coarse-fine division based on number PDF.....	215
Figure 4.53 Solids and fines content profiles at 200, 600 and 2000 second for simulation of SB3. D31 is calculated using 5.5 micron as coarse-fine division based on number PDF.....	216
Figure 4.54 Effects of coarse-fine division on the solids and fines content profiles at 200 second for simulation of SB3. D31 is calculated based on number PDF. ....	216
Figure 4.56 Comparison of solids and fines content profiles at 200 second for simulation of SB3. D31 is calculated using 44 micron as coarse-fine division based on number PDF and mass PDF.....	218
Figure 4.57 Comparison of solids and fines content profiles at 2000 second for simulation of SB3. D31 is calculated using 44 micron as coarse-fine division based on number PDF and mass PDF.....	218
Figure 4.58 Comparison of solids and fines content profiles at 200 second for simulation of SB3. D31 is calculated using 22 micron as coarse-fine division based on number PDF and mass PDF.....	219
Figure 4.59 Comparison of solids and fines content profiles at 2000 second for simulation of SB3. D31 is calculated using 22 micron as coarse-fine division based on number PDF and mass PDF.....	219
Figure 4.60 Comparison of solids and fines content profiles at 200 second for simulation of SB3. D31 is calculated using 5.5 micron as coarse-fine division based on number PDF and mass PDF.....	220
Figure 4.61 Comparison of solids and fines content profiles at 2000 second for simulation of SB3. D31 is calculated using 5.5 micron as coarse-fine division based on number PDF and mass PDF.....	220
Figure 4.62 Coarse Volume Fraction for SB1_Run3 at time of 250, 500, 750 and 1000 second, respectively (Segregation Slope = 0.9) .....	224
Figure 4.63 Fine Volume Fraction for SB1_Run3 at time of 250, 500, 750 and 1000 second (Segregation Slope = 0.9) .....	224
Figure 4.64 Coarse Volume Fraction for SB1_Run4 at time of 250, 500, 750 and 1000 second (Segregation Slope = 0.6) .....	225
Figure 4.65 Fine Volume Fraction for SB1_Run4 at time of 250, 500, 750 and 1000 second (Segregation Slope = 0.6) .....	225
Figure 4.66 Coarse Volume Fraction for SB1_Run5 at time of 250, 500, 750 and 1000 second (Segregation Slope = 0.3) .....	226
Figure 4.67 Fine Volume Fraction for SB1_Run5 at time of 250, 500, 750 and 1000 second (Segregation Slope = 0.3) .....	226
Figure 4.68 Coarse Volume Fraction for SB1_Run6 at time of 250, 500, 750 and 1000 second (Segregation Slope = 0.0) .....	227

Figure 4.69 Fine Volume Fraction for SB1_Run6 at time of 250, 500, 750 and 1000 second (Segregation Slope = 0.0) .....	227
Figure 4.70 Coarse and Fine Volume Fraction for SB1_Run3 (Segregation Slope = 0.9) .....	228
Figure 4.71 Coarse and Fine Volume Fraction for SB1_Run4 (Segregation Slope = 0.6) .....	228
Figure 4.72 Coarse and Fine Volume Fraction for SB1_Run5 (Segregation Slope = 0.3) .....	229
Figure 4.73 Coarse and Fine Volume Fraction for SB1_Run6 (Segregation Slope = 0.0) .....	229
Figure 4.74 Effects of Segregation Slope on Coarse and Fine Volume Fraction for SB1 at Time of 250 second .....	230
Figure 4.75 Effects of Segregation Slope on Coarse and Fine Volume Fraction for SB1 at Time of 1000 second.....	230
Figure 4.76 Coarse Volume Fraction for SB3_Run4 at time of 250, 500, 750 and 1000 second .....	232
Figure 4.77 Fine Volume Fraction for SB3_Run4 at time of 250, 500, 750 and 1000 second.....	233
Figure 4.78 Coarse Volume Fraction for SB3_Run5 at time of 250, 500, 750 and 1000 second .....	233
Figure 4.79 Fine Volume Fraction for SB3_Run5 at time of 250, 500, 750 and 1000 second.....	234
Figure 4.80 Coarse Volume Fraction for SB3_Run6 at time of 250, 500, 750 and 1000 second .....	234
Figure 4.81 Fine Volume Fraction for SB3_Run6 at time of 250, 500, 750 and 1000 second.....	235
Figure 4.82 Coarse and Fine Volume Fraction for SB3_Run4 (Segregation Slope = 0.0) .....	235
Figure 4.84 Coarse and Fine Volume Fraction for SB3_Run6 (Segregation Slope = 0.9) .....	236
Figure 4.85 Effects of Segregation Slope on Coarse and Fine Volume Fraction for SB3 at Time of 250 second .....	237
Figure 4.86 Effects of Segregation Slope on Coarse and Fine Volume Fraction for SB3 at Time of 1000 second.....	237
Figure 4.87 Coarse Volume Fraction for SB3_Run2 at time of 250, 500, 750 and 1000 second .....	238
Figure 4.88 Fine Volume Fraction for SB3_Run2 at time of 250, 500, 750 and 1000 second.....	239

Figure 4.89 Coarse and Fine Volume Fraction for SB3_Run2 (Segregation Slope = 0.0, modified solid rheological model) .....	239
Figure 4.90 Effects of rheological model on Coarse and Fine Volume Fraction for SB3 at time of 250 second.....	240
Figure 4.91 Effects of rheological model on Coarse and Fine Volume Fraction for SB3 at Time of 1000 second.....	240
Figure 4.92 Comparison of solids and fines content profiles from CFX and FLUENT and experiment for SB1 test.....	242
Figure 4.93 Comparison of solids and fines content profiles obtained from CFX, FLUENT and experiment for SB3 test.....	242
Figure 4.94 Comparison of interface development process in CFX and FLUENT simulation as well as in experiment for SB3 .....	243
Figure 4.95 Segregation boundaries for tailing slurry .....	244
Figure 4.96 Comparisons of Solids and Fines Content Profile at Time of 250 Second. The solids and fines content profile for simulations using enhanced solid-solid drag coefficient, regular solid-solid drag coefficient and enhanced water viscosity are shown .....	244
Figure 4.97 Sand volume fraction at flow time of 2500 second for SB3.....	246
Figure 5.1 Setup of Flume Tests: (a) Top View (From Scott et al. 1993); (b) Cross Section (From Scott et al. 1993).....	252
Figure 5.2 Dimensions of Flume Used in the Tests .....	253
Figure 5.3 Test 3: The Profile of Tailings Immediate after Deposition and 19 Hours Later (reproduced from Scott et al. 1993).....	256
Figure 5.4 Test 3: Solids Content Profile (After Scott et al. 1993).....	257
Figure 5.5 Test 3: Fines Content Profile (After Scott et al. 1993).....	257
Figure 5.6 Test 10: Advance of Tailings (from Scott et al. 1993).....	258
Figure 5.7 Test 10: The Profile of Tailings Immediate after Deposition and 66 Hours Later (from Scott et al. 1993).....	258
Figure 5.8 Test 10: Solids Content Profiles (from Scott et al. 1993) .....	259
Figure 5.9 Test 10: Fines Content Profiles (from Scott et al. 1993) .....	259
Figure 5.10 Grids Used in the Free Surface Model (14,514 nodes).....	263
Figure 5.11 Variation of MFT Volume Fraction with Time: (a) MFT Volume Fraction profile at 10 second; (b) MFT volume fraction profile at 50 second; (c) MFT Volume Fraction profile at 100 second; (d) MFT volume fraction profile at 150 second; (e) MFT Volume Fraction profile at 200 second; (f) MFT Volume Fraction profile at 240 second.....	265
Figure 5.12 Advance of the Deposit with Time in Simulation .....	266

Figure 5.13 Comparison of the Simulated and Measured Slope of the Deposit Immediately After Stopping Pumping .....	266
Figure 5.14 Influence of Tailing Viscosity on the Slope of the Deposit.....	267
Figure 5.15 Influence of Tailing Viscosity on the Advance of the Deposit.....	267
Figure 5.16 Mesh Used in Particle Model Simulation (8,882 nodes).....	270
Figure 5.17 Variation of Clay Volume Fraction with Time.....	272
Figure 5.18 Variation of Sand Volume Fraction with Time.....	274
Figure 5.19 Comparison of the Advance of the Slurry Stream with Time for Particle Model and Free Surface Model .....	275
Figure 5.20 Comparison of the Deposit Depth at 240 seconds.....	275
Figure 5.21 Variation of Sand Volume Fraction with Time.....	278
Figure 5.22 Variation of Clay Volume Fraction with Time.....	280
Figure 5.23 Variation of Solids Contents with Time .....	282
Figure 5.24 Comparison of the Advance of the Slurry Stream with Time for Free Surface Model and Particle Models Using Water Viscosity and MFT Viscosity .....	282
Figure 5.25 Comparison of the Deposit Depth at 240 seconds.....	283
Figure 6.1 Location of Suncor Pond 1 (Google Earth, 2009) .....	286
Figure 6.2 Close view of Suncor Tailing Pond 1 (Google Earth, 2009) .....	287
Figure 6.3 Suncor Pond 1 Typical Tailing Composition Variation with Elevation (from MRRT, 2002).....	288
Figure 6.4 Suncor Pond 1 Average Peak Shear Strength Variation with Elevation (from MRRT, 2002) .....	289
Figure 6.5 Suncor Pond 1 Pond Bottom Change with Sand Infilling (after MRRT, 2002).....	290
Figure 6.6 Suncor Pond 1 Sand Capture in MFT above Beach Infill at Site 34 (from MRRT, 2002) .....	291
Figure 6.7 Suncor Pond 1 Sand Capture in MFT above Beach Infill at Site 35 (from MRRT, 2002) .....	292
Figure 6.8 Post-Infilling Idealized Cross-Section Interpreted from 2 Sampling Sites (from MRRT, 2002) .....	293
Figure 6.9 Dimension and grids of the cylinder .....	295
Figure 6.10 Grain size distribution of MFT used in all the simulations.....	296
Figure 6.11 Volume fraction profile and velocity vectors for sand particles and clay particles using Particle Model. (a) volume fraction profile for sand particles; (b) volume fraction profile for clay particles; (c) velocity vector for sand particles; (d) the velocity vector for clay	

particle. All the profiles are drawn on the symmetry plane that passes through the tremie discharge pipe center. The profiles are snap shops taken at time of 1413.5 s. ....	297
Figure 6.12 Geometry and dimension of the frustum domain.....	298
Figure 6.13 Grid of the frustum domain .....	299
Figure 6.14 Contours for volume fractions for sand particle, clay particles and release water at time of 276 second respectively: (a) Volume fraction contour for sand; (b) Volume fraction contour for clay; (c) Volume fraction contour for water.....	300
Figure 6.15 Viscosity and Yield Stress of MFT (From FTFC 1995).....	302
Figure 6.16 Contours of volume fraction for sand particles at time of 146 s for Cylinder domain.....	302
Figure 6.17 Contours of volume fraction MFT at time of 146 s for Cylinder domain.....	303
Figure 6.18 Contours of volume fraction of release water at time of 146 s for Cylinder domain.....	303
Figure 6.20 Contours of volume fraction of MFT at time of 276.5 second for Frustum Domain .....	305
Figure 6.21 Contour of volume fraction for release water at time of 276.5 second for Frustum Domain.....	305
Figure 6.22 Contour of volume fraction for sand particle at time of 476.5 second for Frustum Domain.....	306
Figure 6.23 Sand particle distributions at time of 50.2, 150.2 and 497.2 second respectively (from top to bottom) for Frustum Domain.....	307
Figure 6.24 Geometry and Dimension of the 2-D Frustum Domain.....	309
Figure 6.25 2D Grid for Frustum Domain(27,078 nodes).....	309
Figure 6.26 Sand Volume Fraction at Time of 10 Seconds .....	310
Figure 6.27 Sand Volume Fraction at Time of 30 Seconds .....	311
Figure 6.28 Sand Volume Fraction at Time of 68 Seconds .....	311
Figure 6.29 Sand Velocity Vector at Time of 10 Seconds.....	312
Figure 6.30 Sand Velocity Vector at Time of 30 Seconds.....	312
Figure 6.31 Sand Velocity Vector at Time of 68 Seconds.....	313
Figure A.1: Raw Data for Slurry with Solids Content of 66% and fines content of 37% (a: Plot of Torque vs. Shear Strain from Vane Shear Test; b-o: Plot of Torque vs. Time from Viscosity Measurements) .....	326
Figure A.2 Raw Data for Slurry with Solids Content of 65% and Fines Content of 32% (a: Plot of Torque vs. Shear Strain from Vane Shear Test; b-n: Plot of Torque vs. Time from Viscosity Measurements) .....	329

Figure A.3 Raw Data for Slurry with Solids Content of 43% and Fines Content of 75% (a: Plot of Torque vs. Shear Strain from Vane Shear Test; b-k: Plot of Torque vs. Time from Viscosity Measurements) .....	332
Figure A.4 Raw Data for Slurry with Solids Content of 52% and Fines Content of 60% (a: Plot of Torque vs. Shear Strain from Vane Shear Test; b-v: Plot of Torque vs. Time from Viscosity Measurements) .....	338
Figure A.5 Raw Data for Slurry with Solids Content of 40% and Fines Content of 94% (a: Plot of Torque vs. Shear Strain from Vane Shear Test; b-o: Plot of Torque vs. Time from Viscosity Measurements) .....	343
Figure A.6 Raw Data for Slurry with Solids Content of 61% and Fines Content of 95% (a: Plot of Torque vs. Shear Strain from Vane Shear Test; b-o: Plot of Torque vs. Time from Viscosity Measurements) .....	344
Figure A.7 Raw Data for Slurry with Solids Content of 50% and Fines Content of 95% (a: Plot of Torque vs. Shear Strain from Vane Shear Test; b-p: Plot of Torque vs. Time from Viscosity Measurements) .....	350
Figure A.8 Raw Data for Slurry with Solids Content of 49% and Fines Content of 68% (a: Plot of Torque vs. Shear Strain from Vane Shear Test; b-o: Plot of Torque vs. Time from Viscosity Measurements) .....	354
Figure A.9 Raw Data for Slurry with Solids Content of 51% and Fines Content of 78% (a: Plot of Torque vs. Shear Strain from Vane Shear Test; b-n: Plot of Torque vs. Time from Viscosity Measurements) .....	359
Figure A.10 Raw Data for Slurry with Solids Content of 49% and Fines Content of 86% (a: Plot of Torque vs. Shear Strain from Vane Shear Test; b-r: Plot of Torque vs. Time from Viscosity Measurements).....	364
Figure A.11 Raw Data for Slurry with Solids Content of 41% and Fines Content of 95% (a: Plot of Torque vs. Shear Strain from Vane Shear Test; b-o: Plot of Torque vs. Time from Viscosity Measurements) .....	368
Figure A.12 Raw Data for Slurry with Solids Content of 19% and Fines Content of 24% (a: Plot of Torque vs. Shear Strain from Vane Shear Test).....	369
Figure A.13 Raw Data for Slurry with Solids Content of 25% and Fines Content of 49% (a: Plot of Torque vs. Shear Strain from Vane Shear Test).....	369
Figure A.14 Raw Data for Slurry with Solids Content of 27% and Fines Content of 94% (a: Plot of Torque vs. Shear Strain from Vane Shear Test).....	369

## CHAPTER 1 INTRODUCTION

Oil sands tailings, which are the by-products of the bitumen production from oil sands, pose serious environmental issues and lay significant liability on the oil sands mining operators. Due to increasing volume of soft tailings in Fort McMurray region and increasing public concerns, Alberta government released a tailings directive (ERCB, 2008) to regulate the oil sand tailings and requires the oil sands companies to capture more fine tailings and form a trafficable surface in shorter time period. This research program is intended to explore a feasible technology to deal with oil sand tailings.

In this chapter, the background for this research project is introduced first, followed by the objectives and scope of this research project. Finally, the organization of this thesis is presented.

### **1.1 Backgrounds**

#### 1.1.1 Overview of Bitumen Extraction and Production of Tailings

Oil sands from Athabasca are composed of 83% sand, 3% clay, 4% water and 10% bitumen, of which the bitumen can be upgraded into crude oil (Alberta Energy, 2004). Depending on the ratio of cutoff total volume to bitumen in place (TV/BIP<sup>1</sup>) and grade of the ore, bitumen is recovered using either open pit mining or in-situ recovery methods. In open pit mining, the main bitumen extraction processes involve crushing, slurry preparation, separation, aerated recovery, de-aeration and froth treatment.

After stripping the overburden, oil sands are excavated using shovels. Depending on whether trucks are involved in the transportation process, the oil sands ore is either transported to a permanent Ore Preparation Plant (OPP) in the traditional shovel and truck method, or is directly placed into the mobile ore preparation plant which is located at the mining face in the latest Slurry at Face (SAF) method. In either method,

---

<sup>1</sup> TV/BIP is calculated as the ratio of total volume of overburden, interburden and ore to the volume of bitumen in place. The cutoff grade for the ore is 7 wt% bitumen and the minimum vertical mining selectivity is 3 m. See EUB ID-2001-7 for more information.

the ore is crushed and hot water is added into the crushed ore. As a result, slurry is formed and the slurry can be hydro transported using pipelines.

The bitumen is recovered from the oil sands slurry in the extraction plant where a primary separation vessel is used to separate bitumen from coarse sand. The bitumen in the middling stream that is discharged from the primary separation vessel is further recovered in the secondary separation vessel. The residual bitumen in the tailings is further recovered with hydrocyclones and floatation cells. The bitumen recovered during all of these steps is then deaerated.

Tailings are, therefore, the by-product of bitumen extraction and they can be classified as coarse tailings and fluid fine tailings. The coarse tailings consist mainly of sand particles while fluid fine tailings are those with low solids content and high fines content. Solids content is defined as the total weight of solids divided by total weight of solids, water and bitumen in percent. The fines content is defined as the weight of the fines (< 44 micron) divided by the total weight of solids in percent. The fluid fine tailings which are a warm aqueous suspension of sand, silt, clay residual bitumen, are transported into large fluid tailings ponds to release water for recycle in processing the bitumen. In the ponds, the sand particles settle quickly on the beaches while fine particles are dispersed into water forming a suspension (fine tailings). Over time, three layers have been formed in the settling ponds which from top to bottom are clear water, transition zone of water and settling clay particles, and fine tailings. The fine tailings are composed of average about 85% water, 13% clays and 2% bitumen by volume. It will consolidate to a solids content of approximately 30% after several years, which is called mature fine tailings (MFT). After this, the rate of consolidation is significantly decreased (FTFC, 1995).

Clark Hot Water Extraction process disperses the clay particles in the tailings. As a result, releasing water from fine tailings, that is the consolidation of the fine tailings, is an extremely slow process on the order 100's years. Meanwhile, 2 to 2.5 m<sup>3</sup> of tailings is produced for each barrel of bitumen (Hilderbrand, 2008). In addition to that, more companies are joining the development of the oil sands and the fine tailings can not be consumed as planned in their proposal documents. The result is that a huge volume of

fine tailings are produced and have to be stored in the thin fine tailing ponds. Currently, over 730 million cubic meters of mature fine tailings are stored in the tailing ponds in Fort McMurray region and it is predicted that the total MFT volume will reach 2.2 billion cubic meters as shown in Figure 1.1 (Houlihan et al, 2008). In addition, the tailings ponds amount to a 130 km<sup>2</sup> of land area and they are the largest human-made structures in the world (Grant et al., 2008).

Therefore, consuming fine tailings is a critical component for the oil sand mining developments and also a commitment to environment protection. Currently, producing non-segregating tailings, also called composite tailings or consolidated tailings (CT), is a proven technology at the commercial scale to capture the fine tailings. The idea is to mix MFT with coarse tailings and chemical additives to form a homogeneous mixture which possesses non-segregating properties under the pond environment. Since at least 3 years are required to form MFT from fluid fine tailings, oil sand companies usually start with pumping the fluid fine tailings into external tailing dykes, where MFT will form by self-weight consolidation. The reason for building external tailing dykes first is the limited space in the mine pit during start-up. As soon as enough space is created by mining the oil sands ore and overburden, in-pit tailing dykes are built. Thereafter, the MFT from the fluid tailing ponds is pumped to CT Plant to mix with coarse tailing stream from extraction plant and chemical additives to produce CT. The produced CT usually is stored in CT ponds which are in-pit tailing ponds. During the mine life, several tailing ponds are required to store excessive volume of fluid fine tailings. By transferring fluid fine tailings and MFT from ponds to ponds, oil sands companies are trying to manage their total volume of MFT by producing CT from MFT.

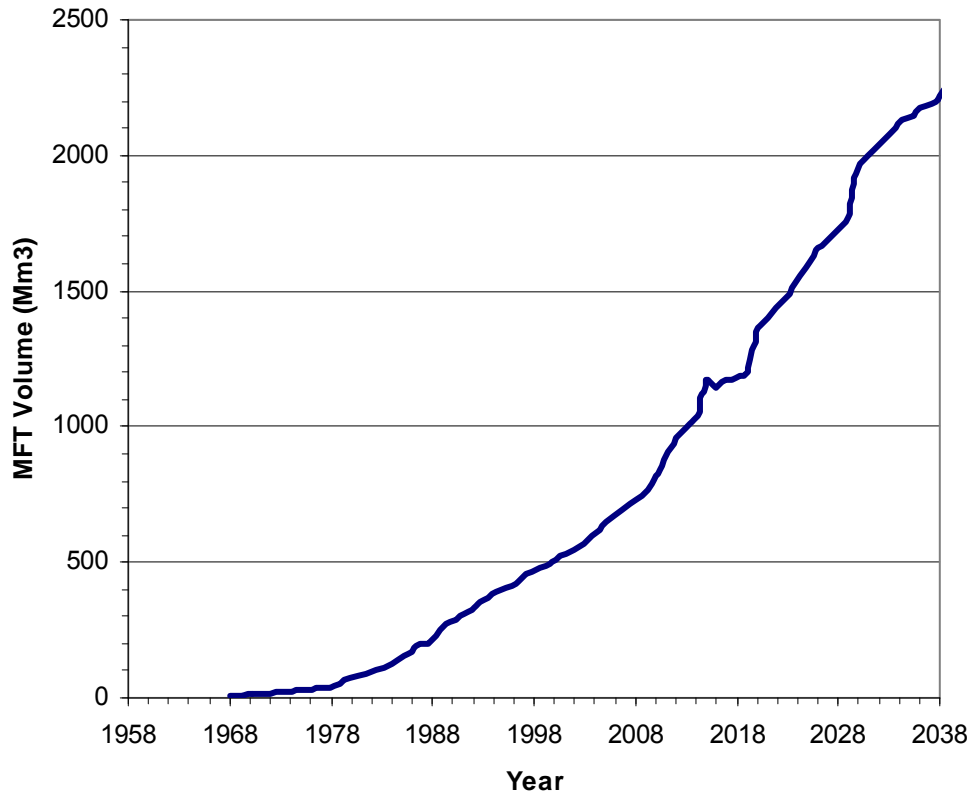


Figure 1.1 Current and Predicted MFT Volume in Fort McMurray (after Houlihan et al, 2008)

### 1.1.2 Reclamation of Tailing Ponds

Reclamation is referred to as the process by which disturbed lands are reclaimed back to a beneficial land use (CEMA, 2007). Reclamation of tailing ponds requires the considerations of end land use, environment and sustainability. Depending on the material in the ponds, water capping or sand capping is used to convert the disturbed land to land suitable for certain end use.

Water capping is applicable to ponds containing fluid tailings and process-affected water. An end pit lake (EPL) is an engineered water body built below grade in oil sands post-mining pits which may contain oil sands by-product materials and will receive surface and groundwater from surrounding reclaimed and undisturbed landscapes. End pit lakes will be permanent features in the final reclaimed landscape, discharging

water to the downstream environment (CEMA, 2007). So far, there is no successful demonstration of reclaiming the fluid tailing ponds in a commercial scale using the end pit lake and the end pit lake is under research to study the feasibility of reclaiming a fluid tailing pond by water capping.

On the other hand, efforts have been made to form a trafficable surface over the composite tailing ponds by both Suncor and Syncrude. The idea is to store non-segregating tailings in the CT ponds and the water in the tailings is released with time. Within ten years, the tailings are sufficiently consolidated to allow placing coarse sand or overburden material on the top. Trafficable surface will form with the aids of these surcharge caps.

#### 1.1.3 Brief Discussion of Suncor Pond 1 Issues

It is required to reclaim the Suncor Tailing Pond 1 by 2010. Suncor decided that the pond will be infilled with hydraulically placed tailings sand and concurrently transfer MFT from the pond. A number of issues have been identified as critical for the technical integrity and success of the Pond 1 infilling and decommissioning process. One of issues is the mechanism of deposition of densified tailings (DT) or cyclone underflow tailings into MFT which is capped by a layer of water. Currently there is a lack of understanding of the mechanism. Furthermore, a risk of a significant failure of the tailing slope generating a large wave exists due to the Plant 4 tailings in Pond 1. The Plant 4 tailings have high bitumen content which may potentially causes brittle failure of the Plant 4 tailing deposit (AMEC, 2001).

#### 1.1.4 Challenges

Although there is a large body of knowledge available on the deposition of sand slurry into water, little is known about deposition of sand slurry into soft deposits, such as CT, MFT and thickened tailings. These deposits are additionally complicated with non-uniform properties in that they have viscosity, yield stress and density which is a function of age, depth in the pond, the sand to fine mineral grain size ratio and in-situ water chemistry. The major uncertainty is the degree of mixing of the sand slurry with the in-situ soft deposit and the resulting engineering behavior of the mixture related to development of a stable reclaimable surface with tolerable long-term settlements.

Failure to optimize these issues is likely to increase the difficulty, volume and cost of MFT transfer and/or to increase the cost of reprocessing of materials in order to achieve the reclamation objectives. These incremental costs could easily reach the 10's of millions of dollars range.

In order to further understand the mechanisms of mixing of the sand slurry with the in-situ soft deposit, the factors affecting the degree of mixing and then optimization of the mixing process, experiments and numerical simulations have to be carried out. A beaching trial test was undertaken in Suncor's tailing Pond 1 in 2002. The results show that the fines content of the mixture at the bottom of the pond was lowered and some of the sand mixed with the overlying MFT deposits. However, questions regarding the detailed mixing process remain open. These experiments are costly and the results obtained are limited by our measuring techniques and instruments. In contrast, numerical tests can be carried out at a relatively low cost and the model with original scale can be built in numerical simulation. The materials prior to and after infilling of the sand slurry into MFT are mixture composed of solid and liquid, which makes the multiphase computational fluid dynamics (CFD) method a promising tool.

## **1.2 Objectives of Research Program**

The objectives of the research program is to study the feasibility of using computational fluid dynamics (CFD) approaches to modeling dense slurry flow with a special emphasis on sand slurry inflow into oil sands mature fine tailings (MFT). The research project will include the following components:

- Detailed state-of-the-art review of the modeling of slurry flows;
- Completion of an experimental program to evaluate the rheological properties of a range of oil sand slurries compositions and varying shear stress rate;
- Modeling of rheological properties testing results to evaluate the most suitable modeling approach with CFX, FLUENT and MFX;
- Modeling of small scale flume test to validate the modeling approaches chosen for different boundary conditions; and
- Modeling of the 2002 Pond 1 Densified Tailing Beaching Trail.

This research will focus on simulation of sand deposition into MFT using computational fluid dynamics. Commercial CFD packages CFX 5, CFX 10, FLUENT 6 and open source CFD package MFIX will be used as modeling tools. In order to simulate the dense sand slurry, viscosity model of the slurry will be obtained by viscometric tests. The model will be tested using these CFD packages and then the tested model will be input into CFX and FLUENT in the subsequent simulations.

In fact, viscosity is not the only factor that affects the simulation results. Discretization scheme for convection terms, drag model and grid also are important numerical factors affecting the success of the simulation. These models will be reviewed in the second part of the thesis. The sensitivity analyses will be performed and the optimum model will be used in the simulation.

The validation of the simulation and model will be conducted using one beach trial. The profile of sand and MFT concentration will be the most important results to verify the simulation results.

### **1.3 Scope of This Work**

Commercial CFD package FLUENT and CFX as well as open source CFD code MFIX will be applied as a tool to evaluate the feasibility of CFD modeling to simulate the dense slurry. It is not expected to establish any new numerical techniques or to code a new program. Viscosity properties of MFT will be measured and the field data and the data from literature will be used to evaluate the CFD model.

### **1.4 Organization of Thesis**

Literature regarding the general properties of clay-sand-water mixture as well as the particular properties of oil sand tailings is reviewed in Chapter 2. The sedimentation and segregation of the tailing slurry are also summarized in this chapter. Subsequently, the numerical techniques in computational fluid dynamics (CFD), specifically the multiphase simulation in CFX, FLUENT as well as MFIX are introduced.

Chapter 3 deals with the measurements of viscosity and yield stress of the oil sand tailings with specified solids and fines contents. The measurement results are analyzed

followed by fitting the flow curves for the oil sand tailings measured in the tests. The viscosity model then is used in CFD simulation of the viscosity and yield stress measurement.

Chapter 4 describes the CFD simulation of segregation of the oil sand tailings. First, the experiment data from literature is used to validate the CFD model. Then the segregation tests conducted on oil sand tailing slurry with solids contents of 45% and 65% are simulated using CFX, FLUENT and MFX. The main factors controlling the simulation results are described.

Chapter 5 describes the CFD simulation of Flume Tests. The solids content and fines content profiles as well as the travel distance with time from simulations are compared with those from laboratory tests.

In Chapter 6, the infilling of the coarse sand tailing slurry into simplified tailing ponds is simulated using CFX. The objective of the chapter is to reproduce the sand distribution obtained in a field trial test at Suncor's Pond 1. The challenges dealing with CFD simulation of the infilling process are described.

The last chapter summarizes the main factors influencing the success in simulating the deposition of oil sand slurry into mature fine tailings, including sedimentation and segregation. This chapter also presents the recommendation for the future research.

## Reference

Alberta Energy, Oil Sands Facts, December 2004.

[Http://www.energy.gov.ab.ca/89.asp](http://www.energy.gov.ab.ca/89.asp).

AMEC, Pond 1 Decommissioning December 2001 Progress Report, submitted to Suncor Energy OSG, Fort McMurray, Alberta, December 2001.

Cumulative Environmental Management Association (CEMA), 2007. Oil Sands End Pit Lake: A Review to 2007. pp. viii. [Http://www.cemaonline.ca](http://www.cemaonline.ca).

Energy Resources Conservation Board. Directive 074: Tailings Performance Criteria and Requirements for Oil Sands Mining Schemes. February 3, 2009. <http://www.ercb.ca>.

Fine Tailing Fundamentals Consortium, 1996. Meeting the Challenge: Solutions for Managing Oil Sands Tailings. Edmonton, Alberta.

Hilderbrand, J. Reclamation Illusions in Oil Sands Country. Wild Land Advocates, vol. 16, pp. 11. June 2008. Available at: <http://issues.albertawilderness.ca/ML/Archive/200806AR11.pdf>.

Houlihan, R., and Mian, H., Oil Sand Tailings: Regulatory Perspective. Proceedings of the First International Oil Sand Tailing Conference, edited by Dr. Dave Segó, Edmonton, Alberta, Canada, December 7-10, 2008.

Grant, J., Woynillowicz, D., and Dyer, S. Fact or Friction (Fact Sheet): Oil Sands Reclamation. Pp.2, May 26, 2008. Published by the Pembina Institute. Available at: <http://www.oilsandswatch.org/pub/1643>.

## CHAPTER 2 LITERATURE REVIEW

The goal in this chapter is to review the properties of the oil sand tailing slurry, the oil sands tailing management, and the state-of-art of computational fluid dynamics (CFD) in simulating concentrated clay-sand-water mixture. The properties of tailing slurry and oil sands tailing management are summarized, followed by the concepts regarding CFD, and then the current status of single-phase CFD and multi-phase CFD is reviewed. Specific problems regarding dispersed phase simulation, discretization schemes and solvers are analyzed. The literature regarding the CFD simulation of dense slurry is reviewed. Physical properties of the tailing slurry and capability of three CFD packages (CFX, FLUENT and MFX) are the focus of this evaluation.

Oil sand tailing slurry can be considered as a particular clay-sand-water mixture with bitumen residual. Therefore, the properties of the general clay-water-sand mixture are reviewed and then the particularity of the properties of oil sand tailing slurry is presented. This section serves as the base for the subsequent CFD simulations. Then, the general concepts of fluid mechanics, fluid dynamics and computational fluid dynamics are introduced.

### **2.1 Introduction to Oil Sand Tailings**

#### 2.1.1 Oil Sands and Origin of Oil Sand Tailings

Containing almost all the bitumen resource in Canada, Alberta has three oil sand deposit regions: Peace River, Fort McMurray and Cold Lake (Figure 2.1). These three areas cover approximately 140,200 square kilometers (NEB, 2004).

Oil sands are composed of sand, clay, water and bitumen, a heavy viscous black oil. Unlike traditional oil, the bitumen in the oil sands will not flow under natural state, thus heating or diluting with lighter hydrocarbon is required to reduce its viscosity. Surface Mining method (also referred to as Open Pit Mining) is used to mine the shallow oil sands (TV:BIP < 12) and the bitumen in the deep oil sand deposits (TV:BIP > 12) are mined using Thermal Recovery methods (Figure 2.2 and Figure 2.3).

The surface mining process is illustrated in Figure 2.4. Large hydraulic or electrical shovels are used to remove the oil sands from the pit and load the trucks. The oil sands are transported with the trucks to crushers/cyclofeeder where the hot water and caustic soda (NaOH) is added to the sand and to release bitumen. Bitumen froth floats to the top of the separation vessels while the sand settles at the bottom. The bitumen froth is further treated in the primary separation vessel (see Figure 2.4) and air-bitumen bubble is separated from water. The solid is removed as tailings.

The froth then is diluted with Naphtha and is completely separated in a centrifugal device. In new process, paraffinic solvent is added into the froth in a separation vessel. The product is diluted bitumen which is transported to an upgrading unit and the separated material is removed as tailing slurry. The residual bitumen in the tailing slurry is recovered at Tailing Oil Recovery unit (see Figure 2.4). Thus, oil sand tailing slurry is a by-product of all oil sand processing.

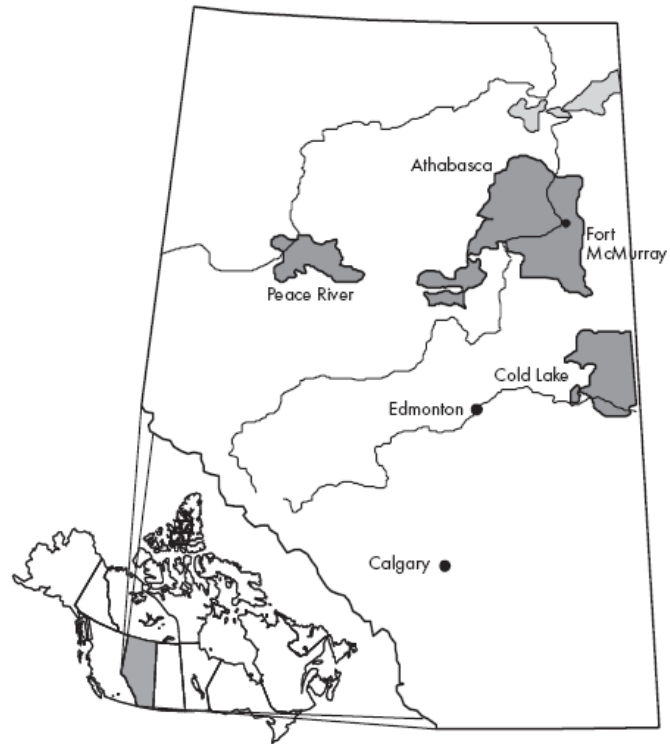


Figure 2.1 Alberta's Oil Sand Deposit in Peace River, Fort McMurray and Cold Lake areas (NEB, 2004)

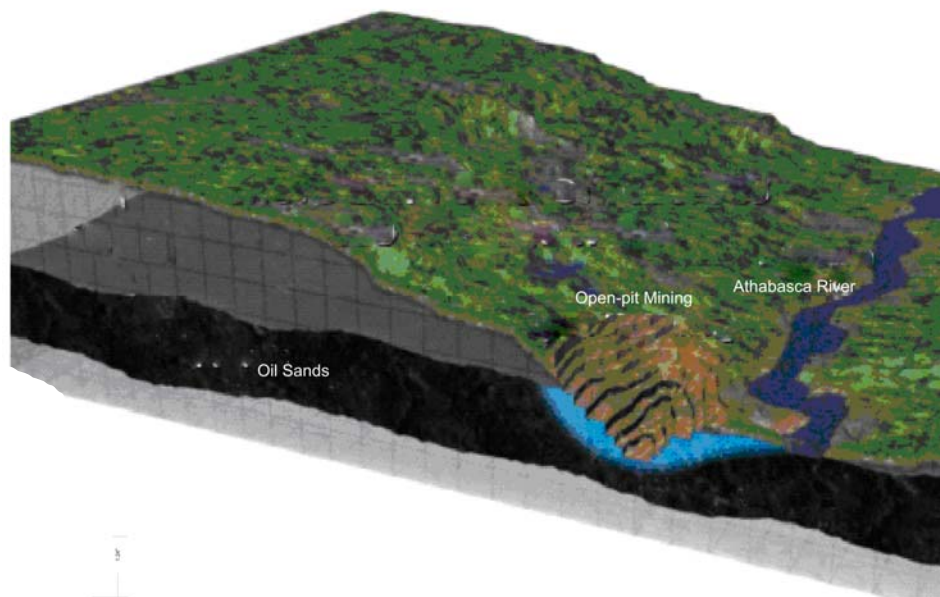


Figure 2.2 Illustration of the depth of the overburden and surface mining area (from AMEC, 2007)

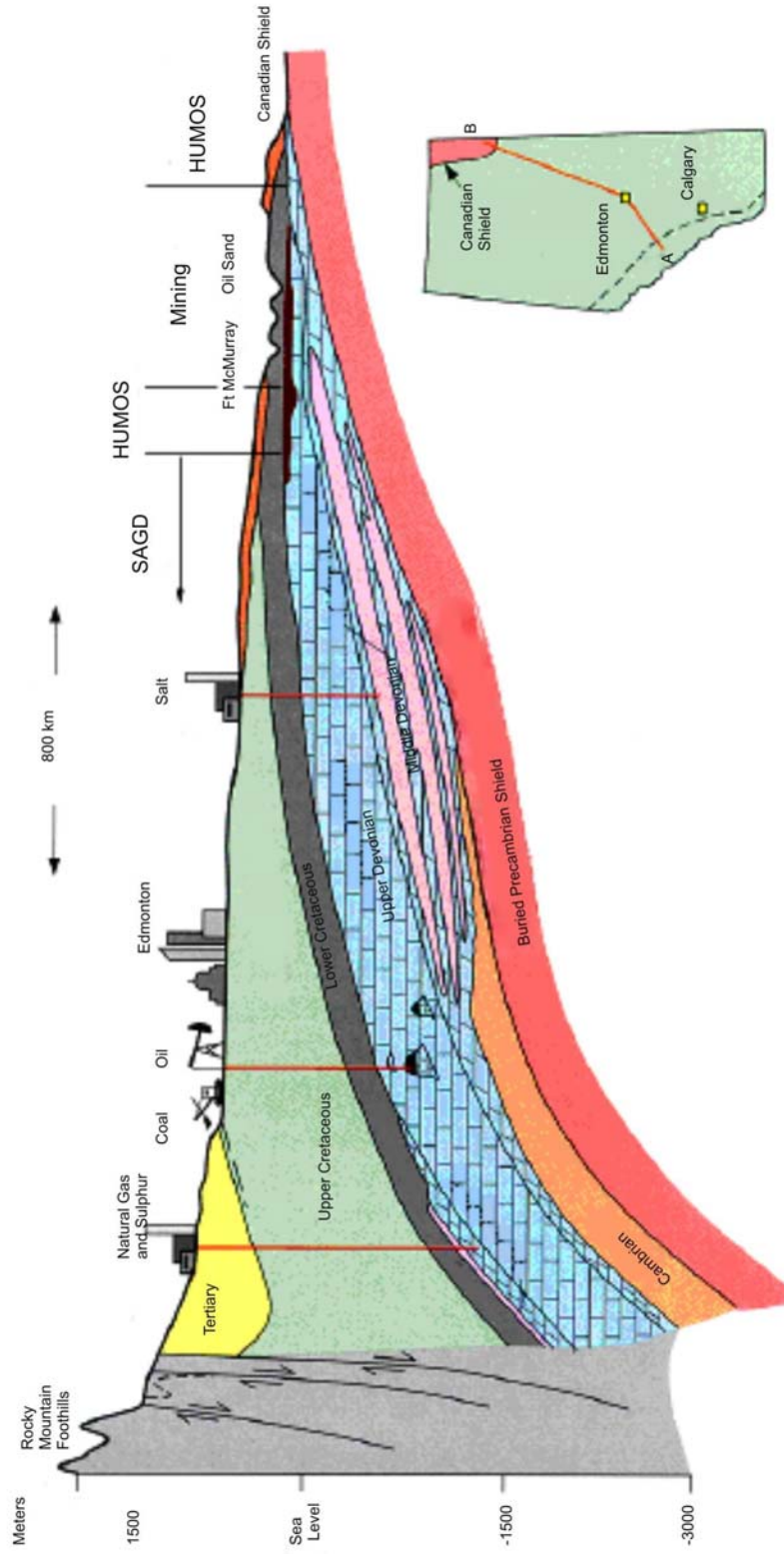


Figure 2.3 Illustration of cross-section and mining methods for oil sands deposit with different depth of overburden (from Syncrude Canada)

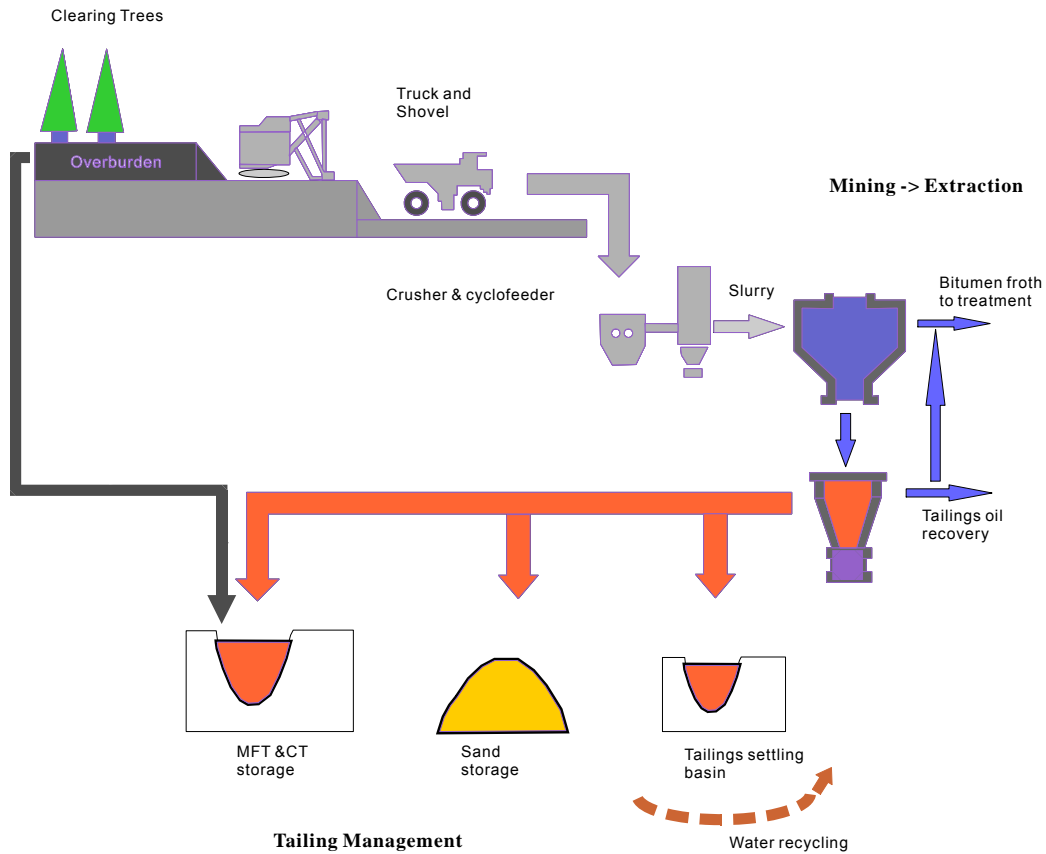


Figure 2.4 Generalized scheme for surface mining (based on Alberta Chamber of Resources, 2004.)

### 2.1.2 Tailings Composition

As described above, the tailings are mainly from primary separation and froth from treatment vessels with insignificant quantities of tailings coming from upgrading units. They are transported to tailing management area through pipeline. Upon discharge, segregation between sand and fine occurs, resulting in coarse solids settling adjacent to the discharge point while fines are carried further into the pond. At a certain stage, the fine tailings will consolidate to a solids content approaching 30%, which is called

mature fine tailings (MFT). The typical size distributions for coarse tailings, flotation tailings and MFT are shown in Figure 2.5 (Fair, 2008).

MFT is composed of 30-60% solids, 2-10% bitumen and 30-68% of water. Figure 2.6 shows ranges of grain size distribution of the mineral grain portion of MFT (FTFC, 1995). It is shown that typically it contains 3-10% sand particles size, 40-60% clay size particle and 30-57% of silt size particles, where sand particles are referred as to the particles greater than 44 microns, and clay particles are those smaller than 2 micron. The silt particles are the particles between 44 microns and 2 microns. The clays are mainly kaolite (80%), including minor portion of illite (15%), montmorillonite and chlorite (Roberts et al., 1980).

Table 2.1 Composition of Syncrude and Suncor MFT (from FTFC, 1995)

Components	Suncor (w/w %)	Syncrude (w/w %)
Total Solids	26.3	26
Bitumen	1.9	1
Water	71.8	73

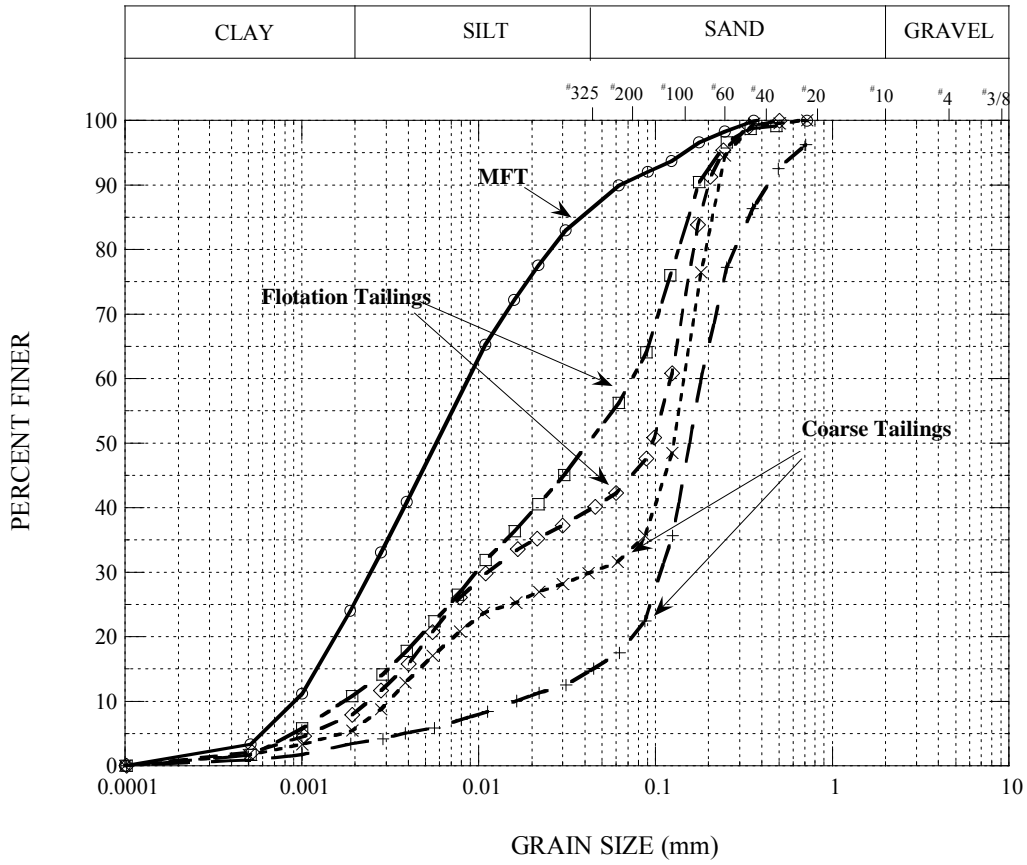


Figure 2.5 Typical Range of Grain size distribution of Oil Sand Tailings (Modified from Fair, 2008)

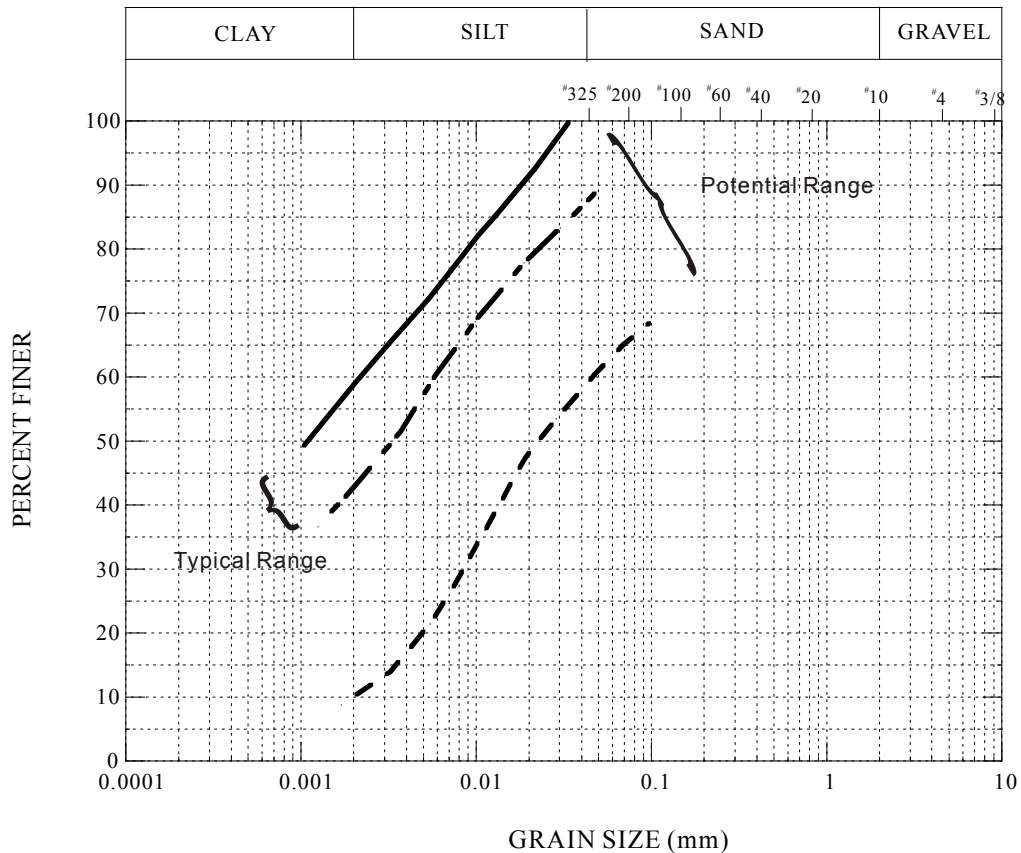


Figure 2.6 Typical Grain Size Distribution of Oil Sand Fine Tailings (after FTFC, 1995)

MFT also contains several components that distinguish it from the natural slurry such as slurry in debris flows. The most significant distinctions are residual bitumen and some chemicals left from the extraction and treatment process. It also contains trace amount of ultra-fine particles with sizes ranging from 20 to 300 nm (FTFC, 1995). The influences of those particles on the settling, segregation and other geotechnical properties of MFT are discussed in the following sections.

## 2.2 Oil Sands Tailing Properties

### 2.2.1 Uniqueness of Oil Sands Mature Fine Tailings

Bitumen residual, water chemistry and clay mineral make MFT different from other industrial tailings. These components interact at the microscopic level and determine the bulk geotechnical and physical properties of the mature fine tailings. For example, the surface properties of the minerals control the rate of consolidation and forces

including electrostatic, steric, Van der Waals, and hydration, which affect colloidal particles in suspension, determine the final settled volume, permeability, and strength of the material (FTFC, 1995). On the other hand, water chemistry and solids' surface determine the nature of the interaction. As most of the fine particles are kaolite and illite clays with some quartz and other components, NaOH additive cause swelling of clays with water. Dispersion of clay minerals causes more mineral surface area exposed to water, resulting in higher water holding capacity, lower permeability, slower settlement, and more MFT. Physical (centrifugation) or chemical process is required to form an aggregate structure which possesses greater mineral-mineral interactions compared to the dispersed clay structures.

### 2.2.2 Geotechnical Properties of Oil Sand Mature Fine Tailings (MFT)

MFT is called a soil after the effective stress exists between particles. Carrier et al (1983) measured the liquid limit and plastic limit of MFT, which range from 40% to 75% and 10% to 20%, respectively. It was also reported that the yield stress of MFT varies from 0 to 520 Pa and viscosity varies from 0 to 5000 cP. Barnes et al. (1991) show that the strength of fine tailings depends on time (independent of consolidation), which is called thixotropy (FTFC, 1995). Consolidation tests were conducted for MFT and it was found that the effective stress is very low even at the full consolidation. The rate of consolidation decreases as consolidation proceeds.

### 2.2.3 Non-Segregating Tailings (NST)

Segregating tailing stream has gap-graded nature, therefore, the majority of the fine particles in the oil sand tailing stream segregate from the main sand deposit and form a fluid deposit called "fine tailings." The accumulation of large quantities of fine tailings leads to increased operating costs and a long term reclamation challenge.

A non-segregating tailing stream is defined as a tailings mixture in which the fine and sand particles settle simultaneously to form a uniform deposit. It is formed by increasing the solids content, increasing fines content, or changing the apparent grain size of the fines. Flocculating or aggregating the fines with chemical agents, such as lime, sulphuric acid, CaSO<sub>4</sub>, flyash and their combinations, can change the tailing stream into non-segregating slurry (FTFC, 1995).

A low energy discharge environment is important in producing non-segregating tailing deposits under dynamic deposition conditions. Air entrainment during deposition causes some segregation of fine from the main deposit (FTFC, 1995).

With the addition of chemicals, fine particles in oil sand tailings become flocculated or coagulated. This process enhances the permeability of tailings especially at relatively low solids contents. As a result, non-segregating tailings undergo a significant volume reduction during sedimentation and initial consolidation. The rate of initial consolidation largely depends on the fines content of the tailings. Once the fines content is greater than 25%, the rate of consolidation decreases considerably. The field and laboratory tests indicate that approximately two-thirds of the ultimate volume change or settlement takes place during sedimentation and initial consolidation. The amount of volume reduction in NST decreases as the tailings consolidate under increased effective stresses especially when a stable grain structure is reached. Similarly, the permeability of NST decreases as the void ratio of the tailings decrease due to consolidation (FTFC, 1995).

## **2.3 Management of Tailings**

### **2.3.1 Management of Tailings**

There are various tailing management technologies, which will produce tailings in the following forms (Deer Creek Energy Limited, 2006):

- Conventional whole tailings
- Thickened fine tailings
- Non-segregating tailings
- Alternative tailings (paste, filtered tailing, polymer-added, freeze-thaw dewatered, cyclo-stacked, dry MFT, and poldered)
- End Pit Lake (EPL)

#### **Conventional Whole Tailings**

The whole tailing stream produced from the caustic Clark hot water extraction (CHWE) process will segregate into coarse tailings and Thin Fine Tailings (TFT), when deposited into ponds. TFT is comprised of finely dispersed clay particles. After

TFT slowly consolidated into mature fine tailings (MFT), releasing water from MFT, and subsequently its consolidation, is extremely slow. Therefore, storage of the TFT and MFT requires large volumes and external tailing ponds are required at the initial mining stage due to the lack of in-pit tailings pond space. As space becomes available with the advance of mining faces, in-pit tailing ponds are built to store TFT and MFT.

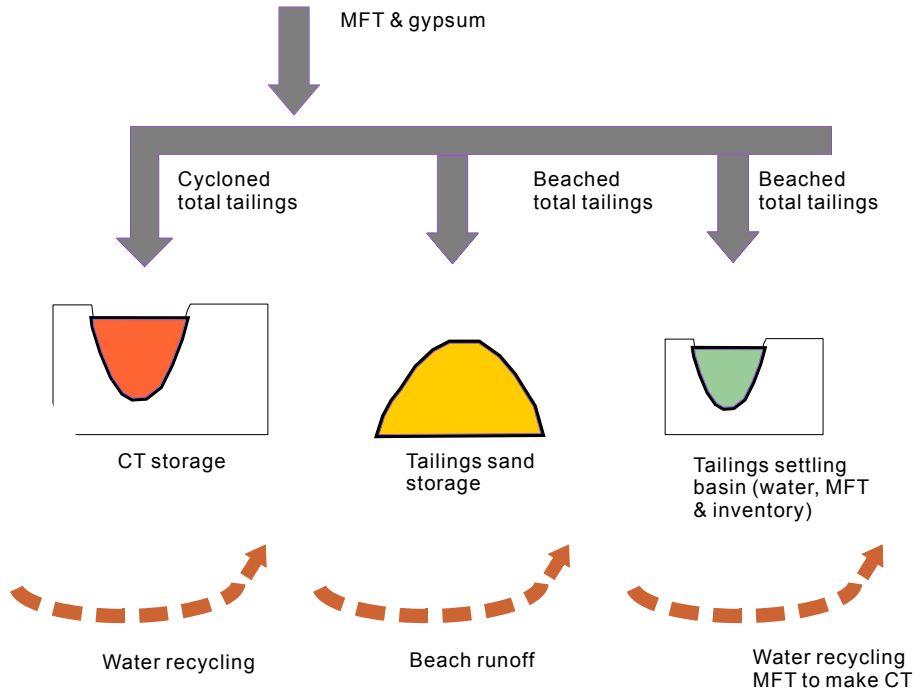


Figure 2.7 Tailings management (based on Alberta Chamber of Resources, 2004.)

In recent years, Non-Caustic and low temperature extraction process have been developed. The whole tailings originating from this process tend to be less segregated when deposited based on laboratory and limited field trials. The results also show that the consolidation of fine tailings deposits and potentially higher ultimate solids content can be achieved for the whole tailings. The downside of this extraction process is lower extraction recovery rate of in situ bitumen.

## **Thickened Tailings**

Thickeners can be used to concentrate the fine tailings prior to deposition into a tailings pond. Flocculant is added into the fine tailings and a concentrated tailing stream is produced as a thickener underflow and warm water is produced from thickener overflow. The main issue associated with the thickener is the variation of oil sands feed quality, which may cause operational control challenges. In addition, current thickener technology can only produce a tailing stream with solids and fines contents equivalent to MFT in the pond. Secondary thickener is utilized to further increase the solids content of the tailings in some mining operations (Deer Creek Energy Limited, 2006).

The benefits of thickener fine tailings include heat recovery and reduced total tailings disposal volume. However, separate disposal of coarse tailings and thickened fine tailings will eliminate the advantage of capturing fine tailings within the void space in the sand during the traditional hydraulic placing of coarse tailings.

## **Non-segregating Tailings or Consolidated Tailings**

Non-segregating tailings (NST), also called consolidated tailings or composite tailings (CT), are tailings in which coarse particles do not settle appreciably through the matrix composed of fines when deposited. NST can be produced by addition of coagulants, such as gypsum, or flocculating agents, such as polymers into the mixture of MFT or thickened tailings with coarse tailings from cyclone underflow.

NST or CT is usually stored in external tailing facilities when in-pit space is not available during the mine start up stage, or in in-pit tailing storage area when the ore is mined out and space is available at later mining stage. The performance of the NST or CT relies on using the right sand to fine ratio (SFR), dosage of coagulant or flocculant, as well as the deposition method. In current NST production, coarse tailing stream comes directly from cyclone underflow. The following factors may affect the efficiency of the NST production, therefore the consolidation and segregation of the NST:

- Reliability of MFT recovery using barges;
- Cyclones plugging with rock;
- Variations in the cyclone feed;
- Competing demands for clean tailings sand; and
- Other plant inefficiencies.

### **Paste**

Tailings paste is defined as a dense, viscous mixture of tailings and water which, unlike slurries, does not segregate when not being transported (Verburg, 2001). Paste thickener can be used to produce a paste material from fine tailings. The paste has sufficiently high solids content so that it can be stacked in a separate disposal area; therefore, tailing storage volume is greatly reduced. However, due to its high solids content, it is difficult to pump over the long distances. Small scale tests have been conducted in the oil sands industry and the commercial scale tests are required before industrial application (Deer Creek Energy Limited, 2006).

### **Filtered Tailings**

The whole tailings stream can be mechanically filtered and dewatered to form a filter cake. The filter cake contains much less moisture than paste tailings so that it can be transported using mine haul trucks or conveyors. Pressure filters or vacuum belt filters can be used to produce the filter cake. Winter conditions, blocking of filter cloth by bitumen, breakdown of filter system as well as variance of oil sands fines content affect the efficiency of filtered tailings technology. The technology is also associated with higher capital costs and transportation costs. However, those disadvantages are balanced by reduced water intake requirements, smaller external tailings pond area, accelerated reclamation, and a more manageable closure plan (Deer Creek Energy Limited, 2006).

### **Whole Tailings**

Producing non-segregating tailings by addition of polymers to the whole tailings stream is being studied in the industry. It is also demonstrated that the overburden or

interburden material can be mixed with the whole tailings to produce a non-segregating tailings (Deer Creek Energy Limited, 2006).

### **Freeze-Thaw Dewatering**

Freeze-thaw cycles of the fine tailings will accelerate the dewatering of the fine tailings. The method uses the natural phenomena and formation of ice lenses, and creating a network of cracks and fissures can accelerate consolidation of the tailings. However, the thickness of the deposition is limited to 2 m and the operation requires large area for the huge volume of tailings in both winter and summer period (Deer Creek Energy Limited, 2006).

### **2.3.2 Reclamation of Tailing Ponds**

Natural consolidation of the fine tailings to produce a trafficable surface, capable of supporting a productive soil layer, would require hundreds of years. The slow rate of consolidation of the existing fine tailings is compounded by the continuous addition of new fine tailings from the extraction process. Consequently, reclamation of the tailing ponds is considered to be the major environmental issue facing the surface mining oil sand industry (FTFC, 1995).

Currently, no single reclamation option can handle the projected volume of fine tailings in a manner which is technically, environmentally, and economically acceptable. The reclamation of the fine tailings material will be accomplished through a combination of the so called “dry” and “wet” landscape technique. The dry approach involves dewatering or incorporation of fine tailings into a solid deposit which is capable of being reclaimed as a land surface, or a wetland. The wet approach involves a lake system, whereby contained fluid fine tailings are capped with a layer of water of sufficient depth to isolate the fine tailings from direct contact with the surrounding environment. The reclamation objective is to produce an area that is stable (good erosion control and geotechnically stable), productive (for both terrestrial and aquatic biota, with no longer term toxic effects), and self-sustaining (diverse ecosystem development, maintenance-free) (FTFC, 1995).

### 2.3.2.1 Dry Landscape Options

Dry landscape techniques aim to significantly reduce the water content of fine tailings and potentially produce a solid deposit which would be capable of being capped with soil as part of terrestrial (or wetlands) reclamation scenario. The following is some of dry landscape options (FTFC, 1995):

- (a) Dewatering of the fine tailings to a more fully consolidated clay through process such as evaporation and freeze-thaw;
- (b) Incorporation of fine tailings with overburden clays (absorption of fine tailings pore water with clay mixes) and with coarse tailings sand (enhanced capture of fine tailings solids in the coarse tailing deposit); and
- (c) Chemical alteration of clay components in tailings prior to deposition (e.g., lime, acid/lime, and calcium sulphate addition to extraction tailings to produce a non-segregating or consolidated tailings).

In all of these dry landscape approaches, the fluid character of the fine tailings is reduced significantly, and in some cases, the produced material will be strong enough to allow for soil capping and terrestrial reclamation. Inherent within all dry landscape option is the requirement to deal with waters that may drain or leach from the reclamation areas because these waters may contain unacceptable levels of organic acids or dissolved ions (FTFC, 1995).

There are changes in particle size, mineralogy, and elemental composition of the MFT with depth in the tailings/settling ponds. Both density and particle size increase with depth in all ponds as total solids content increases. These changes are a result of segregation and settling of the coarser sand particles through the fine tailings.

Sand layering is one of these choices. Although a thin sand layer could be established on fine tailings having a solids content in the 24 to 28% range, the layer would consistently prove to be quite unstable and failures, when initiated, would tend to progress across the entire deposit. With a solids content greater than 30% and with aging of the deposit prior to layering, significant differential loading across a layer

could be supported and a relatively thin layer would exhibit significant resistance to progressive failure induced by layer penetration (FTFC, 1995).

#### 2.3.2.2 Wet Landscape Options

The wet landscape option leaves the fine tailings as a fluid. Mined-out pits serve as a containment area. In this option, the mature fine tailings are disposed as a fluid, over which a layer of water is placed (Boerger et al., 1992). A layer of water is capped onto the fine tailings to isolate the fine tailings zone from physical mixing with the overlying water layer, and to establish a viable, self-sustaining aquatic ecosystem in the climatic conditions (FTFC, 1995).

### **2.4 Rheological Properties of Natural Clay-Water Mixture and Clay-Sand-Water Mixture**

Coussot (1997) reviewed the physical properties of mud suspension in detail from the perspective of mudflow and debris flow. He considered the natural water-debris mixture as a suspension of coarse grains in a colloidal dispersion (clay-water mixture). Based on the difference of clay particles in structure and interaction with water, he divided the solid particles into clay (up to 2 micron) and grains (from 2 micron). The criteria for defining a clay particle are consistent with that in the Unified Soil Classification System (USCS) in ASTM D2487-00 regarding the standard classification of solid for engineering purpose. He further mentioned that clay particles are fundamentally Brownian, colloidal particles in sufficient slow flows. The following review of rheological properties of clay-water and clay-water-sand mixture is mainly based on the work by Coussot (1997).

#### 2.4.1 Rheological Properties of Clay-Sand-Water Mixture

##### 2.4.1.1 Rheological Properties of Clay-Water Mixture

###### *2.4.1.1.1 Effects Influencing the Rheological Properties of Clay-Water Mixture*

Clay-water mixture is a uniform suspension where clay particles suspend in water. Coussot (1997) argued that five mesoscopic effects influence the rheological (macroscopic) properties of the clay-water mixture: Brownian, hydrodynamic, packing effects, inertial effects and colloidal effects. Brownian motions are random motions in addition to the mean motion of particles due to the flow of the suspension. The

motion dominates only when other motions are insignificant. Hydrodynamic effects cause viscosity increase as the solid volume fraction increases. The packing effects dominate when the solid concentration increases to a point where shearing particles will lead to configuration changes. Inertial effects are significant when the collisions between particles become significant in turbulent flow. For the slow flows of colloidal particles, colloidal effects will dominate.

#### 2.4.1.1.2 Formulae for Clay-Water Mixture Viscosity

A large number of formulae were proposed to calculate the Newtonian viscosity of a suspension theoretically or empirically. For very dilute suspensions where total solid volume fraction,  $\phi$ , is less than 2%, the viscosity of suspensions of non-interacting spheres or ellipsoids in a Newtonian fluid was given by Einstein (1956):

$$\mu = \mu_0(1 + 2.5\phi) \quad (\text{Eq. 2.1})$$

where  $\mu$  and  $\mu_0$  are the viscosity of suspension and liquid medium respectively. The solid volume fraction is the ratio of the volume of the solid to the total volume of the suspension.

Later, Batchelor and Green (1972) proposed an equation for a higher solid fraction ( $\phi < 10\%$ ) for elongational flow:

$$\mu = \mu_0(1 + 2.5\phi + 7.6\phi^2) \quad (\text{Eq. 2.2})$$

When the solid fraction increases, non-linear increase in viscosity is demonstrated. Many empirical or semi-empirical formulae approximated this trend. For example, Chong (1971) proposed an empirical formula which fitted to various data corresponding to mono- and polydisperse sphere suspensions:

$$\mu = \mu_0 \left( 1 + \frac{0.75}{\frac{\phi_m}{\phi} - 1} \right)^2 \quad (\text{Eq. 2.3})$$

Where  $\phi_m$  is the maximum solid packing volume fraction.

For moderately concentrated and concentrated suspension, prediction of configuration changes during flow is required in order that a theoretical approach can be used to evaluate the viscosity of the suspension. Simha (1952) deduced the exact theoretical expression for suspension viscosity based on a “cage” model in which each spherical particle of radius  $a$  inside a spherical enclosure of radius  $b$ :

$$\mu = \mu_0(1 + 2.5\lambda\phi) \quad (\text{Eq. 2.4})$$

where  $\lambda$  is a function of the ratio of the particle radius  $a$  to the spherical enclosure radius  $b$ .

For concentrated suspensions several other models have been proposed based on the assumption that hydrodynamic effects were predominant. Frankel and Acrivos (1967) obtained a formula to calculate the viscosity of suspension:

$$\mu = \frac{9}{4}\mu_0 \frac{1}{\varepsilon} \quad (\text{Eq. 2.5})$$

where  $\varepsilon$  is the ratio of the mean distance between two spheres to their radius. Other researchers assumed that the suspension’s viscosity is a function of the solid fraction and the suspending medium viscosity:

$$\mu = \mu_0 f(\phi) \quad (\text{Eq. 2.6})$$

Quemada (1985) proposed a formula by using ratio of solid fraction to maximum packing fraction:

$$\mu = \mu_0 \left(1 - \frac{\phi}{\phi_m}\right)^{-a} \quad (\text{Eq. 2.7})$$

Although all the above models can be used to estimate the viscosity of concentrated suspension, some complex rheological properties resulting from orientation of anisotropic particles (Jeffery, 1922) or particle distribution variation during shearing were not taken into account.

#### *2.4.1.1.3 Thixotropy, Yield Stress and Viscoelasticity of Clay-Water Mixture*

Thixotropy is the changes of viscosity with time. It can be detected in a shear strain rate vs. shear stress diagram for ramp tests where the hysteresis loops demonstrate viscosity changes with flow history. Usually, clay-water mixture exhibits thixotropy behavior (Hu and Fang 1985, Moore 1959, Neumann and Sansom 1971, Wan 1982). However, anti-thixotropy (or rheopexy) was also reported for natural clay-water mixture (Wang et al., 1994).

Suspension exhibits yield stress when a minimum force is required to break the bonds between particles forming a continuous network (Navickis and Bagley 1983, Coussot et al. 1993, Mewis and Spaul 1976). Elastic behavior occurs when external force is small (Coussot et al. 1993) and the dispersion flows only when the external force is large enough or when a critical strain rate is applied.

Once the suspension starts to flow, the energy dissipation via bond ruptures and restoration does not increase dramatically with shear rate. Therefore, dispersion also exhibit shear-thinning behavior where the viscosity reduces with increasing shear strain rate.

If the suspension has the ability to store energy before bond rupture, the system may exhibit viscoelastic behavior. This usually occurs in a concentrated clay-water suspension and is reflected in creep curves. Below the yield value, the suspension exhibits elastic behavior while above this yield value there is an irreversible strain. In addition, dynamic tests show the viscoelastic behavior of clay-water suspension.

Table 2.2 Equations relating viscosity to solid concentration (from Ferraris, 2001)

Equation Name	Equation	Hypothesis
Einstein	$\mu = \mu_0(1 +  \mu \phi)$	No particle interaction, dilute suspension
Roscoe	$\mu = \mu_0(1 - 1.35\phi)^K$	Consider particle interactions
Krieger-Dougherty	$\frac{\mu}{\mu_0} = \left(1 - \frac{\phi}{\phi_{\max}}\right) -  \mu \phi_{\max}$	Relation between viscosity and particle packing. Take into account the maximum packing factor
Mooney	$\mu = \mu_0 \exp\left(\frac{ \mu \phi}{1 - \frac{\phi}{\phi_{\max}}}\right)$	Takes into account the maximum packing factor

Note:  $\mu$  – viscosity of the suspension;  $K$  – constant;  $\phi$  - volume fraction of solid;  $\mu_0$  – viscosity of liquid media;  $|\mu|$  - infinity viscosity of the suspension (2.5 for spheres);  $\phi_{\max}$  - maximum packing factor.

#### 2.4.2 Rheological Properties of Clay-Sand-Water Mixture

As discussed by Coussot (1997) fine particle such as clay particles induce colloidal interactions and Brownian motions may have a significant effects on the behavior of the suspension. In contrast, non-colloidal particles interact hydrodynamically or via direct contact (friction or collision). Coussot (1997) used 40 micron as the limit for colloidal and non-colloidal particles to simplify the problem. He also pointed out that clay fraction rather than fine solid fraction is of significance for the properties of the water-fine mixture and further assumed that most of fine particles are clay particles. Based on this assumption, he considered the clay-sand-water mixture as the mixture of sand with clay-water mixture and the final mixture is a suspension of non-colloidal particles in dispersion.

##### 2.4.2.1 Rheology of Clay-Sand-Water Mixture

Coussot (1997) discussed the concentrated clay-sand-water mixture in which clay (or fine particle) fraction is high enough to support the coarse particles (grains). He considered the final mixture of clay-sand-water mixture to be a mixture of clay-water

interstitial fluid with increasing volume fraction of coarse grains. Coussot and Piau (1995) experimentally showed an increasing apparent viscosity of the whole mixture resulted from addition of force-free particles into clay-water interstitial fluid. Coussot and Boyer (1995) found that a Herschel-Bulkley model, which combines the yield stress and a power law model, can fit the experimental data. They also found that the yield stress in the Herschel-Bulkley model can be expressed in a similar form to the equation for the yield stress for clay-water suspension:

$$\tau_c = c' \exp(s' \phi) \quad (\text{Eq. 2.8})$$

where  $c'$  and  $s'$  are suspension parameters and  $\phi$  is the total solid fraction:

$$\phi = \phi_s + (1 - \phi_s) \phi_a \quad (\text{Eq. 2.9})$$

in which  $\phi_s$  denotes sand to total mixture volume ratio, and  $\phi_a$  is volume ratio of clay to the sum of clay and water. Finally, the following equation was obtained from Eq. 2.8 and Eq. 2.9:

$$\tau_c = c \exp(s \phi_a + s'(1 - \phi_a) \phi_s) \quad (\text{Eq. 2.10})$$

Coussot (1997) found that Eq. 2.10 is also not valid for the sand-clay-water mixture that exhibit instability (minimum in flow curve). Coussot (1997) also argued that the exponential increase of yield stress for increasing grain fraction demonstrated that the interstitial clay-water mixture is the main factor affecting the suspension behavior when the grain volume fraction is below certain critical value. Once the critical value is exceeded, a new network of direct contact between all solid particles may form. The effect of grain size distribution on the yield stress of the sand-clay-water mixture was studied by Boyer (1994) and Coussot and Piau (1995). They demonstrated that adding poorly sorted grain particles will cause more rapid increase in yield stress.

By compiling the data in the literature, Coussot (1997) found that two regions can be distinguished in a solid fraction versus fine to solid ratio diagram: Herschel-Bulkley behavior region and the unstable behavior region where simple shearing flow exhibits a minimum in flow curves. Coussot (1997) also developed a general classification of

the behavior of water-debris mixture based on the total solid fraction and fine to solid ratio (fine fraction). Five zones were distinguished (Figure 2.8):

Due to high grain solid fraction, the water-debris mixture in Zone A can not flow without grain breakage. In Zone B, both the fine to solid particle ratio and total solid fraction are high, and material can flow slowly without fracture. Material in Zone C has low fine to solid particle ratio and the grain solid fraction is approaching the maximum packing limit. The mixture can flow due to slight dilatancy. The transition zone – Zone C-D – contains high concentration of interstitial fine particle-water mixture and fracture will take place before a slow or moderate flow occurs. In Zone D the overall behavior is controlled by the interstitial fine particle-water mixture. Herschel-Bulkley model can be used to represent the flow behavior in this zone. In Zone E an immediate settling of coarsest particle may occur at rest.

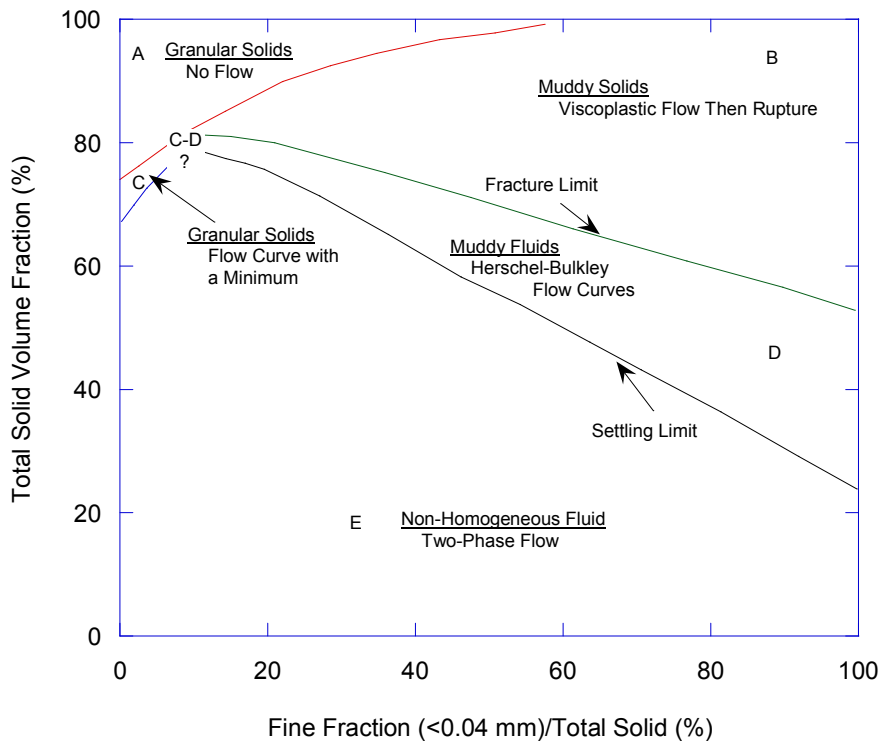


Figure 2.8 Rheological Classification of Water-debris Mixture (after Coussot 1997). The total solid volume fraction is defined as the total volume of the solids divided by the sum of the solid volume and liquid volume in percent.

### 2.4.3 Measurement of Viscosity

Modeling and simulation is meaningless if it is independent of the reality they are supposed to represent. The accuracy of the simulation must be checked, or validated, against data obtained from real operating systems. This experimental validation is critical to ensuring that there are meaningful representations of the applications for which they are intended. The experiments must be designed to challenge the model and push it to the limits at which it fails.

Coussot (1997) pointed out several factors that may affect the rheology measurements in dense suspension: observable strain field, changes of free surface form with time, evaporation rate, wall slip, particle migration and any slow or rapid changes of recorded shear stress or shear rate. He also stressed that a whole range of tests under different conditions are required in order to appreciate the behavior transition and evolution for the most clay-water suspensions.

Capillary and rotational are two common methods used for measuring the rheology of the fluids. Measuring apparatus can be divided into viscometer and rheometer. The former is primarily used to measure viscosity while latter is used to measure rheological properties over a varied and wide range of shear conditions. The inclined plane rheometer was recommended by Coussot (1997) for rheological measurement of clay-sand-water suspension systems. The flow curve can be determined by using the experiment procedure proposed by Coussot and Boyer (1995) and the analysis procedure by Asarita et al. (1974).

## 2.5 Sedimentation and Segregation of Mixture

### 2.5.1 Sedimentation of a Sphere in an Infinite Fluid

When a single sphere is suspended at rest in a fluid it is subjected to two opposite force, gravitational force  $G$ , and buoyancy force  $B$ . If the density of the particle is different from that of liquid, the spherical particle will be accelerated under the unbalanced force  $G-B$ . The skin friction which is the resistance offered by a liquid to the motion of a solid results in the development of a drag force  $D$ . The direction of the drag is opposite to the velocity of the solid particle and increase with the increase in velocity of a particle. Due to the action of drag force on the particle, a balance will

be achieved finally between drag force, buoyancy force and gravitational force and the particle moves at a constant velocity, which is termed terminal settling velocity,  $u_\phi$ . At that point, the drag force can be determined as follows:

$$D = G - B = (\rho_s u g) - (\rho_l u g) = (\rho_s - \rho_l) u g$$

(Eq. 2.11)

This relationship has been formulated for a sphere in an infinite fluid for slow flows. The general solution of the equation depends on the type and magnitude of flow around the particle as described by a dimensionless entity known as Reynolds number:

$$Re = \frac{d_p (u_p - u_l) \rho_l}{\mu} \quad (\text{Eq. 2.12})$$

where  $Re$  is the Reynolds number,  $d_p$  and  $u_p$  are the diameter and velocity of the particle,  $u_l$ ,  $\rho_l$  and  $\mu$  are velocity, density and viscosity of the liquid. For particles, laminar flow occurs below  $Re \sim 0.3$  and turbulent flow takes place when  $Re$  is above  $2 \times 10^5$ . In between them is the transitional region where the inertial forces become increasingly significant (Perry et al 1984).

#### 2.5.1.1 Laminar Flow

The analytical solution for the magnitude of the drag on a single sphere, settling under laminar flow conditions in an infinite liquid, is given by Stokes (1851) as:

$$D = 3\pi\mu d_p u_\phi \quad (\text{Eq. 2.13})$$

where  $u_\phi$  is the terminal velocity of the sphere in an infinite fluid in laminar flow. This equation is only a close approximation. For greater accuracy, additional terms have been included in the solution. Proudman and Pearson (1957) advocate the following equation:

$$D = 3\pi\mu d_p u_\phi \left[ 1 + \frac{3}{16} Re + \frac{9}{160} (Re)^2 \ln\left(\frac{Re}{2}\right) + \dots \right] \quad (\text{Eq. 2.14})$$

Usually, the forces exerted on the moving bodies are expressed in terms of a dimensionless drag coefficient  $C_D$ , which is obtained by dividing the drag force  $D$  by  $\rho_l u_{sr}^2 / 2$  and by the area of the body projected onto a plane normal to the relative velocity  $u_{sr}$ . Hence, for a sphere the drag coefficient is:

$$C_D = \frac{D}{\frac{\rho_l u_{sr}^2}{2} \cdot \frac{\pi d_p^2}{4}} \quad (\text{Eq. 2.15})$$

Using the drag force given by Stoke and expression of Reynolds number, the drag coefficient can be expressed in terms of Reynolds number by settling  $u_{sr} = u_\phi$

$$C_D = \frac{24}{\text{Re}} \quad (\text{Eq. 2.16})$$

Similarly, drag coefficient obtained from the solution given by Proudman and Pearson (1957) will be:

$$C_D = \frac{24}{\text{Re}} + \frac{9}{2} + \frac{27}{20} \text{Re} \ln\left(\frac{\text{Re}}{2}\right) + \dots \quad (\text{Eq. 2.17})$$

If the drag coefficient in the form of  $C_D = 24/\text{Re}$  is acceptable, the terminal velocity of a sphere can be calculated as:

$$u_\phi = \frac{d_p^2 (\rho_s - \rho_l) g}{18\mu} \quad (\text{Eq. 2.18})$$

### 2.5.1.2 Transitional and Turbulent Flow

The drag coefficient varies with Reynolds number as shown in Figure 2.9 (Wasp et al. 1977). Four regions can be divided based on the Reynolds number. Region a ( $\text{Re} < 1$ ) is called Stokes regime, and  $C_D = \frac{24}{\text{Re}}$  is applicable. Region b ( $1 < \text{Re} < 1000$ ) is called intermediate law region. Region c ( $1000 < \text{Re} < 2 \times 10^5$ ) is the regime where laminar-turbulent transition of the boundary layer has occurred prior to separation. In region d, the separation occurred. In region a, it is assumed that skin friction alone is responsible for the drag, and in regions c and d, only form drag, which is the drag due to pressure gradient and separation, dominates.

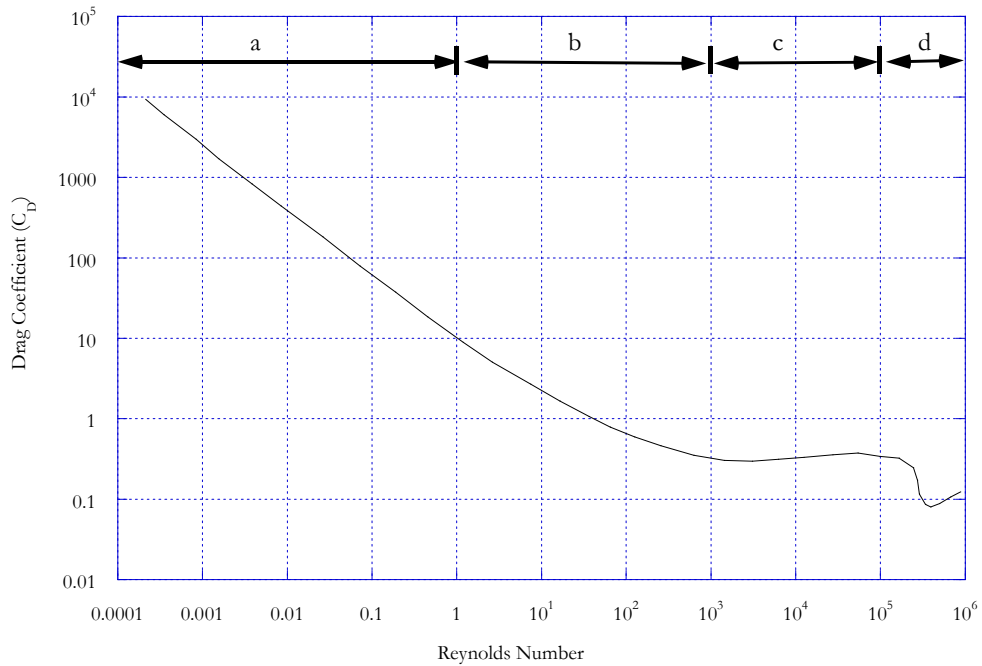


Figure 2.9 Drag coefficient versus Reynolds number for a spherical particle (from Wasp et al, 1977)

### 2.5.2 Nonspherical Particles in an Infinite Fluid

The drag on a nonspherical particle depends on its shape and its orientation with respect to the direction of motion (Perry et al. 1984). If the particles are not symmetrical, they experience drag and lift force during the settlement. This may cause drift to one side during settling, rotation to a position of maximum resistance, steady rotation, or even a wobbling motion (Chen et al. 1997). Alberston (1953) proposed a shape factor of the form

$$F_s = \frac{c}{\sqrt{ab}} \quad (\text{Eq. 2.19})$$

where  $a$  is the longest and  $c$  is the shortest of three mutually perpendicular axes of the particle. Albertson obtained a curve in which the drag coefficient of particles with different shape factor is given (Figure 2.10)

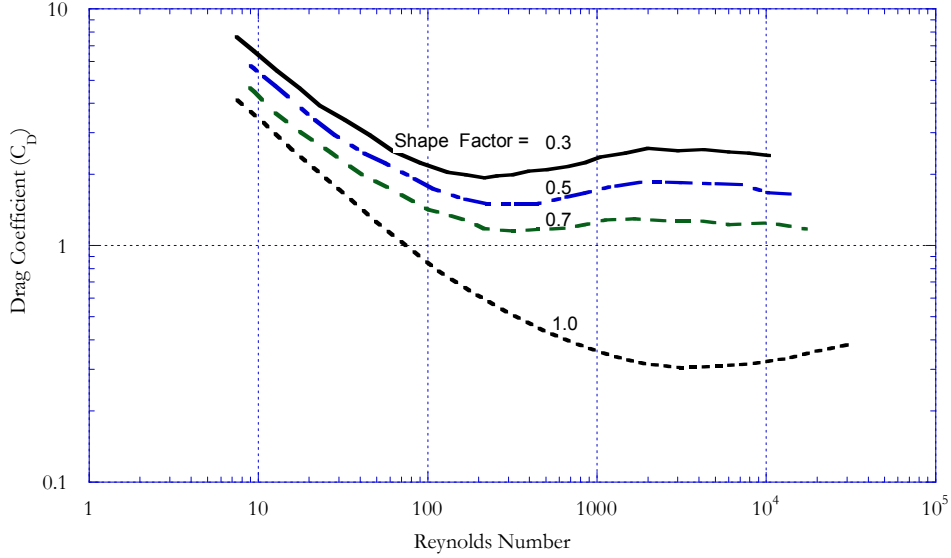


Figure 2.10 Drag coefficient versus Reynolds number for different shape factors (after Albertson, 1953)

Skin friction is related to surface area. The skin friction and hence drag for non-spherical particles will thus be greater because their terminal settling velocities are correspondingly lower than that for a sphere of the same volume. Hawksley (1954) derived a shape factor as

$$K_p = \frac{d_p}{d_A} = \frac{u_{ns}}{u_{\phi t}} \quad (\text{Eq. 2.20})$$

where  $u_{\phi t}$  is settling rate of sphere of diameter  $d_p$  having the same volume as the non-spherical particle,  $u_{ns}$  is the settling rate of non-sphere of diameter  $d_p$ ,  $d_A$  is the diameter of sphere having the same surface area as the non-spherical particle,  $K_p$  is shape factor.

### 2.5.3 Settling in the Presence of Other Particles

At least two effects of high solids concentration on the settling rate of uniformly distributed particles are observed. One is that clusters of particles form during the settling and the other is that as concentration increases each particle is subject to the higher volume of return flow fluid displaced by the settling particles. For the case of

cluster formation, it is observed that the velocity of the cluster is larger than that of individual particles when a group of randomly oriented particles settle in a fluid (Davies and Kaye, 1971). Cluster is often transient and their occurrence has been observed predominantly at low particle concentration (Kaye et al. 1962; Koglin et al. 1973). As the suspension concentration increases, particle acceleration due to cluster formation decreases as the increased drag from the return flowing fluid begins to slow them down. At still higher concentration, solids settle as a mass with an interface between solid phase and the fluid. This type of settling behavior is defined as hindered settling.

### 2.5.3.1 Suspension of Uniform Particle

When the solid concentration increases, the interface between suspensions and liquid descends over time. Richardson and Zaki (1954) proposed an equation describing the settling velocity of the interface,  $u_s$ :

$$u_s = u_\phi(1 - \phi_s)^n \quad (\text{Eq. 2.21})$$

where,  $u_s$  is the mean settling rate of particles in a container in the presence of many other particles,  $u_\phi$  is the terminal velocity of a single representative particle,  $\phi_s$  is the volume fraction of particles, and  $n$  is a constant.

### 2.5.3.2 Suspensions Consisting of a Range of Particle Sizes, Shapes, and Densities

In a suspension made up of a mixture of different size particles, the coarse particles settle in a matrix of smaller particles. For a binary mixture, Davies and Kaye (1971) showed that the mixture settles without segregation when the distance between larger particles is such as to trap the smaller size particles. Thus particle segregation would occur up to a critical concentration beyond which the smaller particles will remain trapped between larger particles.

The following equation has been proposed to predict the velocity of interface (Chen and Scott, 1997):

$$u_s = u_\phi(1 - k_v\phi_s)^{4.7} \quad (\text{Eq. 2.22})$$

where  $k_v$  is the slope of the curve in the plot of settling velocity versus solid volume fraction.

### 2.5.3.3 Concentrated Solid-Fluid System

When the particle concentration becomes large, the influence of particle-particle interactions (mediated by continuous-phase fluid motion and direct collisions) become important or dominant (Hanratty et al. 2003). Two theories were developed to analyze these flows based on analogies with the kinetic theory of dense gas but allowing for dissipative effects of fluid viscosity and inelastic particle collisions. The theory of “rapid granular flow” neglects all influence of the continuous phase. The theory of gas-solid suspensions adds the effect of a low Reynolds number gas. The major issue in extending these theories is to account for the effect of the continuous phase when the particle Reynolds number is large.

It is important to understand the conditions leading to transition from a fluid-like to a solid-like behavior, where the particles interact through enduring contacts between each other and the boundaries. Understanding cohesive interparticle forces, frictional contact between particles and the stability of the system are crucial. An interesting aspect of this problem is that interparticle forces depend on the shape of the particles, the size distribution and frictional contact.

### 2.5.4 Segregation

Williams (1963) discovered the phenomena called “Brazil nut” effect in which the large particles rise to the top of a shaken container of mixed nuts. Similar phenomena for granular mixture with different size or density also are observed. This behavior of the mixture is referred as segregation, a term describing the tendency for certain sizes or components with similar properties to preferentially collect in one or another physical zone of collective (de Silva et al., 1999). The segregation of particles with different properties is of significance in many areas of science and technology, including material science, engineering, agriculture and geophysics (Jullien et al, 1990). Understanding the mechanisms behind the phenomena is important for preventing or promoting the occurrence of it as it may be either beneficial (e.g., segregation process) or disadvantageous (e.g., segregating tailings).

#### 2.5.4.1 Segregation in granular flow

Segregation of granular material has been studied in the literatures. Segregation will occur when granular mixtures of dissimilar materials flow, or undergo shaking or vibration. Slight difference in either size or density causes flow-induced segregation. Segregation of granular material is complex and the understanding of the mechanism is limited. Many attempts have been made to unveil the segregation behavior of the different nuts. Trujillo et al. (2003) proposed that competition between buoyancy and geometric forces leads to “Brazil nut” effect. Buoyancy force is due to the difference between the energies of two granular species. Two geometric forces, one of which is compressive and the other tensile in nature, due to size difference, contribute to the behavior. Another mechanism that has been proposed for this effect is the percolation mechanism, which suggests that small particles can squeeze into small voids below a large particle, but the reverse can not occur (Rosato et al, 1987). Another proposed mechanism is convection, which suggests that large particles can rise with the mean flow, but are too large to fit into a narrow down-welling region near the boundary (Knight et al., 1993).

Jullien et al. (1990) used a three dimensional model to study the mechanism of the size segregation. In the model, the spheres are added, one at a time, to a growing heap on an infinite planar surface or a cylinder of finite radius. They concluded that the segregation is caused by the ability of the large spheres to roll over a random packing of small spheres. The mechanism is of significance when the particles are poured on to a surface or into a container.

There is a variety of other segregation mechanisms including percolation (Bridgewater et al., 1969; Bridgewater 1976; Jullien 1988), and segregation brought about by the filling of voids beneath the large particles by small particles during vibration and shaking (Haff et al., 1986; Rosato et al., 1987). Shear, freeze-thaw cycling, saltation, fluidization and other processes can lead to size segregation as well.

#### 2.5.4.2 Modeling of Segregation in rapid granular flow

Olhero and Ferreira (2004) investigated the effect of particle size and grain size distribution on the rheological behavior and particle packing of silica suspensions. The

results show that the flow properties of slips are strongly influenced by the particle size distribution. The viscosity of suspensions increases with the addition of fine particles. On the other hand, increasing the size ratio enhanced the shear thinning character of the suspensions, while decreasing the size ratio led to an accentuation of the shear thickening behavior.

Dahl and Hrenya (2004) simulate the size segregation in rapid granular flow with Gaussian and lognormal particle size distribution. Two dimensional (dissipative) molecular-dynamics simulations were conducted to evaluate the influence of the granular temperature gradient on the size segregation, where the granular temperature is a term to account for the kinetic energy of the random fluctuation of the disperse particles. They found that particles of all sizes move toward regions of low granular temperature. Especially, large particles possess a higher affinity for the low-temperature regions. It was also found that the local grain size distribution remains of the same form.

Firstly, two system types can be divided: the flows in which species segregation does not occur, and the flows in which species segregation occur. For rapid granular flow, spatial variations in the granular temperature and the application of external forces can lead to species segregation. Simple shear flows do not display species segregation because constant velocity gradient gives rise to a uniform granular temperature. However, species segregation was observed in systems that include external forces and/or exhibit a granular temperature gradient. In molecular-dynamics investigations the stress tensor is calculated based on the motion of individual particles and the averaging region is taken as the entire domain.

For rapid granular flow, investigations based on a kinetic-theory description indicate that several driving forces affect species segregation: granular temperature gradients, species concentration gradients and external forces (Jenkins 1998; Arnarson and Jenknins 1999; Hsiau and Hunt 1996). Hsiau and Hunt used the kinetic theory of Jenkins and Mancini to study segregation in two flow configurations. In the first configuration, a system with zero mean flow and a granular temperature gradient was employed for the case of perfectly elastic particles. The results indicate that an increase

in size or mass difference between the two particle species results in increased species segregation, with the larger particles concentrating in areas of low granular temperature. Additionally, an increase in the granular temperature gradient results in more pronounced segregation. The second flow geometry investigated by these researchers was the shearing of inelastic particles between two parallel walls. It was found that larger particles move preferentially into areas of lower granular temperature. Arnarson and Willits (1998) used an updated form of the kinetic theory of Jenkins and Mancini to study the influence of particle size and mass difference, granular temperature gradients, and gravity on segregation in rapid granular flows. It was found that the larger, denser particles tend to accumulate in regions of low granular temperature. They also observed that the amount of segregation increases with the magnitude of the gravity force for a given granular temperature gradient. Luding et al. (2000) performed molecular-dynamics simulation of inelastic, binary mixtures exposed to two, independent, granular temperature sources. The results show that all particles prefer regions of low granular temperature, but large particles appear to have a higher affinity for cold regions. Luding et al. (2000) also reported that significant segregation occurs in the presence of larger granular temperature gradients. Louge et al (2000) experimentally evaluated the influence of the gravity on the segregation of rapid granular flow with binary particle mixture. The experiment results agree with the simulation results well. Khakhar et al. (1997) used hard-sphere simulations and kinetic theory to study segregation due to pressure and granular temperature gradient in chute flows, and found that the segregation of inelastic, frictionless particles of the same size, but different mass, is not significantly affected by the granular temperature gradient. However, these researchers also found that inelastic, frictionless particles of identical material densities, but different sizes, do segregate in response to a granular temperature gradient, particularly at high solid fractions. Jenkins and Yoon (2002) performed a kinetic-theory analysis and determined that particles of different size and/or mass can segregate, even in the absence of a granular temperature gradient, when gravity is included.

In Dahl and Hrenya's simulation (2004), the velocities of the particles after colliding with the wall are calculated from a Maxwellian distribution. The post-collision velocity

of the particle is obtained using the Box-Muller method. The collisions between particles are treated as hard-sphere collisions. Linear momentum is conserved during the collision while kinetic energy is dissipated via inelastic collisions. The simulation proceeds in time via a hard-particle/overlap technique.

Eskin and Kalman (2000) investigated the radial size segregation of binary mixtures in a partially filled slowly rotating drum. The mathematical model which is capable of predicting a time-dependent as well as steady-state distribution of granular components in the drum was applied in the analysis.

Sundaresan et al. (2003) summarized in their report that segregation issues in granular material is unavoidable. Both models for flows and constitutive models for segregation fluxes under various flow states are required to describe segregation. The bulk of the studies in the literature consider only two special cases: a mixture of particles of the same size and shape, but different densities, and a mixture of the same density and shape, but two different sizes. Models for combined size and density segregation remain to be developed. Particle shape is an even more complicated issue. Virtually nothing is known about how to incorporate the role of cohesion.

#### 2.5.4.3 Modeling of Segregation of Suspension

Willimas et al. (1989 and 1991) showed in their papers that the following factors affecting the sedimentation characteristics of a polydisperse system:

- Particle size distribution, described by mean diameter and standard deviation
- Surface charge: measured by zeta potential
- Density of the particles
- Initial solid concentration

In their papers, two models were developed to simulate the sedimentation (more specific the solid flux in terms of settling velocity) of polydisperse suspension. One is hydrodynamic-based model in which a particle is assumed to reach a terminal velocity immediately after collision with other particle and the terminal velocity is calculated by assuming the drag force is balanced by buoyancy and gravity of the particle. Then

iterations were conducted to track the position of a particle in the space. In each time step the velocity of the particle is assumed to be terminal setting velocity. This model is only suitable for the suspension where non-hydrostatic interaction between particles is negligible.

The other model is empirical model which is a correlation of hindrance factor with independent variables affecting the sedimentation of a mixed non-colloidal colloidal suspension. The independent variables include mean diameter of the particles, standard deviation of the particle size distribution, initial solid volume fraction and zeta potential of the solid phase. Multiple-regression is required to relate the dependent variable to the independent variables. Large volume of experiment data is the basis for this correlation.

In the model mentioned above, hindrance factor is a term that is introduced to describe the discrepancy of the actual solid flux from the ideal solid flux calculated using Stokes drag law. Some important factors and its effects on the sedimentation of polydisperse suspension are as follows:

- Initial solid concentration: Extent of size segregation decreased as the solid volume fraction increase. High volume fraction suspensions are more stable than low volume fraction suspension. However, electro kinetic properties of the particle and size distribution will change the condition.
- Zeta potential: The authors stated that the value of zeta potential has a profound effect on the sedimentation behavior of Mixed-Colloidal-Noncolloidal-Suspension (MCNCS) system. Generally speaking, since fine particles tend to be negative-charged, less negative zeta potential will lead to particle coagulation, consequently increase the solid flux. More specifically, at low solid volume fraction (no more than 0.2), solid flux increase as the zeta potential becomes less negative. However, when the solid volume fraction is 0.3 or 0.4, the suspension behaves conversely to that at lower concentration.

- Particle size distribution: Zeta potential has little effect on the behavior of the coarser particles in the mixture. Sensitivity of the sedimentation behavior of MCNCS system to the changes in the proportions of particles within and either side of the range 15-30 micron is most important.
- Density of the particles: As the solid density increase, particles settle at higher velocities and over a wide range of velocity, thus the extent of the differential settling and solid flux is greater.

The authors pointed out some very important factors that are required to consider in modeling the segregation of a polydisperse suspension, as in oil sand tailings case. First of all, the grain size distribution can not be simplified using two groups. Secondly, as the portion of fine particle increases, colloidal effects are significant such that they can not be neglected if the segregation is to be simulated. The interaction between particles due to van der Waals force, repulsion and electrostatic force has to be taken into account. Zeta potential may not be sufficient to describe the effects resulting from the non-hydrodynamics forces such as gravity, drag and buoyancy force. In addition to these, the shape of the particles has to be considered in the model.

## **2.6 Computational Fluid Dynamics (CFD)**

Complexity of most fluid dynamic problems leads to originating and development of numerical method in this area. Computational fluid dynamics (CFD) provides a tool that can solve the problem for which analytical method cannot be used. Application of CFD can be found in chemical process, biological engineering, medicine manufacture, meteorology, geology and mining engineering (Bates et al, 2005; Tu et al., 2008). Great improvement has been achieved in CFD since 1990's due to the quick development of computer and computing technology.

Tu et al. (2008) summarized the advantages of computational fluid dynamics. CFD make it possible to achieve new paths of theoretical development. In addition, CFD complements experimental and analytical approaches and provides an alternative cost-effective method of modeling real fluid flows. CFD also is able to simulate the flow conditions that can not reproduced in experimental tests. Finally, CFD is able to

provide more detailed, visualized and comprehensive information, compared with analytical and experimental fluid dynamics.

The first step to carry out CFD simulation is to find the appropriate physical and mathematical model. Then a set of partial differential equations is obtained, based on the mathematical model. Discretization methods such as finite element, finite volume method and finite difference method are used to obtain a system of algebraic equations. Finite volume method becomes the first choice in discretizing the partial differential equations due to its property of inherent conservation. The algebraic equations are solved on the suitable grid scheme and a solution method designed for the equations is used to solve the system.

### 2.6.1 Basic Concepts of Fluid Dynamics

Fluid flow is the motion of fluid particles under surface forces and/or body forces. The fluid flow can be classified into several categories based on various criteria. If the speeds of the flow is low enough, the inertia of the fluid can be ignored and the flow is called creeping flow. As the speed increases, inertia forces become significant. When the fluid particle follows a smooth trajectory, the flow is laminar flow. Turbulent flow may be produced when the further increasing in speeds leads to a random and instable flow. If the ratio of flow speed to that of sound exceeds 0.3, the flow is called compressible flow as the exchange between kinetic energy of the motion and internal degree of freedom requires to be counted in (Ferziger et al., 2002). In the following Section 2.6.2 , the conservation equations and numerical techniques are reviewed based on the textbook by Ferziger and Peric (2002).

### 2.6.2 Conservation Equations

By considering changes of a conserved intensive property within a certain spatial region, which is referred to as control volume, the Reynolds' transport theorem can be derived as follows (Ferziger et al., 2002):

$$\frac{d}{dt} \int_{\Omega_{CM}} \rho \phi d\Omega = \frac{d}{dt} \int_{\Omega_{CV}} \rho \phi d\Omega + \int_{S_{CV}} \rho \phi (\bar{v} - \bar{v}_b) \cdot \bar{n} dS \quad (\text{Eq. 2.23})$$

Where  $\phi$  is any conserved intensive property;  $\rho$ ,  $\Omega$  and  $S$  are density, volume and surface, respectively. The subscript  $CV$  represents Control Volume and  $CM$  represents Control Mass.  $\bar{v}$ ,  $\bar{v}_b$  and  $\bar{n}$  are fluid velocity, velocity of control volume boundary surface and the unit vector orthogonal to the  $S_{CV}$  and pointing outward, respectively. The theory state the fundamental principle that change rate of the property within a control mass is equal to sum of the change rate of the property within the control volume plus the convective flux of the property through the control volume boundary. For a fixed control volume (i.e.  $\bar{v}_b = 0$ ), the continuity equation and momentum conservation equation can be obtained by replacing the  $\phi$  with 1 and  $\bar{v}$ , respectively. Thus, the continuity equation can be derived by assuming there is no change of mass within the control mass (Ferziger et al., 2002):

$$\frac{\partial}{\partial t} \int_{\Omega} \rho d\Omega + \int_S \rho \bar{v} \cdot \bar{n} dS = 0 \quad (\text{Eq. 2.24})$$

Where,  $\Omega$  and  $S$  are volume and surface of the control volume, respectively.

After applying the Gauss's divergence theorem to the second term on the left hand side, the continuity equation becomes (Ferziger et al., 2002):

$$\frac{\partial \rho}{\partial t} + \text{div}(\rho \bar{v}) = 0 \quad (\text{Eq. 2.25})$$

The momentum conservation equation is derived by considering the balance of surface and body force due to change of the momentum within the control volume and through the control volume boundary (Ferziger et al., 2002):

$$\frac{\partial}{\partial t} \int_{\Omega_{CV}} \rho \bar{v} d\Omega + \int_{S_{CV}} \rho \bar{v} \bar{v} \cdot \bar{n} dS = \sum \bar{f} \quad (\text{Eq. 2.26})$$

Where  $\bar{f}$  is the force, which includes body forces and surface forces. For Newtonian fluids, the constitutive relationship between stress and strain is as follows:

$$\bar{T} = -\left(p + \frac{2}{3}\mu \cdot \text{div}(\bar{v})\right)\bar{I} + 2\mu\bar{D} \quad (\text{Eq. 2.27})$$

Where  $\bar{T}$  is the stress tensor,  $p$  is the pressure,  $\mu$  is dynamic viscosity, and  $\bar{I}$  is the unit tensor. The symbol  $\text{div}$  is divergence operator of a tensor and  $\bar{D}$  is the rate of the strain tensor as follows:

$$\bar{D} = (\text{grad}(\bar{v}) + (\text{grad}(\bar{v}))^T) \quad (\text{Eq. 2.28})$$

where the symbol  $\text{grad}$  is the gradient operator of a tensor. These two tensors can be written in index notation in Cartesian coordinates as follows (Ferziger et al., 2002):

$$T_{ij} = -\left(p + \frac{2}{3}\mu \frac{\partial u_i}{\partial x_j}\right)\delta_{ij} + 2\mu D_{ij} \quad (\text{Eq. 2.29})$$

The viscous part of the stress tensor,  $\bar{\tau}$ , can be separated from the stress tensor  $\bar{T}$ :

$$\tau_{ij} = 2\mu D_{ij} - \frac{2}{3}\mu \delta_{ij} \cdot \text{div}(\bar{v}) \quad (\text{Eq. 2.30})$$

By substituting the right hand side of Eq. 2.27 with the body force  $b$  and surface force  $T$ , the equation becomes:

$$\frac{\partial}{\partial t} \int_{\Omega_{cv}} \rho \bar{v} d\Omega + \int_{S_{cv}} \rho \bar{v} \cdot \bar{n} dS = \int_{S_{cv}} \bar{T} \cdot \bar{n} dS + \int_{\Omega_{cv}} \rho \bar{b} d\Omega \quad (\text{Eq. 2.31})$$

By applying Gauss' divergence theorem, the momentum conservation equation becomes (Ferziger et al., 2002):

$$\frac{\partial(\rho \bar{v})}{\partial t} + \text{div}(\rho \bar{v} \bar{v}) = \text{div}(\bar{T}) + \rho \bar{b} \quad (\text{Eq. 2.32})$$

By separating stress tensor  $\bar{T}$  into viscous part  $\tau$  and pressure part  $p$ , and considering gravity,  $g$ , as the only body force, the index notation format of above equation becomes (Ferziger et al., 2002):

$$\frac{\partial(\rho u_i)}{\partial t} + \frac{\partial(\rho u_j u_i)}{\partial x_j} = \frac{\partial \tau_{ij}}{\partial x_j} - \frac{\partial p}{\partial x_i} + \rho g_i \quad (\text{Eq. 2.33})$$

### 2.6.3 Finite Volume Method

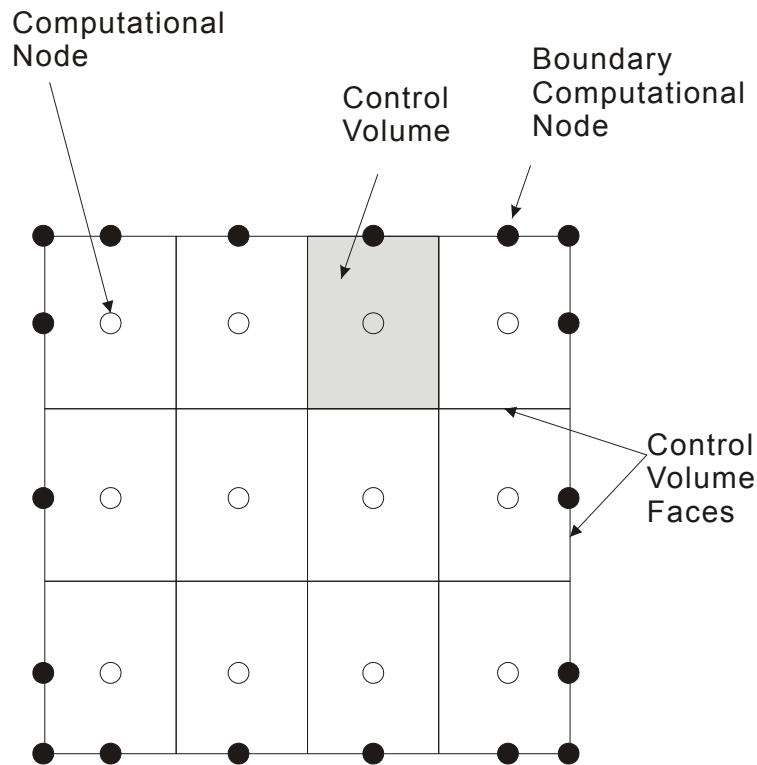


Figure 2.11 Finite Volume Grid

Considering solving the following generic conservation equation for a quantity  $\phi$  in a solution domain as shown in Figure 2.11 (Ferziger et al., 2002):

$$\int_S \rho \phi \bar{v} \cdot \bar{n} dS = \int_S \Gamma \text{grad}(\phi) \cdot \bar{n} dS + \int_{\Omega} q_{\phi} d\Omega \quad (\text{Eq. 2.34})$$

The solution domain is subdivided into a finite number of control volumes which is represented by a rectangular in the figure. Each term in the conservation equation is approximated on each control volume. For the surface integrals, the net flux through the control volume boundary is the sum of integrals over the control volume faces:

$$\oint_S f dS = \sum_k \oint_{S_k} f dS \quad (\text{Eq. 2.35})$$

Where  $f$  is the components of the convective ( $\rho \phi \bar{v} \cdot \bar{n}$ ) or diffusive ( $\Gamma \text{grad}(\phi) \cdot \bar{n}$ ) flux vector in the direction normal to control volume face, and  $k$  is the number of control volume boundary. The approximation of the right hand of the above equation can be made by replacing the integral with a product of the integrand at the cell-face center and cell-face area as follows (Ferziger et al., 2002):

$$\sum_k \oint_{S_k} f dS = \sum_k \bar{f}_k S_k \approx f_k S_k \quad (\text{Eq. 2.36})$$

Where  $\bar{f}_k$  is the interpolation of  $f$  over the control volume boundary  $k$ , and  $S_k$  is the surface area of the boundary  $k$ .

The approximation of the volume integrals is simple compared to the surface integrals. The volume integral can be replaced by the product of the mean value of the integrand and the control volume. The mean value of the integrand over the volume can be approximated as the value at the control volume center. The following equation shows the approximation of the integral (Ferziger et al., 2002):

$$Q_p = \int_{\Omega} q d\Omega = \bar{q} \Delta\Omega \approx q_p \Delta\Omega \quad (\text{Eq. 2.37})$$

Where  $q_p$  represents the value of  $q$  at the control volume center.

As the values of variables at the computational nodes except control volume centers are unknown, interpolation and differentiations are required to obtain the values of variables at the computational nodes from the neighbor nodes. Numerous interpolation and differentiation schemes exist in the text books and in literature.

Upwind interpolation (UDS), Linear Interpolation (CDS), Quadratic Upwind Interpolation (QUICK), Fourth-Order CDS, Linear Upwind Scheme (LUDS), and Skew Upwind Scheme are some of examples. The details of these schemes can be found in the text book (Ferziger et al., 2002).

The convective and diffusive flux at boundaries are either specified or interpolated using the interior values and the boundary data. After all the terms are approximated in each control volume, an algebraic equation system can be obtained by summing all the flux approximations and source terms. The obtained algebraic equation system is either linear or non-linear, depending on nature of the partial differential equations from which they are derived. The non-linear algebraic system can be solved using Gauss Elimination method, LU Decomposition, Tridiagonal Matrix Algorithm (TDMA), or Cyclic Reduction methods. Details of these methods can be found in text book (Ferziger et al., 2002).

Momentum equations contain a contribution from the pressure, which has no separate equations. Due to the close connection of the pressure and the continuity equation, special attention needs to be paid to the choice of variable arrangement on the grid and discretization of pressure terms. In order to avoid checkerboard effect, staggered grids are used in which grids for velocity and for pressure are different. However, due to simplicity of collocated grids in complex geometry and non-orthogonal grids, collocated arrangement regains the favor. Pressure is calculated on a staggered control volume even though all data is stored on the same grid. Most commercial codes use the method proposed by Rhie and Chow (1983).

SIMPLE, SIMPLER, SIMPLEC and PISO solvers can be applied to solve the pressure-velocity coupling problems. In SIMPLE method, a pressure field is assumed then velocity field is solved and then the velocity and pressure field is corrected respectively. During the correction of velocity field, a term is neglected for numerical reason. Contrast to SIMPLE, SIMPLER uses the velocities from previous iteration to approximate the term neglected in SIMPLE, leading to more accurate correction. Instead of suppressing the term as in SIMPLE and SIMPLER, SIMPLEC neglects a term much close to zero, resulting in a more consistent and often more efficient

solution method. PISO uses predictor-corrector with 2 corrections. The method can serve for both incompressible and compressible flows.

#### 2.6.4 CFD Modeling Newtonian Flow and Non-Newtonian Flow

As elasticity is referred as the linear relationship between stress and strain in solid mechanics, Newtonian flow is referred to the flow where the relationship between shear stress and shear strain rate is linear. In other words, the dynamic viscosity of the fluid is constant in relation to the shear strain rate. Any flow that is not within the definition of Newtonian flow is referred to as Non-Newtonian flow.

If the functional relationship between the dynamic viscosity and the shear strain rate is known, modeling of non-Newtonian flow in most of CFD packages can be achieved by modifying the viscosity of the fluid using an expression or user defined function. However, the non-Newtonian relationship can jeopardize the convergence of the CFD model, which means that simplification is required.

#### 2.6.5 Overview of Single-phase CFD

State-of-the-art CFD models are capable of quantitatively predicting laminar flow and mixing of Newtonian fluids with complex geometry. Temperature- and composition-dependent properties and other practical issues such as the end effects, local hot and cold spots, complex geometry, scale-up, and so on can be solved with sufficient accuracy (Joshi and Ranade, 2003). Free surface flow and turbulent flow bring in complexity in single-phase CFD. Presently the flow of simple non-Newtonian and Newtonian flow can be simulated with accuracy. However, prediction for rheologically complex fluids with viscoelastic characteristics is difficult. RANS-based turbulence models dominate the simulation, and large eddy simulations (LES) and direct numerical simulation (DNS) are gaining more and more popularity due to the accessibility of large computer resource. State of art DNS is mainly used as a learning model, which are useful in evaluating and validating more approximate models and may lead to the development of better models (Joshi et al., 2003).

## 2.6.6 Overview of Multiphase CFD

### 2.6.6.1 Multiphase Flow

Strictly speaking, physical phases of matter are gas, liquid and solid; however, in multiphase flow, a phase can be defined as an identifiable class of material that has a particular inertial response to and interaction with the flow and the potential field in which it is immersed (FLUENT, 2003). As shown in Figure 2.12, each solids phase in multiphase flow has identical density and diameter. A mixture composed of particles that differs in diameter or density or both is regarded as a separate phase. Each phase has its own set of governing hydrodynamic equations. Therefore, the particles with identical density but discrete particle sizes have to be treated as individual phases. When the solids particles sizes have continuous distribution, discrete particles sizes have to be used to approximate the continuous distribution.

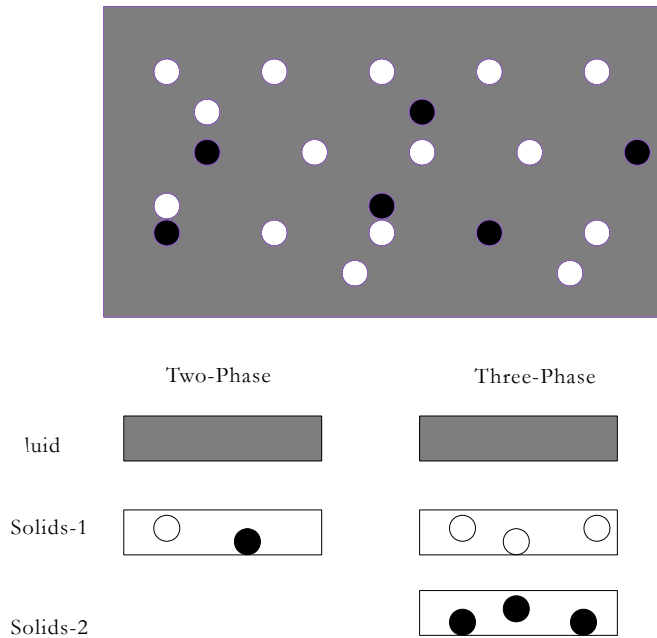


Figure 2.12 Multiphase Description of a Fluid-Solid Mixture (after Syamlal et al., 1993)

### 2.6.6.2 Lagrangian and Eulerian Description

Lagrangian description and Eulerian description are two ways of describing a fluid motion. In the Lagrangian description, the history of individual fluid particles is essentially tracked (Figure 2.13). In this description, any flow variable  $F$  is expressed as a function of time,  $t$ , and the position vector of the particle at reference zero time,  $x_0$ . On the other hand, Eulerian description focuses on the change of variables at a fixed spatial point,  $x$ , thus, a flow variable is a function of spatial position,  $x$ , and time,  $t$ .

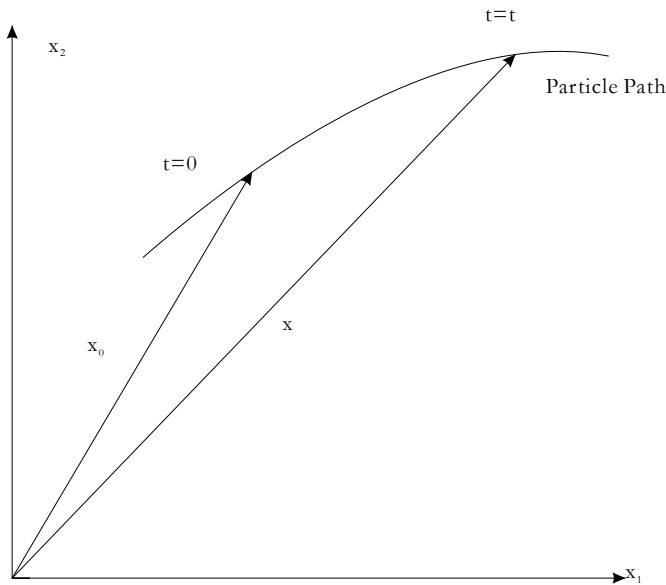


Figure 2.13 Lagrangian Description of Fluid Motion(after Kundu and Cohen, 2002)

In modeling the liquid-solid, gas-solid or liquid-gas-solid flow, the solid phase can be described using Eulerian or Lagrangian description. However, the liquid phase in liquid-solid flow or gas phase in granular flow is almost always described using Eulerian methods as the distribution of the fluid is relatively continuous compared to the solid particles and this description is relatively effective in terms of computational cost. This is due to the fact that each particle has to be tracked at any time during the simulation if Lagrangian description is used. The difference and comparison of these two methods are detailed in the following two sections.

### 2.6.6.3 Euler-Lagrange Methods

In Euler-Lagrange methods, the particulates are tracked through the flow using Lagrangian description while the fluid is described in Eulerian way. Since it is not realistic to track each particle even in dilute suspension, the full particulate phase is modeled by just a sample of individual particles (Ansys, 2003). The behavior of the particles in the flow is tracked by integrating a set of ordinary differential equations in time for each sample particle. As this method is not used in this research program, the detailed information will not be provided here.

### 2.6.6.3 Euler-Euler Methods

As shown in Figure 2.12, strictly speaking, the solid phase in the mixture is not a continuum. To simplify the derivation of the hydrodynamic equations, it is assumed that both the discrete solid particle phase and continuous liquid phase are continua and they are interpenetrating. As the computational domain is divided into control volumes, the total volume of the solid particles is summed up in each control volume. The ratio of the volume of each phase (solid or liquid) to the total volume of the control volume is treated as a variable and solved (Figure 2.14). This ratio is defined as volume fraction. By following the volume fraction of each phase, especially the solid phase, in each control volume, rather than tracking each individual solid particle, the cost of modeling the solid-liquid flow is significantly reduced. The detailed hydraulic equations and the closure will be described further in the following sections.

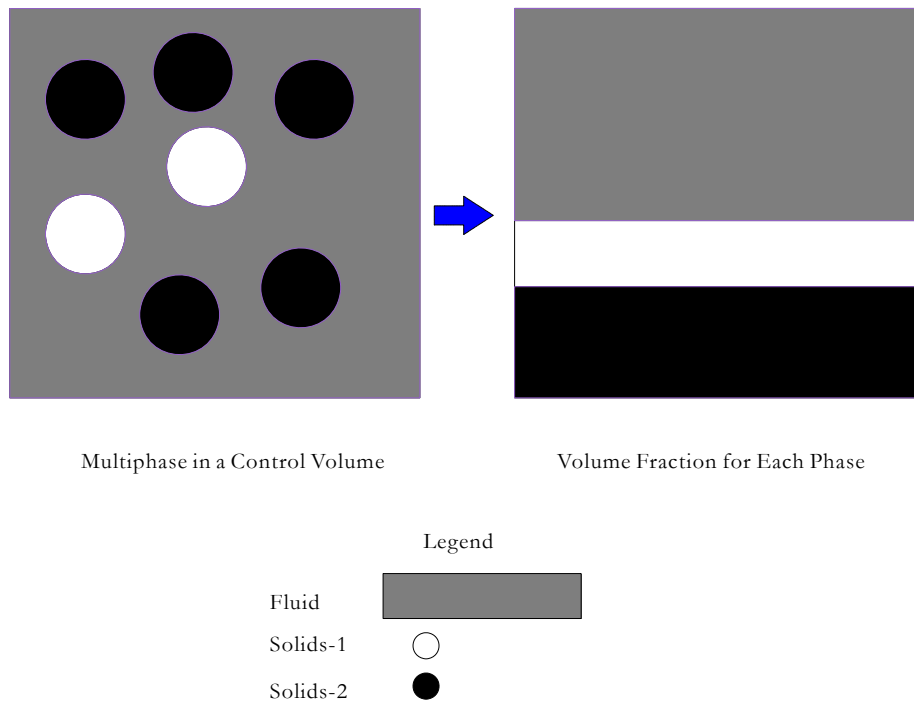


Figure 2.14 Concepts of Interpenetrating Continua and Volume Fractions for a Fluid-Solid Mixture

#### 2.6.6.4 General Hydrodynamic Equations for Multiphase Flow

The conservation equation can be derived by ensemble averaging the local instantaneous balance for each of the phase or by using the mixture theory approach (Syamlal et al., 1993). In this approach, the multiphase flow is described as interpenetrating continua and the concept of phasic volume fractions  $\alpha_f$  is introduced. Volume fractions reflect the portion of volume occupied by each phase in a control volume (Figure 2.14). The governing equations of conservation of mass and momentum are derived based on the concept that these conservation equations are satisfied by each phase individually.

As the definition of volume fraction states, all the volume fractions have to sum up to unity in any control volume as follows:

$$\sum_{q=1}^n \alpha_q = 1 \quad (\text{Eq. 2.38})$$

where,  $\alpha_q$  is volume fraction for each phase,  $n$  is the total number of phases. From the definition, the volume of phase  $q$ ,  $V_q$  is calculated as

$$V_q = \int_V \alpha_q dV \quad (\text{Eq. 2.39})$$

The effective density is defined as

$$\hat{\rho}_q = \alpha_q \rho_q \quad (\text{Eq. 2.40})$$

where  $\rho_q$  is the physical density of phase  $q$ .

#### 2.6.6.4.1 Continuity Equations

The continuity equation for phase  $q$  is

$$\frac{\partial}{\partial t} (\alpha_q \rho_q) + \nabla \cdot (\alpha_q \rho_q \vec{v}_q) = \sum_{p=1}^n \dot{m}_{pq} \quad (\text{Eq. 2.41})$$

where  $\vec{v}_q$  is the velocity of phase  $q$  and  $\dot{m}_{pq}$  is the mass transfer from the  $p^{th}$  to  $q^{th}$  phase.

#### 2.6.6.4.2 Conservation of momentum

The conservation of momentum for a liquid phase  $q$  is

$$\begin{aligned} \frac{\partial}{\partial t} (\alpha_q \rho_q \vec{v}_q) + \nabla \cdot (\alpha_q \rho_q \vec{v}_q \vec{v}_q) = & -\alpha_q \nabla p + \nabla \cdot \bar{\bar{\tau}}_q + \alpha_q \rho_q \bar{\bar{g}} + \alpha_q \rho_q (\bar{\bar{F}}_q + \bar{\bar{F}}_{lift,q} + \bar{\bar{F}}_{vm,q}) \\ & + \sum_{p=1}^n (K_{pq} (\vec{v}_p - \vec{v}_q) + \dot{m}_{pq} \vec{v}_{qp}) \end{aligned}$$

(Eq. 2.42)

where  $\vec{g}$  is the acceleration due to gravity  $\bar{\tau}_g$  is the  $q^{th}$  phase stress-strain tensor,  $p$  is the pressure,  $\bar{F}_q$  is an external body force,  $\bar{F}_{lift,g}$  is a lift force, and  $\bar{F}_{vm,g}$  is a virtual mass force.  $K_{pq}$  is the momentum exchange coefficient between  $p^{th}$  and  $q^{th}$  phases. The term  $\dot{m}_{pq}$  characterizes the mass transfer from  $p^{th}$  to  $q^{th}$  phase.  $\vec{v}_{qp}$  is the relative velocity between  $q^{th}$  and  $p^{th}$  phase.

The conservation of momentum for  $s^{th}$  solid phase is

$$\begin{aligned} \frac{\partial}{\partial t}(\alpha_s \rho_s \vec{v}_s) + \nabla \cdot (\alpha_s \rho_s \vec{v}_s \vec{v}_s) = & -\alpha_s \nabla p - \nabla p_s + \nabla \cdot \bar{\tau}_s + \alpha_s \rho_s \vec{g} + \\ & \alpha_s \rho_s (\bar{F}_s + \bar{F}_{lift,s} + \bar{F}_{vm,s}) + \sum_{l=1}^N (K_{ls} (\vec{v}_l - \vec{v}_s) + \dot{m}_{ls} \vec{v}_{ls}) \end{aligned} \quad (\text{Eq. 2.43})$$

where  $p_s$  is the  $s^{th}$  solids pressure,  $K_k = K_{sl}$  is the momentum exchange coefficient between fluid or solid phase  $l$  and solid phase  $s$ ,  $N$  is the total number of phases.  $\bar{\tau}_s$  is the  $s^{th}$  phase stress-strain tensor,  $\bar{F}_s$  is an external body force,  $\bar{F}_{lift,s}$  is a lift force, and  $\bar{F}_{vm,s}$  is a virtual mass force.  $K_k$  is the momentum exchange coefficient between  $l^{th}$  and  $s^{th}$  phases.  $\dot{m}_{ls}$  characterizes the mass transfer from  $l^{th}$  to  $s^{th}$  phase.  $\vec{v}_{ls}$  is the relative velocity between  $l^{th}$  and  $s^{th}$  phase.

#### 2.6.6.4.3 Closure of Momentum Conservation Equation

As indicated in the above momentum conservation equations, the solid shear stress, fluid shear stress as well as momentum exchanges between solid and fluid and between solid and solid phase are to be determined.

The difference in closing the momentum conservation equations makes each CFD package different, no matter whether it is commercial or non-commercial. The following discussion will be based on the programs that will be used in this research program: MFIIX, FLUENT 6.2, and CFX (version 5 and 10). The formulations for liquid-solid momentum transfer and solid-solid momentum transfer are briefed for each software package.

#### 2.6.6.4.3.1 MFIX

##### (A) FLUID STRESS TENSOR

In MFIX, the fluid viscous stress tensor,  $\bar{\bar{\tau}}_g$ , is assumed to be of Newtonian form:

$$\bar{\bar{\tau}}_g = 2\alpha_g \mu_g \bar{\bar{D}}_g + \alpha_g \lambda_g \text{tr}(\bar{\bar{D}}_g) \bar{\bar{I}} \quad (\text{Eq. 2.44})$$

Where  $\bar{\bar{D}}_g$  is the strain tensor for fluid phase,  $\mu_g$  and  $\lambda_g$  are dynamic viscosity and bulk viscosity for fluid phase.

##### (B) MOMENTUM EXCHANGE BETWEEN FLUID AND SOLID PHASE

The momentum exchange coefficient,  $K_{pq}$ , characterizes the momentum exchange between fluid phase and solid phase. MFIX adopts the momentum exchange coefficient proposed by Syamlal and O'Brien (1987) which was based on a simplified version of kinetic theory as follows:

$$K_{pq} = \frac{3\alpha_p \alpha_q \rho_q}{4v_{rp}^2 d_p} C_D \left( \frac{\text{Re}_p}{V_{rp}} \right) |\bar{v}_p - \bar{v}_q| \quad (\text{Eq. 2.45})$$

Where  $v_{rp}$  is the terminal velocity correlation for the  $p^{\text{th}}$  solids phase. A closed formula for  $v_{rp}$  derived by Garside and Al-Dibouni (1977) is shown in the following equation:

$$v_{rp} = 0.5 \left( A - 0.06 \text{Re}_p + \sqrt{(0.06 \text{Re}_p)^2 + 0.12 \text{Re}_p (2B - A) + A^2} \right) \quad (\text{Eq. 2.46})$$

Where

$$A = \alpha_q^{4.14} \quad (\text{Eq. 2.47})$$

$$B = \begin{cases} 0.8\alpha_q^{1.28} & \text{if } \alpha_q \leq 0.85 \\ \alpha_q^{2.56} & \text{if } \alpha_q > 0.85 \end{cases} \quad (\text{Eq. 2.48})$$

And the Reynolds number for  $p^{th}$  solids phase is given by

$$\text{Re}_p = \frac{d_p |\bar{v}_p - \bar{v}_q| \rho_q}{\mu_q} \quad (\text{Eq. 2.49})$$

And  $C_D$  is the coefficient of drag for a single sphere particle in the fluid. MFIX chooses the formula proposed by Dalla Valle (1948):

$$C_D = \left( 0.63 + \frac{4.8}{\sqrt{\text{Re}_p}} \right) \quad (\text{Eq. 2.50})$$

The fluid-solid momentum exchange coefficient shown above is the default option. Due to the characteristics of this open source code, Gidaspow Drag Model, Wen-Yu Drag Model, Koch & Hill (2001) Drag Model are also included in the code. The details of these models will be introduced in the following sections.

### (C) SOLID PRESSURE AND SOLID PHASE STRESS TENSOR

The simplest formula for solid phase stress tensor is the one that only includes the hydrostatic part of the stress tensor (solids pressure) with an intention to prevent the total solid volume fraction becoming exceeding the one in a packed bed. MFIX adopts the theory proposed for granular flows, in which two distinct flow regimes are classified. One is a viscous or rapid shearing regime where collisions and translations contribute to the momentum transfer, consequently to the stress. The other flow regime is a plastic or slowly shearing regime where the Coulomb friction between particles in enduring contact lead to the stress. It is assumed that the transition from viscous flow regime to plastic flow regime occurs once the void fraction is less than the critical packing,  $\alpha_q^*$ , which is usually the packed-bed void fraction. Accordingly, the solid pressure and solid stress tensor are calculated as follows:

$$P_s = \begin{cases} K_{1s} \alpha_s^2 \Theta_s & \text{if } (\alpha_q > \alpha_q^*) \\ \alpha_s P^* & \text{if } (\alpha_q \leq \alpha_q^*) \end{cases} \quad (\text{Eq. 2.51})$$

where

$$K_{1s} = 2(1 + e_{ss})\rho_s g_{0,ss} \quad (\text{Eq. 2.52})$$

where  $\rho_s$  is density of the solid phase,  $e_{ss}$  is the restitution coefficient between  $s^{\text{th}}$  solid particles.  $\Theta_s$  is the granular temperature of the  $s^{\text{th}}$  solid phase,  $P^*$  is an empirical power law function allowing exceedingly high pressure value when void fraction  $\alpha_q$  is less than the critical void fraction,  $\alpha_q^*$ , as shown in the following formula:

$$P^* = A(\alpha_q^* - \alpha_q)^n \quad (\text{Eq. 2.53})$$

With  $A = 10^{25}$  and  $n = 10$  used in MFIX.

The solid shear stress tensor in viscous flow regime has different form from that in plastic flow regime. Particularly, a solid stress tensor based on the critical state theory (Gray and Stiles's, 1988) was included in MFIX, which applies three-dimensional generalization of a yield function proposed by Pitman and Schaeffer (1987). On the other hand, a modified form of kinetic theory of smooth, inelastic, spherical particles developed by Lun et al. (1984) is applied to derive the viscous stress tensor. Both of the stress tensors are given in the following equations:

$$\bar{\bar{\tau}}_s = \begin{cases} 2\mu_s^v \bar{\bar{D}}_s + \lambda_s^v \text{tr}(\bar{\bar{D}}_s) \bar{\bar{I}} & \text{if } (\alpha_q > \alpha_q^*) \\ 2\mu_1^p \bar{\bar{D}}_1 & \text{if } (\alpha_q \leq \alpha_q^*) \end{cases} \quad (\text{Eq. 2.54})$$

where  $\mu_s^v$  and  $\lambda_s^v$  are shear viscosity and bulk viscosity for  $s^{\text{th}}$  solid phase in viscous flow regime respectively,  $\bar{\bar{D}}_s$  is the strain tensor,  $\mu_1^p$  and  $\bar{\bar{D}}_1$  are shear viscosity and strain tensor for the  $1^{\text{st}}$  solid phase respectively. This implies that the stress tensor in plastic flow regime is only calculated for the  $1^{\text{st}}$  solid phase even if multiple solid phases are presented. The detailed formula for those terms will not be listed here and can be found in the MFIX Documentation Theory Guide (Syamlal et al. 1993).

#### (D) SOLIDS-SOLIDS MOMENTUM EXCHANGE COEFFICIENT

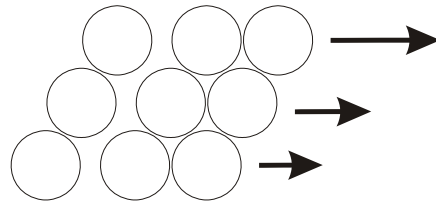
MFIX uses a momentum exchange coefficient derived by Syamlal (1987) based on a simplified version of kinetic theory:

$$K_{ls} = \frac{3(1 + e_{ls})\left(\frac{\pi}{2} + C_{fr,ls} \frac{\pi^2}{8}\right) \alpha_s \rho_s \alpha_l \rho_l (d_l + d_s)^2 g_{0,ls}}{2\pi(\rho_l d_l^3 + \rho_s d_s^3)} |\vec{v}_l - \vec{v}_s| \quad (\text{Eq. 2.55})$$

where  $e_{ls}$  is the coefficient of restitution,  $C_{fr,ls}$  is the coefficient of friction between the  $l^{\text{th}}$  and  $s^{\text{th}}$  solid phase particle  $s$ ,  $d_{ls}$  is the diameter of the particles of solid  $l$ , and  $g_{0,ls}$  is the radial distribution coefficient.

##### Plastic Flow

- slowly shearing
- enduring contacts
- frictional transfer of momentum



##### Viscous Flow

- rapidly shearing
- transient contacts
- translational or collisional transfer of momentum

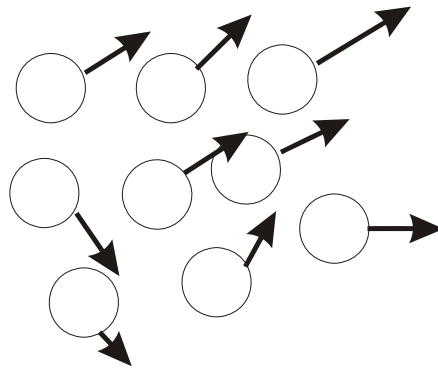


Figure 2.15 Slowly and Rapidly Shearing Granular Flow (after Syamlal et al., 1993)

#### 2.6.6.4.3.2 FLUENT

##### (A) FLUID STRESS TENSOR

The same stress tensor as the one in MFIX is used in FLUENT. The detailed format of the tensor can be found in Eq. 2.44.

##### (B) FLUID-SOLID MOMENTUM EXCHANGE COEFFICIENT

The fluid-solid exchange coefficient takes the form

$$K_{st} = \frac{\alpha_s \rho_s f}{\tau_s} \quad (\text{Eq. 2.56})$$

where drag function,  $f$ , is defined differently for the different exchange-coefficient models, and  $\tau_s$ , the particulate relaxation time, is defined as

$$\tau_s = \frac{\rho_s d_s^2}{18\mu_l} \quad (\text{Eq. 2.57})$$

where  $d_s$  is the diameter of particles of phase  $s$ .

Following models for drag function,  $f$ , which may includes drag coefficient based on the relative Reynolds number are available in FLUENT:

- Syamlal-O'Brien Model

$$f = \frac{C_D \text{Re}_s \alpha_l}{24v_{r,s}^2} \quad (\text{Eq. 2.58})$$

where the drag coefficient has a form derived by Dalla Valle

$$C_D = \left( 0.63 + \frac{4.8}{\sqrt{\text{Re}_s / v_{r,s}}} \right)^2 \quad (\text{Eq. 2.59})$$

where  $Re_s$  is defined as

$$Re_s = \frac{\rho_l d_s |\vec{v}_s - \vec{v}_l|}{\mu_l} \quad (\text{Eq. 2.60})$$

where the subscript  $l$  is for the  $l^{\text{th}}$  fluid phase,  $s$  is for the  $s^{\text{th}}$  solid phase, and  $d_s$  is the diameter of the  $s^{\text{th}}$  solid phase particles. The terminal velocity correlation for the solid phase is

$$v_{r,s} = 0.5 \left( A - 0.06 Re_s + \sqrt{(0.06 Re_s)^2 + 0.12 Re_s (2B - A) + A^2} \right) \quad (\text{Eq. 2.61})$$

where  $A = \alpha_l^{4.14}$  and  $B = 0.8 \alpha_l^{1.28}$  for  $\alpha_l \leq 0.85$  and  $B = \alpha_l^{2.65}$  for  $\alpha_l > 0.85$ .

This model is appropriate when the solid shear stresses are defined according to Syamlal et al (1993).

- Wen and Yu Model

The solid-liquid exchange coefficient is of the following form:

$$K_{sl} = \frac{3}{4} C_D \frac{\alpha_s \alpha_l \rho_s |\vec{v}_s - \vec{v}_l|}{d_s} \alpha_l^{-2.65} \quad (\text{Eq. 2.62})$$

where the drag coefficient

$$C_D = \frac{24}{\alpha_l Re_s} \left[ 1 + 0.15 (\alpha_l Re_s)^{0.687} \right] \quad (\text{Eq. 2.63})$$

This model is appropriate for dilute systems.

- Gidaspow Model

This model is a combination of the Wen and Yu model and the Ergun equation.

When  $\alpha_l > 0.8$ , the fluid-solid exchange coefficient  $K_{sl}$  is of the following form:

$$K_{sl} = \frac{3}{4} C_D \frac{\alpha_s \alpha_l \rho_s |\vec{v}_s - \vec{v}_l|}{d_s} \alpha_l^{-2.65} \quad (\text{Eq. 2.64})$$

where

$$C_D = \frac{24}{\alpha_l \text{Re}_s} \left[ 1 + 0.15 (\alpha_l \text{Re}_s)^{0.687} \right] \quad (\text{Eq. 2.65})$$

When  $\alpha_l \leq 0.8$ ,

$$K_{sl} = 150 \frac{\alpha_s (1 - \alpha_l) \mu_l}{\alpha_l d_s^2} + 1.75 \frac{\rho_l \alpha_s |\vec{v}_s - \vec{v}_l|}{d_s} \quad (\text{Eq. 2.66})$$

This model is recommended for dense fluidized beds.

### (C) SOLID PRESSURE AND SOLID STRESS TENSOR

#### (a) Solid pressure

For granular flows in the compressible regime (i.e., where the solids volume fraction is less than its maximum allowed value, a solid pressure is calculated independently and used for the pressure gradient term,  $\nabla p_s$ , in the granular-phase momentum equation. Due to the fact that a Maxwellian velocity distribution is used for the particles, a granular temperature is introduced into the model, and appears in the expression for the solids pressure and viscosities. The solids pressure is composed of a kinetic term and a second term due to particle collisions:

$$p_s = \alpha_s \rho_s \Theta_s + 2 \rho_s (1 + e_{ss}) \alpha_s^2 g_{0,ss} \Theta_s \quad (\text{Eq. 2.67})$$

where  $e_{ss}$  is the coefficient of restitution for particle collisions,  $g_{0,ss}$  is the radial distribution function, and  $\Theta_s$  is the granular temperature. The granular temperature  $\Theta_s$  is proportional to the kinetic energy of the fluctuating particle motion. The function  $g_{0,ss}$  is a distribution function that governs the transition from the

compressible condition with  $\alpha < \alpha_{s,\max}$ , where the spacing between the solid particles can continue to decrease, to the incompressible condition with  $\alpha = \alpha_{s,\max}$ , where no further decrease in the spacing can occur.

Radial Distribution Function,  $g_0$ , is a correction factor that modifies the probability of collisions between grains when the solid granular phase becomes dense. This function may be regarded as the non-dimensional distance between spheres:

$$g_0 = \frac{s + d_p}{s} \quad (\text{Eq. 2.68})$$

where  $s$  is the distance between grains. FLUENT implemented the radial distribution function proposed by Ranz (1958):

$$g_0 = \left[ 1 - \left( \frac{\alpha_s}{\alpha_{s,\max}} \right)^{\frac{1}{3}} \right]^{-1} \quad (\text{Eq. 2.69})$$

If the number of solid phase is greater than 1, the radial distribution function is extended to

$$g_{0,ll} = \left[ 1 - \left( \frac{\alpha_l}{\alpha_{l,\max}} \right)^{\frac{1}{3}} \right]^{-1} \quad (\text{Eq. 2.70})$$

and

$$g_{0,lm} = \frac{d_m g_{0,ll} + d_l g_{0,mm}}{d_m + d_l} \quad (\text{Eq. 2.71})$$

(b) Solid shear stress

The solid shear stress tensor appears in the liquid-solid momentum equations. It contains shear and bulk viscosities arising from particle momentum exchange due to

translation and collision. A friction component of viscosity can be included to account for the viscous-plastic transition that occurs when particles of a solid phase reach the maximum solid volume fraction.

The solid shear viscosity is the sum of the collisional and kinetic parts, and the optional friction part:

$$\mu_s = \mu_{s,col} + \mu_{s,kin} + \mu_{s,fr} \quad (\text{Eq. 2.72})$$

(b.1) Collisional Viscosity

$$\mu_{s,col} = \frac{4}{5} \alpha_s \rho_s d_s g_{0,ss} (1 + e_{ss}) \left( \frac{\Theta_s}{\pi} \right)^{1/2} \quad (\text{Eq. 2.73})$$

(b.2) Kinetic Viscosity

Expressions for kinetic viscosity, proposed by Syamlal et al. (1993) and Gidaspow et al. (1992) are available in FLUENT. The expression proposed by Syamlal et al (1993) takes the following form:

$$\mu_{s,kin} = \frac{\alpha_s \rho_s d_s \sqrt{\Theta_s \pi}}{6(3 - e_{ss})} \left[ 1 + \frac{2}{5} (1 + e_{ss})(3e_{ss} - 1) \alpha_s g_{0,ss} \right] \quad (\text{Eq. 2.74})$$

The expression proposed by Gidaspow et al. (1992) is:

$$\mu_{s,kin} = \frac{10 \rho_s d_s \sqrt{\Theta_s \pi}}{96 \alpha_s (1 + e_{ss}) g_{0,ss}} \left[ 1 + \frac{4}{5} \alpha_s g_{0,ss} (1 + e_{ss}) \right]^2 \quad (\text{Eq. 2.75})$$

(b.3) Frictional Viscosity

In dense flow at low shear rate, the generation of stress is mainly due to friction between particles when the secondary volume fraction for a solid phase approaches the packing limit. The frictional viscosity proposed by Schaeffer (1987) is realized in FLUENT:

$$\mu_{s,fr} = \frac{p_s \sin \phi}{s \sqrt{I_{2D}}} \quad (\text{Eq. 2.76})$$

where  $p_s$  is the solid pressure,  $\phi$  is the angle of internal friction, and  $I_{2D}$  is the second invariant of the deviatoric stress tensor.

#### (b.4) Bulk Viscosity

The solids bulk viscosity accounts for the resistance of the granular particles to compression and expansion. The form proposed by Lun et al. (1984) is available in FLUENT:

$$\lambda_s = \frac{4}{3} \alpha_s \rho_s d_s g_{0,ss} (1 + e_{ss}) \left( \frac{\Theta_s}{\pi} \right)^{1/2} \quad (\text{Eq. 2.77})$$

#### (D) SOLID-SOLID MOMENTUM EXCHANGE COEFFICIENT

The momentum exchange coefficient implemented in FLUENT is identical to the one used in MFIx. The detailed form of the equation can be found in the corresponding section for MFIx.

#### (E) GRANULAR TEMPERATURE

The granular temperature for the  $s^{\text{th}}$  solid phase is proportional to the kinetic energy of the random motion of the particles. The transport equation derived from kinetic theory takes the form:

$$\frac{3}{2} \left[ \frac{\partial}{\partial t} (\alpha_s \rho_s \Theta_s) + \nabla \cdot (\alpha_s \rho_s \vec{v}_s \Theta_s) \right] = (-p_s \bar{I} + \bar{\tau}_s) : \nabla \vec{v}_s + \nabla \cdot (k_{\Theta_s} \nabla \Theta_s) - \gamma \Theta_s + \phi_{ls} \quad (\text{Eq. 2.78})$$

where  $(-p_s \bar{I} + \bar{\tau}_s) : \nabla \vec{v}_s$  is the generation of energy by the solid stress tensor,  $k_{\Theta_s} \nabla \Theta_s$  is the diffusion of energy,  $\gamma \Theta_s$  is the collisional dissipation of energy, and  $\phi_{ls}$  is the energy exchange between the  $l^{\text{th}}$  fluid or solid phase and the  $s^{\text{th}}$  solid phase. When Syamlal et al. model is used, the diffusion coefficient for granular temperature is given by

$$k_{\Theta_s} = \frac{15\alpha_s \rho_s d_s \sqrt{\Theta_s \pi}}{4(41-33\eta)} \left[ 1 + \frac{12}{5} \eta^2 (4\eta-3) \alpha_s g_{0,ss} + \frac{16}{15\pi} (41-33\eta) \eta \alpha_s g_{0,ss} \right] \quad (\text{Eq. 2.79})$$

where

$$\eta = \frac{1}{2}(1 + e_{ss}) \quad (\text{Eq. 2.80})$$

Following expression is used if the model of Gidaspow is enabled:

$$k_{\Theta_s} = \frac{150\rho_s d_s \sqrt{\Theta_s \pi}}{384(1+e_{ss})g_{0,ss}} \left[ 1 + \frac{6}{5} \alpha_s g_{0,ss} (1+e_{ss}) \right]^2 + 2\rho_s \alpha_s^2 d_s (1+e_{ss}) g_{0,ss} \sqrt{\frac{\Theta_s}{\pi}} \quad (\text{Eq. 2.81})$$

The collisional dissipation of energy  $\gamma_{\Theta_s}$  is represented by the expression derived by Lun et al. (1984):

$$\gamma_{\Theta_m} = \frac{12(1-e_{ss}^2)g_{0,ss}}{d_s \sqrt{\pi}} \rho_s \alpha_s^2 \Theta_s^{3/2} \quad (\text{Eq. 2.82})$$

The transfer of the kinetic energy of random fluctuations in particle velocity from the  $s^{\text{th}}$  solid phase to the  $l^{\text{th}}$  fluid or solid phase is represented by  $\phi_{ls}$ :

$$\phi_{ls} = -3K_{ls} \Theta_s \quad (\text{Eq. 2.83})$$

FLUENT uses an algebraic relation for the granular temperature by neglecting convection and diffusion in the transport equation of granular temperature.

#### 2.6.6.4.3.3 CFX-10

##### (A) FLUID STRESS TENSOR

The fluid stress tensor CFX-10 is the same as those in MFX and FLUENT.

## (B) SOLID-FLUID MOMENTUM EXCHANGE COEFFICIENT

The drag models in CFX-10 is similar to those in FLUENT.

## (C) SOLID PRESSURE AND SOLID STRESS TENSOR

### (a) Solid Pressure

Earlier version of CFX (i.e. CFX-5) implements the Gidaspow Model (Gidaspow, 1994), in which the solid stress tensor is ignored and the solids pressure is assumed to be an empirical function of solid volume fraction,  $P_s = P_s(r_s)$ , so that:

$$\nabla P_s = G(r_s) \nabla r_s \quad (\text{Eq. 2.84})$$

where

$$G(r_s) = \frac{\partial P_s}{\partial r_s} \quad (\text{Eq. 2.85})$$

The Generalized Solids Elasticity Modulus proposed by Bouillard et al (1989) is implemented:

$$G(r_s) = G_0 \exp(c(r_s - r_m)) \quad (\text{Eq. 2.86})$$

where,  $G_0$  is Reference Elasticity Modulus and  $c$  is the Compaction Modulus. The default value for these two parameters are  $G_0 = 1 \text{ Pa}$  and  $c = 20 \sim 600$ .

In CFX-10, a solid pressure model based on kinetic theory was also included:

$$P_s = \rho_s \alpha_s \Theta_s (1 + 2(1 + e_{ss}) g_{0,ss} \alpha_s) \quad (\text{Eq. 2.87})$$

Where  $g_{0,ss}$  is the radial distribution function and  $\Theta_s$  is solid granular temperature, which is determined algebraically in CFX-10.

(b) Solid Stress Tensor

As mentioned in the above section, the solid stress tensor is ignored in CFX-10 if the Gidaspow Model for solid pressure is chosen. Users can implement their own solid stress tensor by writing User Subroutines for solid shear viscosity and bulk viscosity.

When Kinetic Theory Model is selected, the shear viscosity and bulk viscosity in solid stress tensor term are calculated based on the kinetic theory. The solids shear viscosity can be determined using the simple formula proposed by Miller and Gidaspow (1992):

$$\mu_s = 5.35\alpha_s \quad (\text{Eq. 2.88})$$

which leads to a solid shear viscosity in the unit of Poise. More complex model for shear viscosity can be obtained based on the following assumption that shear viscosity is the sum of collisional shear viscosity and kinetic shear viscosity as follows:

$$\mu_s = \mu_{s,col} + \mu_{s,kin} \quad (\text{Eq. 2.89})$$

As in FLUENT,  $\mu_{s,col}$  and  $\mu_{s,kin}$  are collisional shear viscosity and kinetic shear viscosity, respectively. The equations for these two forms of shear viscosity are exactly the same as those in FLUENT.

Summary of models and parameters available in CFX 5 and FLUENT 6 is presented in Table 2.

Table 2.3 Summaries of Models and Parameters in CFX 5 and Fluent 6.

Models	Submodels	CFX-5	Fluent 6	Comments
Euler-Lagrange Model	Momentum Equations	$\pi d^3 \rho_p \frac{dv_p}{dt} = \frac{1}{8} \pi \rho d^2 C_D  v_f - v_p  (v_f - v_p) + F_b$ $--- \frac{\pi d^3 (\rho_p - \rho_f) \omega \times (\omega \times \bar{R})}{3} - \frac{\pi d^3 \rho_p \omega \times v_p}{3}$	$\frac{dy}{dt} = F_y(t-u_p) + \frac{g(\rho_p - \rho)}{\rho_p} + F_x$	Unsteady problem can not be solved using CFX-5;
	Drag Model (solid-liquid)	<p>Stokes's law (<math>Re \ll 1</math>) <math>C_D = \frac{24}{Re}</math></p> <p>Newton's regime: <math>1000 \leq Re \leq 1 \sim 2 \times 10^5</math> <math>C_D = 0.44</math></p> <p>Schiller Naumann Drag Model <math>C_D = \frac{24}{Re} (1 + 0.15 Re^{0.687})</math></p> <p>WEN YU Drag Model</p> $C_D = r_c^{-1.65} \max \left( \frac{24}{Re}, (1 + 0.15 Re^{0.687}), 0.44 \right) \quad Re \leq r_c Re$ <p>Gidaspow Drag Model</p> $C_D = C_D(Wen Yu) \quad r_c > 0.8$ $e_{eff}^{(d)} = 150 \frac{(1-r_c)^2 \mu_c}{r_c d_p^2} + \frac{7(1-r_c) \rho_c  U_c - U_d }{4 d_p} \quad r_c < 0.8$	<p>Morsi and Alexander model <math>C_D = \alpha_1 + \frac{\alpha_2}{Re} + \frac{\alpha_3}{Re^2}</math></p> <p>Haider and Levenspiel <math>C_D = \frac{24}{Re} (1 + b_1 Re^{b_2}) + \frac{b_3 Re}{b_4 + Re}</math></p> <p>Cunningham correction to Stokes' drag law</p>	
	Turbulence Modeling	Turbulence dispersion model (Stochastic method): Gosman and Ioannides (1981)	Stochastic tracking model and particle cloud model	
	Virtual mass force	$F_c^{VM} = -F_d^{VM} = r_d \rho_c C_{VM} \left( \frac{D_d U_d}{Dt} - \frac{D_d U_c}{Dt} \right)$	$F_x = \frac{1}{2} \rho \frac{d}{dt} (u - u_p)$	
	Pressure gradient	$F_p = -\frac{1}{4} \pi d^3 \nabla P$	$F_x = \frac{\rho}{\rho_p} \frac{\partial u}{\partial x}$	
	Mass Transfer	$\frac{dm_c}{dt} = -\pi d \rho D Sh (m_F - m_{FQ})$ and $Sh = 2 + 0.6 Re^{0.5} \left( \frac{\mu}{\rho D} \right)^{1/3}$	Six physical laws available: inert heating or cooling, droplet vaporization, droplet boiling, devolatilisation, surface combustion	
	Heat Transfer	Convective, mass transfer, latent and radiative heat transfer		
	Other forces		Thermophoretic Force, Brownian Force, Sa man's Lift Force,	

Table 2.3 Summaries of Models and Parameters in CFX 5 and Fluent 6 (Continued)

Models	Submodels	CFX-5	Fluent 6	Comments
Eulerian Model	Momentum Equations	<p>Solid phase</p> $\frac{\partial}{\partial t}(\rho_s U_i) + \nabla_j(\rho_s U_j \otimes U_i) = -\tau_j \nabla_j - \nabla_j p_s + \nabla_j(\tau_j) + S_M + M_i$ <p>Liquid phase</p> $\frac{\partial}{\partial t}(\rho_l U_i) + \nabla_j(\rho_l U_j \otimes U_i) = -\tau_j \nabla_j + \nabla_j(\tau_j) + S_M + M_i$	<p>Fluid-Fluid momentum equations</p> $\frac{\partial}{\partial t}(\alpha_s \rho_s \bar{v}_i) + \nabla_j(\alpha_s \rho_s \bar{v}_j \bar{v}_i) = -\alpha_s \nabla_j p + \nabla_j \cdot \bar{\tau}_{ij} + \alpha_s \rho_s \bar{g}_i + \alpha_s \rho_s (\bar{F}_{ij} + \bar{F}_{ip,s} + \bar{F}_{m,s}) + \sum_{p=1}^N (K_{ps}(\bar{v}_p - \bar{v}_i) + m_{ps} \bar{v}_{sp})$ <p>Fluid-Solid momentum equations</p> $\frac{\partial}{\partial t}(\alpha_s \rho_s \bar{v}_i) + \nabla_j(\alpha_s \rho_s \bar{v}_j \bar{v}_i) = -\alpha_s \nabla_j p - \nabla_j p_s + \nabla_j \cdot \bar{\tau}_{ij} + \alpha_s \rho_s \bar{g}_i + \alpha_s \rho_s (\bar{F}_{ij} + \bar{F}_{ip,s} + \bar{F}_{m,s}) + \sum_{p=1}^N (K_{ps}(\bar{v}_p - \bar{v}_i) + m_{ps} \bar{v}_{sp})$	Only one continuous phase can be used in CFX while Fluent can simulate several solid phases dispersed in more than one fluid.
Drag Model (solid-liquid)		<p>Stokes's law (Re &lt; 1)</p> $C_D = \frac{24}{Re}$ <p>Newton's regime: <math>1000 \leq Re \leq 1 - 2 \times 10^5</math> <math>C_D = 0.44</math></p> <p>Schiller-Naumann Drag Model <math>C_D = \frac{24}{Re} (1 + 0.15 Re^{0.687})</math></p> <p>WEN YU Drag Model <math>C_D = r_c^{-1.65} \max\left(\frac{24}{Re}, (1 + 0.15 Re^{0.687}), 0.44\right)</math> <math>Re = r_c Re</math></p> <p>Gidaspow Drag Model <math>C_D = C_D(We_n Yr)</math> <math>r_c &gt; 0.8</math></p> $C_D = 150 \frac{(1 - r_c)^2 \mu_s}{r_c d_p^2} + \frac{7(1 - r_c) \rho_s  U_r - U_d }{4 d_p}$ $r_c < 0.8$	<p>Symahl-O'Brien Model <math>C_D = \left(0.63 + \frac{4.8}{\sqrt{Re_s / Y_r}}\right)^2</math></p> <p>WEN YU Drag Model <math>C_D = \frac{24}{\alpha_i Re_s} \left[1 + 0.15(\alpha_i Re_s)^{0.687}\right]</math></p> <p>Gidaspow Drag Model <math>C_D = \frac{24}{\alpha_i Re_s} \left[1 + 0.15(\alpha_i Re_s)^{0.687}\right]</math> <math>r_i &gt; 0.8</math></p> $K_{ij} = 150 \frac{\alpha_i \rho_i}{\alpha_j d_j^2} + 1.75 \frac{\rho_i \alpha_i}{d_j}  \bar{v}_i - \bar{v}_j $ $r_i < 0.8$	
Drag model (Liquid-Liquid)		Not applicable	<p>Schiller and Naumann Model <math>C_D = \begin{cases} 24(1 + 0.15 Re^{0.687}) / Re &amp; (Re \leq 1000) \\ 0.44 &amp; (Re &gt; 1000) \end{cases}</math></p> <p>Morsi and Alexander Model <math>C_D = \alpha_s + \frac{\alpha_s}{Re} + \frac{\alpha_s}{Re^2}</math></p> <p>Symmetry model <math>C_D = \begin{cases} 24(1 + 0.15 Re^{0.687}) / Re &amp; (Re \leq 1000) \\ 0.44 &amp; (Re &gt; 1000) \end{cases}</math></p>	Momentum transfer of fluid-fluid and solid is not modeled in CFX-5
Drag model (Solid-Solid)		Not modeled	$K_{ij} = \frac{3(1 + \epsilon_{ij})^2}{2} + C_{D,ij} \frac{\pi^2}{8} \rho_i \rho_j \alpha_i \alpha_j (d_i + d_j)^2 k_{s,ij} \frac{\pi^2}{2\pi(\rho_i d_i^2 + \rho_j d_j^2)}  \bar{v}_i - \bar{v}_j $	
Solid Shear Stress model		Solid shear stress $\tau_s$ is neglected.	$\tau_{ij} = 2\mu_s \epsilon_{ij} + \lambda_s \epsilon_{mm} \delta_{ij}$ $\mu_s = \mu_{s,rot} + \mu_{s,loc} + \mu_{s,p}$	

Table 2.3 Summaries of Models and Parameters in CFX 5 and Fluent 6 (Continued)

Models	Submodels	CFX-5	Fluent 6	Comments
			Collision viscosity: $\mu_{e,col} = \frac{4}{5} \alpha_i \rho_i d_i g_{0,im} (1 + e_{iz}) \left( \frac{\Theta_i}{\pi} \right)^{1/2}$	
			Kinetic viscosity: (Syamlal et al) $\mu_{s,kin} = \frac{10 \rho_i d_i \sqrt{\frac{\Theta_i}{\pi}}}{96 \alpha_i (1 + e_{iz}) g_{0,im}} \left[ 1 + \frac{4}{5} \alpha_i g_{0,im} (1 + e_{iz}) \right]^2$ (Gidaspow et al) $\mu_{s,kin} = \frac{\alpha_i \rho_i d_i \sqrt{\frac{\Theta_i}{\pi}}}{G(3 - e_{iz})} \left[ 1 + \frac{2}{5} (1 + e_{iz}) (3e_{iz} - 1) \alpha_i g_{0,im} \right]$	
			Frictional viscosity: $\mu_{i,f} = \frac{p_i \sin \phi}{s \sqrt{I_{2,D}}}$	
			Bulk viscosity: $\lambda_i = \frac{4}{3} \alpha_i \rho_i d_i g_{0,im} (1 + e_{iz}) \left( \frac{\Theta_i}{\pi} \right)^{1/2}$	
	Solid Pressure	$\nabla P_s = G(r_s) \nabla r_s \quad G(r_s) = \frac{\partial P_s}{\partial r_s}$ $G(r_s) = G_0 \exp(c(r_s - r_m))$	$P_s = \alpha_i \rho_i \Theta_i + 2 \rho_i (1 + e_{iz}) \alpha_i^2 g_{0,im} \Theta_i$	
	Lift force	$F_c^L = -F_d^L = r_d \rho_i C_L (U_d - U_c) \times \omega_c$	$\vec{F}_{\phi}^L = -0.5 \rho_i \alpha_i (\vec{v}_p - \vec{v}_p) \times (\nabla \times \vec{v}_p)$	
	Virtual mass force	$F_c^{VM} = -F_d^{VM} = r_d \rho_i C_{VM} \left( \frac{D_s U_d}{Dt} - \frac{D_s U_c}{Dt} \right)$	$\vec{F}_{vm} = 0.5 \rho_i \alpha_i \left( \frac{d \vec{v}_p}{dt} - \frac{d \vec{v}_p}{dt} \right)$	
	Granular temperature	Not applicable	$\frac{3}{2} \left[ \frac{\partial}{\partial t} (\alpha_i \rho_i \Theta_i) + \nabla \cdot (\alpha_i \rho_i \vec{v}_i \Theta_i) \right] = (-p_i \vec{I} + \vec{\tau}_i) : \nabla \vec{v}_i + \nabla \cdot (k_i \nabla \Theta_i) - \gamma \Theta_i + \phi_i$	
	Turbulence modeling	Mixture turbulence model: mixture properties and velocities are used  Dispersed turbulence model: modified k-ε model for continuous phase and Tchen-theory correlations for the disperse phases.	Homogeneous model: mixture properties and velocities are used	
	Interphase mass	Turbulence model for each phase: solves a set of k and ε transport equations for each phase.  Available in library	Phase-dependent turbulence model: each phase can use different turbulence model  Modeled in Fluent	

## 2.6.7 The State-of-The-Art of Multiphase CFD Modeling

Although CFD simulation of single-phase flow is satisfied, many problems in multiphase modeling are yet to be solved. The knowledge of physics for dilute multiphase flow is reasonable but inadequate for dense multiphase flow. Closure for interphase coupling for turbulent and dense dispersions is insufficient. Most constitutive relationship of the multiphase is based on empiricism and the interaction between and within the phases is not completely understood (Joshi et al., 2003). The models involve several parameters, which have to be determined from experiments. All of them affect the capability of CFD in simulating dense multiphase flow. However, attempts have been made to simulate the multiphase using CFD. Eulerian-Lagrangian and Eulerian-Eulerian approaches are used for simulating dilute and dense flows, respectively. It is still impossible to predict the flow regimes. The models are often calibrated without obtaining grid-independent result. Ad hoc models are used to simulate the influence of turbulence or other particles. There are some limitations with current models. Trajectory simulations in turbulent flows regarding drag coefficient, lift coefficient and virtual mass coefficient, turbulent dispersion of particles are not well understood. More research needs to be carried out on the turbulence caused by dispersed particles, momentum transport between different dispersed phases, agglomeration/coalescence/break-up processes and phase change.

### 2.6.7.1 Interactions between Phases

Interphase momentum transfer  $M_{ab}$  occurs due to interfacial forces acting on each phase  $\alpha$  due to interaction with another phase  $\beta$ . Several independent physical effects give rise to the total interfacial forces acting two phases: interphase drag force, lift force, wall lubrication force, virtual mass force, turbulence disperse force and particulate stress (solid contact force). Since other force is not significant in our research, drag force and particulate stress are outlined here only.

#### (a) Drag Force

The resistive, or drag, force experienced by a body moving relative to a fluid can be grouped as viscous drag (or skin friction) and the form drag, depending on the

whether the boundary layer has been separated or not (Wasp, 1977). Stoke first derived the drag force acting on a sphere in a fluid of infinite extent:  $C_D = R_e / 24$ . Wasp (1977) developed the general theory of drag coefficient for the flow outside Stokes regime. He obtained the relationship between drag coefficient and Reynolds number for sphere particles. Then the drag coefficient ( $C_D$ ) for the irregular shapes was investigated by Mcnown et al. (Mcnown 1950, Mcnown 1951). Shape factor was incorporated to account for the irregular shape of the particle. Albertson (1953) studied the effect of shape on gravel particles. He concluded that while it was unlikely that particle shape could ever be accounted for by a single parameter, a shape factor ( $S.F.$ ) of the form appeared to provide a satisfactory representation of particle shape, at least for the degree of refinement that currently exists on this project as a whole. Albertson also addressed the problem of characterization of both maximum-projected area and particle volume for irregular shaped particles, since in the flow regimes under study particles fall with the maximum projected area normal to the flow. He obtained a plot of drag coefficient versus particle Reynolds Number for particles of various shape factors.

The generalized plot of  $C_D$  versus  $R_e$  for irregular shaped particles was first obtained by U.S. Inter-Agency Committee on Water Resources (1957). Superimposed on the  $C_D$ - $R_e$  curves are additional parameters  $C_w$  and  $C_s$ , where  $C_w = (3C_D)/(4R_e)$  and  $C_s = (\pi C_D R_e^2)/8$ . The advantage of the plot is that any one variable of six, i.e. shape factor, fluid density and viscosity, particle density, nominal diameter, and fall velocity, can be determined from the plot.

Theoretically, the drag coefficient depends on particle Reynolds number. In a viscous regime where Reynolds number is less than 1,  $C_D = R_e / 24$  whereas the drag coefficient is independent of Reynolds number if particle Reynolds number is greater than 1000 and less than 100,000 (inertial regime). In the intermediary regime between viscous regime and inertial regime, both viscous and inertial effects are important. Experiments have been conducted to determine the coefficient. There are several empirical models applying for this transitional regime. One of them is proposed by Schiller and Naumann (1935) in the following form:  $C_D = 24(1 + 0.15R_e^{0.687})/R_e$  .

For concentrated solid particles, Wen and Yu (1966) proposed a model in the form similar to that by Schiller Naumann:  $C_D = r_c^{-1.65} \max(24(1 + 0.15R_e'^{0.687})/R_e', 0.44)$  where  $R_e' = r_c R_e$ . Gidaspow (1994) also proposed a model in which Wen Yu correlation is used for low solid volume fractions ( $r_d < 0.2$ ) and Ergun's law for flow in a porous medium is used for larger solid volume fractions. The model can be expressed as:

$$C_D = C_D (Wen Yu) \quad (r_c > 0.8) \text{ (Eq. 2.90)}$$

(Eq. 2.90)

$$C_D = C_D (Ergun) = 150(1 - r_d)^2 \mu_f / (r_c d_p^2) + 7(1 - r_d) \rho_c |U_c - U_d| / (4d_p) \quad (r_c < 0.8)$$

(Eq. 2.91)

### (b) Particulate Stress

Buyevich (1999) reviewed the progress as achieved to date in the matter of describing the particulate contact interaction between the particles in dense disperse flow. The author pointed out that the particulate stresses are of primary importance for highly dense suspension. Present practice (Lun et al, 1984; Johnson, 1987; Campell, 1990; Goldstein 1995) treats the particulate stresses in disperse flow in the same way as it has been done in the mechanics of granular flow. The disadvantage of such an approach is that it completely ignores a crucial difference in the physical mechanisms causing flow of granular system and of suspended particles. In granular flow, particles move due to externally applied shear stresses which are transmitted directly by interparticle contacts. In contrast, the continuous phases cause the flow of suspended particles through the drag and other interphase interactions (Buyevich, 1999).

Buyevich (1999) also summarized the primary mechanisms of generating particulate stress in a suspension. The first mechanism is the direct momentum transport over a transient network of particles separated by thin lubricating films of the intervening fluid. As a result, the apparent suspension viscosity is caused by its disperse phase.

The second mechanism that generates normal and tangential particulate stresses is random fluctuation of particles. The fluctuation is caused by the following three mechanisms:

- Their pair interactions as the particles are brought closer together and pass one another in mean shear flow;
- The relative fluid flow and an external body force field as they interact with random fluctuations of suspension concentrations; and
- Random macroscopic flow patterns, such as bubble rising in fluidized beds that produce a system of Reynolds-like stresses.

Buyevich (1999) then derived the particulate stresses caused by different physical mechanisms and factors. The formula was verified by the experimental data and a good agreement was shown.

Gidaspow (1994) proposed a solid pressure model, which is widely used in commercial CFD programs. In this model, solids stress tensor is ignored and solid pressure is assumed to be expressed as an empirical function of solid volume fraction  $P_s = P_s(r_s)$ , therefore,  $\nabla P_s = G(r_s) \nabla r_s$ , where  $G(r_s) = \partial P_s / \partial r_s$ . Bouillard et al. (1989) assumed the following functional form of the Generalized Solids Elasticity Modulus:  $G(r_s) = G_0 \exp(-c (r_s - r_m))$ , where  $G_0$  is the Reference Elasticity Modulus,  $c$  is the Compaction Modulus and  $r_m$  is the maximum packing parameter which is represented as  $\phi_m$  in some models.

Chen et al. (2002) proposed a procedure to avoid the void fraction below those realizable in practice. It is based on a computation of the particle-particle contact forces which come into play only when computed void fractions fall to values below those corresponding to random packing of the particles.

#### 2.6.7.2 Eulerian or Lagrangian Approach

Sundaresan (2000) stated that the most practical approach to simulating multi-phase flow is through continuum models that treat the coexisting phases as interpenetrating continua. The general structure of the continuity and momentum balance equations is the same for all dispersed two-phase flow problems, although the closure relationship

is system-dependent. This is rather convenient, as one can use a single general-purpose multi-phase CFD code for all the systems.

Snider et al. (1998) reviewed the mathematical models of particulate multiphase flow. It was found that either a continuum approach for all phases (Gidaspow, 1986; Batchelor, 1988) or a continuum for the fluid and a Lagrangian model for particle (Amsden et al., 1989) have been used. The continuum/continuum model readily allows modeling of particle-particle stresses in dense particle flow using spatial gradients of particulate volume fractions (Batchelor, 1988; Gidaspow, 1994). However, modeling a distribution of types and sizes of particles complicates the continuum formulation because separate continuity and momentum equations must be solved for each size and type (Risk, 1993; Gidaspow, 1994). Using a continuum model for the fluid phase and a Lagrangian model for the particle phase allows economical solution for flow with a wide range of particle type, sizes, shapes and velocities (O'Rourke, 1981; Gidaspow, 1994). However, the collision frequency is high for volume fraction above 5% and cannot be realistically resolved by current Lagrangian collision calculations (O'Rourke, 1981).

Goldschmidt et al (2002) reviewed the fundamental method to model the multiphase reactor. Broadly speaking two different types of hydrodynamic models can be distinguished, Eulerian (continuum) model and Lagrangian (discrete element) model. Both consider the gas phase as a continuum. The flow fields at sub-particle level are not solved and empirical equations are applied for fluid-particle drag.

Owing to the continuum description of the particulate suspension, Eulerian models require additional closure laws to describe particle-particle and/or particle-wall interactions. In most recent continuum models constitutive relations according to the kinetic theory of granular flow are incorporated. This theory is basically an extension of the classical kinetic theory of dense gases to particulate flows, which takes non-ideal particle-particle collisions and gas-particle drag into account.

Lagrangian (discrete particle) models on the contrary do not require additional closure for the suspended particulate phase, since they compute the motion of every individual

particle, taking collision and external force acting on the particle directly into account. However, the number of the particles that this model can handle (typically  $<10^6$ ) is always orders of magnitude lower than encountered in the fluidized beds. Therefore the continuum model consist of a more natural choice for hydrodynamic modeling of engineering scale systems, whereas discrete Particle Model can be applied as a valuable research tool to verify and further develop closure laws for these continuum models.

### 2.6.7.3 Turbulence Simulation

Turbulence consists of fluctuation of flow in space and time. Its main characteristics are three-dimensional, unsteady and consisting of many scales. When inertial effects predominate over viscous effects, turbulence will take place. According to its kinetic energy  $\kappa$ , three scales can be divided within the whole spectrum: the region where turbulence interact with the mean flow and extract energy from the mean flow; dissipation range where the turbulence is small and isotropic and kinetic energy is dissipated into a thermal energy; in-between is the inertial sub-range where energy coming from large turbulence is given off to the dissipation range.

Direct Numerical Simulation (DNS), Large Eddy Simulation (LES) and Reynolds Average Navier-Stoke Equation (RANS) are three methods used to simulate turbulence flow. Since Navier-Stoke equations describe turbulence, all length scales of turbulence can be solved. This method is called Direct Numerical Simulation (DNS) in which no averaging or approximation other than necessary numerical discretization is used. DNS capture all of the kinetic energy dissipation including Kolmogoroff scale; therefore, the size of the grid must be no larger than a viscously determined scale.

In contrast to DNS, Large Eddy Simulation (LES) aims to solve all the features on a length scale larger than a given value ( $\delta$ ) as the large scale motions are generally are much more energetic than the small scale one. Compared to DNS, LES is less accurate than DNS but much less costly, therefore LES is the preferred method for flows in which the Reynolds number is too high or the geometry is too complex for the application of DNS.

In most situations, only some time-average quantities interest engineers or prohibitive computer resource is not accessible. Therefore, attempts have been made to separate turbulence flow into time average and fluctuation parts and only time-average parts are solved. When inserting sum of time-average and fluctuation parts into Navier-Stoke equations, a closure problem induced. Introduction of Reynolds stress tensor needs a model to close. Many models applying this idea were proposed, which can be divided into four groups in general depending on the method to solve closure problem: Algebraic models, one-equation models, two-equation models and Reynolds stress models.

In the following sections, three methods are outlined and sub-models in each category will be briefed.

#### *2.6.7.3.1 Direct Numerical Simulation*

DNS solves Navier-Stoke equations without any approximation using turbulence model (Moin et al. 1998). The number of grid point in each coordinate direction has to be enough for Kolmogoroff scale to be solved. This limited the method to flow with low Reynolds number, even using the latest computer processor and memory (Moin et al. 1998). On parallel computers, Reynolds range can be extended greatly. The biggest DNS in the world, up to this date, used  $4096^3$  mesh points and was carried out in the Japanese Earth Simulator supercomputer in 2002 (Ishihara et al., 2007; Ishihara et al., 2009).

Quite a few applications of DNS in multiphase flow simulation can be found in literature presently. DNS of multiphase flows may help to understand some key issues: relating the distributor geometry and characteristics of generated dispersed-phase particles, extrapolation of cold flow data to higher temperature/pressures, and entrainment of the continuous phase due to bubble or drop collapse at the free surface. DNS may also be used to develop appropriate closure models for Eulerian-Eulerian approach. For relatively denser multiphase flows, where DNS becomes impractical to use, the Eulerian-Lagrangian approach is commonly used. For dense dispersed-phase flows, the Eulerian-Eulerian approach is used, in which appropriate closure models are needed (Moin et al., 1998; Joshi et al., 2003; Joseph, 2002).

### 2.6.7.3.2 Large Eddy Simulation (LES)

In LES, filtering (Leonard, 1974) is applied to extract the large-scale components from the total velocity field. The resolved large-scale field is essentially a local average of the complete field. After the Navier-Stoke equations are filtered, a set of equations similar in form to the RNAS equations is obtained (Ferziger et al., 1996). In order to maintain equality of the quantity, a term called subgrid scale Reynolds stress has to be incorporated to compensate the difference between two sides of the equations. Models are required to approximate the subgrid scale Reynolds stress.

#### (A) SMAGORINSKY AND RELATED MODELS

Subgrid scale model proposed by Smagorinsky (1963) is widely used (Ferziger et al., 1996). It is based on the assumption that SGS Reynolds stresses are proportional to the modulus of the strain rate and tensor of the filtered large-scale flow. The Smagorinsky model can be thought of as combining the Reynolds averaging assumptions given by  $L_{ij} + C_{ij} = 0$  with a mixing length based eddy viscosity model for the Reynolds SGS tensor. The subgrid scale eddy viscosity can be derived by dimensional analysis. The problem of this model occurs when flow near wall or surface is simulated and the model parameter  $C_s$  required to be modified. Van Driest damping that has been used in RANS models was an alternative to reduce the near-wall eddy viscosity.

Another choice is use the subgrid scale model that reduces the eddy viscosity when the subgrid scale Reynolds number becomes small (Ferziger et al., 1996). McMillan and Ferziger (1980) and Yakhot and Orszag (1986) proposed such kind of subgrid scale models.

There are many difficulties with Smagorinsky model. DNS result shows that Smagorinsky model is very poor (Ferziger et al., 1996).

Bardina et al. (1980) proposed a scale similarity model based on the idea that the small scales of a simulation are similar in many ways to the still smaller scales that are treated via the model. The main argument is that the significant interactions between the resolved and resolved scales involve eddies that are a little larger or a little smaller

than the length scale  $\Delta$  associated with the filter. This model correlates well with the actual SGS Reynolds stress but hardly dissipates any energy.

#### *(B) DYNAMIC MODELS*

If the idea underlying the scale similarity model is further extended, a dynamic model is introduced (Gernano et al. 1991). Idea is that supposing one of subgrid scale models is applicable one can compute the subgrid scale Reynolds stress tensor by filtering the velocity field and multiplying the procedure. From the large-scale field, estimation of the field can be obtained. The value of the model parameter can then be computed by comparing this two-subgrid scale Reynolds stress tensor. This model solves the difficulties associated with Smagorinsky model. Disadvantage of this model is that numerical instability may occur when negative eddy viscosity is too large. An alternative is to use mixed Smagorinsky-scale-similarity model (Zang et al. 1993; Shah and Ferziger 1995). In addition, wall function similar to that used in RANS modeling is used in LES (Piomelli et al., 1989).

#### *2.6.7.3.3 RANS Models*

In Reynolds averaged Navier-Stoke models, all unsteadiness are regarded as part of the turbulence. Due to the occurrence of Reynolds stress tensor, model is required to close the problem.

##### *(a) Algebraic Models*

Boussinesq assumption is used in this model. It assumed that the Reynolds stresses are a function of velocity gradients and turbulence viscosity. By dimension analysis, the turbulence viscosity is expressed in term of turbulence scale and velocity gradients. In this model, mixing length must be determined. This model is outdated and rarely used now (Davidson, 2003).

##### *(a.1) One Equation Models*

In one-equation models, a transport equation is often solved for turbulent kinetic energy. The unknown turbulence length scale must be given and often an algebraic expression is used. The advantage of this type of model is that it is not applicable to

general flow. Some proposals have been made where the turbulence length scale is computed in a more general way (Davidson, 2003).

#### (a.2) Two Equation Models

In this kind of models, two transport equations are derived which describe the transport of two scalars, for example the turbulent kinetic energy and its dissipation. The Reynolds tensor is computed using Boussinesq assumption.

Wall boundaries need to be treated specially in these models. Sharp gradient near the wall boundaries requires complex three-dimensional flow computation, therefore, a large volume of computer resource. An alternative is to assume that flow near wall behaves like a fully developed turbulent boundary layer. Wall function is employed for the boundary condition.

There are several models depending on the scalar solved in the transport equations. In  $\kappa - \varepsilon$  Model the modeled transport equations are that for turbulent kinetic energy  $\kappa$  and its dissipation  $\varepsilon$ . In  $\kappa - \omega$  Model transportation equations for turbulent kinetic energy and its specific dissipation  $\omega$  are solved. Another model is  $\kappa - \tau$  Model in which the transport equation for the turbulent time scale  $\tau$  is solved (Davidson, 2003).

#### (b) Low-Re Number Turbulence Model

In some situation the flow near the boundary is very important so the wall function is not suitable. Low Reynolds number models should be used, in which high Reynolds number models are modified such that it can be used all the way down to the wall. Low-Re  $\kappa - \varepsilon$  Model, Launder-Sharma Low-Re  $\kappa - \omega$  Model, Two-Layer  $\kappa - \varepsilon$  Models, Low-Re  $\kappa - \omega$  Model can be grouped into Low-Re Number Turbulence Model (Davidson, 2003).

#### (c) Reynolds Stress Models

In this kind of models a transportation equation for the stress tensor is derived from the Navier-Stoke equation and Boussinesq assumption is not used. This is done in the same way as for the turbulent kinetic energy equation (Davidson, 2003).

Whenever non-isotropic effects are important RSMs should be used. Advantages with RSMs is the production terms need not to be modeled and it can selectively argument or damp the stresses due to curvature effects, acceleration/retardation, swirling flow, buoyancy etc. Disadvantages include complexity, numerical instability and CPU consuming.

Eddy viscosity models have the advantages of simplicity, numerical stability and suitability for a large number of engineering flow problems. Disadvantages with eddy viscosity models are that they are isotropic and not good in predicting normal stresses and are unstable to account for curvature effects and irrotational strain.

## **2.7 Conclusions**

Oil sand tailing slurry is composed of clay, silt, sand, bitumen and water. Similar to the rheological properties of clay-sand-water mixture, the rheological properties of the oil sands are mainly controlled by the mixture of clay-water, probably influenced by the presence of bitumen. The sedimentation and segregation of the oil sand tailings are controlled by the solids and fines contents of the slurry and essentially by the rheological properties of the clay-water mixture.

CFX and FLUENT 6 are two most widely used commercial CFD packages, both of which have the capability to model multiphase flow. The most significant difference between the two packages lies in the way how to treat solid-solid interaction. In FLUENT-6, the solid-solid interaction is accounted for by considering the collision, friction, kinetic and bulk viscosity of the solid particles. In CFX-5, only solid pressure is modeled in order to prevent the volume fraction of the solid particles from exceeding certain limit. Latest version 10 of CFX has the similar capability to model the solid-solid interaction, in addition to the simplified model inherited from CFX-5. The open-source CFD code MFIx has similar features as in FLUENT except only structured mesh is allowed in MFIx.

## Reference

- Alberta Chamber of Resources. Oil Sands Technology Roadmap: Unlocking the Potential. January 30, 2004.
- Albertson, M. L., Effects of Shape on the Fall Velocity of Gravel Particles. Proc. 5th Iowa Hyd. Conf., Iowa, 1953.
- ANSYS Inc., CFX 5.6 User Manual, 2003.
- ANSYS Inc., CFX 5.7 Solver Theory, 2004.
- ANSYS Inc., CFX 10 Solver Theory, 2005.
- AMEC. Analysts and investors Visit - Canadian Oil Sands Presentation, July 2007. [http://www.amec.com/investors/presentations/presentations\\_2007.htm](http://www.amec.com/investors/presentations/presentations_2007.htm).
- Amsder, A.A., O'Rourke, P.J., and Butler, T.D., KIVA-II: A computer program for chemically reactive flows with sprays. LA-11560-MS, Los Alamos National Laboratory, 1989.
- Arnarson, B. O. and Jenkins, J. T. Particle Segregation in the Context of the Species Momentum Balance. Traffic in Granular Flows '99: Social, Traffic, and Granular Dynamics, Edited by Helbing, D., Hermann, H. J., Schreckenberg, M., and Wolf, D. E. Springer, Berlin, 1999. p.1.
- Arnarson, B. O. and Willits, J. T. Thermal Diffusion in Binary Mixtures of Smooth, Nearly Elastic Spheres with and without Gravity. Phys. Fluids, vol. 10, p. 1324, 1998.
- Astarita, G., et Marrucci, G. Principles of non-Newtonian fluid mechanics. McGraw Hill, New York, 1974.
- Bardina, J., Ferziger, J.H., Reynolds, W.C., Improved subgrid scale models for large-eddy simulations. Am. Inst. Aeronaut. Astronaut, Paper 89-1357.
- Barnes, H.A., Jomha, A.I., Lips, A., Merrington, A., and Woodcock, L.V. Recent developments in dense suspension rheology. Powder Technology, vol. 65, pp. 343-370, 1991.
- Bates, P.D., Lane, S.N., and Ferguson, R.I., Computational Fluid Dynamics Modeling for Environmental Hydraulics. In: Computational fluid dynamics, edited by Bates, P.D., Lane, S.N., and Ferguson, R.I., pp. 7 -14. John Wiley & Sons, Ltd. 2005.

- Batchelor, G.K., A new theory of the instability of a uniform fluidized bed. *Journal of Fluid Mechanics*, vol. 193, pp. 75-110, 1988.
- Batchelor, G.K., and Green, J.T. The determination of the bulk stress in a suspension of spherical particles to order  $c^2$ . *J. Fluid Mechanics*, vol.56, p.375, 1972.
- Boerger, H., MacKinnon, M., Meer, T.V., and Verbeek, A., 1992. Wet Landscape Option for Reclamation of Oil Sands Fine Tailings. *Proceedings of Second International Conference on Environmental Issues and Management of Waste in Energy and Minerals Production*, edited by Singhal R.K., A.K. Mehrotra, K. Fytas, and J-L Collins. A.A. Balkema. Rotterdam, pp. 1249-1261.
- Bouillard, J. X., Lyczkowski, R. W., and Gidaspow, D, Porosity Distribution in a Fluidized Bed with an Immersed Obstacle, *AIChE J.*, 35, 908-922, 1989.
- Bridgewater, J. *Powder Technol.* Vol. 15, p. 215-236m 1976.
- Bridgewater, J., Sharpe, N. W. and Stoker, D. C., *Trans. Inst. Chem. Engng* 47, T114-T119 (1969).
- Buyevich, Y.A., Particulate Stress in Dense Disperse Flow, *Ind. Eng. Chem. Res.*, vol. 38, pp. 731-743, 1999.
- Campell, C.S., Rapid Granular Flow, *Annual Rev. Fluid Mech.*, 1990, 22, 57.
- Carrier III, W.D., Bromwell, L.G., and Somogyi, F. Design Storage of Capacity of Slurried Mineral Waste Ponds. *ASCE Journal of the Geotechnical Engineering Division*, 109 (GT2): 699-716, 1983.
- Chalaturnyk, R. J. and Scott, J. D. Soil Structure Behavior Diagram. *Proceedings of High Density and Paste Tailings 2001 Seminar*, University of the Witwatersrand, South Africa, May 10 – 11, 2001.
- Chen, W., and Scott, K. J. Sedimentation. In *Handbook of Powder Science and Technology*, 2<sup>nd</sup> edn, ed. M.E. Fayed and L. Otten, Chapman & Hall, NY, 1997, pp. 635 – 683.
- Chen, Z., Gibilaro, L. G. and Jand, N., Particle packing constraints in fluid-particle system simulation, *Computers and Chemical Engineering*, Vol.27, Issue 5, 681-687, 2002.

- Chong, J.S., Christiansen, E.B., and Baer, A.D., Rheology of Concentrated Suspensions, *J. Appl. Polymer Sci.*, 152007-2021, 1971.
- Coussot, P. and Ancey, C., Rheophysical Classification of Concentrated Suspensions and Granular Pastes, *Physical Review E*, Vol. 59, Number 4, April 1999.
- Coussot, P. and Piau, J.M. On the behavior of fine mud suspensions. *Rheol. Acta*, 33, 175-184, 1994a.
- Coussot, P. Rheology of debris flows - Study of concentrated dispersions and suspensions. Ph.D Thesis, INPG, Grenoble.1992. (in French)
- Coussot, P. Structural similarity and transition from Newtonian to Non-Newtonian behavior for water-clay suspension. *Phys. Rev. Lett.*, vol. 74, pp. 3971-3974, 1995.
- Coussot, P., and Piau, J.-M. A larger-scale field coaxial cylinder rheometer to study the rheology of natural coarse suspensions. *J. Rheol.*, vol. 39, vol. 105-124, 1995.
- Coussot, P., and Boyer, S. Determination of yield stress fluid behavior from inclined plane test. *Rheol. Acta*, 34, 534-543, 1995.
- Coussot, P., and Piau, J.-M. Rheology of very concentrated suspensions of force-free particles. *Les Cahiers de Rheologie (Groupe FranFais de Rheologie)*, XIII, 266-277, 1994. (in French)
- Coussot, P., Leonov, A.J. and Piau, J.-M. Rheology of concentrated dispersed systems in a low molecular weight matrix. *J. Non-Newt. Fluid Mech.*, vol.46, pp. 179-217, 1993.
- Coussot, Philippe, *Mudflow Rheology and Dynamics*, 1997, A.A.Balkema.
- Dahl, S. R. and Hrenya, C. M. Size Segregation in Rapid, Granular Flows with Continuous Size Distributions. *Physics of Fluids*, vol. 16, No. 1, January 2004.
- Dalla Valle, J.M., *Micromeritics*, Pitman, London, 1948.
- Davidson, L. *An Introduction to Turbulence Models*. Chalmers University of Technology, Sweden, 2003.  
[http://www.tfd.chalmers.se/~lada/postscript\\_files/kompendium\\_turb.pdf](http://www.tfd.chalmers.se/~lada/postscript_files/kompendium_turb.pdf)
- Davies, R. and Kaye, B. H., Experimental Investigation into Settling Behavior of Suspensions. *Proceedings of Powtech '71: International Powder Technology & Bulk Granular Solids Conference*, 1971.

- de Silva, S., A. Dyroy, (1999). Segregation Mechanism and Their Quantification using Segregation Testers. Proceedings of the IUTAM Symposium on Segregation in Granular Flows, Cape May, NJ, Kluwer Academic Publishers.
- Deer Creek Energy Limited, Joslyn North Mine Project Application, Section B “Project Description”, B.5-1 – B.5-4, February 2006.
- Einstein, A., Investigation of the Brownian Movement, Dever Publication, New York, 1956. [English translation of Ann. Physik, 19, 286, 1906, et 34, 591, 1911]
- Eskin, D. and Kalman, H., A Numerical Parametric Study of Size Segregation in a Rotating Drum. Chemical Engineering and Processing, vol. 39, p. 539-545, 2000.
- Fair, A., The Past, Present and Future of Tailings at Syncrude. Presentation on the First International Oil Sands Tailings Conference, Edmonton, Alberta, Canada, December 7, 2008. <http://www.ostrf.com/seminars>.
- Ferraris, C., Larrard, F.D., and Martys, N., Fresh Concrete Rheology: Recent Developments, Material Sciences of Concrete VI, Edited by S. Mindess and J.Skalny, The American Ceramic Society, 2001, 215-241.
- Ferziger, J.H and Peric, M, Computational Methods for Fluid Dynamics, Springer, New York, 1996.
- Ferziger, J.H., and Peric, M., Computational Methods for Fluid Dynamics, 2<sup>nd</sup> edit., Springer-Verlag, New York, 2002.
- FLUENT Inc., FLUENT 6.1 User Guide. Chapter 20 Introduction to Modeling Multiphase Flow; Chapter 21 Discrete Phase Model; Chapter 22 General Multiphase Models. February 2003.
- Frankel, N. A., and Acrivos, A. On the viscosity of a concentrated suspension of solid spheres. Chem. Eng. Sci., vol.22, pp.847-853, 1967.
- FTFC (Fine Tailings Fundamental Consortium), 1995. In: Advances in Oil Sands Tailings Research, Alberta Department of Energy, Oil Sands and Research Division.
- Garside, J., and Al-Dibouni, M.R., Velocity-Voidage Relationships for Fluidization and Sedimentation. I&EC Proc. Des. Dev., 16, 206-214, 1977.

- Germano, M., Piomelli, U., Moin, P., Cabot, W.H., A dynamic subgrid-scale eddy viscosity model. *Physics of Fluids A – Fluid Dynamics*, vol. 3, issue 7, pp. 1760-1765, 1991.
- Gidaspow, D., Bezburuah, R., and Ding, J. Hydrodynamics of Circulating Fluidized Beds, Kinetic Theory Approach. In *Fluidization VII, Proceedings of the 7th Engineering Foundation Conference on Fluidization*, p. 75-82, 1992.
- Gidaspow, D., Hydrodynamics of fluidization and heat transfer: supercomputer modeling. *Applied Mechanics Review*, vol. 39, pp. 1 -22, 1986.
- Gidaspow, D., *Multiphase Flow and Fluidization*, Academic Press, 1994.
- Goldschmidt, M. J. V., Beetstra, R. and Kuipers, J. A. M. Hydrodynamic modeling of dense gas-fluidized beds: Comparison of the kinetic theory of granular flow with 3D hard-sphere discrete particle simulations, *Chemical Engineering Science*, Vol. 57, Issue 11, pp. 2059-2075, June 2002.
- Goldstein, A., Shapiro, M., *Mechanics of Collisional Motion of Granular Material, Part 1: General Hydrodynamic Equations*, *J. Fluid Mech.*, 1995, 282, 75.
- Gray, D.D., and Stiles, J.M. On the Constitutive Relation for Frictional Flow of Granular Materials. Topical Report, DOE/MC/21353-2584, NTIS/DE88001089, National Technical Information Service, Springfield, VA, 1988.
- Haff, P. K. and Werner, B. T. *Powder Technol.* Vol.48, p. 239-245, 1986.
- Hanratty, T. J., Theofanou, T., Delhay, J., Eaton, J., McLaughlin, J., Prosperetti, A., Sundaresan, S., and Tryggvason, G., Workshop Finding. *International Journal of Multiphase Flow*, vol. 29, p.1047-1059, 2003.
- Hawksley, P. G. W., Survey of the Relative Motion of Particles and Fluids. *Br. J. App. Phys.*, vol. 5, p. S1-S5, 1954.
- Hsiau, S. S. and Hunt, M. L. Granular Thermal Diffusion in Flows of Binary-sized Mixtures. *Acta Mech.* Vol. 114, p. 121, 1996.
- Hu, G., and Fang, Z. Antithixotropic model for fluid with hyperconcentration of sediment. Proc. Int. Workshop on Flow of Hyperconcentrations and Sedimentation, Beijing, China, 1.3, IRTCES Publication, I-9, 1985.

- Ishihara, T, Gotoh, T., and Kaneda, Y. Study of High-Reynolds Number Isotropic Turbulence by Direct Numerical Simulation. *Annual Review of Fluid Mechanics*, vol. 41, pp. 165-180, 2009.
- Ishihara, T., Kaneda, Y., Yokokawa, M., Itakura, K., and Uno, A. Small-scale Statistics in High-resolution Direct Numerical Simulation of Turbulence: Reynolds Number Dependence of One-point Velocity Gradient Statistics. *J. Fluid Mech.*, vol. 592, pp. 335–366, 2007.
- Jeffery, G.B., The Motion of Ellipsoidal Particles Immersed in a Viscous Fluid, *Proc. R. Soc. London*, A102, 161-179, 1922.
- Jenkins, J. T. Particle Segregation in Collisional Flows of Inelastic Spheres, *Physics of Dry Granular Media*, edited by Hermann, H. J., Hovi, J. P. and Luding, S. Kluwer, Dordrecht, 1998, p.645.
- Jenkins, J.T., and Yoon, D.K., Segregation in binary mixtures under gravity. *Physical Review Letters*, vol. 88, issue 19, pp. 194301, 2002.
- Johnson, P.C., Jackson, R., Frictional-Collisional Constitutive Relations for Granular Material with Application to Plane Shearing. *J. Fluid Mechanics*, 1987,176, 67.
- Joseph, D. D. Interrogations of Direct Numerical Simulation of Solid-Liquid Flows. University of Minnesota, 2002.  
[Http://www.efluids.com/efluids/books/joseph.htm](http://www.efluids.com/efluids/books/joseph.htm).
- Joshi, J. B., and Ranade, V.V. Computational fluid dynamics for designing process equipment: Expectations, current status, and path forward. *Industrial & Engineering Chemistry Research*, Vol. 42, pp. 1115-1128, 2003.
- Jullien, R. and Meakin, P. *Europhysics Letter*, vol. 6, p. 629-634, 1988.
- Jullien, R. and Meakin, P. A mechanism for particle size segregation in 3 dimensions. *Nature*, vol. 344, issue 6265, pp. 425-427, March 29, 1990.
- Kaye, B. H., and Boardman, R. P., Cluster Formation in Dilute Suspensions. *Proc. Symp. Interaction Between Fluids and Particles*, Inst. Chem. Engr. A17-21, 1962.
- Knight, J.B., Jaeger, H.M., and Nagel S.R., Vibration Induced Granular Segregation in Granular Media: the Convection Connection. *Phys. Rev. Lett.* 70:3728-31, 1993.

- Khakhar, D.V., McCarthy, J.J., and Ottino, J.M., Radial segregation of granular mixtures in rotating cylinders. *Physics of Fluids*, vol. 9, issue 12, pp. 3600 – 3614, 1997.
- Koch, D.L., and Hill, R.J., Inertial effects in suspension and porous-media flows. *Annual Review of Fluid Mechanics*, vol. 33, pp. 619-647, 2001.
- Koglin, B., Dynamic Equilibrium of Settling Velocity Distribution in Dilute Suspension of Spherical Irregularly Shaped Particles. *Proceedings of the Conference on Particle Technology*, IIT Research Institute of Chicago, pp. 266-271, August 21-24, 1973.
- Kundu, P.K., and Cohen, I.M. *Fluid Mechanics*, second edition. Academic Press, 2002 (page 52).
- Leonard, A., Dissipation of turbulent energy and scalar variance in large eddy simulations of turbulent flows. *Transactions – American Geophysical Union*, vol. 55, issue 3, pp. 137-138, 1974.
- Louge, M. Y., Jenkins, J. T., Xu, H. and Arnarson, B. O., Granular Segregation in Collisional Shearing Flows. *Mechanics for a New Millennium*, edited by Aret, A. and Philips, Kluwer Academic, Dordrecht, 2000, p. 239.
- Luding, S., Strauss, O. and Mcnamara, S. Segregation of Polydisperse Granular Media in the Presence of a Temperature Gradient. *IUTAM Symposium on Segregation in Granular Flows*, edited by Rosato, A. D. and Blackmore, D. L. Kluwer Academic, Dordrecht, 2000, p. 297.
- Lun, C. K. K., Savage, S. B., Jeffrey, D. J., and Chepuruiy, N. Kinetic Theories for Granular Flow: Inelastic Particles in Couette Flow and Slightly Inelastic Particles in a General Flow Field. *J. Fluid Mech.*, vol. 140, p.223-256, 1984.
- McMillan, O.J., and Ferziger, J.H., Tests of new subgrid scale models in strained turbulence, *AIAA Pap.* 80-1339, 1980.
- Mcnown, J.S. and Malaika, J., Effects of Particle Shape on Settling Velocity at Low Reynolds Numbers, *Trans. Amer. Geophys. Union*, V. 31 (1950).
- Mcnown, J.S., Malaika, J. and Pramanik, H., Particle Shape and Settling Velocity, *Pro. In. Asso. Hyd. Res.*, 4th Meeting, Bombay, Indian (1951).

- Mewis, J., and Spaul, A.J.B. Rheology of concentrated dispersions. *Adv. Colloid Interface Sci.*, vol. 6, pp. 173-200, 1976.
- Miller, A., and Gidaspow, D., Dense, vertical gas flow in a vertical pipe. *AICHE Journal*, vol. 38, issue 11, pp. 1801-1815, 1992.
- Mills, P. and Snabre, P. Rheology and Structure of Concentrated Suspensions of Hard Spheres. Shear Induced Particle Migration. *J. Phys. II (Paris)*, pp. 1597, vol. 5, 1995.
- Moin, P. and Mahesh, K. Direct Numerical Simulation: A Tool in Turbulence Research. *Annu. Rev. Fluid Mech.* Vo. 30, pp539–78, 1998.
- Moore, F. The rheology of ceramic slips and bodies. *Trans. Brit. Ceram. Soc.*, 58, 470-492, 1959.
- National Energy Board. *Canada's Oil Sands: Opportunities and Challenges to 2015.* Canada, May 2004.
- Navickis, L.L., and Bagley, E.B. Yield stresses in concentrated dispersions of closely packed, deformable gel particles. *J. Rheol.*, vol. 27, pp. 519-536, 1983.
- Neumann, B.S., and Sansom, K.G. The rheological properties of dispersions of laponite, a synthetic hectorite-like clay, in electrolyte solutions. *Clay Minerals*, 9, 231-243, 1971.
- Olhero, S.M. and Ferreira, J.M.F. Influence of Grain size distribution on Rheology and Particle Tracking of Silica-based Suspensions. *Powder Technology*, vol. 139, p. 69-75, 2004.
- O'Rourke, P.J., Collective drop effects on vaporizing liquid sprays. Ph.D thesis, Princeton University, 1981.
- Perry, R. H., and Green, D., *Chemical Engineer's Handbook*, 6th edit., McGraw-Hill, New York, pp. 5-64, 1984.
- Piomelli, U., Ferziger, J., Moin, P., Kim, J., New Approximate boundary conditions for large eddy simulations of wall-bounded flows. *Phys. Fluids*, vol. 1, pp. 1061-1068, 1989.
- Pitman, B., and Schaeffer, D. Stability of Time Dependent Compressible Granular Flow in Two Dimensions. *Comm. Pure Appl. Math.*, 40, 421-447, 1987.

- Proudman, I, and Pearson, J.R.A., Expansions at Small Reynolds Numbers for the Flow Past a Sphere and a Circular Cylinder. *J. Fluid Mech.* Vol. 2, p. 237-262, 1957.
- Quemada, D. Phenomenological rheology of concentrated dispersions: I. Clustering effects and structure-dependent packing fraction. *J. Theor. Appl. Mech., Numéro Spécial*, pp. 267-288, 1985.
- Ranz, W. E. Some Experiments on Orifice Sprays. *Canadian Journal of Chemical Engineering*, p. 175, 1958.
- Rhie, C.M., Chow, W.L., A numerical Study of Turbulent Flow Past an Isolated Airfoil with Trailing Edge Separation. *AIAA J.*, 21 1525-2532, 1983.
- Richardson, J. F., and Zaki, W. N., Sedimentation and Fluidization: Part 1. *Trans. Inst. Chem. Eng.* Vol. 32, p.35-53, 1954.
- Risk, M.A., Mathematical modeling of densely loaded particle laden turbulent flows. *Atomization and Sprays*, vol. 3, pp. 1-27, 1993.
- Roberts, J.O.L., Yong, R.N. and Erskine, H.L. 1980. Surveys of Some Tar Sand Sludge Ponds: Results and Interpretations. *Proceedings of Applied Oil Sands Geoscience 1980 Conference*, Edmonton, Alberta, June 11-13, p.46.
- Rosato, A., Prinze, F., Standburg, K.J., and Sevensen, R., Why Brazil Nuts Are On Top: Size Segregation of Particulate Matter by Shaking. *Physical Review Letter*, vol. 58, p. 1038-40, 1987.
- Sundaresan, S. Modeling the Hydrodynamics of Multiphase Flow Reactors: Currents Status and Challenges. *AIChE Journal Perspective*, vol. 46, No. 6, pp. 1102-1105, 2000.
- Schaeffer, D. G. Instability in the Evolution Equations Describing Incompressible Granular Flow. *J. Di. Eq.*, vol. 66, p.19-50, 1987.
- Schiller, L. and Naumann, Z. *Z. Ver. Deutsch. Ing.*, 77 : 318, 1935.
- Shah, K.B., Ferziger, J., A new non-eddy viscosity subgrid-scale model and its application to channel flow, in: *CTR Annual Research Briefs 1995*, Center for Turbulence Research, Stanford University and NASA Ames Research Center, Stanford CA 1995.

- Simha, R. A treatment of the viscosity of concentrated suspension. *J. Appl. Phys.*, vol. 23, p. 1020-1024, 1952.
- Smagorinsky, J., General circulation experiments with the primitive equations: I. The basic experiment. *Mon. Weather Rev.*, vol. 91, pp. 99-164, 1963.
- Snider, D. M., O'Rourke, P. J., and Andrews, M. J., Sediment Flow in Inclined Vessels Calculated Using a Multiphase Particle-In-Cell Model for Dense Particle Flows. *International Journal of Multiphase Flow*, vol. 24, p. 1359-1382, 1998.
- Stokes, C. G., On the Effect of the Internal Friction of Fluids on the Motion of Pendulums. *Trans. Cambridge Philos. Soc.* Vol. 9 (II), p. 8-106, 1851.
- Sundaresan, S., Eaton, J., Koch, D. L., and Ottino, J. M., Appendix 2: Report of Study Group on Dispersed Flow. *International Journal of Multiphase Flow*, vol.29, pp.1069-1087, 2003.
- Syamlal, M, and O'Brien, T.J., A generalized drag correlation for multiparticle systems, unpublished report, 1987.
- Syamlal, M., Rogers, W., and O'Brien T.J., MFIx Documentation Theory Guide. U.S. Department of Energy, Morgantown Energy Technology Center, Technical Note DOE/MET-94/1004 (1993).
- Trujillo1, L., Alam, M. and Herrmann, H. J. Segregation in a fluidized binary granular mixture: Competition between buoyancy and geometric forces. *EUROPHYSICS LETTERS*, vol. 64, pp. 190-196, October 2003.
- Tu, J., Yeoh, G. H., and Liu, C. *Computational Fluid Dynamics: A Practical Approach*. pp 6 – 24. Elsevier Inc., 2008.
- U.S. Inter-Agency Committee. Some fundamentals of particle size analysis. A study of methods used in measurement and analysis of sediment loads in streams. Subcommittee on Sedimentation. U.S. Inter-Agency Committee on Water Resources, Report No. 12, St. Anthony Fall Hydr. Lab., Minneapolis, Minn., 1957.
- Verburg, R. B. M. Use of Paste Technology for Tailings Disposal: Potential Environmental Benefits and Requirements for Geochemical Characterization. *Proceedings of International Mine Water Association*, pp. 1-13. Belo Horizonte, Brazil, 2001.

- Wan, Z. Bed material movement in hyperconcentrated flow. Series Paper 31, Inst. of Hydrodynamics and Hydr. Eng., Tech. Univ. of Denmark, 1982.
- Wang, Z., Larsen, P., and Xiang, W. Rheological properties of sediment suspensions and their implications. *J Hydr. Res.*, 32, 560-580, 1994. .
- Wasp, E. J., Kenny, J. P., and Gandhi, R. L. Solid-Liquid Flow Slurry Pipeline Transportation. Series on Bulk Material Handling, vol. 1, No. 4, 1st edit., 1977.
- Wen, C.-Y. and Yu, Y. H. Mechanics of Fluidization. *Chem. Eng. Prog. Symp. Series*, 62:100-111, 1966.
- Williams, J.C., The segregation of powders and granular materials. *Fuel Soc. J.*, vol. 14, pp. 29-34, 1963.
- Williams, R. A., Amarasinghe, and W. P. K., Simons, Measurement and Simulation of Sedimentation Behavior of Concentrated Polydisperse Suspensions. *Trans. Instn Min. Metal.*, vol. 98, C68-C82, 1989.
- Williams, R. A., Amarasinghe, W. P. K., Simons, S. J. R., and Xie, C. G., Sedimentation Behavior of Complex Polydisperse Suspensions. *Powder Technology*, vol. 65, p. 411-432, 1991.
- Yakhot, V., Orszag, S.A., Renormalization group analysis of turbulence I. Basic theory. *J. Sci. Computing*, vol. 1, issue 3, 1986.
- Zang, Y., Street, R.L., Koseff, J.R., A dynamic mixed subgrid-scale model and its application to turbulent recirculating-flows. *Physics of Fluids A – Fluid Dynamics*, vol. 5, issue 12, pp. 3186-3196, 1993.

### 3.1 Measurement of the Rheological Properties of Tailing Slurry

#### 3.1.1 Introduction

The aim of the rheometry is to determine the rheological properties of material subject to continuous deformations at a macroscopic scale (Coussot, 1997). As a consequence, discontinuity in shear strain field and material heterogeneities should be prevented. Furthermore, a theoretical flow within the rheometer has to be assumed in order to deduce the rheological properties of the material from measurements. Ideally, a perfectly homogeneously flow field with specific boundary conditions should be formed between viscometric tools.

Rheology is the study of the deformation and flow of matter. Accurate determination of the rheological properties of the oil sand slurry is of importance to numerical simulation of the behavior of the slurry. Tailing slurry belongs to particulate fluids which demonstrate complex rheological properties such as yield stress and/or thixotropy. Classification of the particulate fluids into settling and non-settling slurry is useful to understand the rheological properties of the fluids. According to whether their viscosities vary with shear strain rate, the suspensions also can be classified as Newtonian and Non-Newtonian fluid. Non-Newtonian flows are the focus of this study and the major features of non-Newtonian fluid behaviour in shear are as follows:

#### 1. Time-independent non-Newtonian fluids

In this category the rheological equation is given by

$$\frac{du}{dy} = \dot{\gamma} = f(\tau) \quad (\text{Eq. 3.1})$$

Where  $u$  is velocity,  $\dot{\gamma}$  the shear strain rate, and  $\tau$  the shear stress.

---

<sup>1</sup> A version of part of this chapter has been published. Yang, J. and Chalaturmyk, R.J., Development of Rheological Model for Computational Fluid Dynamics Simulation of Sand Deposition into MFT. Proceedings of the 57<sup>th</sup> Canadian Geotechnical Conference, Quebec, Canada, October 19- 22, 2004.

The viscosity of the fluids is a function of shear strain rate and is independent of time. According to the change of shear stress and viscosity with shear strain rate, three distinct types of fluids can be subdivided as follows and they are shown in Figure 3.1:

- (i) Bingham plastic
- (ii) Pseudo-plastic fluids
- (iii) Dilatant fluids

## 2. Time-dependent fluids

For such fluids the viscosity depends not only on the rate of shear but also on the time when the shearing has been applied. These fluids are subdivided into two classes based on the trends of the variation of viscosity with time:

- (i) Thixotropic fluids: As shown in the left figure in Figure 3.2, the viscosity decreases with duration of shearing due to breakdown of the structure by shear. Thixotropic materials are those whose consistency depends on the duration of shear as well as on the rate of shear.
- (ii) Rheopectic fluids: The variation of viscosity with time was shown in the right figure in Figure 3.2. Formation of structure by shear occurs in these fluids.

The apparent viscosity is the ratio of shear stress to the shear strain rate. Concentrated tailing slurry also possesses yield stress, which is defined as the critical shear stress that must be exceeded before irreversible deformation and flow to occur. Tailing suspension also demonstrates shear-thickening or shear-thinning and thixotropy (Danielson et al., 1999). Shear-thinning refers to the property of the fluid to show a decreasing viscosity with increasing shear rate. Shear-thickening or dilatant material exhibits an increase in viscosity with increasing shear rate. Thixotropy refers to the time dependence of rheological properties (yield and viscosity) on time.

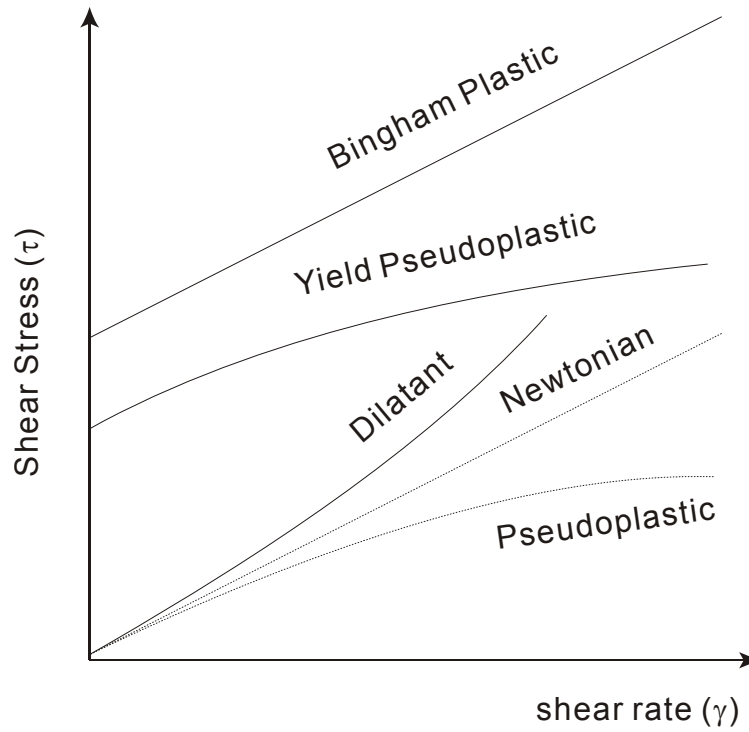


Figure 3.1 Shear stress – shear rate curves for typical time independent Non-Newtonian fluids (after Wasp et al., 1977)

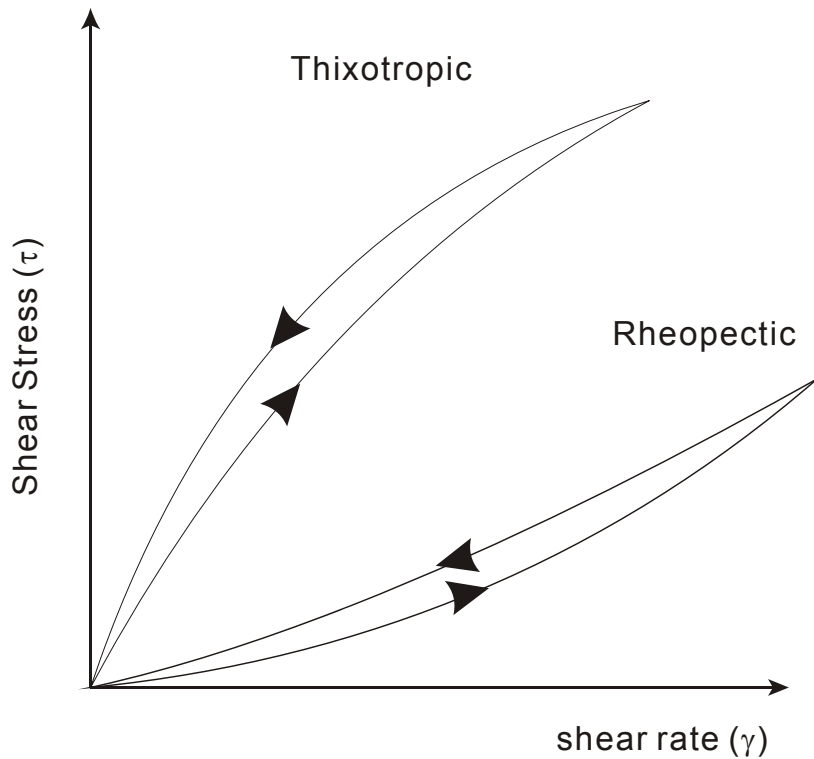


Figure 3.2 Shear diagrams for thixotropic and rheopectic fluids (after Wasp et al., 1977)

For the different fluid categories, various empirical flow models are used to describe the flow behavior. Ostwald-De Waele model, Bingham model and Herschel Bulkley model are among the most widely used equations:

1. Ostwald-De Waele (de Waele, 1923; Ostwald, 1925) or Power Law model:

$$\tau = k\dot{\gamma}^n \quad (\text{Eq. 3.2})$$

Where  $\tau$  is shear stress,  $\dot{\gamma}$  the strain rate, and  $k$  is a parameter defining the measure of consistency (viscosity). The bigger is  $k$  the more viscous is the fluid. The parameter  $n$  defines the measure of distortion of a fluid from the Newtonian fluid (Gonet et al., 2004).

2. Bingham model (Bingham, 1916):

$$\tau = \tau_B + \eta_B \dot{\gamma} \quad (\text{Eq. 3.3})$$

where  $\tau_B$  is yield point and  $\eta_B$  is plastic viscosity.

3. Herschel Bulkley model (Herschel and Bulkley, 1926):

$$\tau = \tau_{HB} + k\dot{\gamma}^n \quad (\text{Eq. 3.4})$$

Where  $\tau_{HB}$  is the yield point.

4. Casson model (Casson, 1959):

$$\tau^{1/2} = \tau_c^{1/2} + (\eta_c \dot{\gamma})^{1/2} \quad (\text{Eq. 3.5})$$

Where  $\tau_c$  is yield point, and  $\eta_c$  is Casson's viscosity.

Danielson et al. (1999) studied the rheological properties of Syncrude tailing pond slurry with solids content ranging from 10% to 50%. The authors found that shear thickening behavior were demonstrated up to shear rates of  $\sim 32 \text{ sec}^{-1}$  after which the slurry shows shear-thinning behavior. They also found that the upper yield stress (the maximum of the flow curve at low shear rates) of the slurry increased with undisturbed

time in the viscometer, indicating the thixotropic nature of the sludge. Based on the time-dependent rheological properties of the slurry, they argued that the time-dependent structure formation occurs in sludge quite rapidly after stirring. An interesting finding of this research is that the yield strengths (upper and Bingham) and fluid viscosity (at  $2770 \text{ sec}^{-1}$ ) are strongly correlated with the square of the total solids and the total solids content of the sludge. They found that the mineral solids were the only significant parameter in the linear multiple regression equation. This statement contradicted the argument by Scott et al. (1985) that the yield stress of the sludge is attributed to its bitumen contents. Yong et al. (1981) did not find a simple relationship between the fines contents and the measured yield stress in sludge. In the following sections, the apparatus, samples, procedures and the test results will be presented.

### 3.1.2 Apparatus, Samples and Procedures

#### 3.1.2.1 Apparatus

The slurry viscosity is measured using a Brookfield DV-II+ Programmable Viscometer (Figure 3.3). The tests were carried out by controlling the shear strain rates. Cylindrical spindles with designation of SC4-27/13R (RV) are used for these tests. The range of the viscosity for this spindle is 125 - 2,500,000 cp with an error of  $\pm 1\%$  of full scale. It is designed to be used with a disposable Small Sampler Adaptor. The cylinder spindle has a diameter of 11.76 mm with effective length of 33.02 mm. The Small Sample Adaptor (SC4-13RD) has an inner diameter of 19.05 mm and depth of 67.9 mm. As a result, the gap between the spindle and the Adaptor is 3.645 mm. Coussot (1997) discussed the required dimensions of the measuring tools. For coaxial cylinders the minimum gap is 30 times of the particle characteristic diameter. If we assume that the largest diameter of the particles in the mixture of MFT and sand is 0.8 mm, the gap between two coaxial cylinders has to be greater than 24 mm. For the case of MFT with no addition of sand, the minimum gap should be larger than 6 mm if a particle characteristic diameter of 0.2 mm is assumed. For sand-silt-clay-water mixtures, a special large device (O'Brien and Julien, 1988) may be required. The small space between the spindle and the sample adaptor will significantly disturb the viscosity measurement when the largest particle size is considered. For this reason, a beaker of 500 ml capacity is used in the measurement. The inner diameter of the beaker is 81.30

mm. The temperature is controlled by Therмосel and all the measurements are made at room temperature of 20 Celsius degree.



Figure 3.3 Brookfield DV-II+ Programmable Viscometer



Figure 3.4 Brookfield R/S Soft Solid Rheometer

A Brookfield R/S Soft Solid Rheometer (Figure 3.4) is used in this study to measure the yield stress of the slurry. Three vanes with length-diameter (in millimeter) ratio of 2 are used in the experiments: V30-15, V40-20 and V80-40. According to the operation manual, selection of the vane is based on the consideration of working torque ranges, vane-to-container diameter ratios and the clearance between the lower end of the vane and the base of the container. A vane-to-container diameter of less than 0.75 is desired for the vane measuring method. And an ample clearance should be ensured when measuring large-particle suspensions. As mentioned in the manual, reliable range of 3% (or 1.5 mNm) to 100% (or 50 mNm) torque has to be guaranteed in operating the SST2000 Rheometer. In all the vane tests, a 400-ml beaker is used to contain the samples.

### 3.1.2.2 Samples

The material used in the experiments is MFT slurry with various solids contents and fines contents by weight (Table 3.2) and is shown in Figure 3.5. The fines content remained identical for all the yield stress measurements in an effort to exclude the influence of this variable on the measured yield stress. Slurry with different solids contents is produced by mixing MFT from Syncrude's tailing pond with different volumes of pond release water. Pond release water is used to ensure aqueous chemistry is unchanged in the specimens. The grain size distribution of MFT is shown in Figure 3.6. The samples of MFT contain 40.2% solids content and 94.5% fines content. The MFT is centrifuged to obtain a material with solids content of 60.5% and fines content of 95.4%. In case a slurry with solids content greater than 40.2% and fines content of less than 94.5, the centrifuged MFT is used to prepare the samples. In some cases, the sand with grain size distribution shown in Figure 3.7 is added into MFT in order to increase the sand: fine ratio in the mixture.

Table 3.1 The Source Materials and Corresponding Solids and Fines Contents

Material	Solids Content (%)	Fines Content (%)
MFT	40.2	94.5
Coarse Sand	82.0	4.8
Release Water	0.0	0.0
Centrifuged MFT	60.5	94.5

Table 3.2 Matrix of Samples for Viscosity and Yield Stress Measurements

Test Series	Materials	Test Types	Solids Content (%)	Fines Content (%)	Sands: Fines Ratio (SFR)	Fines Water Ratio (FWR)
1	MFT+Sand+Water	V, Y	66	37	1.7	0.5
2	MFT+Sand+Water	V, Y	65	32	2.1	0.5
3	MFT+Sand+Water	V, Y	43	75	0.3	0.6
4	MFT+Sand+Water	V, Y	52	60	0.7	0.6
5	MFT+Sand	V, Y	40	94	0.1	0.6
6	Centrifuged MFT	V, Y	61	95	0.1	0.7
7	Diluted Centrifuged MFT	V, Y	50	95	0.1	0.7
8	MFT+Sand (5:1)	V, Y	49	68	0.5	0.6
9	MFT+Sand (10:1)	V, Y	51	78	0.3	0.6
10	MFT+Sand (20:1)	V, Y	49	86	0.2	0.6
11	Only MFT	V, Y	41	95	0.1	0.6
12	MFT+Sand+Water	Y	19	24	3.2	0.2
13	MFT+Sand+Water	Y	25	49	1.0	0.4
14	MFT+Sand	Y	27	94	0.1	0.6

Where:

Solids Content = Mass of Solids / (Mass of Solids + Mass of Water)

Mass of Solids = Mass of Fines + Mass of Sands

Fines Content = Mass of Fines / (Mass of Fines + Mass of Sands)

Sands Fines Ratio (SFR) = Mass of Sands / Mass of Fines

Fine Water Ratio (FWR) = Mass of Fines / (Mass of Fines + Mass of Water)

Fines = Solids with grain size less than 44 micron

Sands = Solids with grain size greater than 44 micron

V = Viscometer Tests

Y = Vane Shear Tests

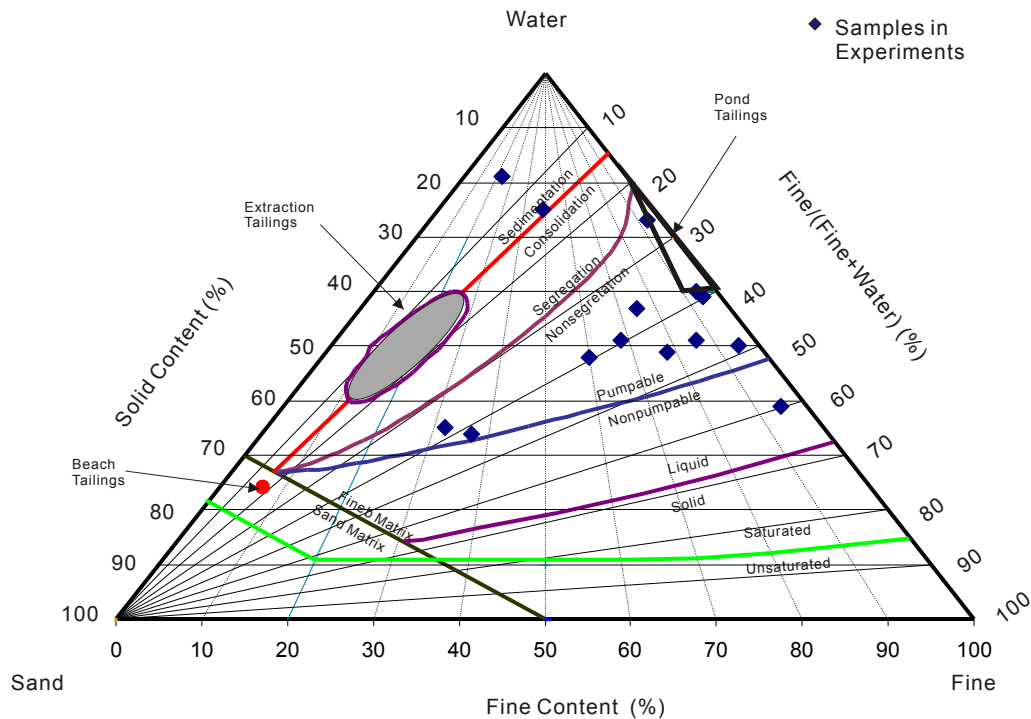


Figure 3.5 Sample Matrix on Tailing Properties Diagram (based on Chalaturnyk and Scott, 2001; Azam & Scott, 2005)

### 3.1.2.3 Procedures

#### 3.1.2.3.1 Procedures for Viscosity Measurements

Following procedures are followed for the viscosity measurements using Brookfield DV-II+ Programmable Viscometer (Brookfield Operation Manual):

1. Mount the guard leg on the DV-II+ Viscometer (RV series).
2. Zero the reading by removing the spindle and hooks and pressing any key.
3. The sample is mixed in a 500-ml beaker until a homogeneous mixture is reached. The sample then is rested for 2 minute. Insert and center the spindle in the test material until the fluid level is at the immersion groove on the spindle shaft. Attach the spindle to the lower shaft of the viscometer. Lift the shaft slightly, holding it firmly with one hand while screwing the spindle on with the other (note left-hand thread). Avoid putting side thrust on the shaft. Verify the proper spindle immersion depth and that the viscometer is level.

4. Select a spindle and corresponding speed by trial and error method. An important rule is that the torque reading has to be in the range of 10% and 100% of maximum torque. Viscosity range is inversely proportional to the size of the spindle and the rotational speed. Small spindle and/or a slow speed can be used to measure high viscosity. Reducing the spindle speed or choosing a smaller spindle will help to avoid a reading above 100%. Any combination of the spindle and speed can be chosen if a satisfactory result between 10-100% is obtained. Non-Newtonian fluid behaviour can result in the measured viscosity changing if the spindle and or speed are changed. Allow time for the indicated reading to stabilize. The time required for stabilization will depend on the speed at which the Viscometer is running and the characteristics of the sample fluid. For maximum accuracy, readings below 10% should be avoided.
5. Press the MOTOR ON key to start a test. The tests are started from lowest RPM and the speed is increased step by step. The measurements started with lowest shear strain rate (or RPM) and then the speed of the rotation is increased gradually until the percentage of maximum torque approaches 100%. The data is transferred from the apparatus to a laptop using Hyper Terminal under Windows XP OS. The motor “OFF” when changing a spindle or changing samples. Remove spindle before cleaning.
6. Interpret the measurement results. The measured data are imported into Excel worksheets. The calculation of the shear strain rate and shear stress are carried out according to Brookfield (2005):

$$\gamma = \frac{2\omega R_c^2 R_b^2}{x^2 (R_c^2 - R_b^2)} \quad (\text{Eq. 3.6})$$

$$\tau = \frac{M}{2\pi R_b^2 L} \quad (\text{Eq. 3.7})$$

where  $\omega$  is the angular velocity of the spindle (rad/sec),  $R_c$  and  $R_b$  the diameter (cm) of the container and the spindle respectively,  $x$  the radius at which the shear strain rate is calculated,  $M$  the torque input by the instrument (dyne/cm), and  $L$  the effect length of

the spindle. The angular velocity of the spindle can be calculated by  $\omega = \frac{2\pi N}{60}$  where  $N$  is RPM of the spindle. The torque  $M$  can be calculated based on the full scale torque of the RV spring  $M = M_f p/100$  where  $p$  is the percent of the torque in the reading.

#### *3.1.2.3.2 Procedures for Yield Stress Measurements*

The procedures for the measurement of the yield stress by vane tests are as follows.

1. The prepared MFT slurry is mixed for 3 minutes prior to the viscometer measurement in order to obtain a homogeneous clay-water matrix. The slurry is allowed to rest for 2 minutes in order to preclude the effects of fluid movement on the measured yield stress. Effects of segregation of the slurry on the yield stress value are neglected due to its high fines content. In order to determine the yield stress, a constant shear rate test is run, in which the vane is rotated at a constant low rotational rate (typically 0.1 to 0.5 rpm) and torque or stress is measured against time, rotational angle or strain.
2. The measurement of the yield stress is controlled by Rheo2000 software remotely. After the rheometer is connected to the computer, the software is started up by clicking Rheo2000 software icon. The communication between the rheometer and the computer would be checked and then the required test method is selected by clicking Load Program File in which the Step Time in seconds and number of measurement points are set in advance.
3. The vane spindle is also selected prior to the measurements.
4. The sample is mixed and then is placed on the center of the base plate. It is fixed in place with the clamps.
5. The instrument head is lowered by pushing down on the periscope handles so that the vane enters the sample to the required depth.
6. The test runs for the period that is specified in measurement method after clicking OK.

Vane method is the most accurate method to measure the yield stress. This method is similar to the field vane shear tests in soil mechanics. The conventional approach

employed in soil mechanics assumes that the material yields along a cylindrical surface having an area of  $\pi DH + 2(\pi D^2/4)$ , where  $D$  and  $H$  are diameter and length of the vane, respectively. Also the shear stress is assumed to be uniformly distributed everywhere on the cylinder, and equal to the yield stress  $\tau_y$  when the torque is at maximum  $T_m$  (Dzuy and Boger, 1983, 1985.)

The relationship between  $\tau_y$ ,  $T_m$  and the vane dimension is obtained as

$$T_m = \frac{\pi D^3}{2} \left( \frac{H}{D} + \frac{1}{3} \right) \tau_y \quad (\text{Eq. 3.8})$$

In addition, measurements are made with the vane immersed at various depths into the suspension sample, and thus allowance must be made for the extra shearing surface area  $\pi D_s L$ , where  $D_s$  is the shaft diameter and  $L$  is the excess immersed depth beyond the blade height  $H$ . According to Turian et al (1993), for an immersed depth,  $L$ :

$$T_m = \left[ \frac{\pi D^3}{2} \left( \frac{H}{D} + \frac{1}{3} \right) + \frac{\pi D_s^3}{2} \left( \frac{L}{D_s} - \frac{1}{6} \right) \right] \tau_y \quad (\text{Eq. 3.9})$$

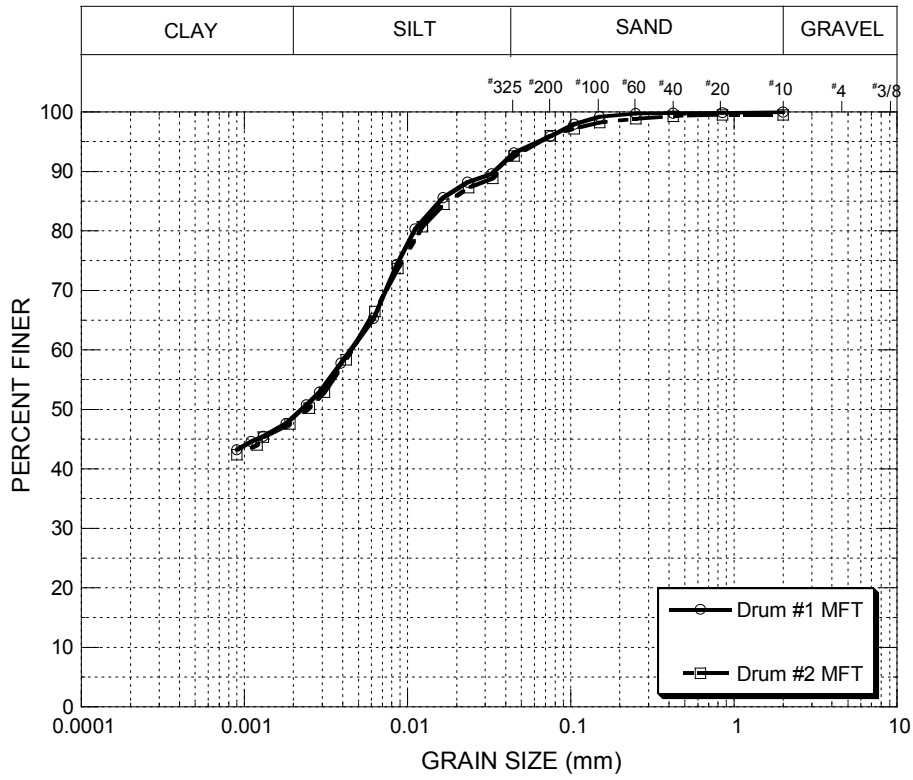


Figure 3.6 Grain size distribution of MFT from Syncrude

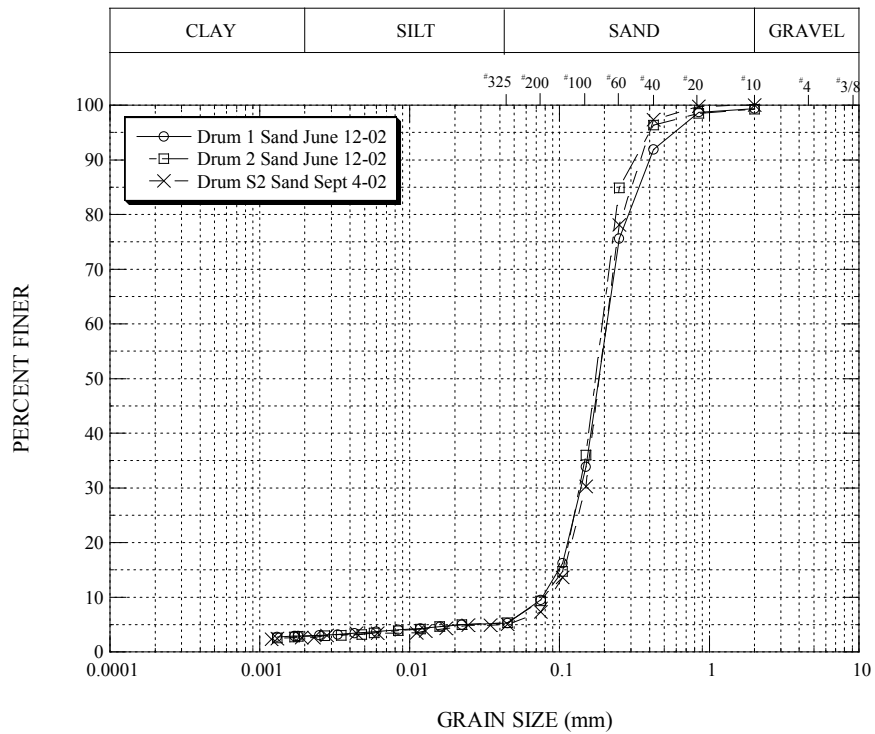


Figure 3.7 Grain size distribution of Cyclone Underflow Sand from Syncrude

### 3.1.3 Test Results

In this section, the results of viscometer tests and vane shear tests for each sample are presented. For each sample, the viscosity measurements results are shown first followed by the yield stress test results provided that both tests lead to meaningful results and the measured torques are within 10% - 100% of maximum torque for that equipment. As for the vane shear tests, the shear stress as calculated in Eq. 3.8 are plotted against shear strain for each sample. The raw data of measured torque vs. shear strain are included in Appendix A.

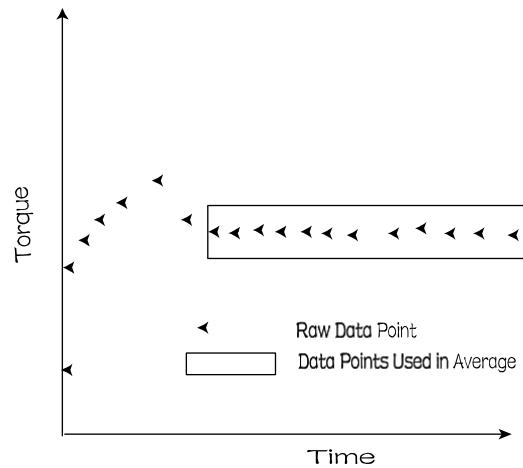


Figure 3.8 Illustration for typical plot of torque vs. time and the data points used to obtain averaged torque

As illustrated in Figure 3.8 typically the torque will fluctuate immediately after the rotation speed is changed in viscometer tests. It will level out after a period of time. The constant torque is used to calculate the shear stress on the cylinder spindle. In cases nearly constant torque is not obtained, the torque data, consequently the shear stress data, for the corresponding shear rate is omitted. All the raw data for the torque variation with time for viscometer tests is included in Appendix A.

#### 3.1.3.1 Test 1: Slurry with Solids Content of 66% and Fines Content of 37%

The raw data for this test can be found in Figure A.1. The change in shear stress with shear strain for the vane shear test is demonstrated in Figure 3.9. The variation of the shear stress and apparent viscosity with shear rate for the viscometer test are presented

in Table 3.3 and the corresponding plots of shear stress vs. shear rate and apparent viscosity vs. shear rate are shown in Figure 3.10 and Figure 3.11.

Table 3.3 Calculated Shear Stress and Apparent Viscosity for Slurry with s%=66 and f%=37

RPM	Strain Rate (1/s)	Average Shear Stress (Dyne/cm <sup>2</sup> )	Viscosity (cp)	Shear Stress (Pa)	Viscosity (Pa.s)
0.03	0.006	178.1	2776754.4	17.8	2776.8
0.05	0.011	175.1	1637552.3	17.5	1637.6
0.07	0.015	175.0	1169144.1	17.5	1169.1
0.09	0.019	171.4	890508.4	17.1	890.5
0.1	0.021	170.0	795284.4	17.0	795.3
0.2	0.043	175.6	410724.7	17.6	410.7
0.3	0.064	187.9	292996.9	18.8	293.0
0.4	0.086	205.6	240445.4	20.6	240.4
0.6	0.128	218.7	170476.0	21.9	170.5
0.8	0.171	155.8	91091.6	15.6	91.1
1	0.214	230.5	107821.0	23.1	107.8
2	0.428	249.6	58365.7	25.0	58.4
40	8.552	337.8	3950.2	33.8	4.0
120	25.657	407.6	1588.6	40.8	1.6

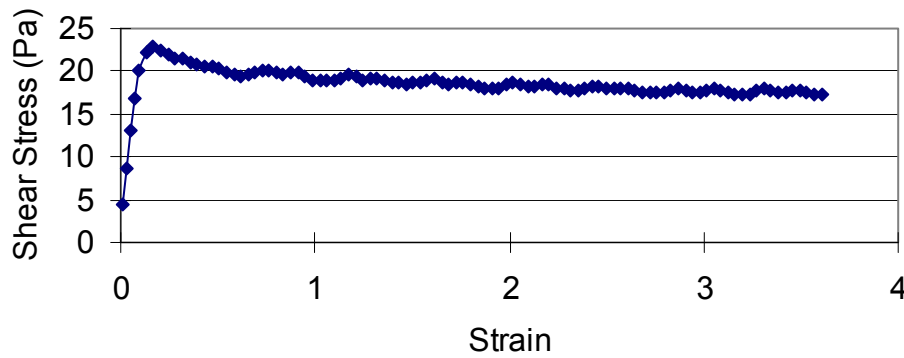


Figure 3.9 Shear Stress vs. Strain for Mixture with s% = 66 and f% = 37 in the Vane Shear Tests (Vane 80-40, Constant Strain Rate=0.03 s<sup>-1</sup>)

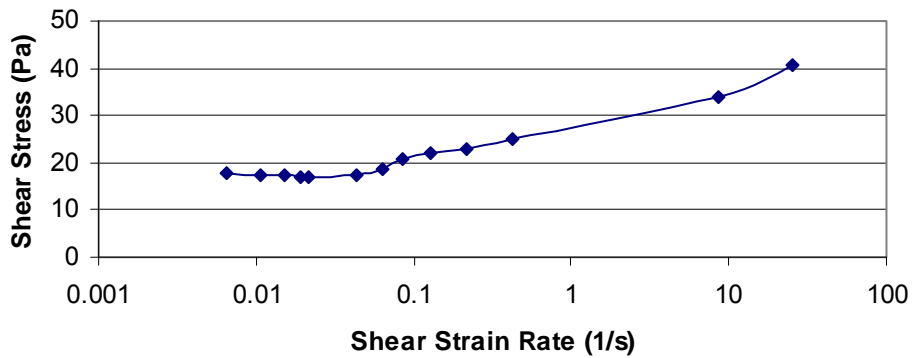


Figure 3.10 Plot of Shear Stress vs. Shear Rate in Semi-Log Scale for Slurry with s%=66 and f%=37

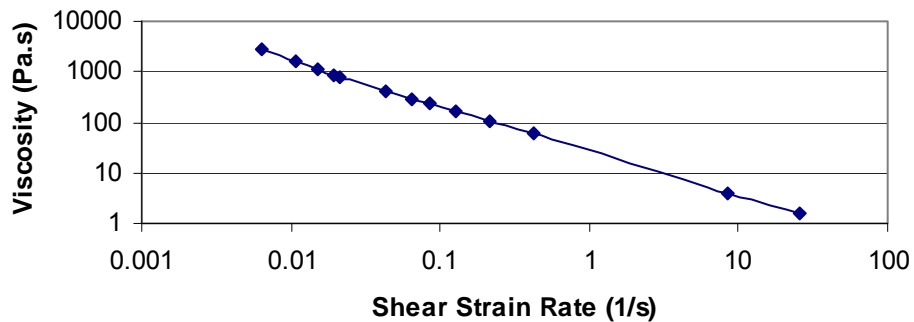


Figure 3.11 Plot of Apparent Viscosity vs. Shear Rate in Log-Log Scale for Slurry with s%=66 and f%=37

### 3.1.3.2 Test 2: Slurry with Solids Content of 65% and Fines Content of 32%

The raw data for this test can be found in Figure A.2. The change in shear stress with shear strain for the vane shear test is demonstrated in Figure 3.12. The variation of the shear stress and apparent viscosity with shear rate for the viscometer tests are presented in Table 3.4 and the corresponding plots of shear stress vs. shear rate and apparent viscosity vs. shear rate are shown in Figure 3.13 and Figure 3.14.

Table 3.4 Calculated Shear Stress and Apparent Viscosity for Slurry with s%=65 and f%=32

RPM	Strain Rate (1/s)	Average Shear Stress (Dyne/cm <sup>2</sup> )	Viscosity (cp)	Shear Stress (Pa)	Viscosity (Pa.s)
0.05	0.011	173.6	1624280.3	17.4	1624.3
0.07	0.015	174.6	1166786.9	17.5	1166.8
0.09	0.019	172.4	895839.4	17.2	895.8
0.1	0.021	170.5	797503.7	17.1	797.5
0.2	0.043	175.8	411066.3	17.6	411.1
0.3	0.064	188.2	293443.1	18.8	293.4
0.4	0.086	205.6	240445.4	20.6	240.4
0.6	0.128	217.9	169851.6	21.8	169.9
0.8	0.171	224.1	131015.1	22.4	131.0
1	0.214	229.8	107457.7	23.0	107.5
2	0.428	249.7	58397.6	25.0	58.4
40	8.552	337.9	3950.9	33.8	4.0
120	25.657	410.6	1600.2	41.1	1.6

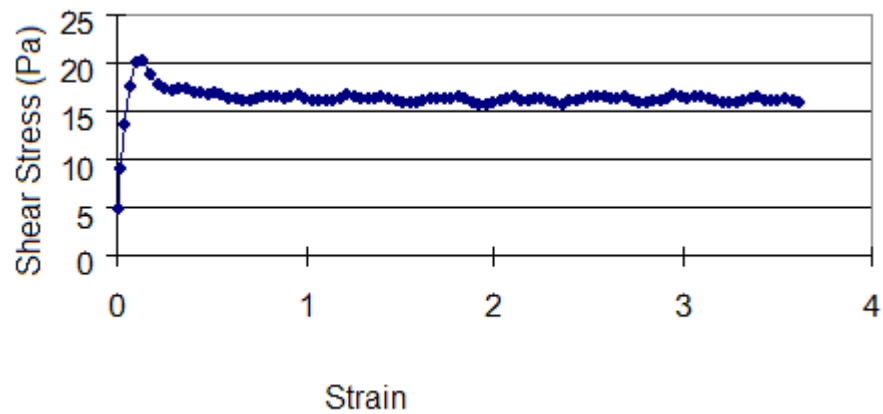


Figure 3.12 Shear Stress vs. Strain for Mixture with s% = 65 and f% = 32 (Vane 80-40, Constant Strain Rate=0.03 s<sup>-1</sup>)

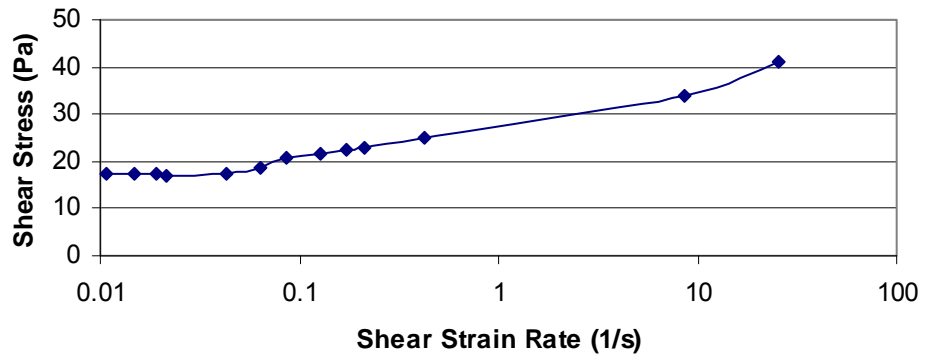


Figure 3.13 Plot of Shear Stress vs. Shear Rate in Semi-Log Scale for Slurry with s%=65 and f%=32

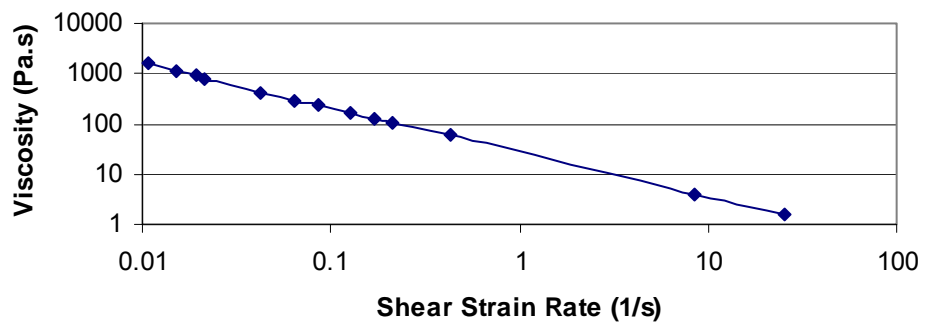


Figure 3.14 Plot of Apparent Viscosity vs. Shear Rate in Log-Log Scale for Slurry with s%=65 and f%=32

### 3.1.3.3 Test 3: Slurry with Solids Content of 43% and Fines Content of 75%

The raw data for this test can be found in Figure A.3. The change in shear stress with shear strain for the vane shear test is demonstrated in Figure 3.15. The variation of the shear stress and apparent viscosity with shear rate for the viscometer tests are presented in Table 3.5 and the plots of shear stress vs. shear rate and apparent viscosity vs. shear rate are shown in Figure 3.16 and Figure 3.17.

Table 3.5 Calculated Shear Stress and Apparent Viscosity for Slurry with s%=43 and f%=75

RPM	Strain Rate (1/s)	Average Shear Stress (Dyne/cm <sup>2</sup> )	Viscosity (cp)	Shear Stress (Pa)	Viscosity (Pa.s)
0.8	0.272	86.6	31855.5	8.7	31.9
1	0.34	90.2	26519.6	9.0	26.5
1.5	0.51	90.9	17824.5	9.1	17.8
2	0.68	90.4	13286.8	9.0	13.3
4	1.36	92.5	6804.3	9.3	6.8
8	2.72	92.8	3413.3	9.3	3.4
20	6.8	95.0	1397.1	9.5	1.4
40	13.6	100.5	738.8	10.0	0.7
80	27.2	108.2	398.0	10.8	0.4
160	54.4	122.3	224.8	12.2	0.2

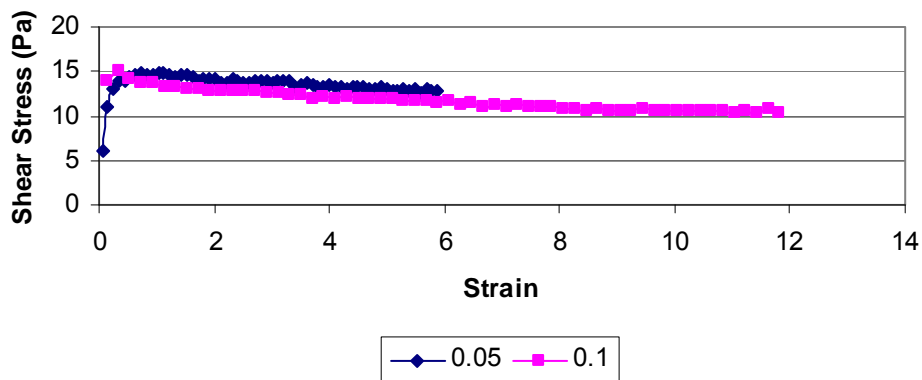


Figure 3.15 Comparison of Averaged Shear Stress vs. Strain for Mixture with s% = 43 and f% = 75 (Vane 80-40, Constant Strain Rate=0.05 and 0.1 s<sup>-1</sup>)

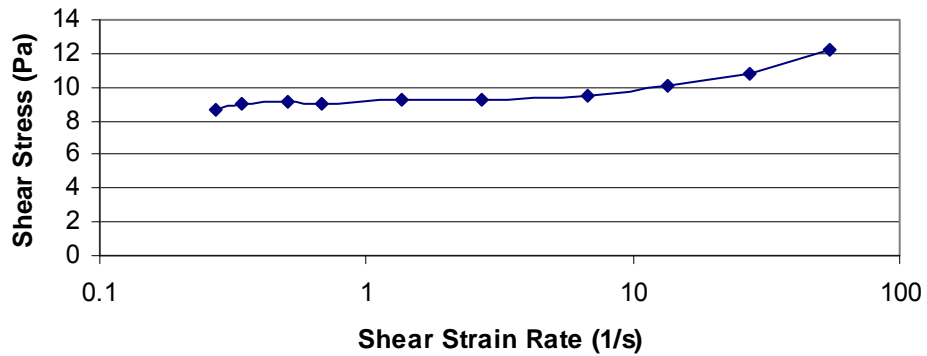


Figure 3.16 Plot of Shear Stress vs. Shear Rate in Semi-log Scale for Slurry with  $s\% = 43\%$  and  $f\% = 75\%$

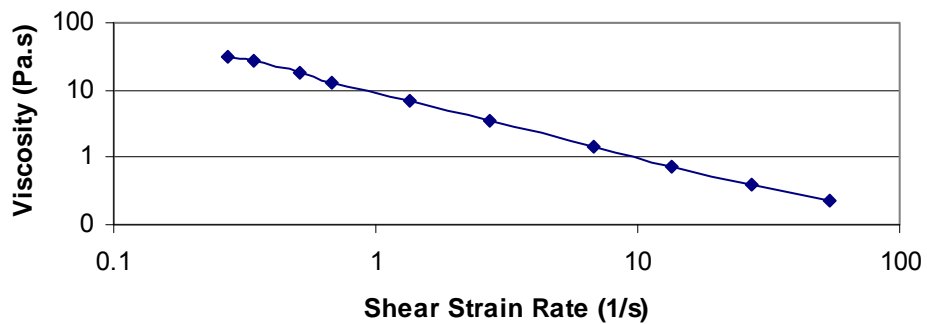


Figure 3.17 Plot of Apparent Viscosity vs. Shear Rate in Log-Log Scale for Slurry with  $s\% = 43\%$  and  $f\% = 75\%$

#### 3.1.3.4 Test 4: Slurry with Solids Content of 52% and Fines Content of 60%

The raw data for this test can be found in Figure A.4. The change in shear stress with shear strain for the vane shear test is demonstrated in Figure 3.18. The variation of the shear stress and apparent viscosity with shear rate for this sample are presented in Table 3.6 and the corresponding plots of shear stress vs. shear rate and apparent viscosity vs. shear rate are shown in Figure 3.19 and Figure 3.20.

Table 3.6 Calculated Shear Stress and Apparent Viscosity for Slurry with s%=52 and f%=60

RPM	Strain Rate (1/s)	Average Shear Stress (Dyne/cm <sup>2</sup> )	Viscosity (cp)	Shear Stress (Pa)	Viscosity (Pa.s)
0.03	0.006	117.6	1832970.4	11.8	1833.0
0.05	0.011	106.5	995859.6	10.6	995.9
0.07	0.015	105.7	705995.6	10.6	706.0
0.09	0.019	105.1	546112.1	10.5	546.1
0.1	0.021	105.1	491749.8	10.5	491.7
0.2	0.043	114.5	267789.0	11.5	267.8
0.3	0.064	121.8	189850.9	12.2	189.9
0.4	0.086	129.3	151183.2	12.9	151.2
0.6	0.128	140.2	109257.0	14.0	109.3
0.8	0.171	148.6	86876.1	14.9	86.9
1.5	0.321	170.9	53297.8	17.1	53.3
2	0.428	182.8	42752.3	18.3	42.8
10	2.138	204.9	9585.3	20.5	9.6
20	4.276	217.0	5074.7	21.7	5.1
40	8.552	232.3	2716.7	23.2	2.7
80	17.105	252.1	1474.0	25.2	1.5
120	25.657	271.1	1056.5	27.1	1.1

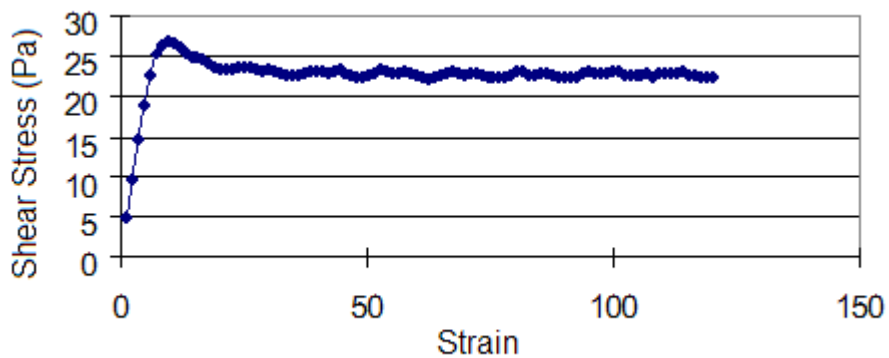


Figure 3.18 Comparison of Averaged Shear Stress vs. Strain for Mixture with s% = 52 and f% = 60 (Vane 80-40, Constant Strain Rate=0.05 and 0.1 s<sup>-1</sup>)

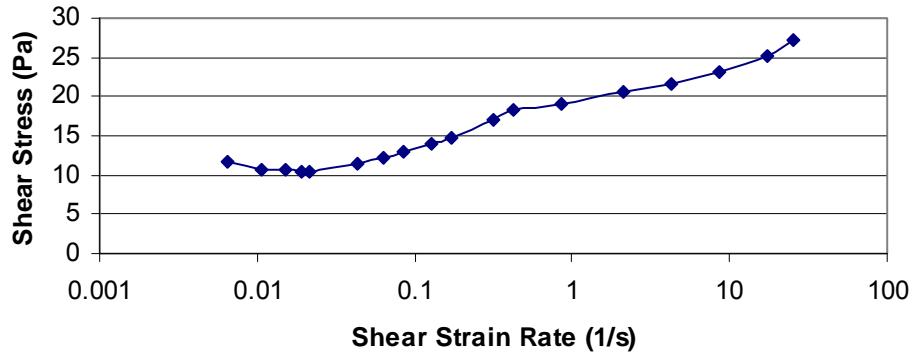


Figure 3.19 Plot of Shear Stress vs. Shear Rate in Semi-Log Scale for Slurry with  $s\%=52$  and  $f\%=60$

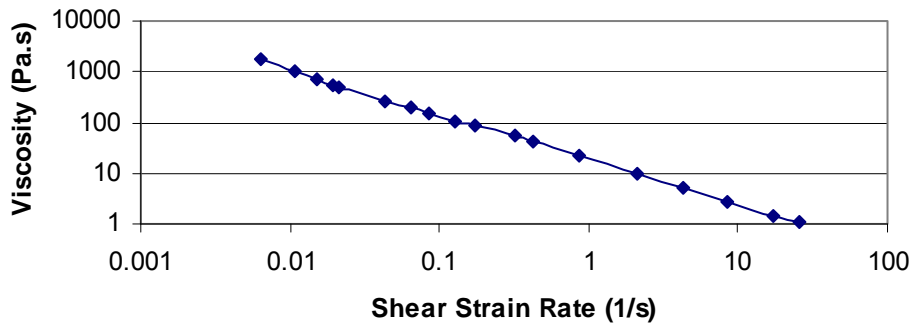


Figure 3.20 Plot of Apparent Viscosity vs. Shear Rate in Log-Log Scale for Slurry with  $s\%=52$  and  $f\%=60$

### 3.1.3.5 Test 5: Slurry with Solids Content of 40% and Fines Content of 94%

The raw data for this test can be found in Figure A.5. The change in shear stress with shear strain for the vane shear test is demonstrated in Figure 3.21. The variation of the shear stress and apparent viscosity with shear rate for the viscometer tests are presented in Table 3.7 the corresponding plots of shear stress vs. shear rate and apparent viscosity vs. shear rate are shown in Figure 3.22 and Figure 3.23.

Table 3.7 Calculated Shear Stress and Apparent Viscosity for Slurry with s%=40 and f%=94

RPM	Strain Rate (1/s)	Average Shear Stress (Dyne/cm <sup>2</sup> )	Viscosity (cp)	Shear Stress (Pa)	Viscosity (Pa.s)
0.05	0.017	113.1	665201.2	11.3	665.2
0.07	0.024	110.8	465604.2	11.1	465.6
0.09	0.031	111.4	363897.5	11.1	363.9
0.2	0.068	120.6	177303.9	12.1	177.3
0.3	0.102	128.5	125975.2	12.8	126.0
0.4	0.136	137.3	100960.2	13.7	101.0
0.6	0.204	148.1	72587.7	14.8	72.6
0.8	0.272	159.4	58590.7	15.9	58.6
1	0.340	165.9	48800.3	16.6	48.8
1.5	0.510	173.2	33969.0	17.3	34.0
4	1.360	185.6	13644.0	18.6	13.6
8	2.720	186.3	6849.3	18.6	6.8
20	6.800	187.5	2757.7	18.8	2.8
40	13.600	193.3	1421.3	19.3	1.4
80	27.200	205.2	754.2	20.5	0.8
120	40.800	216.0	529.5	21.6	0.5

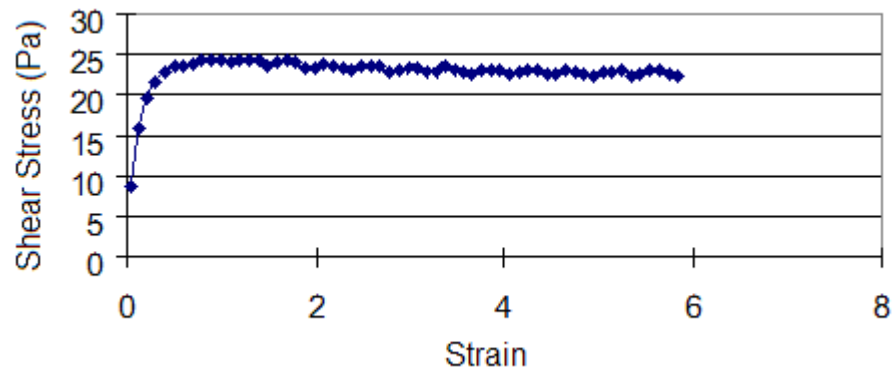


Figure 3.21 Comparison of Averaged Shear Stress vs. Strain for Mixture with s% = 40 and f% = 94 (Vane 80-40, Constant Strain Rate=0.03 s<sup>-1</sup>)

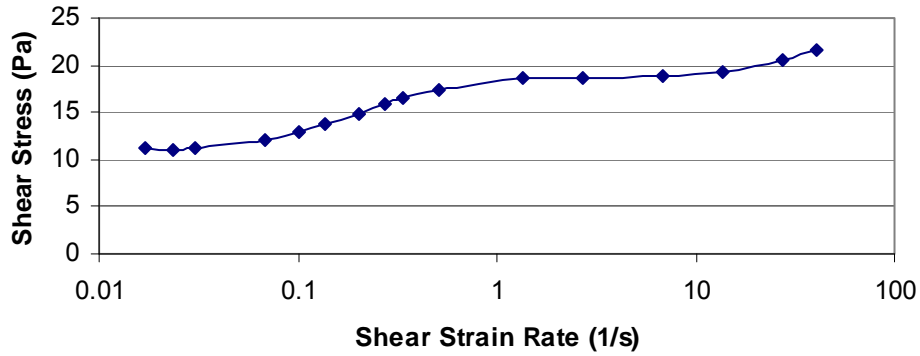


Figure 3.22 Plot of Shear Stress vs. Shear Rate in Semi-Log Scale for Slurry with s%=40 and f%=94

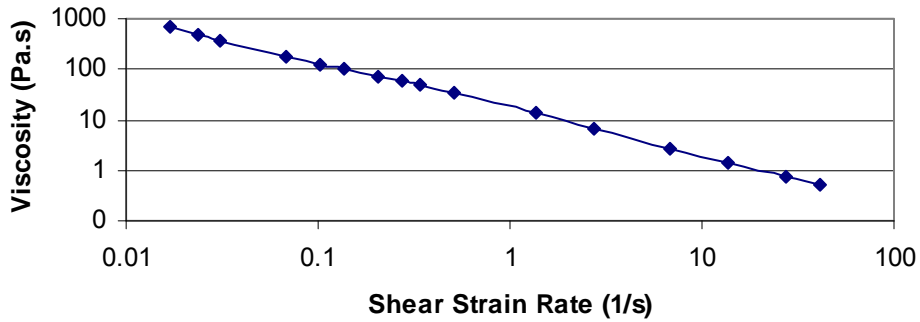


Figure 3.23 Plot of Apparent Viscosity vs. Shear Rate in Log-Log Scale for Slurry with s%=40 and f%=94

### 3.1.3.6 Test 6: Centrifuged MFT with Solids Content of 61% and Fines Content of 95%

The raw data for this test can be found in Figure A.6. The change in shear stress with shear strain for the vane shear test is demonstrated in Figure 3.24. The variation of the shear stress and apparent viscosity with shear rate for the viscometer tests are presented in Table 3.8 and the corresponding plots of shear stress vs. shear rate and apparent viscosity vs. shear rate are shown in Figure 3.25 and Figure 3.26.

Table 3.8 Calculated Shear Stress and Apparent Viscosity for Slurry with s%=61 and f%=95

RPM	Strain Rate (1/s)	Average Shear Stress (Dyne/cm <sup>2</sup> )	Viscosity (cp)	Shear Stress (Pa)	Viscosity (Pa.s)
0.03	0.0102	799.2	7835612.1	79.9	7835.6
0.05	0.017	810.0	4764745.6	81.0	4764.7
0.07	0.0238	825.1	3466994.1	82.5	3467.0
0.1	0.034	843.9	2482070.7	84.4	2482.1

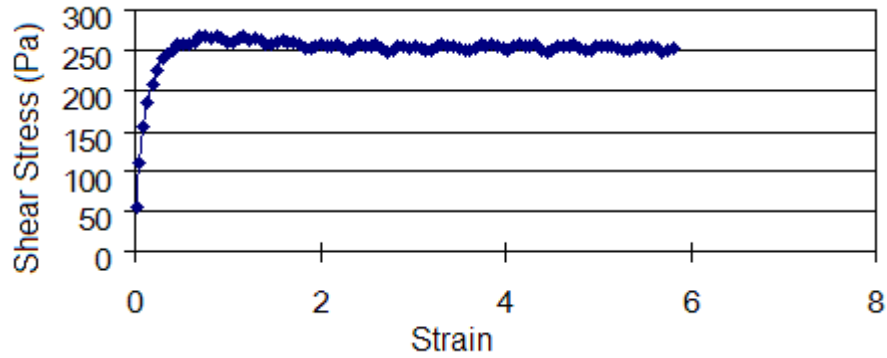


Figure 3.24 Shear Stress vs. Strain for Mixture with s% = 61 and f% = 95 (Vane 40-20, Constant Strain Rate=0.05 s<sup>-1</sup>)

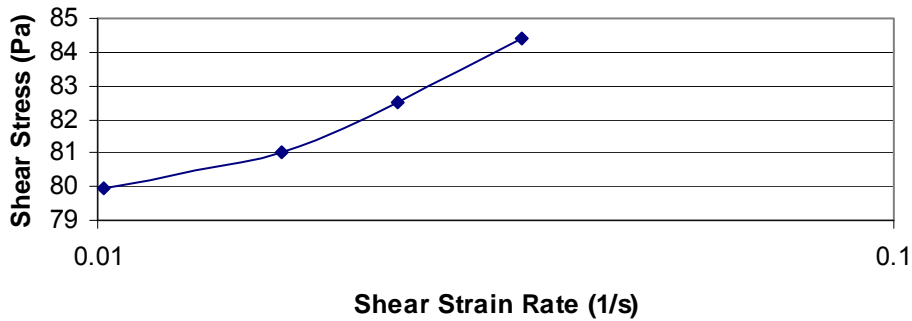


Figure 3.25 Plot of Shear Stress vs. Shear Rate in Semi-Log Scale for Slurry with s%=61 and f%=95

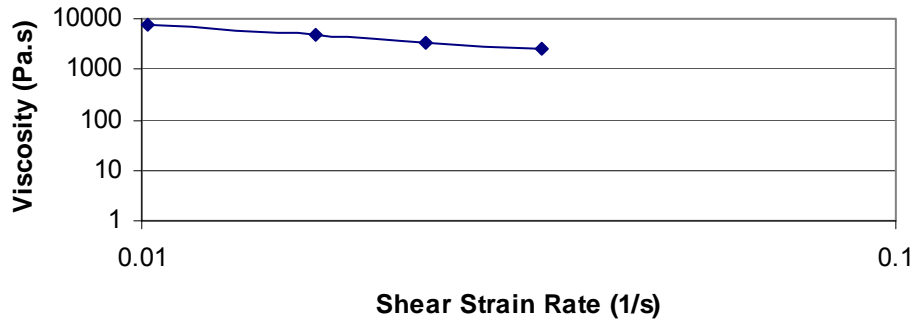


Figure 3.26 Plot of Apparent Viscosity vs. Shear Rate in Log-Log Scale for Slurry with s%=61 and f%=95

3.1.3.7 Test 7: Diluted Centrifuged MFT with Solids Content of 50% and Fines Content of 95%

The raw data for this test can be found in Figure A.7. The change in shear stress with shear strain for the vane shear test is demonstrated in Figure 3.27. The variation of the shear stress and apparent viscosity with shear rate for viscometer tests are presented in Table 3.9 and the corresponding plots of shear stress vs. shear rate and apparent viscosity vs. shear rate are shown in Figure 3.28 and Figure 3.29.

Table 3.9 Calculated Shear Stress and Apparent Viscosity for Slurry with s%=50 and f%=95

RPM	Strain Rate (1/s)	Average Shear Stress (Dyne/cm <sup>2</sup> )	Viscosity (cp)	Shear Stress (Pa)	Viscosity (Pa.s)
0.03	0.006	186.8	2912367.5	18.7	2912.4
0.05	0.011	187.1	1749909.1	18.7	1749.9
0.07	0.015	190.7	1273932.4	19.1	1273.9
0.1	0.021	197.2	922445.6	19.7	922.4
0.2	0.043	224.5	524993.5	22.4	525.0
0.3	0.064	237.4	370181.1	23.7	370.2
0.4	0.086	248.0	289923.3	24.8	289.9
0.6	0.128	275.8	214953.9	27.6	215.0
0.8	0.171	293.1	171377.2	29.3	171.4
1	0.214	307.2	143696.6	30.7	143.7
1.5	0.321	337.9	105351.2	33.8	105.4
80	17.105	572.407	3346.521	57.241	3.347
160	34.209	618.905	1809.181	61.890	1.809

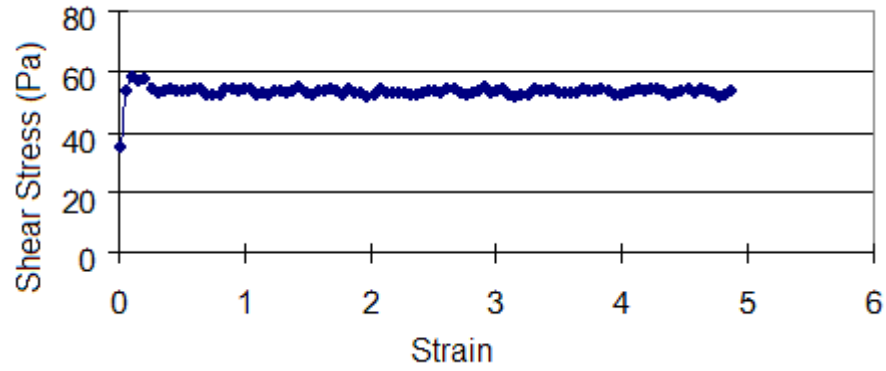


Figure 3.27 Shear Stress vs. Strain for Mixture with  $s\% = 50$  and  $f\% = 94.5$  (Vane 40-20, Constant Strain Rate= $0.05 \text{ s}^{-1}$ )

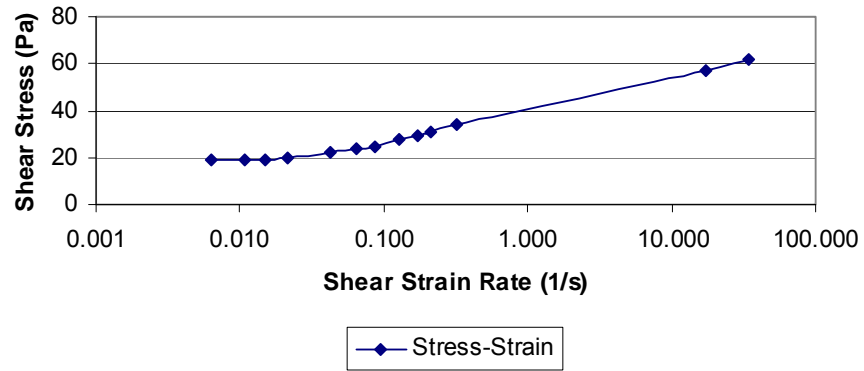


Figure 3.28 Plot of Shear Stress vs. Shear Rate in Semi-Log Scale for Slurry with  $s\%=50$  and  $f\%=95$

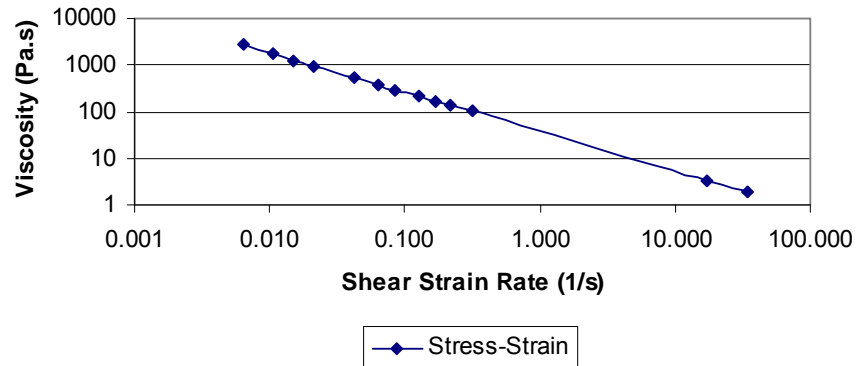


Figure 3.29 Plot of Apparent Viscosity vs. Shear Rate in Log-Log Scale for Slurry with  $s\%=50$  and  $f\%=95$

3.1.3.8 Test 8: Slurry with Solids Content of 49% and Fines Content of 68%

The raw data for this test can be found in Figure A.8. The change in shear stress with shear strain for the vane shear test is demonstrated in Figure 3.30. The variation of the shear stress and apparent viscosity with shear rate for viscometer tests are presented in Table 3.10 and the plots of shear stress vs. shear rate and apparent viscosity vs. shear rate are shown in Figure 3.31 and Figure 3.32.

Table 3.10 Calculated Shear Stress and Apparent Viscosity for Slurry with  $s\%=49$  and  $f\%=68$

RPM	Strain Rate (1/s)	Average Shear Stress (Dyne/cm <sup>2</sup> )	Viscosity (cp)	Shear Stress (Pa)	Viscosity (Pa.s)
0.03	0.006	115.2	1795257.2	11.5	1795.3
0.05	0.011	111.8	1046046.6	11.2	1046.0
0.07	0.015	113.2	756360.3	11.3	756.4
0.1	0.021	113.7	531940.9	11.4	531.9
0.2	0.043	123.8	289612.2	12.4	289.6
0.3	0.064	130.9	204066.2	13.1	204.1
0.6	0.128	152.8	119142.3	15.3	119.1
0.8	0.171	159.1	93011.9	15.9	93.0
1	0.214	165.2	77250.7	16.5	77.3
2	0.428	179.8	42057.5	18.0	42.1
8	1.710	207.4	12126.8	20.7	12.1
40	8.552	230.4	2694.4	23.0	2.7
80	17.105	245.0	1432.5	24.5	1.4
160	34.209	264.9	774.4	26.5	0.8

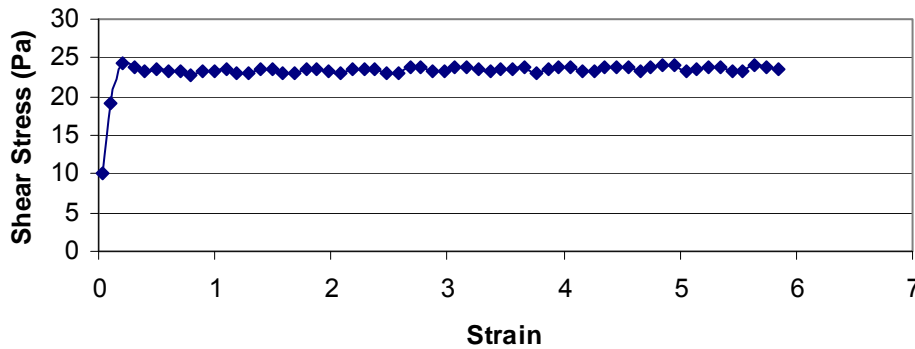


Figure 3.30 Shear Stress vs. Strain for Mixture with  $s\% = 49$  and  $f\% = 68$  (Vane 40-20, Constant Strain Rate= $0.05 \text{ s}^{-1}$ )

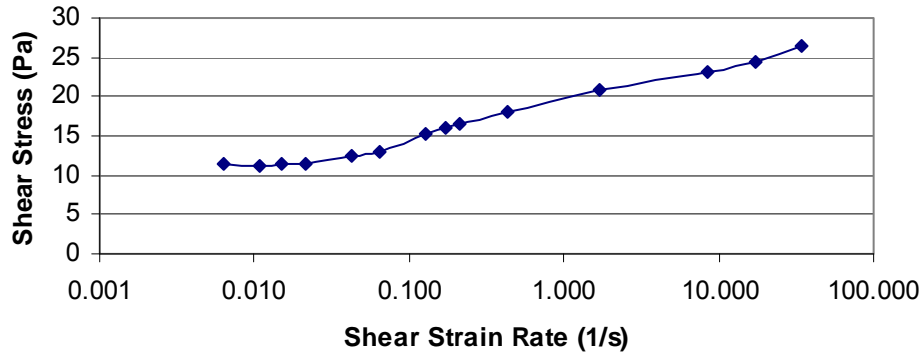


Figure 3.31 Plot of Shear Stress vs. Shear Rate in Semi-Log Scale for Slurry with s%=49 and f%=68

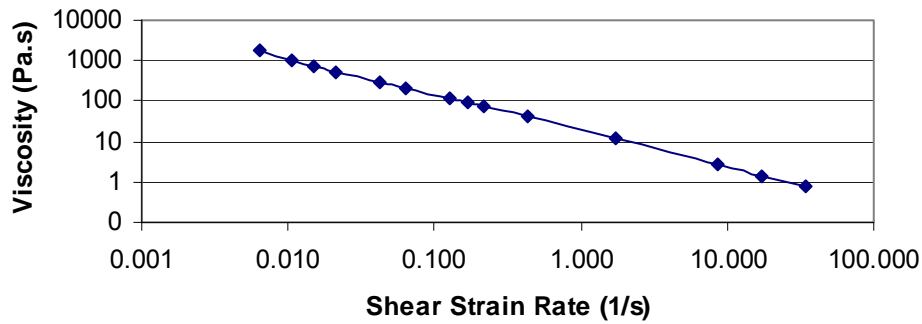


Figure 3.32 Plot of Apparent Viscosity vs. Shear Rate in Log-Log Scale for Slurry with s%=49 and f%=68

### 3.1.3.9 Test 9: Slurry with Solids Content of 51% and Fines Content of 78%

The raw data for this test can be found in Figure A.9. The change in shear stress with shear strain for the vane shear test is demonstrated in Figure 3.33. The variation of the shear stress and apparent viscosity with shear rate for the viscometer tests are presented in Table 3.11 and the corresponding plots of shear stress vs. shear rate and apparent viscosity vs. shear rate are shown in Figure 3.34 and Figure 3.35.

Table 3.11 Calculated Shear Stress and Apparent Viscosity for Slurry with s%=51 and f%=78

RPM	Strain Rate (1/s)	Average Shear Stress (Dyne/cm <sup>2</sup> )	Viscosity (cp)	Shear Stress (Pa)	Viscosity (Pa.s)
0.05	0.01069	175.6	1642898.8	17.6	1642.9
0.07	0.014966	175.1	1170240.2	17.5	1170.2
0.1	0.021381	177.0	827878.3	17.7	827.9
0.2	0.042761	189.2	442517.9	18.9	442.5
0.3	0.064142	198.0	308726.2	19.8	308.7
0.4	0.085523	209.9	245387.5	21.0	245.4
0.8	0.171046	234.8	137288.4	23.5	137.3
1	0.213807	242.9	113625.9	24.3	113.6
4	0.855228	310.7	36333.7	31.1	36.3
8	1.710455	307.0	17950.8	30.7	18.0
40	8.552277	337.2	3942.4	33.7	3.9
80	17.10455	349.0	2040.1	34.9	2.0
120	25.65683	361.5	1409.0	36.2	1.4
160	34.20911	372.7	1089.5	37.3	1.1

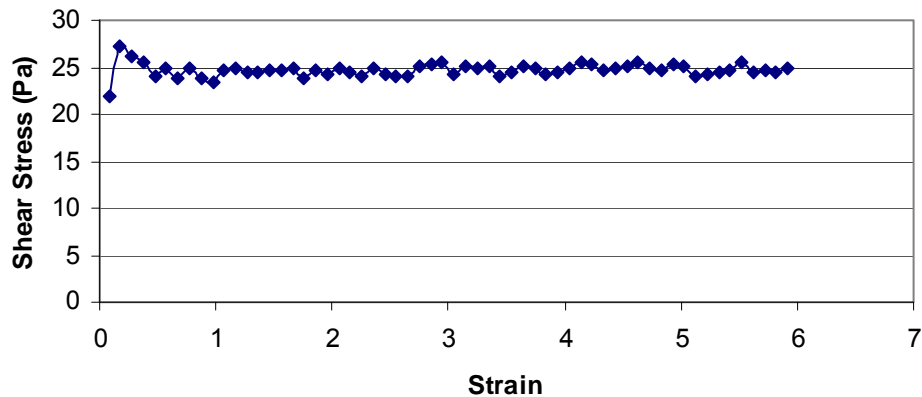


Figure 3.33 Shear Stress vs. Strain for Mixture with s% = 44 and f% = 79 (Vane 40-20, Constant Strain Rate=0.05 s<sup>-1</sup>)

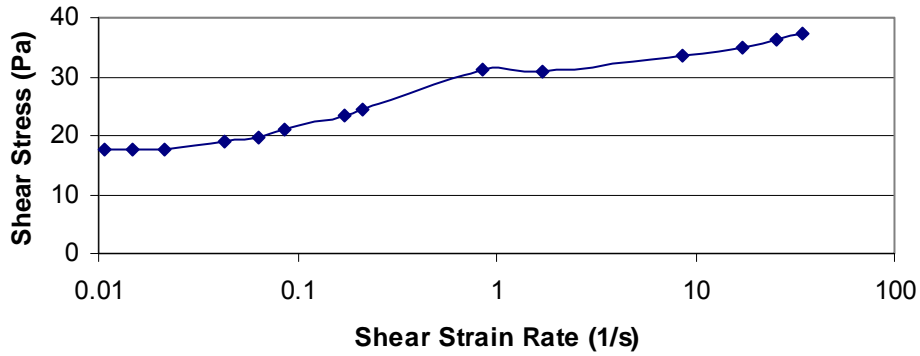


Figure 3.34 Plot of Shear Stress vs. Shear Rate in Semi-Log Scale for Slurry with s%=51 and f%=78

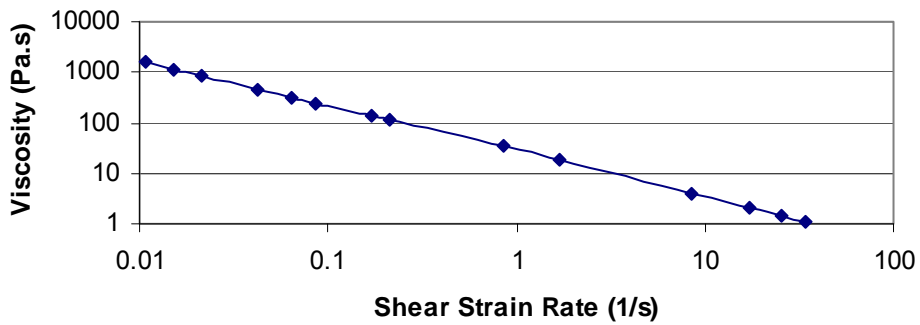


Figure 3.35 Plot of Apparent Viscosity vs. Shear Rate in Log-Log Scale for Slurry with s%=51 and f%=78

### 3.1.3.10 Test 10: Slurry with Solids Content of 49% and Fines Content of 86%

The raw data for this test can be found in Figure A.10. The change in shear stress with shear strain for the vane shear test is demonstrated in Figure 3.36. The variation of the shear stress and apparent viscosity with shear rate for the viscometer tests are presented in Table 3.12 and the plots of shear stress vs. shear rate and apparent viscosity vs. shear rate are shown in Figure 3.37 and Figure 3.38.

Table 3.12 Calculated Shear Stress and Apparent Viscosity for Slurry with s%=49 and f%=86

RPM	Strain Rate (1/s)	Average Shear Stress (Dyne/cm <sup>2</sup> )	Viscosity (cp)	Shear Stress (Pa)	Viscosity (Pa.s)
0.03	0.006	202.8	3161920.0	20.3	3161.9
0.05	0.011	200.1	1871851.1	20.0	1871.9
0.07	0.015	199.4	1332592.6	19.9	1332.6
0.1	0.021	205.6	961433.8	20.6	961.4
0.2	0.043	218.2	510378.6	21.8	510.4
0.3	0.064	271.7	423655.5	27.2	423.7
0.4	0.086	276.6	323452.5	27.7	323.5
1	0.214	298.2	139486.7	29.8	139.5
1.5	0.321	312.8	97522.5	31.3	97.5
2	0.428	331.8	77599.3	33.2	77.6
4	0.855	351.5	41102.3	35.2	41.1
8	1.710	359.3	21003.7	35.9	21.0
20	4.276	365.9	8557.8	36.6	8.6
40	8.552	366.5	4285.1	36.6	4.3
80	17.105	374.5	2189.3	37.4	2.2
120	25.657	384.5	1498.8	38.5	1.5
160	34.209	395.7	1156.8	39.6	1.2

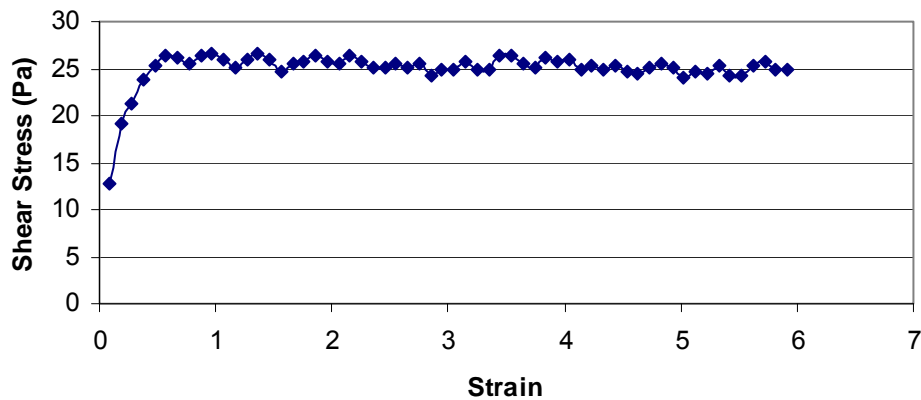


Figure 3.36 Shear Stress vs. Strain for Mixture with s% = 49 and f% = 86 (Vane 40-20, Constant Strain Rate=0.05 s<sup>-1</sup>)

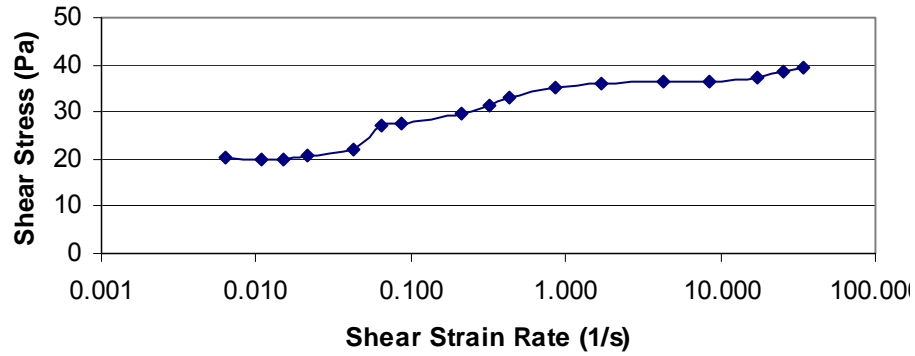


Figure 3.37 Plot of Shear Stress vs. Shear Rate in Semi-Log Scale for Slurry with s%=49 and f%=86

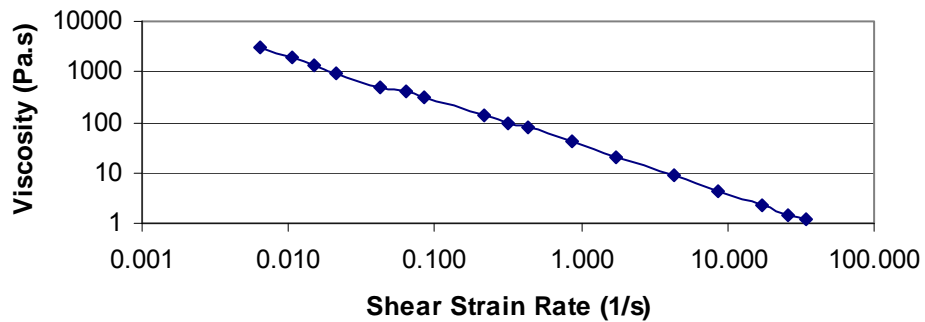


Figure 3.38 Plot of Apparent Viscosity vs. Shear Rate in Log-Log Scale for Slurry with s%=49 and f%=86

### 3.1.3.11 Test 11: Slurry with Solids Content of 41% and Fines Content of 95%

The raw data for this test can be found in Figure A.11. The change in shear stress with shear strain for the vane shear test is demonstrated in Figure 3.39. The variation of the shear stress and apparent viscosity with shear rate for the viscometer tests are presented in Table 3.13 and the plots of shear stress vs. shear rate and apparent viscosity vs. shear rate are shown in Figure 3.40 and Figure 3.41.

Table 3.13 Calculated Shear Stress and Apparent Viscosity for Slurry with s%=41 and f%=95

RPM	Strain Rate (1/s)	Average Shear Stress (Dyne/cm <sup>2</sup> )	Viscosity (cp)	Shear Stress (Pa)	Viscosity (Pa.s)
0.03	0.0102	120.0	1176301.6	12.0	1176.3
0.05	0.017	110.3	649019.6	11.0	649.0
0.07	0.0238	105.3	442252.5	10.5	442.3
0.09	0.0306	102.8	335846.6	10.3	335.8
0.1	0.034	103.0	302819.5	10.3	302.8
0.2	0.068	109.2	160565.0	10.9	160.6
0.8	0.272	157.0	57723.2	15.7	57.7
1.8	0.612	182.3	29793.7	18.2	29.8
40	13.6	198.0	1455.9	19.8	1.5
150	51	228.5	448.0	22.9	0.4
200	68	234.6	345.0	23.5	0.3

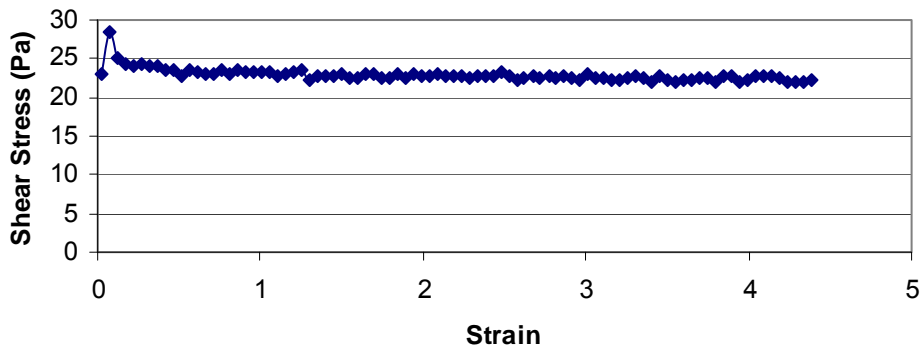


Figure 3.39 Diagram of Averaged Shear Stress vs. Strain for Mixture with s% = 41 and f% = 95 (Vane 40-20, Constant Strain Rate=0.05 s<sup>-1</sup>)

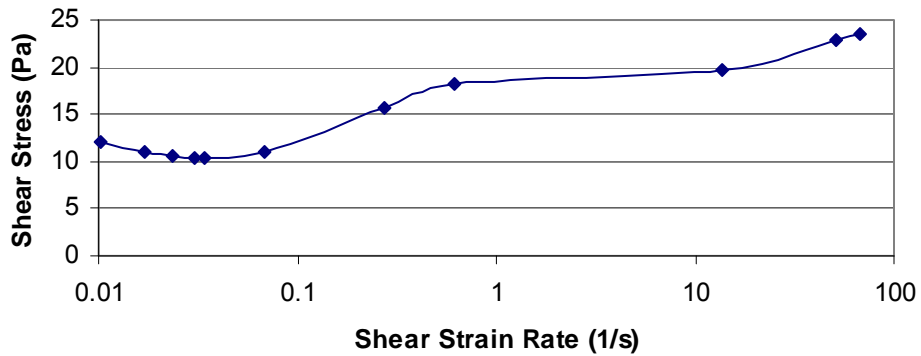


Figure 3.40 Plot of Shear Stress vs. Shear Rate in Log-Log Scale for Slurry with s%=41 and f%=95

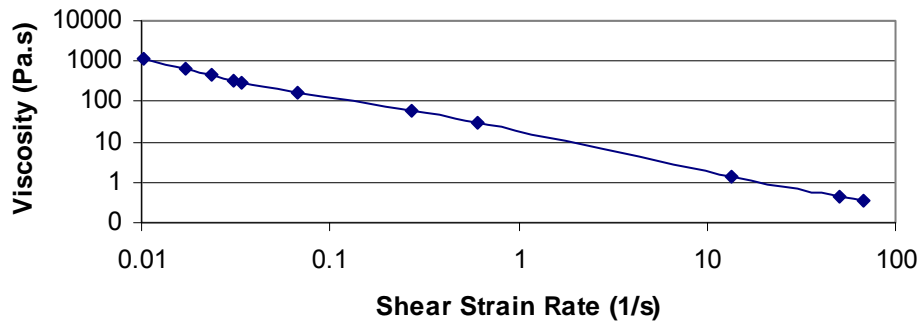


Figure 3.41 Plot of Apparent Viscosity vs. Shear Rate in Log-Log Scale for Slurry with s%=41 and f%=95

### 3.1.3.12 Test 12: Slurry with Solids Content of 19% and Fines Content of 24%

The raw data for this test can be found in Figure A.12. The change in shear stress with shear strain for the vane shear test is demonstrated in Figure 3.42. Since the torque measured in the viscometer tests is less than 10% of maximum torque for the instrument, the plots for viscosity measurements are not shown here.

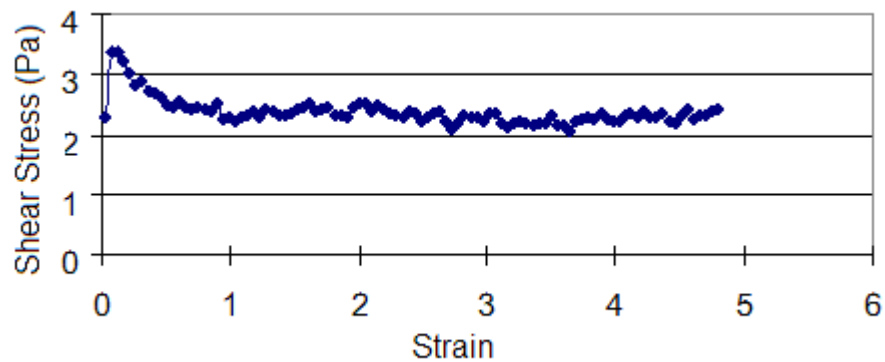


Figure 3.42 Diagram of Averaged Shear Stress vs. Strain for Mixture with s% = 19 and f% = 24 (Vane 80-40, Constant Strain Rate=0.05 s<sup>-1</sup>)

### 3.1.3.13 Test 13: Slurry with Solids Content of 25% and Fines Content of 49%

The raw data for this test can be found in Figure A.13. The change in shear stress with shear strain for the vane shear test is demonstrated in Figure 3.43. Since the torque measured in the viscometer tests is less than 10% of maximum torque for the instrument, the plots for viscosity measurements are not shown here.

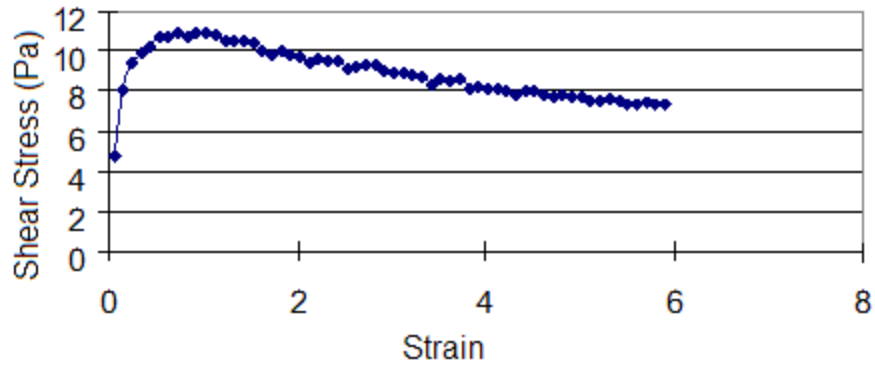


Figure 3.43 Diagram of Averaged Shear Stress vs. Strain for Mixture with  $s\% = 25$  and  $f\% = 49$  (Vane 80-40, Constant Strain Rate= $0.05 \text{ s}^{-1}$ )

#### 3.1.3.14 Test 14: Slurry with Solids Content of 27% and Fines Content of 94%

The raw data for this test can be found in Figure A.14. The change in shear stress with shear strain for the vane shear test is demonstrated in Figure 3.44. Since the torque measured in the viscometer tests is less than 10% of maximum torque for the instrument, the plots for viscosity measurements are not shown here.

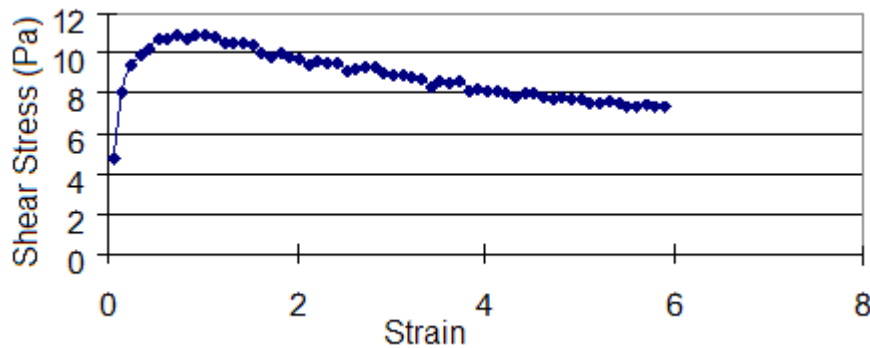


Figure 3.44 Diagram of Averaged Shear Stress vs. Strain for Mixture with  $s\% = 27$  and  $f\% = 94$  (Vane 80-40, Constant Strain Rate= $0.05 \text{ s}^{-1}$ )

### 3.1.4 Analysis and Discussion of the Results

#### 3.1.4.1 Analysis of the Results of Vane Shear Tests

The peak value of the shear stress is determined as the yield stress. The static yield stress for the mixture with various solids and fines contents is summarized in Table 3.14. The variation of the yield stress with solids and fines contents is shown in Figure 3.45. The general trends shown in Figure 3.45 are that the static yield stress increases

with both solids and fines contents. The variation of the static yield stress with increasing solids content at the same fines content is shown in Figure 3.46. It can be seen that the yield stress increases dramatically when the solids content approaches 60%. The trends of the static yield stress with fines content at the similar solids content are represented in Table 3.16. The table demonstrates that the yield stress increases with fines content. Moreover, greater increase in yield stress results from the increase of fines content for the mixture with higher solids content.

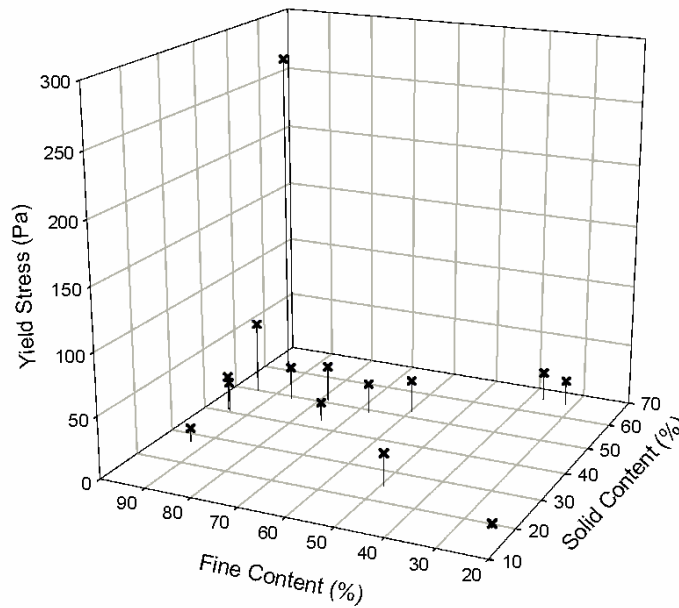


Figure 3.45 Diagram of Variation of Static Yield Stress with Solid sand Fines Contents

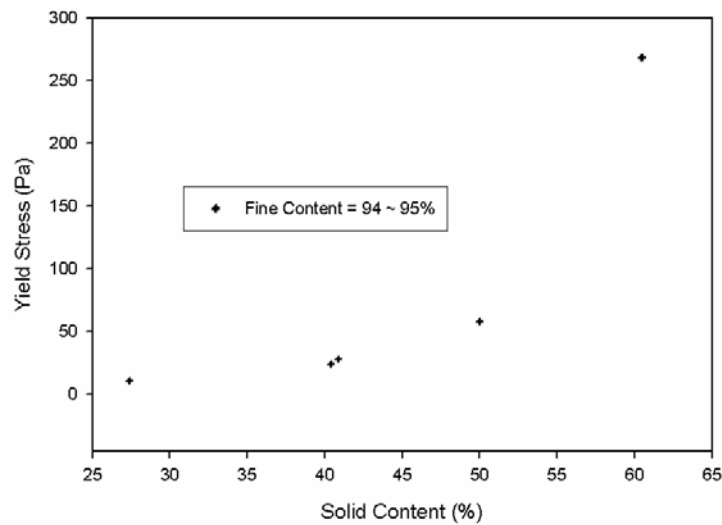


Figure 3.46 Diagram of Variation of Static Yield Stress with Solids Content

Table 3.14 Static Yield Stress for Mixture with Various Solids and Fines Contents

Test Series	Solids Content (%)	Fines Content (%)	Sand: Fine Ratio	Fine/ ( Fine+ Water )	Yield Stress (Pa)
1	66	37	1.7	0.4	22.8
2	65	32	2.1	0.4	20.2
3	43	75	0.3	0.4	14.9
4	52	60	0.7	0.4	26.8
5	40	94	0.1	0.4	24.4
6	61	95	0.1	0.6	268.6
7	50	95	0.1	0.5	58.1
8	49	68	0.5	0.4	24.3
9	51	78	0.3	0.4	29.2
10	49	86	0.2	0.5	27.5
11	41	95	0.1	0.4	28.1
12	19	24	3.2	0.1	3.4
13	25	49	1.0	0.1	26.4
14	27	94	0.1	0.3	10.9

Table 3.15 Comparison of Static Yield Stress for Mixture with Similar Solids Content and Different Fines Content

Test Series	Solids Content (%)	Fines Content (%)	Sand: Fine Ratio	Fine/ ( Fine+ Water )	Yield Stress (Pa)
14	27	94	0.1	0.3	10.9
5	40	94	0.1	0.4	24.4
11	41	95	0.1	0.4	28.1
7	50	95	0.1	0.5	58.1
6	61	95	0.1	0.6	268.6

Table 3.16 Comparison of Static Yield Stress for Mixture with Similar Solids Content and Different Fines Content

Test Series	Solids Content (%)	Fines Content (%)	Sand: Fine Ratio	Fine/ ( Fine+ Water )	Yield Stress (Pa)
4	52	60	0.7	0.4	26.755
8	49	68	0.5	0.4	24.252
9	51	78	0.3	0.4	29.163
10	49	86	0.2	0.5	27.467
7	50	95	0.1	0.5	58.082

Our focus is the variation of the yield stress for MFT with different solids content at the same fines content. Following this idea, the measured static yield stress for MFT with different solids content is listed in Table 3.17. The yield stress data can be regressed using the following equation (Coussot 1997):

$$\tau_c = ce^{(s\phi)} \quad (\text{Eq. 3.10})$$

where  $\tau_c$  and  $\phi$  are static yield stress and solid volume fraction in percent respectively. The parameters  $c$  and  $s$  in Eq. 3.10 are fitting parameters.

The first step to regress the data in Table 3.17 is to calculate the volume fraction of the solid particles from solids and fines contents by assuming a density of 2700 kg/m<sup>3</sup> for both coarse and fine particles and a density of 1000 kg/m<sup>3</sup> for water. The data pairs,  $\phi$  and  $\tau_c$ , are regressed using the Exponential Growth equation in the software SigmaPlot

9. The parameters  $c$  and  $s$  obtained from the regression are 1.1436 and 0.1487 respectively with R-square of 0.9985 for the data presented in Table 3.17. The measured and predicted yield stresses are shown in Figure 3.47.

Table 3.17 Static Yield Stress for MFT with Various Solids Contents

Test Series	Solids Content (%)	Fines Content (%)	Solid Volume Fraction (%)	Sand Fine Ratio	Fine/ ( Fine+ Water )	Yield Stress (Pa)
14	27	94	12.0	0.1	0.3	10.9
5	40	94	19.8	0.1	0.4	24.4
11	41	95	20.5	0.1	0.4	28.1
7	50	95	27.0	0.1	0.5	58.1
6	61	95	36.7	0.1	0.6	268.6

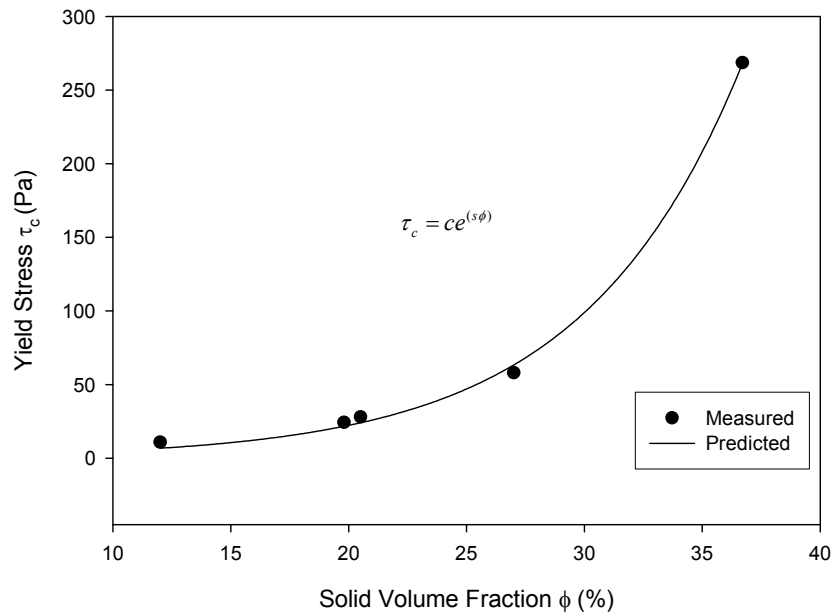


Figure 3.47 Comparison of Measured and Predicted Yield Stress Using Exponential Equation

### 3.1.4.2 Analysis of the Viscometer Tests

#### 3.1.4.2.1 Overall Observations

According to Coussot (1997), it is advantageous to plot the experimental data in a logarithm scale of diagram of shear strain rate vs. shear stress such that Herschel-Bulkley model can be used to fit the data in a wider range of shear strain rate. The flow curves are shown in Figure 3.48. The apparent viscosity of the mixture is demonstrated

in Figure 3.49. These curves indicate that the slurry is yield stress fluid with viscosity decreasing with shear strain rate. The yield stress and viscoplastic properties of the slurry are also demonstrated in Figure 3.10 to Figure 3.41. Shear-thinning behavior is associated with floc breakage because the energy dissipated via bond ruptures and restorations does not increase significantly with shear rate (Coussot, 1997).

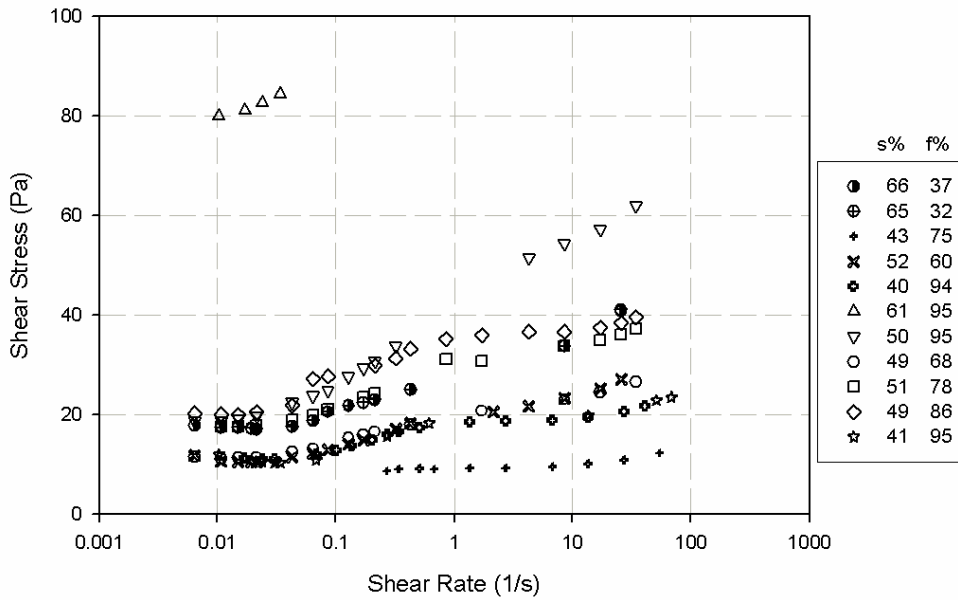


Figure 3.48 Shear stress vs. shear strain rate curves for various solids and fines contents

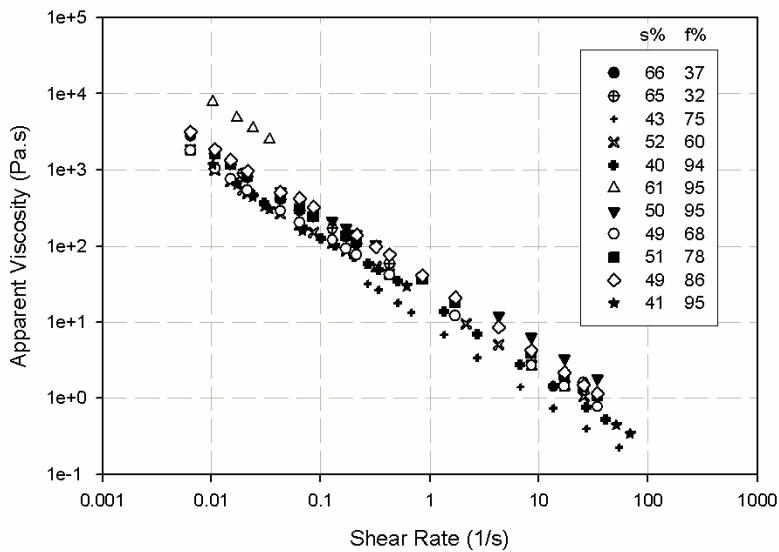


Figure 3.49 Apparent viscosity for mixture with various solids and fines contents

### 3.1.4.2.2 Effects of Solids Content on Viscosity of the Slurry

Figure 3.50 shows that the increasing solids content results in an increase in apparent viscosity and shear stress at the same shear strain rate. This has been supported by the viscosity measurements for Syncrude's tailing pond slurry (Danielson et al., 1990), clay-water (Boyer, 1994) and polystyrene-kaolin-water suspension (Coussot, 1997). As stated by Coussot (1997), the average liquid strain increases with the solid concentration if all other things are equal. As a result, the macroscopic viscosity of the suspension increases with the solid fraction. In fact, the viscosity approaches infinity when the solid fraction tends towards the maximum packing fraction (Figure 3.50).

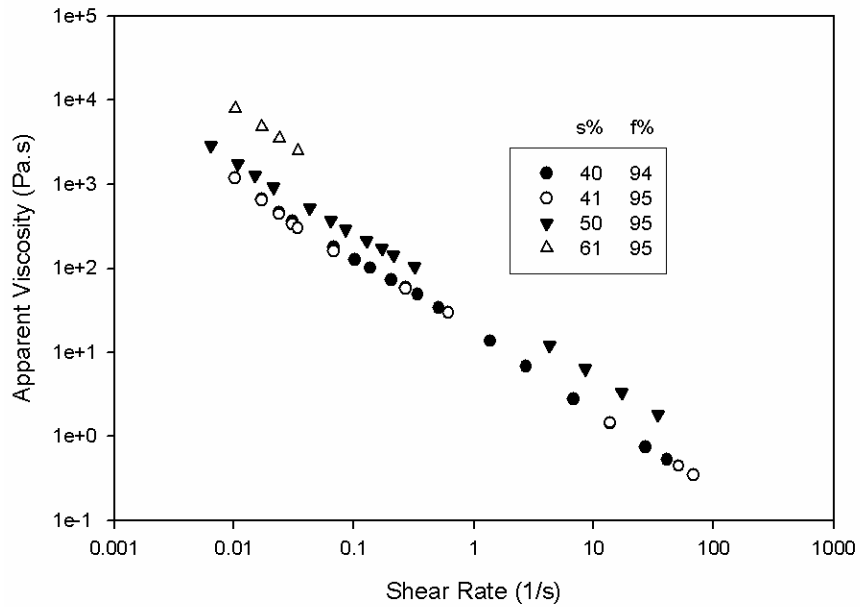


Figure 3.50 Effects of solids contents on apparent viscosity

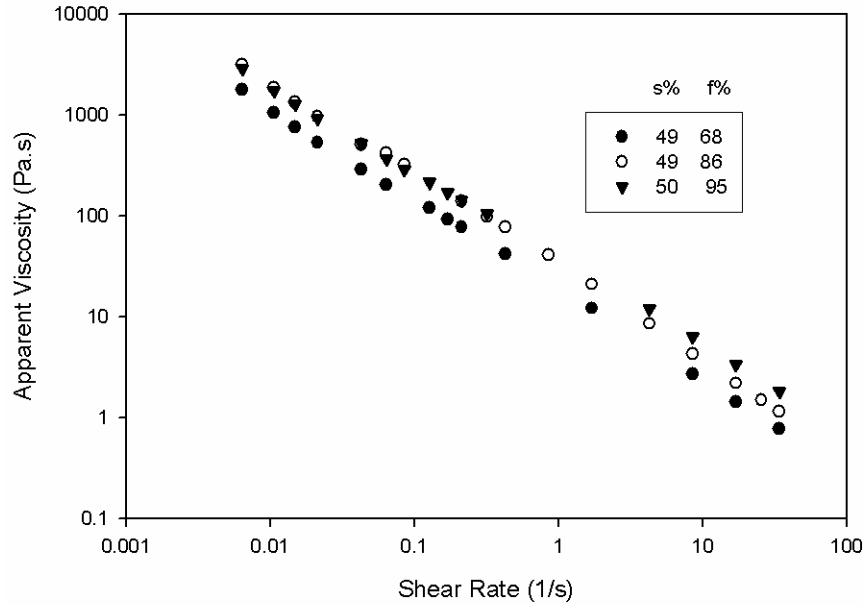


Figure 3.51 Effects of fines contents on apparent viscosity

### 3.1.4.2.3 Effects of Fines Contents on Viscosity of the Slurry

Influences of the fines contents on the shear stress and apparent viscosity are shown in Figure 3.51. Increasing shear stress and apparent viscosity are observed from these figures. Sufficient small suspended particles within slow flows give rise to various colloidal forces. For a polydisperse suspensions made up of fine (colloidal) and coarse (non-colloidal) particles, Sengun and Probstein (1989a and 1989b) proved that the interstitial phase composing of interaction between fine colloidal particles and water imparts most of its rheological properties to the entire suspension by experiments. Ancy (2001) studied the bulk behavior of addition of Kaolin into suspensions of glass beads (Figure 3.52). The author found that the bulk behavior of the mixture is viscoplastic when the Kaolin fraction  $\phi_k$  is high enough. The influence of the Kaolin on the bulk behavior of the mixture is negligible when  $\phi_k$  is small. Odd behavior is observed at an intermediate concentration  $\phi_k$ . The shear stress first increases rapidly and reaches a maximum (short-term behavior), then decreases slowly and flattened out, and rises once again to finally attain its late-time value, when a shear rate is applied.

### 3.1.4.2.4 Influence of Addition of Sand into MFT

Figure 3.53 shows the flow curves for mixture of coarse sand with MFT. From the figure it can be seen that when the solids content matches each other, the shear stress, consequently the apparent viscosity, increases with fines content. However, once there is a significant difference in solids content, the fines content will be the minor factor that controls the shear stress, and consequently the apparent viscosity.

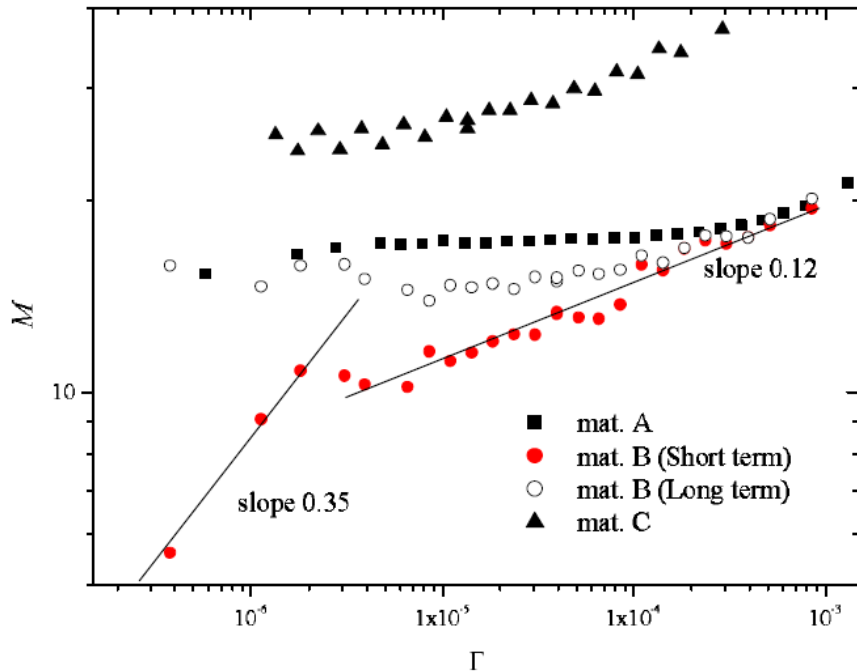


Figure 3.52 Variation of the dimensionless torque as a function of  $\Gamma$  where  $M = C/(Q'gbR^3)$  (where  $C$  is the measure torque) exerted on the vane by the tested suspensions and  $\Gamma$  is the rotational speed. Material A:  $\phi_k = 3.2\%$ ,  $\phi_c = 60.6\%$ ,  $\phi_l = 61.8\%$ . Material B:  $\phi_k = 9.8\%$ ,  $\phi_c = 58.9\%$ ,  $\phi_l = 62.9\%$ . Material C:  $\phi_k = 15.4\%$ ,  $\phi_c = 47.9\%$ ,  $\phi_l = 55.9\%$ , where  $\phi_k = V_k/(V_k + V_w)$ ;  $\phi_c = V_c/(V_k + V_w + V_d)$ , and  $\phi_l = (V_c + V_k)/(V_k + V_w + V_d)$  with  $V$  representing volume and subscripts  $k$ ,  $c$ , and  $w$  for kaolin, coarse particles and water respectively (from Ancey, 2001)

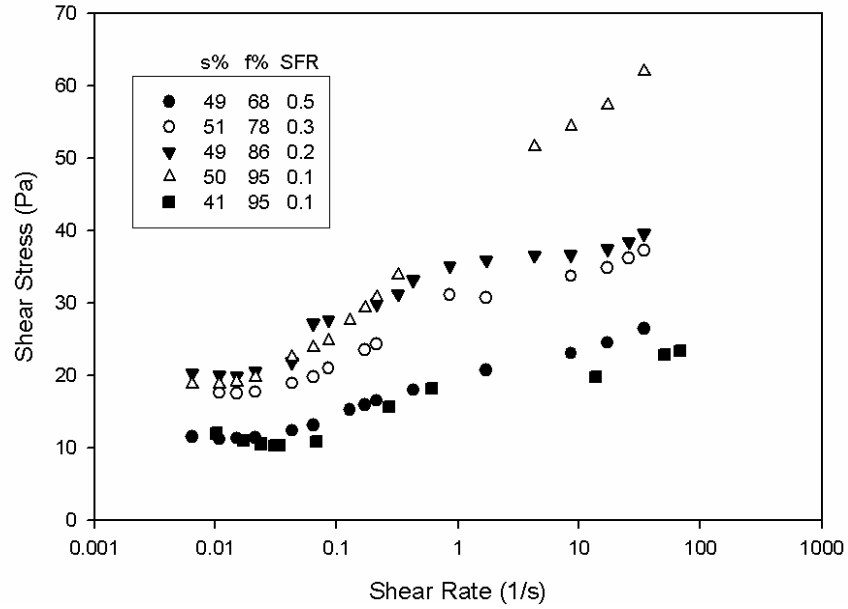


Figure 3.53 Effects of addition of coarse sand into MFT

#### 3.1.4.2.5 Regression of Flow Curves

The relationship between shear stress and shear strain rate is fitted using Herschel-Bulkley Model (Eq. 3.4) and Power Law Model (Eq. 3.2). It is found that the Power Law Model is the most appropriate model to fit all the measurement data. The fitting coefficients are presented in Table 3.18. The measured data and predicted shear stress using the models mentioned above are shown in Figure 3.54 to Figure 3.63.

Coussot and Piau (1995) found that  $k$  in Herschel-Bulkley model increase with sand fraction but no simple relationship between  $k$  and the solid volume fraction  $\phi$  were found. Attempts here are made to regress these  $k$  and (or)  $n$  values in either Power Law model or Herschel-Bulkley Model, a reliable regression equation can not be found.

Table 3.18 Parameters for Viscosity Regression Equations

Test #	Power Law $\tau = k\dot{\gamma}^n$			Herschel-Bulkley $\tau = \tau_y + k\dot{\gamma}^n$			
	k	n	R <sup>2</sup>	$\tau_y$	k	n	R <sup>2</sup>
1	27.4119	0.1133	0.9766	17.5	6.9359	0.382	0.955
2	27.3561	0.1174	0.9867	17	7.8298	0.3523	0.9608
3	9.165	0.0526	0.8238	9	0.1088	0.8467	0.9851
4	18.241	0.1208	0.9736	9.5	7.7319	0.2669	0.9449
5	16.3923	0.08	0.9045	9.8	6.2408	0.1859	0.8449
6*	N/A	N/A	N/A	N/A	N/A	N/A	N/A
7	37.2045	0.1483	0.9934	22.64	9.5975	0.4172	0.9255
8	18.5266	0.1051	0.9808	10.2	7.4079	0.2403	0.9387
9	27.2873	0.0953	0.9593	19.5	6.3618	0.3154	0.8581
10	31.6538	0.0765	0.885	13	18.2247	0.1278	0.8503
11	16.0199	0.0929	0.9263	7	8.4754	0.1637	0.9106

Note \*: Not enough data for data fitting for Test 6.

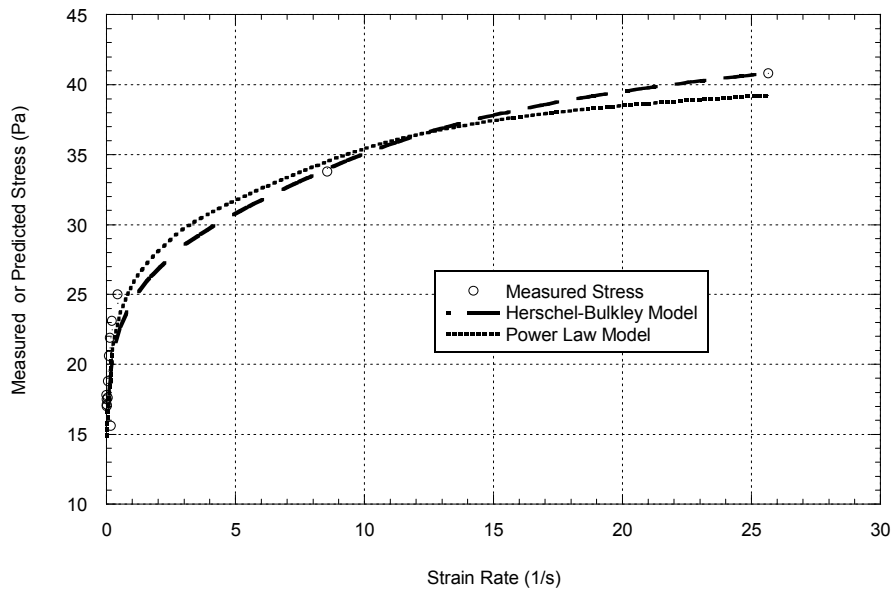


Figure 3.54 Herschel-Bulkley Model and Power Law Model Fitting of Relationship between Shear Stress and Strain Rate for Test 1

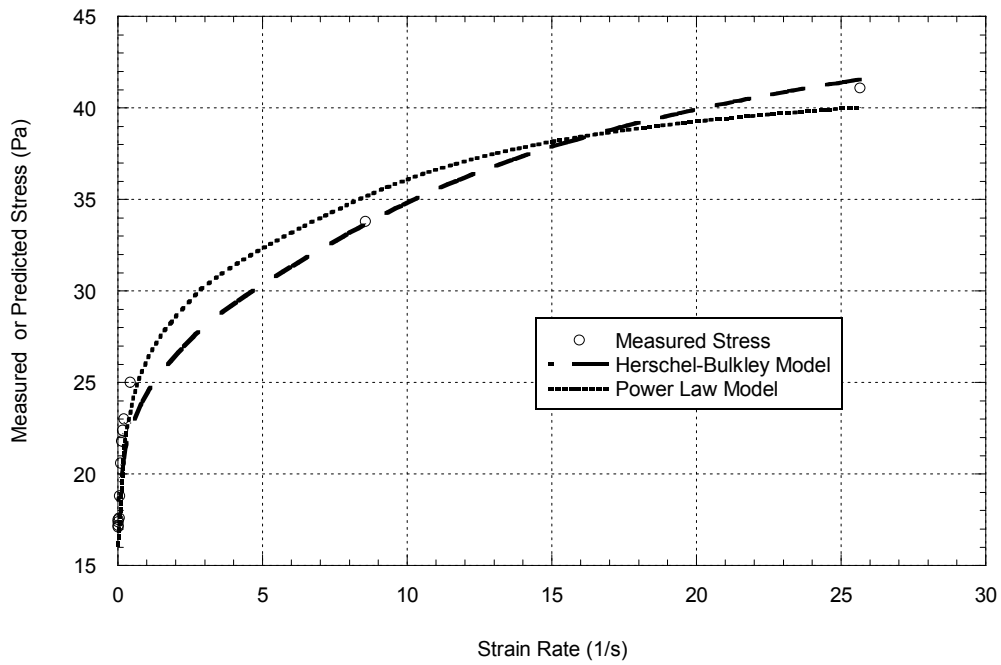


Figure 3.55 Herschel-Bulkley Model and Power Law Model Fitting of Relationship between Shear Stress and Strain Rate for Test 2

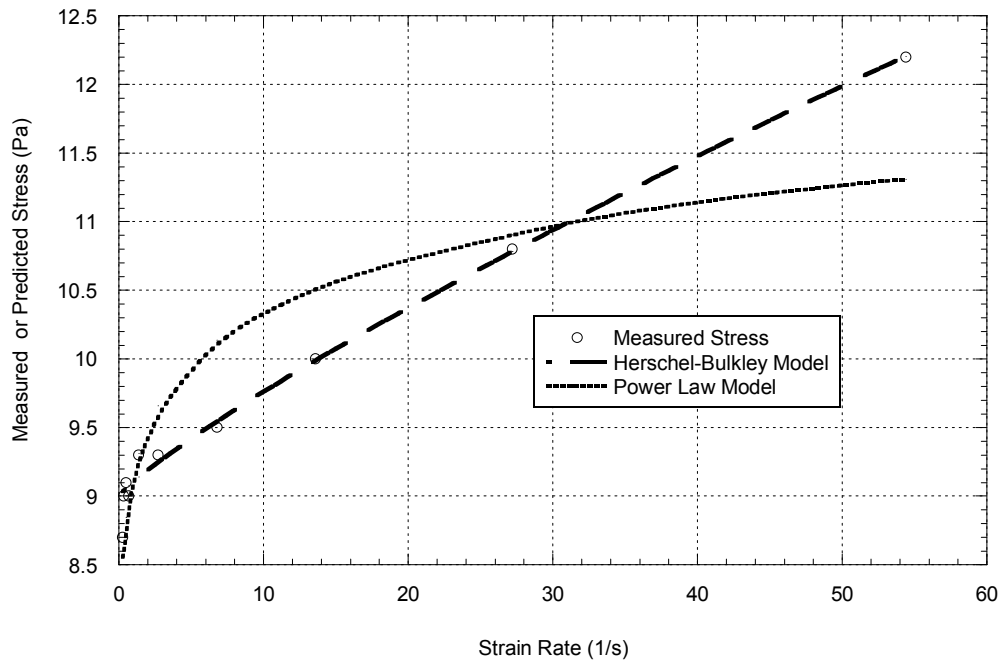


Figure 3.56 Herschel-Bulkley Model and Power Law Model Fitting of Relationship between Shear Stress and Strain Rate for Test 3

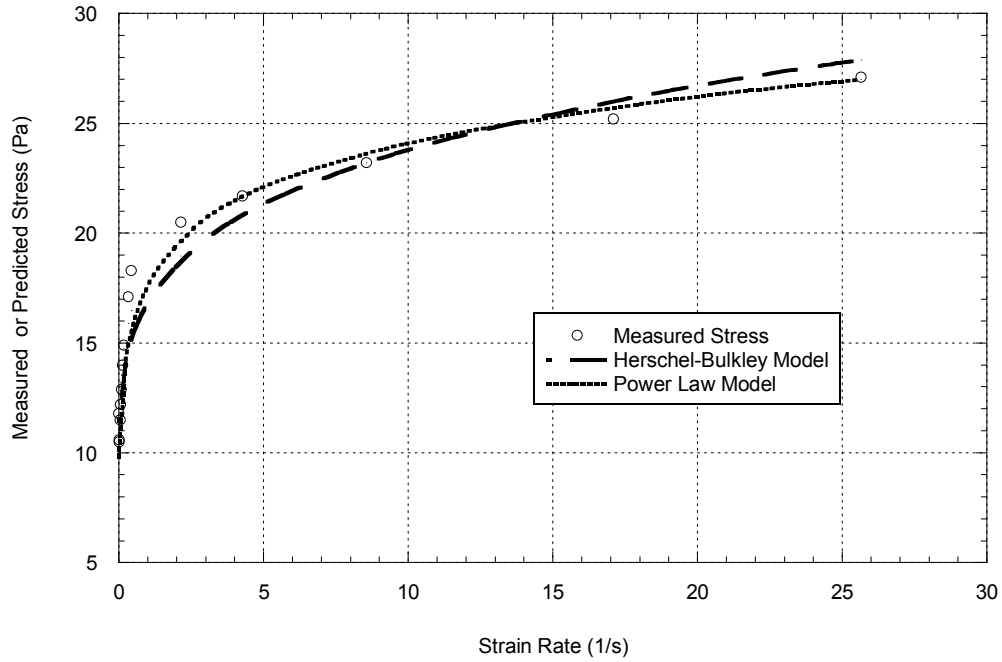


Figure 3.57 Herschel-Bulkley Model and Power Law Model Fitting of Relationship between Shear Stress and Strain Rate for Test 4

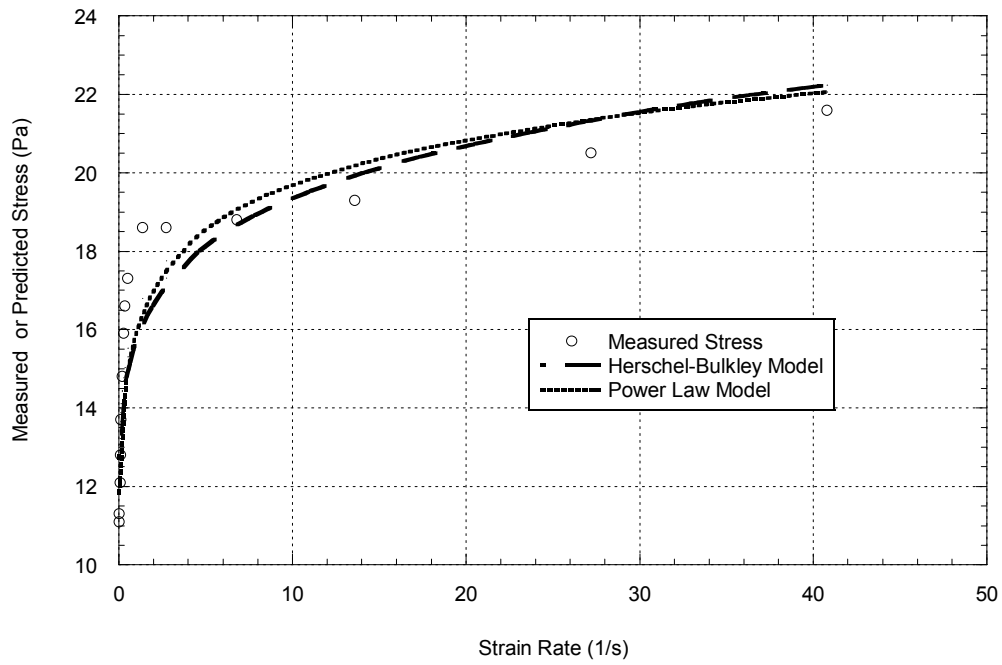


Figure 3.58 Herschel-Bulkley Model and Power Law Model Fitting of Relationship between Shear Stress and Strain Rate for Test 5

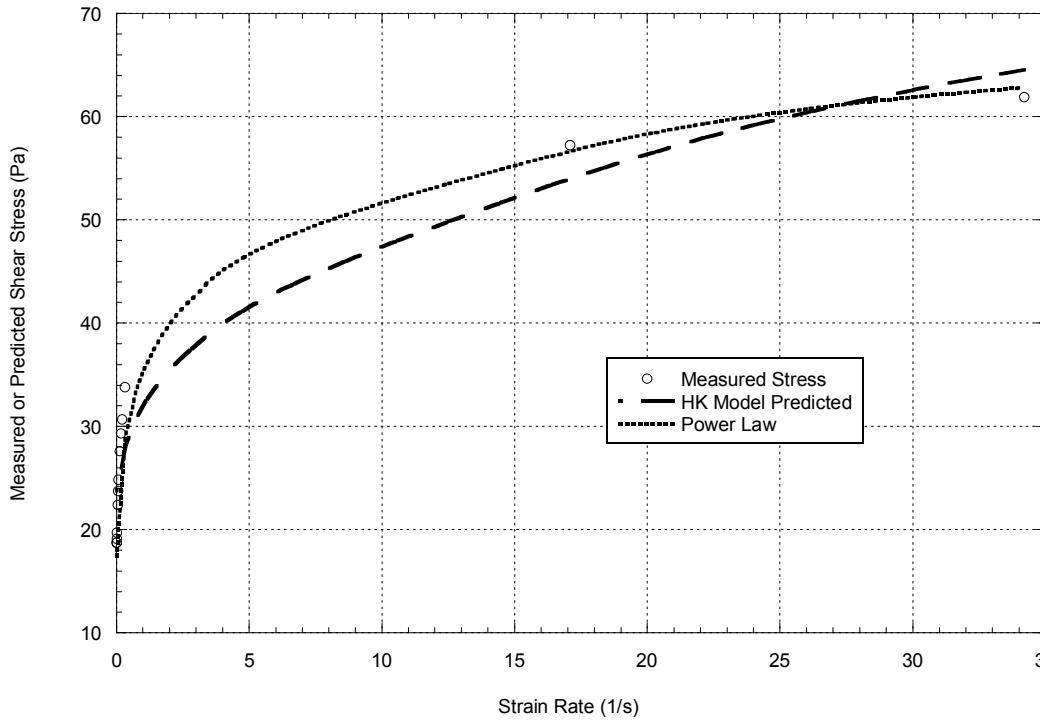


Figure 3.59 Herschel-Bulkley Model and Power Law Model Fitting of Relationship between Shear Stress and Strain Rate for Test 7

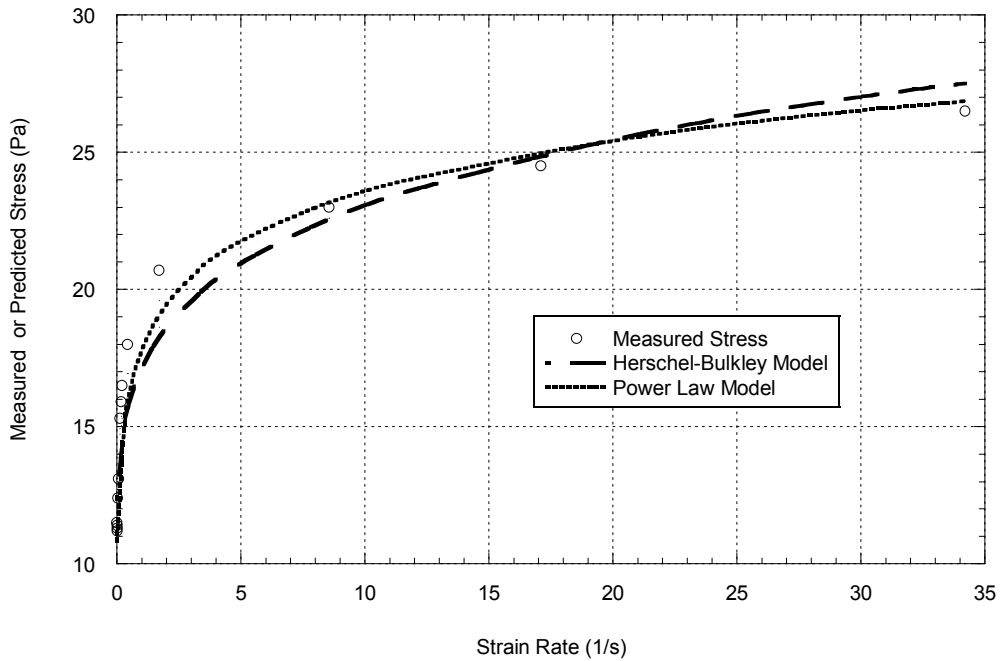


Figure 3.60 Herschel-Bulkley Model and Power Law Model Fitting of Relationship between Shear Stress and Strain Rate for Test 8

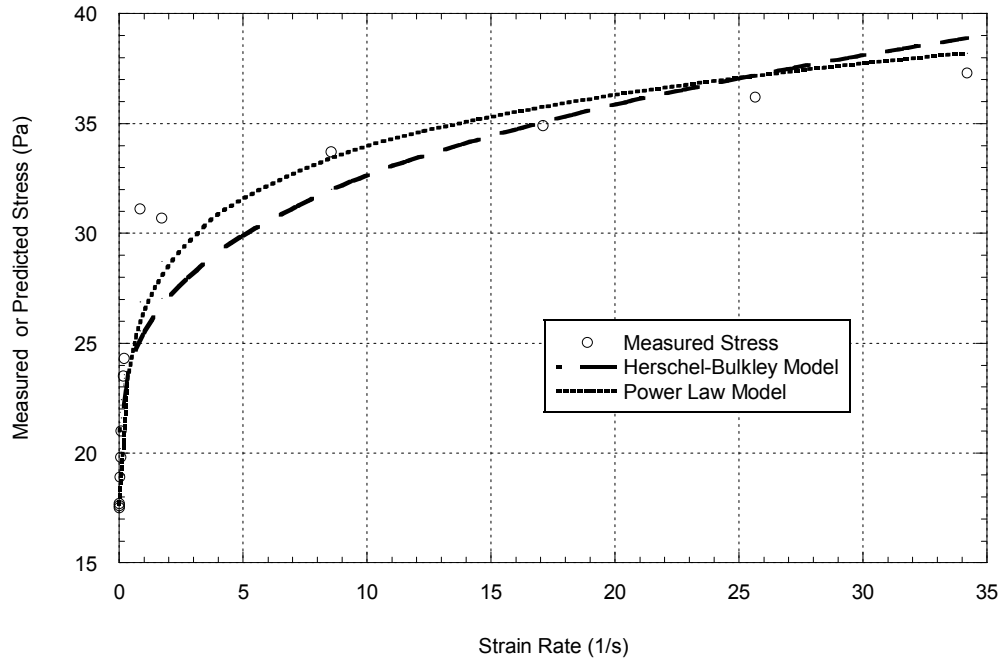


Figure 3.61 Herschel-Bulkley Model and Power Law Model Fitting of Relationship between Shear Stress and Strain Rate for Test 9

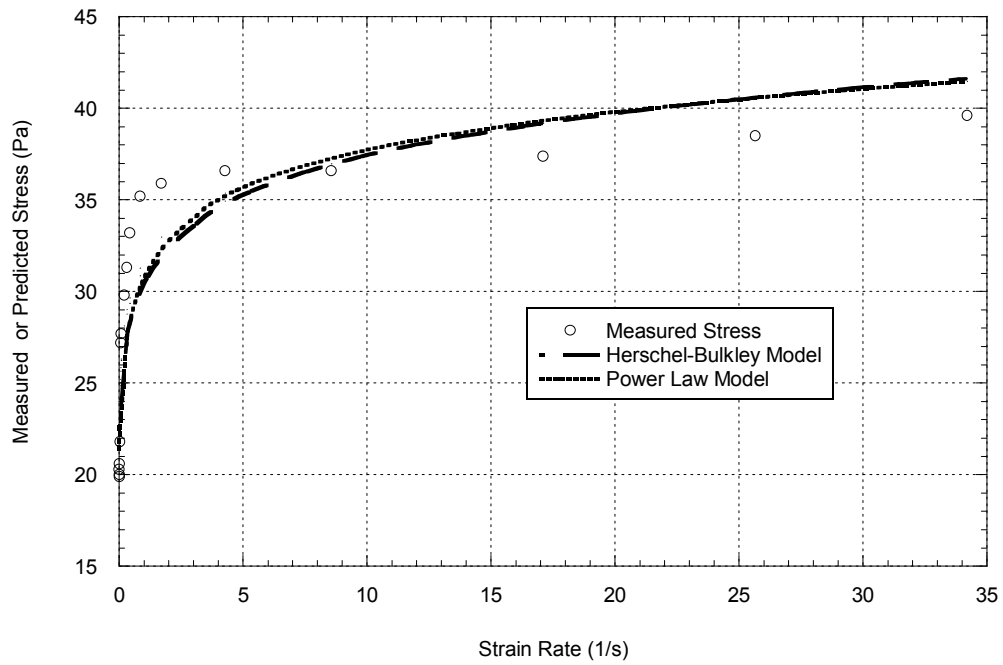


Figure 3.62 Herschel-Bulkley Model and Power Law Model Fitting of Relationship between Shear Stress and Strain Rate for Test 10

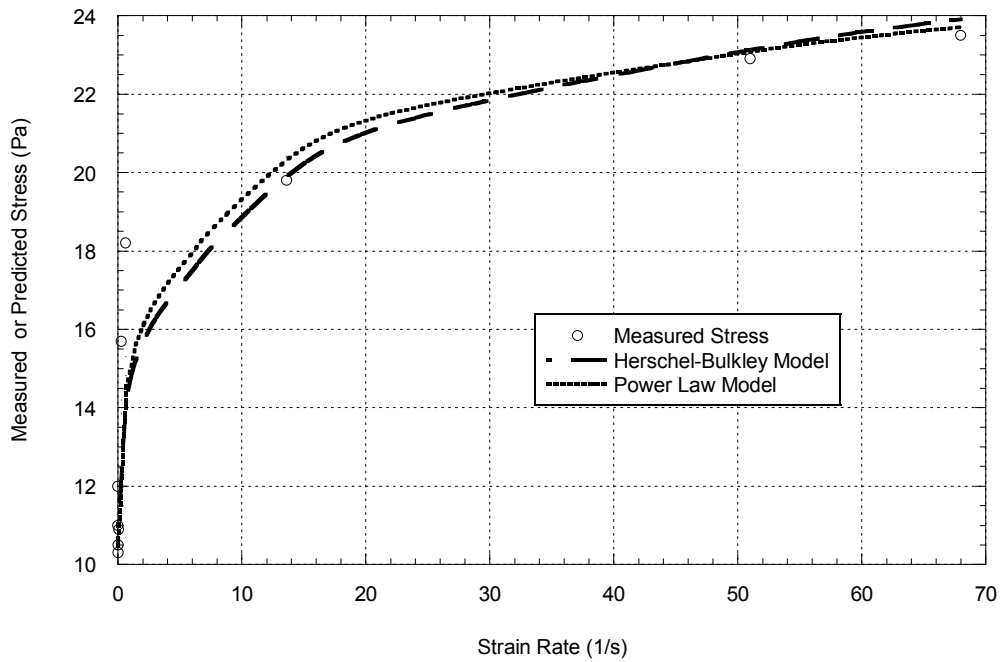


Figure 3.63 Herschel-Bulkley Model and Power Law Model Fitting of Relationship between Shear Stress and Strain Rate for Test 11

### 3.2 Verification of CFD Model Using Rheological Model Obtained from Experiments

#### 3.2.1 Simulation of Viscosity Measurements Using DV-II Viscometer by Single-Phase Model

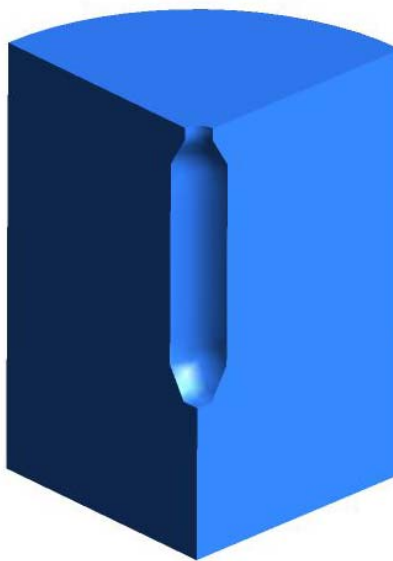


Figure 3.64 Geometry of DV-II Viscometer Model

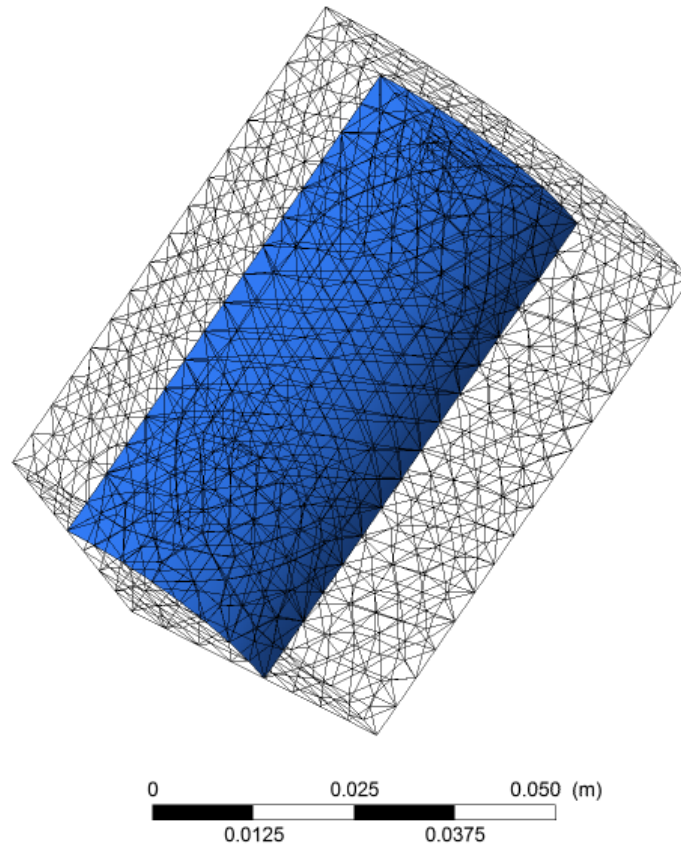


Figure 3.65 Coarse Mesh of DV-II Viscometer Model (3,791 nodes)

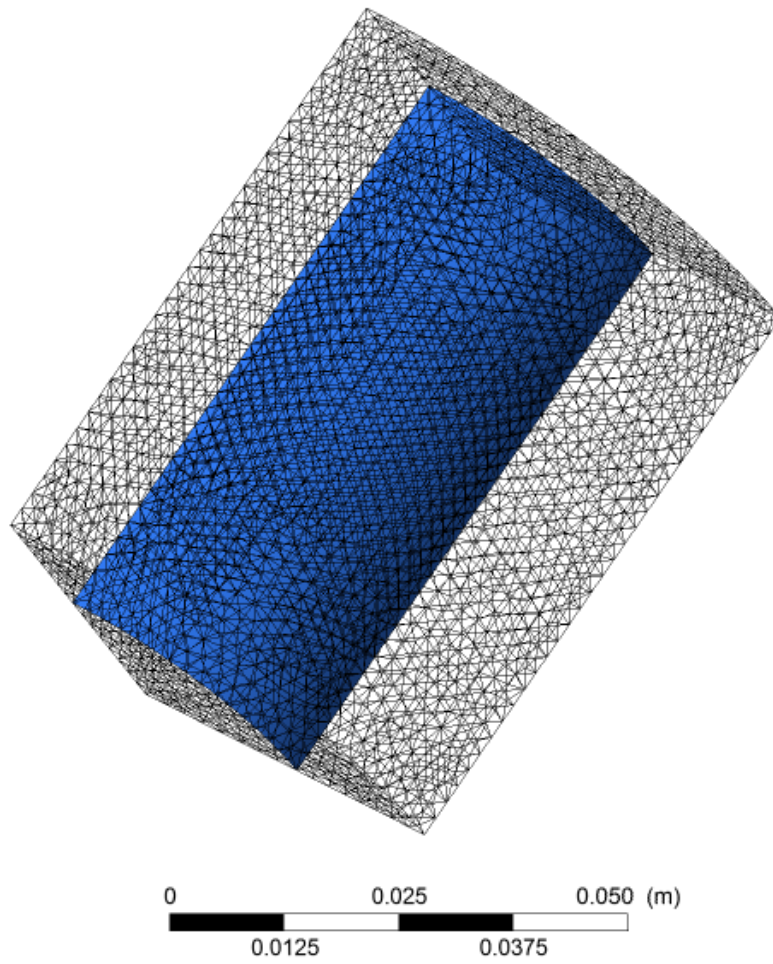


Figure 3.66 Medium Mesh of DV-II Viscometer Model (24,294 nodes)

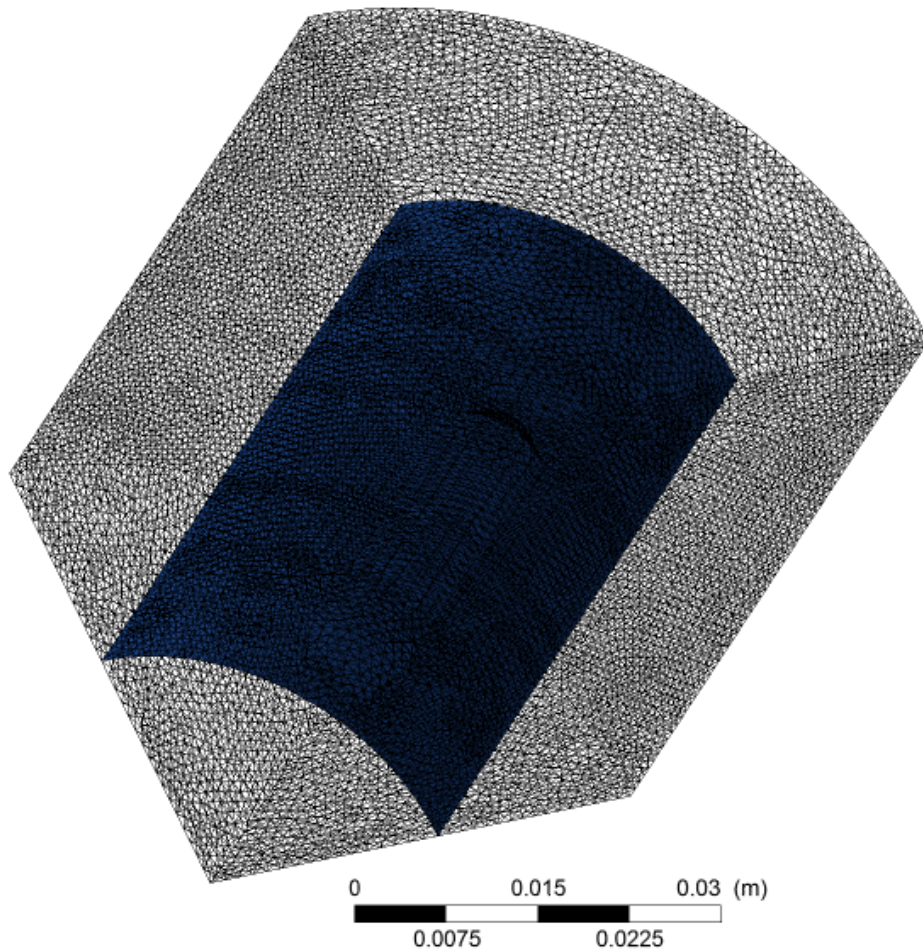


Figure 3.67 Fine Mesh of DV-II Viscometer Model (185,464 nodes)

Test 11 listed in Table 3.2 is used to evaluate the viscosity model obtained from viscosity measurements. The mixture contains a solids content of 41% and a fines content of 95%, consequently the density of the mixture is 1338 kg/m<sup>3</sup> if specific gravity of 2.7, 2.6 and 1.0 are assumed for coarse particle (sand), fine particles (clay) and water respectively. The slurry is treated as a single phase and the Herschel-Bulkley rheological model as shown in Table 3.18 is adopted. Since the Reynolds number for maximum of rotation speed is 6.72, the flow is laminar. Axial symmetric flow field also is assumed and thus a quarter of the flow field is simulated.

The capacity of the Multiple Frame of Reference (MFR) in CFX-10 allows to model the rotation of the spindle in the outer cylinder. According to the Theory Manual

(Ansys, 2005), Frozen Rotor option produces a steady state solution to the multiple frame of reference problems. In this model, the relative orientation of the components (stators and rotors) is fixed while the frame of reference is changed. By simplifying the relative orientation of the components, significant computation cost is saved. This method is most useful when the circumferential variation of the flow is large in relation to the machine speed at the interface. The consequence of the simplification is that the transient mixing of the stationary components with rotating components is ignored. Nevertheless, the transient mixing effects is negligible with consideration of the assumption of laminar flow while measuring the viscosity of the slurry. As a result, the Frozen Stator model is selected for the simulation of viscosity measurements.

The geometry of the model is shown in Figure 3.64. The cylinder shown in the figure has a diameter of 5.76 mm and the diameter of the cup is 81.30 mm. The height of the model is 70.02 mm. The grid sensitivity is performed using the mesh with coarse, medium and fine grid density. The three meshes are shown in Figure 3.65 to Figure 3.67. The coarse mesh contains 3,791 nodes and the medium mesh 24,294 nodes. The fine mesh has 185,464 nodes. The meshes are generated by reducing the Body Space and the Face Space by 50% each time.

The computing domain is divided into rotating inner domain and stationary outer one. The rotating domain rotates around the z axis at a speed of 0.1 RPM. The interface between rotating domain and stationary domain is a cylindrical surface with diameter of 44 mm. It is assumed that the pattern of the flow have a periodically repeating nature in the Azimuthal direction. Therefore, the faces that are parallel to the axis of rotation are specified as Rotationally Periodic boundary condition. The cylindrical spindle and the external wall are assigned as Non-slip Wall. The top faces of the both domains are specified as Slip Wall.

The Generalized Richardson Extrapolation method presented by Baker (2005) and Franke et al. (2007) is used here to calculate the value of the simulated torque. The grid refinement ratios  $r_{21}$  and  $r_{32}$  are defined as follows:

$$r_{21} = h_2 / h_1 \quad (\text{Eq. 3.11})$$

$$r_{32} = h_3 / h_2 \quad (\text{Eq. 3.12})$$

Where the subscripts 1, 2 and 3 are referred to the fine mesh, medium mesh and coarse mesh, respectively, and hence  $h_1$ ,  $h_2$  and  $h_3$  are the lengths of the grids for fine, medium and coarse meshes, respectively.

In this simulation, the length of the mesh is reduced by 50% each time. Therefore,  $r_{21} = r_{32} = 2$ . As a result, the order of the numerical solution can be calculated explicitly from the following equation:

$$p = \frac{\log[(f_2 - f_3)/(f_1 - f_2)]}{\log(r)} \quad (\text{Eq. 3.13})$$

Where  $p$  is order of the numerical solution,  $r$  the grid refinement ratio, and  $f_1$ ,  $f_2$  and  $f_3$  are the solution obtained from the fine grid, medium grid and coarse grid, respectively. The estimated exact solution is then calculated as follows:

$$f_{ex} = f_1 + \frac{f_1 - f_2}{r^p - 1} \quad (\text{Eq. 3.14})$$

The estimated exact solution for the torque in this simulation case is  $1.02 \times 10^{-4}$  N.m. Compared with the measured torque of  $8.70 \times 10^{-5}$  N.m, the error of 18% occurs in the simulation.

Table 3.19 Richardson Extrapolation for Simulated Torque

<b>k</b>	<b>Mesh</b>	<b>Grid Length</b>	<b>Obtained Torque (f) (N.m)</b>
1	Fine	0.925 mm	1.10E-4
2	Medium	1.85 mm	1.34E-4
3	Coarse	3.7 mm	1.67E-4

### 3.2.2 Simulation of Vane Shear Tests Using R/S Solid Rheometer by Single-Phase Model

Barnes (1999) questioned the existence of yield stress. The author concluded that soft solids will demonstrate a creep behavior when the stress is below the apparent yield stress and a Newtonian-plateau viscosity can be used to describe the creep behavior. The yield stress is more or less related to our capability of measuring the shear stress at very tiny shear strain rate. Increasingly, the utility of the vane shear test to measure yield stress of a Non-Newtonian fluid and soft solids slurries is being recognized. Nguyen et al. (2006) have shown that the yield stress determined by the vane shear test is a reliable and reproducible measurement method for the concentrated Non-Newtonian slurry. From the field of geotechnical engineering and the use of vane shear tests to determine undrained shear strength, it is understood that several assumptions are involved in calculating the yield stress parameters using the vane method. It is assumed that an imaginary cylinder with the same dimensions as those of vane blades is formed when the slurry yields under shearing by the vane. A yield surface coinciding with the imaginary cylinder surface is assumed in the interpretation of the test results. It is also assumed that the fluid between two adjacent vane blades is stationary in relation to the movement of blades - that is no secondary flow occurs when shearing the slurry in vane tests. The most important assumption is that the distribution of the shear stress on the yield surface is uniform and the magnitude of the shear stress is equal to the yield stress of the Non-Newtonian slurry (Nguyen et al. 1983; Keentok et al. 1985).

Several authors have verified these assumptions. Barnes et al. (1990) confirmed the existence of the fluid cylinder within the periphery of vane blades. Keentok (1985) demonstrated that the stress concentration at the tips of the blades and the diameter of the fluid cylinder is larger than the vane diameter. Yan et al. (1997) evaluated the existence of the yield surface for viscoelastic and plastic fluids in a vane viscometer using finite element method. They also validated the assumption of uniform shear on a rotating cylinder of material included in the blades of a vane. They further concluded that for Herschel-Buckley and Casson fluid, a rotating rigid cylinder of fluid is attached

at the vane blades and the shear stress on the surface of the fluid cylinder is uniformly distributed.

Within the field of soil mechanics and the measurement of undrained shear strength on soft deposits, De Alencar et al. (1988) challenged the assumption of uniform distribution of the shear stress over the cylinder surface for the progressive failure in the vane test. The authors used a strain softening finite element model to evaluate the shear stress distribution around the perimeter of the vane and concluded that the stress distribution is not known and the assumption of uniform mobilization of shear strength will lead to an incorrect evaluation of the peak strength of the material.

In this section, CFX-10 is used to simulate the measurement of yield stress of the MFT using the Brookfield R/S Soft Solid Rheometer. The torque from the simulation is compared with that from measurement. The yield surface of MFT is evaluated in three dimensions.

Steady state, quasi transient and transient calculations are three methods that have been applied for simulating the interactions between the rotor and stator (Belardini 2003). The rotor refers to the vane and the stator is the mixing vessel. Although transient rotor-stator methods using a sliding mesh provides a more accurate time solution, excessive computing resources required for this method limits its applications to this case. Given that the mixing vessel contains no baffles to cylindrical flow, the frozen rotor interface method is applied for the simulations presented here.

The geometry of the vane is shown in Figure 3.68. The diameter of the vane blades is 20 mm and the height is 40 mm. The vane is immersed into a beaker with an internal diameter of 80.13 mm and a height of 90 mm. The computing domain is subdivided into rotating and stationary parts, with the rotating domain rotating with vane blades at a speed of 0.05 radian/s. A quarter of the domains is simulated as the axisymmetry is assumed in the simulation.

As homogeneity of the measured slurry is assumed, a single phase model is applied in the simulations. In the experiments, turbulent flow is avoided in order to obtain an

accurate yield stress measurement. Consequently, laminar flow is assumed for the CFD simulations. In the following sections, the MFT sample in Test 7 in Table 3.18 with solids content of 50% and fines content of 95% is simulated. The viscosity model for the MFT sample based on the regression of the measured viscosity data is applied in the CFD model. The flow curve for the sample is as follows:

$$\tau = 22.64 + 9.5975\dot{\gamma}^{0.4172} \quad (\text{Eq. 3.15})$$

A non-slip wall boundary condition is set for the vane blades and the shaft of the vane. The domain containing the vane is assumed to rotate at an angular velocity of 0.05 radian/s. Similar to the simulation of viscosity measurement, the external faces that are parallel to the axis of rotation are specified as Rotationally Periodic boundary condition. The top faces of the both domains are specified as Slip Wall.

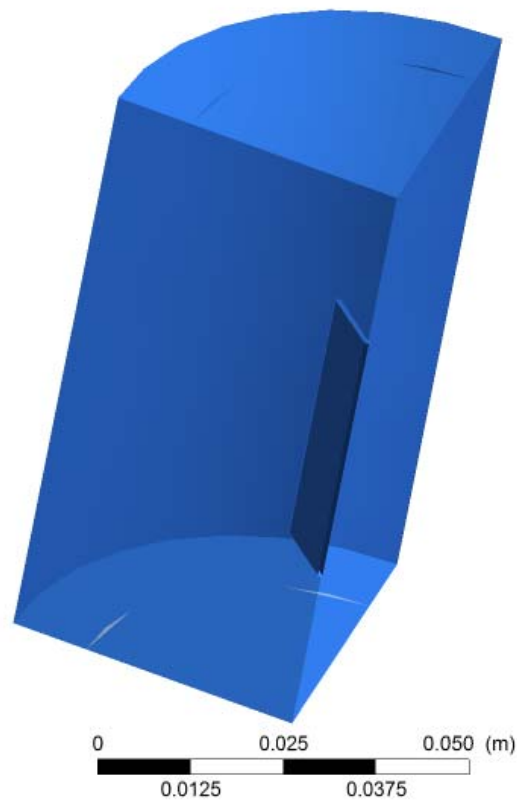


Figure 3.68 Geometry of Brookfield R/S Soft Solid Rheometer Model

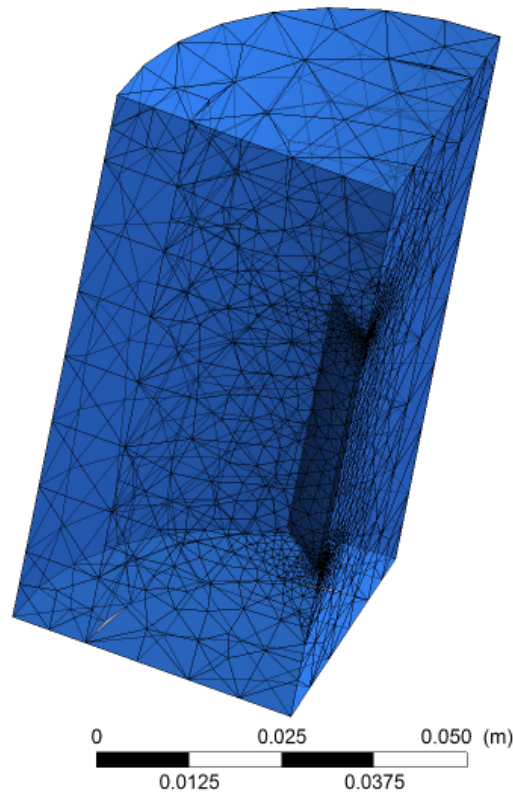


Figure 3.69 Coarse mesh of Brookfield R/S Soft Solid Rheometer model  
(27,320 nodes)

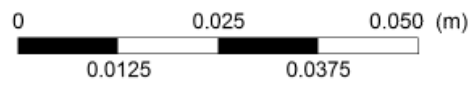
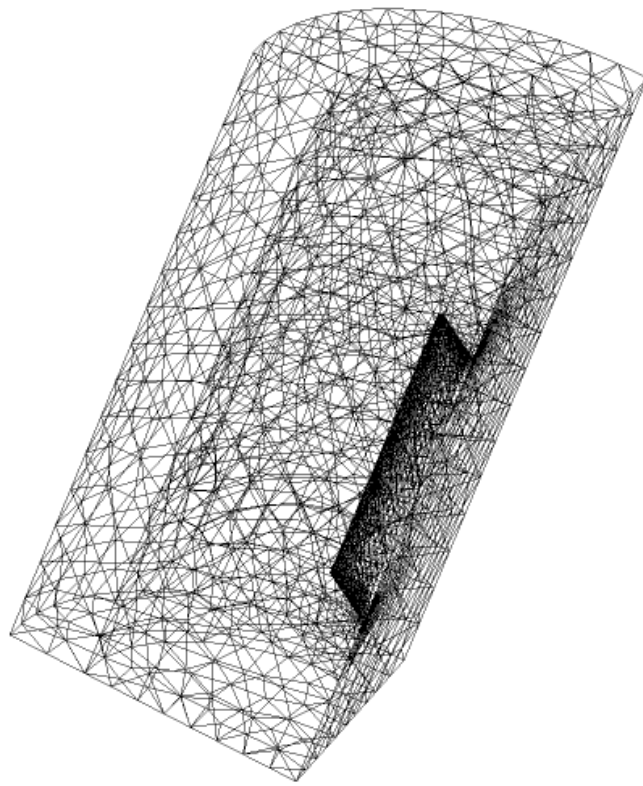


Figure 3.70 Medium mesh of Brookfield R/S Soft Solid Rheometer model  
(28,212 nodes)

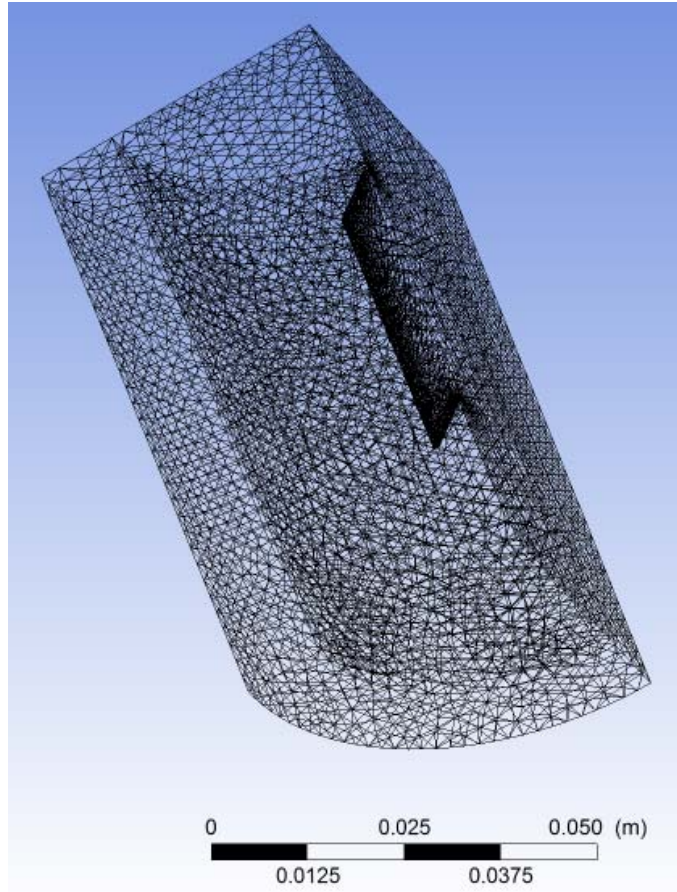


Figure 3.71 Fine mesh of Brookfield R/S Soft Solid Rheometer model (41,597 nodes)

In order to conduct grid sensitivity test, three meshes with coarse, medium and fine grid density are used in the simulation. The meshes are shown in Figure 3.69 to Figure 3.71. The length of the grids is shown in Table 3.20. Therefore, the refinement ration  $r_{21}$  is equal to  $r_{32}$ , which simplifies the Richardson Extrapolation. The exact solution for the torque based on these simulations can be calculated using Eq. 3.14. A value of  $1.46 \times 10^{-3}$  N.m is obtained from the calculation, which is 6% lower than the measured torque value of  $1.55 \times 10^{-3}$  N.m.

Table 3.20 Richardson Extrapolation for Simulated Torque

<b>k</b>	<b>Mesh</b>	<b>Grid Length</b>	<b>Obtained Torque (f) (N.m)</b>
1	Fine	2.25 mm	1.43E-03
2	Medium	4.5 mm	1.35E-03
3	Coarse	9 mm	1.32E-03

The contours of shear strain rate on the plane passing through the middle of the vane blades are shown in Figure 3.72. It shows that the shear strain rate is almost uniform in the circumferential direction except for the higher shear strain rate in the proximity of the tip of the blades. In order to evaluate the shear strain rate over the virtual fluid cylinder surface in detail, the shear strain rate over a polyline located at a radius equal to the tip of the vanes is computed and is shown in Figure 3.73. The location of the polyline is shown in Figure 3.74. Noting that the blades are located at  $\theta = 0^\circ$ , it is evident that the mobilized shear strain rate is not uniform to a certain extent. In addition, the maximum shear strain rate occurs around the vane blade tip. As expected, the minimum shear strain rate appears between two blades, which is consistent with experimental observations and experience with vane shear testing in geotechnical engineering.

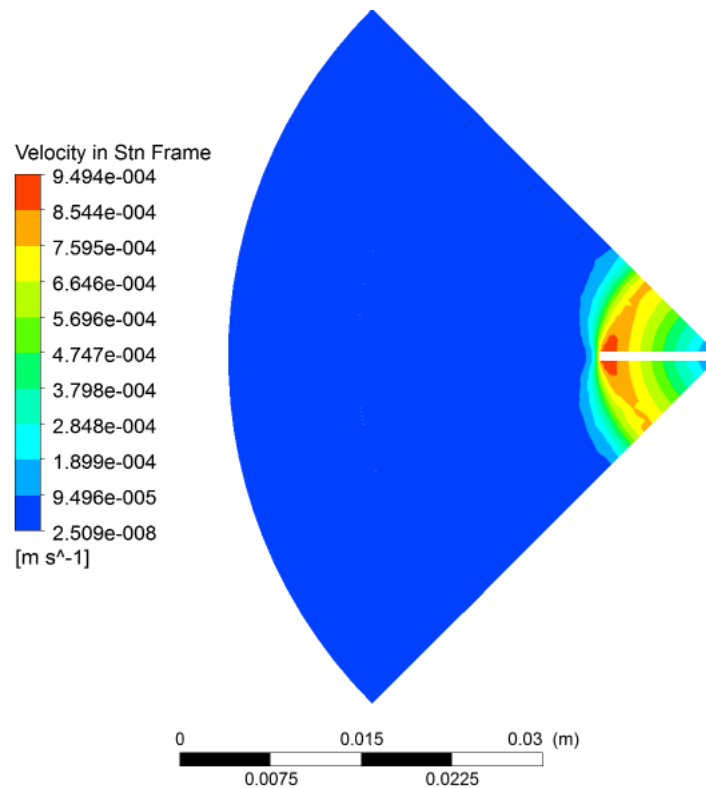


Figure 3.72 Shear strain rate for MFT yield stress measuring

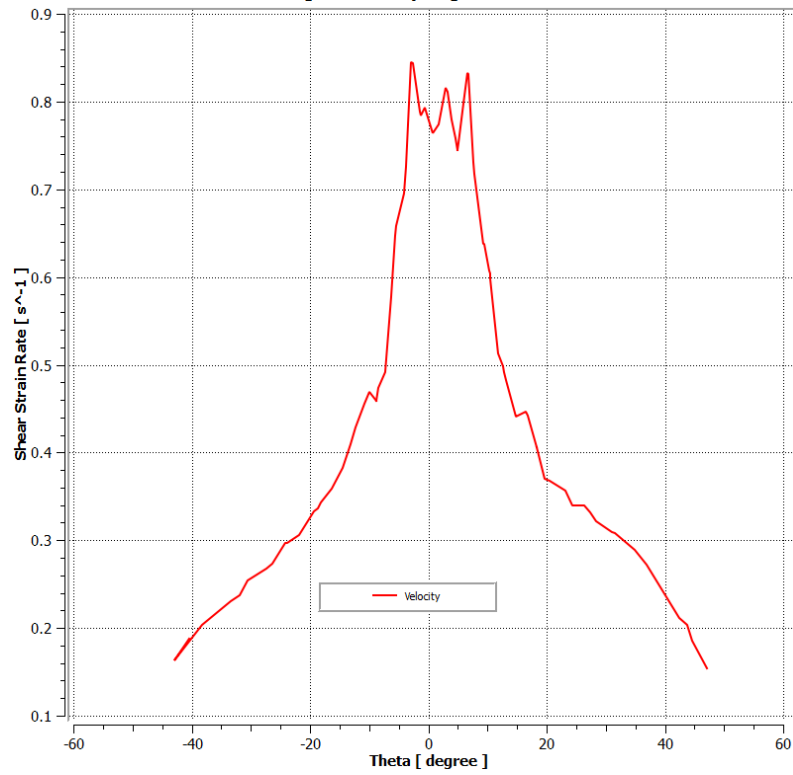


Figure 3.73 Shear strain rate for MFT along a curve with radius of 0.010 m on the horizontal mid-plane passing through the blade

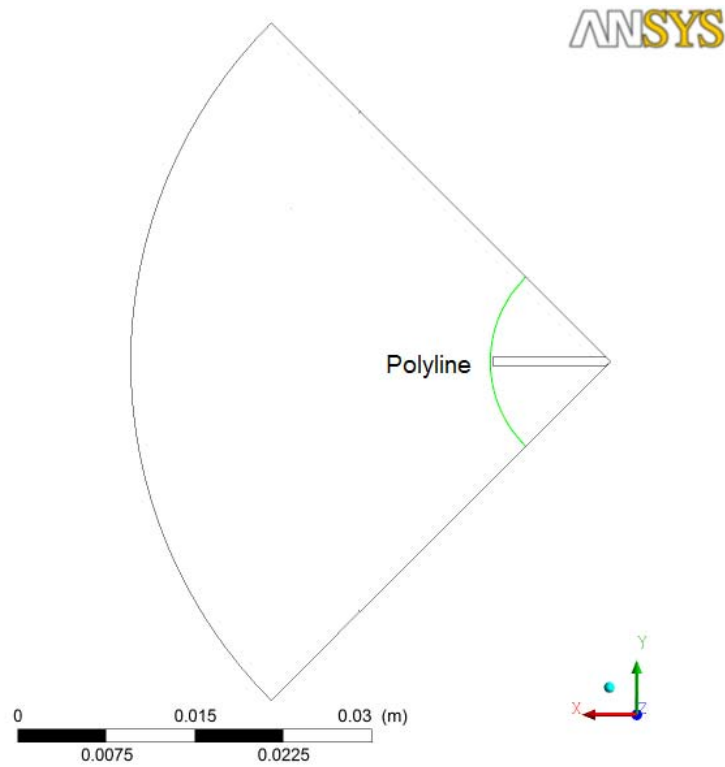


Figure 3.74 Location of the curve for shear rate plot

The shear strain rate on a plane passing through the vane blades is shown in Figure 3.75. If the yield surface is the surface where the shear strain rate is greatest, the shape of the intersection of the yield surface with the horizontal plane can be approximated as a circle. The peak of the shear strain rate is almost the same, indicating further that the assumption of cylindrical yield surface is valid for MFT. The shear strain rate inside the circle with radius equal to that of vane blades is approximately equal to zero, which supports the assumption that the fluid entrapped in the imaginary cylinder is acting in a rigid manner and there is no secondary flow between the adjacent blades.

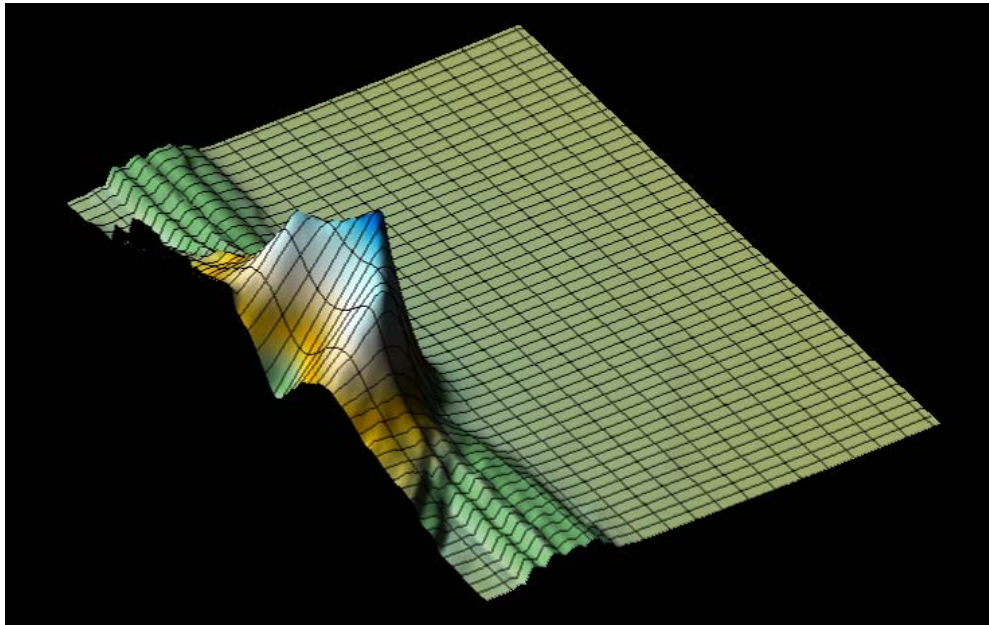


Figure 3.75 Shear strain rate surface plot for MFT slurry over the plane passing through the middle of the vane

The velocity vectors on the plane passing through the middle of this plane are shown in Figure 3.76. Approximately uniform velocity in the tangential direction can be observed. It also can be observed that the velocity of the fluid outside the imaginary fluid cylinder is very small and the fluid between the vane blades rotate at the same angular velocity as that of vane blades.

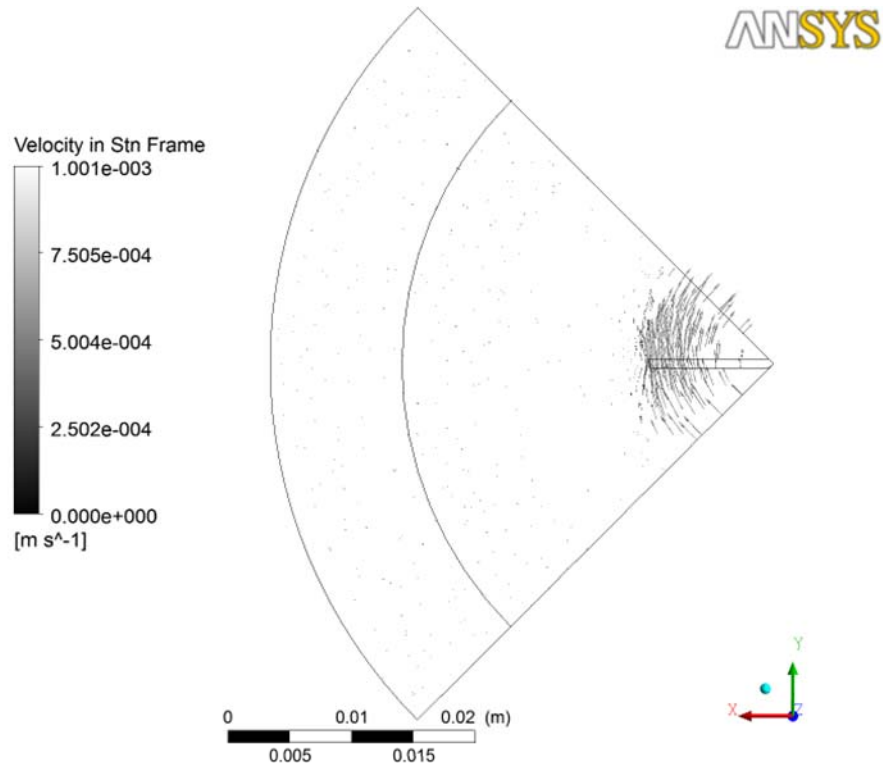


Figure 3.76 Vector of velocity on the plane passing through the middle of the vane blades for MFT

### 3.3 Summary and Conclusions

1. Tailings samples are prepared by mixing MFT, coarse sand and pond water in the specified proportion to achieve certain solids and fines contents. Brookfield DV-II+ Programmable Viscometer is used to measure the viscosity of the samples and Brookfield R/S Soft Solid Rheometer is used to obtain the static yield stress.
2. Similar to any other non-Newtonian material, the viscosity of the samples changes with the strain rate at which the samples are sheared. As a result, a curve of shear stress versus shear strain rate is obtained for each sample. All the samples show shear-thinning properties in the tests, that is, viscosity decreases with the increasing shear strain rate.
3. The static yield stress is obtained from the vane shear tests using above mentioned Rheometer. The peak value of the shear stress is determined to be the yield stress. Analysis of the variation of static yield stress with solids content and fines content

indicates that the static yield stress increases with both solids and fines contents. At the same fines content, the static yield stress increases dramatically when the solids content approaches 60%. Likewise, the static yield stress increases with fines content at the same solids content. Available data suggests that greater increase in yield stress results from the fines content for the mixture with higher solids content. The variation of yield stress with solids content for MFT is curve fitted using the equation proposed by Coussot (1997).

4. It is observed that increases in either solids content or fines content cause increase in apparent viscosity. It is found that fines content affects the shear stress and consequently the apparent viscosities when the solids contents are similar. Fines content becomes a minor factor when a significant difference in solids content exists.
5. Herschel-Bulkley model and Power Law model are used to fit the viscosity measurement data. It is found that the Power Law model is more appropriate to fit the relationship between shear stress and shear strain rate for the samples with a wide range of solids and fines contents.
6. Herschel-Bulkley model obtained from curve fitting for MFT is used in CFD simulations of the viscosity and yield stress measurements. The simulated torque for the MFT reasonably agrees with the measured torques from viscosity test using Brookfield DV-II+ Programmable Viscometer. The torque obtained from the simulation of the yield stress measurement is also in agreement with that from vane shear test using Brookfield R/S Soft Solid Rheometer. These simulation results indicate that the obtained Herschel-Bulkley model for the MFT is able to characterize this material in the CFD simulations. The assumptions made in vane shear tests are verified using CFD and it is found that these assumptions are generally true.

## Reference

- Ancey, C., Role of Lubricated Contacts in Concentrated Polydisperse Suspensions, *J. Rheol.* Volume 45, Issue 6, pp. 1421-1439, 2001.
- ANSYS Inc., CFX 10 Solver Theory, 2005.
- Azam, S. and Scott, J.D., Revision the Ternary Diagram for Tailings Characterization and Management. *Geotechnical News*, December, 2005.
- Baker, T. J. Mesh generation: Art or science? *Progress in Aerospace Sciences*, vol. 41, pp. 29–63, 2005.
- Barnes, H., 1999. The yield stress--a review or 'παντι ρει'—everything flows? *Journal of Non-Newtonian Fluid Mechanics*, 81, 133-178.
- Barnes, H.A. and Carnali, J.O., 1990. The vane-in-cup as a novel rheometer geometry for shear thinning and thixotropic materials. *Journal of Rheology*, vol.34, No.6, pp. 841.
- Belardini, E., State of the art in rotor-stator interaction for turbines. *QNET-CFD Network Newsletter*, vol.2 No.3 pp.22-26, 2003.
- Coussot, P., and Piau, J.-M. A larger-scale field coaxial cylinder rheometer to study the rheology of natural coarse suspensions. *J. Rheol.*, vol. 39, vol. 105-124, 1995.
- Franke, J., Hellsten, A., Schlünzen, H., and Carissimo, B. Best Practice Guideline for the CFD Simulation of Flows in the Urban environment, Cost Action 732.. pp. 33-36, May 1, 2007, University of Hamburg, Meteorological Institute, Centre for Marine and Atmospheric Sciences, Hamburg, Germany.
- Bingham, E.C. An Investigation of the Laws of Plastic Flow. U.S. Bureau of Standards Bulletin, 13, 309-353, 1916.
- Boyer, S. Détermination des propriétés rhéologiques des laves torrentielles à laide d'expériences d'écoulements sur un plan incliné. DEA MMGE, INPG, Grenoble, 1994.
- Brookfield Engineering Labs., Inc. More solutions to sticky problems: A guide to getting more from your Brookfield viscometer. 2005.

- Casson, N. in Rheology of dispersive systems, ed. C. C. Mills, Pergamon Press, Oxford, pp. 84, 1959.
- Chalaturnyk, R. J. and Scott, J. D. Soil Structure Behavior Diagram. Proceedings of High Density and Paste Tailings 2001 Seminar, University of the Witwatersrand, South Africa, May 10 – 11, 2001.
- Coussot, P. and Piau, J.M. On the behavior of fine mud suspension. Rheol. Acta, vol. 33, pp. 175-184, 1994.
- Coussot, P., Mudflow Rheology and Dynamics. International Association for Hydraulic Research, A.A.Balkema Publishers, Brookfield, USA., 1997.
- Danielson, L.J. and MacKinnon, M.D., Rheological Properties of Syncrude's Tailing Pond Sludge. AOSTRA Journal of Research, vol. 6, 99-121, 1999.
- De Alencar, J.A., Chan, D.H. and Morgenstern, N.R., 1988. Progressive failure in the vane test. Vane Shear Strength Testing in Soils: Field and Laboratory Studies, ASTM STP 1014, A.F. Richard, Ed., American Society for Testing and Materials, Philadelphia, pp.150-165.
- de Waele, A. Viscometry and Plastometry. Journal of the Oil & Colour Chemists Association, vol. 6, pp33-69, 1923.
- Dzuy, N.Q., Boger, D.V., Yield stress measurement for concentrated suspensions. Journal of Rheology, vol. 27, issue 4, pp. 321-349, 1983.
- Dzuy, N.Q., Boger, D.V., Direct yield stress measurement with vane method. Journal of Rheology, vol. 29, issue 3, pp. 335-347, 1985.
- Gonet, A., Stryczek, S., Pinka, J. Analysis of Rheological Models of Selected Cement Slurries .Acta Montanistica Slovaca Ročník 9 (2004), číslo 1, 16-20.
- Herschel, W.H. and Bulkley, R. Konsistenzmessungen von Gummi-Benzollösungen. Kolloid Zeitschrift, vol. 39, pp. 291–300, 1926.
- Keentok, M., Milthorpe, J. F. and O'Donovan, E., On the shearing zone around rotating vanes in plastic liquids: Theory and experiment. Journal of Non-Newtonian Fluid Mechanics, vol.17, pp.23, 1985.
- Keetok, M. The measurement of the yield stress of liquids. Rheol. Acta, 21, 325-332, 1982.

- Nguyen, Q.D., Akroyd, T., De Kee, D.C., and Zhu L.X. Yield stress measurements in suspensions: an inter-laboratory study. *KOREA-AUSTRALIA RHEOLOGY JOURNAL*, vol. 18, pp. 15-24, 2006.
- Nguyen, Q.D., and Boger, D.V. Yield stress measurement for concentrated suspensions. *J. Rheol.*, vol. 27, pp. 321-349, 1983.
- O'Brien, J.S. and Julien, P.Y. Laboratory analysis of mudflows properties. *J. Hydraulic Eng.*, 114, 877-887, 1988.
- Ostwald, W. Speed function of viscosity of disperse systems. I. *Kolloid-Zeitschrift*, vol. 36, pp. 99-117, 1925.
- Scott, J.D., Dusseault, M.B., and Carrier, W.D. Behavior of the Clay/Bitumen/Water Sludge System From Oil Sands Extraction Plants, *Applied Clay Science*, vol. 1, p. 207, 1985.
- Sengun, M.Z. and Probstein, R.F. Bimodal model of slurry viscosity with applications to coal slurries. Part 1. Theory and experiment. *Rheologica Acta*, vol. 28, pp. 382-393, 1989a.
- Sengun, M.Z. and Probstein, R.F. Bimodal model of slurry viscosity with applications to coal slurries. Part 2. High shear limit behavior. *Rheologica Acta*, vol. 28, pp. 394-401, 1989b.
- Turian, R.M., Fakhreddine, M.K., Avramidis, K.S. and Sung, D.J., Yield stress of coal-water mixtures. *Fuel*, vol. 72, issue 1, pp. 1305 – 1315, 1993.
- Yan, J. and James, A.E., The yield surface of viscoelastic and plastic fluid in a vane viscometer. *Journal of Non-Newtonian Fluid Mechanics*, vol.70, pp.237-253, 1997.
- Yong, R.N., Sheeran, D.E., Sethi, A.J., and Erskine, H.L. The Dynamics of Tar-Sand Tailings, presented at the 33rd Annual Tech. Mtg. of the Petrol. Soc. Of the CIM, pp. 116, 1981.

## CHAPTER 4 CFD SIMULATION OF OIL SAND SLURRY SEGREGATION<sup>1,2</sup>

### 4.1 Introduction

Although segregation of the solid particles in gas is studied thoroughly, limited research on the segregation of slurry or suspension can be found in the literature. In contrast to the segregation occurring in granular flow, the influence of the liquid media on the solid particle, as well as on the interactions between solid particles complicates the problem.

Segregation mechanisms are introduced and numerical simulation of the segregation of solid particles in granular media is reviewed in Chapter 2. This chapter will present the simulation of segregation of solid particles in liquid media. The simplest scenario of two solid size groups is verified first followed by the validation of the simulation of segregation of slurry with four solid size groups. These verifications will lead to the more complicated and more realistic scenarios in real oil sand tailing slurry.

### 4.2 Verification of the CFD Simulation of Sedimentation

#### 4.2.1 Bidisperse Suspension

Burger et al. (2000) modeled the sedimentation experiments reported by Schneider et al. (1985) using shock-capturing numerical schemes for the solution of systems of conservation laws. The authors claimed that the simulation results agreed well with the experiment data. The material used in the experiment is glass beads with density of  $2790 \text{ kg/m}^3$ . The particles of the diameter  $d_1 = 0.496 \text{ mm}$  and  $d_2 = 0.125 \text{ mm}$  respectively are settled in a column of height  $L = 0.3 \text{ m}$ . The diameter of the column is assumed to be  $0.03 \text{ m}$ . The density and viscosity of the fluid are  $1208 \text{ kg/m}^3$  and

---

<sup>1</sup> A version of part of this chapter has been published. Yang, J. and Chalaturnyk, R.J., Computational Fluid Dynamics Simulation of Very Dense Liquid-Solid Flow Using Eulerian Model. Proceedings of the Third International Conference on Computational Methods in Multiphase Flow 2005, Portland, Maine, U.S.A., October 31 – November 2, 2005.

<sup>2</sup> A version of part of this chapter has been published. Yang, J. and Chalaturnyk, R.J., Computational Fluid Dynamics Simulation of Standpipe Tests. Proceedings of the First International Oil Sands Tailings Conference, Edmonton, Alberta, Canada, December 7 – 10, 2008.

0.02416 kg/m.s respectively. The initial solid volume fractions for coarse and fine particles are 0.2 and 0.05 respectively, which is equivalent to a mixture with a solids content of 43% and a fines content of 0%. The volume fractions are the ratio of the volume of the solid particles to the total volume of the mixture.

Grid independence tests are conducted for the model. Three grids with density of 6 x 30, 12 x 60 and 24 x 120 nodes are tested. The simulation time is 100 seconds. The profiles of the volume fractions for the coarse and fine particles are shown in Figure 4.1. It can be observed that the obtained profiles are almost the same except in the region between the elevation of 0.075 m and that of 0.125 m. In this region, the interface between supernatant liquid and suspension develops. The simulation with a grid of 24 x 120 nodes obtains sharper interface as the volume fraction of the coarse particles change dramatically within a shorter elevation range. Based on the observation that almost same profiles are obtained in the grid independence test, it is determined that the grid of 12 x 60 is used in the subsequent simulations for both the bidisperse and polydisperse suspension in MFIX.

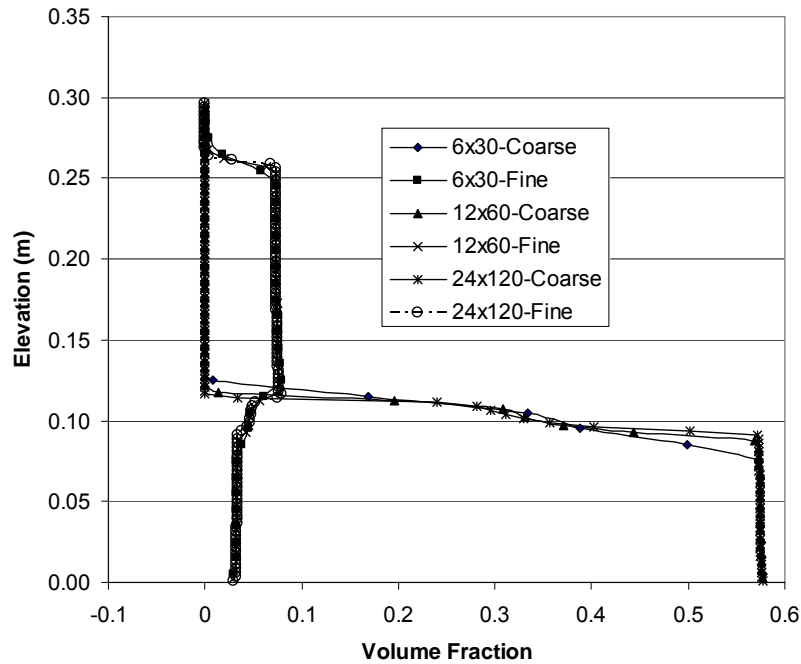


Figure 4.1 The grid independence tests for the bidisperse mixture

The volume fraction profile for coarse and fine solid particles at time of 51.9 s, 299.8 s and 599.7 s are compared in Figure 4.2 to Figure 4.4. A reasonable agreement is achieved using MFIX and FLUENT. It can be seen that these models in the CFD packages can be used to simulate the sedimentation of bidisperse suspension with reasonable accuracy.

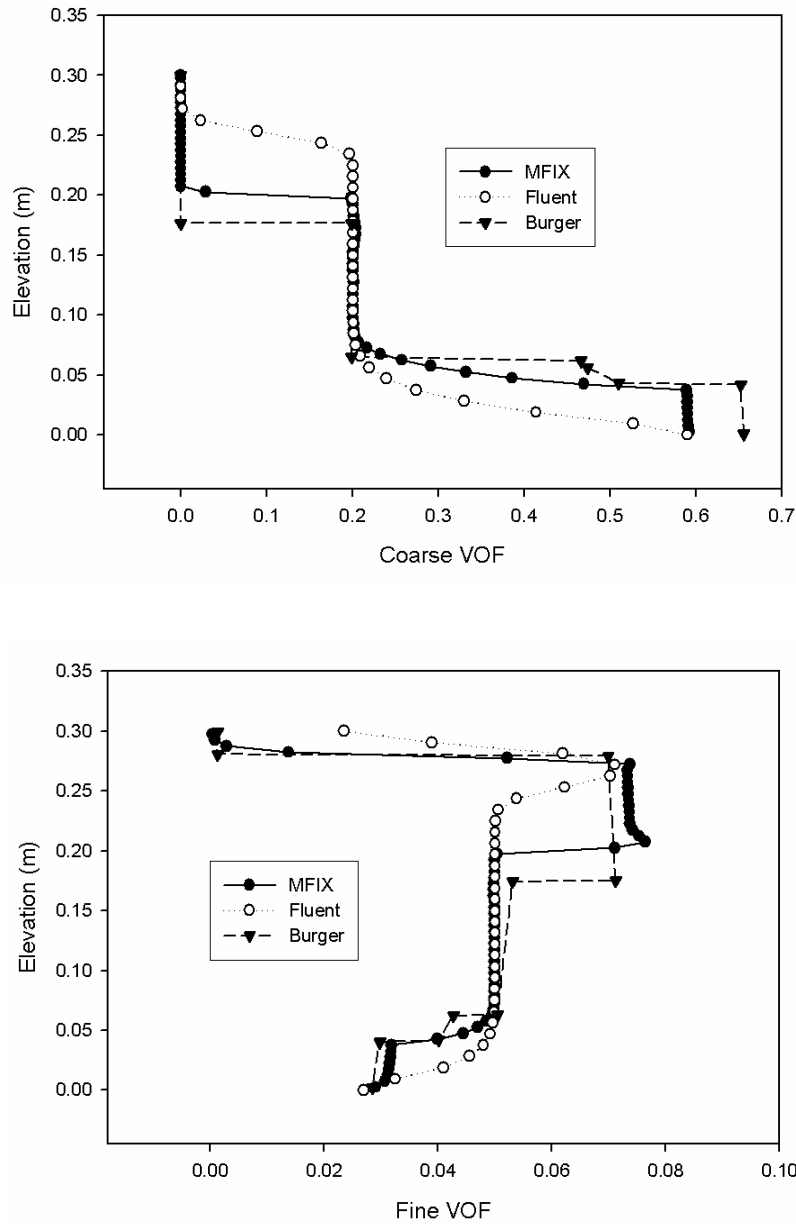


Figure 4.2 Comparison of volume fraction of coarse and fine particles at time = 51.9 seconds

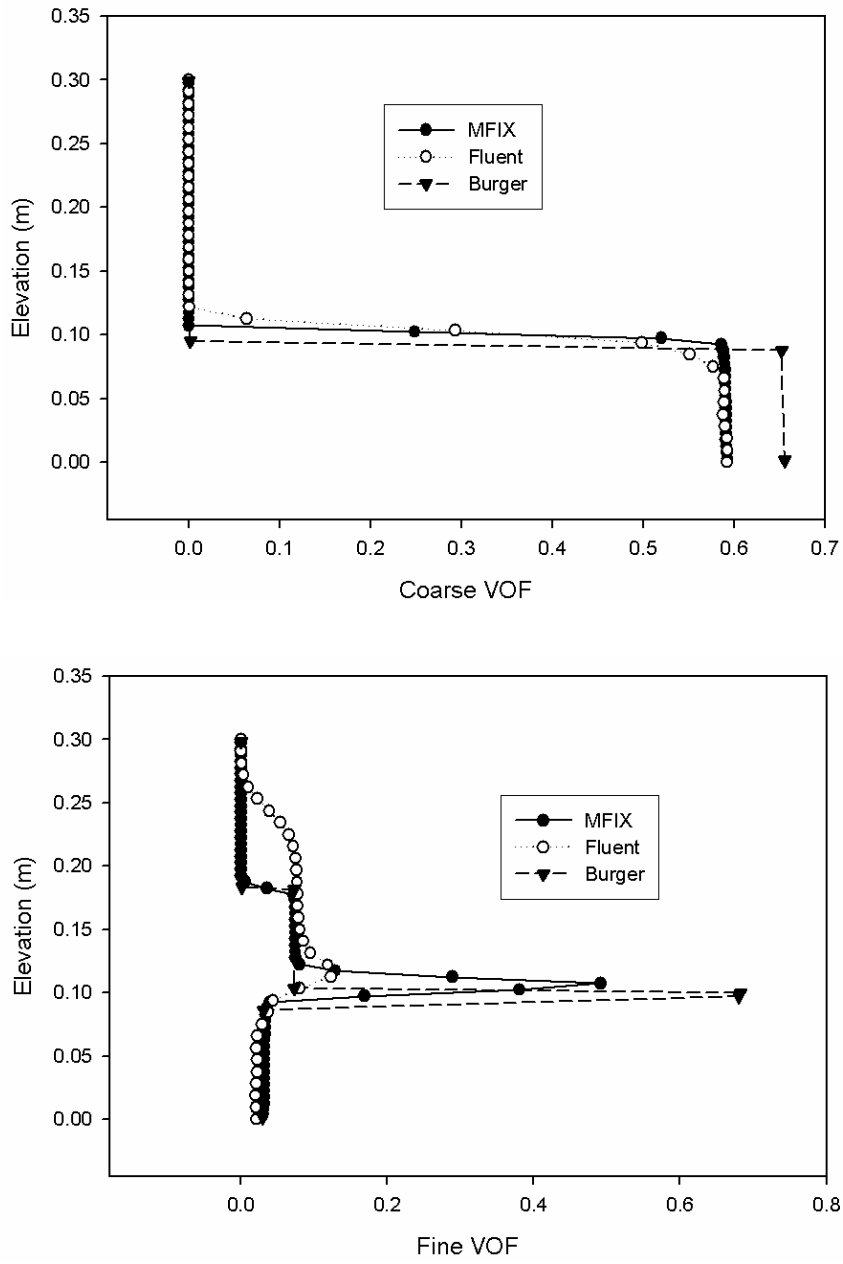


Figure 4.3 Comparison of volume fraction of coarse and fine particles at time = 299.8 seconds

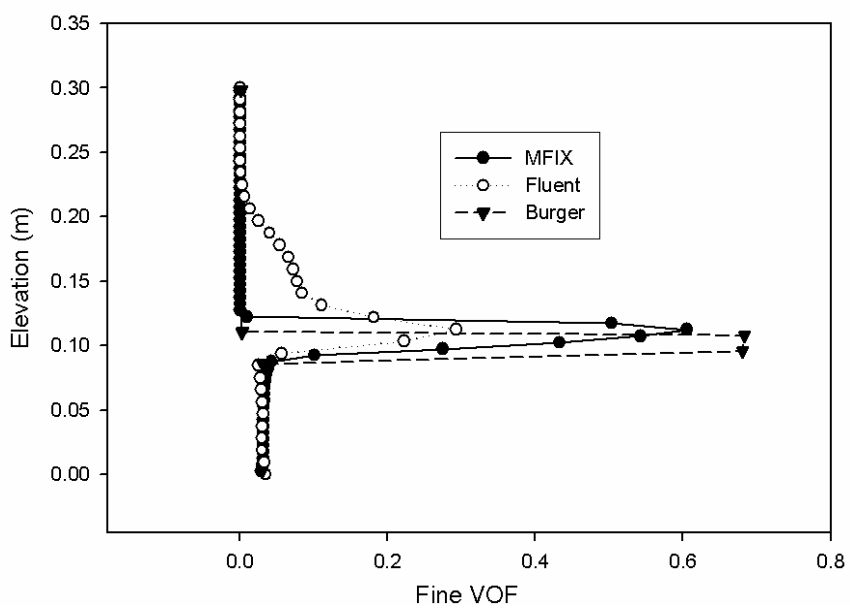
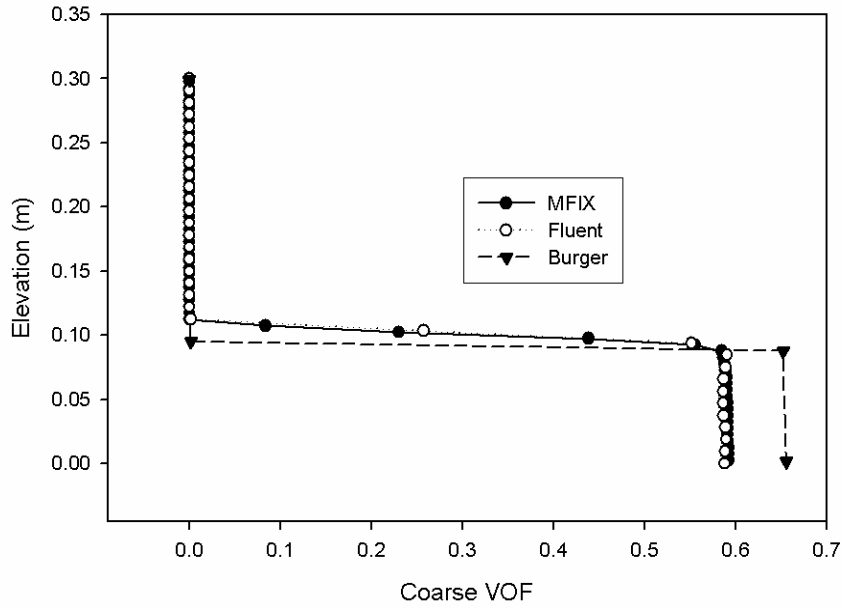


Figure 4.4 Comparison of fine particle volume fraction at time = 599.7 seconds

## 4.2.2 Polydisperse Suspension

### 4.2.2.1 MFIX Simulation

Burger et al. (2000) used shock-capturing numerical scheme to simulate the sedimentation process of four solid particles. The size and density of the particles used in their simulation are shown in Table 4.1. Their simulation results are compared with the solution of Greenspan and Ungarish (1982) and a good agreement is found between those two simulation results. Here the data used in Burger's simulation is used in MFIX and the simulation results are compared with Burger's results.

Table 4.1 lists the properties of the composition of the polydisperse system. The initial volumes of fraction for all the particles are set 0.05, which is equivalent to a solids content of 37%. The grid used in this simulation is shown in Figure 4.5. The volume fraction profile at 150s and 600s are shown in Figure 4.6 and Figure 4.7 respectively. The particle volume fraction at 1000s is shown in Figure 4.8. Those figures show that segregation occurred for the polydisperse system with the largest particles settling at the bottom and the smallest particles at the top of the solid sedimentation. The comparison of the volume fraction profiles obtained from MFIX simulation and from Burger's simulation at time of 615 seconds is shown in Figure 4.9. The MFIX simulation results agree well with Burger's paper.

Table 4.1 The Properties of the Composition of Polydisperse System

Composition	Liquid	Particle 1	Particle 2	Particle 3	Particle 4
Density (kg/m <sup>3</sup> )	1208	2790	2790	2790	2790
Size (mm)	N/A	0.496	0.3968	0.2976	0.1984
Viscosity (kg/m.s)	0.02416	N/A	N/A	N/A	N/A
Initial volume fraction	0.8	0.05	0.05	0.05	0.05

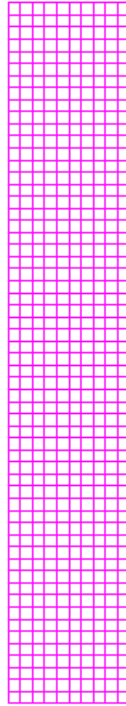


Figure 4.5 Grid Used in Dispersed Simulation (MFIx)

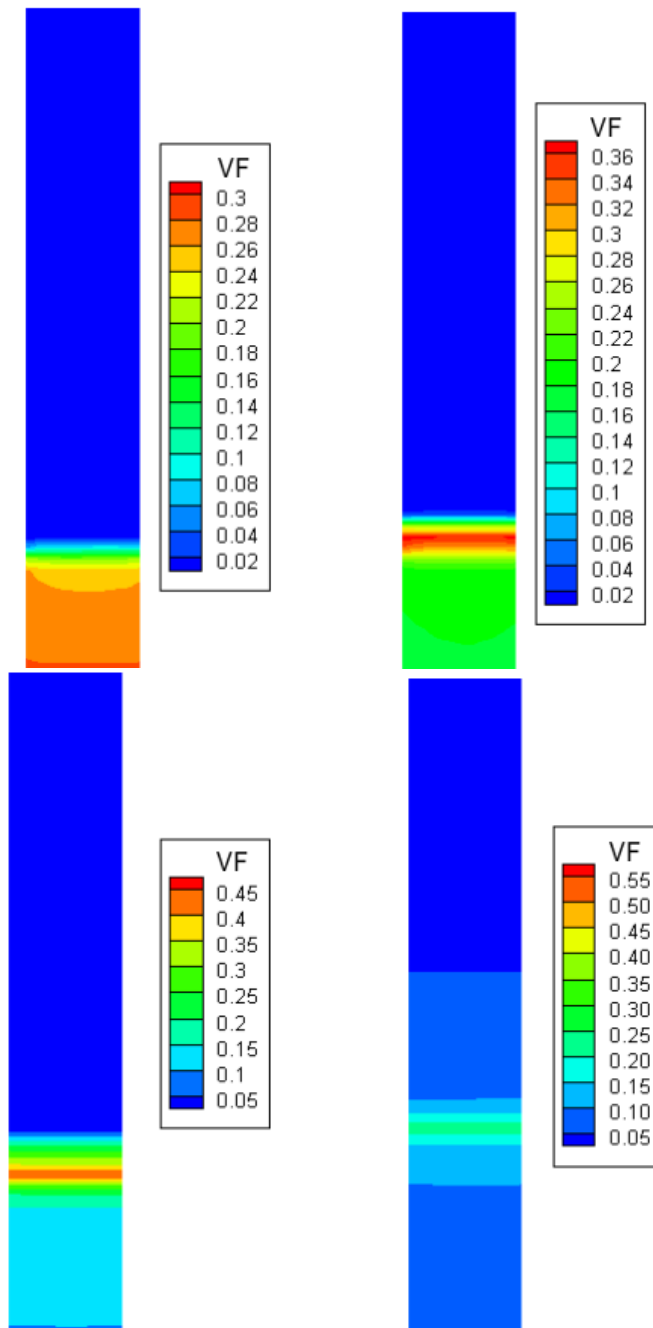


Figure 4.6 The Volume Fraction Profile for Four Solid Phases ( Particle Size Decrease from Left to Right) at the Time of 150 s

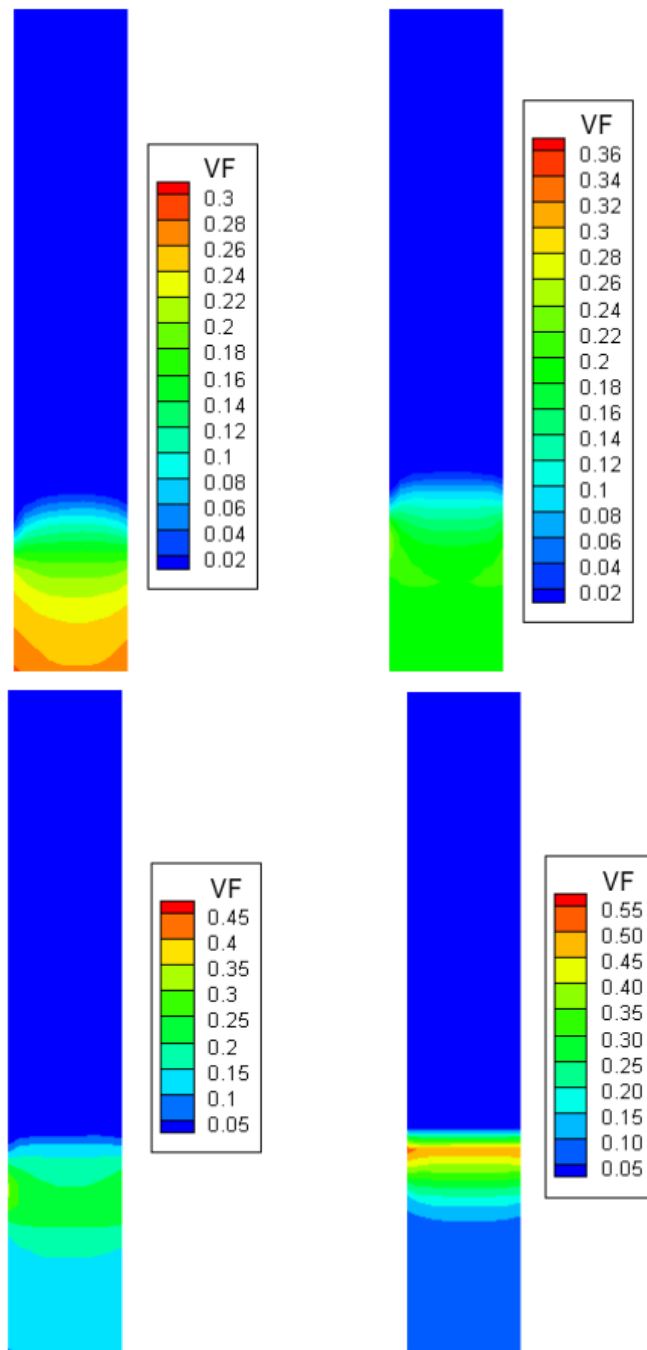


Figure 4.7 The Volume Fraction Profile for Four Solid Phases ( Particle Size Decrease from Left to Right) at the Time of 600 s

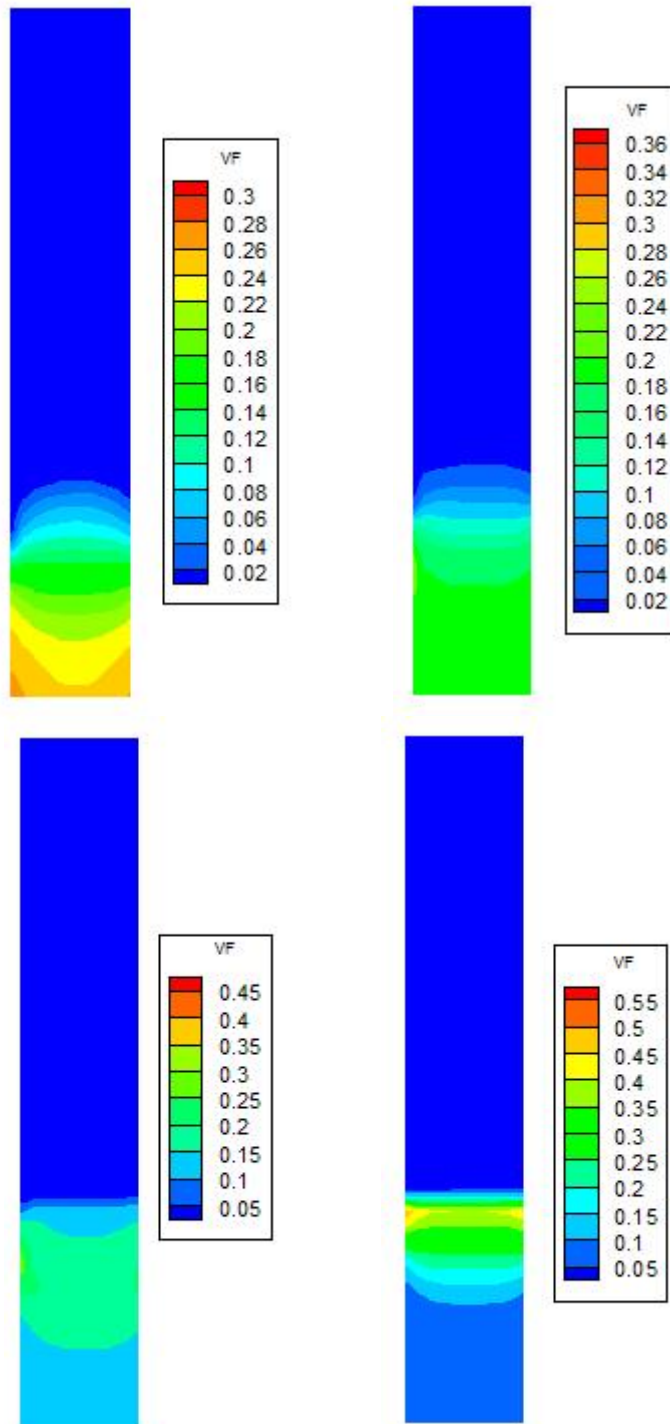


Figure 4.8 The Volume Fraction Profile for Four Solid Phases ( Particle Size Decrease from Left to Right) at the Time of 1000 s

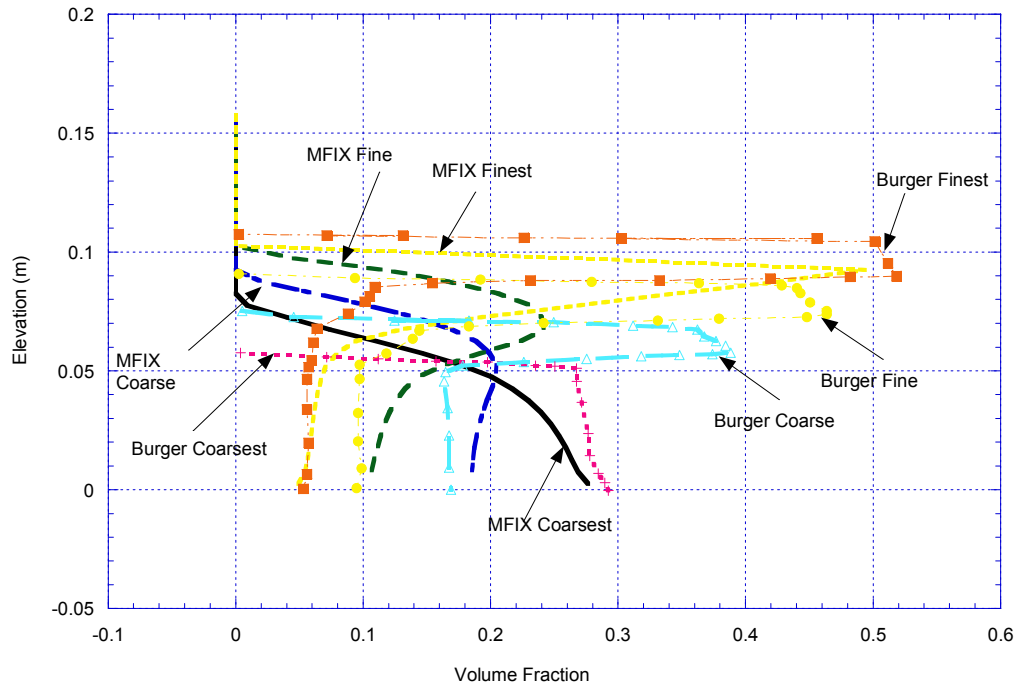


Figure 4.9 Comparison of volume fraction profiles from MFIX simulation and Burger's data at Time = 615.07s

#### 4.2.2.2 FUENT Simulation

The same sedimentation experiment mentioned above is modeled using FLUENT 6. The properties of phases listed in Table 4.1 are assigned to the phases. For each phase, the Gidaspow Model is selected for granular viscosity, the Lun-et-al Model for granular bulk viscosity, the Schaffer Model for frictional viscosity, the based-ktgf model for frictional pressure, the algebraic granular temperature, the Lun-et-al Model for solids pressure and a radial distribution function. A constant internal friction angle of 30 degree is assigned. Friction packing limit and packing limit are 0.61 and 0.63 respectively, in which friction packing limit specifies a threshold volume fraction at which the frictional regime becomes dominant and packing limit specifies the maximum volume fraction for the granular phase. The drag models for solid-liquid and solid-solid used in the simulations are Gidaspow Model and Syamlal-O'Brien-Symmetry model respectively.

The volume fraction of four particles at time of 500, 750 and 1200 seconds are shown in Figure 4.10 to Figure 4.12. The scatter plots of all the four particles at time of 500,

750 and 1200 seconds are demonstrated in Figure 4.13 to Figure 4.15. From these figures it can be observed that the coarsest particles settle first. There are no apparent changes in Volume Fraction profiles for the coarsest and coarse particles from 500 s to 1200 s. However, most fine particles settle on the top of other particles with time.

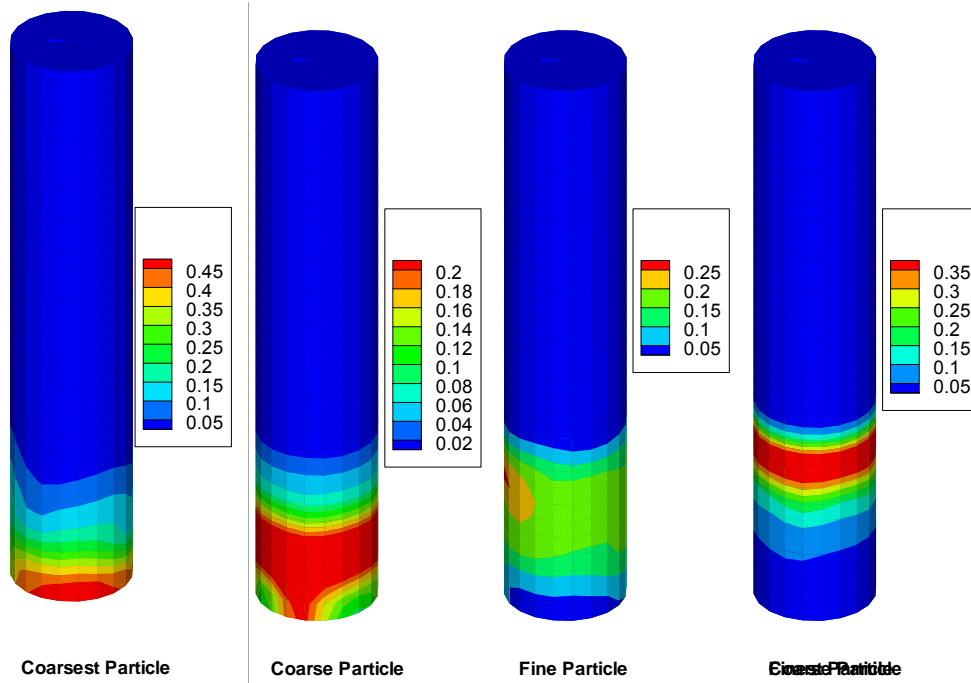


Figure 4.10 Volume Fraction Profile for Largest and Large Particle Sizes at Time = 500s (FLUENT)

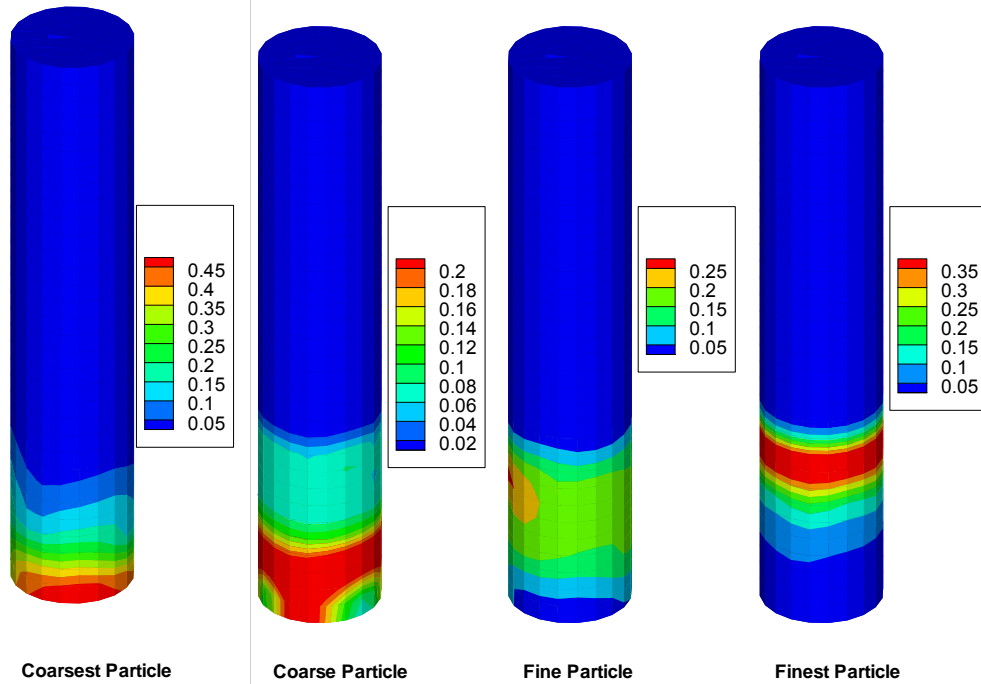


Figure 4.11 Volume Fraction Profile for Largest and Large Particle Sizes at Time = 750s (FLUENT)

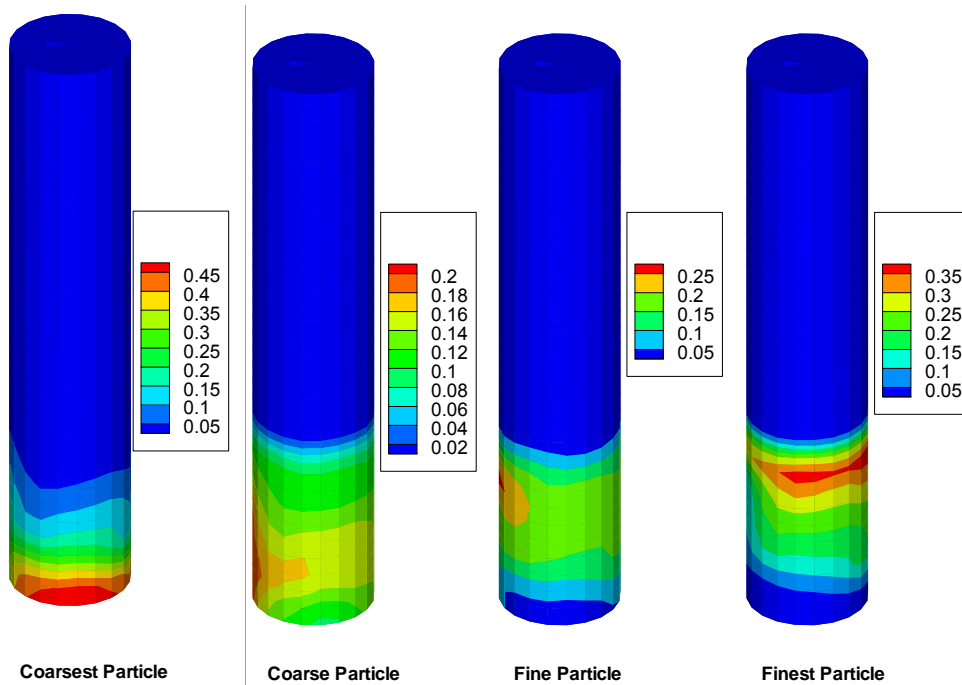


Figure 4.12 Volume Fraction Profile for Largest and Large Particle Sizes at Time = 1200s (FLUENT)

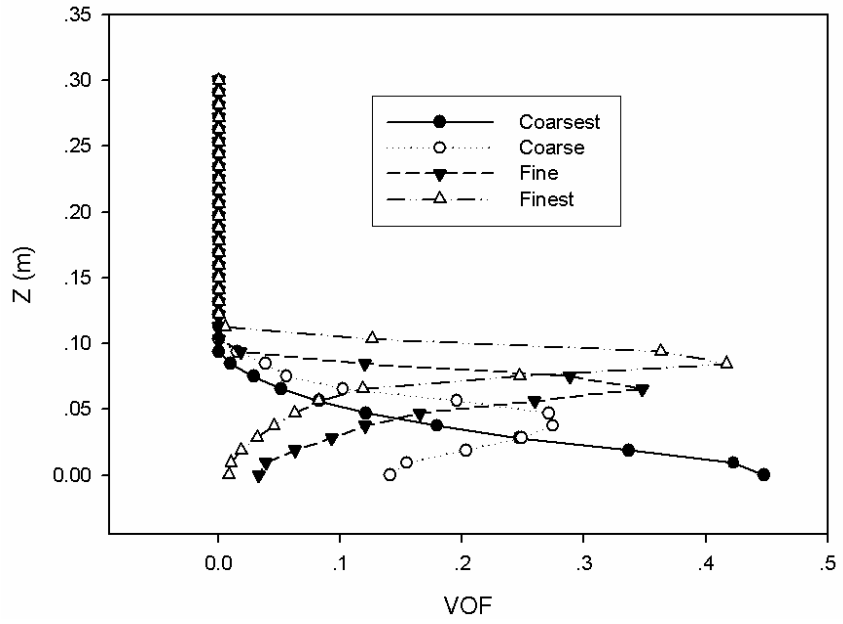


Figure 4.13 Volume Fraction Profile for Four Particle Sizes at Time = 500s (FLUENT)

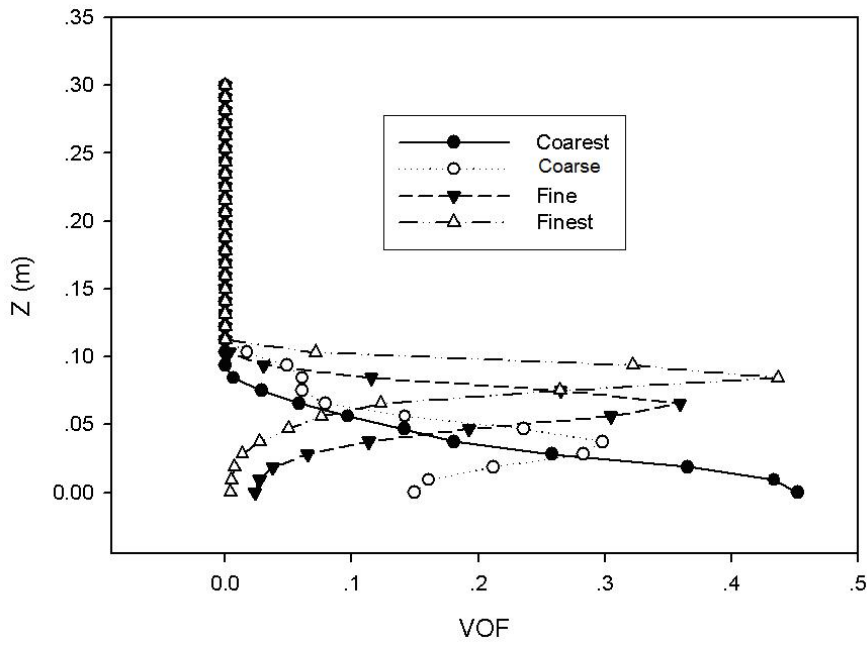


Figure 4.14 Volume Fraction Profile for Four Particle Sizes at Time = 750s (FLUENT)

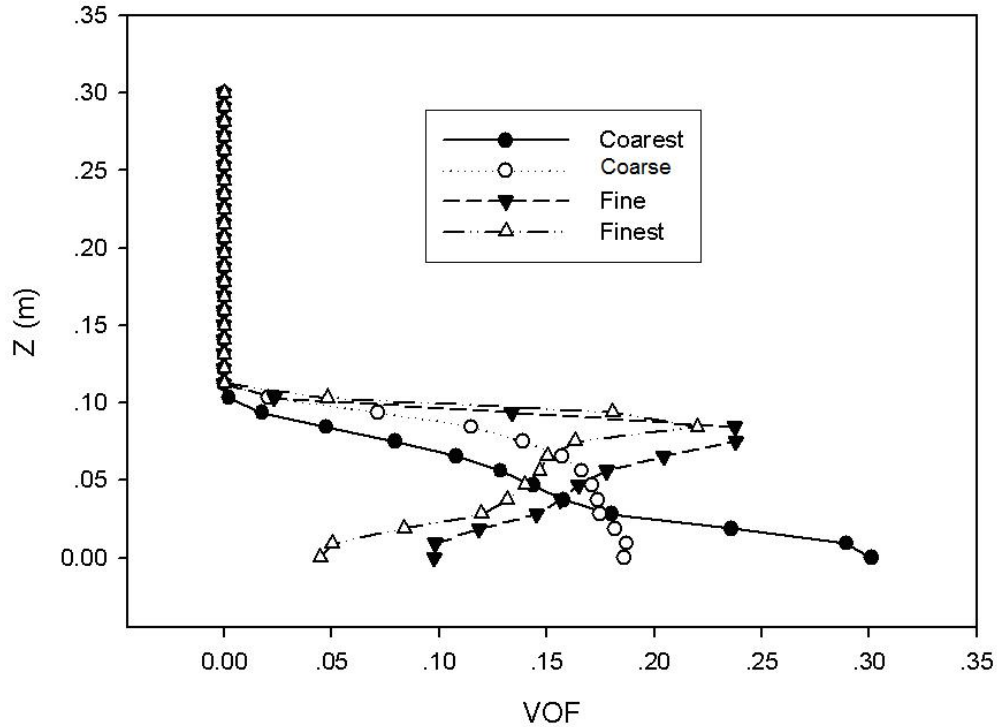


Figure 4.15 Volume Fraction Profile for Four Particle Sizes at Time = 1200s (FLUENT)

#### 4.2.2.3 Comparison

The simulation of polydisperse of four particle sizes with varied particle size using MFIX and FLUENT demonstrates that the polydisperse system can be modeled using CFD method. The applicability of CFD in modeling the polydisperse system involving ultra-fine particles as clay particles in oil sand tailings will be evaluated in the following sections.

### 4.3 Simulation of Segregation of Oil Sand Tailing Slurry

Attempts have been made to model the segregation of oil sand tailings using computational fluid dynamics (CFD) method. The sensitivity of the number of size groups, solids content, sand fine ratio on the segregation is evaluated using CFX 5.7, FLUENT 6.1 and MFIX. Since standpipe tests are simple tests that can be used to verify the segregation models implemented using CFD method, they are used in the following simulations.

#### 4.3.1 Unique Properties of Oil Sand Tailing Slurry

As mentioned in Chapter 2, oil sand tailings composed of water, bitumen, fines and sand, are produced in extracting synthetic crude oil from oil sands. The grain size distribution for the fines and sand is continuous and the mineral solids are composed of clay ( $<2 \mu\text{m}$ ), silt ( $2 \mu\text{m} - 75 \mu\text{m}$ ) and sand ( $>75 \mu\text{m}$ ). Ideally, the continuous distribution of sizes for those particles can be approached by dividing them into infinite number of group sizes. The more size groups, the more the discrete distribution of sizes approaches the continuous distribution. In each group, the particle size is the same. In practice, the continuous distribution of the particle sizes is simplified by dividing the particles into several particle groups with identical particle size. In addition to that, there are strong interactions between ultra-fine particles and water. The bitumen in the oil sand tailings also makes the interactions more complicated.

#### 4.3.2 Segregation Tests in Laboratory

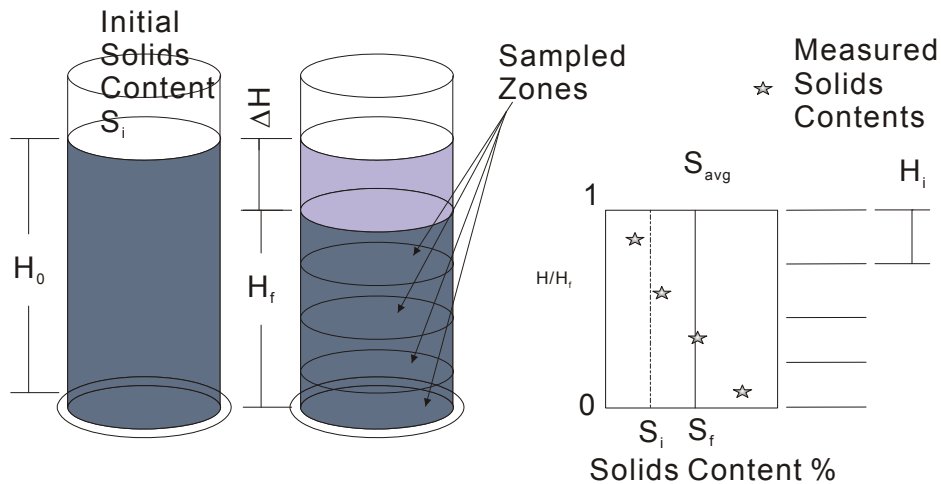


Figure 4.16 Measurement of Segregation and Fines Capture (after Chalaturnyk et al., 2001)

Segregation of oil sand tailing slurry during transportation and deposition is an undesirable behavior. Research has been carried out in finding ways to produce non-segregating oil sand tailings. Batch standpipe tests are conducted on tailing slurry with a wide range of solids content (i.e. percent of solid mass) and fines content (i.e. percent

of fine mass in solid components), where 44 micron is selected as the boundary between fine and coarse particles. After the slurry is uniformly mixed, it is then placed into a standpipe where an interface between upper clear water and lower suspension develops. The time variation of the elevation of the interface with elapsed time is recorded and is used to characterize the properties of the tailing slurry. The observation is ended when the elevation of the interface changed extremely slowly. Then the profiles of the solids content and fines content are obtained by measuring the mass fraction of water, sand and fine. The average solids content (Chalaturnyk et al., 2001) is calculated using Eq. 4.1:

$$S_{avg} = \frac{1}{\frac{1}{S_0} - \left(1 - \frac{H}{H_0}\right) \left(\frac{G_w}{G_s} + \frac{1}{S_0} - 1\right)} \quad (\text{Eq. 4.1})$$

where  $S_{avg}$  is average solids content,  $S_0$  the initial average solids content,  $H_0$  the initial height of the slurry, and  $G_w$  and  $G_s$  are specific gravity of water and solid respectively. In order to describe the segregation, the Segregation Index,  $I_s$ , (Chalaturnyk and Scott, 2001) is defined as follows:

$$I_s = \sum_{i=1}^N \left\{ \frac{1}{2} \left[ \frac{S_i}{S_{avg}} - 1 \right] \left[ \left( \frac{H}{H_f} \right)_{i+1} - \left( \frac{H}{H_f} \right)_{i-1} \right] \right\} * 100\% \quad (\text{Eq. 4.2})$$

Where  $S_i$  is the solids content of layer  $i$  at elevation of  $H$ ,  $H_f$  is the total height of the suspension, and  $N$  is the total number of layers measured. The fine capture is define as  $100 - I_s$  and a mix is defined as a non-segregation matrix if fine capture is at least 95%. The measurement of segregation and calculation of the Segregation Index are illustrated in Figure 4.16.

In order to determine the segregation boundary of the oil tailing slurry, three standpipe tests are conducted on the oil sand tailings with solids and fines contents combination shown in Table 4.2. The grain size distribution of the solid particles is shown in Figure 4.17. It contains 24.8% fine particles and 75.2% coarse particles. The bitumen content is not measured in these experiments. Segregation index for the three CT mixture are

also included in the table. It can be seen that sample SB1 is a segregating slurry while sample SB3 is a non-segregating slurry.

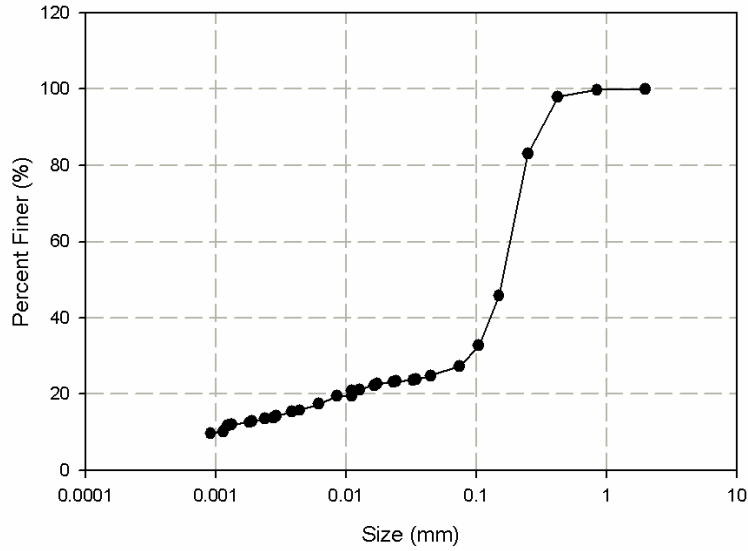


Figure 4.17 Size Distribution of Solid Particles Used in Segregation Tests

Table 4.2 Comparison of three Standpipe Tests for Determining Segregation Boundary

Name	Initial Solids Content $s_0\%$	Initial Fines Content $f_0\%$	Calculated Segregation Index $I_s$	$I_s < 5\%$ (Non-Segregating) Yes or No
SB1	45.00	25.00	44.5	No
SB2	55.00	25.00	8.15	No
SB3	65.00	25.00	1.59	Yes

#### 4.3.3 CFD Simulation of Segregation Tests

The intention here is to verify the capability of their Euler-Euler models in modeling the sedimentation process of segregating and non-segregation slurry. Samples SB1 and SB3 are chosen to verify the Euler-Euler Multiphase model in CFX 5.7, FLUENT 6.2 and MFX since SB1 sample is a segregating matrix and SB3 is non-segregating. As mentioned in Section 4.3.1, simplification of the particle sizes has to be performed in order to apply Euler-Euler model in all the three CFD packages.

The solid particles in the tailing slurry have a size distribution as shown in Figure 4.17. In order to simplify the simulation, the tailing slurry is assumed to be composed of three phases, which are water, fine and coarse particles. Fine particles and sand particles are assumed to have uniform sizes in their size group in all the simulations. A representative or effective diameter is used for the fine particles and sand particles, respectively. Section 4.3.3.1 will discuss the set-up and simulation results for CFX followed by the set-up and results from FLUENT and MFX in Section 4.3.3.2 and 4.3.3.3 respectively. The comparison of the simulation results are presented in Section 4.3.3.4.

Sensitivity of the following factors to the segregation simulation will be evaluated for SB1 and SB3 tests listed in Table 4.2: viscosity of continuous phase and dispersed phases, drag law, density of the solid particles, grain size distribution and ratio, friction and collision, wall, bitumen content. Before that, the geometry, mesh and parameters used in the simulation will be introduced first.

#### 4.3.3.1 CFX-5 Simulation

##### 4.3.3.1.1 CFX5 Set-Up

As mentioned in Chapter 2, the Particle Model in CFX-5 is Euler-Euler model and is applicable for the mixture with high volume fractions of solid dispersed particles, therefore, the Particle Model is chosen in the simulation. In the software, the solid stress tensor is ignored and solid pressure term is added by assuming that solid pressure is a function of solid volume fraction. The main objective of adding the solid pressure term is to prevent the solid volume fraction from exceeding certain value defined as the maximum packing limit.

Three phase simulations were conducted in ANSYS CFX 5.7 using a tetrahedron mesh composed of 4,051 nodes. The properties of each phase are listed in Table 4.3. The flow in the standpipe is assumed to be laminar. The initial volume fraction of sand, clay and water is shown in Table 4.4. The top of the standpipe is set to be a free-slip wall boundary and the wall and bottom of the standpipe are assigned as non-slip walls.

Table 4.3 Material Properties for Each Phase

Name	Density (kg/m <sup>3</sup> )	Diameter (micron)
Water	1000	
Coarse Particle	2700	120
Fine Particles	2600	22

Table 4.4 Initial Volume Fractions for SB1 and SB3

Tests	Water Volume Fraction	Sand Volume Fraction	Clay Volume Fraction
SB1	0.7657	0.1740	0.0602
SB3	0.5902	0.3044	0.1054

#### 4.3.3.1.2 CFX-5 Simulation Sensitivity Tests

##### 4.5.3.1.2.1 DEFAULT SETTINGS

For the simulation of the segregating slurry, the sedimentation process, therefore the transient simulation, is very important. Comparison of the variation of certain variables in simulation with those during experiment is highly desirable. Unfortunately, the variation of the solid-liquid interface with time is the only time-dependent process recorded in the experiments. What make it more challenging is that the scale of time in the simulation is not commensurate. For instance, the first reading for the interface level is 1.87 hours after starting the test while the time step for this simulation in CFX is 0.05 second. Since transient simulation has to be conducted for the sedimentation process, each step requires 5 runs which mean that it is not realistic to simulate the whole process. As a result, the simulation result for the time of only 5 minutes is obtained. The discussion and analysis of the results will be based on this output data. The parameters used in this simulation are shown in Table 4.5, and are applied in both segregation (SB1) and non-segregation (SB3) tests. As mentioned in Chapter 2, the dynamic viscosity of the coarse and fine particles have no effects on the simulation results as the shear stress tensor for the solid particles is ignored in the Particle Model in CFX-5. Any number can be assigned to the parameters.

Table 4.5 shows one set of parameters used in the simulation cases of SB1 and SB3. The solids and fines content profiles for SB1 at simulation time of 300 seconds are shown in Figure 4.18 and Figure 4.19. Comparison of the simulated and measured interface between fine particles and coarse particles is made in Figure 4.20. It is demonstrated that segregation occurred at time of 300 seconds. Although the simulation captured the trends of segregation for SB1, the interface development shown in Figure 4.20 indicates that the sedimentation of the solid particles in the simulation occurs significantly faster than that in the experiments. The solids and fines content profiles and the comparison of simulated and measured interface for SB3 are shown in Figure 4.21 to Figure 4.23. Again it is demonstrated that segregation occurred at the time of 344 s from Figure 4.21 and Figure 4.22. From Figure 4.23 it can be seen that the rate of settling of particles represented by the interface development is much greater in the simulation than that in laboratory measurements.

Table 4.5 Parameters Used in CFX Particle Models for SB1 and SB3

Phase Name	Overall	water	coarse	fine	water-coarse interaction	water-fine interaction	coarse-fine interaction
Max. Time (s)	3000						
Time Step (s)	5.00E-02						
Time Step Adjustment Factor	N/A						
Number of Particulate Phases	2						
Close Packed			N/A	N/A			
Segregation Slope Coefficient			0	0			
Max. solid particle packing			0.6	0.6			
Drag Model					Gidaspow	Gidaspow	N/A
Restitution Coefficient			N/A	N/A			N/A
Dynamic Viscosity (kg/m.s)		8.90E-04	0.05	0.005			
Granular Viscosity (kg/m.s)							
Granular Bulk Viscosity (kg/m.s)							
Frictional Viscosity (kg/m.s)							
Density (Kg/m <sup>3</sup> )		1000	2700	2600			
Diameter (Micron)			120	22			
Coefficient of Frictional Angle	0.1						
Internal Frictional Angle (degree)			30	30			
Solid Pressure Model			Gidaspow	Gidaspow			
Compaction Modulus			600	300			
Reference Elasticity Modulus (Pa)			1	1			
Initial Volume Fraction		varies	varies	varies			
Boundary Conditions	Top Free-slip						

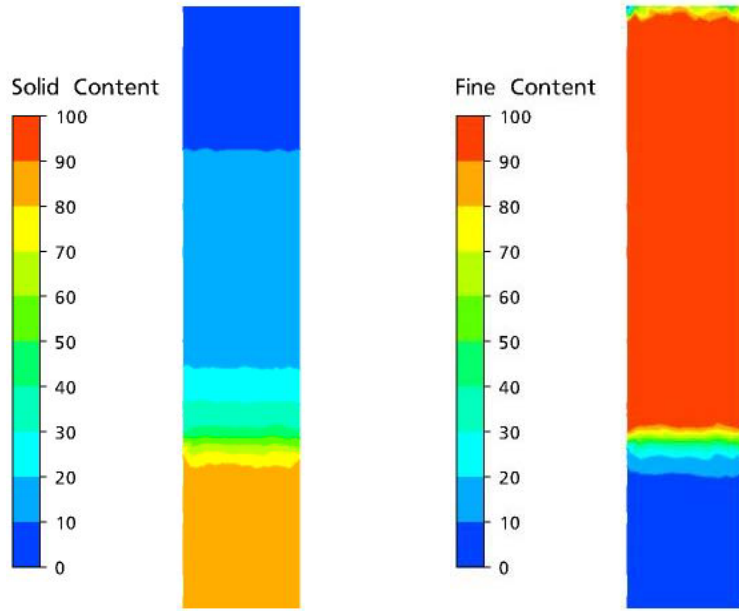


Figure 4.18 Solids and fines content for SB1 at Time = 300s for CFX-Case1

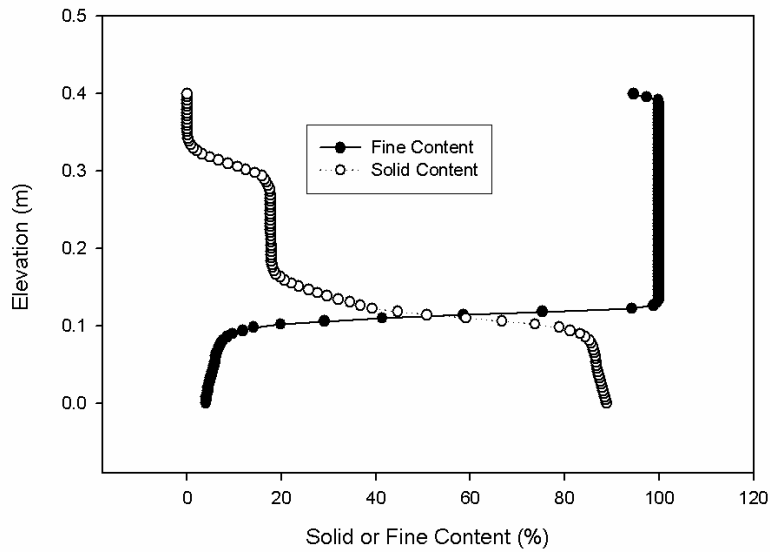


Figure 4.19 Solids and fines contents for SB1 at Time = 300 s for CFX-Case1

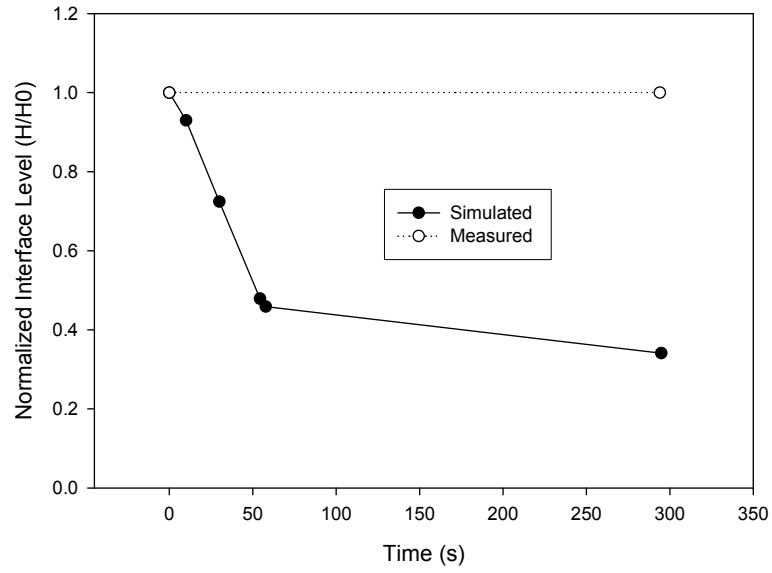


Figure 4.20 Comparison of Interface Development for SB1

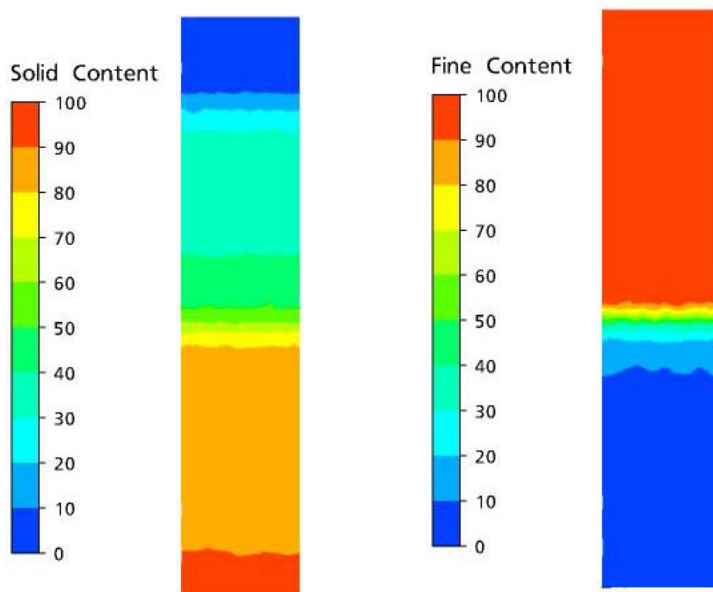


Figure 4.21 Solids and fines contents for SB3 at Time = 344 s

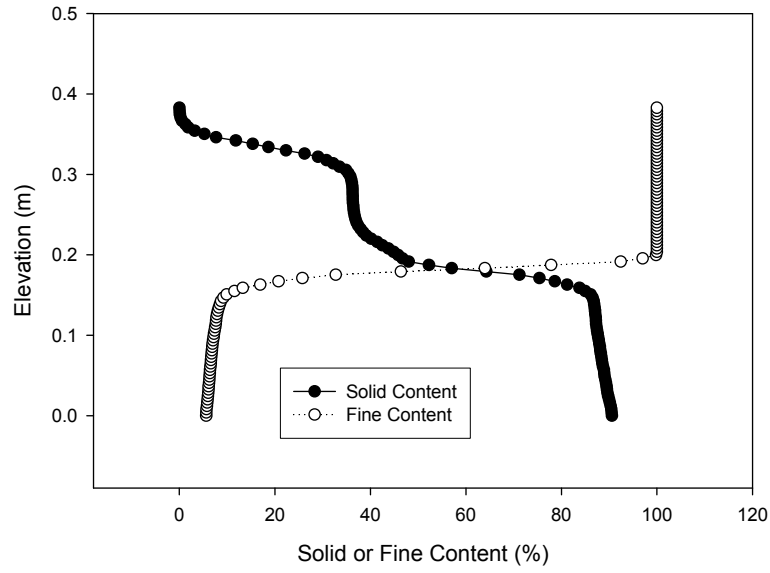


Figure 4.22 Solids and fines contents for SB3 at Time = 344 s for CFX-Case1

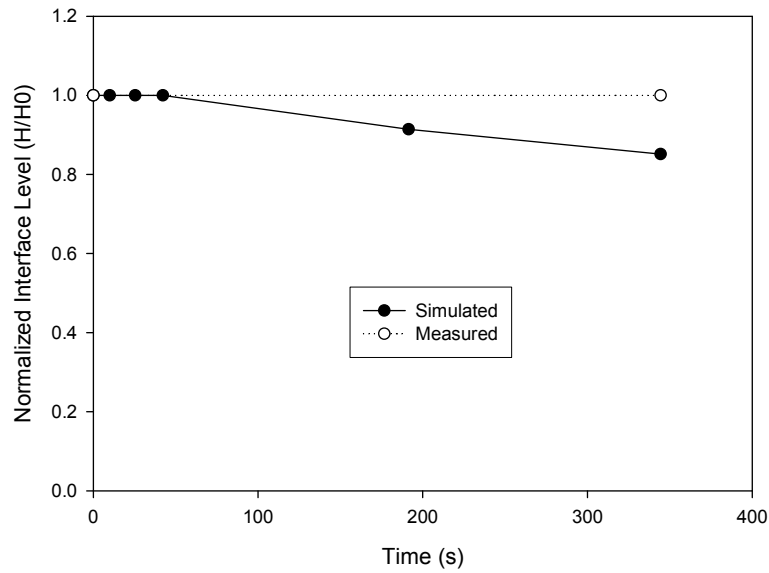


Figure 4.23 Comparison of Interface Development for SB3

#### 4.3.3.1.2.1 MODIFIED SETTINGS

As shown in Figure 4.18 to Figure 4.23, the rate of the coarse-fine particle interface development is faster than that measured in the laboratory for both segregating slurry (SB1) and non-segregating (SB3). Considering the fact that the simulation results using FLUENT and MFIX agrees reasonably with Burger's simulation results, it is reasonable to assume that the unique properties of the oil sand tailing slurry and simplified solid stress tensor model in CFX-5 may cause this discrepancy. Thus, the first attempt is to increase the dynamic viscosity from 0.005 kg/m.s to 150 kg/m.s. The effects of increasing viscosity on the solids and fines content profile at time of 147 s are shown in Figure 4.24. It can be seen that again segregation occurred at the specified simulation time, which is much faster than the segregation process in the laboratory experiment SB1.

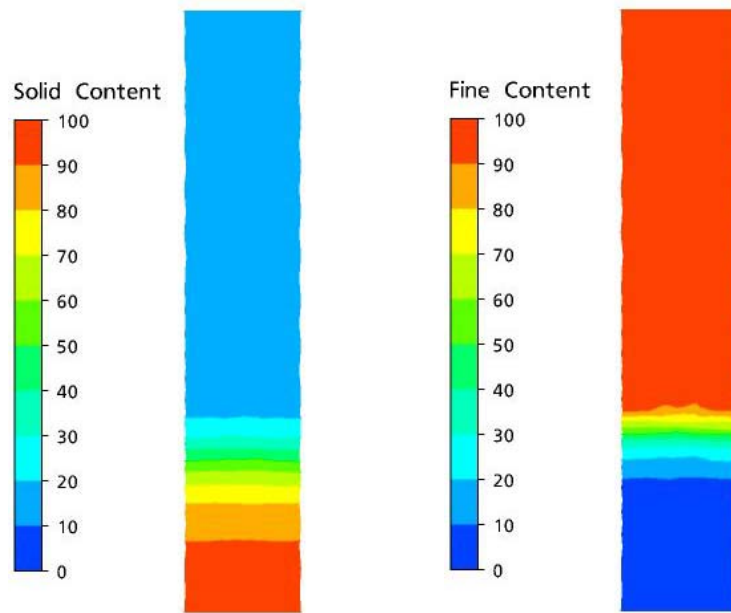


Figure 4.24 Solids and fines contents using fine particle dynamic viscosity of 150 kg/m.s for SB1 at 147 s

The next step is to introduce the segregation criteria artificially into the CFX-5 model. The idea is to conduct regression on the segregation boundaries of the oil sand tailings reported in McMurray Resource's 2002 report and incorporate it into CFX-5 model by modifying the dynamic viscosity of the water phase. The segregation boundaries for

the tailings with Sands Fines Ratio (SFR) less than 0.5 and greater than 0.5 are shown in Figure 4.25 and Figure 4.26 respectively. The regression equation for the boundaries for both conditions is as follows:

$$s = 0.00055f^2 - 1.108f + 87.714 \quad (\text{Eq. 4.3})$$

where  $s$  and  $f$  are solids contents and fines contents in percent. According to Figure 4.25 and Figure 4.26, segregation will occur once the solids content  $s$  is greater than the calculated critical solids content  $s_c$  using this equation. A User Subroutine is implemented to search the segregation boundary. Once the calculated solids contents are greater than the critical solids contents at the fines content calculated in the cell, the maximum dynamic viscosity of 250,000 kg/m.s is assigned to the water phase in that cell. By increasing the drag force between solid particles and liquid, it is expected that the relative movement between solid particles will be lowered at the non-segregation region in the domain.

The effects of the segregation boundary on the sedimentation behavior of the slurry are shown in Figure 4.27. The simulation results at the time of 30 seconds are obtained. Using the User Subroutine requires very small time step during the modeling, therefore, the modeling process is very time-consuming. It can be seen from the figure that segregation behavior is prohibited by introducing the segregation boundary artificially.

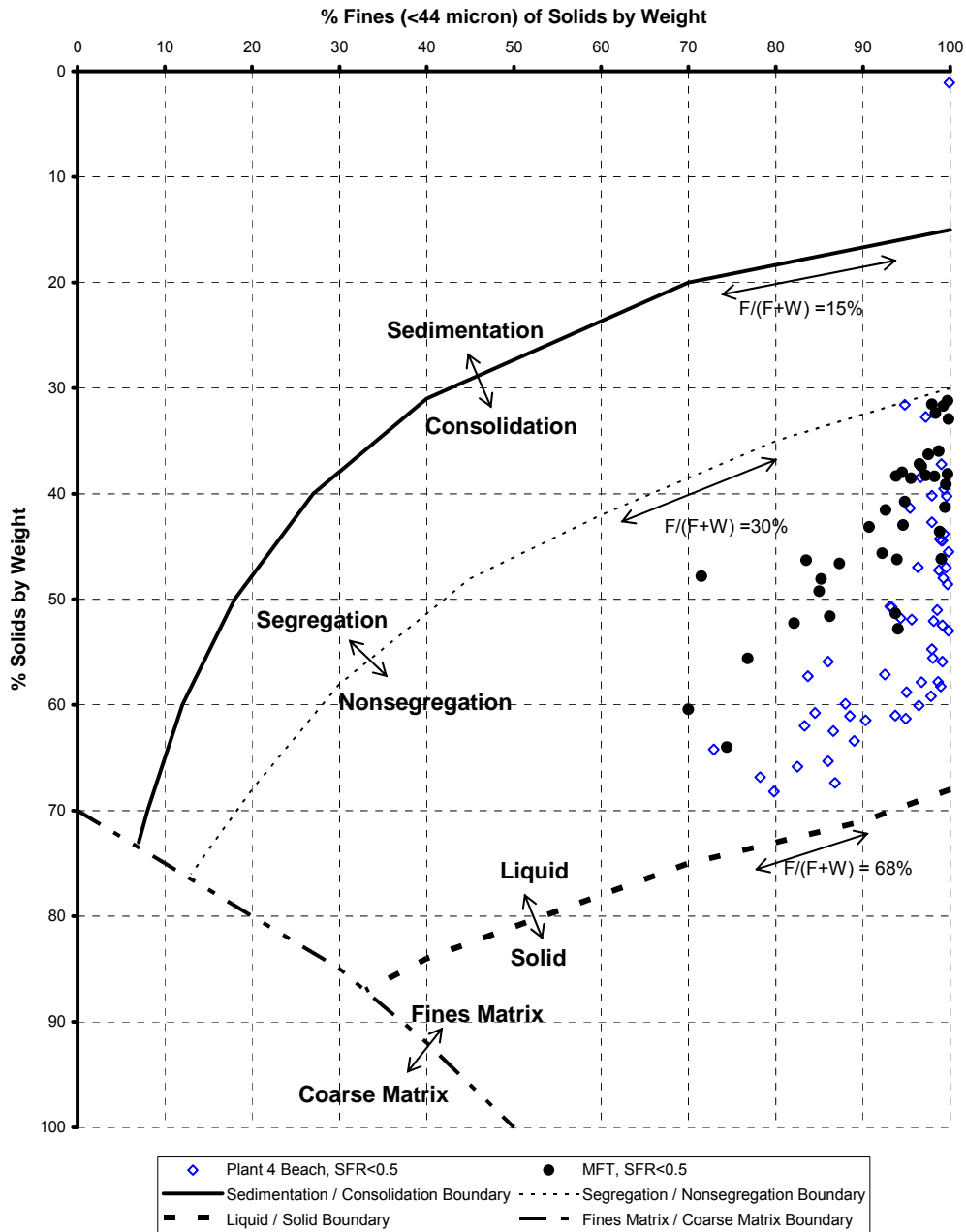


Figure 4.25 Slurry Properties Diagram for Suncor's Pond 1 tailings (SFR<0.5) (From McMurray Resources (Research & Testing) Ltd.'s report, 2002)

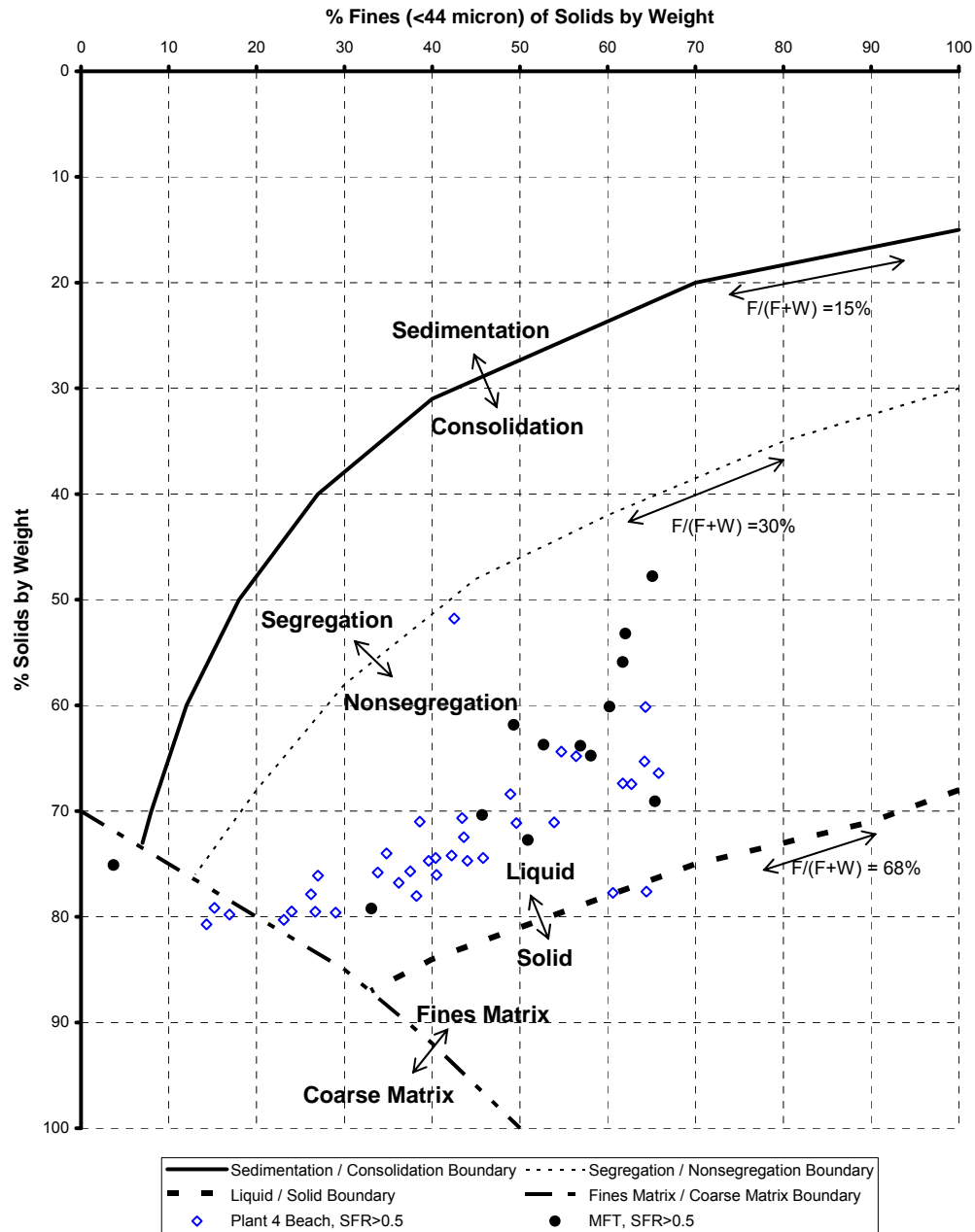


Figure 4.26 Slurry Properties Diagram for Suncor's Pond 1 tailings (SFR>0.5) (From McMurray Resources (Research & Testing) Ltd.'s report, 2002)

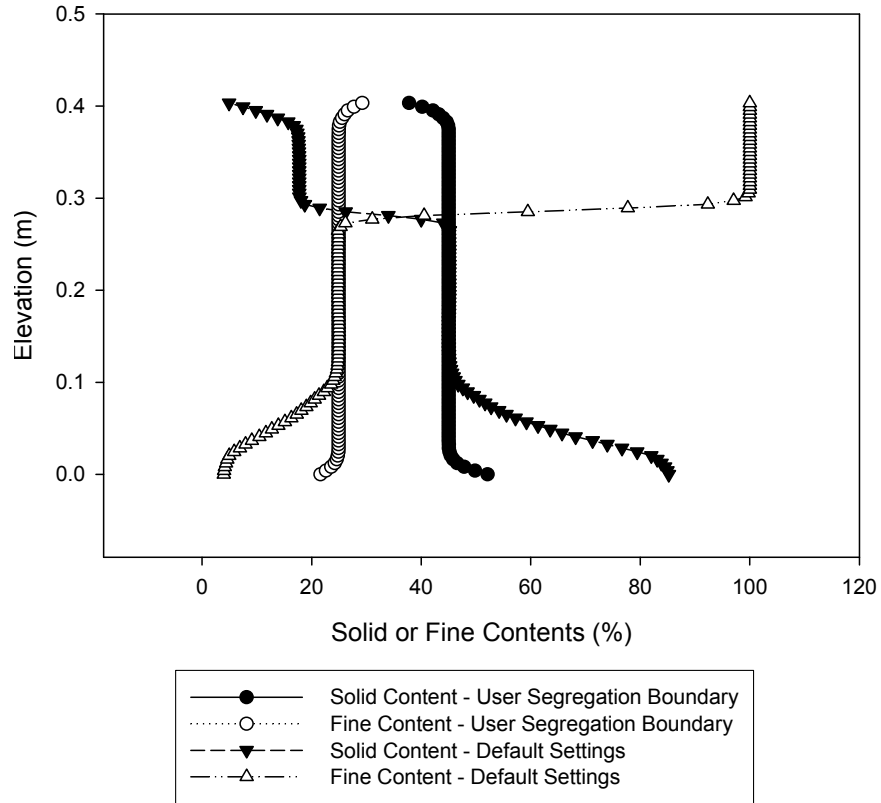


Figure 4.27 Comparison of solids and fines contents using default settings and user segregation boundary for SB1 at 30 second

Since the simulation of segregation by introducing the segregation boundary as shown above is very time-consuming, it is reasonable to use the program with built-in model with capability of being modified as intended. Thus, the focus is on simulating the segregation using Fuent-6 and MFIIX in which users can modify the model using the User Defined Function interface.

### 4.3.3.2 FLUENT-6 Simulation

#### 4.3.3.2.1 FLUENT-6 Set-up

The similar settings used in CFX-5 simulation are adopted in FLUENT simulation. The material properties listed in Table 4.3 are used in FLUENT simulation. The same initial and boundary conditions as those used in CFX 5.7 are applied in FLUENT. The mesh shown in Figure 4.28 is used in FLUENT 6.2.

#### 4.3.3.2.2 FLUENT-6 Sensitivity Tests

Sixteen tests are conducted for SB1 using FLUENT. The settings for each of simulation case are shown in Table 4.6. The explanation of these models and the corresponding parameters is presented in Section 2.6.6.4.3.2 and Table 2.. In all the cases, simulation time of 30 seconds is reached. The influence of some of the parameters on the simulated solids and fines contents is shown in Figure 4.29 to Figure 4.36. The effects of various parameters on the solids and fines contents at simulation time of 30 seconds are presented in the following sections.

The settings for Case 1, 2 and 3 are shown in Table 4.6. Figure 4.29 shows the effects of granular temperature model and solid pressure on the solids and fines contents at the time of 30 seconds. The influence of bulk viscosity is shown in Figure 4.30. It can be seen from these figures that selecting granular temperature model, solid pressure model and bulk viscosity have very limited effects on the solids and fines content profile at the time of 30 seconds.

Figure 4.31 shows the significant influence of frictional viscosity on the solids and fines content profile at the time of 30 seconds. This is expected as the frictional viscosity will predominate among all the viscosities when the volume fraction for solid phases increases, especially when the solid volume fraction exceeds 0.5.

The effects of the Packed Bed are shown in Figure 4.32. The figure demonstrates that choosing Packed Bed does not change the solids and fines contents at the final simulation stage. Enabling the Packed Bed option will freeze the velocity field for the

granular phase. Figure 4.33 shows the effects of choosing granular viscosity model on the solids and fines content profile. Figure 4.34 shows the effects of internal angle of friction for solid phases. It is seen that granular viscosity model has certain influence and frictional angle does not affect the solids and fines contents at the time of 30 second.

The effects of diameter and density for coarse particles on the final solids and fines contents are shown in Figure 4.35 and Figure 4.36. It can be seen that settling rate is reduced as the coarse particle diameter and density decrease.

Table 4.6 Sensitivity Analysis for SB1 using Fluent-6

Case #	Water			Coarse Particles										Fine Particles										Phase-Phase Interactions													
	$\rho_w$ (g/cm <sup>3</sup> )	$\mu_w$ (mPa.s)	$\rho$ (g/cm <sup>3</sup> )	d (μm)	$\mu$ (mPa.s)	Gran. Temp. Model	$\mu_s$ (mPa.s)	$\lambda_s$	$\mu_{s,fr}$ (mPa.s)	Fr. Ang.	$\Theta_s$ (m <sup>2</sup> /s <sup>2</sup> )	$\rho_s$ (Pa)	$G_0$ (Pa)	$g_{0,ls}$ (Pa)	$\alpha_{s,max}$ (Pa)	$\rho$ (g/cm <sup>3</sup> )	$\mu$ (mPa.s)	ed	Pack	Gran. Temp. Model	$\mu_s$ (mPa.s)	$\lambda_s$	$\mu_{s,fr}$ (mPa.s)	Fr. Ang.	$\Theta_s$ (m <sup>2</sup> /s <sup>2</sup> )	$\rho_s$ (Pa)	$G_0$ (Pa)	$g_{0,ls}$ (Pa)	$\alpha_{s,max}$ (Pa)	f-w Drag Model	f-w Drag lift Model	c-w Drag Model	c- Drag lift Model	f-c Drag Model	Vir. M. F.		
1	1	1	2.7	120	50	No	PP	s-o	0	None	none	s-o	s-o	der	0.63	2.6	2.2	5	PP	s-o	0	None	None	s-o	le-a	s-o	der	0.63	gid	no	gid	no	s-o-s	0.7	0.8	0.9	No
2	1	1	2.7	120	50	No	PP	s-o	0	None	none	s-o	s-o	der	0.63	2.6	2.2	5	PP	s-o	0	None	None	s-o	le-a	s-o	der	0.63	gid	no	gid	no	s-o-s	0.7	0.8	0.9	No
3	1	1	2.7	120	50	No	PDE	s-o	0	None	none	s-o	s-o	der	0.63	2.6	2.2	5	PDE	s-o	0	None	None	s-o	s-o	der	0.63	gid	no	gid	no	s-o-s	0.7	0.8	0.9	No	
4	1	1	2.7	120	50	No	PP	s-o	le-a	None	none	s-o	s-o	der	0.63	2.6	2.2	5	PP	s-o	0	None	None	s-o	le-a	s-o	der	0.63	gid	no	gid	no	s-o-s	0.7	0.8	0.9	No
5	1	1	2.7	120	50	No	PDE	s-o	le-a	sch	45	s-o	s-o	der	0.63	2.6	2.2	5	PDE	s-o	le-a	sch	45	s-o	s-o	der	0.63	gid	no	gid	no	s-o-s	0.7	0.8	0.9	No	
6	1	1	2.7	120	50	Yes	PDE	s-o	le-a	sch	45	s-o	s-o	der	0.63	2.6	2.2	5	PDE	s-o	le-a	sch	45	s-o	s-o	der	0.63	gid	no	gid	no	s-o-s	0.7	0.8	0.9	No	
7	1	1	2.7	120	5E+5	Yes	PDE	s-o	le-a	sch	45	s-o	s-o	der	0.63	2.6	2.2	5	PDE	s-o	le-a	sch	45	s-o	s-o	der	0.63	gid	no	gid	no	s-o-s	0.7	0.8	0.9	No	
8	1	1	2.7	120	5E+5	Yes	PDE	s-o	le-a	sch	45	s-o	s-o	der	0.63	2.6	2.2	5E+5	Yes	PDE	s-o	le-a	sch	45	s-o	s-o	der	0.63	gid	no	gid	no	s-o-s	0.7	0.8	0.9	No
9	1	1	2.7	120	50	Yes	PDE	s-o	le-a	sch	45	s-o	s-o	der	0.63	2.6	2.2	5	Yes	PDE	s-o	le-a	sch	45	s-o	s-o	der	0.63	gid	no	gid	no	s-o-s	0.7	0.8	0.9	No
10	1	1	2.7	120	50	Yes	PDE	gid	le-a	sch	45	s-o	s-o	der	0.63	2.6	2.2	5	Yes	PDE	gid	le-a	sch	45	s-o	s-o	der	0.63	gid	no	gid	no	s-o-s	0.7	0.8	0.9	No
11	1	1	2.7	120	50	Yes	PDE	gid	le-a	sch	15	s-o	s-o	der	0.63	2.6	2.2	5	Yes	PDE	gid	le-a	sch	15	s-o	s-o	der	0.63	gid	no	gid	no	s-o-s	0.7	0.8	0.9	No
12	1	1	2.7	120	50	Yes	PDE	gid	le-a	sch	15	s-o	s-o	der	0.63	2.6	2.2	5	Yes	PDE	gid	le-a	sch	15	s-o	s-o	der	0.63	gid	no	gid	no	s-o-s	0.7	0.8	0.9	Yes
13	1	1	2.7	120	50	Yes	PDE	s-o	le-a	sch	45	s-o	s-o	der	0.63	2.6	2.2	5	Yes	PDE	s-o	le-a	sch	45	s-o	s-o	der	0.63	gid	no	gid	no	s-o-s	0.7	0.8	0.9	Yes
14	1	1	2.7	60	50	Yes	PDE	s-o	le-a	sch	45	s-o	s-o	der	0.63	2.6	2.2	5	Yes	PDE	s-o	le-a	sch	45	s-o	s-o	der	0.63	gid	no	gid	no	s-o-s	0.7	0.8	0.9	Yes
15	1	1	2.7	30	50	Yes	PDE	s-o	le-a	sch	45	s-o	s-o	der	0.63	2.6	2.2	5	Yes	PDE	s-o	le-a	sch	45	s-o	s-o	der	0.63	gid	no	gid	no	s-o-s	0.7	0.8	0.9	Yes
16	1	1	2.3	120	50	Yes	PDE	s-o	le-a	sch	45	s-o	s-o	der	0.63	2.6	2.2	5	Yes	PDE	s-o	le-a	sch	45	s-o	s-o	der	0.63	gid	no	gid	no	s-o-s	0.7	0.8	0.9	Yes

**Symbols:**

$\rho$  = density;  $\mu$  = dynamic viscosity;  $\mu_s$  = granular viscosity;  $\mu_{s,col}$  = collisional viscosity;  $\mu_{s,kin}$  = kinetic viscosity;  $\mu_{s,fr}$  = frictional viscosity;  $\lambda_s$  = bulk viscosity;  $\Theta_s$  = granular temperature;  $p_s$  = solid pressure;  $g_{0,ls}$  = radial distribution function;  $G_0$  = elasticity modulus;  $a_{s,max}$  = packing limit;  $e_{fr}$  = restitution coefficient between fine particles;  $e_{fc}$  = restitution coefficient between fine and coarse particles;  $e_{cc}$  = restitution coefficient between coarse particles.

**Abbreviation:**

Packed= Packed Bed; Gran. Temp. Model = Granular Temperature Model; PP = Phase Property; PDE = Partial Differential Equation; s-o = Syamlal-O'Brien; gid = Didaspow; le-l = lun-et-al; sch = schaffer; Fri. Ang. = Internal Angle of Friction; dr = derived; Vir. M. F. = Virtual Mass Force.

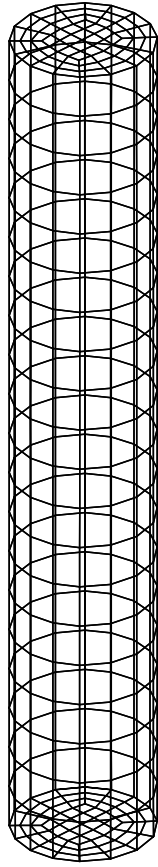


Figure 4.28 The mesh used for all the sensitivity analysis in FLUENT-6.

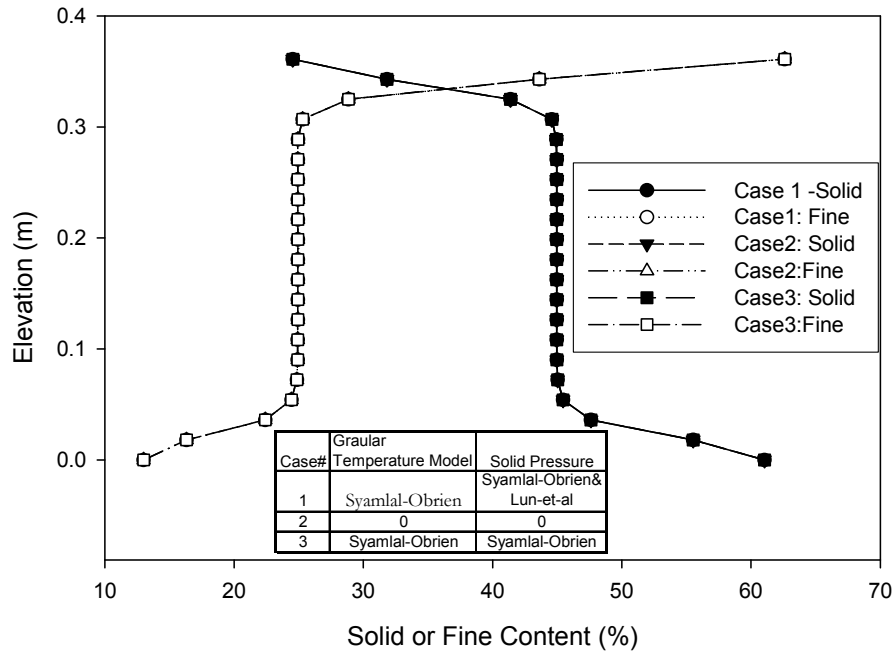


Figure 4.29 Effects of granular temperature model and solid pressure on solids and fines contents

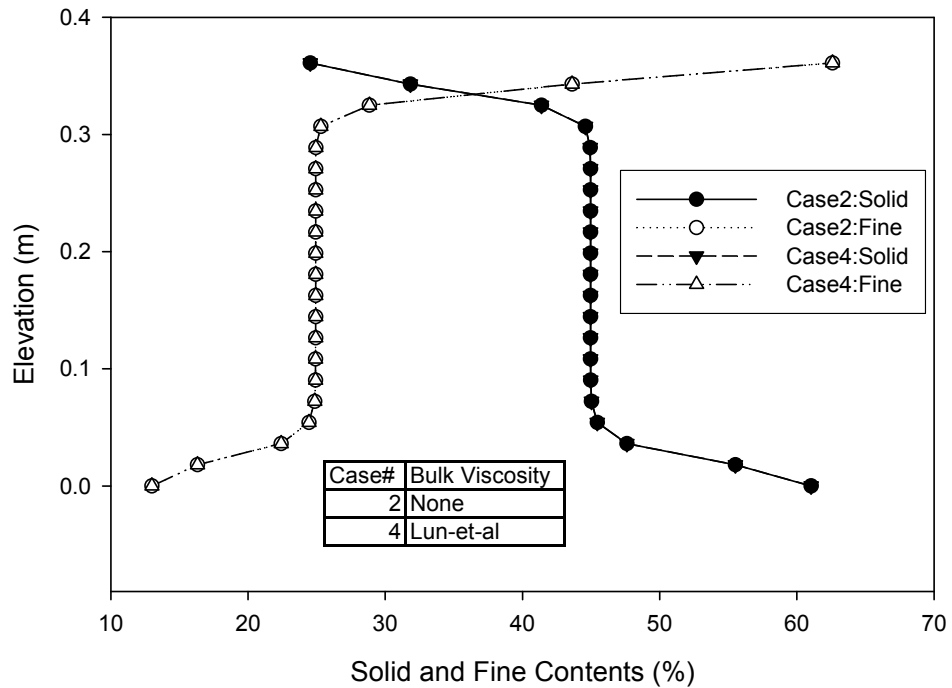


Figure 4.30 Effects of bulk viscosity on solids and fines contents

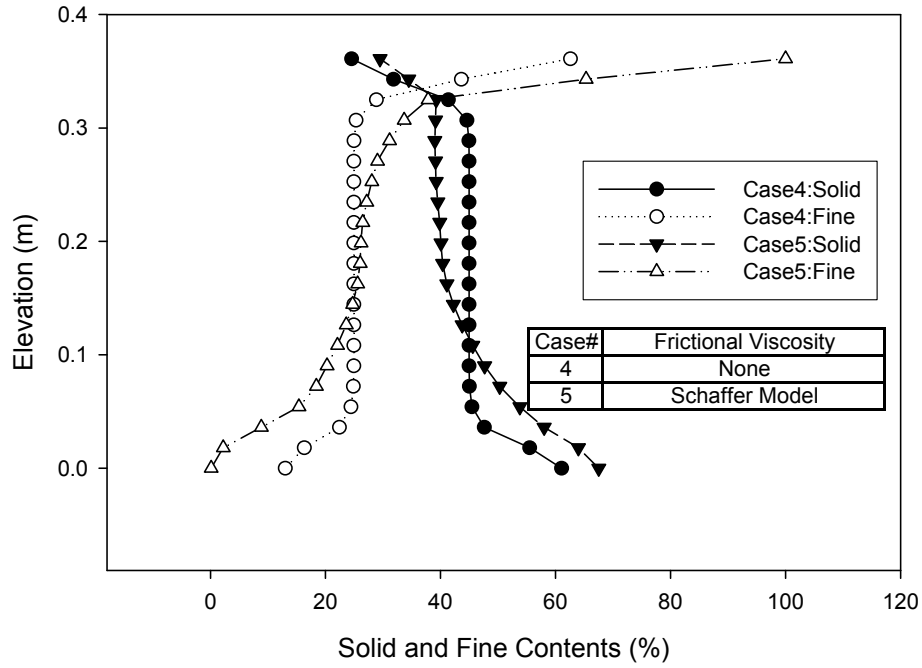


Figure 4.31 Effects of frictional viscosity on solids and fines contents

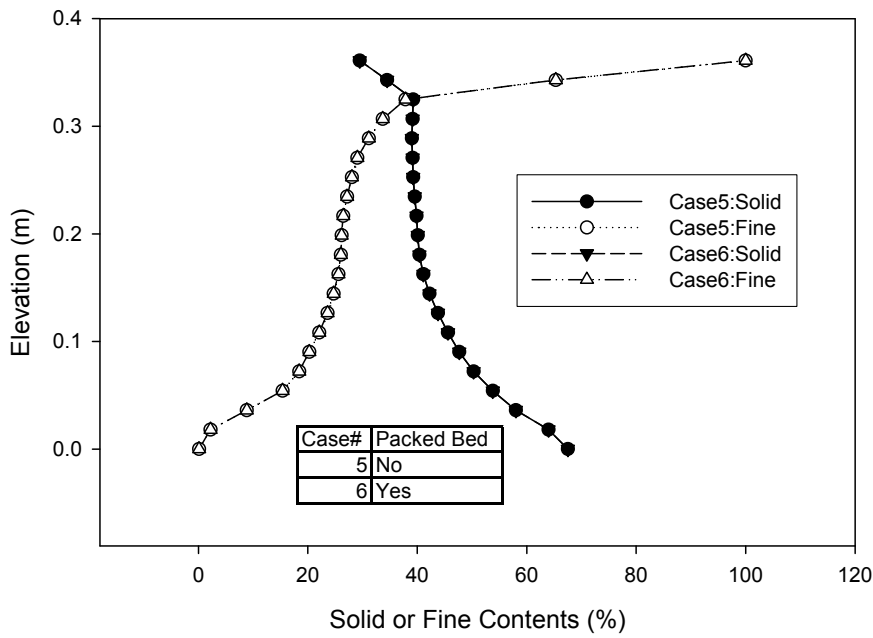


Figure 4.32 Effects of Packed Bed on solids and fines contents

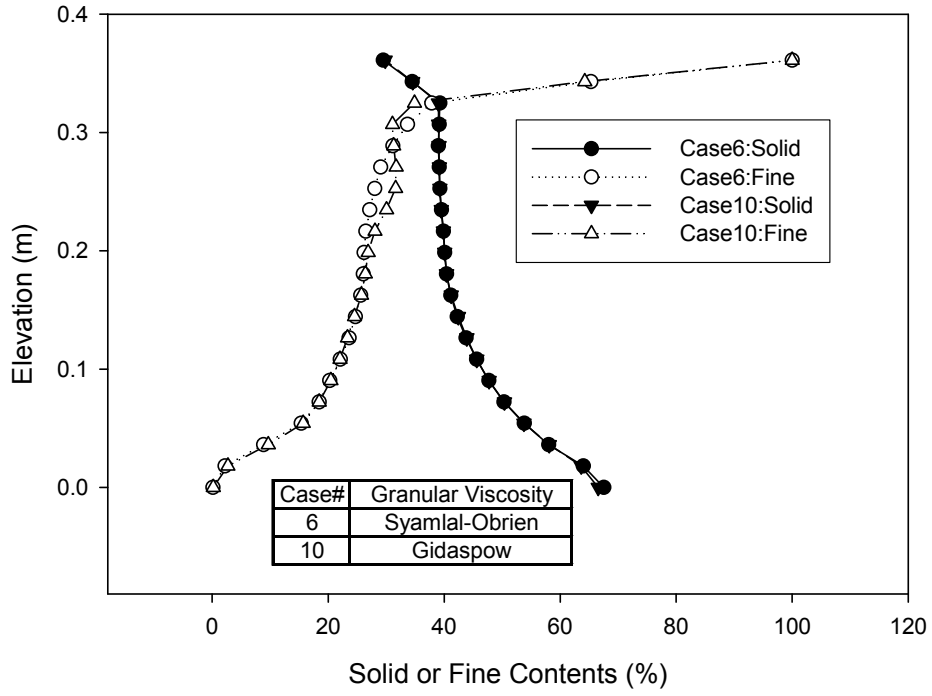


Figure 4.33 Effects of granular viscosity on solids and fines contents

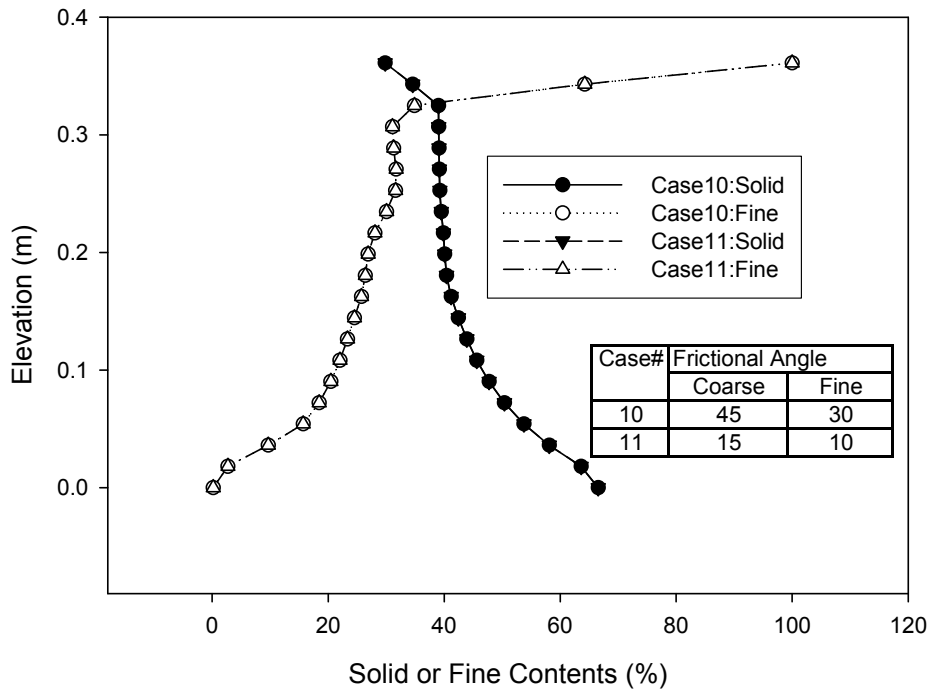


Figure 4.34 Effects of frictional angle on solids and fines contents

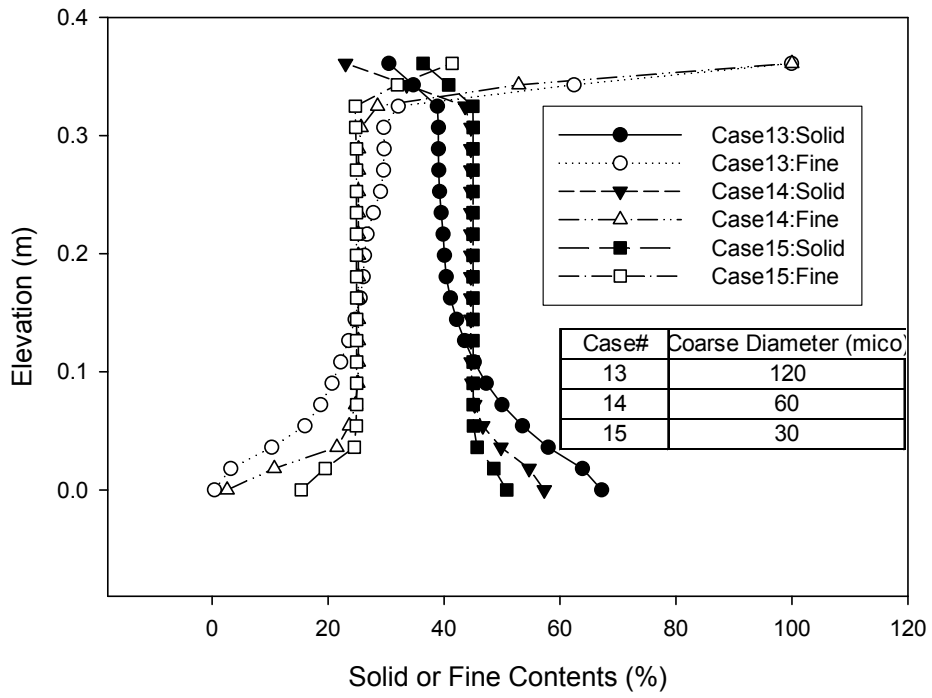


Figure 4.35 Effects of particle diameter on solids and fines contents

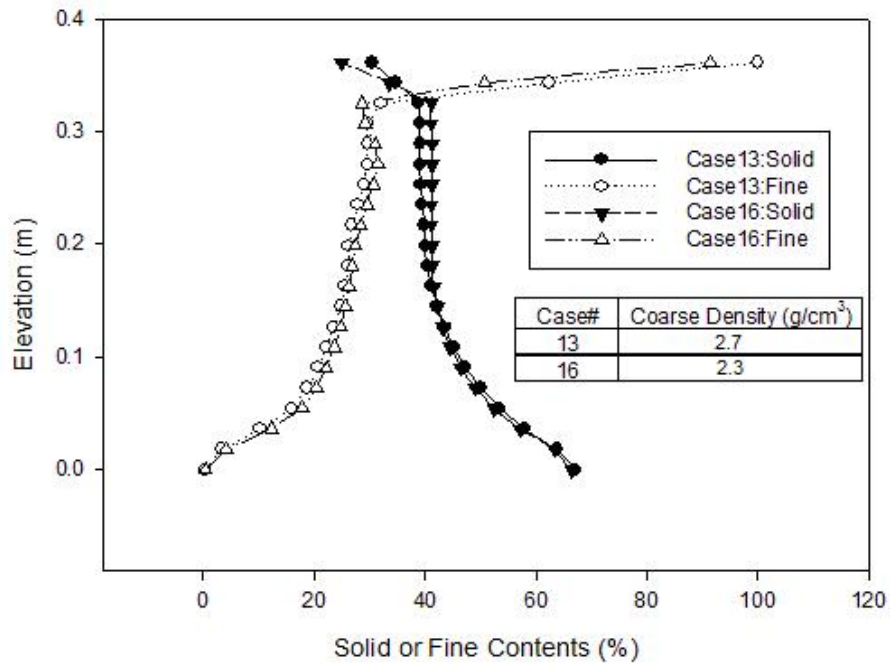


Figure 4.36 Effects of particle density on solids and fines contents

#### 4.3.3.2.3 Simulation of Segregating Slurry Using FLUENT-6 Modified Settings

##### 4.3.3.2.3.1 EFFECTS OF PARTICLE SIZE DIVISION FOR FINE AND COARSE PARTICLES

###### 4.3.3.2.3.1.1 DETERMINATION OF THE EFFECTIVE SIZE FOR POLYDISPERSE SYSTEM

The slurry in SB1 and SB3 is formed by mixing coarse tail sand with mature fine tailings (MFT) at specified mass ratio. The mixture is composed of continuous distribution of particles with diameter ranging from less than 1 micron to more than 2 mm. Since limited number of particle group is allowed in Euler-Euler simulation in FLUENT, attempts are made to divide all the particles into coarse particle and fine particle groups using certain division value. Based on the grouping, an effective or representative diameter is found in each group to represent all the particles in the corresponding group.

Loth et al. (2004) studied the effective diameter for the two-phase flow in which the gravity and drag force determine the particle motion. They found that the volume-width diameter shown in the following equation is the effective diameter for the flow where particle Reynolds number is much less than 1:

$$D_{31}^2 = \frac{\int_0^{\infty} f(D)D^3 dD}{\int_0^{\infty} f(D)D dD} \quad (\text{Eq. 4.4})$$

Where  $f(D)$  is the number Probability Distribution Function (PDF) and  $D$  is the diameter of the particles. The number Probability Distribution Function is the Probability Distribution Function in term of the number of particles within certain size range as shown in the following equation:

$$n_i = \frac{m_i}{\rho_{di} \frac{\pi D_i^3}{6}} \quad (\text{Eq. 4.5})$$

Where  $m_i$  is the mass fraction of particles in Group  $i$ ,  $\rho_{di}$  the dry density of the particles which is assumed to be 2700 Kg/m<sup>3</sup>,  $D_i$  the diameter of particles and  $n_i$  the number of the particles in Group  $i$ . The number PDF can be calculated using the following equation:

$$f(D_i) = \frac{n_i}{\sum_{i=1}^N n_i} \quad (\text{Eq. 4.6})$$

Where N is the number of particle group.

As stated above, several assumptions are made in calculating the probability distribution of particle numbers. The assumption involved in particle shape is prone to errors. Moreover, it is more convenient to determine the fraction of mass for certain sizes of particles than to determine the number distribution in practice. Therefore, the mass Probability Distribution Function is used to calculate the effective particle size D31 for fine and coarse particles, as shown in the following equation:

$$f(D_i) = \frac{m_i}{\sum_{i=1}^N m_i} \quad (\text{Eq. 4.7})$$

Where  $m_i$  is mass fraction of particles in Group  $i$ . The number of the particles is calculated based on the assumption that the particles in each particle group are spherical and have uniform size. Here the number Probability Distribution Function is changed to the mass Probability Distribution Function.

Table 4.7 Calculated Effective size D31 in mm for CT, coarse and fine particles based on number Probability Distribution Function using different fine-coarse particle divisions

Mixture	SB1			SB3		
Division	0.044	0.022	0.0055	0.044	0.022	0.0055
CT	5.48E-01	5.48E-01	5.48E-01	5.47E-01	5.48E-01	5.47E-01
coarse	5.13E-01	5.17E-01	5.39E-01	5.07E-01	5.17E-01	5.30E-01
fine	3.78E-03	2.29E-03	9.81E-04	8.19E-03	2.29E-03	1.33E-03

Table 4.8 Calculated Effective size D31 in mm for CT, coarse and fine particles based on mass Probability Distribution Function using different fine-coarse particle divisions

Mixture	SB1			SB3		
Division	0.044	0.022	0.0055	0.044	0.022	0.0055
<b>CT</b>	5.48E-01	5.48E-01	5.48E-01	5.47E-01	5.47E-01	5.47E-01
<b>coarse</b>	5.48E-01	5.48E-01	5.48E-01	5.47E-01	5.48E-01	5.47E-01
<b>fine</b>	1.74E-02	9.89E-03	1.34E-03	2.00E-02	9.89E-03	1.34E-03

Figure 4.37 shows the grain size distribution of coarse tailing sands (referred as Coarse in the Figure) and MFT. The grain size distribution of the coarse tailing sands and MFT is shown in Figure 3.6 and Figure 3.7. The CT in the figure is referred to the mixture composed of coarse sand tailings and mature fine tailings (MFT). The grain size distribution of CT is calculated based on the grain size distribution and mass fraction of the two components.

The particles in CT are divided into fine and coarse particle groups according to the division of 0.044, 0.022 and 0.0055 mm. The effective particle size, D31, of fine and coarse particles is calculated using the same arithmetic as that used for calculating D31 for CT. The calculation is performed using a MATLAB code. The calculated effective size D31 for CT, coarse particles and fine particles using number PDF is shown in Table 4.7. The table also lists the D31 based on different divisions for fine and coarse particles. Similarly, Table 4.8 shows the effective size D31 based on mass PDF using different divisions for fine particles and coarse particles.

Comparison of the calculated D31 in Table 4.7 and those in Table 4.8 is shown in Figure 4.38, Figure 4.39 and Figure 4.40. Figure 4.38 shows that D31 for CT and coarse particles based on number Probability Distribution agree well with those calculated using mass PDF. However, the D31 for fine particles using number PDF is significantly smaller than D31 using mass PDF. Preference of small particles using number PDF is expected as the probability of smaller particles in terms of the number is larger than that of the same particles based on mass. Figure 4.39 shows the similar results for SB3. Figure 4.40 compares the differences in using division sizes and probability density functions. It can be observed that choosing larger division sizes (22 micron or 44 micron) has larger influence on the calculated fine particle sizes if different PDF is selected.

Another representative particle size used quite frequently in geotechnical engineering is D50. This is the particle size that corresponds to 50 percent of the solid mass finer than the size. Calculated D50 for coarse and fine particles is shown in Table 4.9.

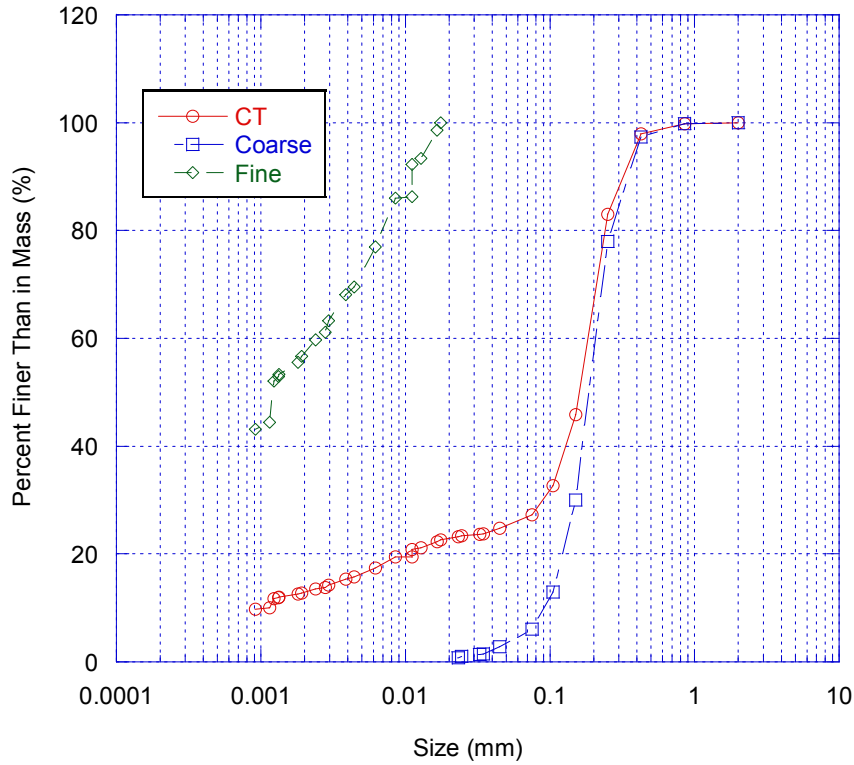


Figure 4.37 Grain size distribution for the mixture of coarse tailing sands and MFT. Here the mixture is referred to as CT. The grain size distribution for the coarse tailings and MDT is shown in Figure 3.6 and Figure 3.7. The grain size distribution of the mixture is calculated based on its solids and fines contents.

Table 4.9 Calculated Effective size D50 in mm for coarse and fine particles based on 50% mass using different fine-coarse particle divisions

Mixture	SB1			SB3		
Division	0.044	0.022	0.0055	0.044	0.022	0.0055
coarse	1.93E-01	1.94E-01	1.94E-01	1.96E-01	1.96E-01	1.95E-01
fine	8.96E-04	7.41E-04	6.87E-04	1.22E-03	1.22E-03	1.21E-03

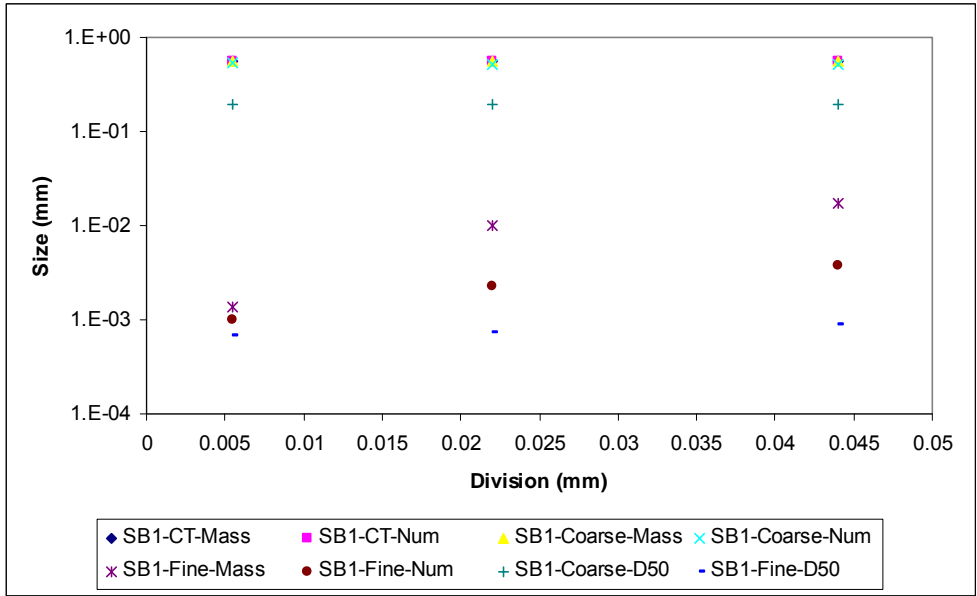


Figure 4.38 Effective particle sizes D31 for CT, coarse and fine particles for SB1 using number PDF, mass PDF and 50 percent mass

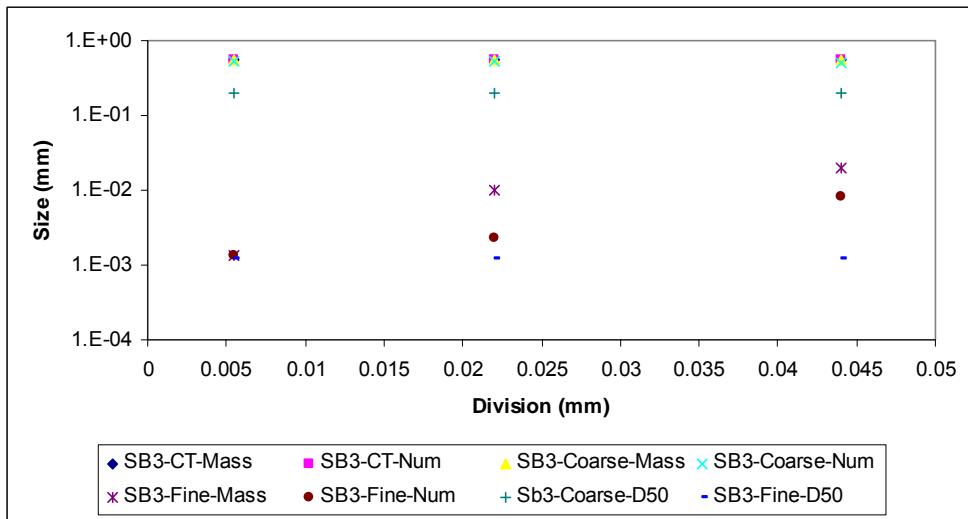


Figure 4.39 Effective particle sizes D31 for CT, coarse and fine particles for SB3 using number PDF, mass PDF and 50 percent mass

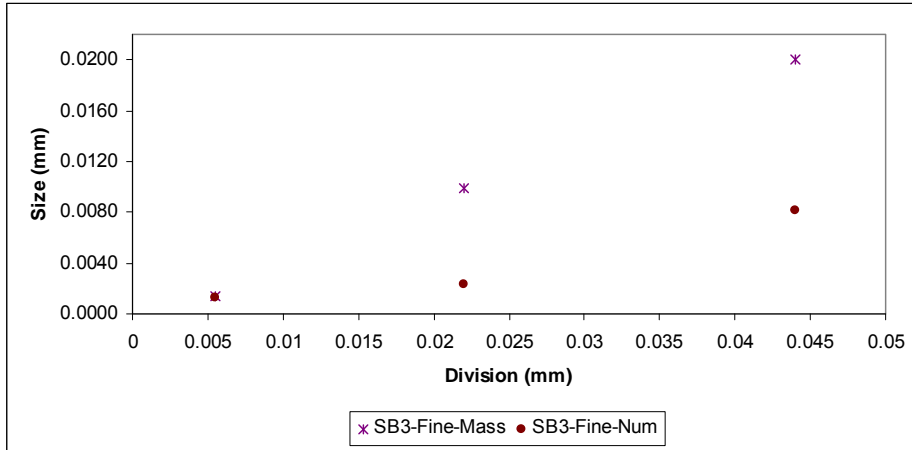


Figure 4.40 Comparison of effective particle sizes D31 for SB3 calculated using number PDF with that calculated using mass PDF

#### 4.3.3.2.3.1.2 SIMULATION RESULTS FOR SEGREGATING SLURRY SB1

Figure 4.41 to Figure 4.45 shows solids and fines contents profiles at 200, 1000 and 2000 s using 44, 22 and 5.5  $\mu\text{m}$  as a coarse fine division for segregating slurry SB1. Figure 4.41, Figure 4.42 and Figure 4.43 show the progress of solids and fines content profiles with time. Comparison of the solids and fines content profiles using different coarse-fine divisions is shown in Figure 4.44 and Figure 4.45. The variations in solids and fines content over the simulation period can be seen from Figure 4.41 to Figure 4.43. Greater variation in solids content for the simulation in the upper 20 cm of the standpipe can be observed for the simulation using the coarse-fine division of 44 micron than those using 22 and 5.5 micron as a division. This is confirmed in Figure 4.44 and Figure 4.45 where simulation results using different coarse-fine division at 200 s and 2000 s respectively are compared.

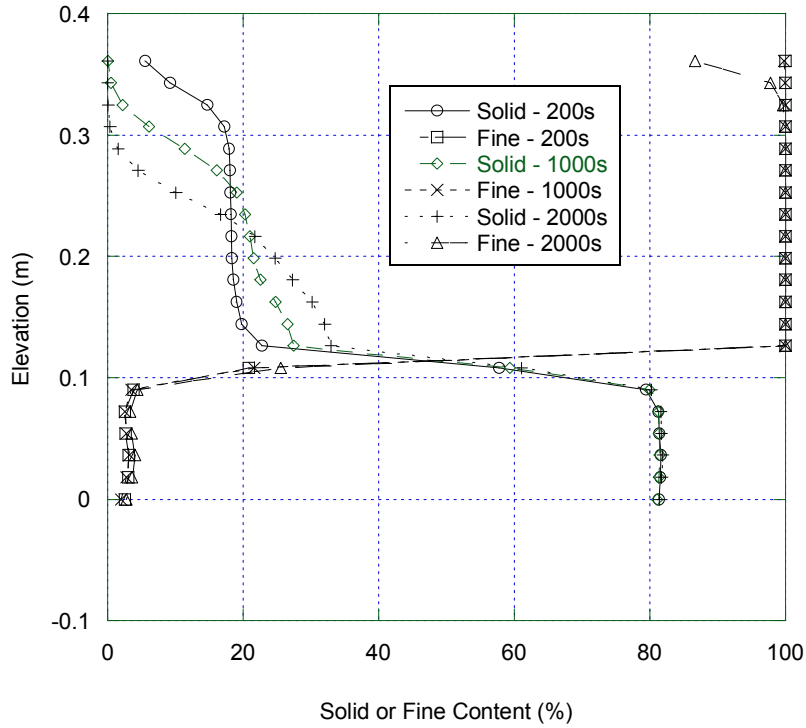


Figure 4.41 Solids and fines content profiles at 200s, 1000s and 2000s for simulation of SB1. D31 is calculated using 44 micron as coarse-fine division based on mass PDF.

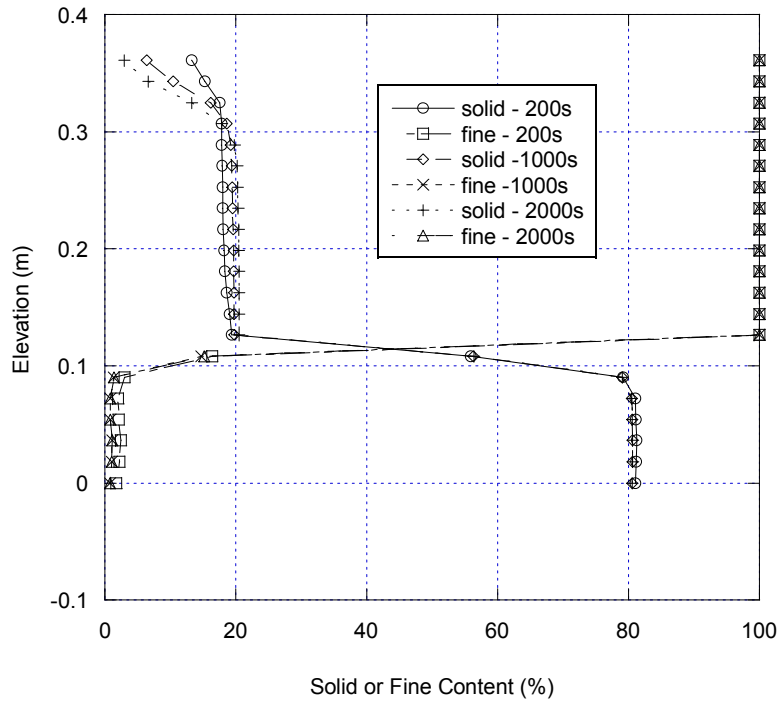


Figure 4.42 Solids and fines content profiles at 200s, 1000s and 2000s for simulation of SB1. D31 is calculated using 22 micron as coarse-fine division based on mass PDF.

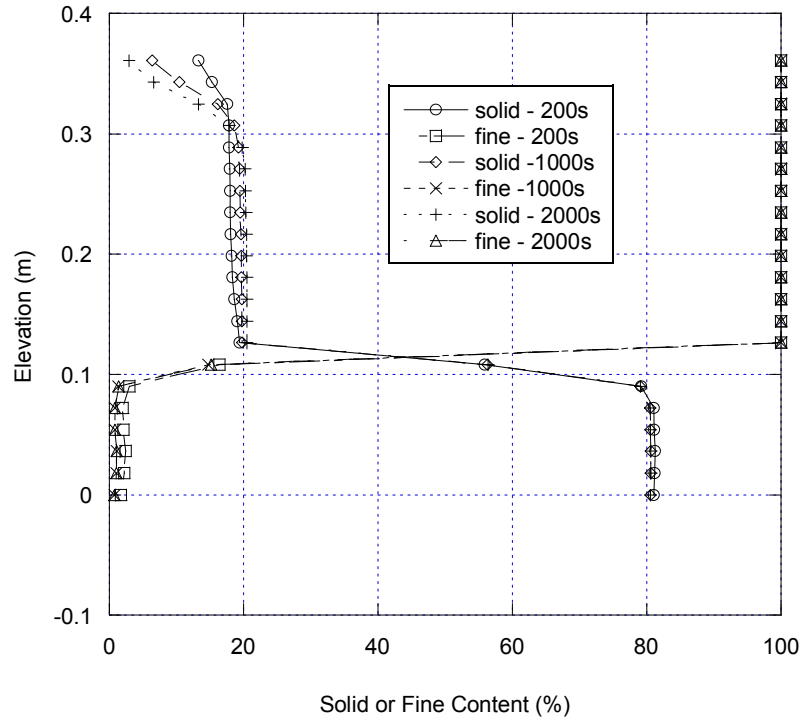


Figure 4.43 Solids and fines content profiles at 200s, 1000s and 2000s for simulation of SB1. D31 is calculated using 5.5 micron as coarse-fine division based on mass PDF.

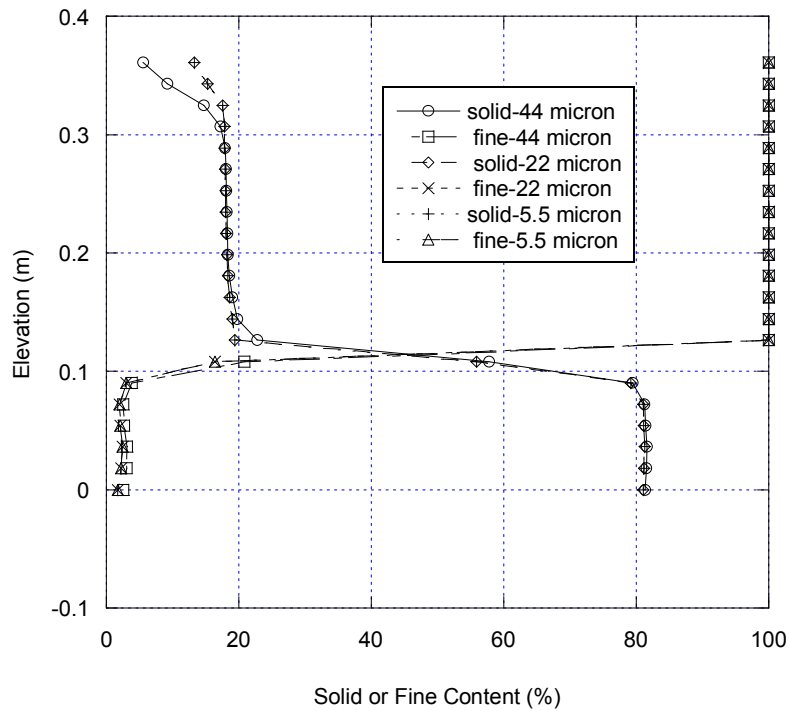


Figure 4.44 Effects of coarse-fine division on solids and fines content profiles at 200s for SB1. D31 is calculated based on mass PDF.

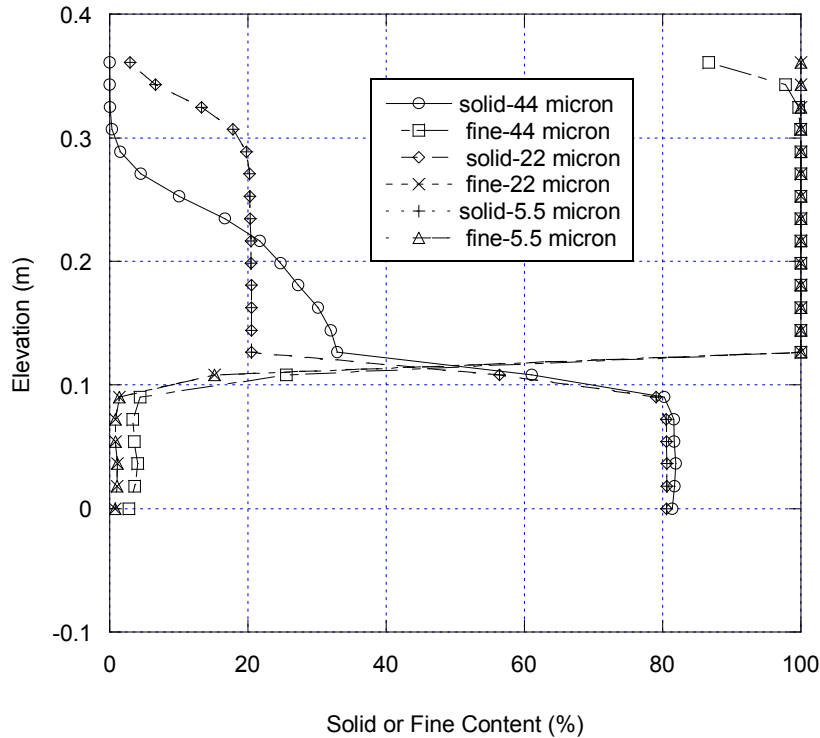


Figure 4.45 Effects of coarse-fine division on solids and fines content profiles at 2000s for SB1. D31 is calculated based on mass PDF.

#### 4.3.3.2.3.1.3 SIMULATION RESULTS FOR NON-SEGREGATING SLURRY

##### 4.3.3.2.3.1.3.1 Simulation Using D31 Calculated on Mass PDF

The solids and fines content profiles at 200, 1000 and 2000 seconds are presented in Figure 4.46, Figure 4.47 and Figure 4.48. The effects of coarse-fine division on the solids and fines contents at various times are shown in Figure 4.49 and Figure 4.50. Figure 4.46, Figure 4.47 and Figure 4.48 demonstrate that the solids content increases with time for the upper part of the domain while the solids content in the lower standpipe domain and the fines contents remain essentially constant after 200 seconds. It can be observed that solids and fines contents remain almost constant for the simulation using 5.5  $\mu\text{m}$  as a coarse-fine division.

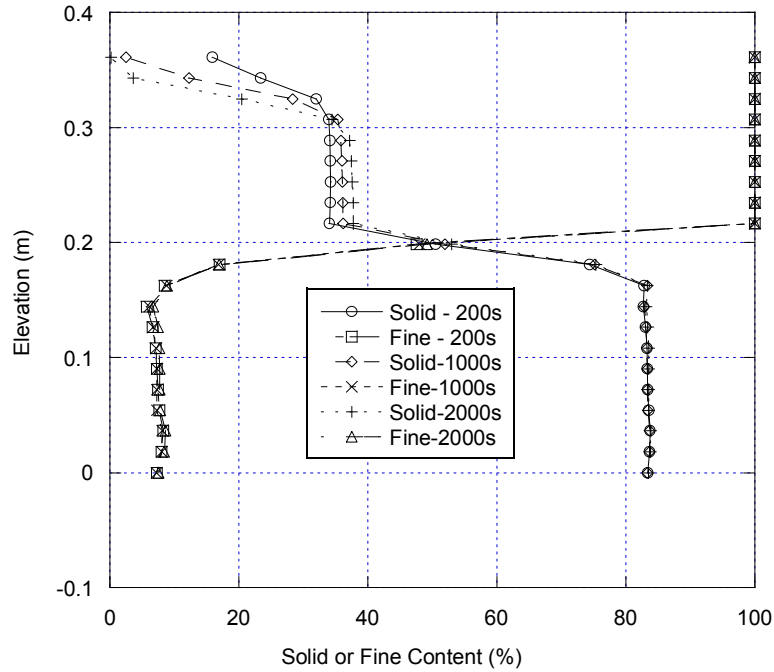


Figure 4.46 Solids and fines content profiles at 200, 1000 and 2000 second for simulation of SB3. D31 is calculated using 44 micron as coarse-fine division based on mass PDF.

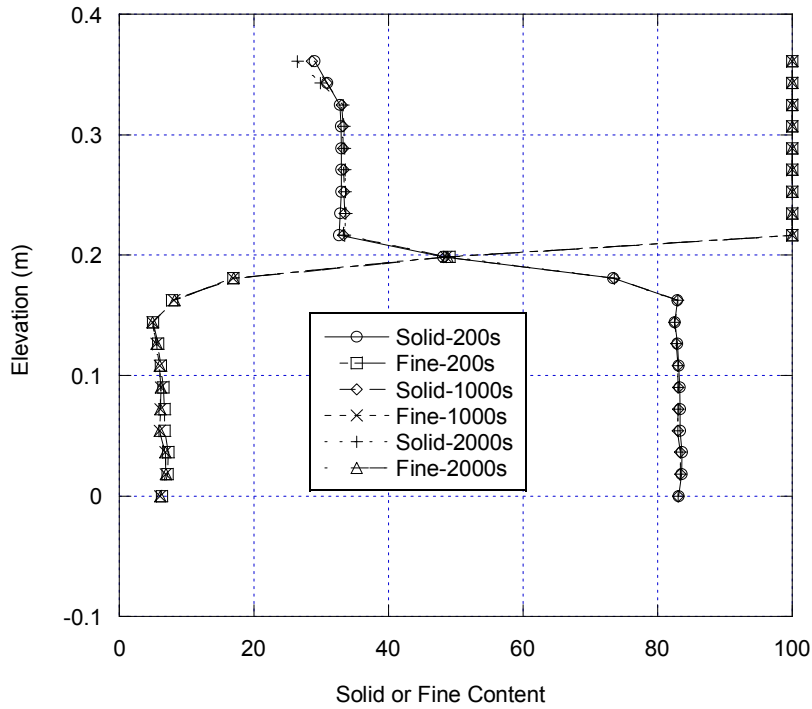


Figure 4.47 Solids and fines content profiles at 200, 1000 and 2000 second for simulation of SB3. D31 is calculated using 22 micron as coarse-fine division based on mass PDF.

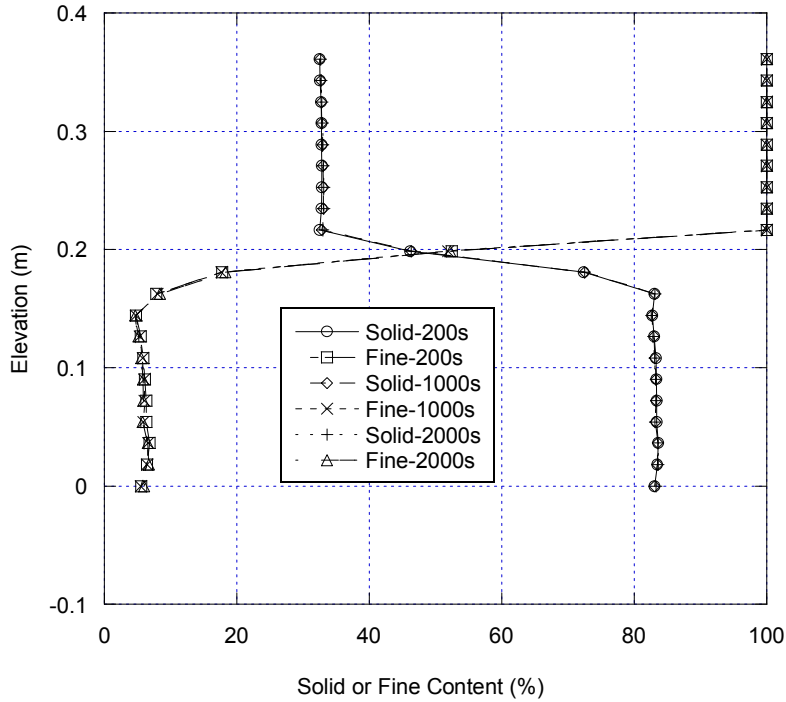


Figure 4.48 Solids and fines content profiles at 200, 1000 and 2000 second for simulation of SB3. D31 is calculated using 5.5 micron as coarse-fine division based on mass PDF.

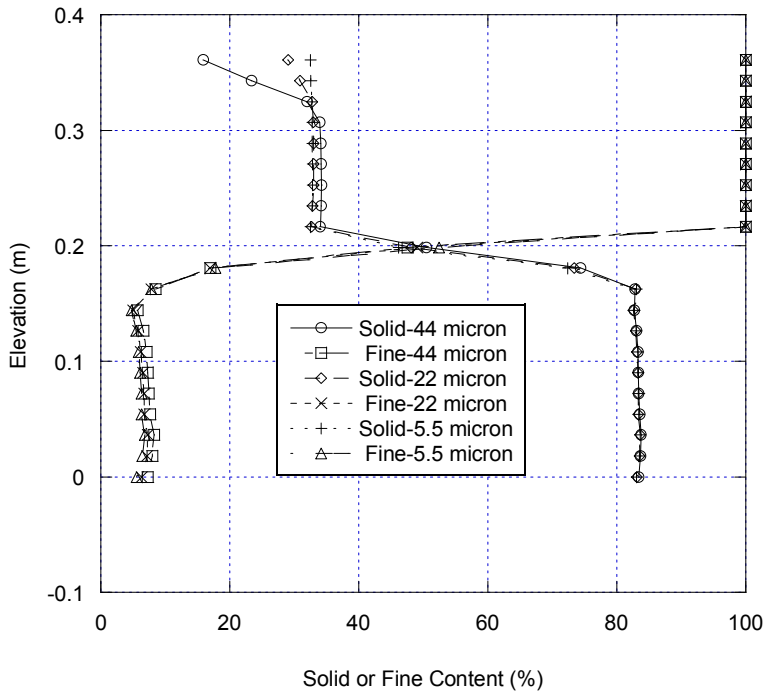


Figure 4.49 Effects of coarse-fine division on the solids and fines content profiles at 200 second for simulation of SB3. D31 is calculated based on mass PDF.

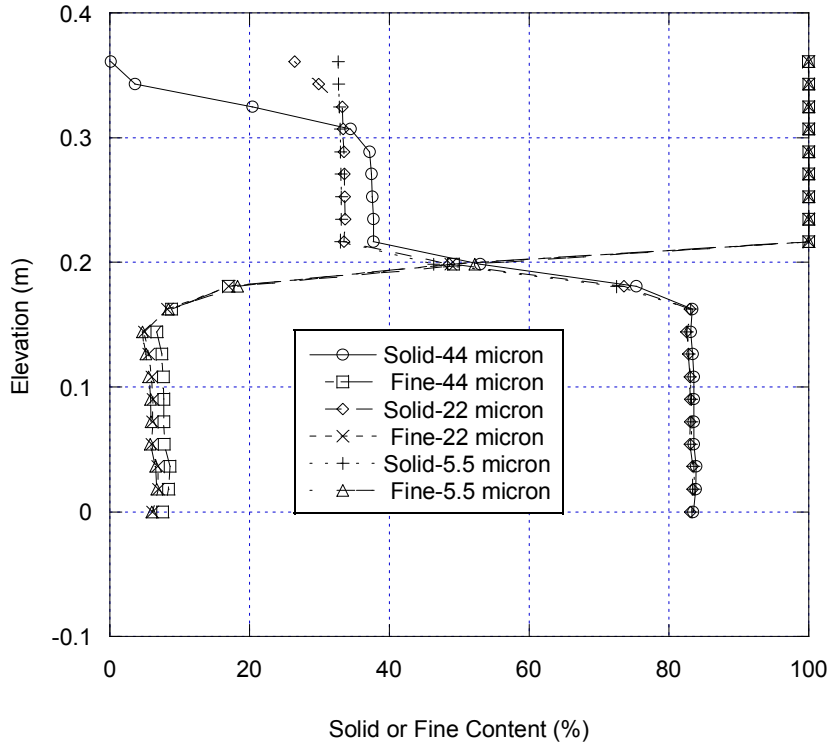


Figure 4.50 Effects of coarse-fine division on the solids and fines content profiles at 2000 second for simulation of SB3. D31 is calculated based on mass PDF.

#### 4.3.3.2.3.1.3.2 Simulation Using D31 Calculated on Number PDF

The evolution of the solids and fines content profiles using different coarse-fine division is presented in Figure 4.51, Figure 4.52 and Figure 4.53. Comparison of solids and fines content profiles using different coarse-fine division is shown in Figure 4.54 and Figure 4.55. These figures show that the variations in solids and fines contents for all the simulations are insignificant. Figure 4.54 and Figure 4.55 show that the difference in solids and fines contents profiles using different coarse-fine division is not evident.

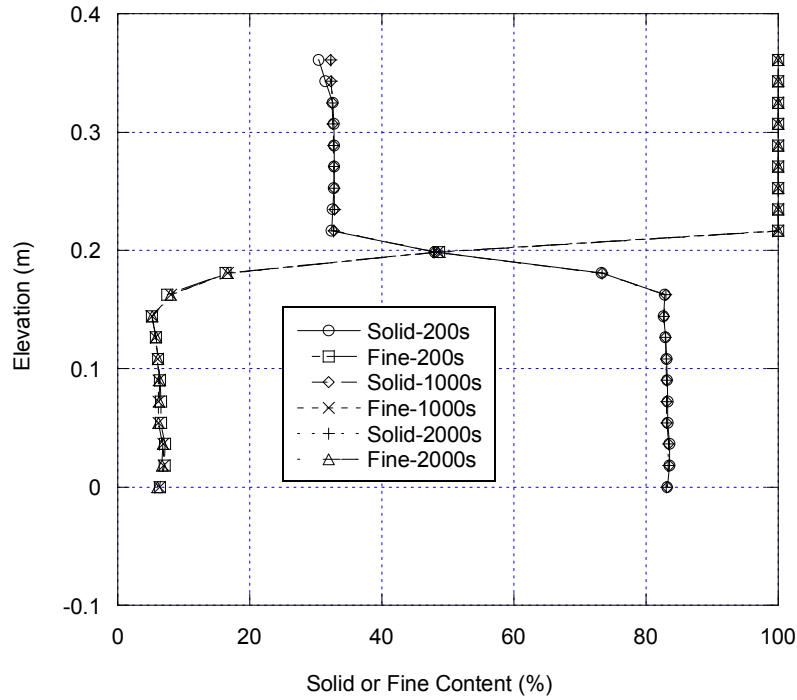


Figure 4.51 Solids and fines content profiles at 200, 1000 and 2000 second for simulation of SB3. D31 is calculated using 44 micron as coarse-fine division based on number PDF.

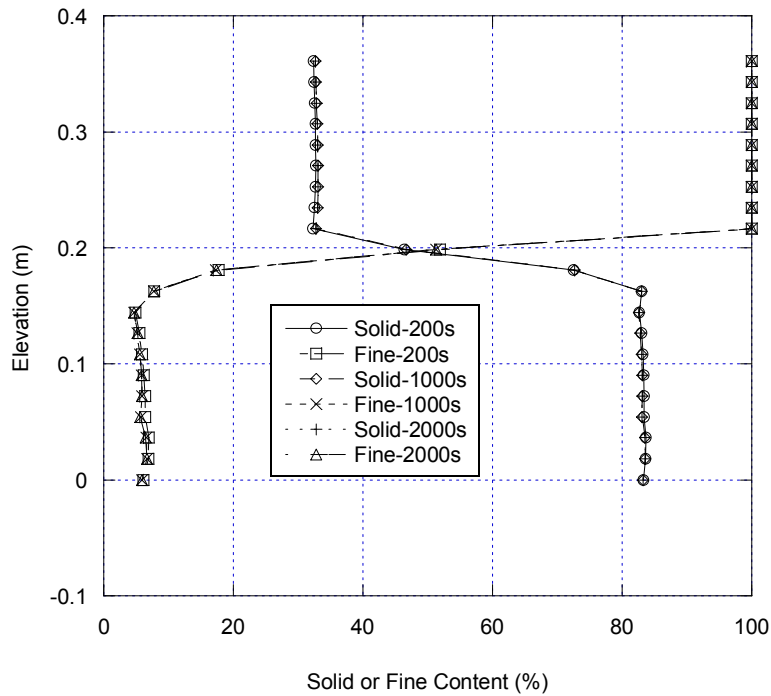


Figure 4.52 Solids and fines content profiles at 200, 1000 and 2000 second for simulation of SB3. D31 is calculated using 22 micron as coarse-fine division based on number PDF.

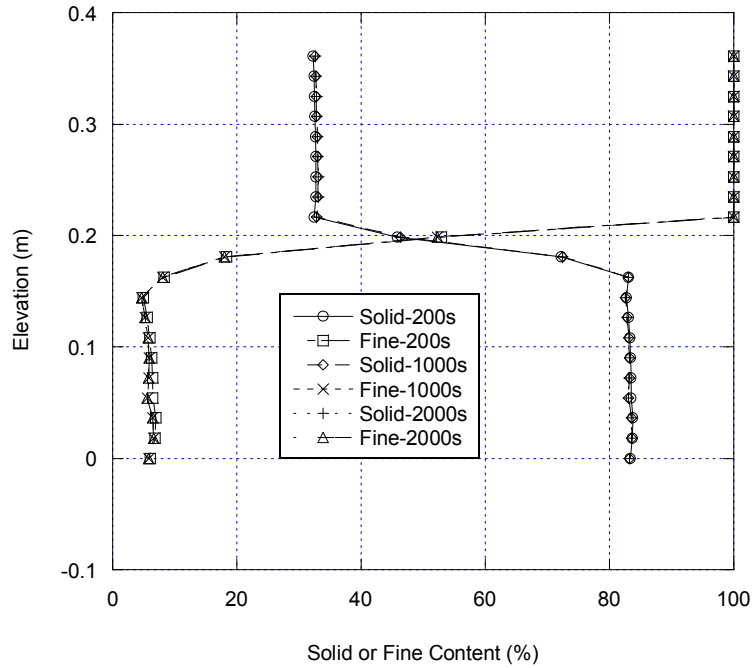


Figure 4.53 Solids and fines content profiles at 200, 600 and 2000 second for simulation of SB3. D31 is calculated using 5.5 micron as coarse-fine division based on number PDF.

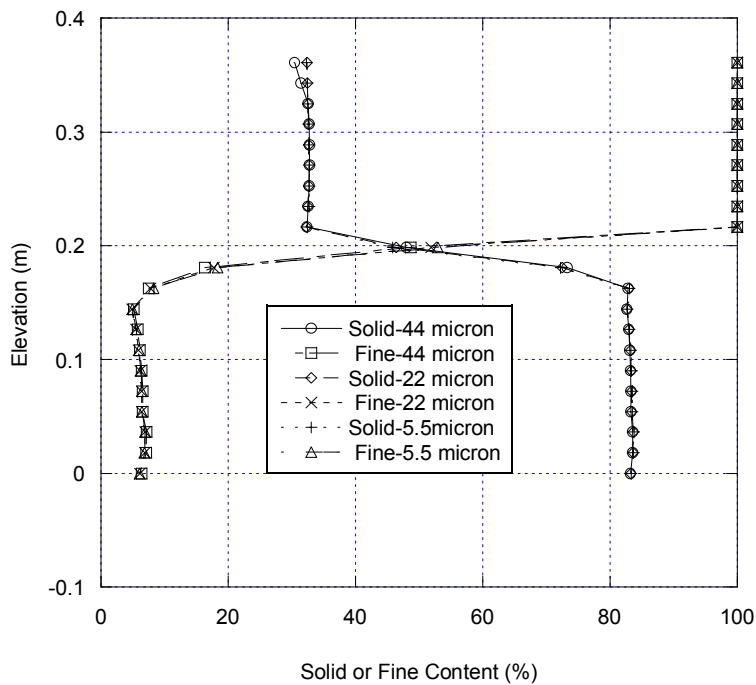


Figure 4.54 Effects of coarse-fine division on the solids and fines content profiles at 200 second for simulation of SB3. D31 is calculated based on number PDF.

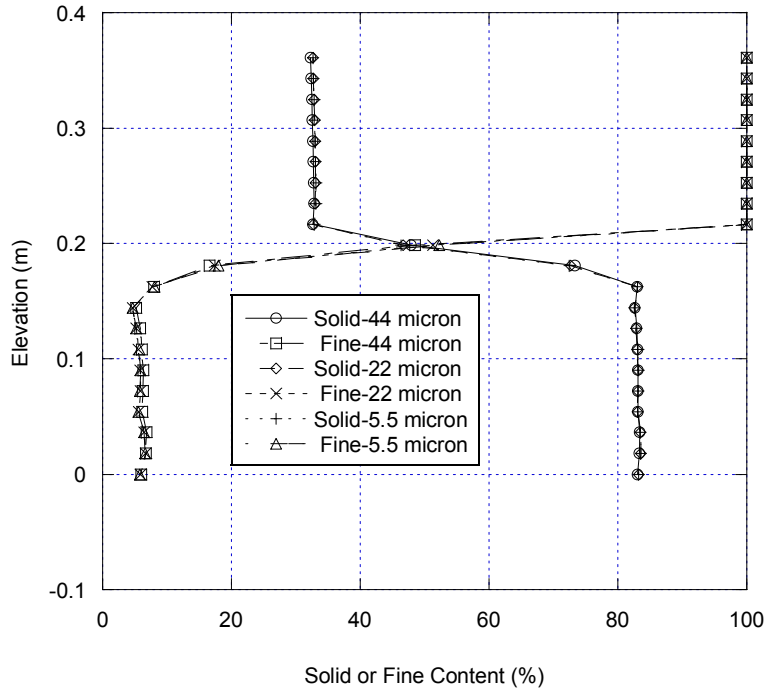


Figure 4.55 Effects of coarse-fine division on the solids and fines content profiles at 2000 second for simulation of SB3. D31 is calculated based on number PDF.

#### 4.3.3.2.3.1.3.3 Comparison of Effects of D31 on the Solids and Fines content

The effects of using mass PDF and using number PDF on the solids and fines contents are shown in Figure 4.56 to Figure 4.61. Figure 4.56 and Figure 4.57 show the solids and fines content profiles obtained using mass PDF and number PDF for SB3 at the simulation time of 200 s and 2000 s respectively. Effective diameters for fine and coarse particles are calculated using 44 micron as a division. The solids and fines content profiles using 22 micron as a division are shown in Figure 4.58 and Figure 4.59. The simulation results using 5.5 micron as a coarse-fine division are presented in Figure 4.60 and Figure 4.61.

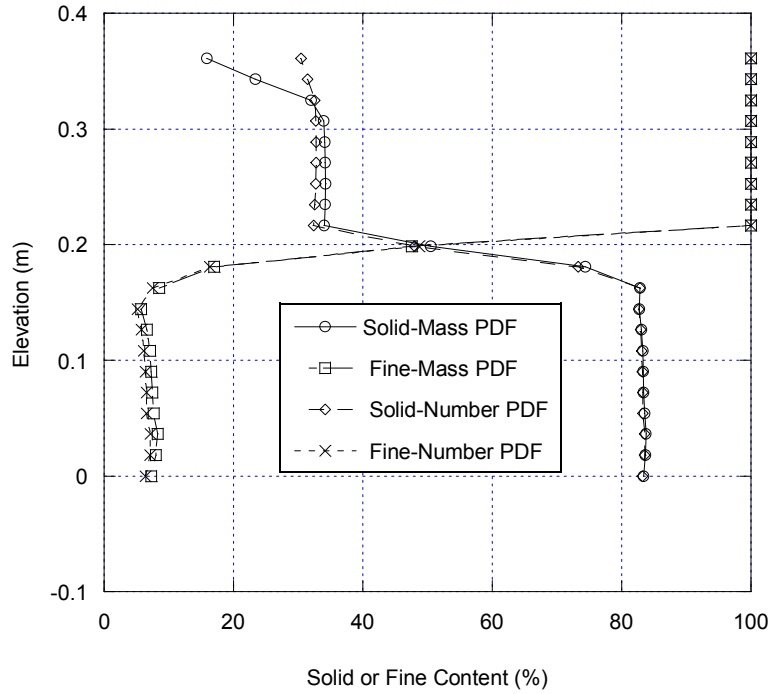


Figure 4.56 Comparison of solids and fines content profiles at 200 second for simulation of SB3. D31 is calculated using 44 micron as coarse-fine division based on number PDF and mass PDF.

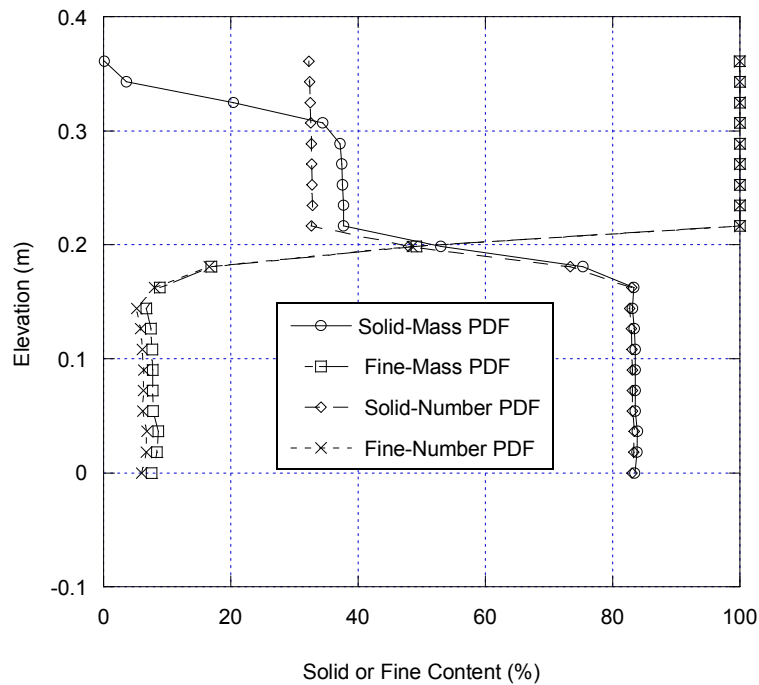


Figure 4.57 Comparison of solids and fines content profiles at 2000 second for simulation of SB3. D31 is calculated using 44 micron as coarse-fine division based on number PDF and mass PDF.

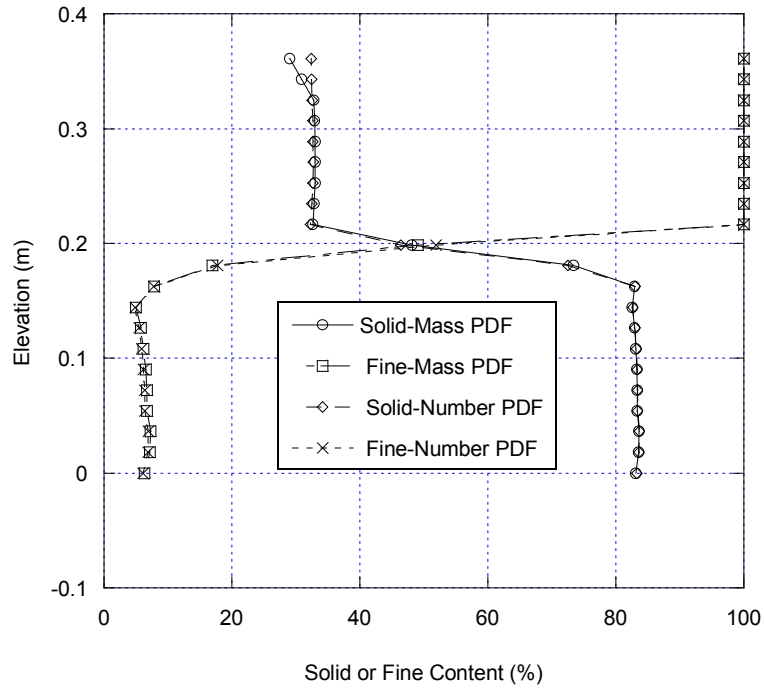


Figure 4.58 Comparison of solids and fines content profiles at 200 second for simulation of SB3. D31 is calculated using 22 micron as coarse-fine division based on number PDF and mass PDF.

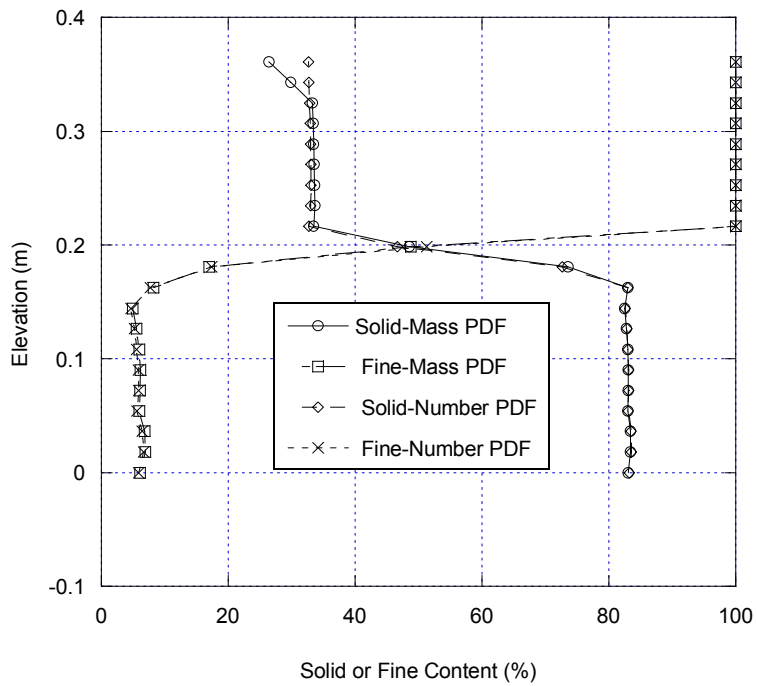


Figure 4.59 Comparison of solids and fines content profiles at 2000 second for simulation of SB3. D31 is calculated using 22 micron as coarse-fine division based on number PDF and mass PDF.

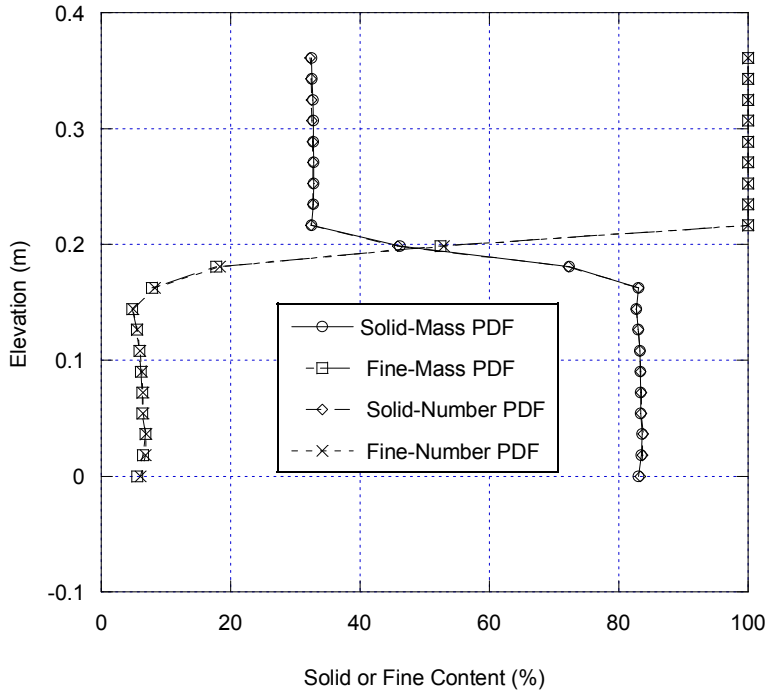


Figure 4.60 Comparison of solids and fines content profiles at 200 second for simulation of SB3. D31 is calculated using 5.5 micron as coarse-fine division based on number PDF and mass PDF.

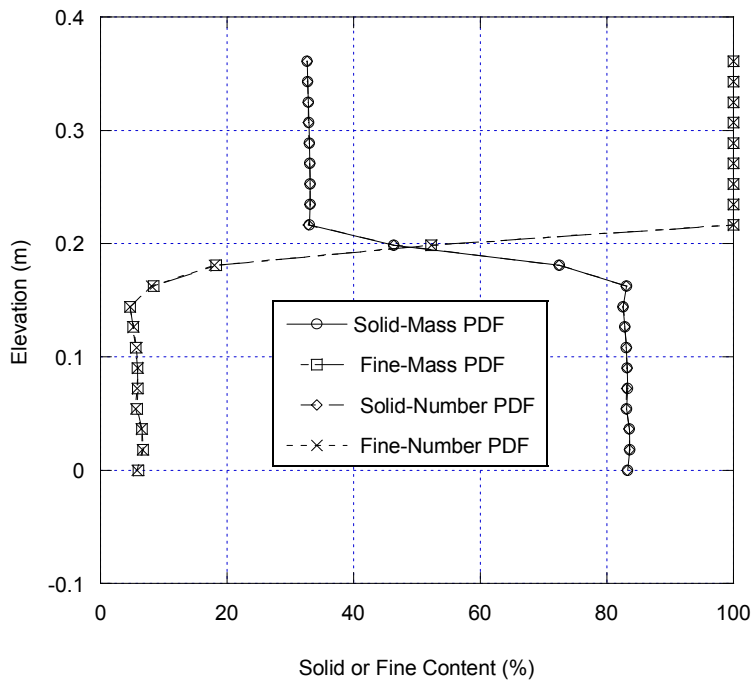


Figure 4.61 Comparison of solids and fines content profiles at 2000 second for simulation of SB3. D31 is calculated using 5.5 micron as coarse-fine division based on number PDF and mass PDF.

### 4.3.3.3 MFIX Simulation

#### 4.3.3.3.1 Backgrounds

Figure 4.20 and Figure 4.23 show that the interface between supernatant water and the suspension develops faster than that in the experiments using CFX-5. The simulation results and the sensitivity tests that are conducted in FLUENT-6 in Section 4.3.3.2 also indicate that the solids and fines content profiles are not sensitive to the parameters in the models. In both models, the non-segregating slurry SB3 is predicted to be segregating. However, segregation occurs in a short time for both segregating slurry (SB1) and non-segregating slurry (SB3).

Efforts then are made to search for the open-source CFD codes which are potentially capable of modeling the segregating and non-segregation process. MFIX became an ideal candidate because of its wide application in granular flow by research institutes (National Energy Technology Laboratory (NETL), Iowa State University, Los Alamos National Laboratory, etc.) Particularly, several researchers studied the particle segregation using the Euler-Euler model in the MFIX code.

Gera et al. (2004) reviewed the literature on the segregation prediction. They found that the prediction in the models by Goldschmidt et al. (2001) and Chen et al. (2002) is contrary to experiment results which show that segregation will not occur at low velocities for the binary system. In order for the model to predict non-segregation at low velocities, they added a new term into the particle-particle drag coefficient. The modified particle-particle drag coefficient is shown in the following equation:

$$F_{ml} = \frac{3(1 + e_{lm})(\pi/2 + C_{fml}\pi^2/8)\varepsilon_l\rho_l\varepsilon_m\rho_m(d_{pl} + d_{pm})^2 g_{0,lm}|\vec{v}_l - \vec{v}_m|}{2\pi(\rho_l d_{pl}^3 + \rho_m d_{pm}^3)} + C_1 P^* \quad (\text{Eq. 4.8})$$

where  $F_{ml}$  is the drag coefficient between the granular phase  $m$  and phase  $l$ . In the first term,  $e_{ml}$  and  $C_{fml}$  are the coefficient of restitution and coefficient of friction, respectively, between  $l^{\text{th}}$  and  $m^{\text{th}}$  granular-phase particles;  $g_{0,lm}$  is the radial distribution function at contact,  $\varepsilon$ ,  $\rho$ ,  $d$  and  $\vec{v}$  are the fraction of volume, density, diameter and velocity, respectively. The subscripts  $l$  and  $m$  indicates the variables for  $l^{\text{th}}$  and  $m^{\text{th}}$

granular-phase particles respectively. In the second term which is the added term by the author,  $P^*$  is the solids pressure.

The authors show both non-segregation at lower velocity and the rate of segregation at intermediate velocity are correctly predicted by the modified model. The performance of this modified model will be evaluated for segregating (SB1) and non-segregating oil sand tailing slurry (SB3).

#### 4.3.3.3.2 MFIX Set-up

The standpipe tests SB1 and SB3 are modeled using MFIX (Multiphase Flow with Interphase eXchanges) code. The standpipe is assumed to be 40 cm high with a diameter of 4 cm. Cylindrical symmetry is assumed, thus only length of the domain in x (radial) direction is 2.0 cm. Two-dimensional simulations are conducted for all the cases by assigning the number of grid in z (Azimuth) direction as 1. With exception of the case Sb1-Run6 in which 4 x 40 x 1 uniform grid is used, a uniform grid of 8 x 80 x 1 is used for all the other simulation cases. The settings that are in common in all the MFIX simulation cases are shown in Table 4.10. The parameters of Segregation Slope are varied from 0 to 0.9 for the simulation of segregating slurry, SB1. The detailed values of Segregation Slope used in each case are presented in Table 4.11. As for the non-segregating slurry, SB3, the influence of the segregation slope and the solid viscosity models on the volume fraction of coarse and fine particles are evaluated. The detailed settings used in the simulation for non-segregating slurry, SB3, are discussed in the following sections.

Table 4.10 Common Settings for MFIX Simulation Cases

	Overall	Water	Coarse	Fine
Max. Time (s)	1000	N/A	N/A	N/A
Time Step (s)	5.00E-04	N/A	N/A	N/A
Time Step Adjustment Factor	0.9	N/A	N/A	N/A
Number of Particulate Phases	2	N/A	N/A	N/A
Close Packed	N/A	N/A	TRUE	TRUE
Drag Type	N/A	Gidaspow	Syamlal-O'Brien-Symmetric	Syamlal-O'Brien-Symmetric
Segregation Slope Coefficient	N/A	N/A	varied	varied
Max. solid particle packing	N/A	N/A	0.6	0.6
Viscosity (g/(cm.s))	N/A	1.00E-02		
Density (g/cm <sup>3</sup> )	N/A	1	2.7	2.6
Coefficient of Restitution	0.97	N/A	N/A	N/A
Coefficient of Frictional Angle	0.1	N/A	N/A	N/A
Internal Frictional Angle (degree)	N/A	N/A	30	30
Boundary Conditions	Top Free-slip; non-slip wall for the rest.	N/A	N/A	N/A

Table 4.11 Segregation Slope Values for MFIX Simulation Cases

Cases	Segregation Slopes	Cases	Segregation Slopes
SB1-Run3	0.9	SB3-Run4	0
SB1-Run4	0.6	SB3-Run5	0.3
SB1-Run5	0.3	SB3-Run6	0.9
SB1-Run6	0		

### 4.5.3.3.3 Effects on Segregation Slope on the Simulation of Segregating Slurry (SB1)

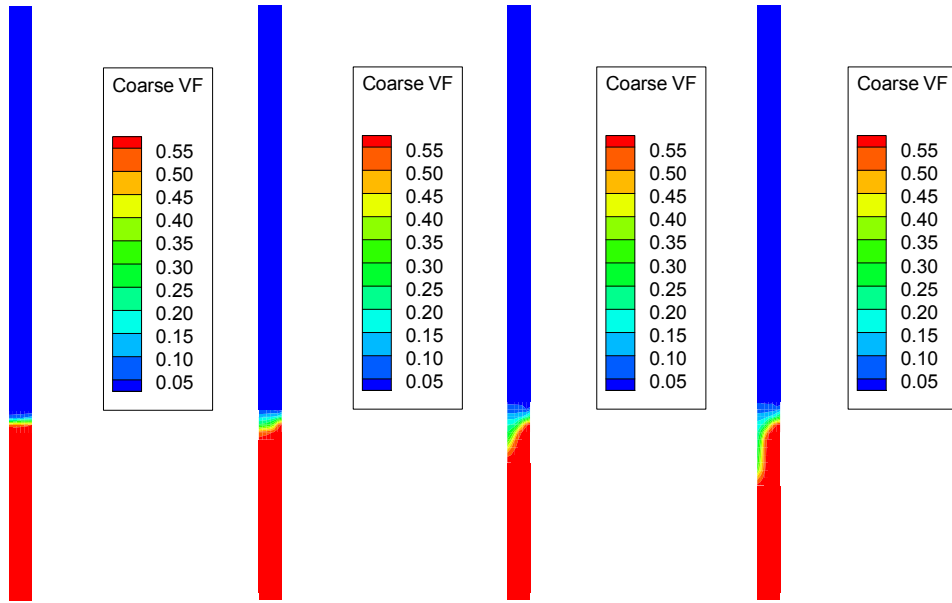


Figure 4.62 Coarse Volume Fraction for SB1\_Run3 at time of 250, 500, 750 and 1000 second, respectively (Segregation Slope = 0.9)

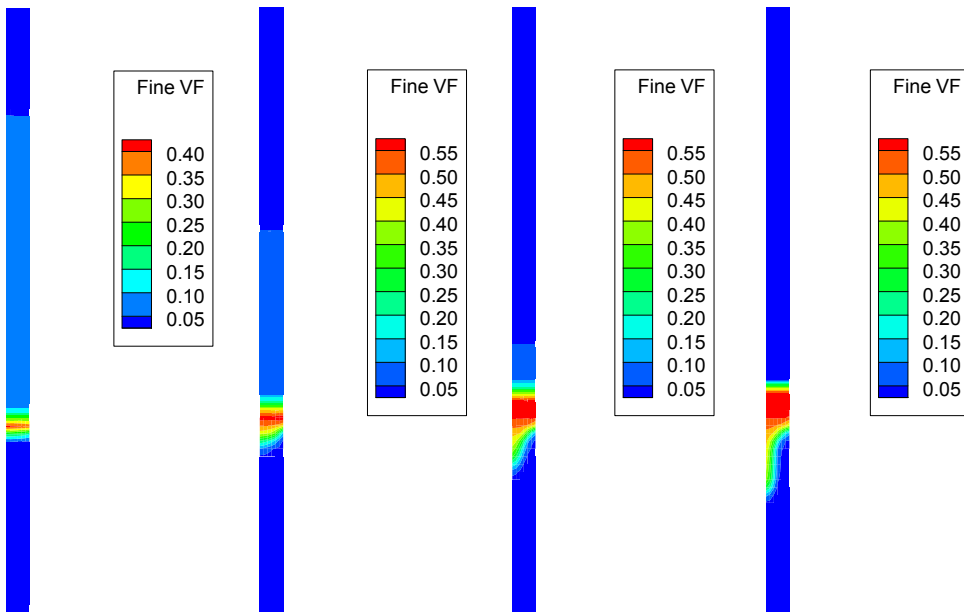


Figure 4.63 Fine Volume Fraction for SB1\_Run3 at time of 250, 500, 750 and 1000 second (Segregation Slope = 0.9)

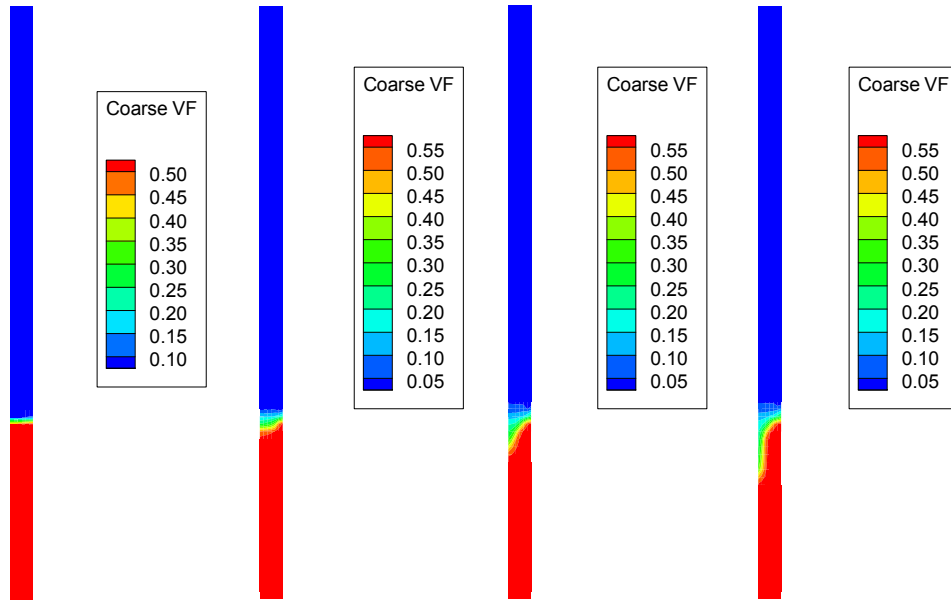


Figure 4.64 Coarse Volume Fraction for SB1\_Run4 at time of 250, 500, 750 and 1000 second (Segregation Slope = 0.6)

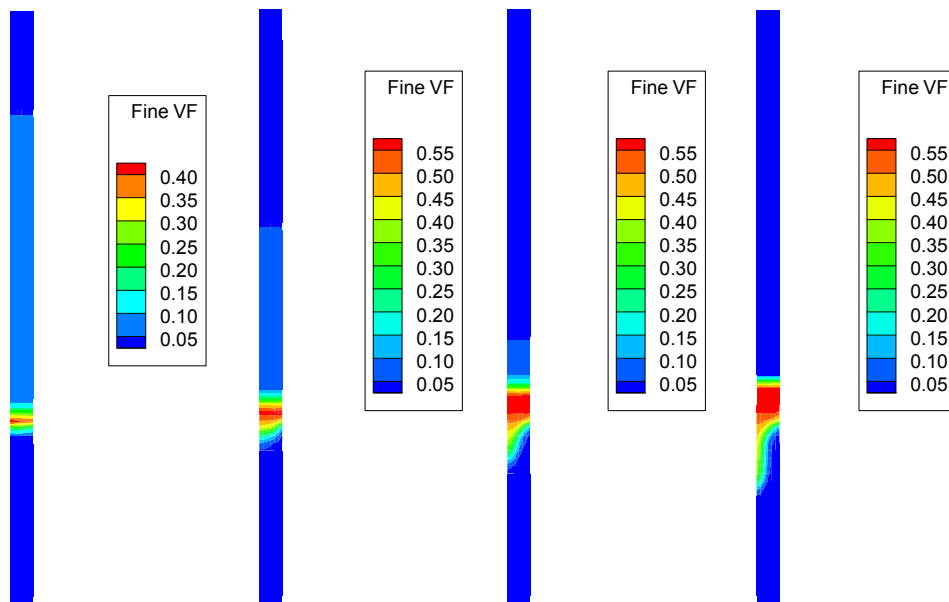


Figure 4.65 Fine Volume Fraction for SB1\_Run4 at time of 250, 500, 750 and 1000 second (Segregation Slope = 0.6)

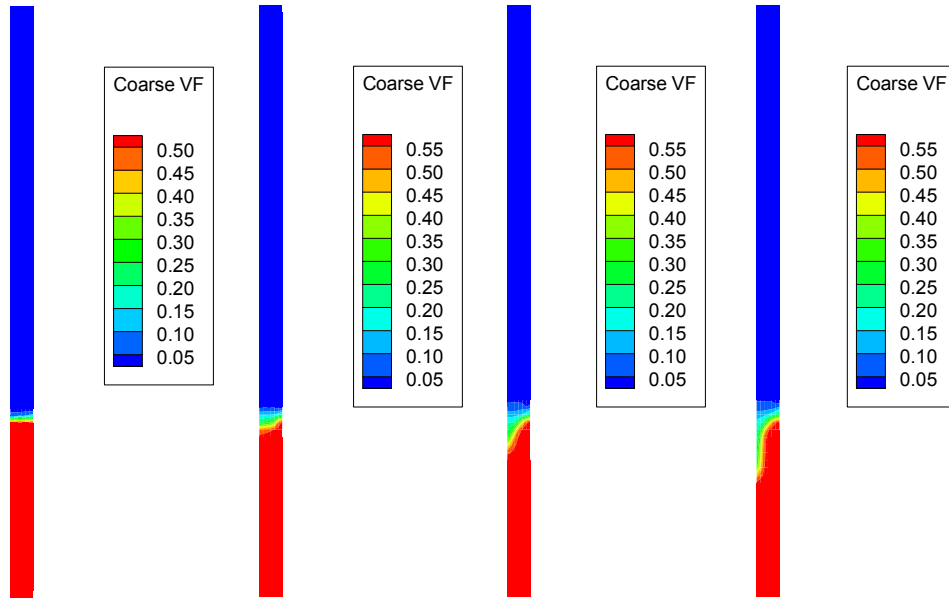


Figure 4.66 Coarse Volume Fraction for SB1\_Run5 at time of 250, 500, 750 and 1000 second (Segregation Slope = 0.3)

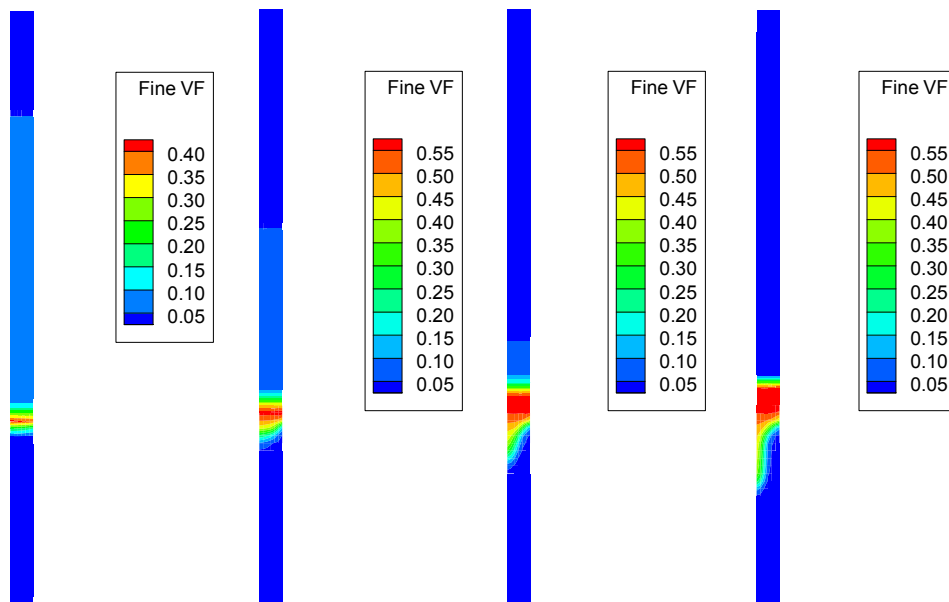


Figure 4.67 Fine Volume Fraction for SB1\_Run5 at time of 250, 500, 750 and 1000 second (Segregation Slope = 0.3)

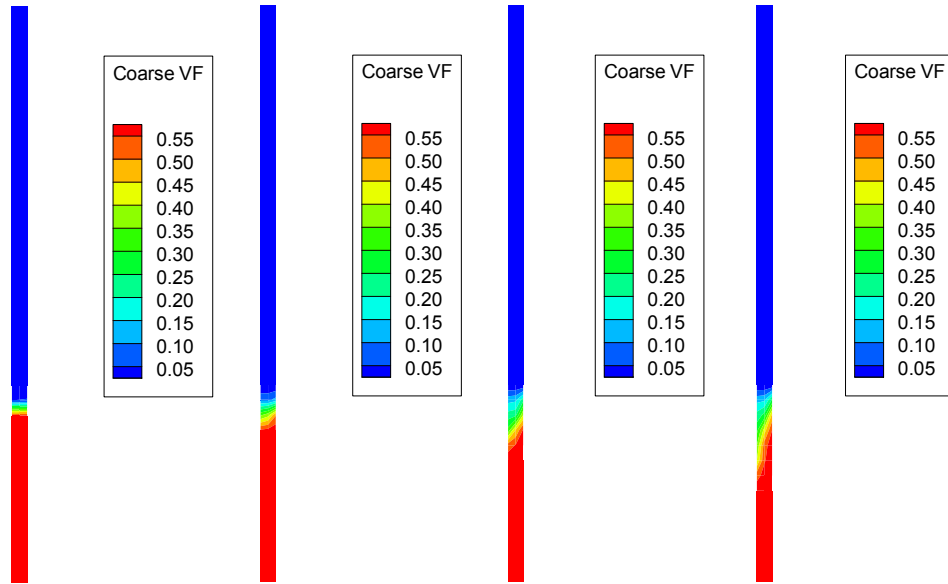


Figure 4.68 Coarse Volume Fraction for SB1\_Run6 at time of 250, 500, 750 and 1000 second (Segregation Slope = 0.0)

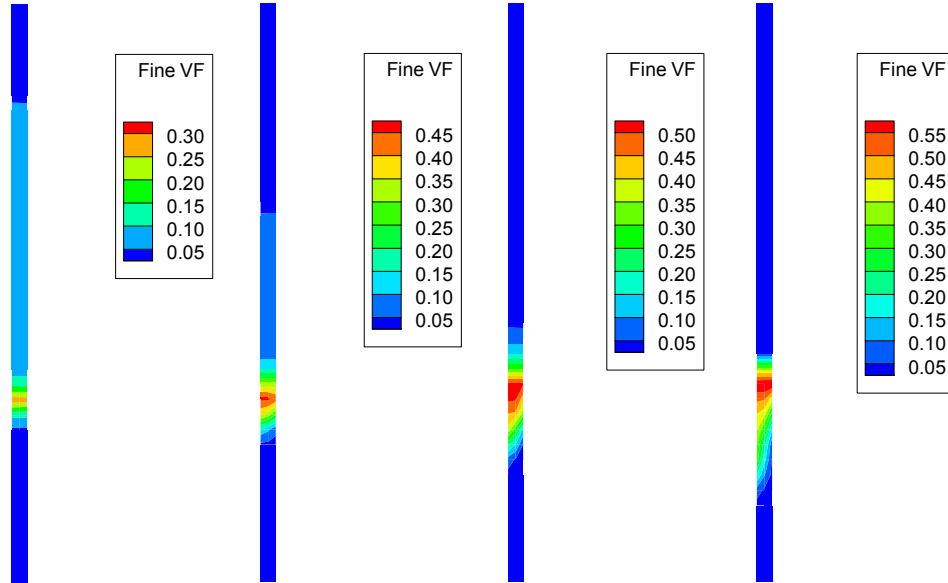


Figure 4.69 Fine Volume Fraction for SB1\_Run6 at time of 250, 500, 750 and 1000 second (Segregation Slope = 0.0)

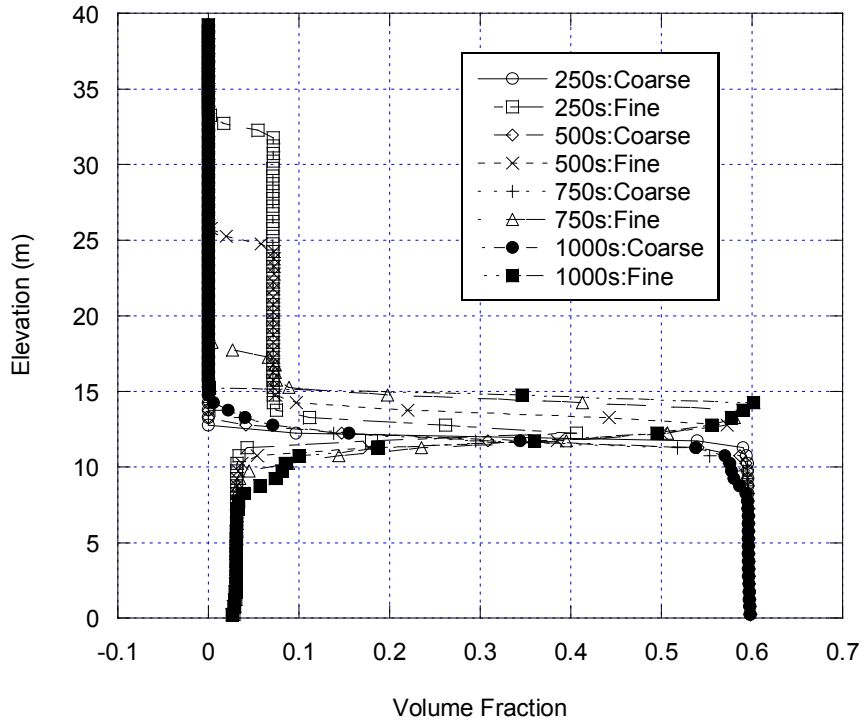


Figure 4.70 Coarse and Fine Volume Fraction for SB1\_Run3 (Segregation Slope = 0.9)

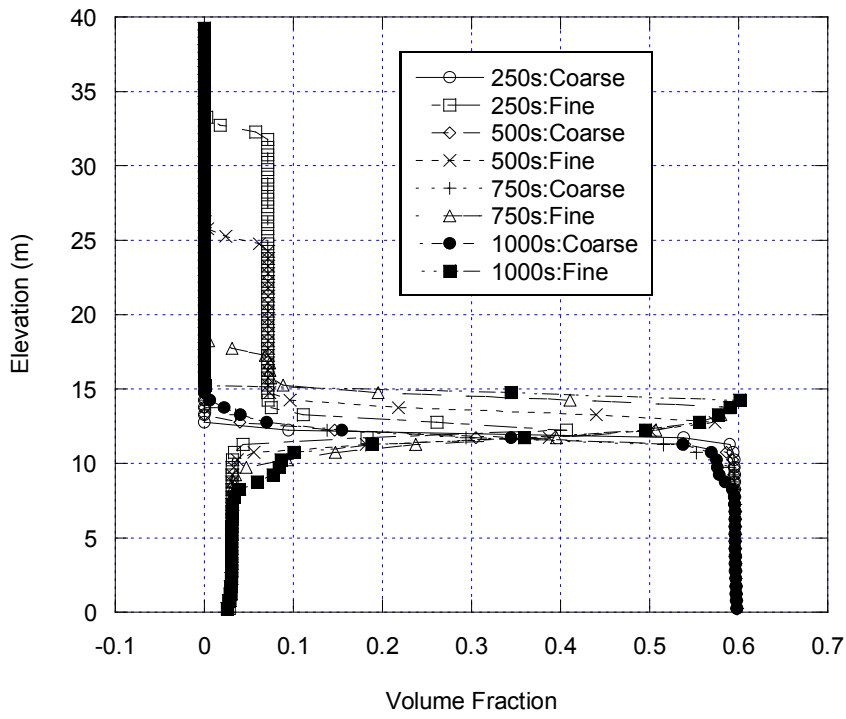


Figure 4.71 Coarse and Fine Volume Fraction for SB1\_Run4 (Segregation Slope = 0.6)

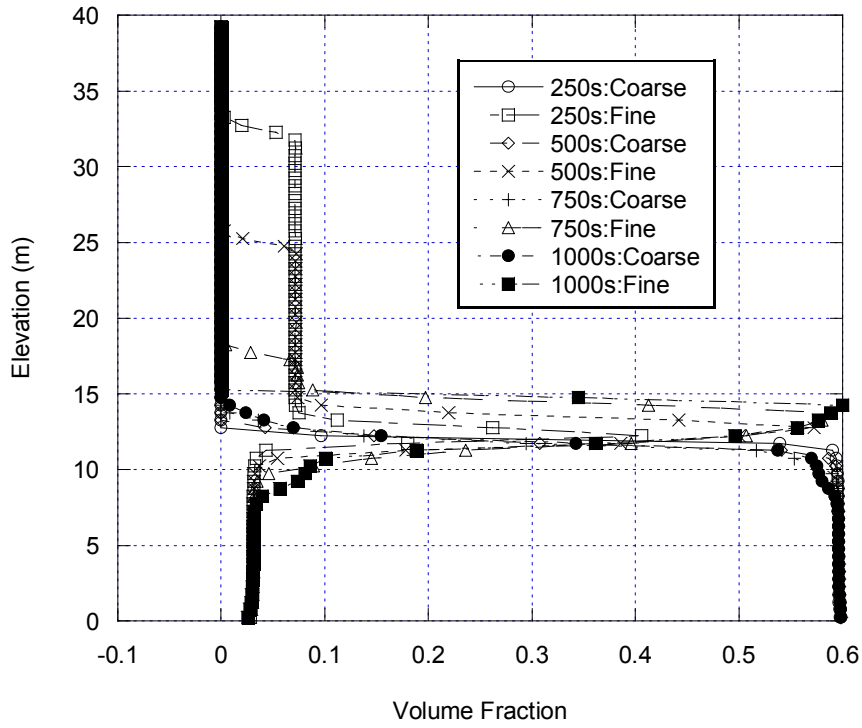


Figure 4.72 Coarse and Fine Volume Fraction for SB1\_Run5 (Segregation Slope = 0.3)

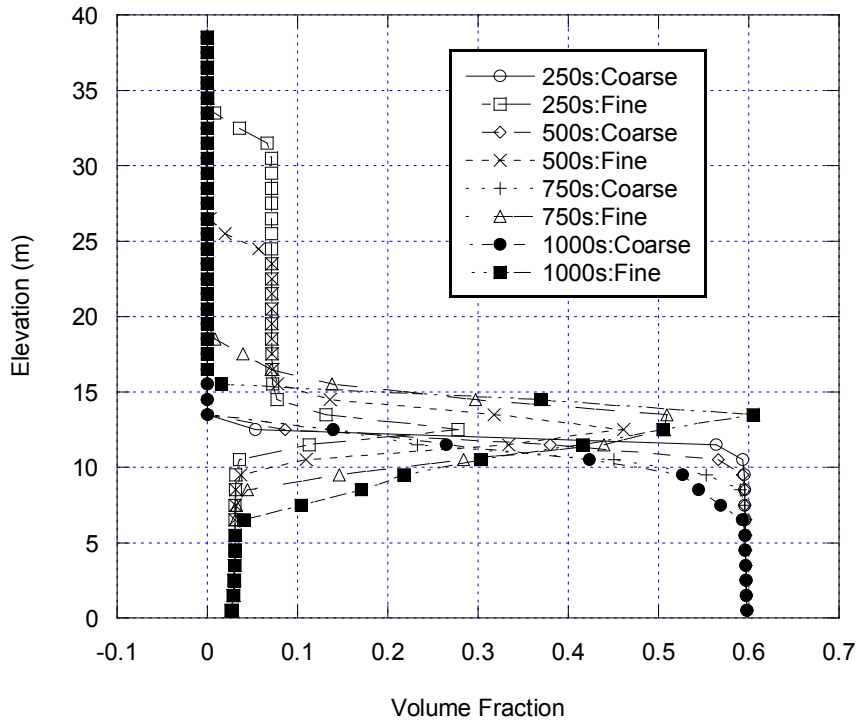


Figure 4.73 Coarse and Fine Volume Fraction for SB1\_Run6 (Segregation Slope = 0.0)

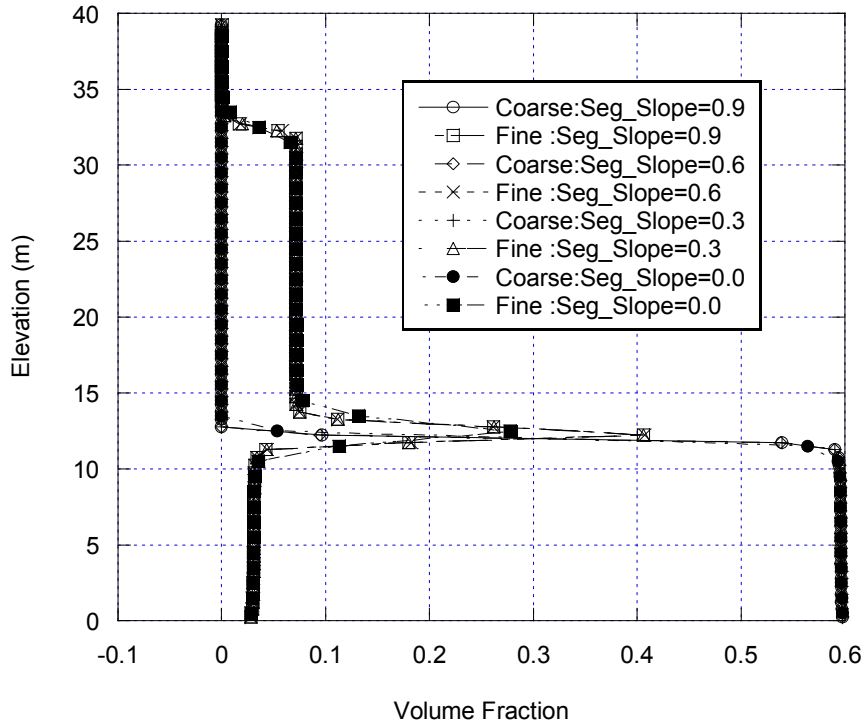


Figure 4.74 Effects of Segregation Slope on Coarse and Fine Volume Fraction for SB1 at Time of 250 second

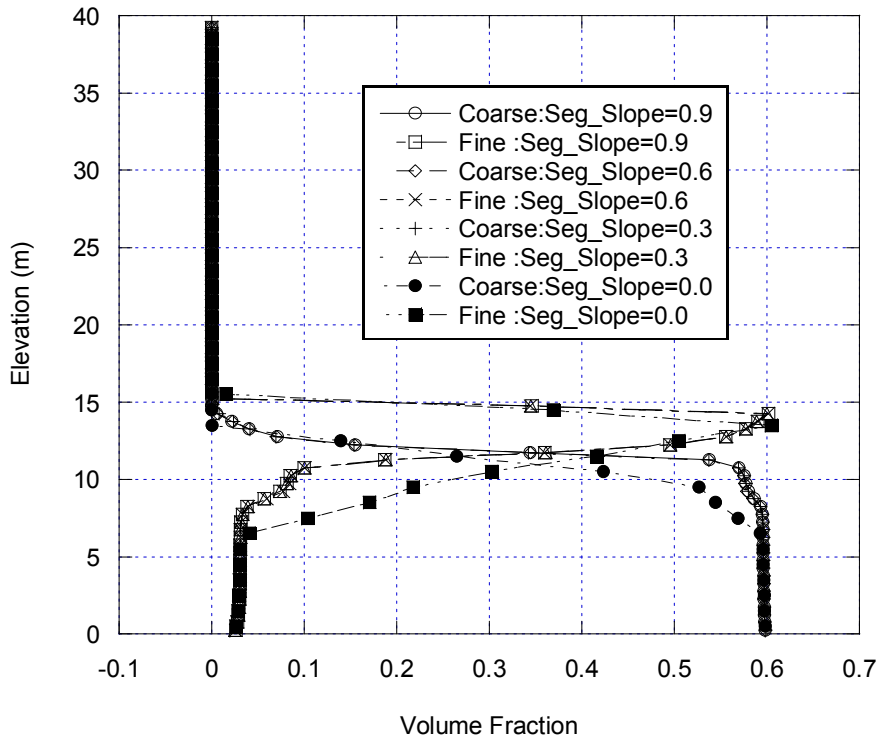


Figure 4.75 Effects of Segregation Slope on Coarse and Fine Volume Fraction for SB1 at Time of 1000 second

The volume fraction profiles for the coarse and fine particles in the simulation cases SB1-Run3, SB1-Run4, SB1-Run5 and SB1-Run6 are shown in Figure 4.62 to Figure 4.73. The coarse volume fraction and fine volume fraction at simulation time of 250 s, 500 s, 750 s and 1000 s are visually presented in Figure 4.62 to Figure 4.69. The figures show that the coarse particles settle at the bottom of the standpipe and the variation of its volume fraction after 250 seconds is negligible. The fine particles are dispersed over the middle part of the standpipe at the time of 250 seconds. Over time, the interface between the fine particle suspension and the supernatant moves downward and approaches to the interface between fine suspension and coarse suspension. In Figure 4.70 to Figure 4.73 it is also shown that the sedimentation of the coarse particles are essentially completed at the time of 250 seconds as the coarse volume fraction contour of 0.10 has limited variation in vertical direction.

The effects of segregation slope on the volume fraction profiles at 250 and 1000 s are shown in Figure 4.74 and Figure 4.75, respectively. The comparison indicates that the effects of segregation slope on the volume fraction profiles for both fine and coarse particles at time of 250 seconds are insignificant. Its effects on the profiles at 1000 seconds seem to be relatively significant as indicated by the discrepancy between the curves representing the segregation slope of zero with those of non-zeros.

#### 4.3.3.3.4 Effects on Segregation Slope on the Simulation of Non-Segregating Slurry (SB3)

Figure 4.76 to Figure 4.81 visually shows volume fraction of coarse and fine particles at the simulation time of 250, 500, 750 and 1000 seconds. Similar observations to those for SB1 can be made on these figures for SB3. It can be seen that the sedimentation of the coarse particles are essentially completed within 250 seconds. Settling of fine particle with time is evident in these figures. Figure 4.82 to Figure 4.84 show changes of volume fraction for coarse and fine particles with time. These figures confirm the observation that the coarse particles settle at the bottom within 250 seconds while fine particles settle with time over the whole simulation time.

Figure 4.85 and Figure 4.86 compare the coarse and fine volume fractions for simulations using various segregation slopes at simulation time of 250 seconds and 1000 seconds, respectively. Both of the figures indicate that the effects of segregation slope values on the coarse and fine particle volume fraction are insignificant in the simulation of the non-segregating slurry using MFIX.

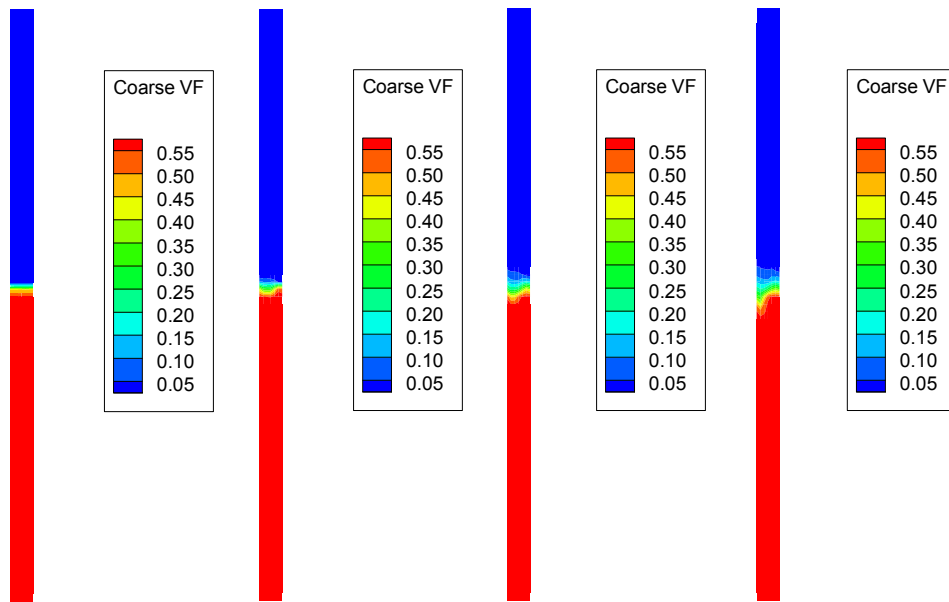


Figure 4.76 Coarse Volume Fraction for SB3\_Run4 at time of 250, 500, 750 and 1000 second

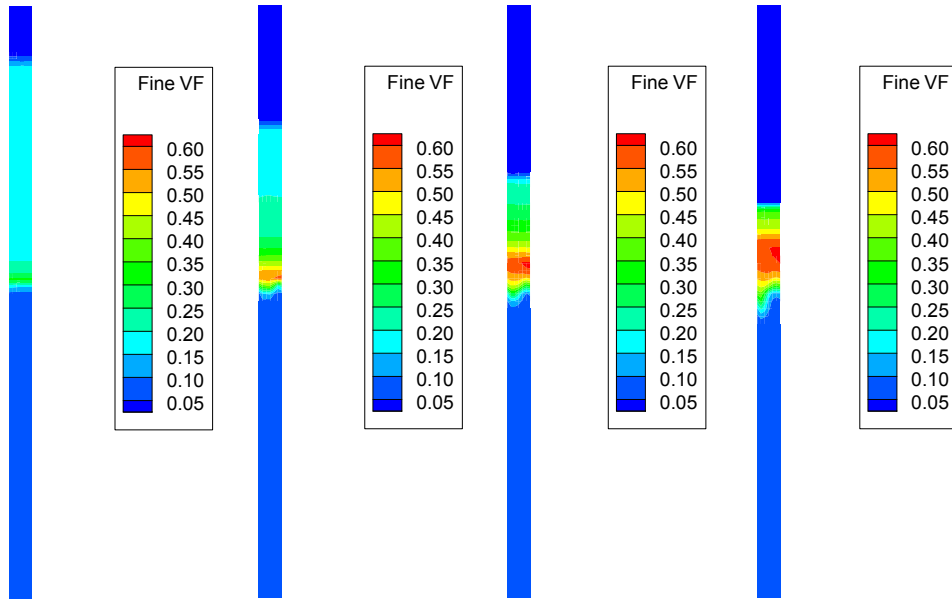


Figure 4.77 Fine Volume Fraction for SB3\_Run4 at time of 250, 500, 750 and 1000 second

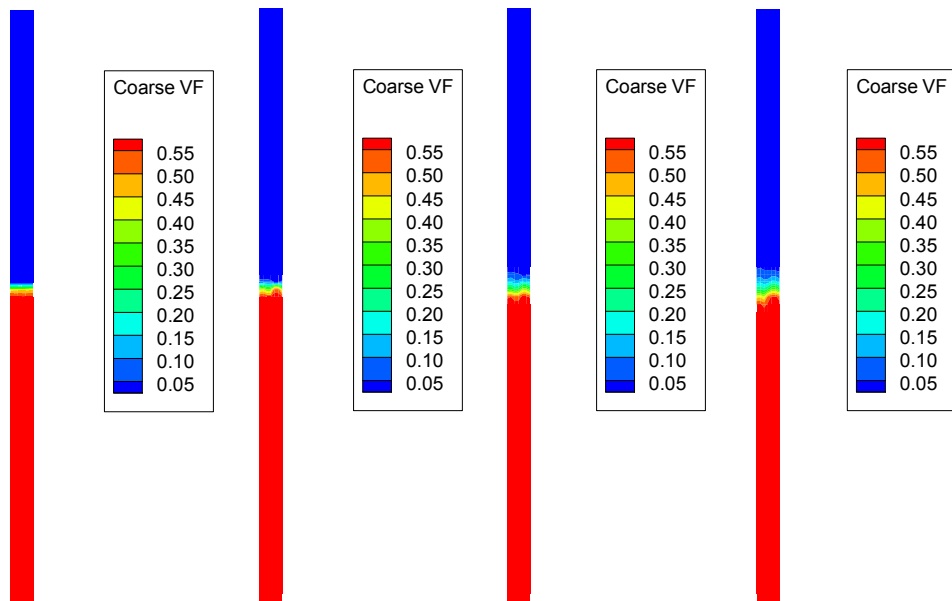


Figure 4.78 Coarse Volume Fraction for SB3\_Run5 at time of 250, 500, 750 and 1000 second

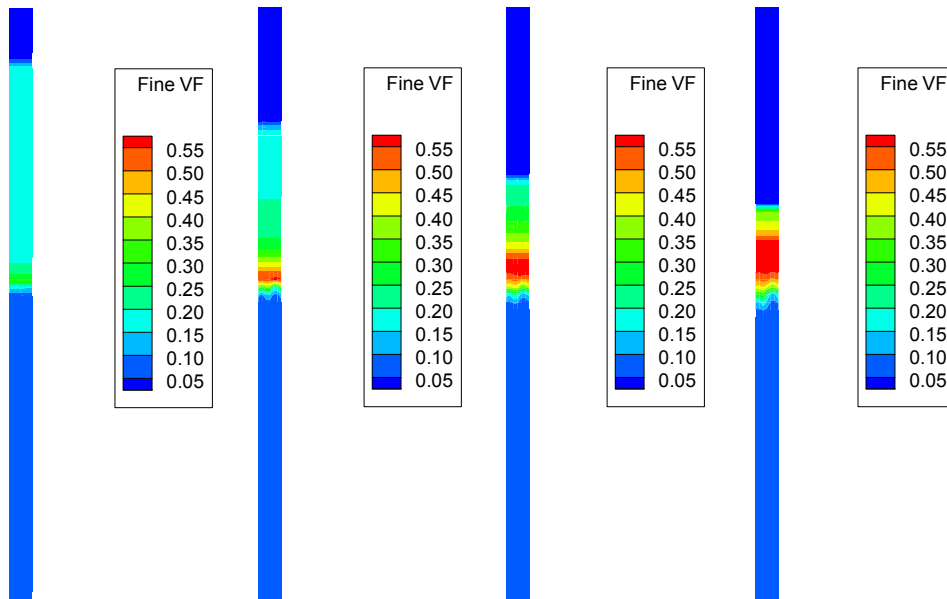


Figure 4.79 Fine Volume Fraction for SB3\_Run5 at time of 250, 500, 750 and 1000 second

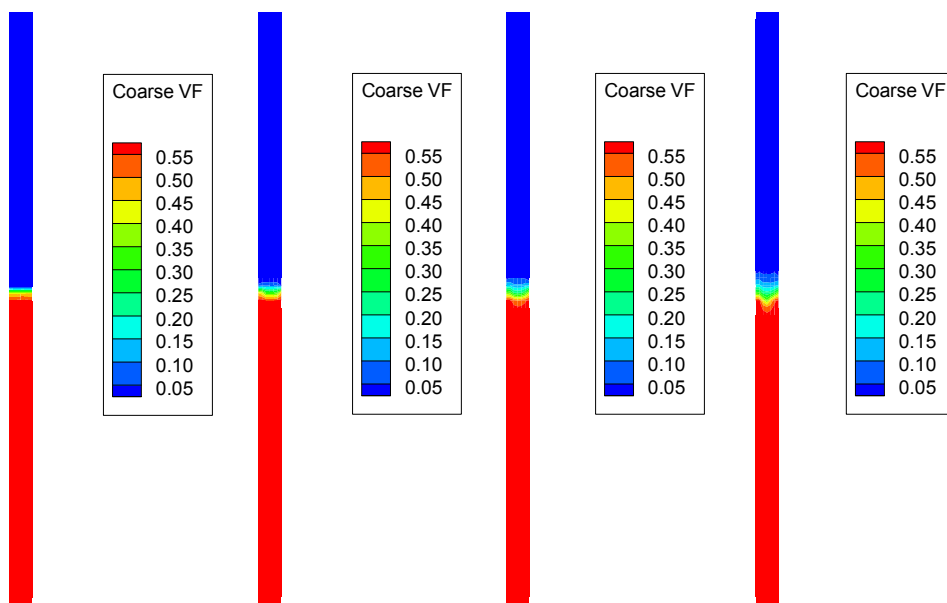


Figure 4.80 Coarse Volume Fraction for SB3\_Run6 at time of 250, 500, 750 and 1000 second

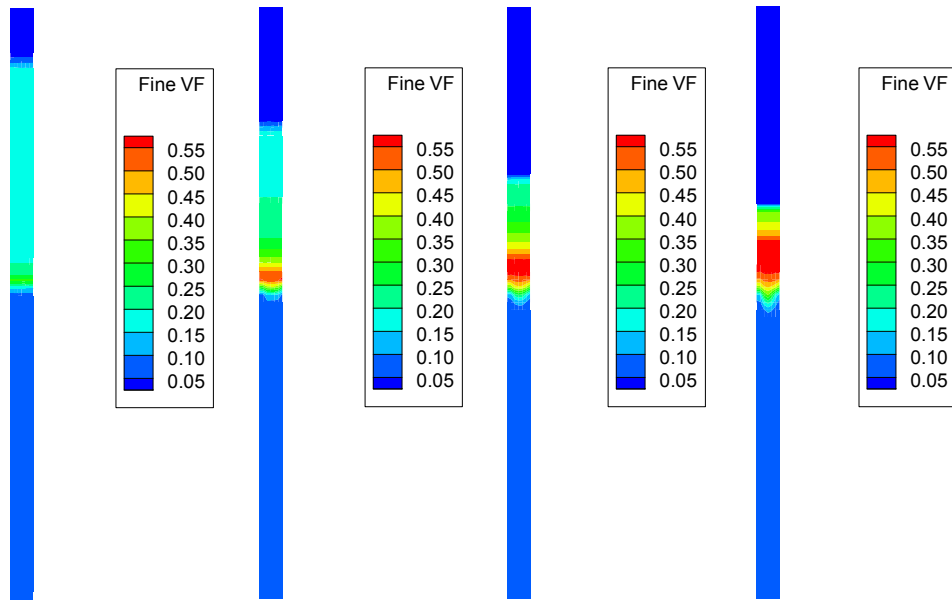


Figure 4.81 Fine Volume Fraction for SB3\_Run6 at time of 250, 500, 750 and 1000 second

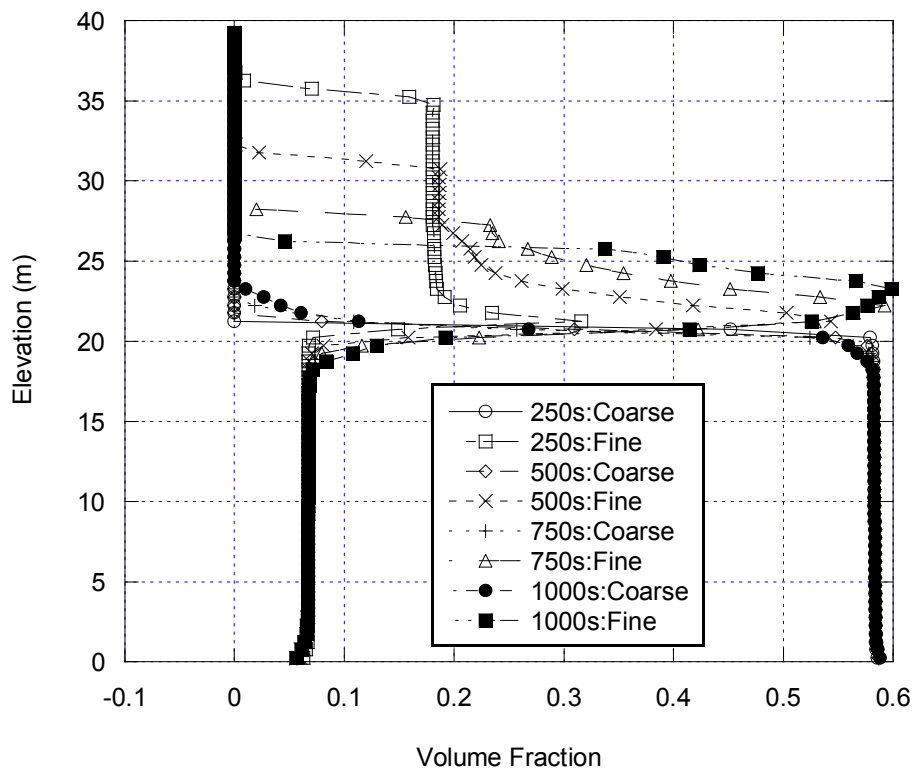


Figure 4.82 Coarse and Fine Volume Fraction for SB3\_Run4 (Segregation Slope = 0.0)

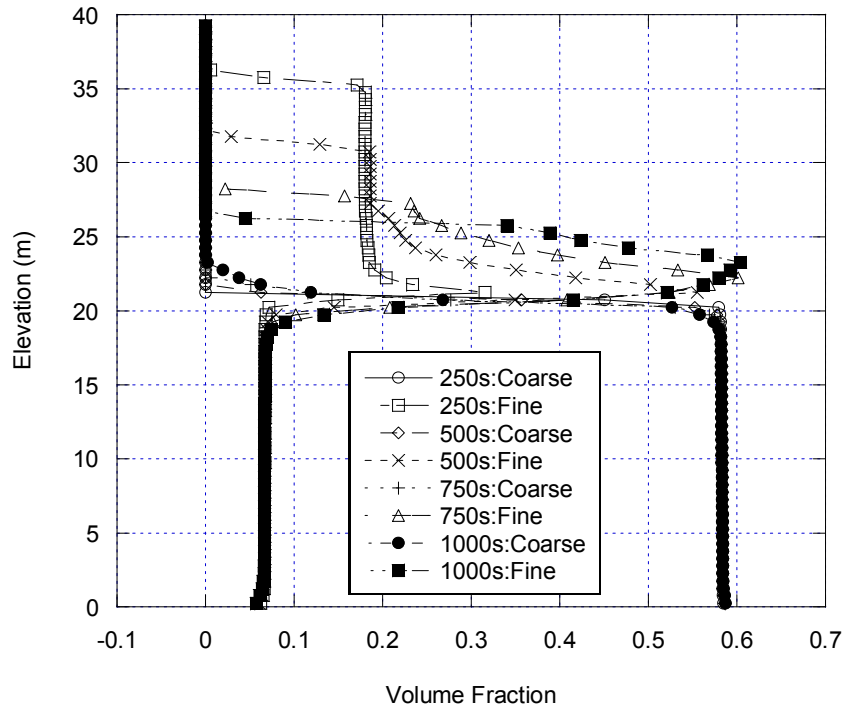


Figure 4.83 Coarse and Fine Volume Fraction for SB3\_Run5 (Segregation Slope = 0.3)

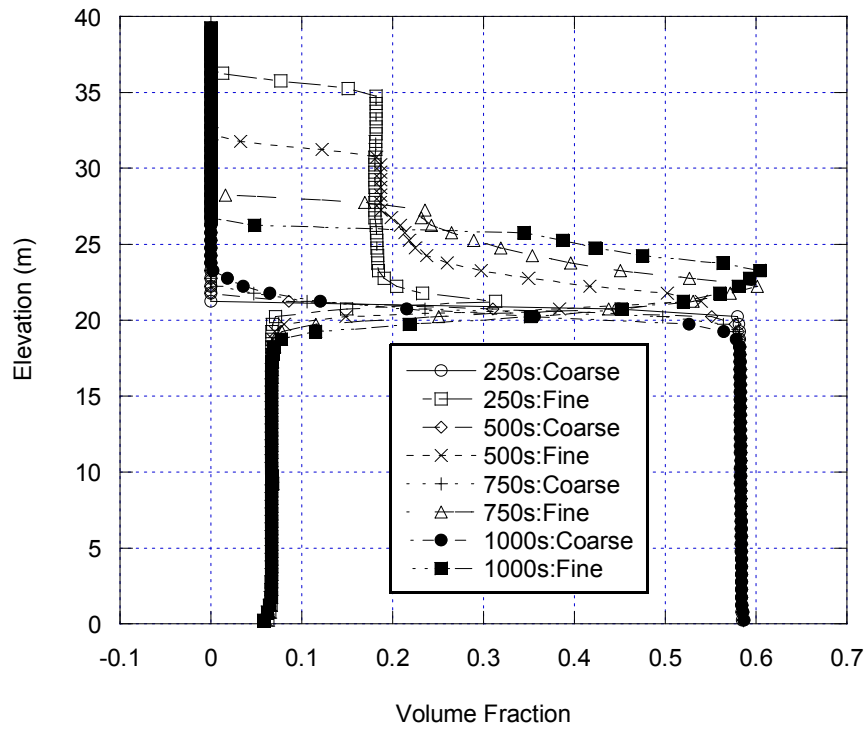


Figure 4.84 Coarse and Fine Volume Fraction for SB3\_Run6 (Segregation Slope = 0.9)

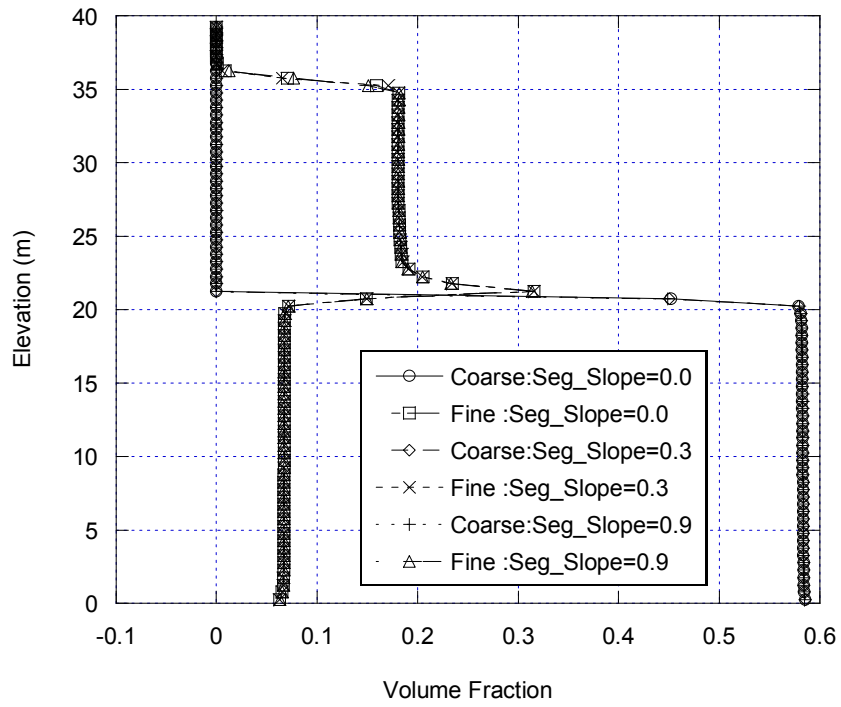


Figure 4.85 Effects of Segregation Slope on Coarse and Fine Volume Fraction for SB3 at Time of 250 second

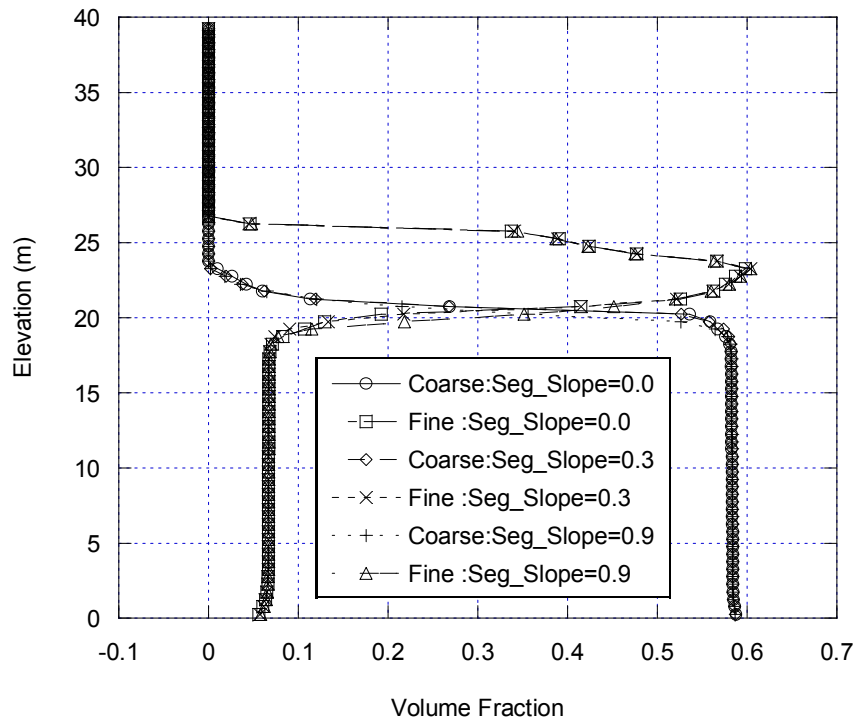


Figure 4.86 Effects of Segregation Slope on Coarse and Fine Volume Fraction for SB3 at Time of 1000 second

#### 4.3.3.3.5 Effects of Solid Rheology Model on the Simulation of Non-Segregating Slurry (SB3)

Variations of volume fractions for the coarse and fine particles over time are shown in Figure 4.87, Figure 4.88 and Figure 4.89. Basically, the same observations as those using default rheology models are applicable for simulations using the modified rheological model which is equivalent Wen-Yu model in both CFX and FLUENT.

Comparison of the volume fraction profiles of the coarse and fine particles for the simulation using modified rheological models with those for the simulation using the default model is made in Figure 4.90 and Figure 4.91. It can be seen that the settling rate is smaller in the cases using modified rheological models than those using the default model at the times of 250 seconds and 1000 seconds.

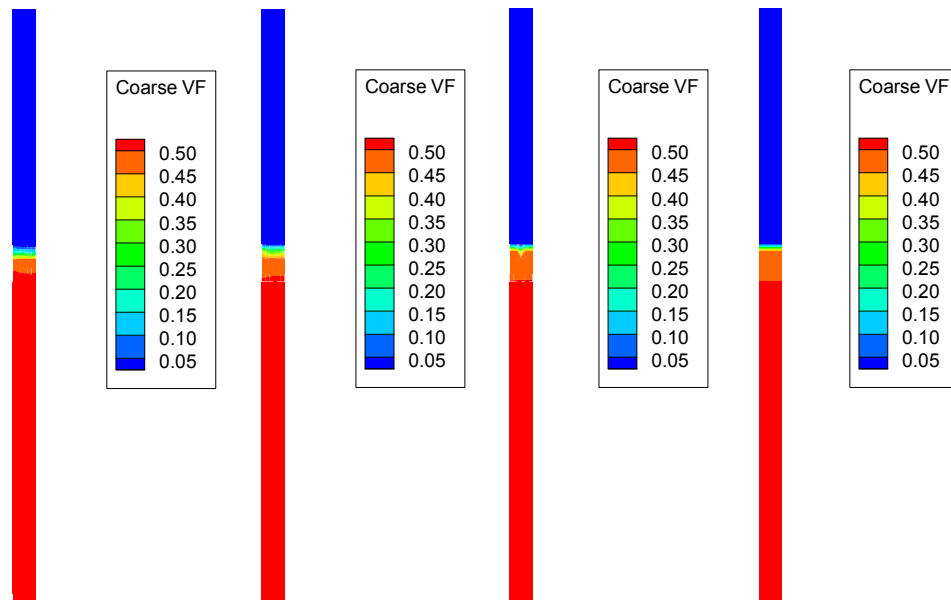


Figure 4.87 Coarse Volume Fraction for SB3\_Run2 at time of 250, 500, 750 and 1000 second

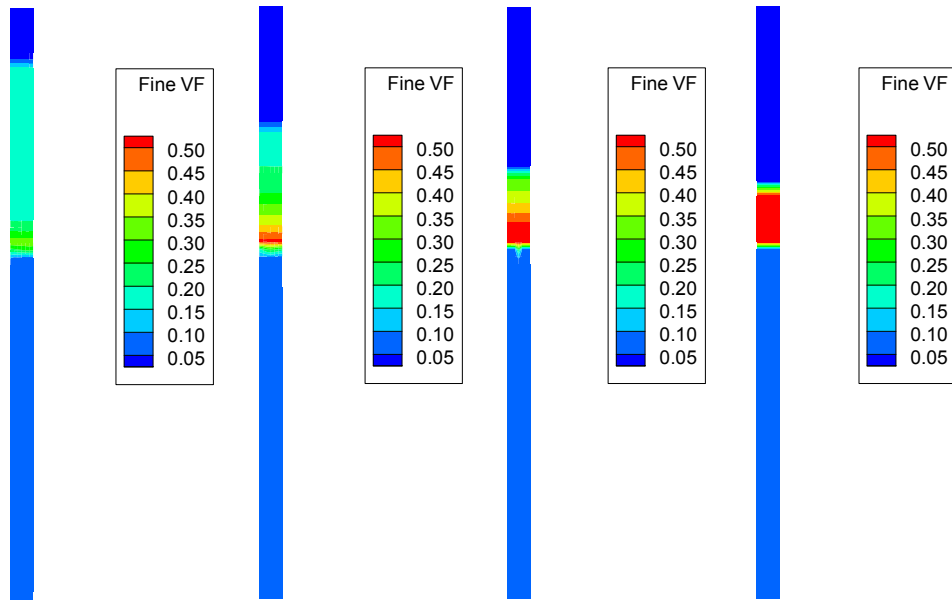


Figure 4.88 Fine Volume Fraction for SB3\_Run2 at time of 250, 500, 750 and 1000 second

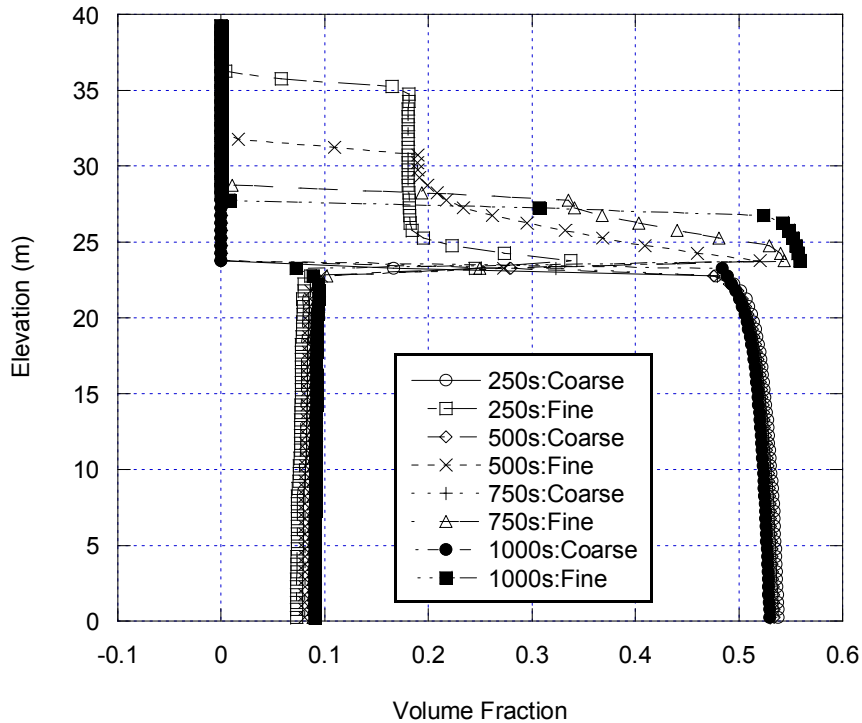


Figure 4.89 Coarse and Fine Volume Fraction for SB3\_Run2 (Segregation Slope = 0.0, modified solid rheological model)

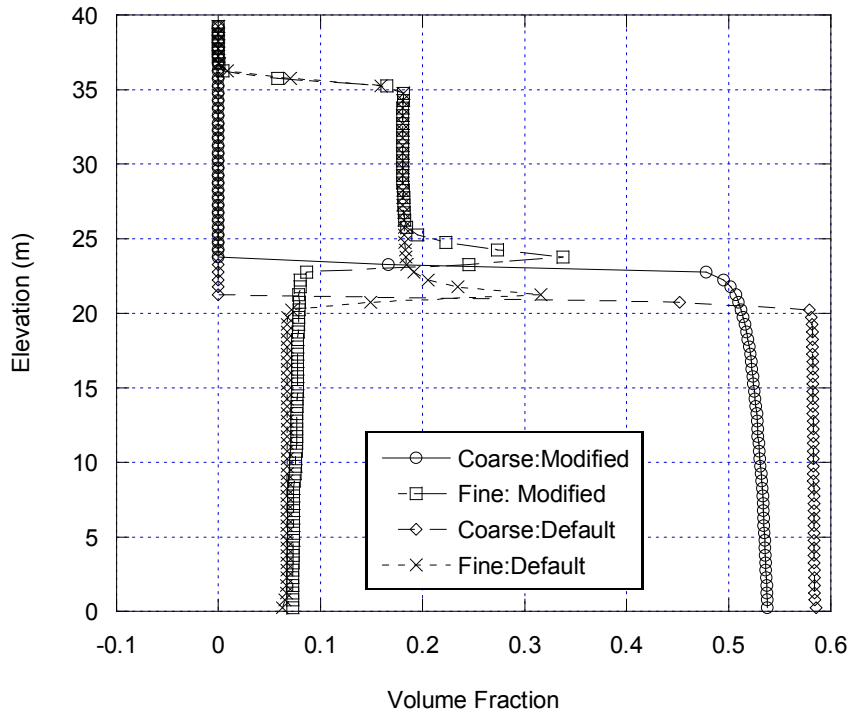


Figure 4.90 Effects of rheological model on Coarse and Fine Volume Fraction for SB3 at time of 250 second

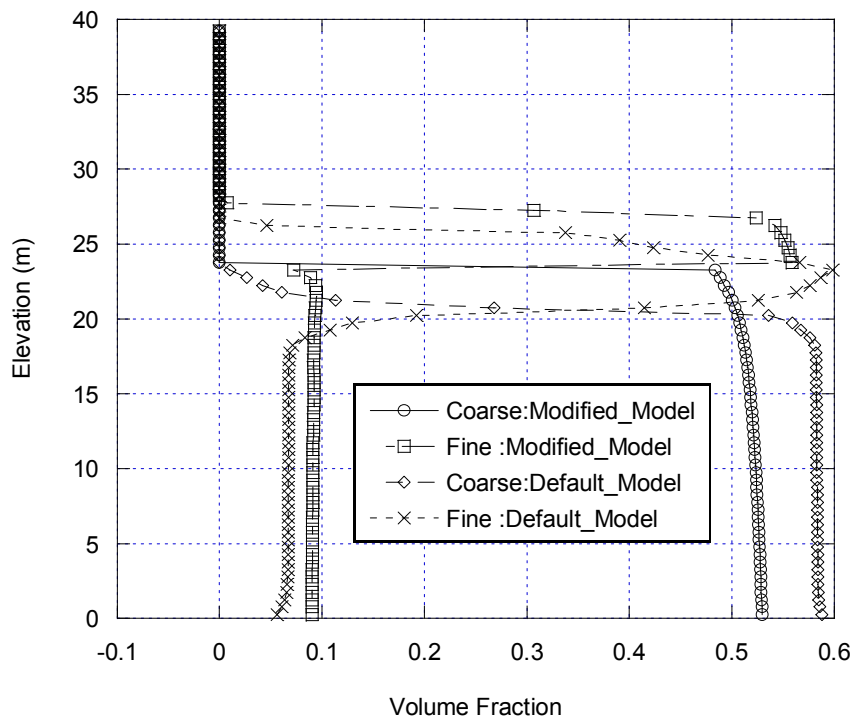


Figure 4.91 Effects of rheological model on Coarse and Fine Volume Fraction for SB3 at Time of 1000 second

#### 4.3.3.4 Comparison of Simulation Results

Figure 4.92 shows the simulated solids and fines content profiles for SB1 from CFX and FLUENT at flow time of 300 seconds. The measured solids and fines content profiles for SB1 are also demonstrated in Figure 4.92. One can observe that the predicted solids content profile approximately matches that obtained from experiment, while the predicted fines content profile deviated from the experiment result. Both CFX and FLUENT predicted that almost all sand particles settle down to the lower part of the standpipe and all the solid particles are clay particles at the elevation of 0.12m up to the top of the standpipe. The Segregation Indexes calculated from the solids and fines content profiles obtained from CFX and FLUENT simulation are 23.5 and 57.6 compared with a value of 69.6 from experiments.

Comparison of solids and fines content profiles for SB3 is shown in Figure 4.93. Segregation Index calculated from experiment result is 1.59 while Segregation Indexes of 24.7 and 31.7 are obtained from CFX and FLUENT simulation. From Figure 4.93 it can be seen that sand particles settle at the bottom of the standpipe while clay particles are suspended in the upper part of the fluid. The development of the level of interface between supernatant and suspension is shown in Figure 4.94. A higher rate of the interface progress in simulations than that in experiments is observed although FLUENT predicted that the interface develops at a lower speed than in CFX. From Figure 4.92 – Figure 4.94 one can see that similar solids and fines content profiles are obtained in CFX and FLUENT. However, one main difference is that CFX can not limit the solid volume fraction in the compaction zone (Figure 4.92 and Figure 4.94). For this reason, the following simulation is conducted in FLUENT only.

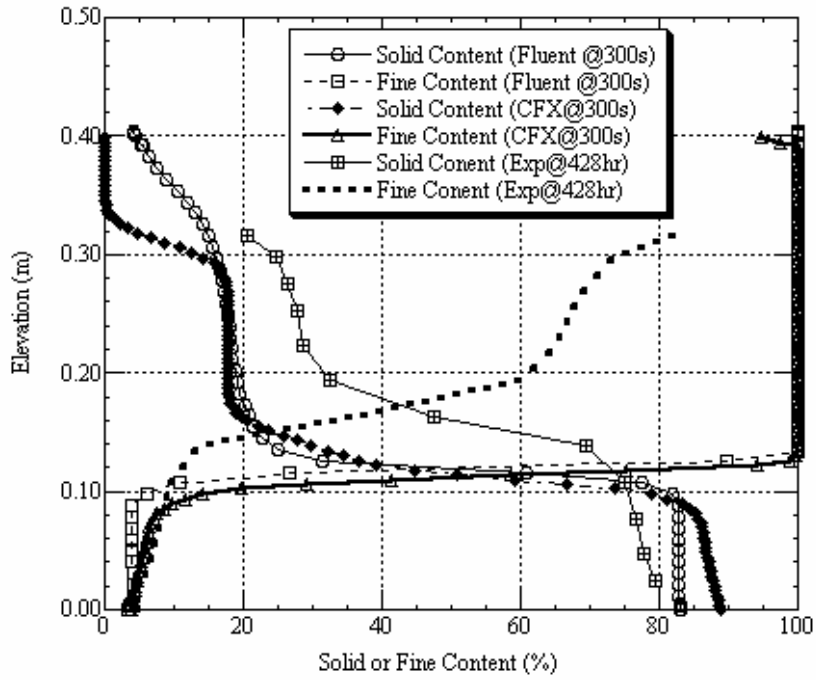


Figure 4.92 Comparison of solids and fines content profiles from CFX and FLUENT and experiment for SB1 test

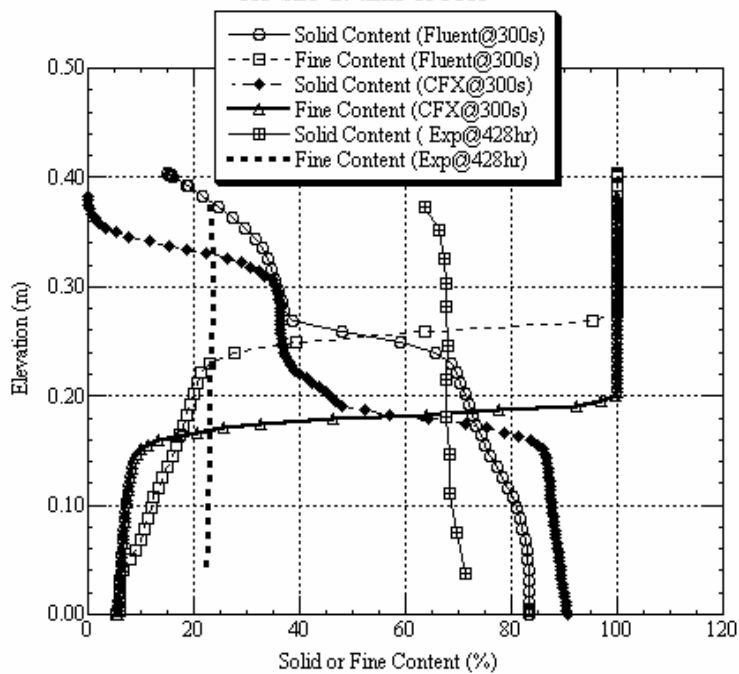


Figure 4.93 Comparison of solids and fines content profiles obtained from CFX, FLUENT and experiment for SB3 test

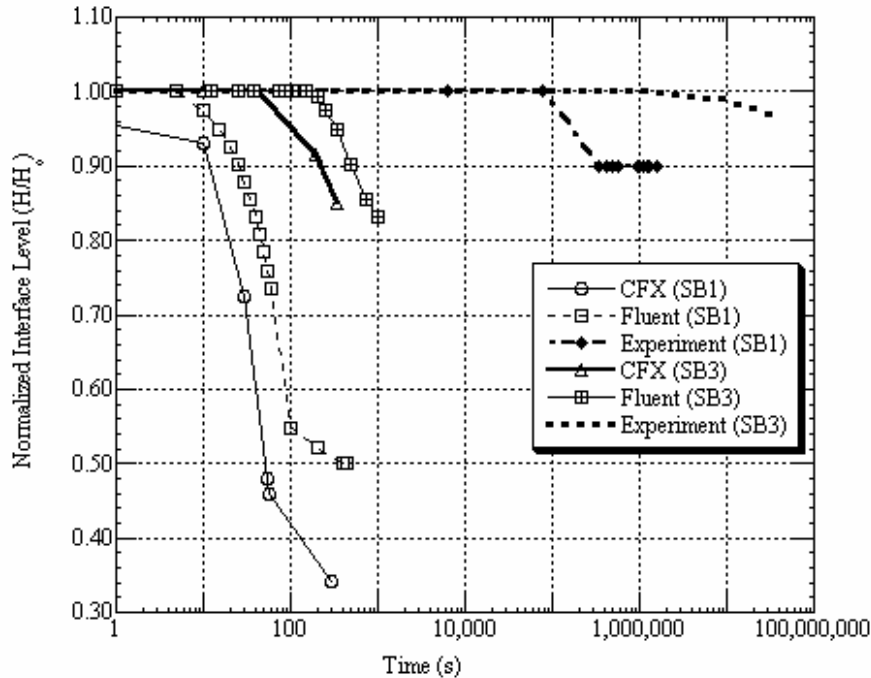


Figure 4.94 Comparison of interface development process in CFX and FLUENT simulation as well as in experiment for SB3

#### 4.3.4 Proposed Solution to Oil Sand Slurry Segregation Simulation

##### 4.3.4.1 Modification of Solid-Solid Exchange Coefficient

The simulations above indicate that the Euler-Euler model in FLUENT and CFX is not capable of capturing the non-segregation behavior of very dense solid-liquid flow under quasi-static conditions. This is similar to the finding by Gera et al. (2004) and is referred in Section 4.3.3.3.1. Then the authors added a term, which is proportional to solid pressure, into solid-solid drag exchange coefficient, as show in Eq. 4.8. In following their conceptual idea, another term is added into solid-solid exchange coefficient. The magnitude of this term depends on the relative volume fraction of sand and clay and the location of the segregation boundary shown in Figure 4.95. If the combination of sand volume fraction and clay volume fraction lies above the segregation boundary curve and below the compacting limit line, the mixture is supposed to be non-segregating slurry. The additional term is calculated as 1000 times the vertical distance of this point to the point on the segregation boundary curve at current clay volume fraction. The effects of the additional term on the sand and clay volume fraction profile are shown in Figure 4.96. It can be seen that the added solid-solid exchange term has insignificant effects on prohibiting the occurrence of

segregation as the solids and fines content profiles in this simulation are the same as those in the simulations using the default solid-solid exchange coefficient.

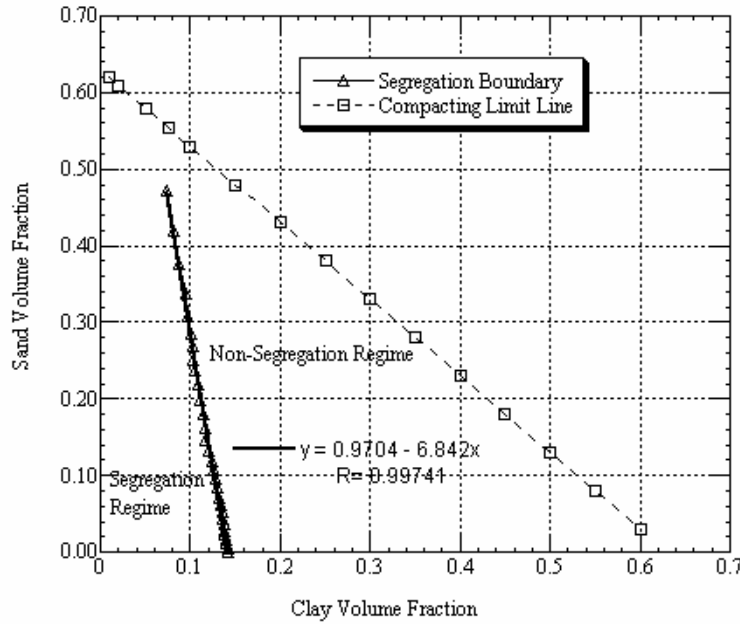


Figure 4.95 Segregation boundaries for tailing slurry

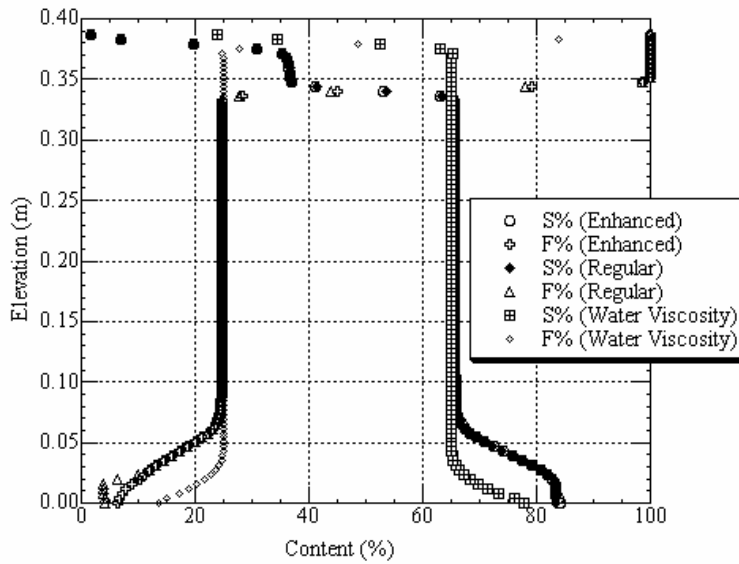


Figure 4.96 Comparisons of Solids and Fines Content Profile at Time of 250 Second. The solids and fines content profile for simulations using enhanced solid-solid drag coefficient, regular solid-solid drag coefficient and enhanced water viscosity are shown

#### 4.3.4.2 Modification of the viscosity of water phase

Several authors (Ha et al., 2002; Narasimha et al., 2007; Wang et al., 2009; Chu et al., 2009) assigned the viscosity of the suspension composed of small particles and fluid to the fluid phase in dealing with the hindered settling of the solid particles in the fluid. Ha et al. (2002) observed that a large particle displaced not only the fluid but also the smaller particles when it settled in a smaller particle. Therefore, the interactions between particles of different sizes were accounted by simply computing the settling velocity of the large particles as if they were settling in an effective fluid medium which has the same viscosity and density as the suspending fluid containing the smaller particles.

According to Thomas (1962), the viscosity of the suspension can be expressed via:

$$\mu_m = \mu_0(1 + 2.5\phi + 10.05\phi^2 + A \exp(B\phi)) \quad (\text{Eq. 4.9})$$

where  $\mu_m$ ,  $\mu_0$  and  $\phi$  are viscosity of suspension, viscosity of suspending medium and the volume fraction of solids;  $A$  and  $B$  are parameters. The suggested values of 0.00273 and 16.6 for these two parameters are used in the simulation. The solids and fines content profiles at flow time of 250 second are shown in Figure 4.96. It can be seen that increasing the viscosity of the suspending medium hindered the occurrence of segregation.

#### 4.3.4.3 Two-Phase Simulation

These simulations demonstrate that some interactions between solid and solid as well as between solid and liquid are not captured in the current models. To circumvent the considerations of the clay-clay and clay-water interactions, clay and water can be considered as a single phase with varying viscosity and density, which can reflect the distribution of clay particles in water due to segregation or non-segregation. For non-segregation mixture, the clay volume fraction almost remains constant, which simplify the simulation.

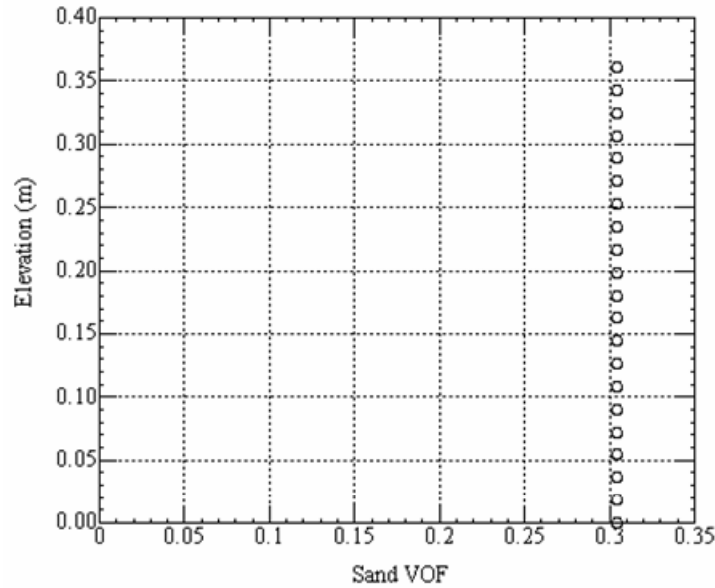


Figure 4.97 Sand volume fraction at flow time of 2500 second for SB3

The maximum viscosity of 1000 Pa.s was assigned for the water phase. The simulation result is shown in Figure 4.97. It can be observed that the sand volume fraction remain almost constant even at time of 2500 seconds.

#### 4.4 Summary and Conclusions

1. The Euler-Euler Model in MFIx and FLUENT-6 is used to model the sedimentation of suspension composed of two or more sizes of solid particles. The sizes of these solid particles range from 125  $\mu\text{m}$  to 496  $\mu\text{m}$  and the sizes are uniform in each size group. The solids contents for the bidisperse and polydisperse suspension are 43% and 36% respectively. The simulated volume fraction profiles reasonably agree with those obtained by Burger et al. (2000) using shock capturing numerical schemes. Since Burger et al. (2000) compared their simulation results with the results from measurements by Schneider et al. (1985) and Greenspan et al. (1982) and claimed that their simulation results agree with the experiment, it is concluded that the CFD tools are able to produce the similar results for the bidisperse and polydisperse suspensions.

2. A series of sensitivity tests are carried out numerically to verify the capability of Euler-Euler models in FLUENT, MFX and CFX in modeling the sedimentation process of oil sand tailing slurry. The oil sand tailings slurry is assumed to be composed of water and solid particles with grain sizes ranging from clay ( $< 2 \mu\text{m}$ ) to sand ( $> 75 \mu\text{m}$ ). The grain size has a continuous distribution. Simulation results indicate that all these models are able to track the trend of the sedimentation process; however, these models are not capable of tracking or predicting the real-time sedimentation process of the tailing slurry when the true viscosity of 0.001 Pa.s is assigned to the water phase.
3. Comparing the bidisperse or polydisperse suspension in the literature with the oil sand tailing slurry, three main differences exist. First, the bidisperse and polydisperse suspension in the literature do not contain colloidal particles, whereas the oil sands tailings do. Second, the suspension reported in the literature contains solid particles with discrete size distribution, while solid particles in oil sand tailings slurry have continuous size distribution. Third, the non-segregating slurry sample SB3 has 65% solids content while the suspensions reported in the literature have solids contents ranging from 37% to 43%. These CFD models are able to capture the time sequence of sedimentation process for suspensions with two or four sizes of non-colloidal solid particles with solids content of approximately 40% while they fail to track the settling process of oil sand tailings slurry. Logically, these differences contribute to the discrepancy.
4. A suspension containing two or four sizes of non-colloidal particles is modeled using CFD successfully by simulating each group of particles as a separate disperse phase. On the other hand, the continuous distribution of solid particles in oil tailing slurry is approximated using bidisperse suspension, which introduced significant errors no matter which method is used to calculate the effective particles size for each group.
5. The ultra-fine solid particles, bitumen and chemistry of the oil tailing slurry make it a unique solid-liquid suspension. The electrostatic and steric effects in the fine tailings make the fine particles in tailing slurry difficult to settle under gravity

- (FTFC, 1995). Interactions between ultra-fine particles are not accounted for in any of these CFD models. Therefore, the uniqueness of the oil sand tailing slurry partially results in the failure of these models to capture the extremely slow process of the sedimentation of the dense tailing slurry.
6. Compared with segregation, non-segregation behavior of the solid-liquid system brings more challenges in the numerical simulations. The interactions between clay and clay as well between clay and water are critical to solution of this problem. One solution to this is to modify the suspending medium viscosity to reflect the influence of the interactions. Considering the clay-water as a single phase can be another way to overcome the complexity of the interactions.

## Reference

- Burger, R., Concha, F., Fjelde, K.K., Karlsen, K.H., Numerical simulation of settling of polydisperse suspension of spheres. *Powder Technology*, vol. 113, pp. 30-54, 2000.
- Chalaturnyk, R. J. and Scott, J. D. Soil Structure Behavior Diagram. Proceedings of High Density and Paste Tailings 2001 Seminar, University of the Witwatersrand, South Africa, May 10 – 11, 2001.
- Chen, A., Grace, J.R., Epstein, N., Lim, C.J., Steady state dispersion of mono-size, binary and multi-size particles in a liquid fluidized bed classifier. *Chem. Eng. Sci.* 57, 991–1002, 2002.
- Chu, K.W., Wang, B., Yu, A.B., and Vince, A. CFD-DEM Modeling of Multiphase Flow in Dense Medium Cyclones. *Powder Technology*, pp. 235-247, vol. 193, 2009.
- Dahl, S. R. and Hrenya, C. M. Size Segregation in Rapid, Granular Flows with Continuous Size Distributions. *Physics of Fluids*, vol. 16, No. 1, January 2004.

- FTFC (Fine Tailings Fundamental Consortium), 1995. Vol. 1, Effects of surfactants on tailing behavior. In: *Advances in Oil Sands Tailings Research*, Alberta Department of Energy, Oil Sands and Research Division.
- Gera, D., Syamlal, M., and O'Brien, T.J., Hydrodynamics of Particle Segregation in Fluidized Beds. *International Journal of Multiphase*, vol. 30, p. 419-428, 2004.
- Goldschmidt, M.J.V., Kuipers, J.A.M., van Swaaij, W.P.M. Segregation in dense gas-fluidized beds: validation of multi-fluid continuum model with non-intrusive digital image analysis measurements. In: *10th Engineering Foundation Conference on Fluidization*, Beijing, China, May 20–25, pp. 795–802, 2001.
- Greenspan, H.P. and Ungarish, M. On hindered settling of particles of different sizes. *Int. J. Multiphase Flow*, vol. 8, pp. 587-604, 1982.
- Ha, Z., and Liu, S. Settling Velocities of Polydisperse Concentrated Suspension. *The Canadian Journal of Chemical Engineering*, pp. 783-790, vol. 80, 2002.
- McMurray Resources (Research & Testing) Ltd, 2001 Pond 1 Tailing Investigation, pg. 32 and 33, Figure 13 and Figure 14. CC , Feb 14, 2002, Project No. 43-443
- Schneider, W., Anestis, G., Schaflinger, U. Sediment composition due to settling of particles of different sizes, *Int. J. Multiphase Flow*, vol. 11, pp. 419-423, 1985.
- Narasimha, M., Brennan, M.S., Holtham, P.N., and Banerjee, P.K. Numerical analysis of the changes in dense medium feed solids on dense medium cyclone performance. *Proceedings of 16th Australasian Fluid Mechanics Conference*, Gold Coast, Australia, 2-7 December 2007. pp. 1042 – 1049.
- Thomas, D.G., Transport characteristics of suspensions: Application of different rheological model to flocculated suspension data. *American Society Mech. Engineers*, Chapter 64, pp. 704-717, New York, 1962.
- Wang, B., Chu, K.W., Yu, A.B., and Vince, A. Modeling the Multiphase Flow in a Dense Medium Cyclone. *Ind. Eng. Chem. Res.*, pp. 3628-3639, vol. 48, 2009.

## CHAPTER 5 CFD SIMULATION OF LABORATORY FLUME TESTS

### 5.1 Introduction

Scott et al. (1993) conducted a series of flume tests to study the chemically treated tailings in a depositional environment. During the tests the tailings are discharged into a flume with 30 centimeters of water at the bottom. Since the environment where the tailings are placed is equivalent to that of deposition of coarse sand tailings into MFT pond, the flume tests are selected as the tests to evaluate the capability of the CFX-10 Particle Model as well as the regressed viscosity model that is obtained from viscosity measurements. In this chapter the objectives, procedure and equipments of the flume tests are introduced first followed by the simulation of the flume tests using CFX-10.

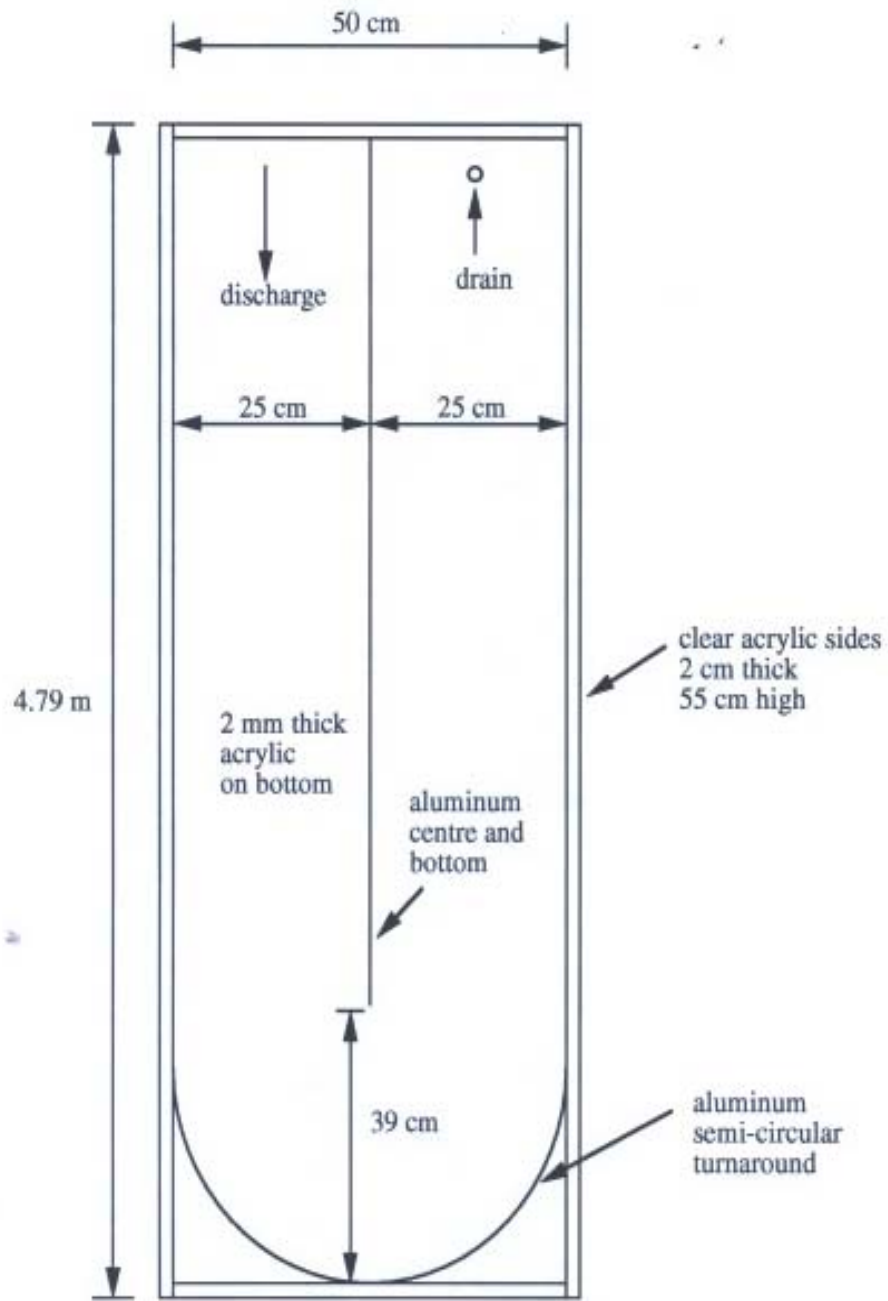
### 5.2 Laboratory Scale Flume Tests

#### 5.2.1 Objectives of the Flume Tests

The flume tests were carried out to determine the amount of additives required to prevent segregation during dynamic deposition and to investigate the effects of the deposition methods on the segregation of the tailing mixes (Scott et al., 1993). The flume tests are conducted to study the behavior of the mix during deposition, such as flow pattern and flow rate and to investigate the changes in water chemistry during mixing and deposition and after deposition.

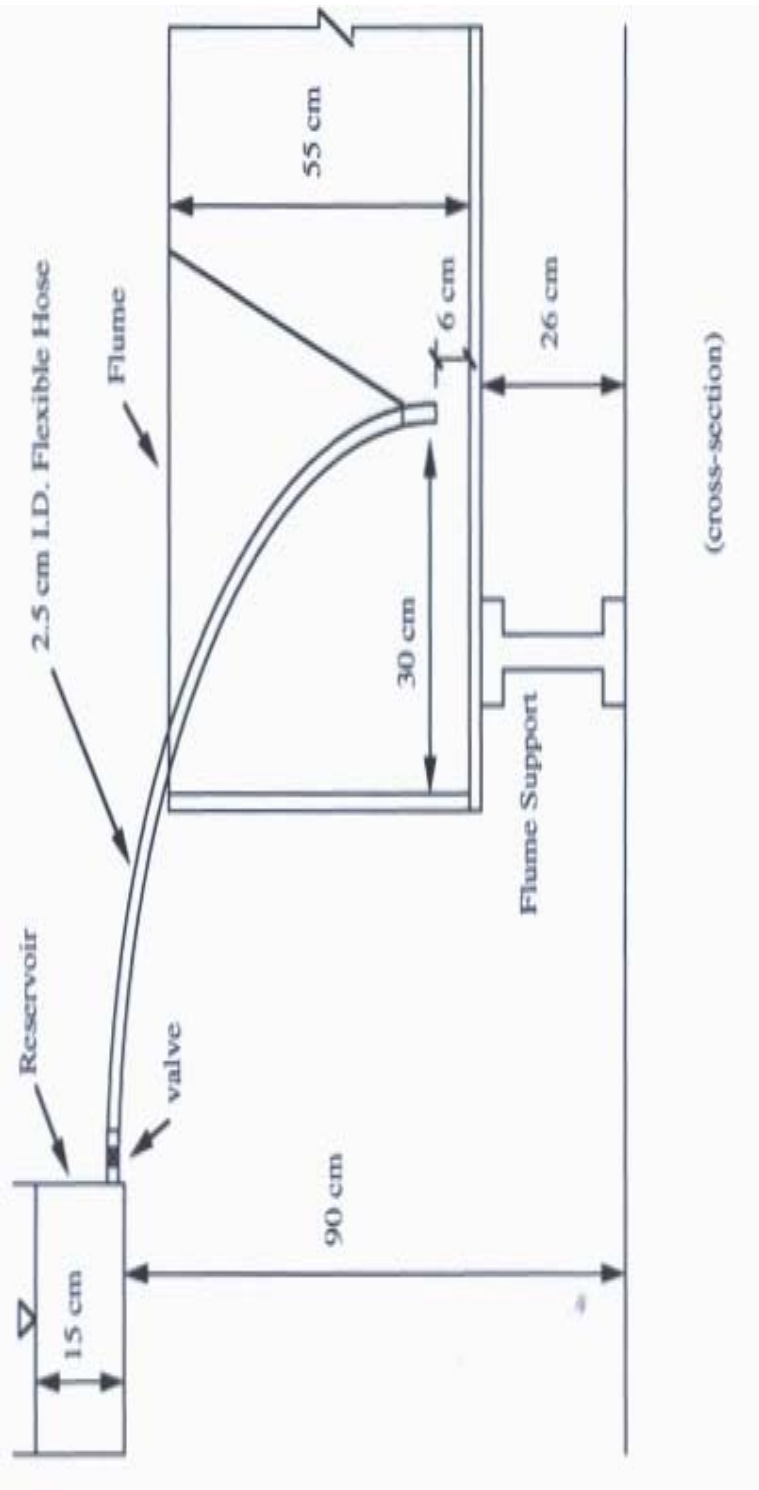
#### 5.2.2 Set-Up of the Tests

The plan and cross-section of the flume used in the flume tests is shown in Figure 5.1 and the dimension of the flume is shown in Figure 5.2. The flume is 4.8 meter in length with a semi-circular turn-around at the end of the flume, resulting in an equivalent length of 9.15 m. Each half of the flume is 25.5 cm wide and the flume is 55 cm deep. In order to observe the deposition and settlement of the tailing, the sides are made from clear acrylic.



(not to scale)

(a)



(b)

Figure 5.1 Setup of Flume Tests: (a) Top View (From Scott et al. 1993); (b) Cross Section (From Scott et al. 1993)

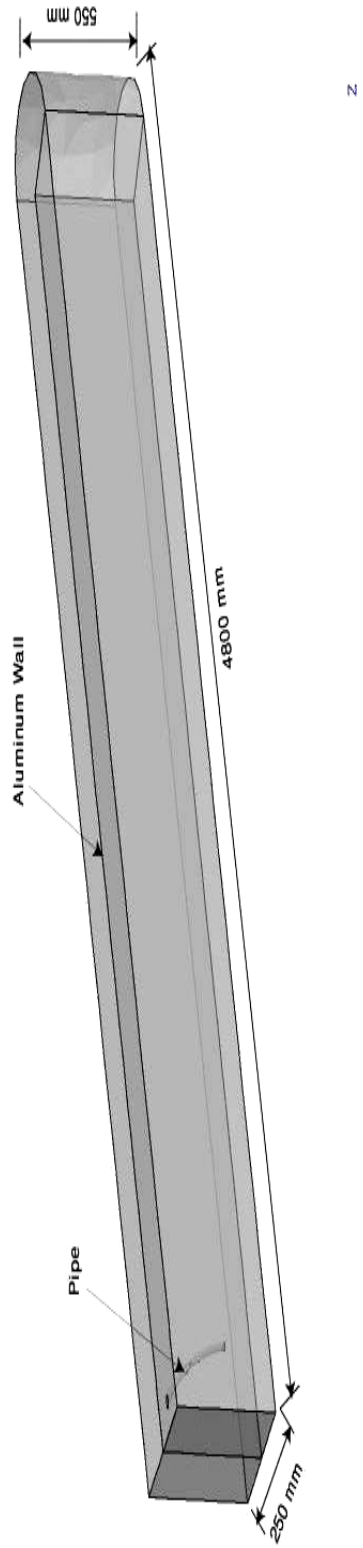


Figure 5.2 Dimensions of Flume Used in the Tests

### 5.2.3 Test Procedure

The desired solids and fines contents of the tailings are achieved by mixing the tailings, beach sand, pond water, fine tailings. The tailings then are mixed for a few minutes in a mixing barrel to obtain a homogeneous suspension. Lime or acid was added to the tailings and mixed for 5 minutes. Following this, the barrel was raised to a position to allow discharge from a valve in the bottom of the barrel into the discharge reservoir. To prevent air entrainment the discharge point was positioned below the surface in the reservoir. The tailings were stirred in the discharge reservoir to prevent any settlement during this operation. After the reservoir was filled with the prepared tailings, the valve at the base of the reservoir was opened. In order to maintain a constant hydraulic head, the level in the reservoir was kept constant during tests. As the tailings are discharged into the flume, the time of advance of the toe of the deposit was recorded at 50 cm intervals along the flume. Discharge was stopped once either the barrel was emptied or the end of the flume was reached. The thickness of the deposits was recorded immediately after deposition. The run-off from the surface of the deposition was collected beneath a drain at the end of the flume and the volume and solids content was measured at time interval of 5 minutes.

### 5.2.4 Test Results

Table 5.1 Summary of Flume Tests (from Scott et al. 1993)

Test	Solids (%)	Fines (%)	Additives (g/cm <sup>3</sup> )	Rate (L/min)	Deposition Method	Segregation	Solids in Runoff (%)
1	56	18	L 1230	5.2	VH	No	<= 1
2	55	18	L 1220	21	VH	No	< 0.5
3	54	18	None	19	VH	Definite	10
4	53	16	A 940	77	HDF	Partial	< 2
5	44	20	L 1380	49	HD	minimal	1
6	35	25	L 1280	46	HD	Partial	< 0.8
7	36	26	L1290	62	VH	Partial	< 0.6
8	37	25	A 1050	57	VH	Partial	< 1.2
9	34	27	L 1020	62	VH	minimal	< 0.7
10	42	21	None	62	VH	Definite	4.5 - 7.5

Test	Solids (%)	Fines (%)	Additives (g/cm <sup>3</sup> )	Rate (L./min)	Deposition Method	Segregation	Solids in Runoff (%)
11	43	25	L 1250	58	HDU	Definite	Fines mixed with water
12	53	18	L 1250	48	VH	No	< 0.4
13	53	18	A 950	56	VH	Partial	< 1.1
14	56	18	L 1250	40	VHU	Partial	
15	57	16	L 1250	40	RS	minimal	< 1.0
16	63	14	L 1250	32	VE	No	< 0.5
17	53	19	L 1250	35	VE	No	< 0.9
18a	55	17	L 1250	36	VE	No	< 0.7
18b	56	16	L 1250	42	VE	No	< 1.1
19a	56	16	L 1250	40	VE	No	< 0.5
19b	56	16	L 1250	40	VE	No	< 0.5
20	57	13	L 1250	40	VE	Partial	< 0.7
21	42	16	L 1250	51	VET	Significant	< 0.7
22	55	21	L 1250	34	VET	No	< 0.6
23	57	13	L 1500	55	VET	No	< 0.5
24	53	13	L 1250	52	VET	Partial	< 1.5

VH= Vertical hose; HDF= Horizontal Distributor with Fin;

HDU=Horizontal Distributor Underwater; RS=Rectangular Spoon; VE=Vertical Elbow;

VET=Vertical Elbow (Tremie); HD=Horizontal Distributor without Fin;

The summary of the test result is presented in Table 5.1 (Scott et al. 1993). Comparing Test 3 and Test 10 with Test 2 and Test 11 in Table 5.1, one can see that the non-treated tailings segregated and formed a steeper beach with higher solids content in runoff. Influence of the deposition method on the slope and segregation of the tailing deposit can be seen from Test 3 and Test 10, where the tailings are deposited beneath 30 cm of water. The slope of the deposit for Test 3 is shown in Figure 5.3. The solids and fines content profiles are demonstrated in Figure 5.4 and Figure 5.5, respectively. The results for Test 10 are shown in Figure 5.6 to Figure 5.9. Figure 5.6 presented the advance of tailings with time. Figure 5.7 shows the deposit thickness immediately after

the deposition and 66 hours after the deposition. The solids and fines content profiles are shown in Figure 5.8 and Figure 5.9.

It can be seen from Figure 5.3 and Figure 5.7 a slope formed in the proximity of discharge points for both tests. However, depositing the tailings at a slower rate caused steeper slope of the beach and higher fine capture, which can be seen by comparing Figure 5.3 and Figure 5.7 for Test 3 and Test 10, respectively. The most obvious effect of the addition of lime or acid to the tailings is that a shallow deposit with gentle slope is formed, with the slope depending on the viscosity of the mixture and rate of deposition. A significant amount of water with low solids content is released due to the hindered settling and possibly some self-weight consolidation.

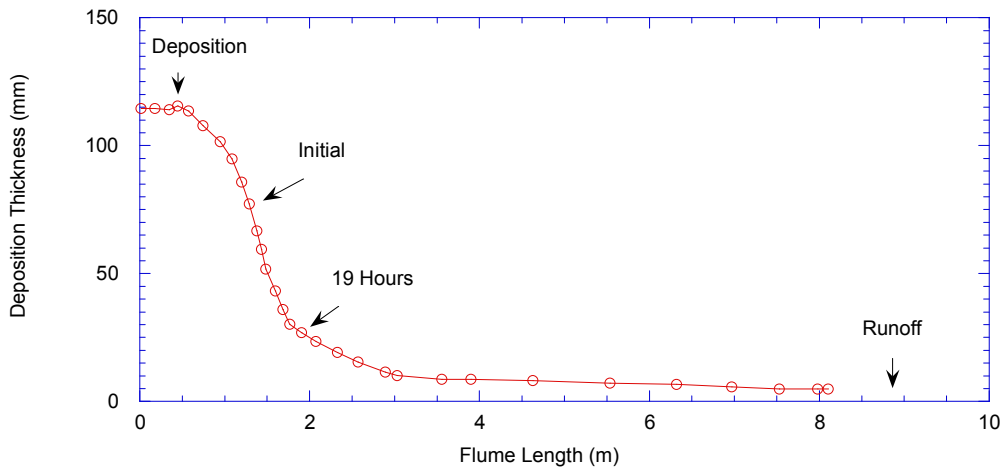


Figure 5.3 Test 3: The Profile of Tailings Immediate after Deposition and 19 Hours Later (reproduced from Scott et al. 1993)

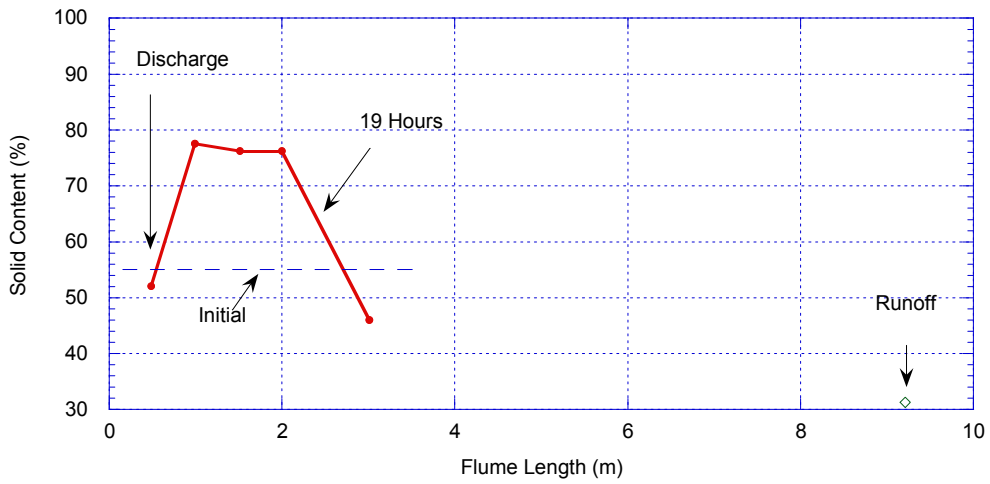


Figure 5.4 Test 3: Solids Content Profile (After Scott et al. 1993)

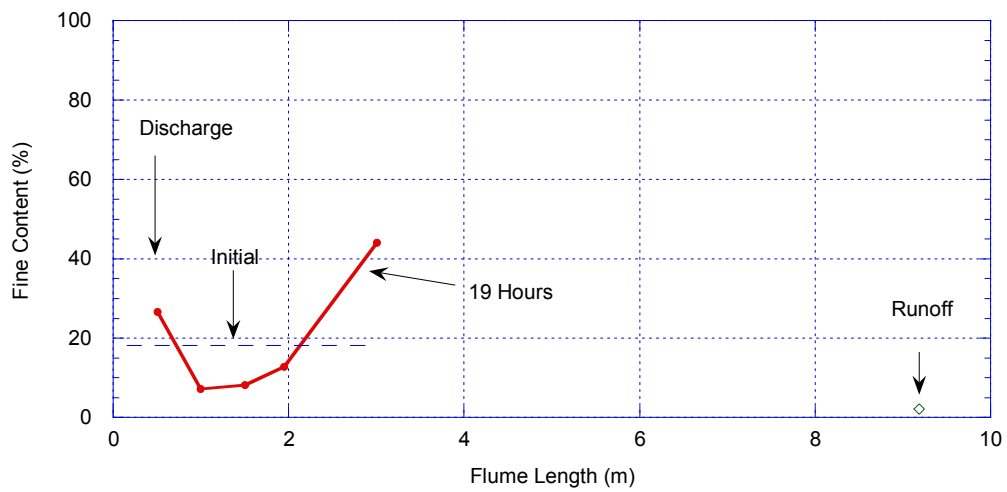


Figure 5.5 Test 3: Fines Content Profile (After Scott et al. 1993)

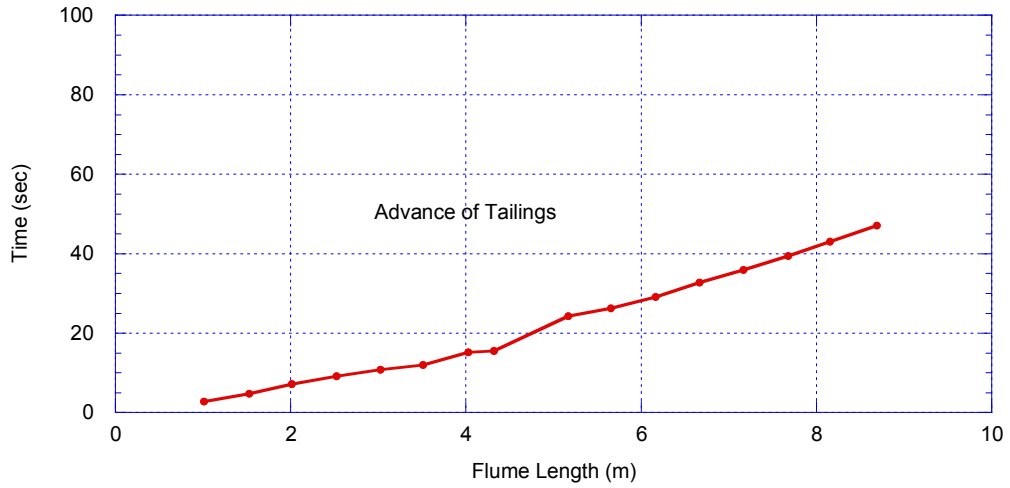


Figure 5.6 Test 10: Advance of Tailings (from Scott et al. 1993)

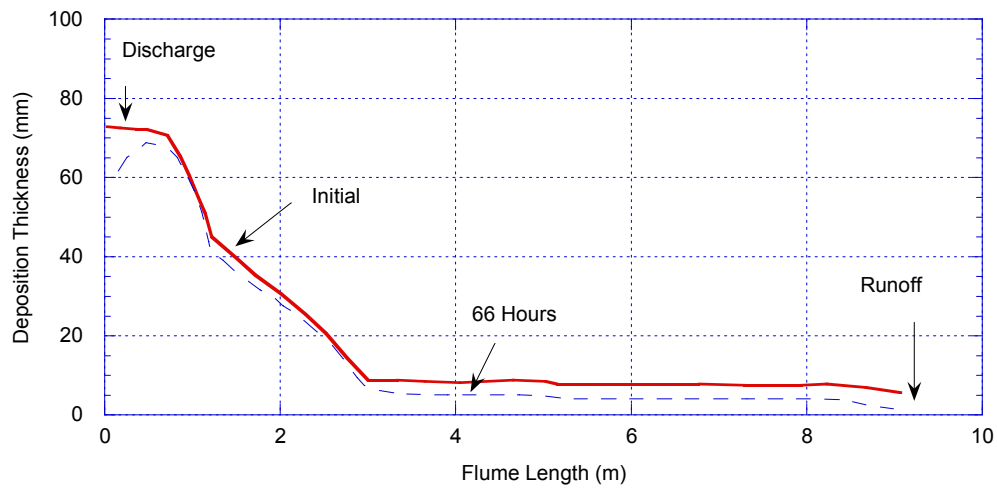


Figure 5.7 Test 10: The Profile of Tailings Immediate after Deposition and 66 Hours Later (from Scott et al. 1993)

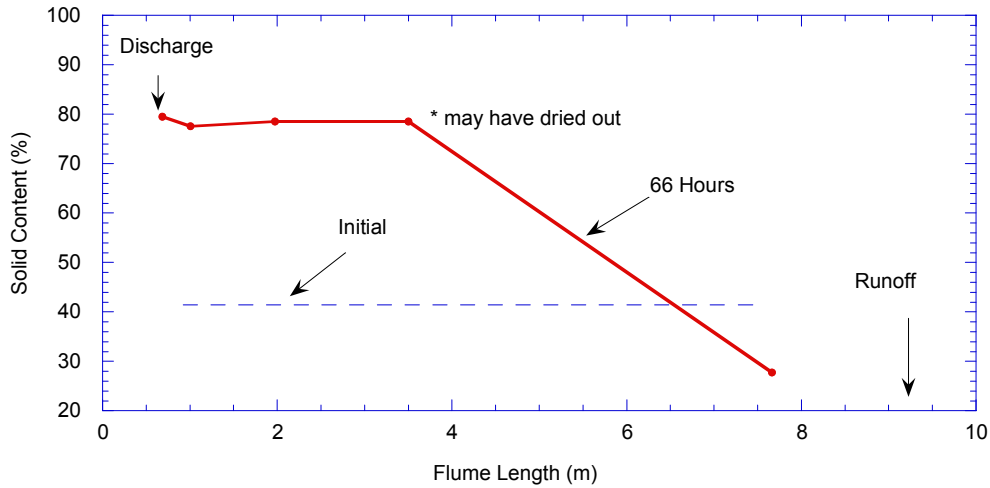


Figure 5.8 Test 10: Solids Content Profiles (from Scott et al. 1993)

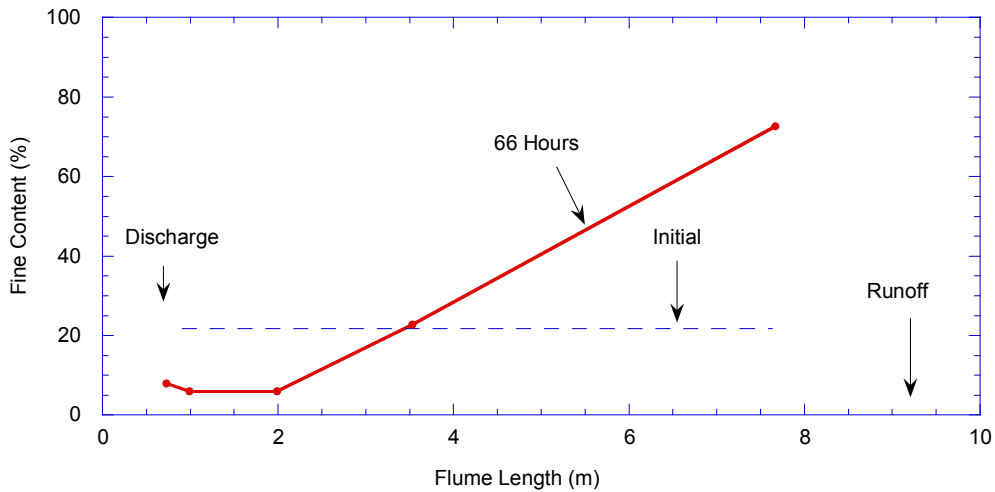


Figure 5.9 Test 10: Fines Content Profiles (from Scott et al. 1993)

Our interest here is focused on the influence of deposition conditions on the tailing properties. According to the report (Scott et al. 1993), the method affects the amount of air entrained in the deposit, thus the solids content of the runoff. The best deposition method was submerged deposition, which are Test 3 and 10 listed in Table 5.1. Partial segregation occurred in Test 3, with approximately 15% of the fines carried in the water to the end of the flume. Test 10 resulted in complete segregation of the tailings, with most of the fines stripped into the overlying water.

### 5.3 CFD Simulation of Flume Tests

Since the deposition environment in Test 3 is very similar to that in Suncor's Pond 1, Test 3 is used to evaluate the Euler-Euler models in CFX in modeling the deposition of tailing slurry and their proper boundary conditions. The tailings are treated as a single phase in subsection 5.3.1 and Particle Model (Euler-Euler) will be used in subsection 5.3.2.

#### 5.3.1 Free-Surface Model

##### 5.3.1.1 Model Set-Up

Free Surface Model is suitable for modeling the multiphase flow where a distinct interface separates two phases (CFX-10 Modeling Manual). In cases such as open channel flow, Free Surface Model can be applied conveniently and an interface between tailings and air can be tracked using Free Surface Model.

In this simulation, air, water at temperature of 25 C° and MFT are three phases that are used in the simulation. Free Surface Model is set for the interphase transfer between air and water, and between air and MFT. The drag coefficients for both above interphase transfer model are default value of 0.44 in the model. Intermixing is allowed to occur between MFT and water, thus Mixture Model with interface length scale of 1 mm and drag coefficient of 0.44 is set up for interphase transfer between MFT and water. For all the interphase transfer models, no mass transfer is assigned in the model. Since MFT with initial solids content of 54% and fines content of 18% is deposited beneath 30 cm water in the experiment, the density of the MFT can be calculated as follows:

$$\rho_{MFT} = \frac{100}{\frac{(100-s)}{\rho_{water}} + \frac{s(100-f)/100}{\rho_{sand}} + \frac{s*f/100}{\rho_{clay}}} \quad (\text{Eq. 5.1})$$

Where  $s$  and  $f$  are the solids content and fines content of the MFT in percent,  $\rho_{water}$ ,  $\rho_{clay}$ ,  $\rho_{sand}$ , and  $\rho_{MFT}$  the density of water, sand, clay and MFT, respectively. It is assumed that the density of water, sand and clay are 1000, 2700 and 2600 kg/m<sup>3</sup> respectively. When the densities of the water, sand and clay along with solids and fines

content are substituted into Eq. 5.1, the MFT density of  $1320 \text{ kg/m}^3$  is obtained. Since the viscosity of MFT is not measured during the experiments, the viscosity of the MFT sample listed in Table 3.2 with solids contents of 52% and fines content of 60% is assigned to the material in the CFD model. The Reynolds number for the test ranges from 0.02 to 208.34 based on the maximum viscosity of 917.4 Pa.s and minimum viscosity of 0.098 Pa.s for the MFT used in the simulation. As a result, laminar flow is assumed in the simulation. The tetrahedron elements as shown in Figure 5.10 are applied and it is assumed that 30 cm of water is overlain by 20 cm of air initially. The MFT slurry is pumped through the 2.5 cm diameter pipe at a velocity of 0.62 m/s. Transient process is assumed for the deposition process. The total time is 243 seconds and time step of 0.5 second is found to be ideal balance between the accuracy of the simulation result and computing time. The end of the pipe submerging into water is assigned as velocity inlet boundary condition and degassing Outlet boundary condition is set for the top surface of the flume, where only air is allowed to exit from the top surface. The aluminum wall shown in Figure 5.2 is modeled using Thin Wall, whose thickness is zero. In order to use Thin Wall setting, the left part of the flume is assigned as Sub-Domain. All other boundary conditions are set to be rough Wall where Use Volume Fraction option is used for Wall Contact Model. It is assumed that the friction between air and the wall is negligible and thus Free Slip wall is assigned for the influence of wall on Air. No-Slip conditions are assigned for MFT and water.

### 5.3.1.2 Simulation Results

The variation of MFT volume fraction with time is shown in Figure 5.11. The volume fraction of MFT is shot on the plane passing through the center line of the pipe. It can be seen that the concentration of MFT is accumulated immediate beneath the pipe inlet, then flowed along the base of the flume away from the pipe inlet. The advance of the deposit with time is demonstrated in Figure 5.12. It can be seen that the speed of the advance of the deposit is almost uniform during the first 125 seconds and after that the deposit advance slowed down. The slope of the deposit immediate after stopping pumping MFT into the flume is shown in Figure 5.13. It can be observed that the front of the tailing flow travels to a shorter distance than that in the experiment. However, the slope of the deposited tailings is steeper than that in the

experiment. The discrepancy in the advance and the slope of the deposit lies in the viscosity value of the MFT phase in the model. Based on the conclusion drawn in Section 3.1.4.2.3, higher fines content will lead to higher apparent viscosity at the same solids content. Therefore, overestimated apparent viscosity is assigned for the tailings with solids content of 54% and fines content of 18%. Another factor is the subjectivity of the measurement in the experiments. The height of the interface between slurry and upper clear water is recorded with time during the test. The boundary value of concentration between tailing slurry and clear water is subjective to the observer. In Figure 5.13 the depth of the deposit is obtained by tracking the contour of the tailing slurry volume fraction on the mid-plane between outer wall and central aluminum wall of the flume. In spite of the discrepancy, a steep slope at the front of the deposit indicates that the relative rigidity of the tailing slurry.

If the viscosity of the tailing slurry is scaled down by 0.01 times, the travel distance of the deposit front would be expected to be greater than the simulation using the original viscosity. As shown in Figure 5.14 and Figure 5.15, the deposit in the simulation using the scaled viscosity travels 1.5 m greater distance than that using the originally assumed viscosity model. The depth of the deposit is reduced correspondingly.

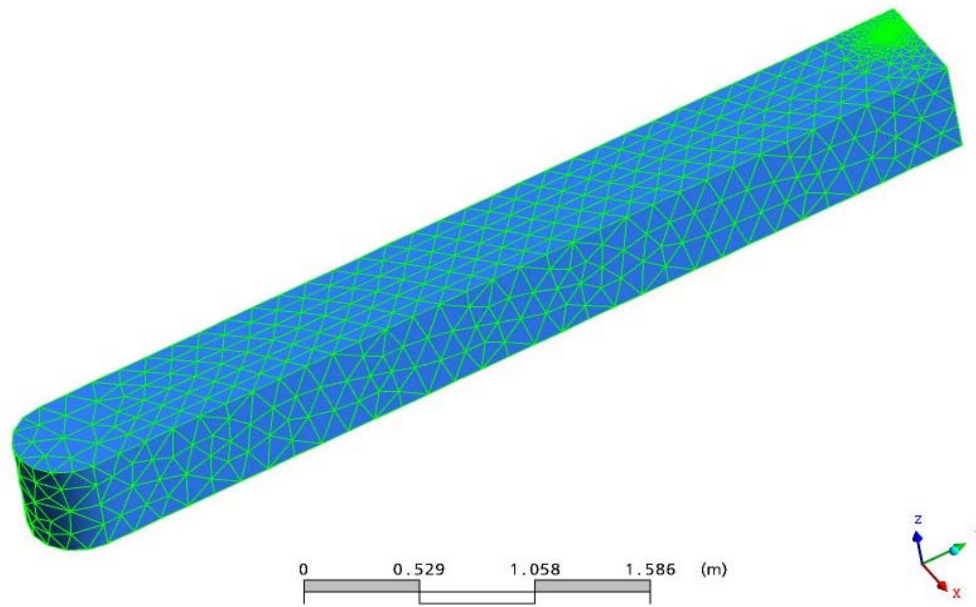
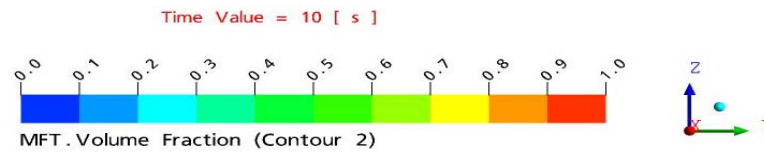


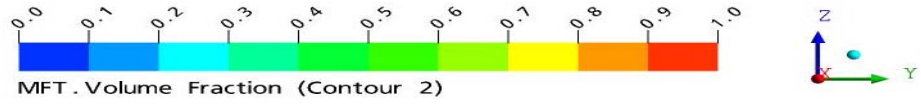
Figure 5.10 Grids Used in the Free Surface Model (14,514 nodes)



(a)



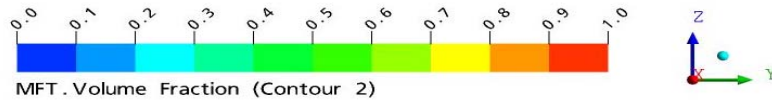
Time Value = 50 [ s ]



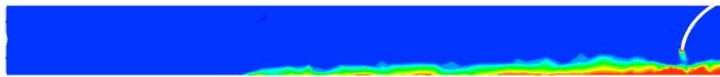
(b)



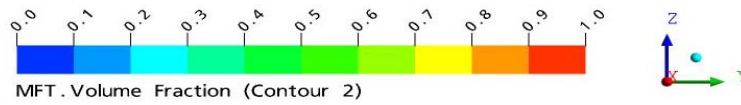
Time Value = 100 [ s ]



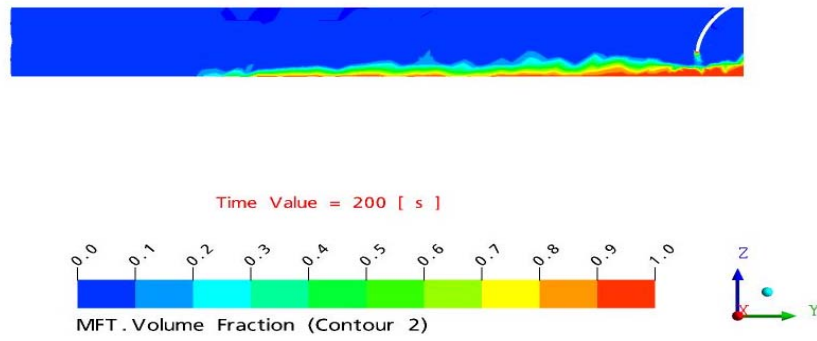
(c)



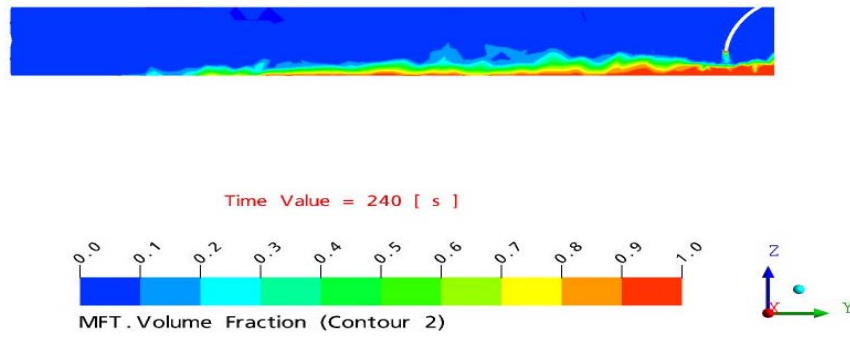
Time Value = 150 [ s ]



(d)



(e)



(f)

Figure 5.11 Variation of MFT Volume Fraction with Time: (a) MFT Volume Fraction profile at 10 second; (b) MFT volume fraction profile at 50 second; (c) MFT Volume Fraction profile at 100 second; (d) MFT volume fraction profile at 150 second; (e) MFT Volume Fraction profile at 200 second; (f) MFT Volume Fraction profile at 240 second

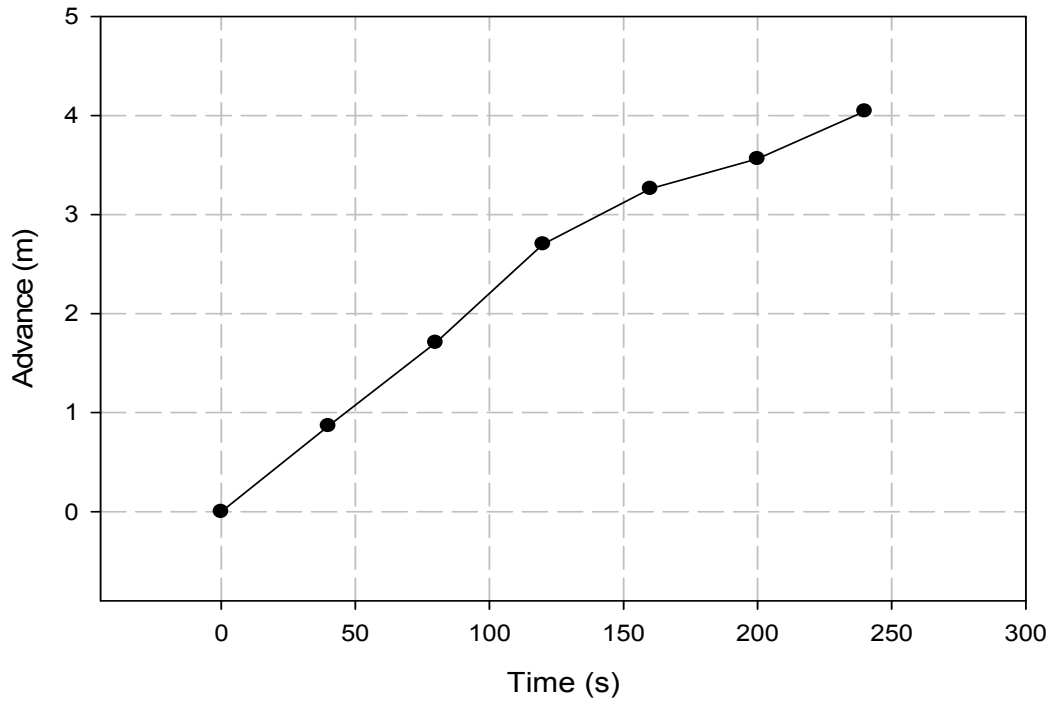


Figure 5.12 Advance of the Deposit with Time in Simulation

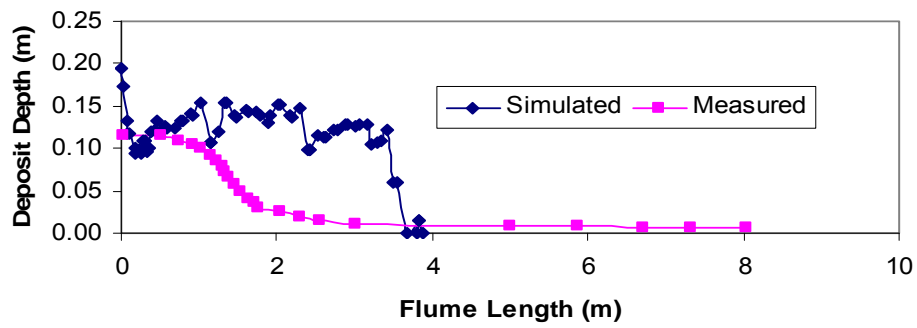


Figure 5.13 Comparison of the Simulated and Measured Slope of the Deposit Immediately After Stopping Pumping

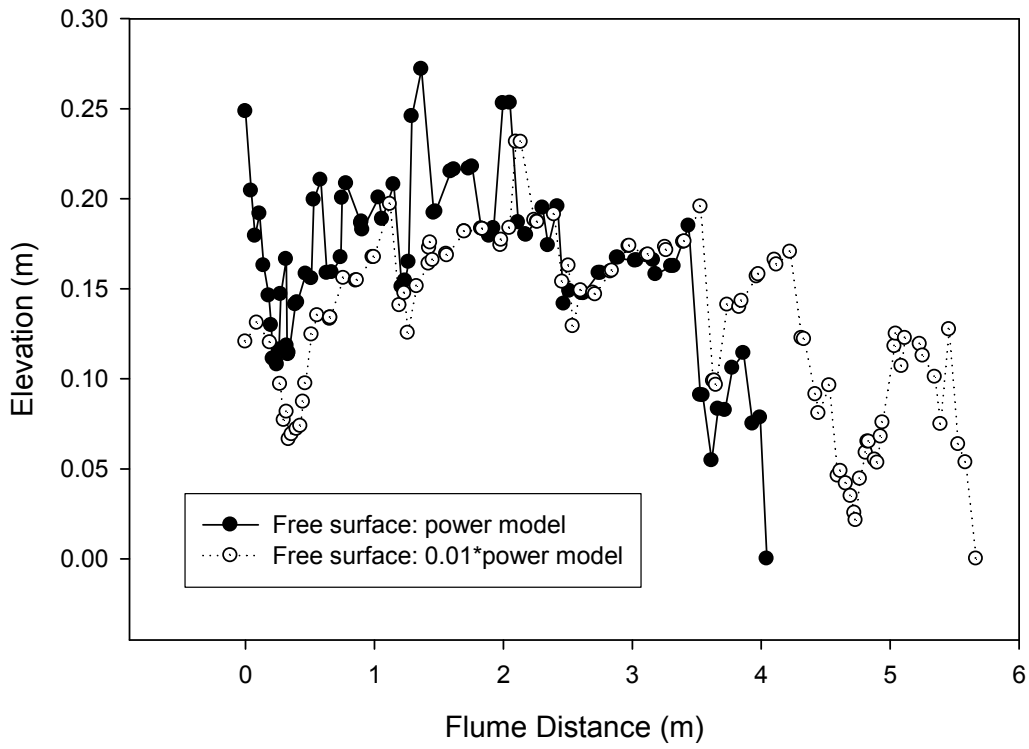


Figure 5.14 Influence of Tailing Viscosity on the Slope of the Deposit

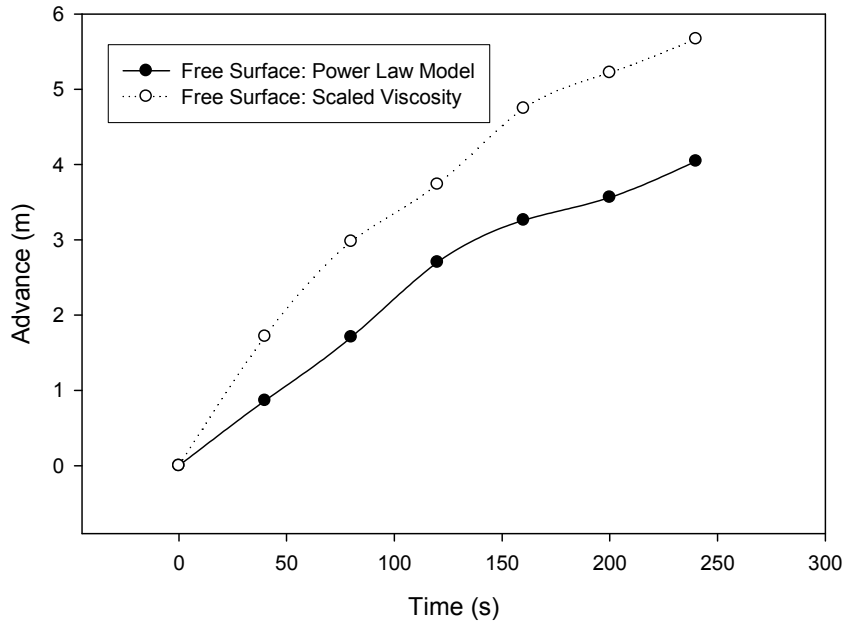


Figure 5.15 Influence of Tailing Viscosity on the Advance of the Deposit

### 5.3.2 Particle Model Using Water Viscosity

#### 5.3.2.1 Model Set-Up

If the distribution of the composition is of interest, Particle Model should be applied as each phase in the model has its own flow field (velocity, temperature etc.). In this case, tailing slurry is decomposed into coarse particles (sand), fine particles (clay) and water. The division for the fine and coarse particles is 44 micron.

The grid used in this simulation is shown in Figure 5.16. The height of the domain of the flume is 30 cm instead of 55 cm in Free Surface Model. Water is assigned as the only continuous phase while sand and clay are set as dispersed phases. The densities of water, sand and clay are assumed to be 1000, 2700 and 2600 kg/m<sup>3</sup> respectively. The viscosity of the water phase is 0.001 Pa.s. K-Epsilon turbulence model is used for water phase while Dispersed Phase Zero Equation is applied for sand and clay phases. Buoyancy force is accounted for in the calculation and the buoyancy reference density is assigned as the density of water. The mean diameters for sand and clay phases are assigned as 75 and 2 micron respectively. The choice of the mean diameter is random since no grain size distribution data is obtained. Based on the recommendation on CFX 10 manual (CFX-10 Modeling Manual), the Gidaspow Solid Pressure Model with Compaction Modulus of 1 and Elasticity Modulus of 100 Pa is assigned for clay phase. The Compaction Modulus and Elasticity Modulus of 1 and 600 Pa, respectively, are set for the sand phase. No solid bulk and shear viscosity are assigned for both the dispersed clay and sand phases. Particle Model is chosen for the momentum transfer between each pair of phases and Gidaspow drag model is used for the drag force between water and clay as well as water and sand. Initially, the flume is assumed to be filled with water. The tailing slurry stored in the tank is decomposed into water, sand and clay with volume fraction of 0.696, 0.248 and 0.056. The normal velocity of 0.62 m/s is set for all the phases at the inlet boundary conditions. The top face of the flume domain is assumed to be Outlet boundary condition. Only water is assumed to exit from this face with the velocity calculated from volume balance of the system.

### 5.3.2.2 Simulation Results

The variations of clay and sand volume fraction profile with time are shown in Figure 5.17 and Figure 5.18. It can be seen that clay particle spreads speedily across the whole depth of the flume and the front of the clay particle stream moves rapidly. The same trends are observed for sand particles. The contour of the total solid volume fraction is drawn on the mid-surface between the outer wall and the central aluminum wall. The travel of the tailings deposit front from the simulation using the Particle Model is compared with that using Free Surface Model in Figure 5.19. It can be seen that the movement of the front in Particle Model is much faster than that in Free Surface Model. The discrepancy resulted from the fact that non-Newtonian properties (yield stress, shear-rate-dependent viscosity etc.) of the tailing slurry are not reflected in the decomposed matrix of water, sand and clay. In other words, the interactions between water, clay particles and sand particles are not completely accounted for in the constitutive model of Particle Model.

Figure 5.20 compares the profiles from the simulation using Particle Model and that from experiments at the time of 4 minutes. It can be observed that the simulated depth of the deposit is greater than that from experiments.

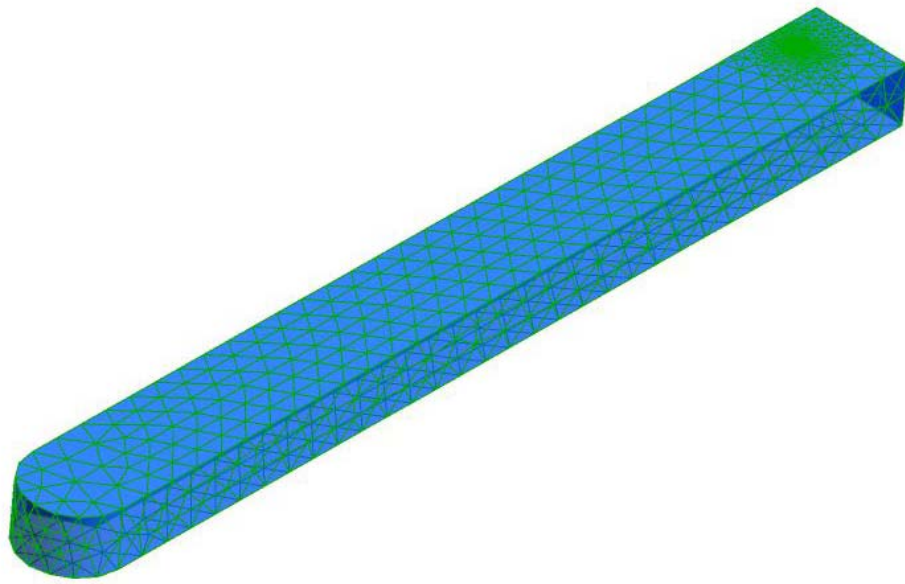
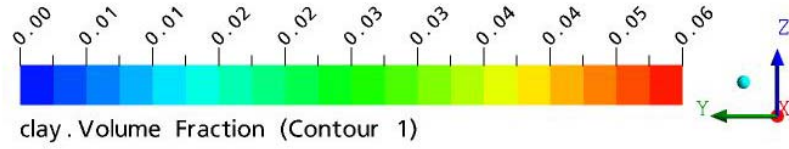


Figure 5.16 Mesh Used in Particle Model Simulation (8,882 nodes)



Time Value = 40 [ s ]

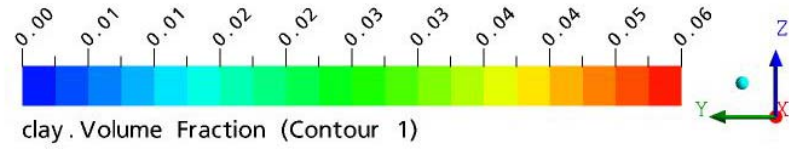


clay . Volume Fraction (Contour 1)

(a)



Time Value = 80 [ s ]

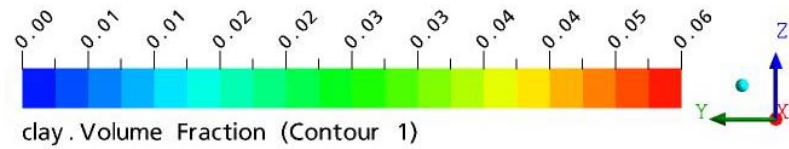


clay . Volume Fraction (Contour 1)

(b)



Time Value = 120 [ s ]

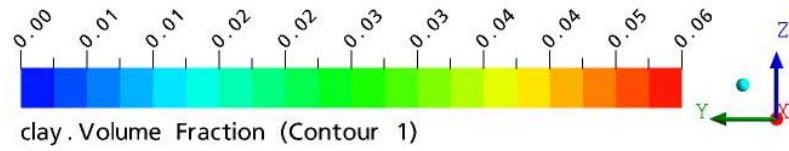


clay . Volume Fraction (Contour 1)

(c)



Time Value = 160 [ s ]

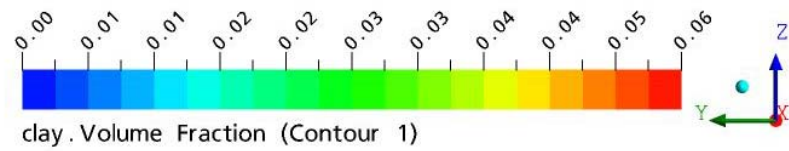


clay . Volume Fraction (Contour 1)

(d)



Time Value = 200 [ s ]

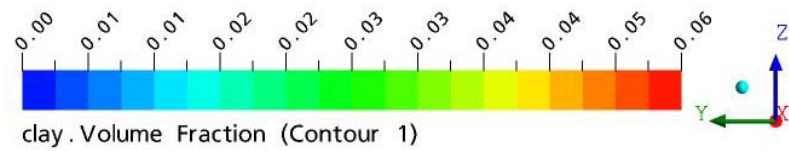


clay . Volume Fraction (Contour 1)

(e)



Time Value = 240 [ s ]



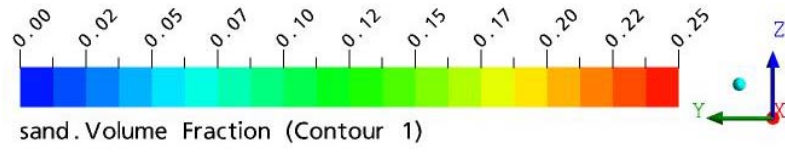
clay . Volume Fraction (Contour 1)

(f)

Figure 5.17 Variation of Clay Volume Fraction with Time



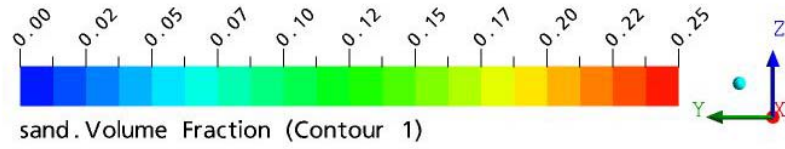
Time Value = 40 [ s ]



(a)



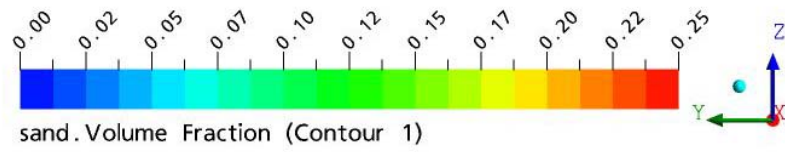
Time Value = 80 [ s ]



(b)



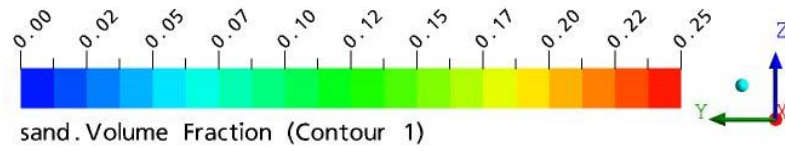
Time Value = 120 [ s ]



(c)



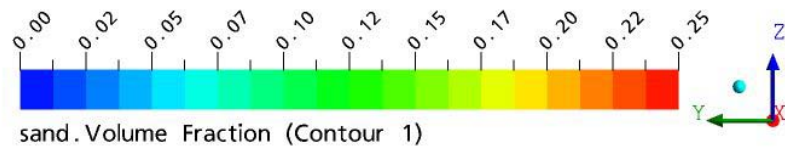
Time Value = 160 [ s ]



(d)



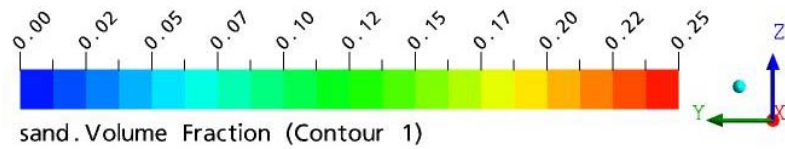
Time Value = 200 [ s ]



(e)



Time Value = 240 [ s ]



(f)

Figure 5.18 Variation of Sand Volume Fraction with Time

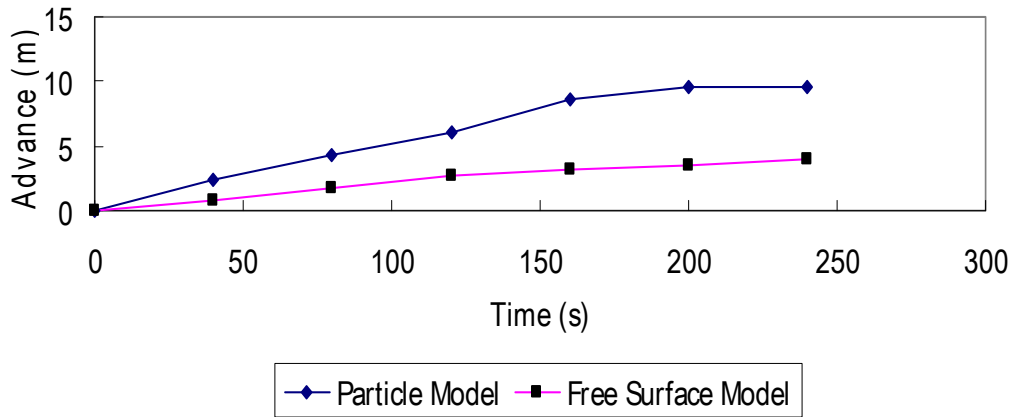


Figure 5.19 Comparison of the Advance of the Slurry Stream with Time for Particle Model and Free Surface Model

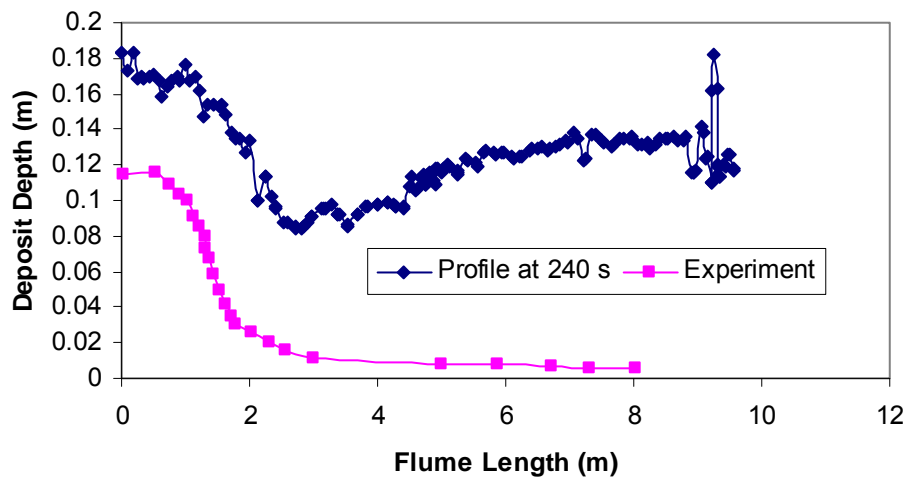


Figure 5.20 Comparison of the Deposit Depth at 240 seconds

### 5.3.3 Particle Model Using MFT Viscosity

#### 5.3.3.1 Model Set-Up

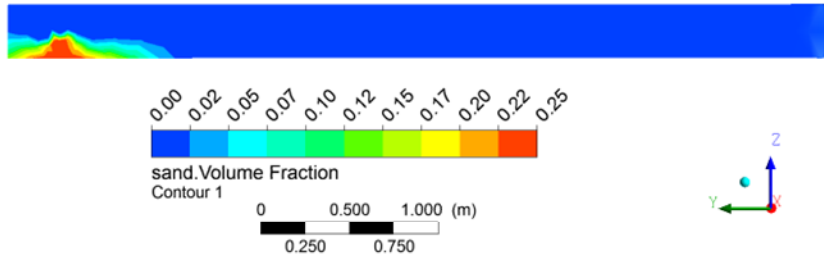
The same grid and model in Section 5.3.2 are used in this simulation. In order to impede the travel of the MFT, the viscosity of the Sample 5 shown in Table 3.18 is assigned to the water phase. The Power Law model with parameters shown in Table 3.18 is used and the maximum viscosity of 50 Pa.s is set in the simulation. The top of the flume is assigned as Free-Slip wall and the side wall that is perpendicular to the flow of the tailings is assumed to be Outlet boundary. It is assumed that the mass flow at the outlet face is equal to that at the inlet.

#### 5.3.3.2 Simulation Results

Figure 5.21 shows the variation of sand volume fraction with time and the Figure 5.22 shows the clay volume fraction changes with time. Compared with the variation of the sand and clay volume fraction with time shown in Figure 5.17 and Figure 5.18, it can be observed that the travel of the MFT front in this simulation is much slower than that in the simulation described in the Section 5.3.2, where the viscosity of the water is set as 0.001 Pa.s. Figure 5.23 shows the variation of the solids content profiles with time. The profiles of the deposit at various times are obtained from the 11% solids content contour line on the mid-plane between two vertical flume walls.

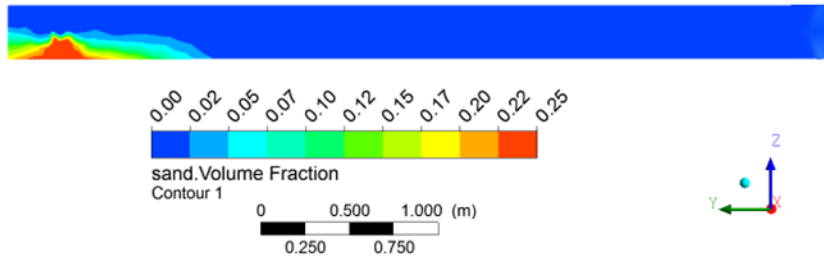
Figure 5.24 compares the advance of the MFT fronts in the three simulation cases above. Figure 5.25 shows the depth of the deposition at time of 240 seconds. The figure shows that the sand and clay particles concentrate in the vicinity of the discharge pipe. The depth of the deposit is greater than measured in the experiment; however, the form of the deposit generally follows the measured deposit depth profile.

Time Value = 40.1399 [ s ]



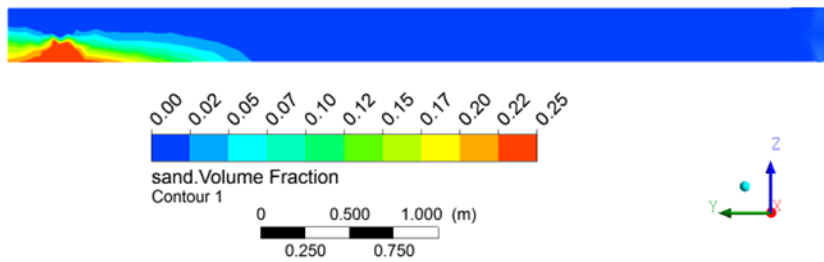
(a)

Time Value = 60.1548 [ s ]

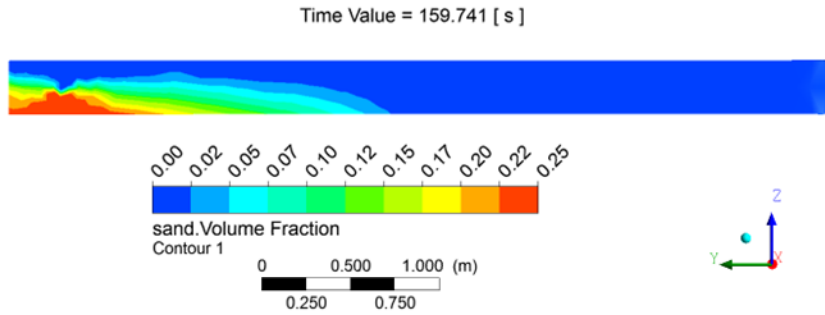


(b)

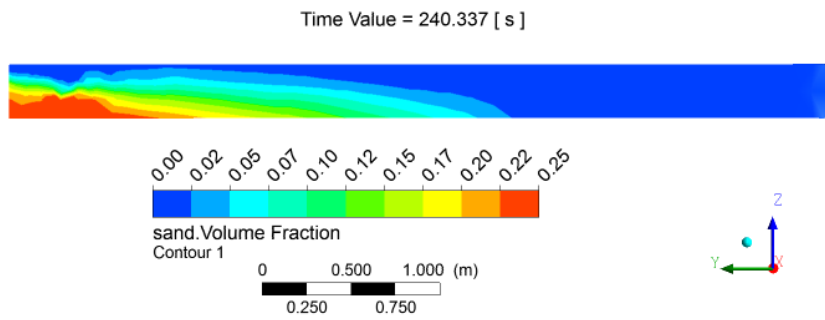
Time Value = 80.17 [ s ]



(c)



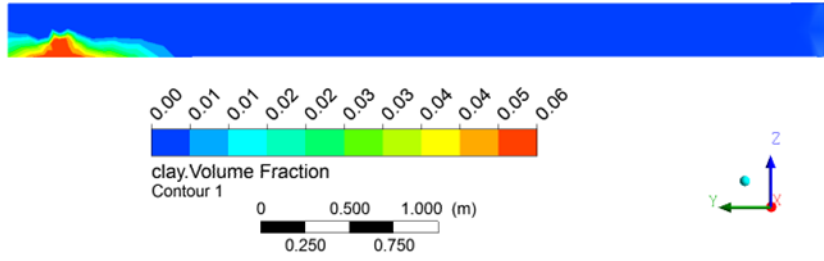
(d)



(e)

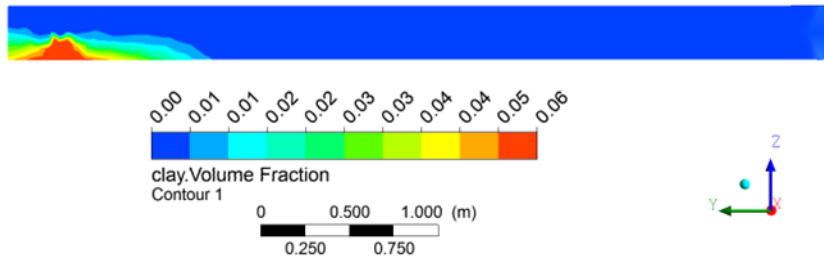
Figure 5.21 Variation of Sand Volume Fraction with Time

Time Value = 40.1399 [ s ]



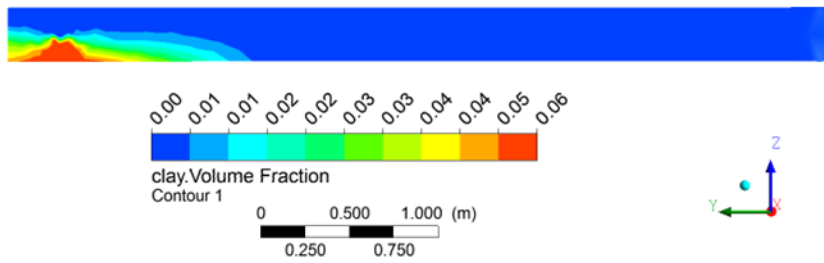
(a)

Time Value = 60.1548 [ s ]



(b)

Time Value = 80.17 [ s ]



(c)

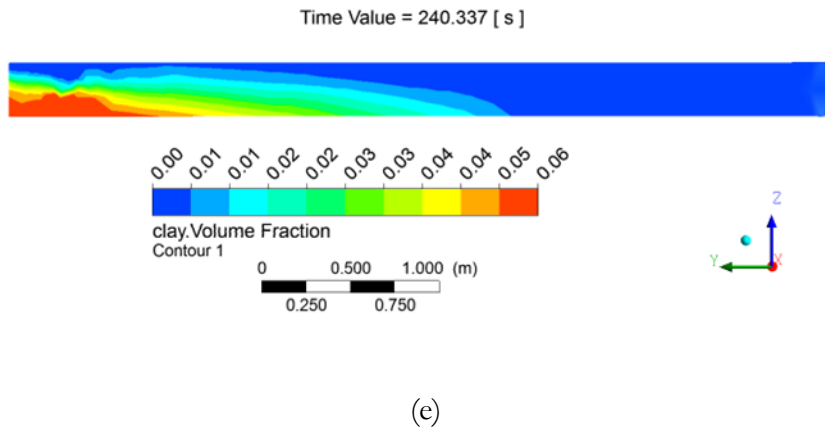
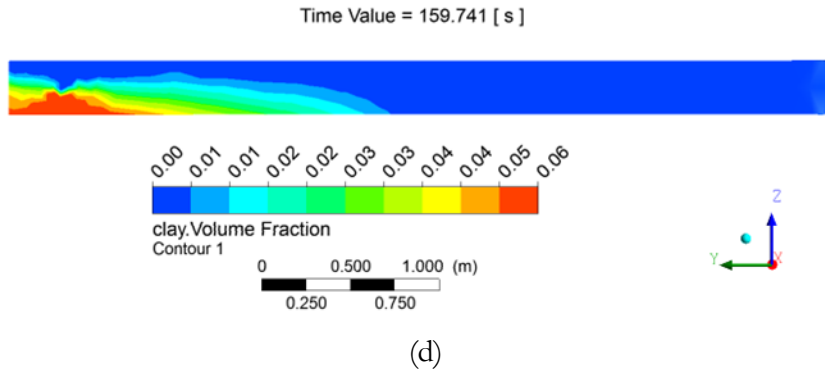
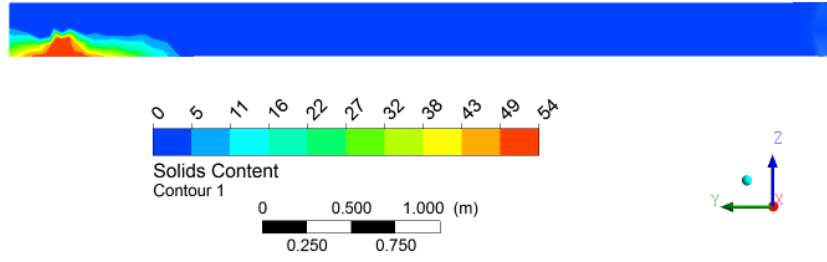


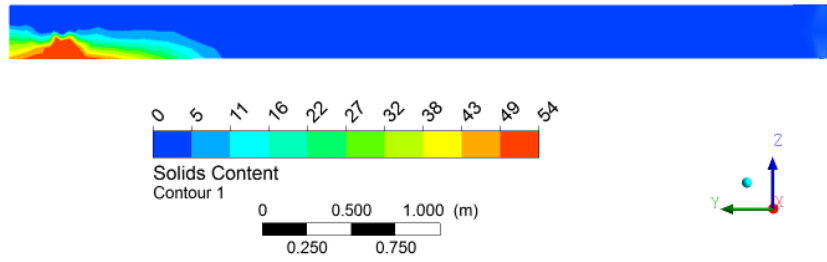
Figure 5.22 Variation of Clay Volume Fraction with Time

Time Value = 40.1399 [ s ]



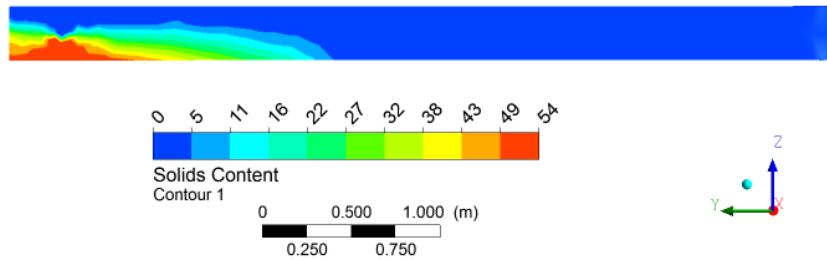
(a)

Time Value = 60.1548 [ s ]

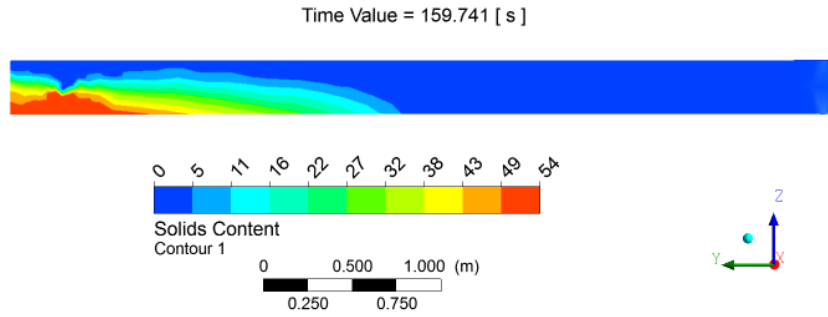


(b)

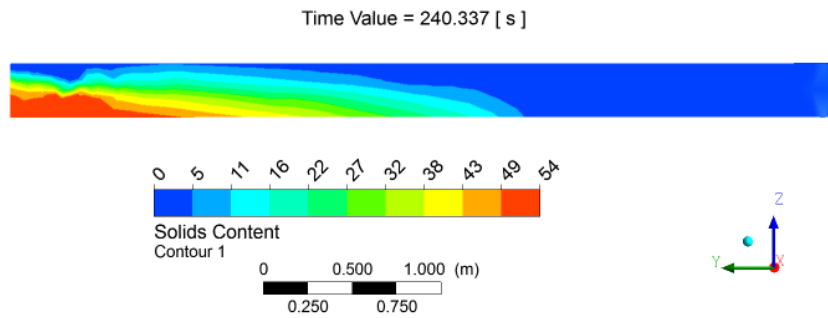
Time Value = 119.981 [ s ]



(c)



(d)



(e)

Figure 5.23 Variation of Solids Contents with Time

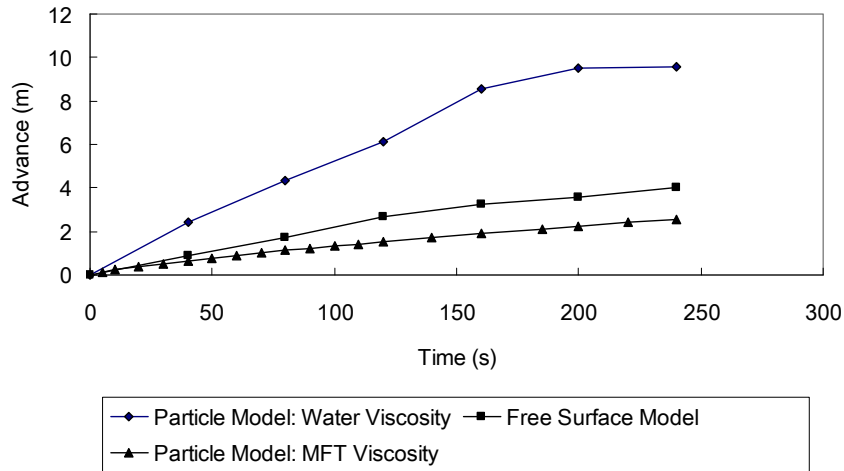


Figure 5.24 Comparison of the Advance of the Slurry Stream with Time for Free Surface Model and Particle Models Using Water Viscosity and MFT Viscosity

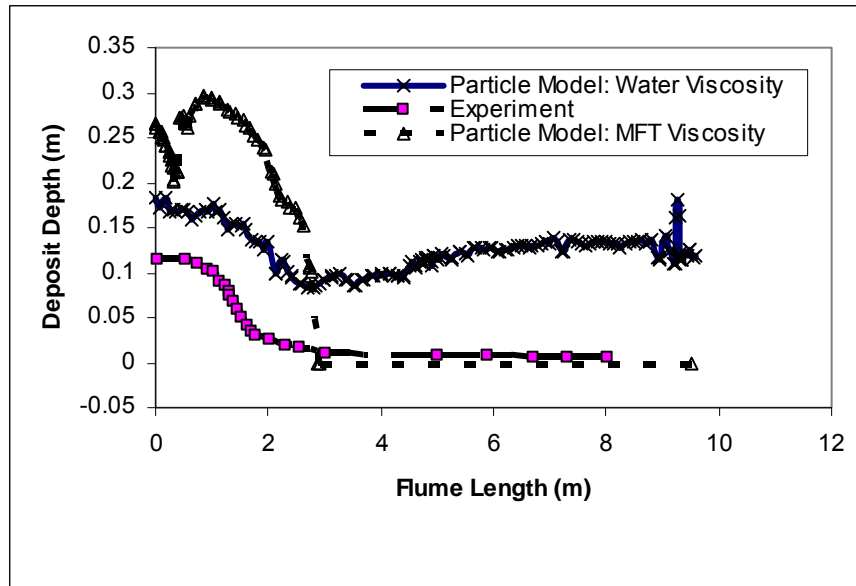


Figure 5.25 Comparison of the Deposit Depth at 240 seconds

#### 5.4 Summary and Conclusion

1. The flume tests conducted by Scott et al. (1993) are presented. The Test 3 is modeled using Free Surface Model and Particle Model in CFX-10.
2. The Free Surface Model is used to simulate the advance of the MFT slurry in the flume. It is found that the advance of the tailing deposit in the Free Surface Model simulation travels at a greater speed than measured in the laboratory tests. One of reasons is that the viscosity of the tailing slurry was not measured in the experiment and an approximate viscosity model is assigned for the MFT in the Free Surface Model.
3. The Particle Model with the true viscosity (0.001 Pa.s) assigned to water phase is applied to capture the advance of the tailing slurry front and the development of the profiles of solids and fines contents. Sand particles settle quickly in the tailing slurry and the front of the tailing slurry travels at a greater speed than that in Free Surface Model. Therefore, the solids and fines content profiles in the simulation do not match with those in the laboratory at the specified time. This result is similar to the simulation results for the sedimentation of the non-segregating slurry in the

standpipe, which is presented in Chapter 4. The reason is that assigning a true viscosity value (0.001 Pa.s) for the water phase does not account for the interactions between fine particles and water, thus the hindered settling of the coarse particles in the suspension of water and fine particles.

4. The Particle Model with MFT viscosity assigned for the water phase is also used in the simulation of the flume Test 3. Comparison of the deposit profiles at 240 seconds obtained from the Particle Model using the real water viscosity of 0.001 Pa.s indicates that the advance of the deposit front from this simulation is significantly slower. The depth of the deposit is greater than that obtained from the experiment although the shape of the deposit in the simulation generally follows that obtained from the experiment.

### **Reference**

Scott, J.D., Caughill, D.L. and Liu, Y. Total Tailing Disposal Research Program Report 6: Analysis of Flume Tests. University of Alberta, Edmonton, Alberta, Canada. November 30, 1993.

## CHAPTER 6 CFD SIMULATION OF SUNCOR'S POND 1 TRIAL TESTS<sup>1</sup>

### 6.1 Introduction

Reducing the volume of fine tailings contained in tailing ponds is one of the main issues during reclamation of the tailing pond in mining industries. Incorporation of fine tailings into coarser tailings by mixing remains one of the more promising strategies for long term containment (Morgenstern et al., 1995). In this process fine tailings will be captured into the space between sand particles. By pumping coarse sand into MFT and then capturing the fine tailings between coarse sands, it is expected that the volume of the fine tailings is reduced. Attempts are made to model the deposition using Mixture Model and Particle Model. Results obtained from simulations are presented and issues related to the numerical simulation are discussed.

### 6.2 Suncor Pond 1 and Sand Infilling Trial in 2002

Suncor's tailings Pond 1 is located approximately 30 kms north of Fort McMurray, Alberta (Figure 6.1 and Figure 6.2). The typical tailing composition and average peak shear strength prior to sand infilling are shown in Figure 6.3 and Figure 6.4. The figures show that the material above elevation 1050 ft is very weak tailings with solids content below 35% and shear strength less than 0.5 kPa. The MFT material between elevation 1050 ft and 1010 ft has mineral content of 35 – 65%. Its peak shear strength is up to 1.5 kPa. The MFT below elevation 1010 ft has increasing shear strength and sand fine ratio. The low strength of the MFT precludes sand capping as a potential reclamation option. It is determined that the pond would be reclaimed by infilling dense tailings (DT) concurrently with MFT removal. Due to the uncertainty of the depositional mechanisms and risks associated with the failure of Plant 4 tailings beach, a large beach test is carried out at Suncor's Tailing Pond 1 (MRRT, 2002).

---

<sup>1</sup> A version of part of this chapter has been published. Yang, J. and Chalaturmyk, R.J., Development of Rheological Model for Computational Fluid Dynamics Simulation of Sand Deposition into MFT. Proceedings of the 57<sup>th</sup> Canadian Geotechnical Conference, Quebec, Canada, October 19- 22, 2004.

Figure 6.5 shows the change in bottom elevations due to infilling dense sand slurry into MFT. It can be seen that overall beach elevation (or pond bottom elevation) increase with DT infilling. The changes of sand fine ratio (SFR) at sites 34 and 35 after infilling of DT are shown in Figure 6.6 and Figure 6.7. From the change of SFR it can be observed that most of the infilling sand is deposited between elevation of 1005 ft and 1025 ft. Based on the samples from three sampling sites, an illustration is developed to conceptually interpret the mechanisms (Figure 6.8). However, the detailed distribution of sand in the fine tailings is unknown at that point. In order to optimize the reclamation process, factors affecting the capture of fine tailings into sand are required to be investigated. Numerical simulation, particularly computational fluid dynamics (CFD), is studied to understand the deposition mechanisms as a component of research program.



Figure 6.1 Location of Suncor Pond 1 (Google Earth, 2009)



Figure 6.2 Close view of Suncor Tailing Pond 1 (Google Earth, 2009)

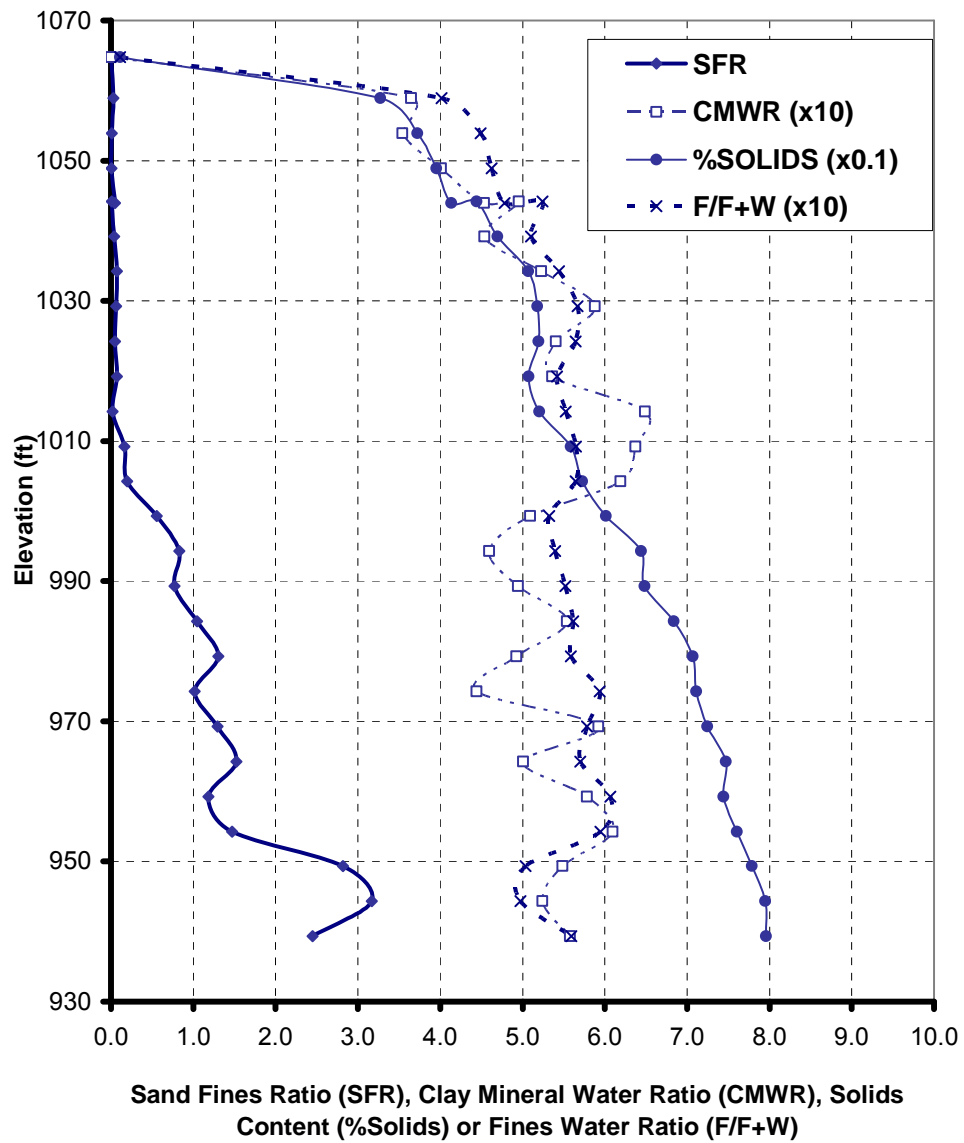


Figure 6.3 Suncor Pond 1 Typical Tailing Composition Variation with Elevation (from MRRT, 2002).

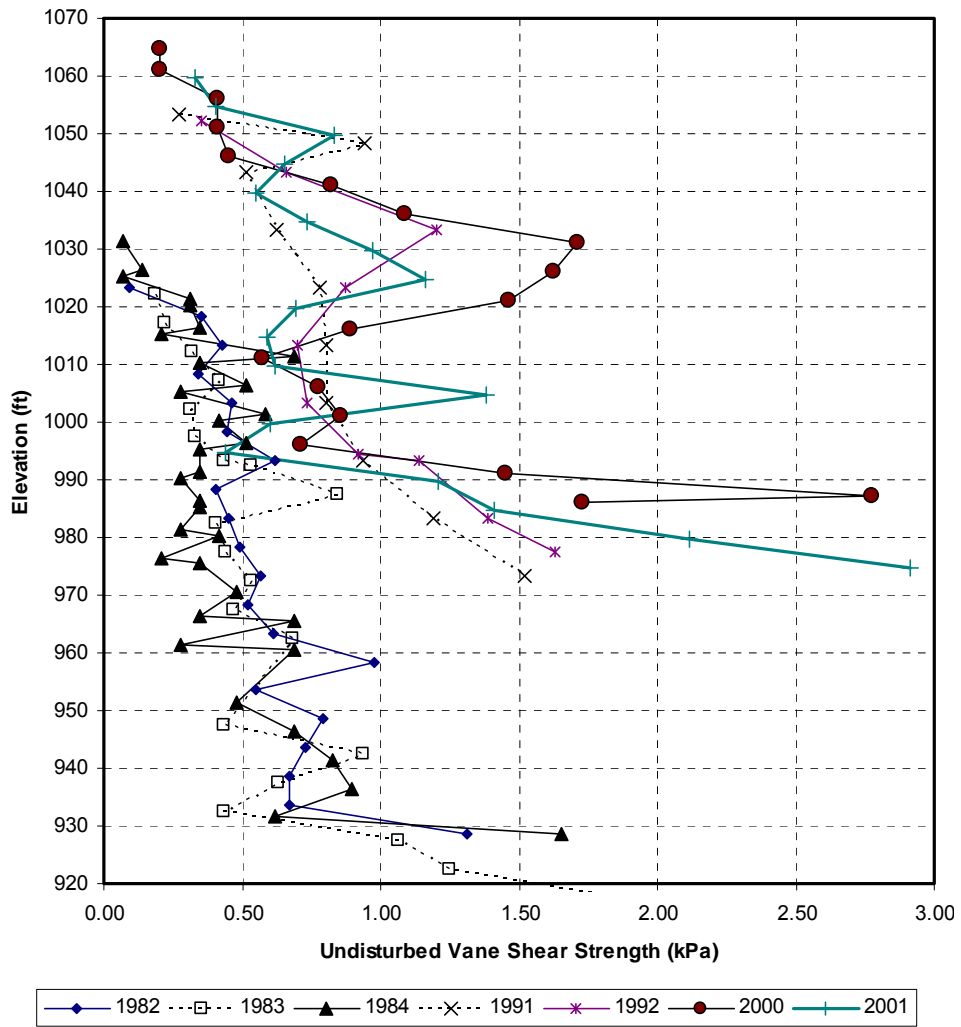


Figure 6.4 Suncor Pond 1 Average Peak Shear Strength Variation with Elevation (from MRRT, 2002)

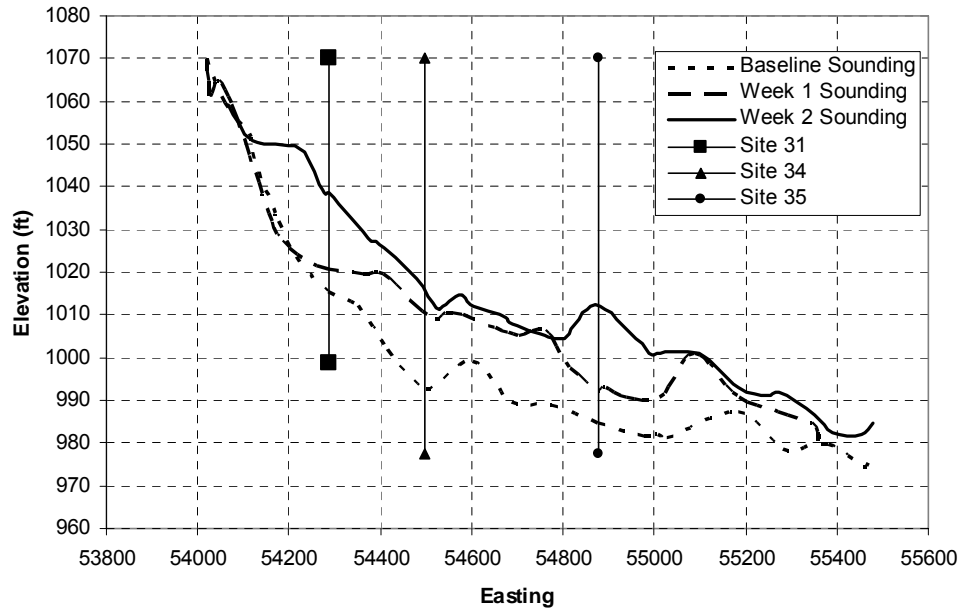


Figure 6.5 Suncor Pond 1 Pond Bottom Change with Sand Infilling (after MRRT, 2002)

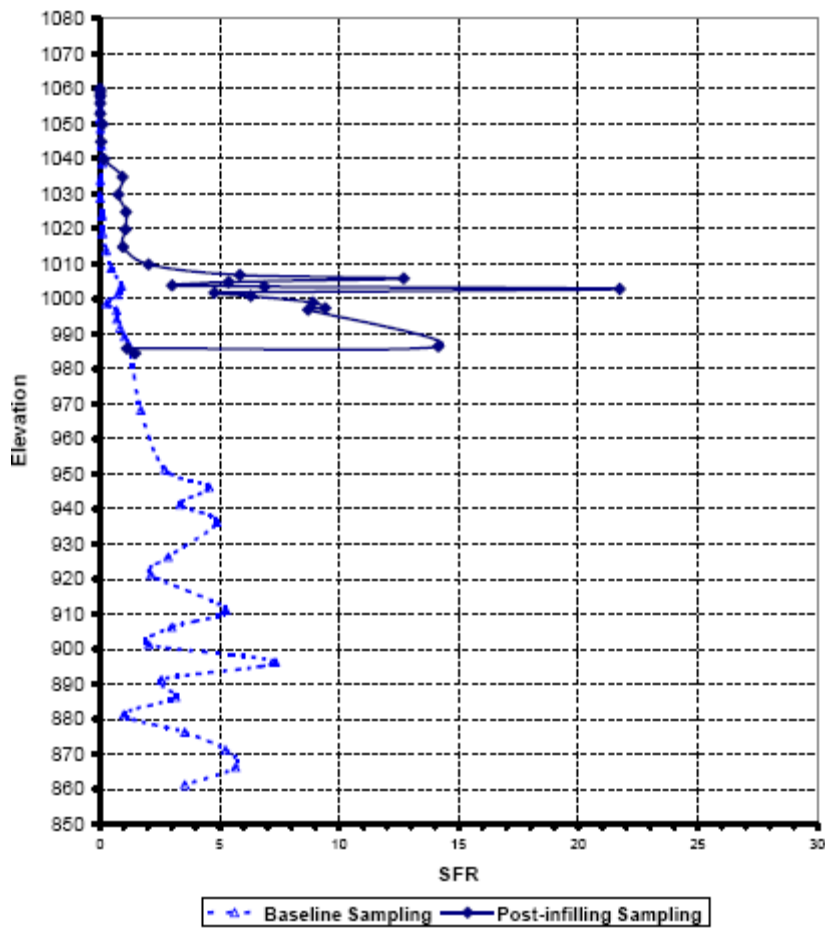


Figure 6.6 Suncor Pond 1 Sand Capture in MFT above Beach Infill at Site 34 (from MRRT, 2002)

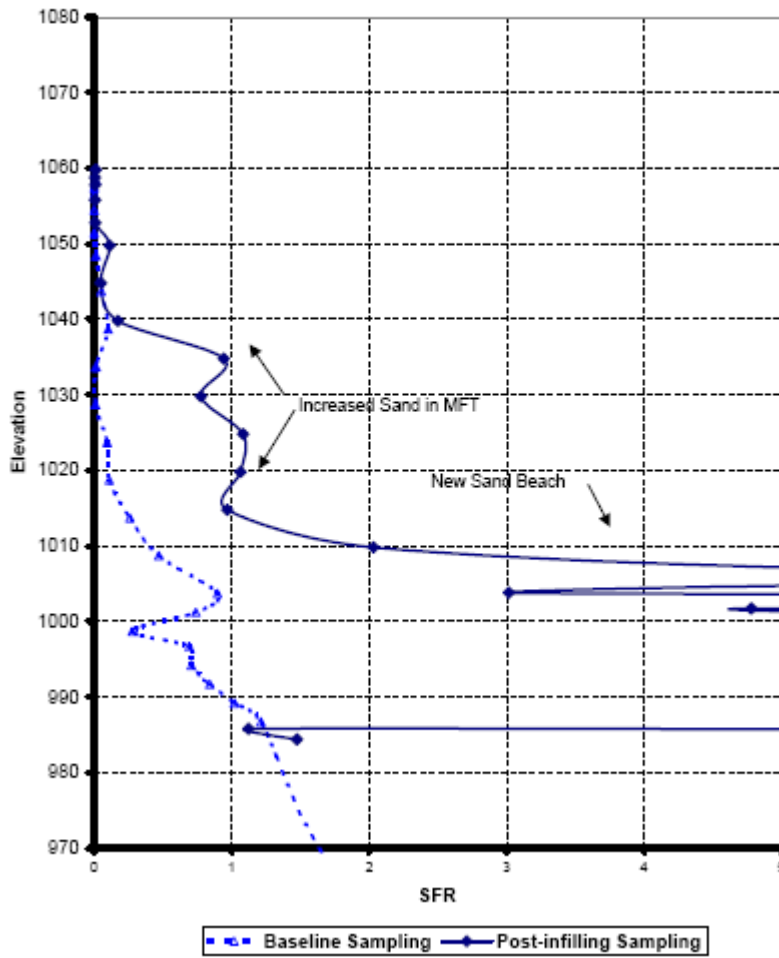


Figure 6.7 Suncor Pond 1 Sand Capture in MFT above Beach Infill at Site 35 (from MRRT, 2002)

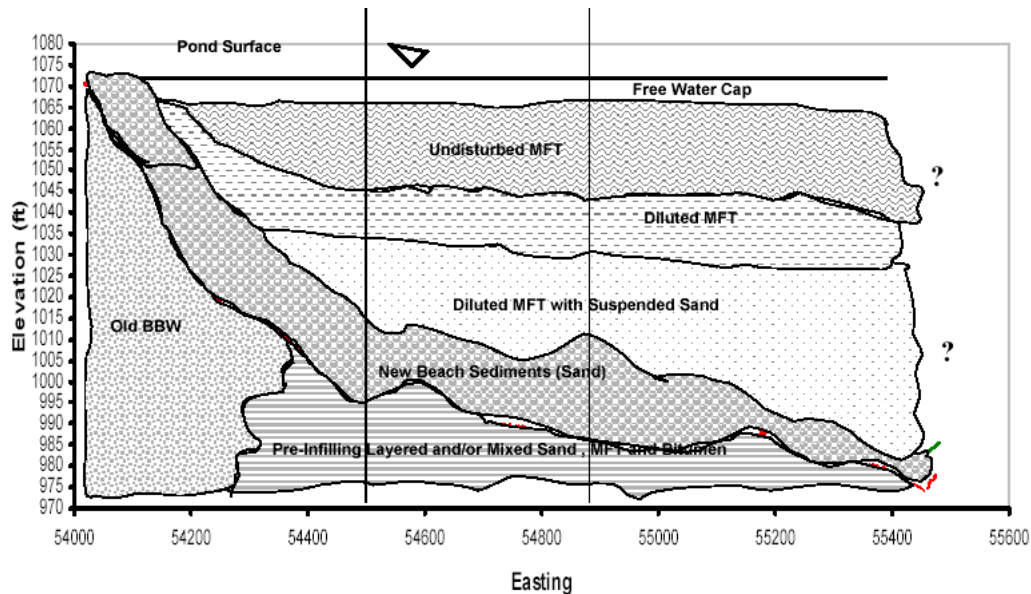


Figure 6.8 Post-Infilling Idealized Cross-Section Interpreted from 2 Sampling Sites (from MRRT, 2002)

### 6.3 Computational Fluid Dynamics Simulation

In this section, MFT is first treated as three phases with sand particles, clay particles and water. The true viscosity of 0.001 Pa.s is assigned to water phase. Following that, MFT is simplified as two phase mixture with sand particles dispersed in the clay-water medium. Finally, MFT is treated as three phases with sand, clay and water with MFT viscosity assigned to water phase.

#### 6.3.1 Three Phases for MFT

The problem to be modeled is simplified as deposition of sand into a pond in which 2 m clear water is underlain by 18 m mature fine tailings. Sand slurry composed of water and sand is pumped into the tailing pond. Since the distribution of sand particles into soft fine tailings is of interest in this simulation, multiphase simulation is necessary, in which transport equations are solved for each phases.

Based on the problem to be simulated, several choices can be made to model the deposition process. Mixture Model is the first choice because more than one continuous phase can be set in this model. Water and MFT are two continuous phases and sand particle is simulated as a dispersed solid phase in Mixture Model.

The second choice is Particle Model, in which one continuous phase can be assigned and unlimited number of dispersed phases can be set. If this model is used, water will be the only continuous phase and fine particle and sand particle will be the dispersed solid phases. Two size groups are divided using 44 micron as fine particle and coarse particle division.

In the following sections, the feasibility of the Particle Model is evaluated using two simplified tailing ponds: a cylinder and a frustum. Following that a combination of Mixture Model and Free Surface Model will be applied for the same domains. Comparison between the Particle Model and combined model is made and the main issues are discussed.

#### 6.3.1.1 Particle Model

In CFX 5, the user can assign a viscosity for the solid phase and the solid viscous shear stress will be calculated based on the viscosity and shear strain tensor of the solid phase. The solid pressure is modeled using Gidaspow model, in which the solid pressure is a function of solid volume fraction. It becomes large when the solid volume fraction approaches the maximum packing limit. Gidaspow drag model is used for momentum transfer between solid and liquid phase. Since MFT is composed of fine particles, coarse particles and water, three phases are modeled in the following simulations. Water is modeled as continuous liquid phase whereas clay and sand particles are modeled as disperse solid phases. The mean diameter of the clay is set to 22 micron and mean diameter of 150 micron is used for sand particles. The specific gravities of the sand and the clay particles are 2.7 and 2.6 respectively.

##### 6.3.1.1.1 Cylinder Domain

In the tailing ponds of Suncor, two to three meters of water caps on the top of MFT. In order to evaluate the movements of the sand particle in the mixture of water and MFT, a domain consisting of a cylinder with diameter of 20 meters and height of 20 meters (Figure 6.9) is modeled first. A tremie discharge pipe of 1 m diameter is located in the center of the top surface. In order to reduce the computing cost, it is assumed that the flow is axially symmetrical and a quarter of the cylinder is simulated. A tetrahedron mesh with 8,359 nodes (Figure 6.9) is used in the simulation. In order to

simplify the simulation, the domain is initially filled with 2 meters of water underlain by 18 meter of MFT. The grain size distribution of MFT shown in Figure 6.10 is adopted in the following simulations. In all the simulations in this section, MFT is assumed to contain 39w/w% of solids content and 92.5w/w% fines content. It is assumed that sand slurry with solids content of 60% and fines content of 1% is pumped into the cylinder at a speed of 0.25 m/s.

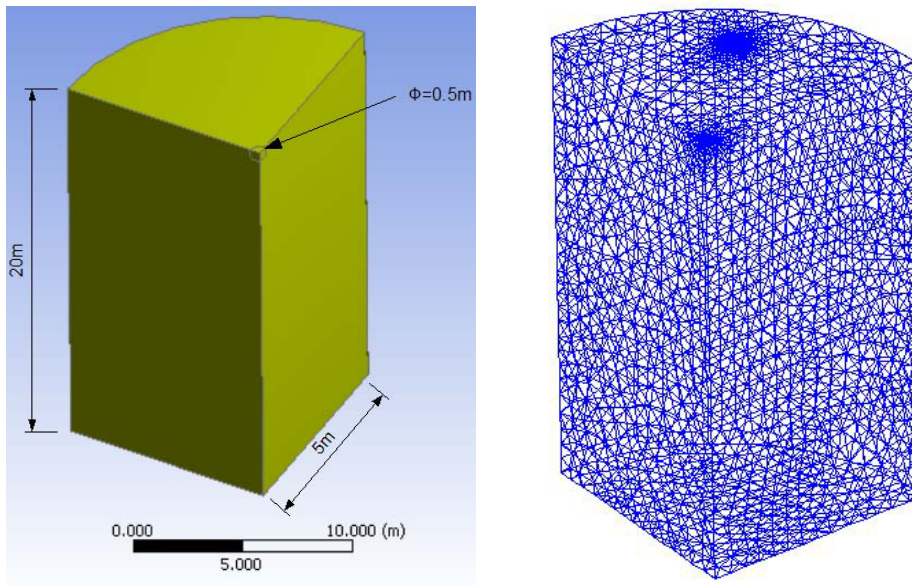


Figure 6.9 Dimension and grids of the cylinder

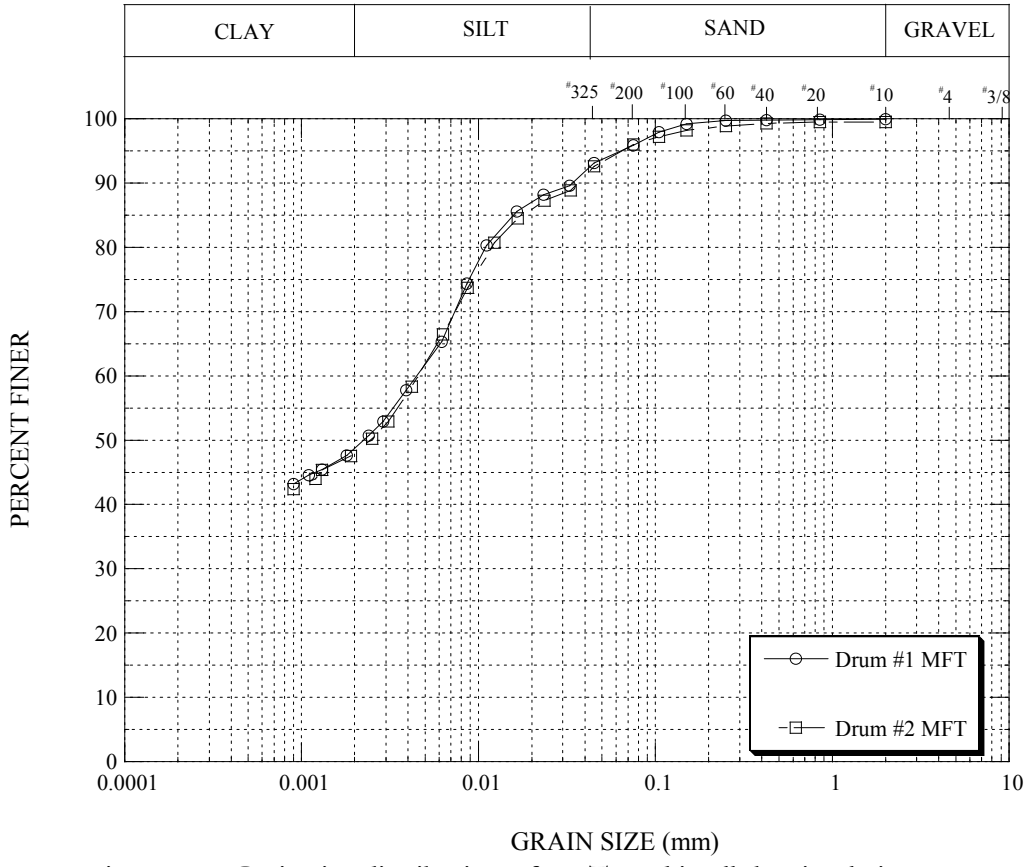
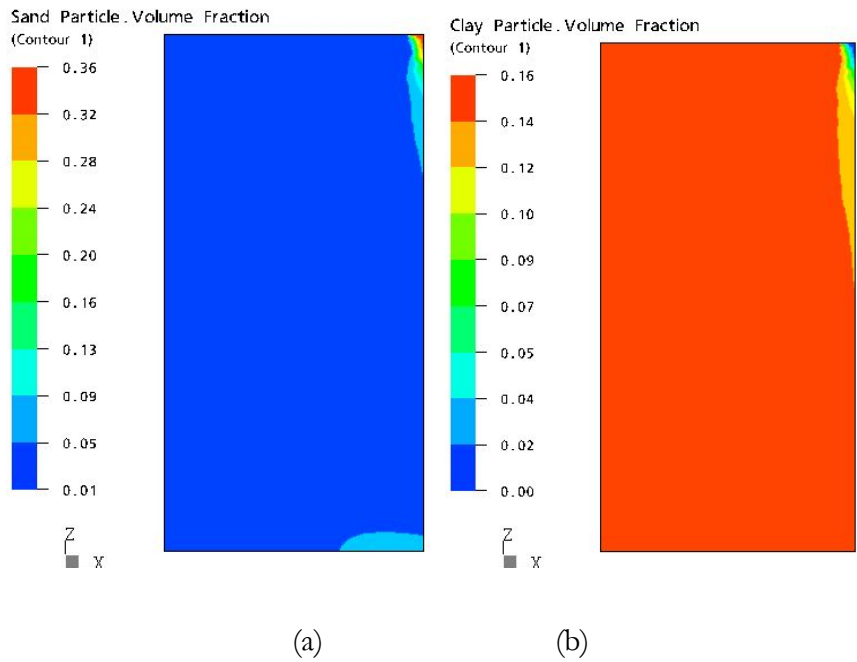


Figure 6.10 Grain size distribution of MFT used in all the simulations



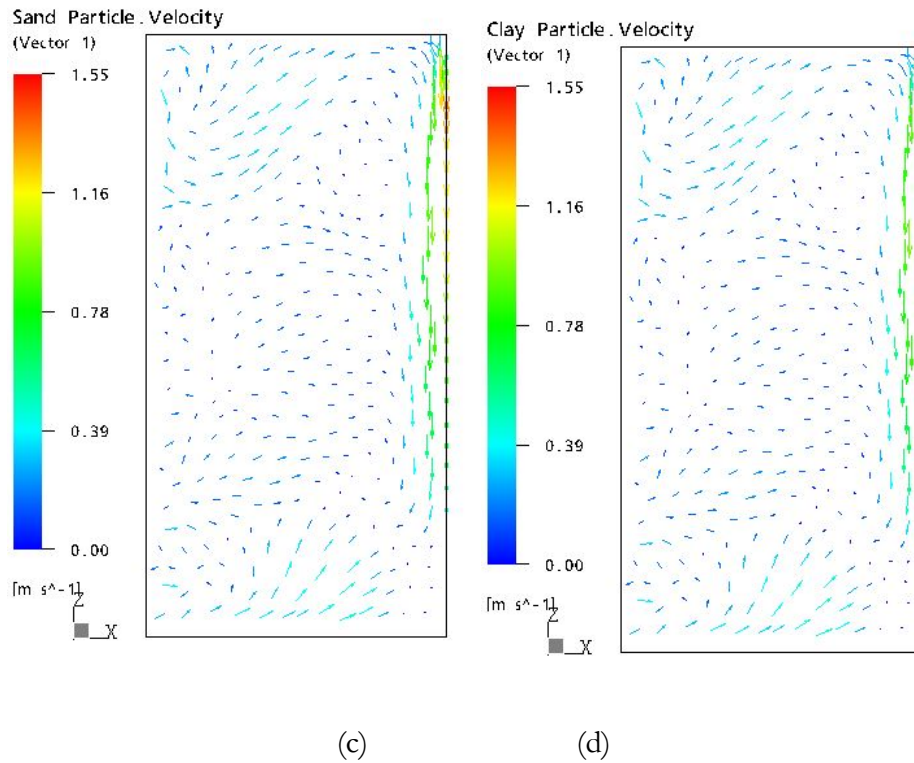


Figure 6.11 Volume fraction profile and velocity vectors for sand particles and clay particles using Particle Model. (a) volume fraction profile for sand particles; (b) volume fraction profile for clay particles; (c) velocity vector for sand particles; (d) the velocity vector for clay particle. All the profiles are drawn on the symmetry plane that passes through the tremie discharge pipe center. The profiles are snapshots taken at time of 1413.5 s.

The sand and clay volume fraction profiles on the symmetry plane passing through the tremie discharge pipe are shown in Figure 6.11 (Figure 6.11 (a) and (b)), which corresponds to the distribution of sand and clay at a time of 1413.5 s. Corresponding velocity vectors are shown in Figure 6.11 (c) and (d). It can be seen that sand flows almost vertically and fall to the base of the cylinder. Sand is accumulated at the base of the cylinder.

#### 6.3.1.1.2 Tailing Pond Domain

In order to evaluate the movement of particle on the slope, pumping sand slurry into a 20 m high tailing pond is simulated. The dimension and geometry of the pond are shown in Figure 6.12. In order to save CPU time, only a quarter of the body is modeled and the fluid field is assumed to be symmetrical about two vertical central

planes. A tetrahedron mesh with totally 24,809 nodes is used in the simulation (Figure 6.13). The same initial conditions as the previous simulation are applied here. The contours for volume fractions for sand particle, clay particles and release water at a time of 276 s are shown in Figure 6.14. It can be seen that the top surface water is replaced by underlying MFT, which consists of sand particles, clay particles and water. Meanwhile, sand slurry penetrates into the top surface water then into MFT and flows along the pond slope.

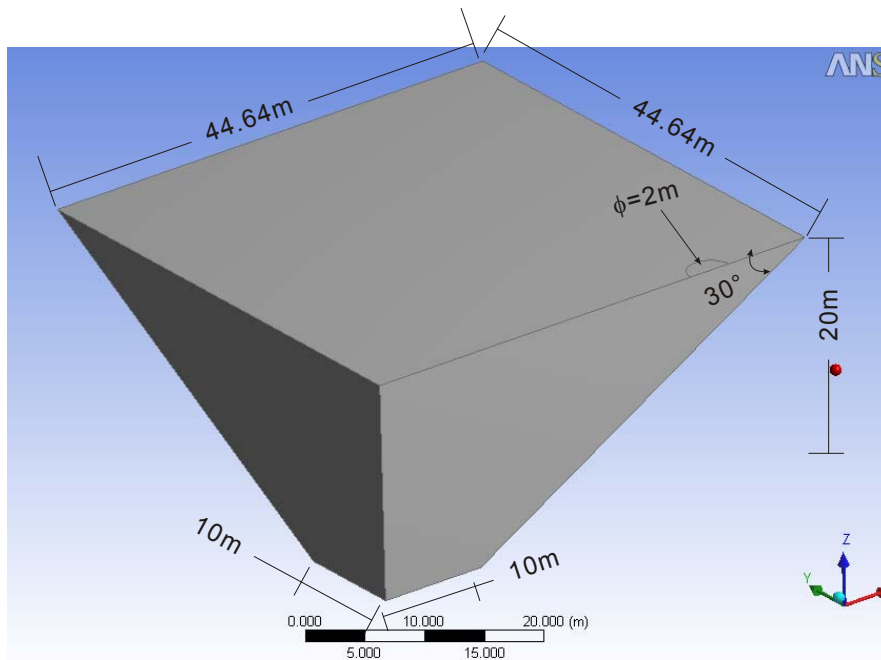


Figure 6.12 Geometry and dimension of the frustum domain

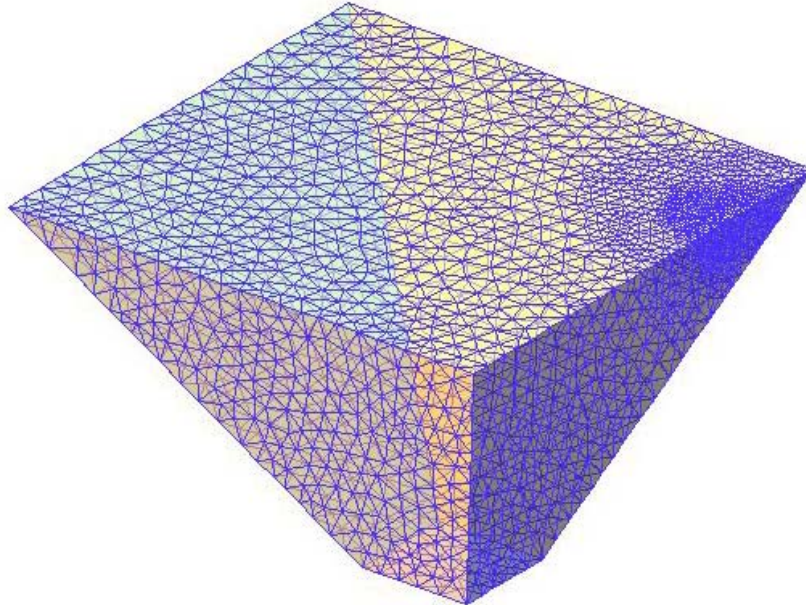
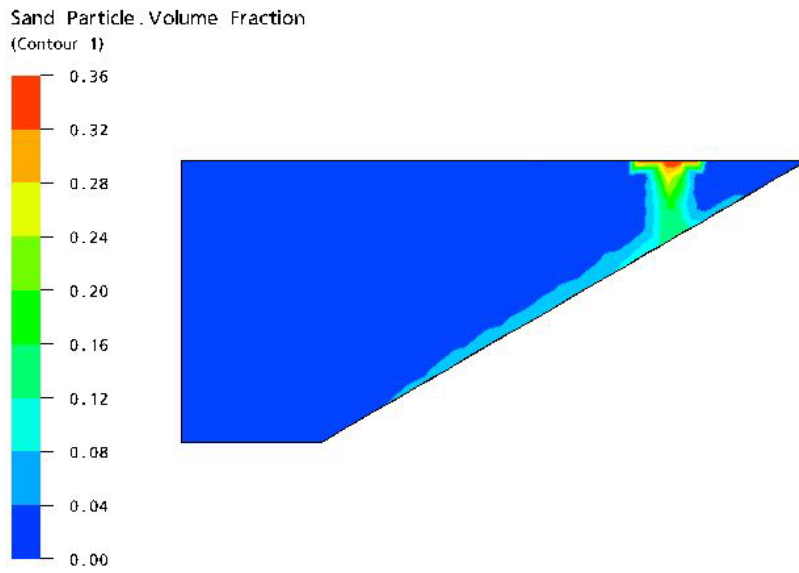
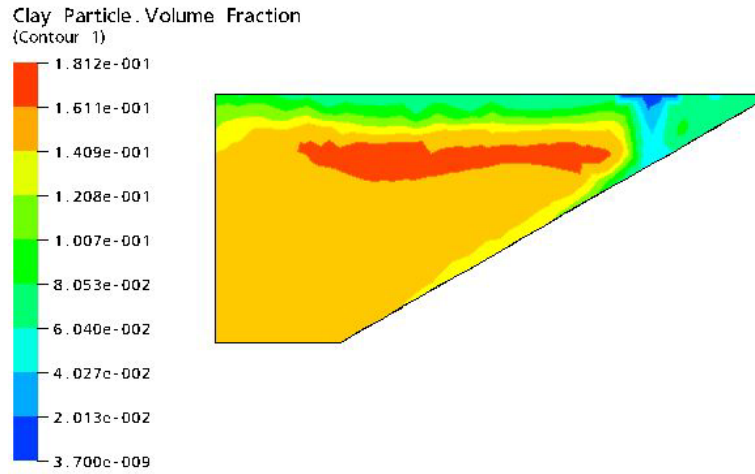


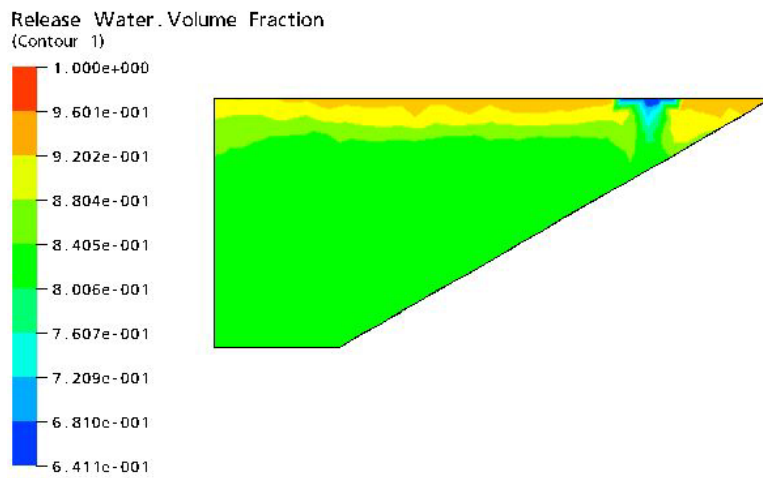
Figure 6.13 Grid of the frustum domain



(a)



(b)



(c)

Figure 6.14 Contours for volume fractions for sand particle, clay particles and release water at time of 276 second respectively: (a) Volume fraction contour for sand; (b) Volume fraction contour for clay; (c) Volume fraction contour for water.

### 6.3.1.2 Mixture Model

Pumping sand slurry into the frustum domain that is initially filled with release water and MFT can be simulated using a Mixture Model. Release water and MFT are simulated as continuous phases and sand particles are modeled as disperse solid phase. The momentum transfer between the two continuous phases is simulated using the Free Surface Model, whereas interactions between sand particles and either of the two continuous phases are simulated using Particle Model. The interface between release water and MFT is modeled using Free Surface Model.

#### 6.3.1.2.1 Cylinder Domain

The viscosity of the continuous phase has a significant effect on the momentum transfer between disperse particle phase and continuous phase, which can be seen from the drag coefficient for the Particle Model. It is known that the MFT possesses complex rheological properties (FTFC, 1995) and it is thixotropic, having yield stress and it is also shear thinning. Figure 6.15 represented the effect of sample handling on the yield stress and thixotropy of MFT. A measurement of yield stress for MFT is carried out at University of Alberta using BrookField R/S SST2000 Soft Solid Tester. In this simulation, the Herschel and Bulkley model in the form of  $\tau = \tau_c + K\dot{\gamma}^n$  was used. In the simulation,  $K$  is set to  $0.02 \text{ Pa}\cdot\text{s}^n$  and  $n$  is 1.25. The yield stress  $\tau_c$  is set to  $27 \text{ Pa}$ .

It is assumed that the sand slurry is pumped at a speed of  $0.25 \text{ m/s}$  into the cylinder. The volume fractions of MFT, release water and sand particle are 0.007, 0.639 and 0.354 respectively, which is equivalent to sand slurry with 60 w/w % of solids content and 1 w/w% of fines content. The initial 2 m of water is placed on the top of MFT. The time step is set to 1 second and transient simulation is carried out. The volume fraction profiles of MFT, release water and sand particle at time of 146 second are shown in Figure 6.18 to Figure 6.18. It can be observed that the sand slurry displaces MFT and the settling of the sand slurry is retarded by the MFT.

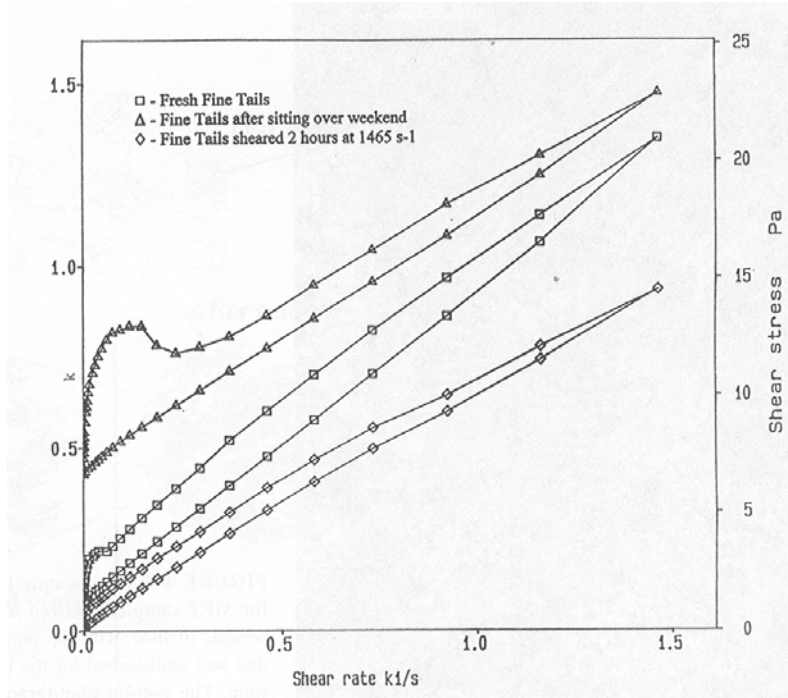


Figure 6.15 Viscosity and Yield Stress of MFT (From FTFC 1995)

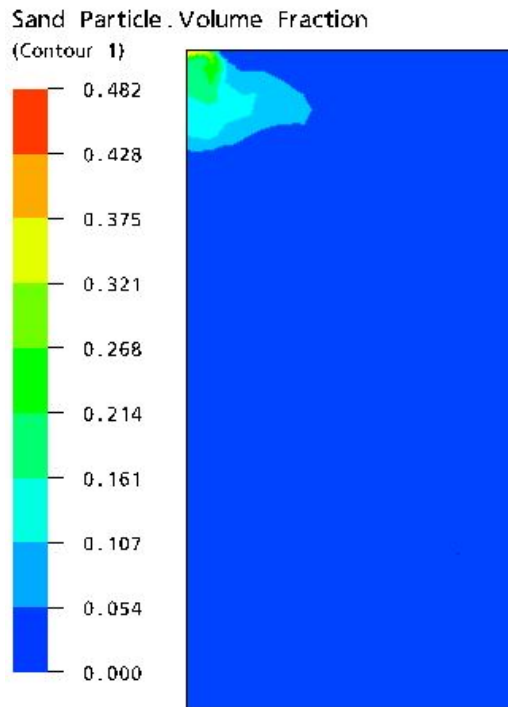


Figure 6.16 Contours of volume fraction for sand particles at time of 146 s for Cylinder domain

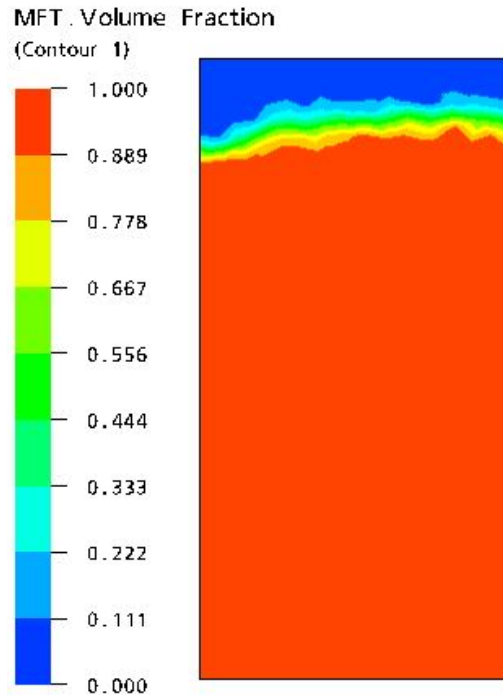


Figure 6.17 Contours of volume fraction MFT at time of 146 s for Cylinder domain

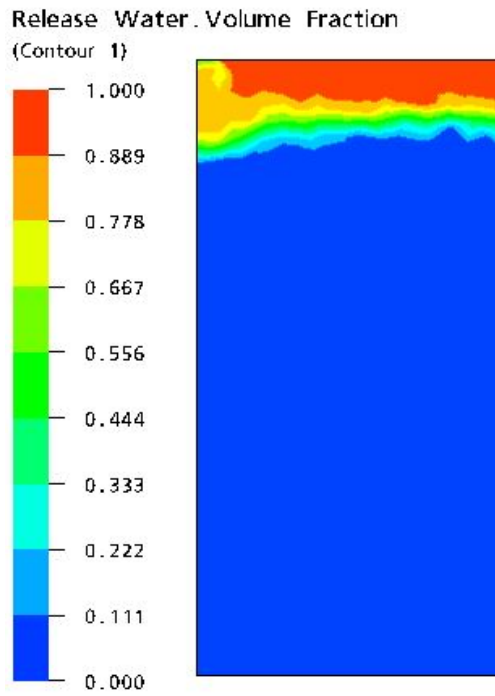


Figure 6.18 Contours of volume fraction of release water at time of 146 s for Cylinder domain

### 6.3.1.2.2 Frustum Domain

Similar boundary conditions and initial conditions to the simulation in Section 3.2 are applied here. Sand slurry is pumped into the pond at a speed of 0.25 m/s. The volume fraction profiles for sand particles, MFT and water at the time of 276 second are shown in Figure 6.20 to Figure 6.21. The sand particle volume fraction profile at the time of 476.5 second is shown in Figure 6.22.

From Figure 6.20 it can be seen that sand slurry is upheld by MFT which possess a yield stress and higher viscosity. This effect is more apparent at the time of 476.5 second, which is demonstrated in Figure 6.22. Figure 6.20 and Figure 6.21 demonstrate that the MFT is displaced by the incoming sand slurry. MFT prevents the sand slurry from flowing along the pond slope due to the yield stress effect of MFT.

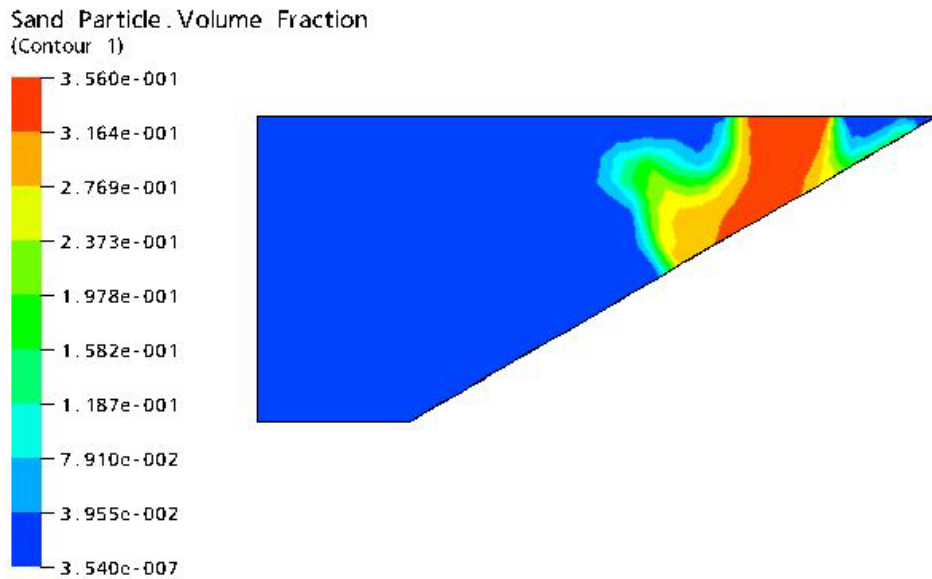


Figure 6.19 Contours of volume fraction of sand particles at time of 276.5 second for Frustum Domain

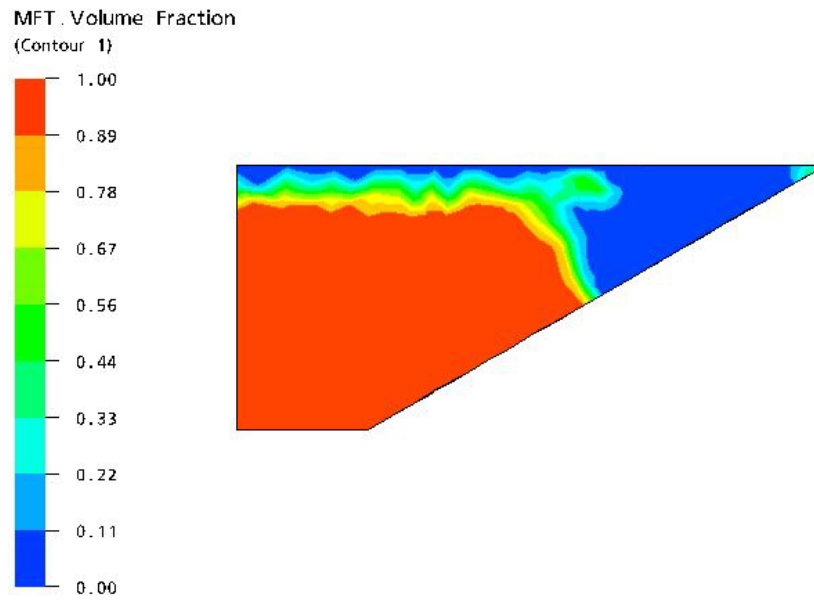


Figure 6.20 Contours of volume fraction of MFT at time of 276.5 second for Frustum Domain

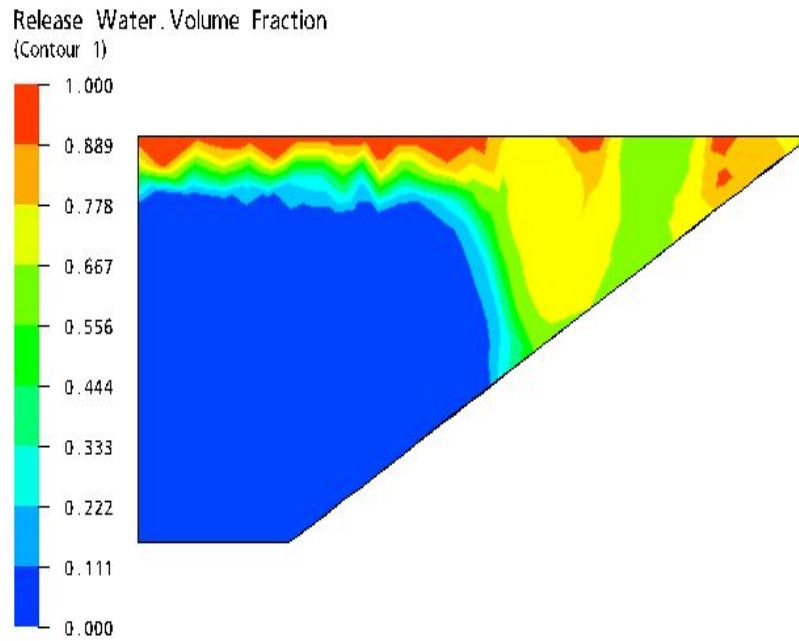


Figure 6.21 Contour of volume fraction for release water at time of 276.5 second for Frustum Domain

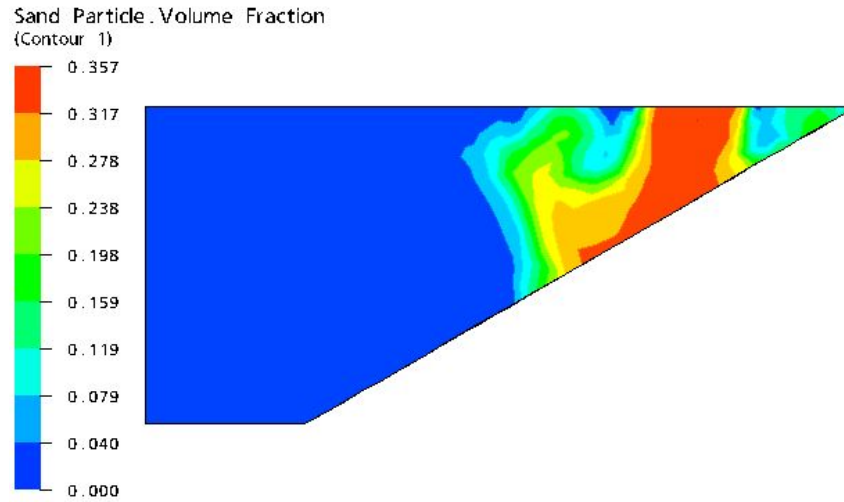


Figure 6.22 Contour of volume fraction for sand particle at time of 476.5 second for Frustum Domain

#### 6.3.1.2.3 Simulation of Deposition of Sand into Release Water

Since sand slurry is upheld by MFT in the above simulation, the effects of the viscosity of MFT on the sand slurry flow can be evaluated by comparing the sand flow in water with the sand slurry flow in MFT. In this simulation the sand particles are pumped at a speed of 0.25 m/s into a pond filled with release water. The simulation results are shown in Figure 6.23. It can be observed that the sand particles follow along the slope, which is opposite to what is observed in the previous simulation of MFT pond.

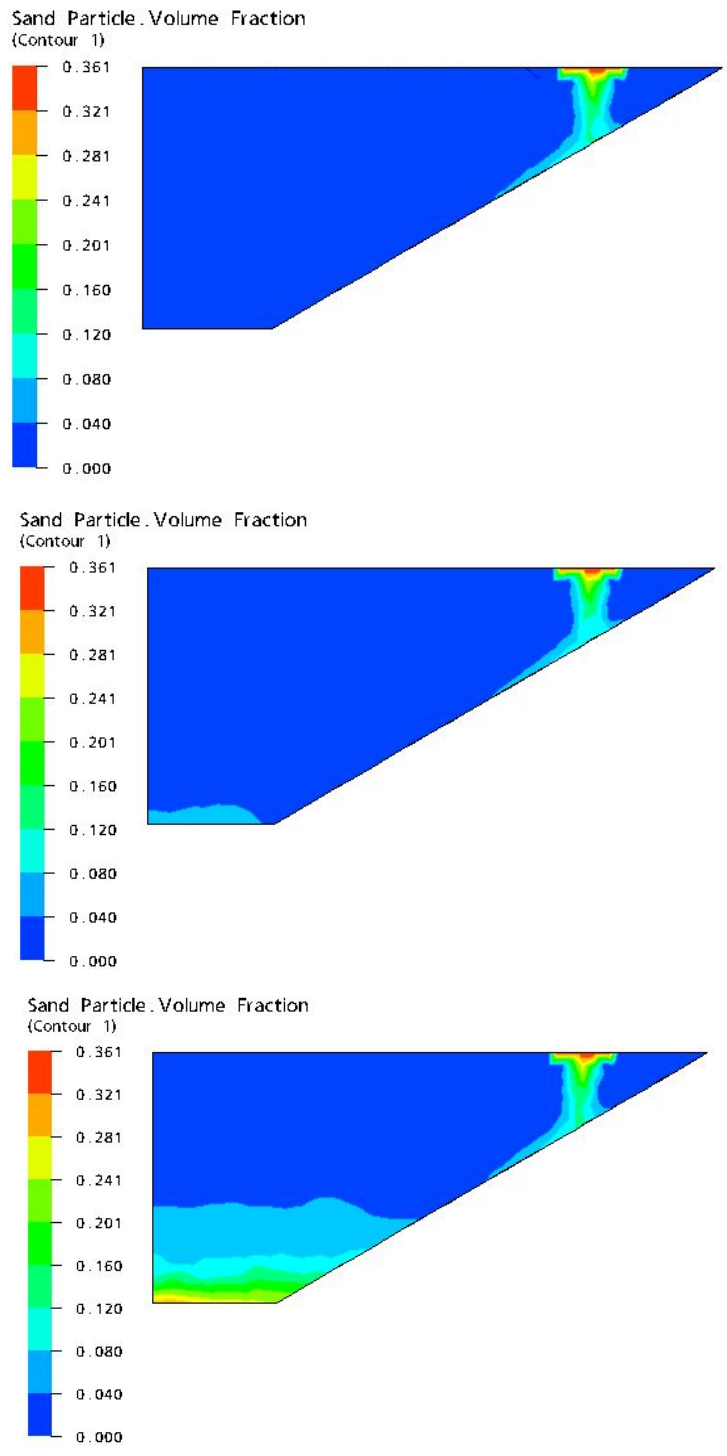


Figure 6.23 Sand particle distributions at time of 50.2, 150.2 and 497.2 second respectively (from top to bottom) for Frustum Domain

### 6.3.2 Two Phases for MFT Using Particle Model

The segregation simulation in Chapter 2 indicates that non-segregating behavior of the tailing slurry can be achieved by considering MFT as a mixture of sand particles with clay-water suspension. This subsection presents the simulation results using two phase Particle Model to simulate the infilling of tailing sand into MFT ponds in a two-dimension domain. The geometry of the simplified 2-D tailing pond is shown in Figure 6.24. The slope of the tailing pond wall is assumed to be  $30^\circ$  and the length of the tailing pond bottom is assumed to be 10 m. The depth of the pond is 10 m. The inlet of the tailing pond is 2 m wide and the left corner of the inlet is 4 m from the upper left corner of the domain.

It is assumed that the MFT contains 50% solids content and 95% fines content. The density of the MFT is assumed to be  $1338 \text{ kg/m}^3$ . The Herschel-Bulkley model for the viscosity of the MFT is assumed in the simulation. The parameters of the Herschel-Bulkley are the same as those used in the viscometer and rheometer tests in Chapter 3, which are shown in Table 3.18. However, the maximum of the dynamic viscosity is set to 50 Pa.s for the MFT in order for the simulation to converge.

It is also assumed that the sand slurry flows at a velocity of 0.25 m/s into the tailing pond. The volume fraction of the sand particles and MFT flowing into the tailing pond are 0.16 and 0.84 respectively. As the density of the sand particles is assumed to be  $2700 \text{ kg/m}^3$  and that of MFT is  $1338 \text{ kg/m}^3$ , the solids content and fines content of the inflow are 64% and 54% respectively, if solids content of 50% and fines content of 95% for the MFT are considered.

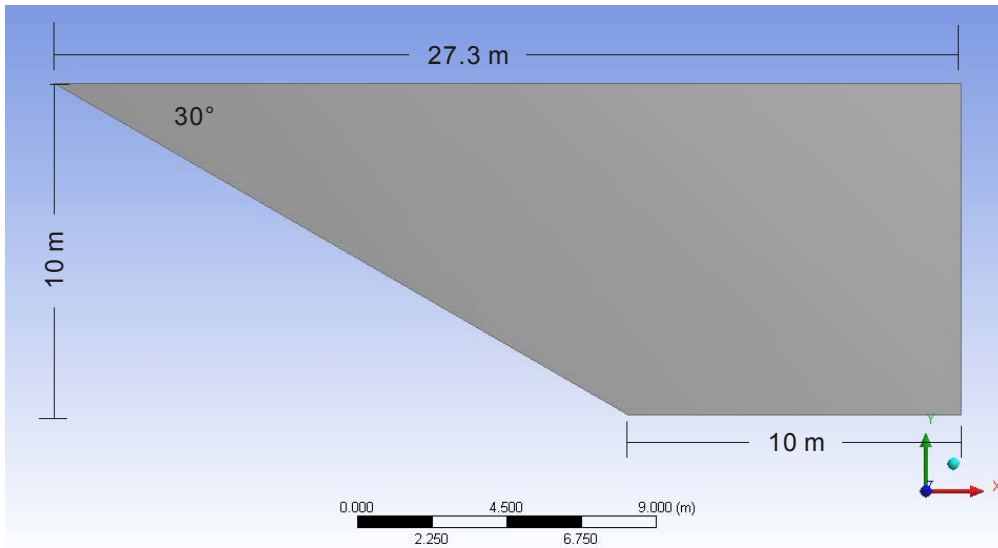


Figure 6.24 Geometry and Dimension of the 2-D Frustum Domain

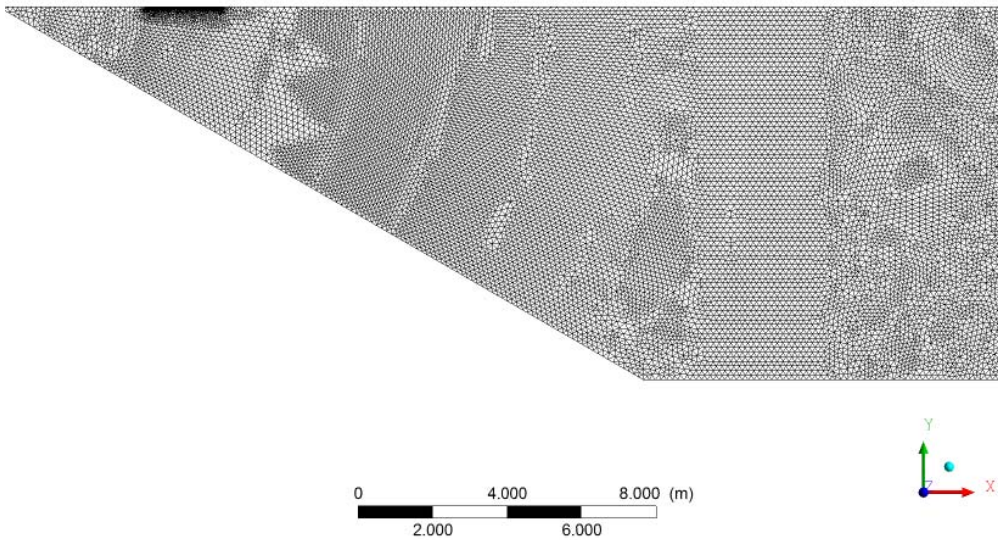


Figure 6.25 2D Grid for Frustum Domain(27,078 nodes)

The grid used in the simulation is shown in Figure 6.25. Totally 27,078 nodes are generated for the grid. The Mass and Momentum option is chosen for the Inlet boundary condition. The Free-Slip Wall boundary condition is assigned to the top

surface. The right vertical surface is assigned as Outlet boundary condition, with the condition of the mass flow equal to the mass flow at the Inlet boundary.

The sand volume fraction profiles at the time from 10 seconds to 68 seconds are shown in Figure 6.26 to Figure 6.28. The velocity vectors for the sand particles are shown in Figure 6.29 to Figure 6.31. These figures show that the sand particles are seized by MFT for first. As the sand particles accumulate in the MFT, they flow along the tailings pond slope and deposit on the bottom of the pond. Comparing with the results presented in Section 6.3.1, the simulation results in this section approximately match the post-infilling idealized cross-section shown in Figure 6.8.

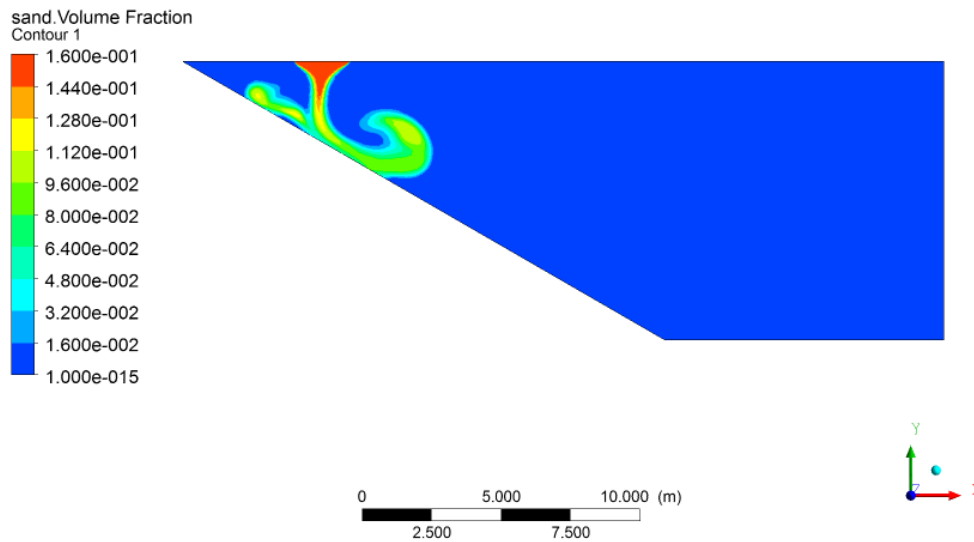


Figure 6.26 Sand Volume Fraction at Time of 10 Seconds

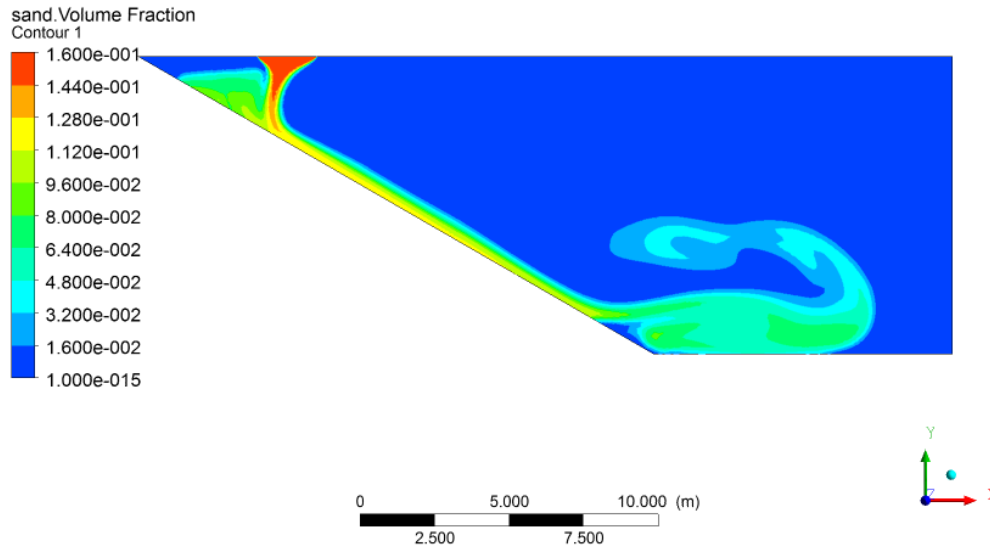


Figure 6.27 Sand Volume Fraction at Time of 30 Seconds

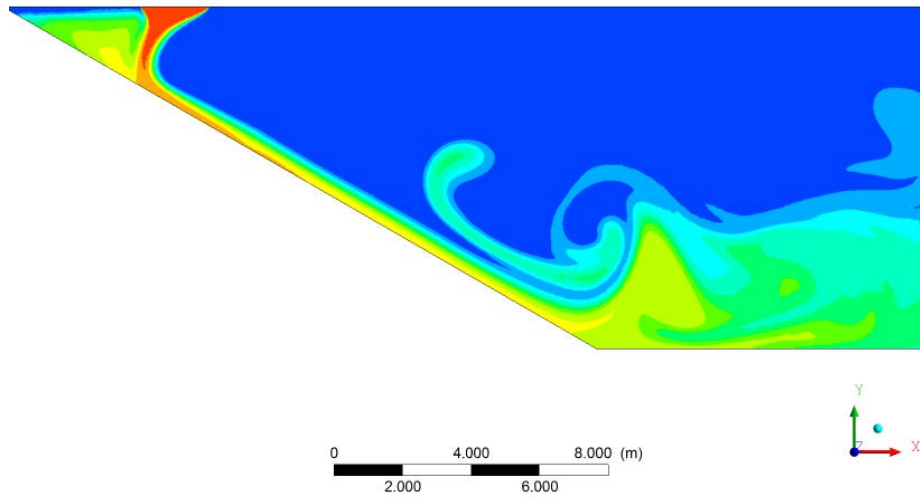


Figure 6.28 Sand Volume Fraction at Time of 68 Seconds

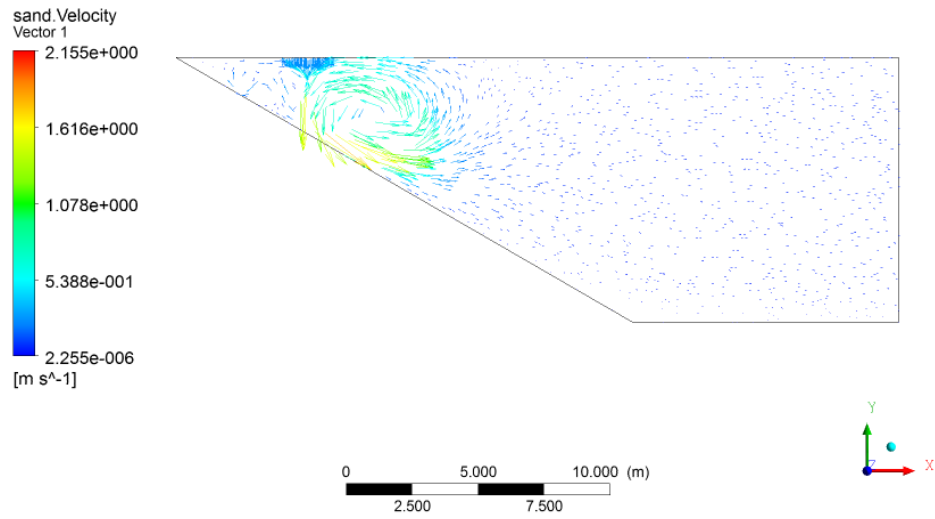


Figure 6.29 Sand Velocity Vector at Time of 10 Seconds

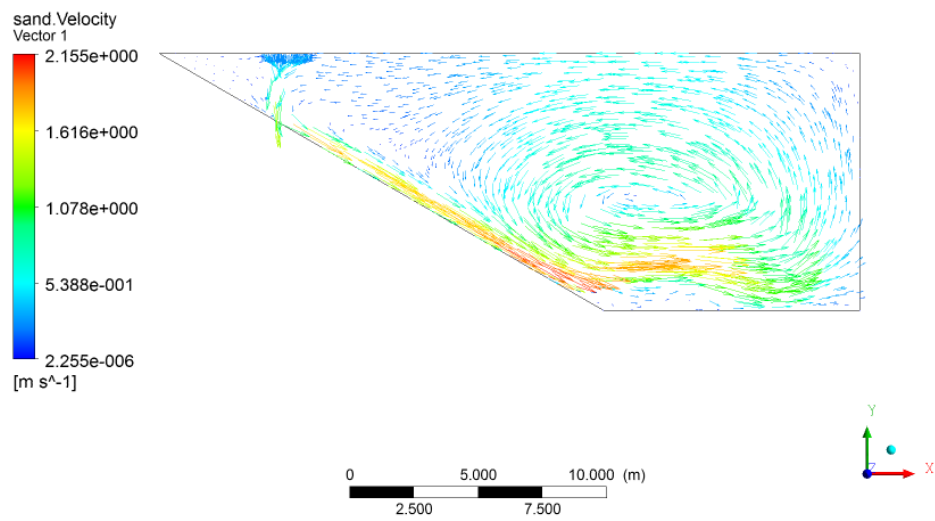


Figure 6.30 Sand Velocity Vector at Time of 30 Seconds

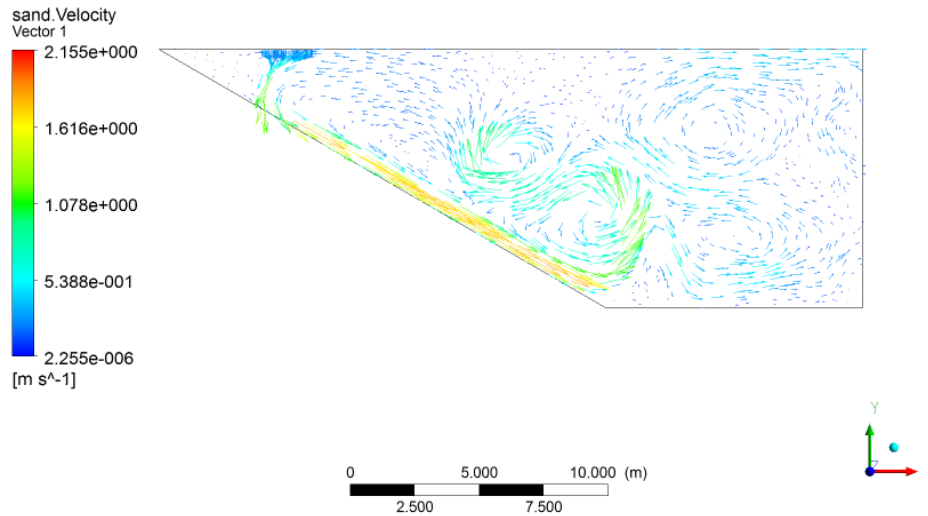


Figure 6.31 Sand Velocity Vector at Time of 68 Seconds

## 6.4 Conclusions

1. If the tailing slurry is considered to be composed of sand particles, clay particles and release water, segregation always occurs for non-segregation mixture in the simulation using the Particle Model if the true water viscosity and density are assigned to the water phase. In addition, due to the lack of sufficient size groups to account for the effect of particle size distribution, the influence of the addition of solid particle into the fluid on the viscosity of suspension medium is not considered in the three phase model where water phase has a viscosity of 0.001 Pa.s. In these simulation cases, the sand particles flow along the slope wall of the simplified tailing pond and settle at the bottom of the pond.
2. One solution is to use Mixture Model, where MFT is treated as one phase and the consideration of the interactions between clay particles and water is not required. By assigning a yield stress to MFT, the sand particles are retained by the MFT in the simulation.
3. The further simplified model is the two phase Particle Model. In this model, the two meter clear water in the tailing pond is not modeled which eliminates the consideration of the water-clay interactions. It is assumed that sand particles and

- MFT are the only components of the coarse tailing slurry and the original tailing pond is filled with MFT. A Herschel-Bulkley model is assigned to the MFT in the simulation. It is found that this simulation more approximately matches the interpreted cross-section from two sampling sites conducted at Suncor Pond 1 during the field test.
4. However, none of the above simulations is completely satisfactory from the perspective of physics. In the Particle Models the effects of size distribution and viscosity of the suspension are not accounted for which is of importance to the settling characteristics of the sand in MFT. As for the Mixture Model, shear-thinning properties for the MFT is obtained from the viscosity measurements. However, there is a lack of model that is capable of describing the shear-thinning viscosity model whose parameters are also a function of solids content and fines content. The difficulty lies in that the parameters in either Herschel-Bulkley model or Power Law model is not a simple function of solids and fines contents which is described in Section 3.1.4.2.5.

## Reference

- AMEC, Pond 1 Decommissioning December 2001 Progress Report, submitted to Suncor Energy OSG, Fort McMurray, Alberta, December 2001.
- CFX Ltd. 2003. Particle Transport Theory, CFX-5 Solver Theory, p. 148-155.
- FTFC (Fine Tailings Fundamentals Consortium), 1995. Volume 1, Fundamental Properties of Fine Tailings, Advances in Oil Sands Tailing Research, Alberta Department of Energy, Oil Sand and Research Division.
- Gidaspow, D, 1994. Multiphase Flow and Fluidization, Academic Press.
- Morgenstern, N.R. and Scott, J.D., 1995. Geotechnics of Fine Tailings Management. GeoEnvironment 2000, ASCE Special Conference, 46(2)1663-1683. New Orleans, USA.
- MRRT (McMurray Resources (Research & Testing) Ltd.), 2001 Pond 1 Tailings Investigation report, prepared for Suncor Energy OSG. February 14, 2002.

## CHAPTER 7 SUMMARIES, CONCLUSIONS AND RECOMMENDATIONS

### 7.1 Summaries and Conclusions

#### 7.1.1 Rheological Properties of Oil Sand Tailings

Brookfield DV-II+ Programmable Viscometer is used to measure the viscosity of the oil sand tailings samples. The samples are prepared by mixing MFT, coarse sand and pond water in the specified proportion to achieve certain solids and fines contents. The flow curves demonstrate shear-thinning properties for all these samples, that is, viscosity decreases with the increasing shear strain rate.

Herschel-Bulkley model and Power Law model are used to fit the viscosity measurement data. It is found that the Power Law model is more appropriate to fit the relationship between shear stress and shear strain rate for the samples with a wide range of solids and fines contents.

The samples with either higher solids content or higher fines content are observed to have greater apparent viscosity. It is found that fines content affects the shear stress and consequently the apparent viscosities when the solids contents are similar. Fines content becomes a minor factor when a significant difference in solids content exists.

Brookfield R/S Soft Solid Rheometer is used to obtain the static yield stress. The peak value of the shear stress vs. time curve is determined to be the yield stress. Analysis of the variation of static yield stress with solids content and fines content indicates that the static yield stress increases with both solids and fines contents. At the same fines content, the static yield stress increases dramatically when the solids content approaches 60%. Likewise, the static yield stress increases with fines content at the similar solids content. Available data suggests that greater increases in yield stress result from the fines content for the mixture with higher solids content. The variation of yield stress with solids content for MFT is curve fitted using the equation (Eq. 3.10) that was proposed by Coussot (1997).

Herschel-Bulkley model obtained from curve fitting for MFT is used in the CFD simulations of the viscosity and yield stress measurements. Single phase model with non-Newtonian properties for MFT is used in the model. The simulated torques for the MFT reasonably agree with the measured torques from viscometer test using Brookfield DV-II+ Programmable Viscometer. The torque obtained from the simulation of the vane shear test is also consistent with that from the rheometer test using Brookfield R/S Soft Solid Rheometer. The simulation results indicate that the Herschel-Bulkley model is suitable for the MFT material. The assumptions made in vane shear tests are verified using CFD and it is found that these assumptions are generally true.

#### 7.1.2 CFD Simulation of Oil Sand Tailing Slurry Segregation

First, the sedimentation of the bidisperse and polydisperse suspensions from literature is validated using the Euler-Euler Model in MFX and FLUENT-6. The suspensions are composed of two or four sizes of solid particles and liquid. The sizes of these solid particles range from 125  $\mu\text{m}$  to 496  $\mu\text{m}$  and the sizes are uniform in each size group. The solids contents for the bidisperse and polydisperse suspension are 43% and 36% respectively. The simulated volume fraction profiles are compared with those reported in Burger et al. (2000). It is found that the simulated profiles reasonably agree with those obtained by Burger et al. using shock capturing numerical schemes. Since Burger et al. (2000) compared their simulation results with the results from measurements by Schneider et al. (1985) and Greenspan et al. (1982) and claimed that their simulation results agree with the experiment, it is concluded that the CFD tools are able to produce the similar results for the bidisperse and polydisperse suspensions.

A series of sensitivity tests are carried out numerically to verify the capability of Euler-Euler models in FLUENT and MFX and Particle Model in CFX in modeling the sedimentation process of oil sand tailing slurry. The oil sand tailings slurry is assumed to be composed of water and solid particles with grain sizes ranging from clay ( $< 2 \mu\text{m}$ ) to sand ( $> 75 \mu\text{m}$ ). The grain size has a continuous distribution and two discrete grain sizes are used to approximate the continuous distribution. Simulation results indicate that all these models are able to track the trend of the sedimentation process;

however, these models are not capable of tracking or predicting the real-time sedimentation process of the tailing slurry when the true viscosity of 0.001 Pa.s is assigned to the water phase.

Comparing the bidisperse or polydisperse suspension in the literature (Burger et al., 2000; Schneider et al., 1985; Greenspan et al., 1982) with the oil sand tailing slurry, three main differences exist. First, the bidisperse and polydisperse suspension in the literature do not contain colloidal particles, whereas the oil sands tailings include clay particles ( $< 2 \mu\text{m}$ ). Second, the suspension reported in the literature contains solid particles with discrete size distribution, while solid particles in oil sand tailings slurry have continuous size distribution. Third, the non-segregating slurry sample SB3 has 65% solids content while the suspensions reported in the literature have solids contents ranging from 37% to 43%. These CFD models are able to capture the time sequence of sedimentation process for suspensions with two or four sizes of non-colloidal solid particles with solids content of approximately 40% while they fail to track the settling process of oil sand tailings slurry. Logically, these differences contribute to the discrepancy.

A suspension containing two or four sizes of non-colloidal particles is modeled using CFD successfully by simulating each group of particles as a separate disperse phase. On the other hand, the continuous distribution of solid particles in oil tailing slurry is approximated using bidisperse suspension, which introduced significant errors no matter which method is used to calculate the effective particles size for each group.

The ultra-fine solid particles, bitumen and chemistry of the oil tailing slurry make oil sand tailing slurry unique in solid-liquid suspension. The electrostatic and steric effects in the fine tailings make the fine particles in tailing slurry difficult to settle under gravity (FTFC, 1995). Interactions between ultra-fine particles are not accounted for in any of these CFD models. Therefore, the uniqueness of the oil sand tailing slurry partially results in the failure of these models to capture the extremely slow process of the sedimentation of the dense tailing slurry.

Compared with segregation, non-segregation behavior of the solid-liquid system brings more challenges in the numerical simulations. The interactions between clay and clay as well between clay and water are critical to solution of this problem. One solution to this is to modify the suspending medium viscosity to reflect the influence of the interactions. Considering the clay-water as a single phase can be another way to overcome the complexity of the interactions.

#### 7.1.3 CFD Simulation of Flume Tests

The flume test conducted at the University of Alberta by Dr. Scott is modeled using Free Surface Model and Particle Model in CFX-10. Attempts are made to capture the advance of the slurry front and the profiles of solids and fines contents using the CFD method. It is found that the traveling speed of the slurry is faster than was measured in the laboratory tests. The solids and fines content profiles in the simulation do not match with those in the laboratory deposit. One of reasons is that the viscosity of the tailing slurry was not measured in the experiment and an approximate viscosity model is assigned for the MFT in the Free Surface Model. In Particle Model, assigning a viscosity value of 0.001 Pa.s for the fluid phase water does not account for the interactions between coarse and fine particles, thus the hindered settling of the coarse particles in the suspension of water and fine particles.

The Particle Model with MFT viscosity assigned for the water phase is also used in the simulation of the flume Test 3. It is observed that the travel speed of the deposit is significantly slower in the Particle Model with MFT viscosity for the water phase than that with the viscosity value of 0.001 Pa.s for the water. It is also seen that the depth of the deposit is greater than that obtained from the experiment although the shape of the deposit in the simulation generally follows that obtained from the experiment.

#### 7.1.4 CFD Simulation of Oil Sand Deposition into MFT Pond

If the tailing slurry is considered to be composed of sand particles, clay particles and release water, segregation always occurs for non-segregation mixture in the simulation using the Particle Model when the true water viscosity and density are assigned to the water phase. In addition, due to the lack of sufficient size groups to account for the

effect of particle size distribution, the influence of the addition of solid particle into the fluid on the viscosity of suspension medium is not considered in the three phase model where water phase has a viscosity of 0.001 Pa.s. In these simulation cases, the sand particles flow along the slope wall of the simplified tailing pond and settle at the bottom of the pond.

One solution is to use Mixture Model, where MFT is treated as one phase and the consideration of the interactions between clay particles and water is not required. By assigning a yield stress to MFT, the sand particles are retained by the MFT in the simulation.

The further simplified model is the two phase Particle Model. In this model, the two meter clear water in the tailing pond is not modeled which eliminates the requirement of the water phase and the water-clay interactions. It is assumed that sand particles and MFT are the only components of the coarse tailing slurry and the original tailing pond is filled with MFT. A Herschel-Bulkley model can be assigned to the MFT in the simulation. It is found that this simulation is more approximately in agreement with the interpreted cross-section from two sampling sites conducted at Suncor Pond 1 during the field test.

However, none of the above simulations is completely satisfactory from the perspective of physics. In the Particle Models the effects of size distribution and viscosity of the suspension are not accounted for which is of importance to the settling characteristics of the sand in MFT. As for the Mixture Model, shear-thinning properties for the MFT are obtained from the viscosity measurements. There is a lack of model that is capable of describing the shear-thinning viscosity model whose parameters are also a function of solids content and fines content. The difficulty lies in that the parameters in either Herschel-Bulkley model or Power Law model is not a simple function of solids and fines contents, which is described in Section 3.1.4.2.5.

## 7.2 Recommendations

All the simulations in this thesis use the Eulerian-Eulerian method, which is suitable for the multiphase flow where the solid volume fraction is high. The suitability of the Eulerian-Lagrangian method in modeling the concentrated tailing slurry flow needs to be explored.

All the models in this thesis do not incorporate the interactions between colloidal particles and the interactions between water and colloidal particles. Those actions significantly influence the settlement and segregation behavior of tailing slurry in the quasi-static status. Incorporating these interactions into the momentum equations requires further research. In addition, the effects of bitumen content on the sedimentation and segregation behavior of tailing slurry needs to be investigated.

As inertial contribution to the momentum equation is minor, other contributions from the particle-particle interactions may dominate the movement of the solid particles. As a result, the influence of the interactions between smaller particles including colloidal particles, and the interactions between those particles and fluid media, on the sedimentation and segregation of the oil sand tailings are significant. Research is needed to bring these factors into the momentum equations and to study their effects on the behavior of oil sands tailings.

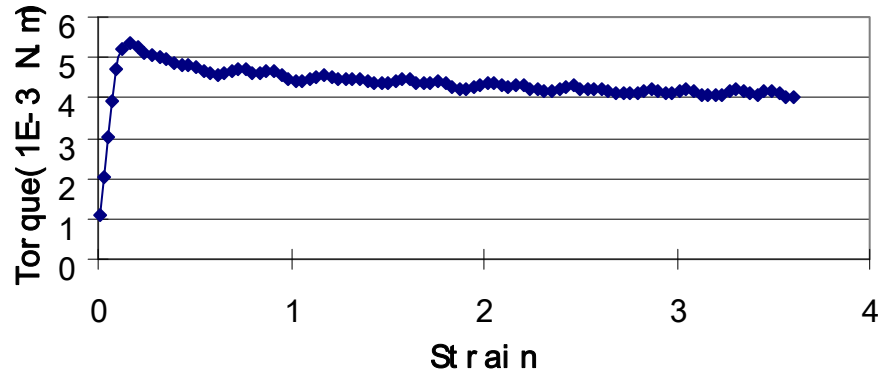
Modeling the sedimentation and segregation behavior of slurry with continuous distribution of particle sizes is challenging. One challenge is the lack of high quality experimental data with respect to the velocities, volume fraction of the sand and clay particles when the sand slurry is injected into MFT. Experiment program is required to characterize the flow field of tailing slurry with many size groups rather than simply measuring the solids and fines content profiles at the end of the experiments.

More research is also required to develop the viscosity model that is capable of modeling the shear-thinning properties and the variation of the viscosity with both solids and fines contents.

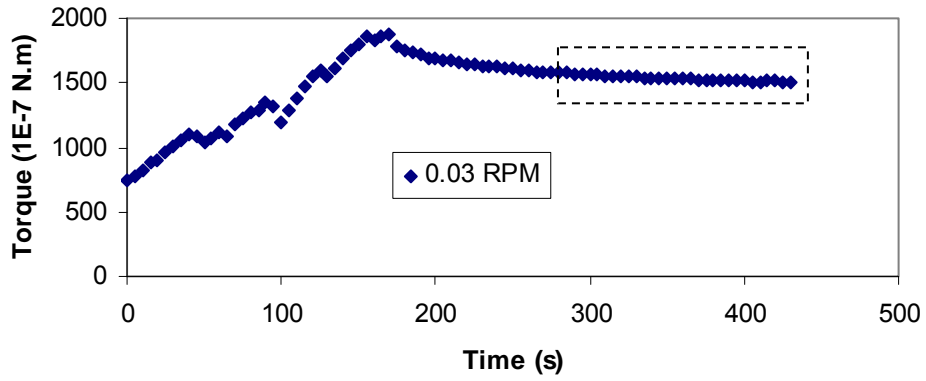
## Reference

- Burger, R., Concha, F., Fjelde, K.K., Karlsen, K.H., Numerical simulation of settling of polydisperse suspension of spheres. *Powder Technology*, vol. 113, pp. 30-54, 2000.
- Coussot, P., *Mudflow Rheology and Dynamics*. International Association for Hydraulic Research, A.A.Balkema Publishers, Brookfield, USA., 1997.
- FTFC (Fine Tailings Fundamental Consortium), 1995. Vol. 1, Section 2.5.4 Effect of Surfactants on Tailing Behavior. In: *Advances in Oil Sands Tailings Research*, Alberta Department of Energy, Oil Sands and Research Division.
- Greenspan, H.P. and Ungarish, M. On hindered settling of particles of different sizes. *Int. J. Multiphase Flow*, vol. 8, pp. 587-604, 1982.
- Schneider, W., Anestis, G., Schaflinger, U. Sediment composition due to settling of particles of different sizes, *Int. J. Multiphase Flow*, vol. 11, pp. 419-423, 1985.

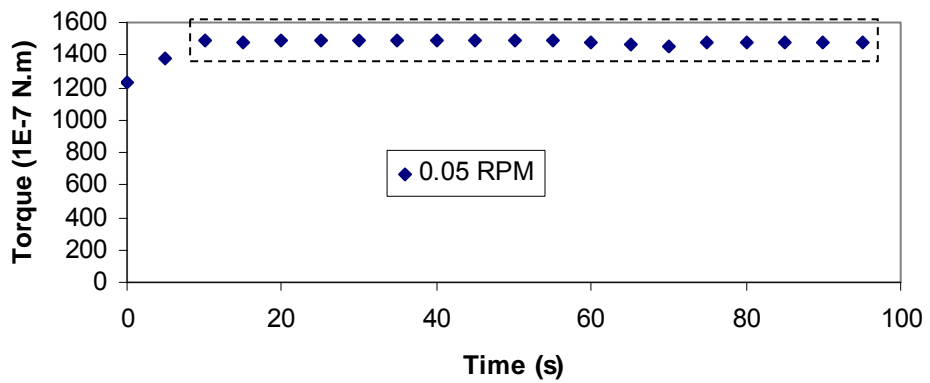
Appendix A: Raw Data for Viscosity Measurement for Tailing Slurry



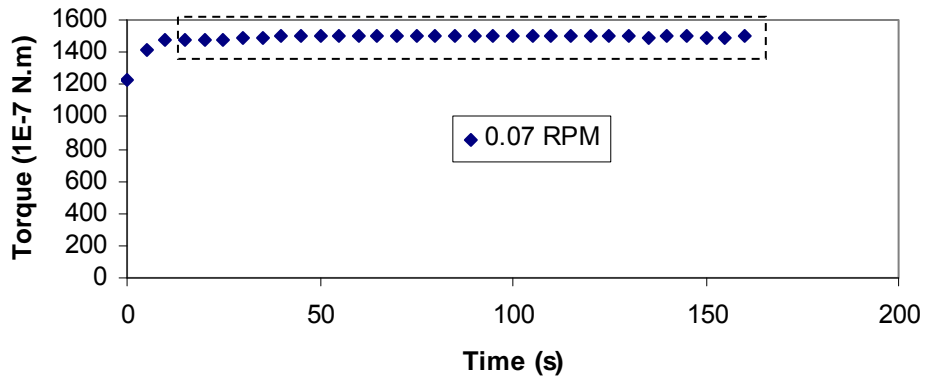
(a)



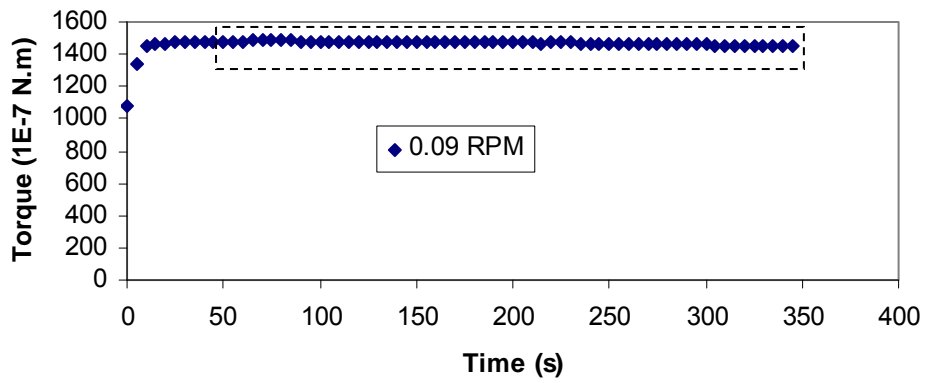
(b)



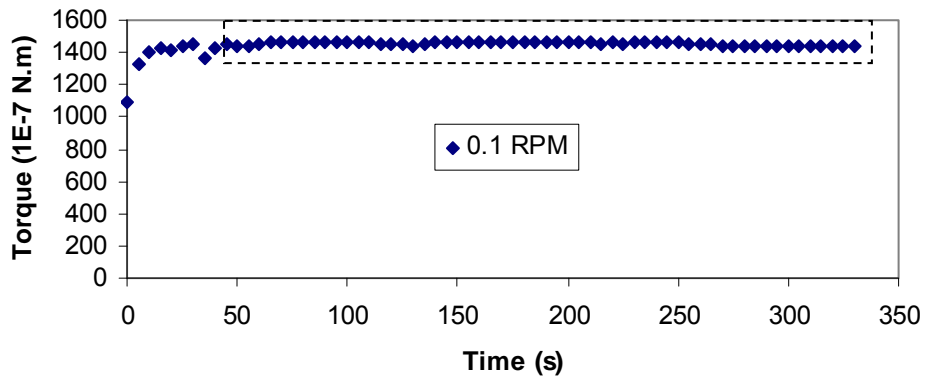
(c)



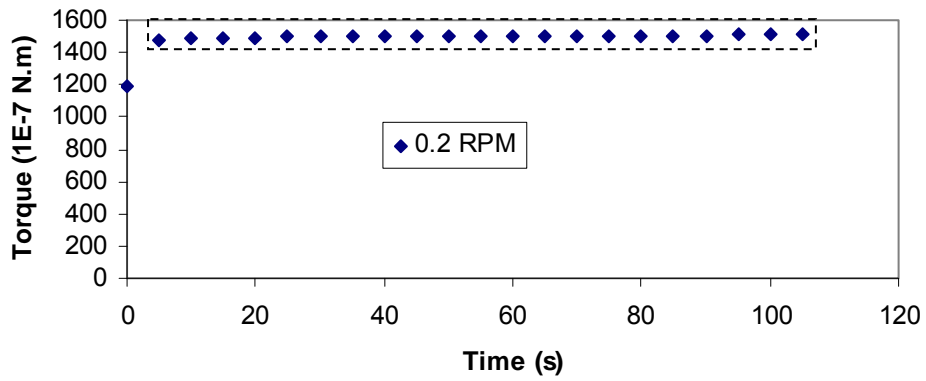
(d)



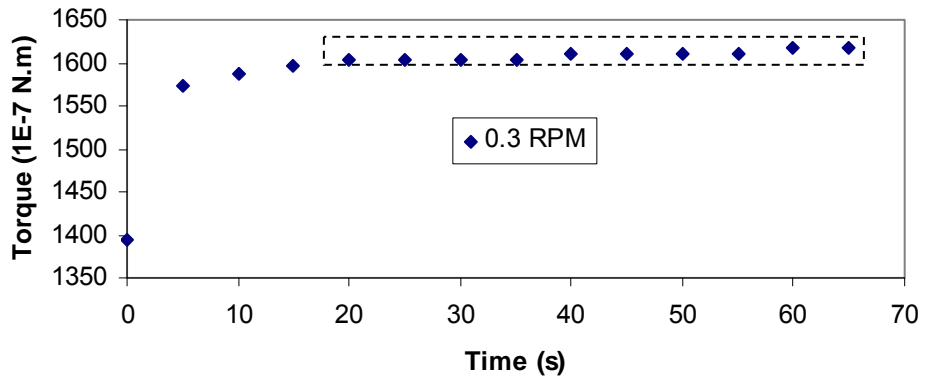
(e)



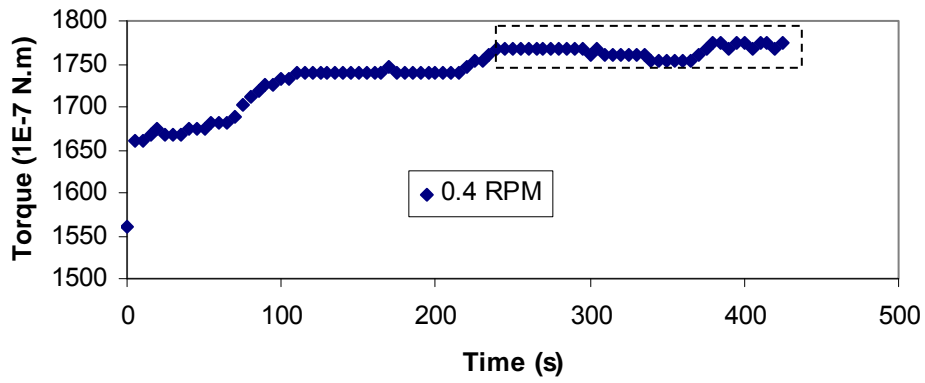
(f)



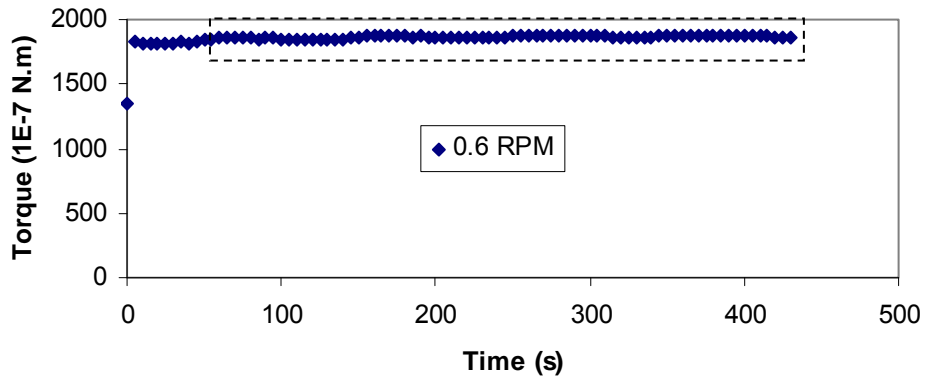
(g)



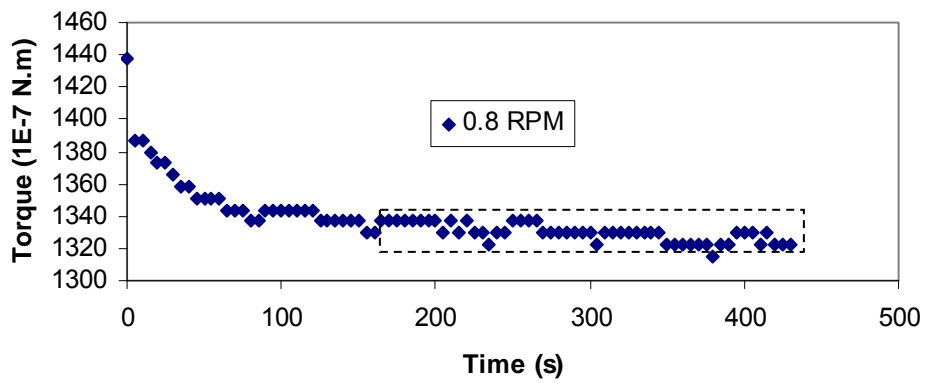
(h)



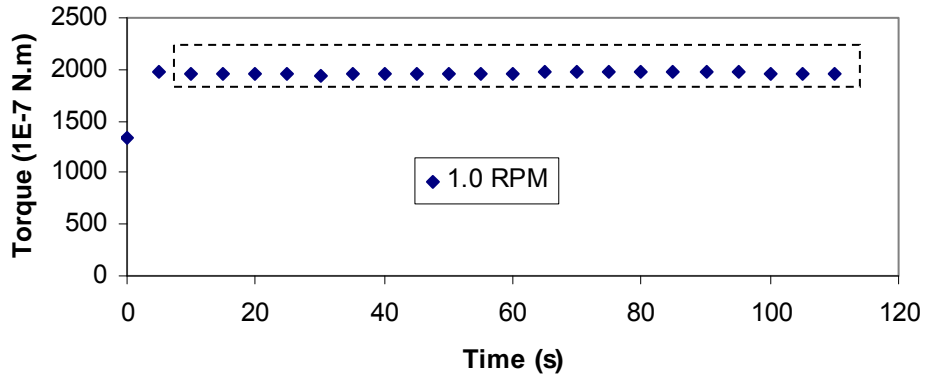
(i)



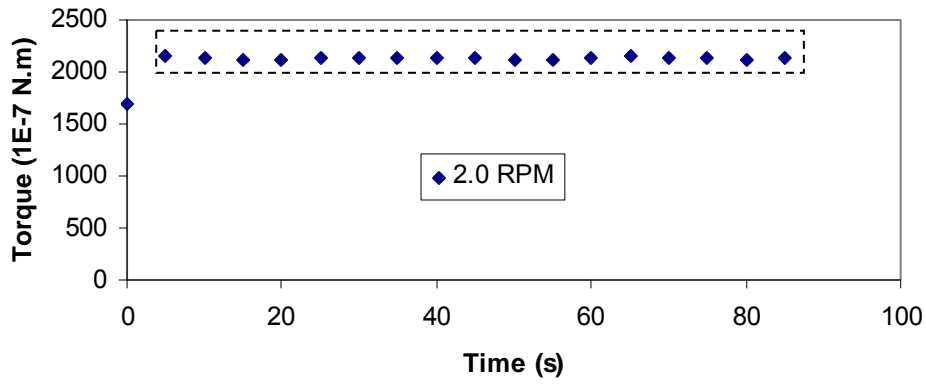
(j)



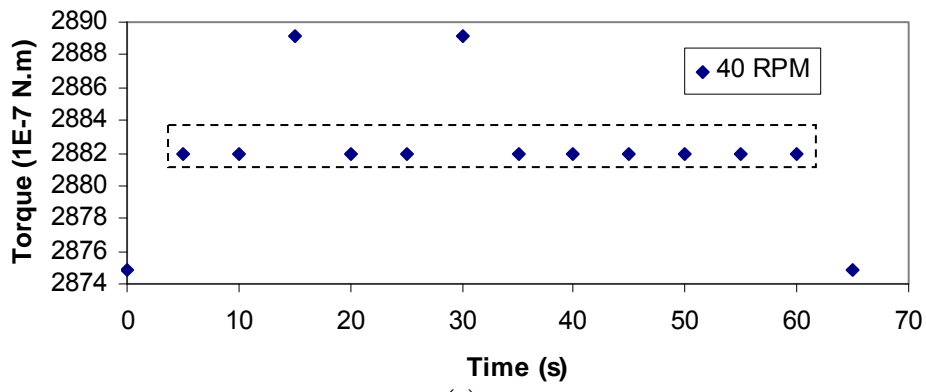
(k)



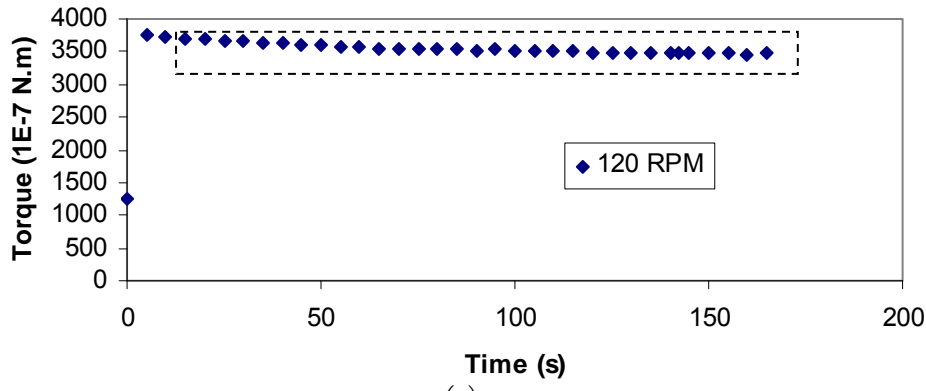
(l)



(m)

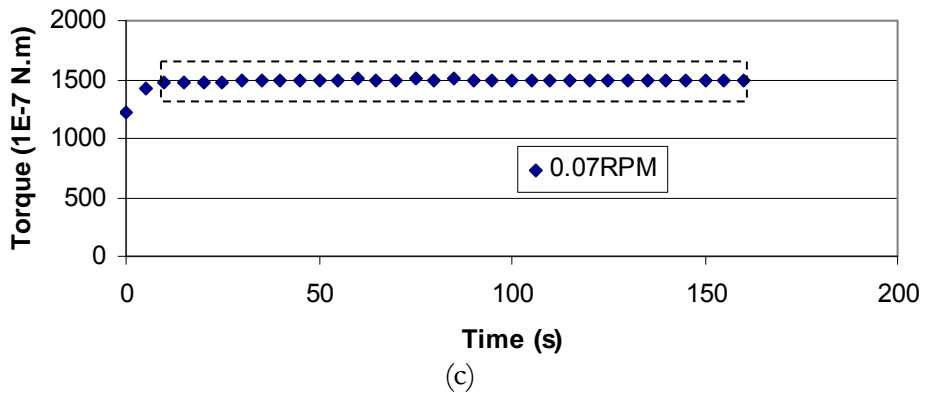
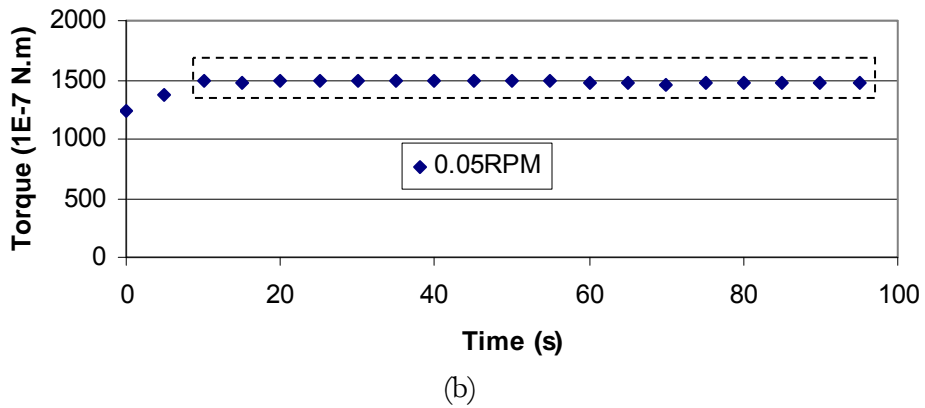
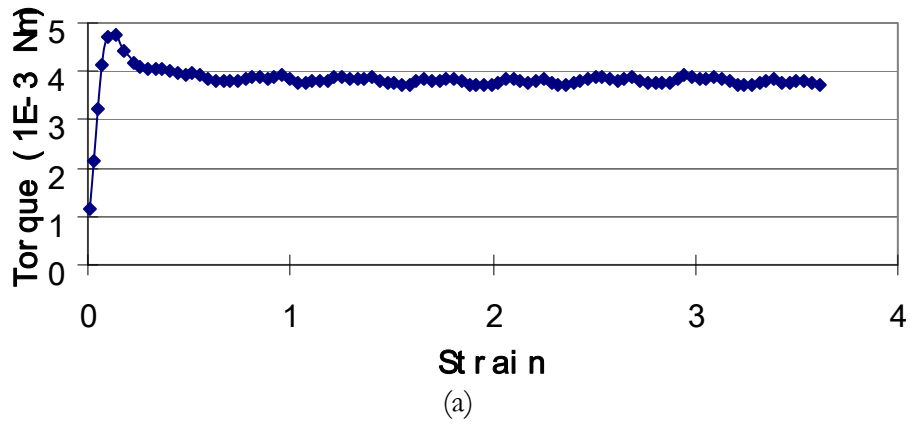


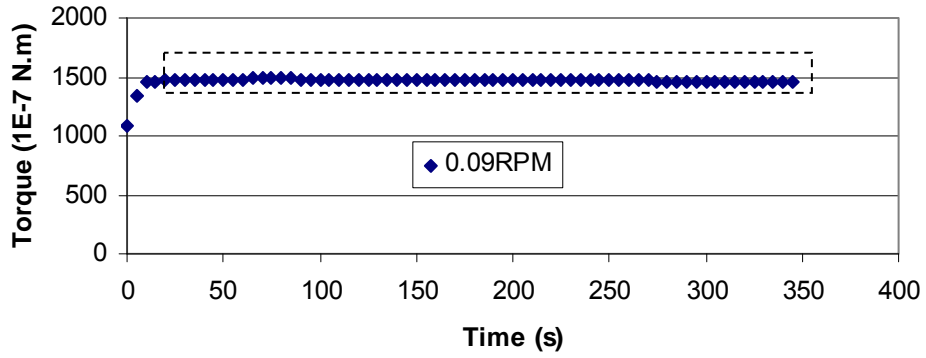
(n)



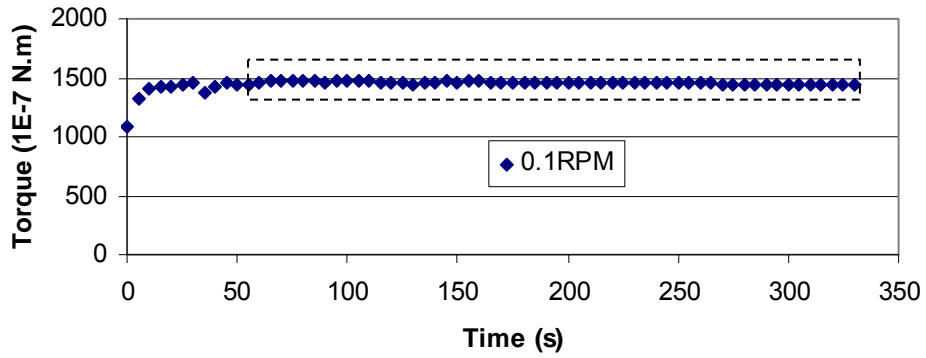
(o)

Figure A.1: Raw Data for Slurry with Solids Content of 66% and fines content of 37%  
 (a: Plot of Torque vs. Shear Strain from Vane Shear Test; b-o: Plot of Torque vs. Time  
 from Viscosity Measurements)

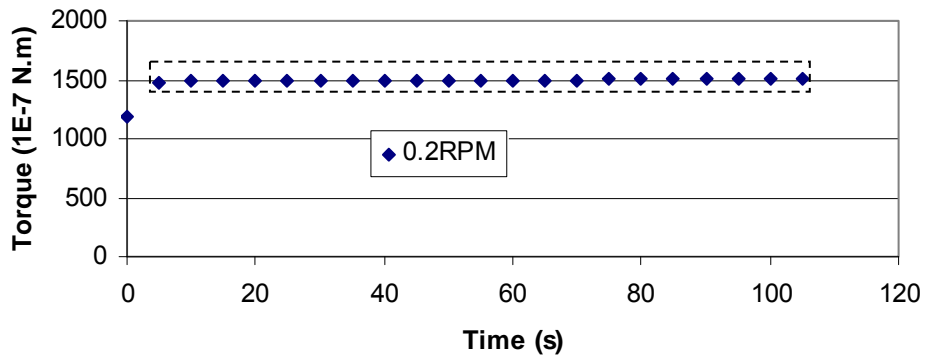




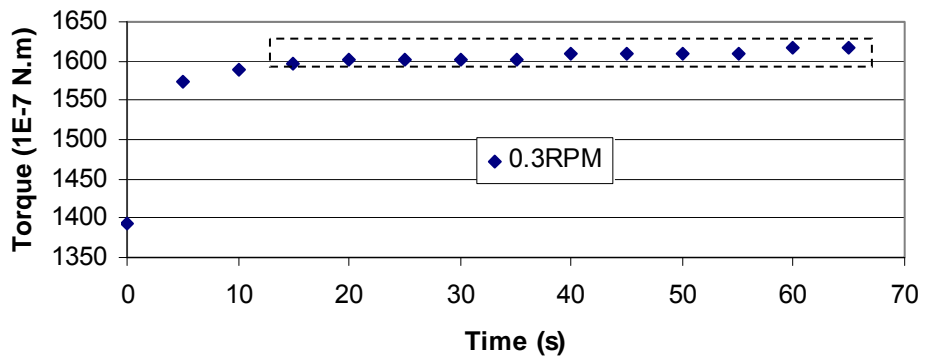
(d)



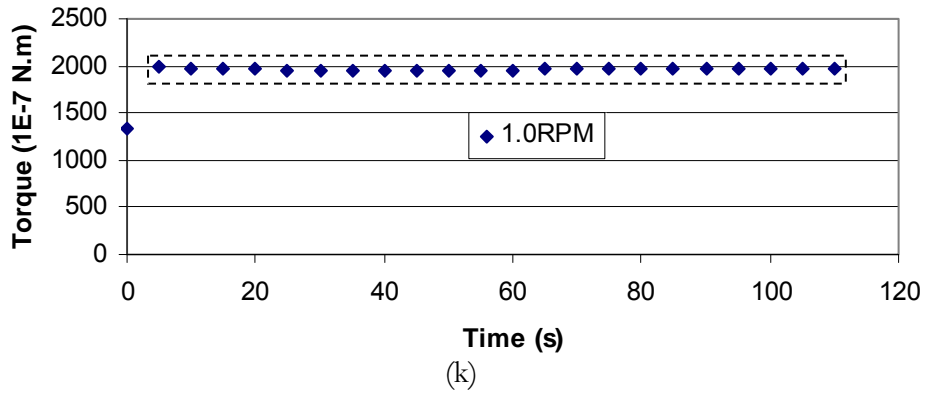
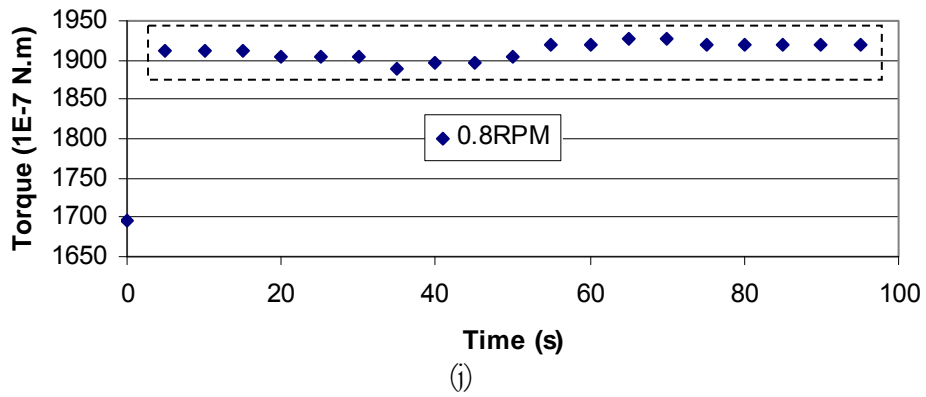
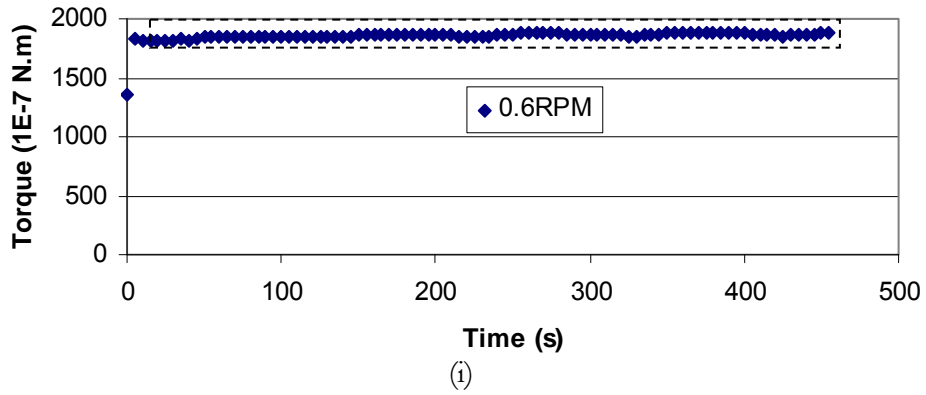
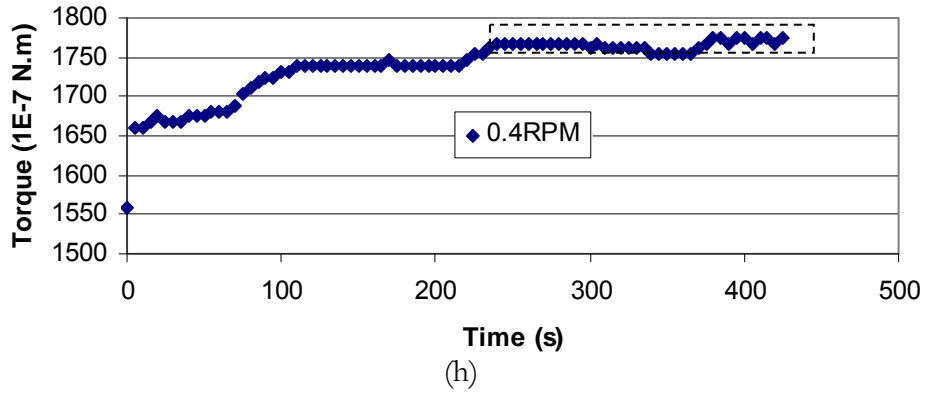
(e)

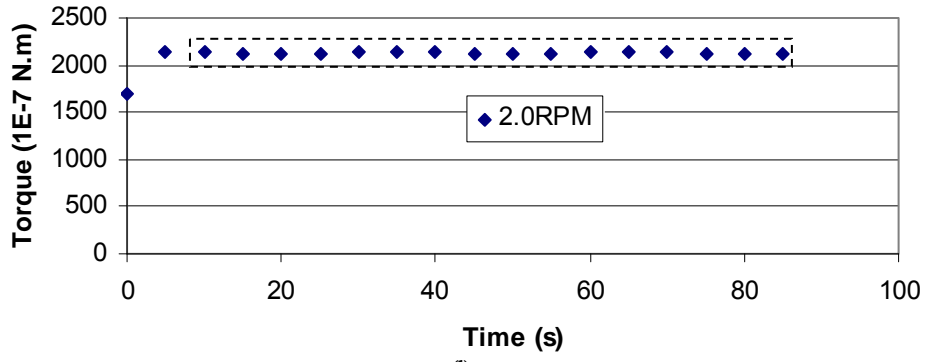


(f)

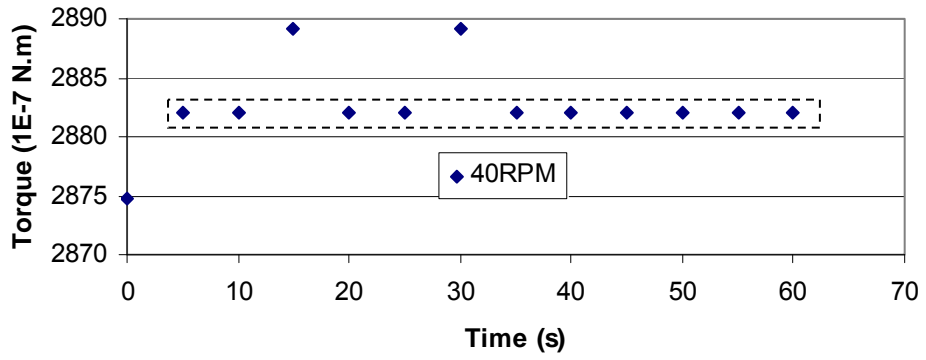


(g)

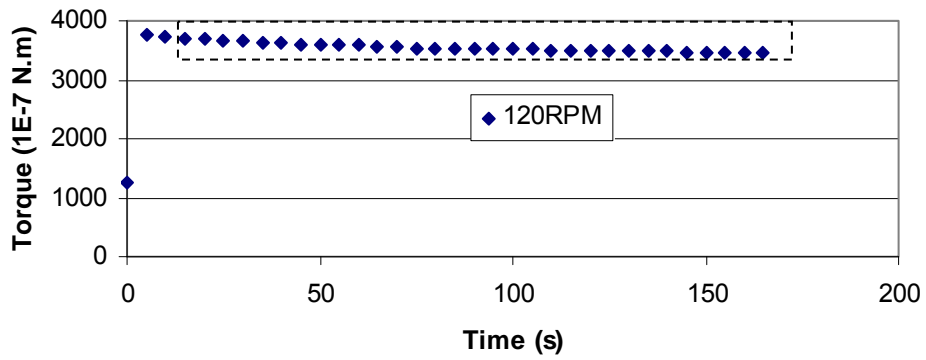




(l)

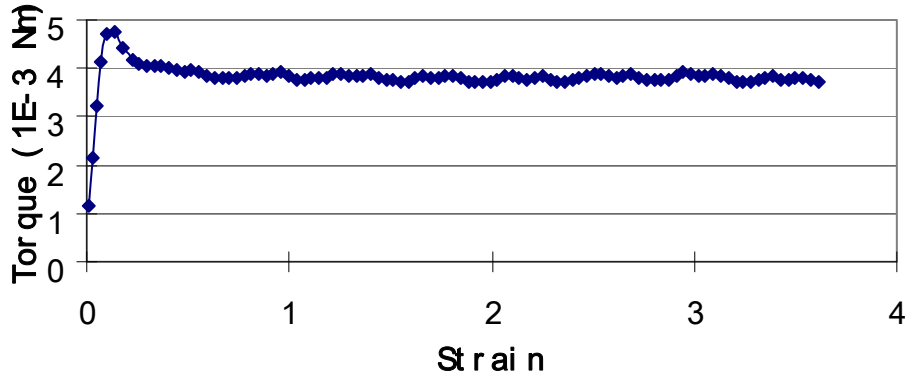


(m)

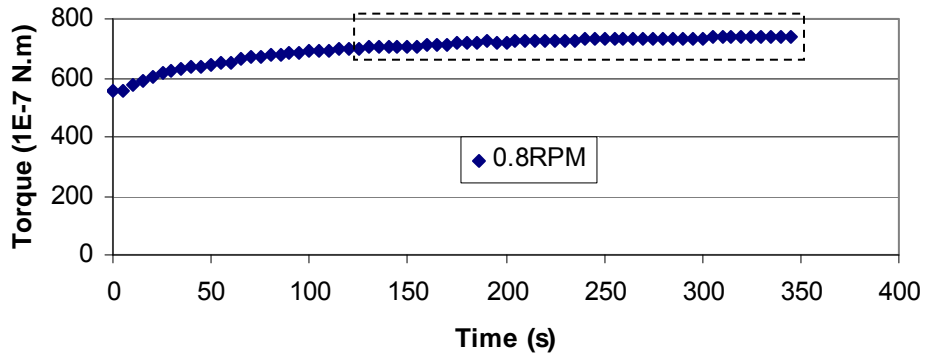


(n)

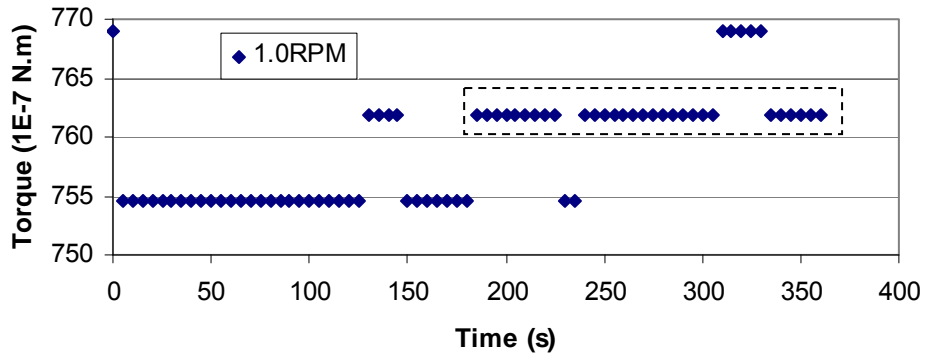
Figure A.2 Raw Data for Slurry with Solids Content of 65% and Fines Content of 32%  
 % (a: Plot of Torque vs. Shear Strain from Vane Shear Test; b-n: Plot of Torque vs.  
 Time from Viscosity Measurements)



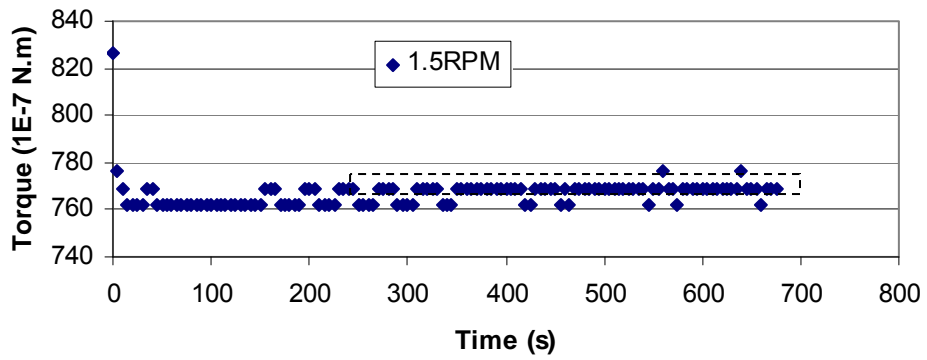
(a)



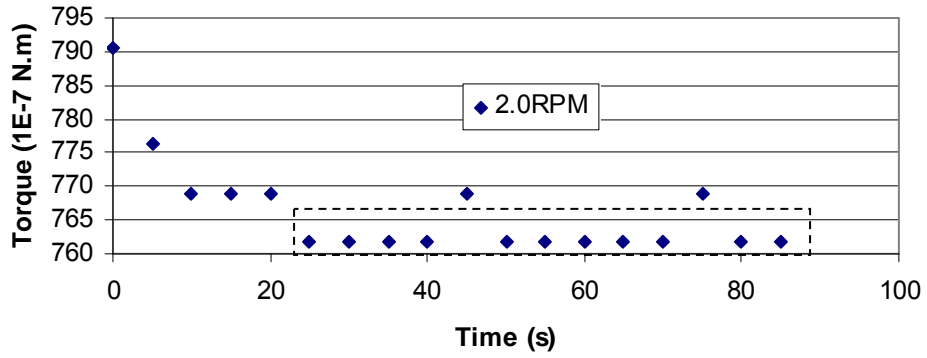
(b)



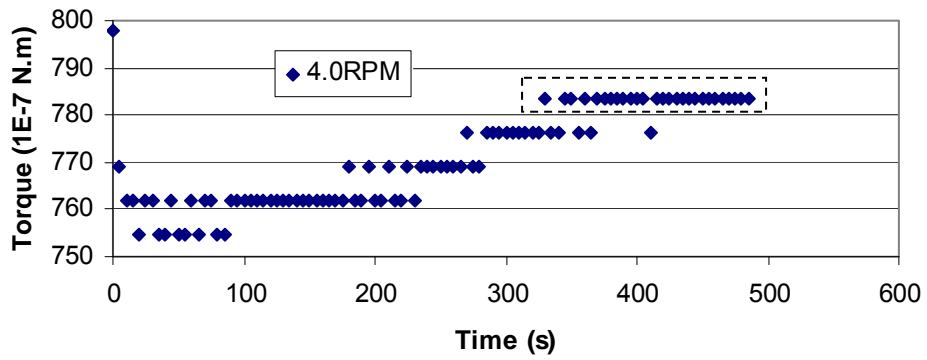
(c)



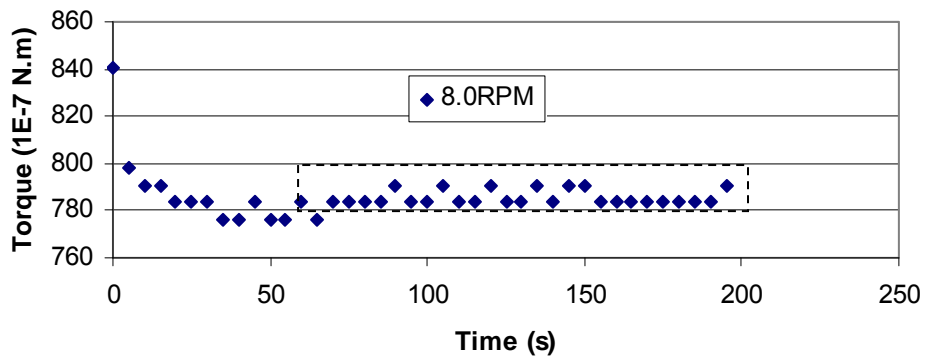
(d)



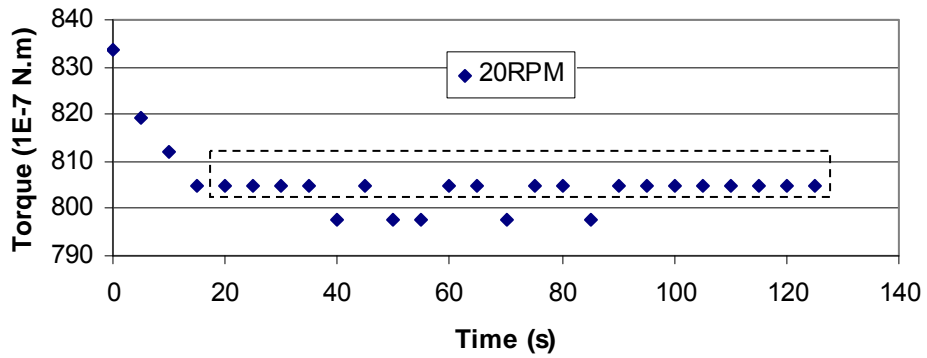
(e)



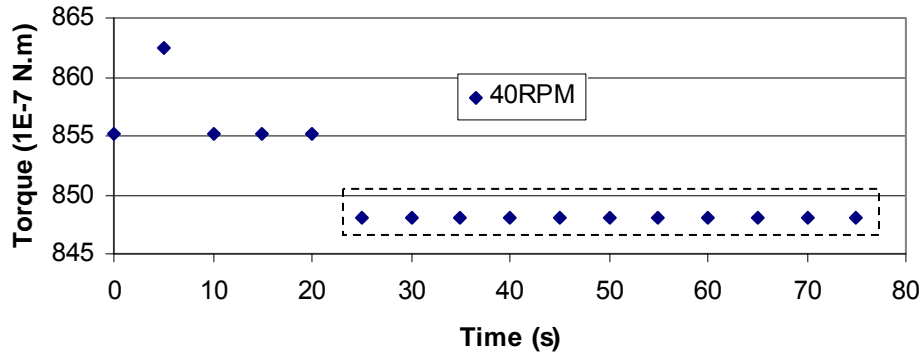
(f)



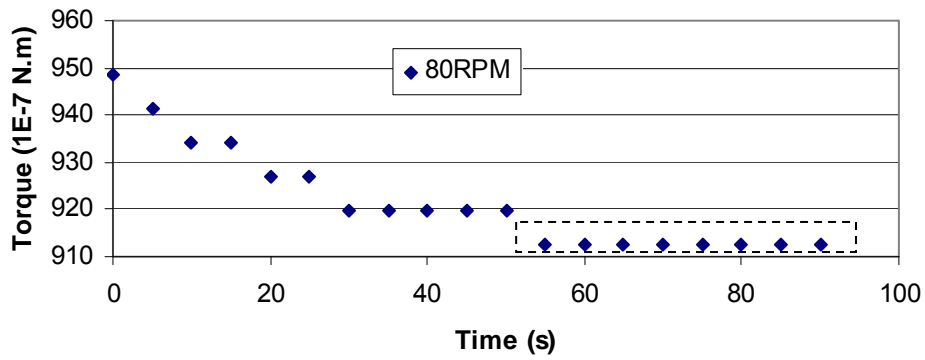
(g)



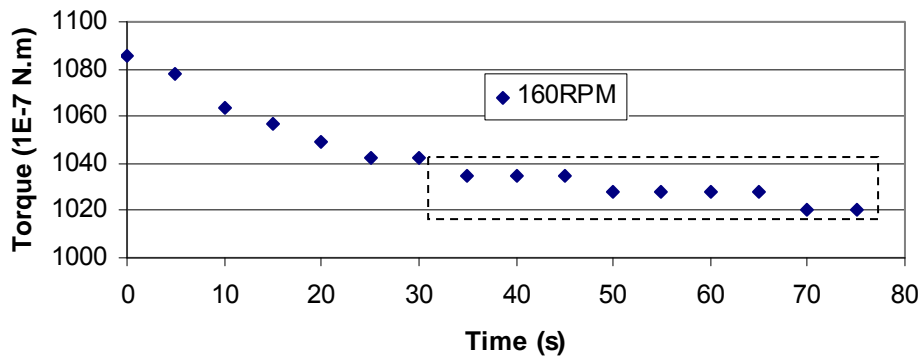
(h)



(i)

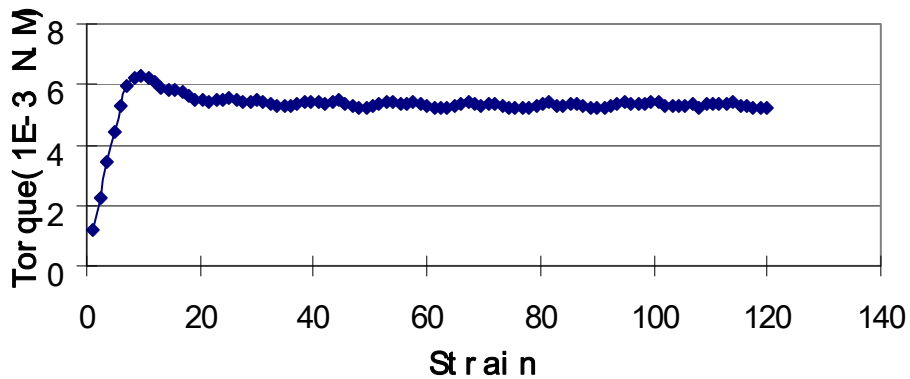


(j)

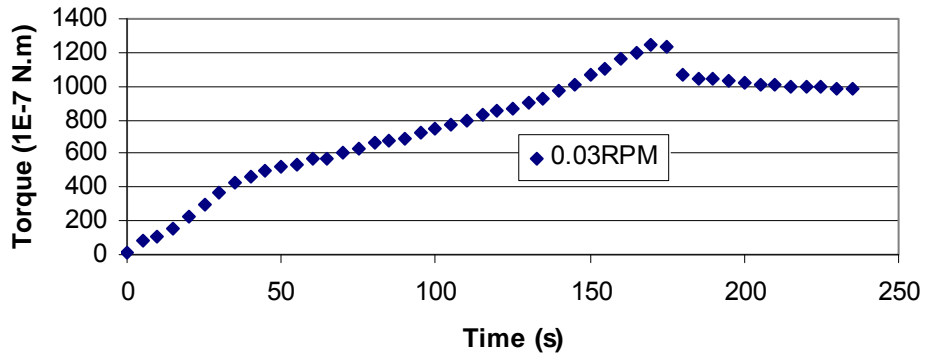


(k)

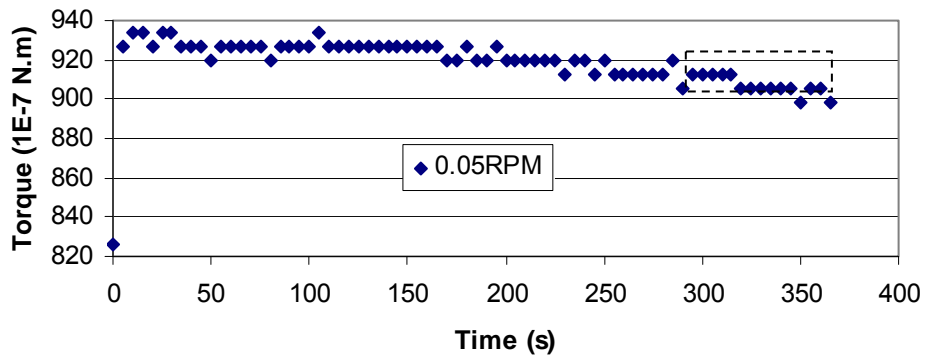
Figure A.3 Raw Data for Slurry with Solids Content of 43% and Fines Content of 75% (a: Plot of Torque vs. Shear Strain from Vane Shear Test; b-k: Plot of Torque vs. Time from Viscosity Measurements)



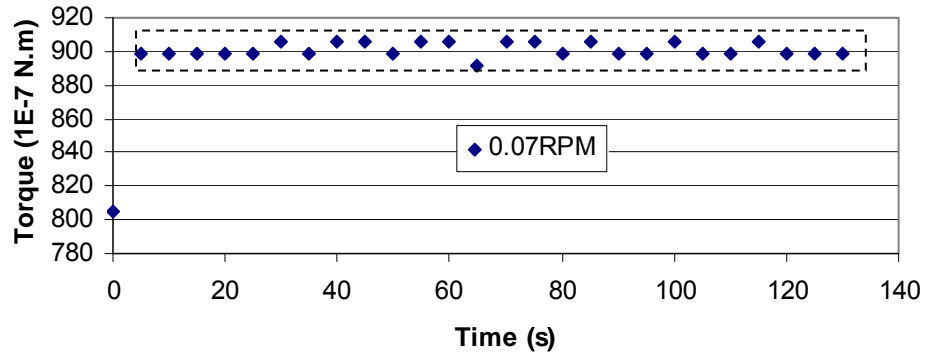
(a)



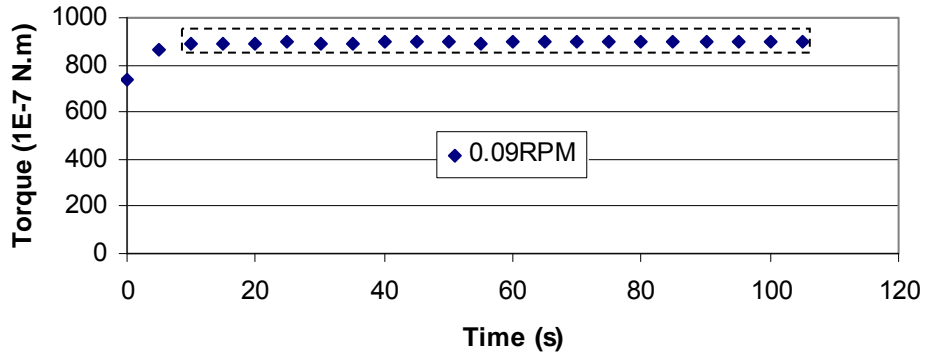
(b)



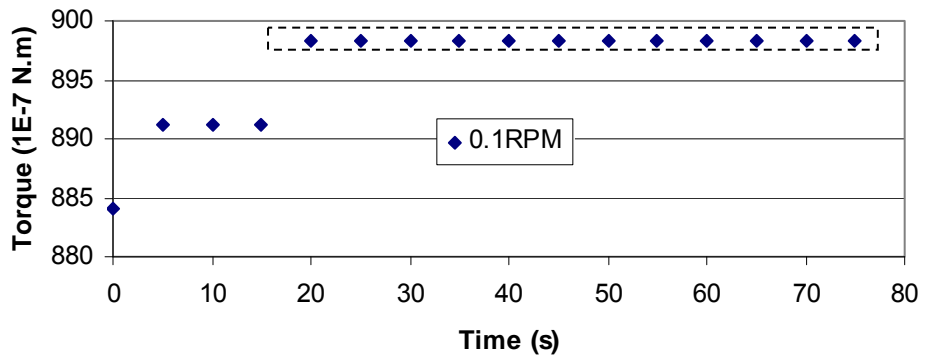
(c)



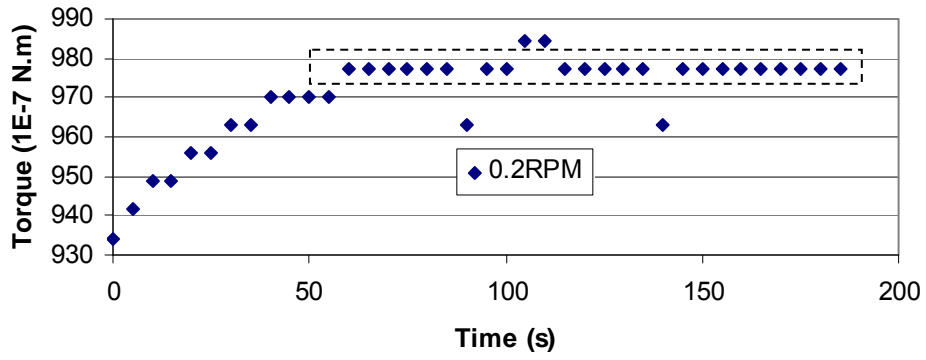
(d)



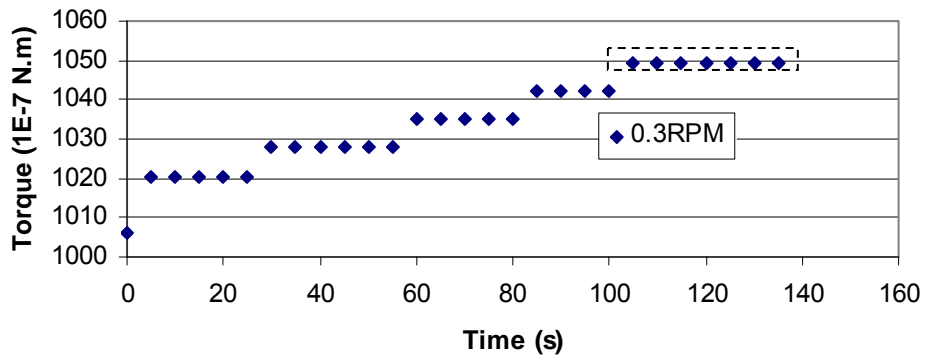
(e)



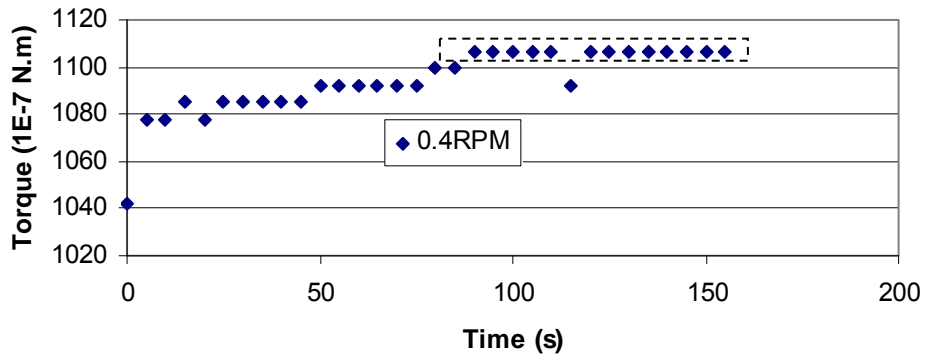
(f)



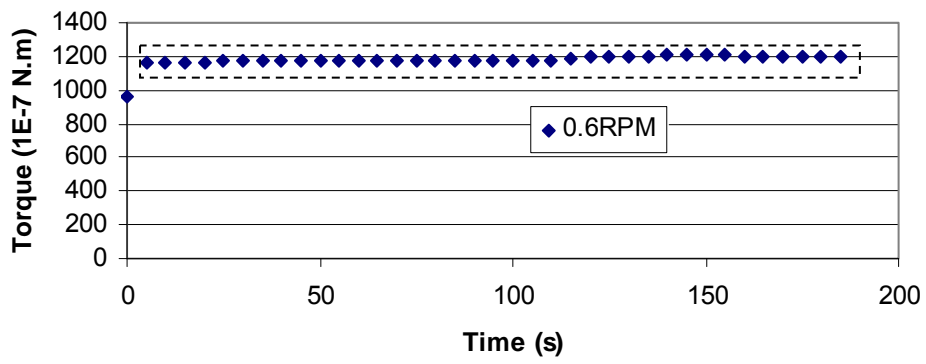
(g)



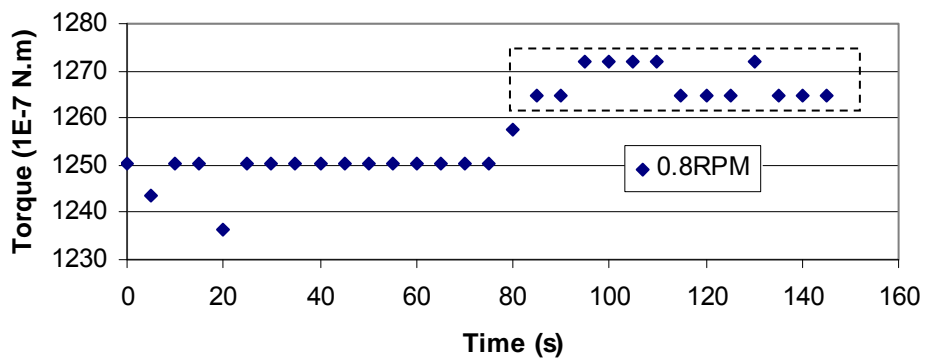
(h)



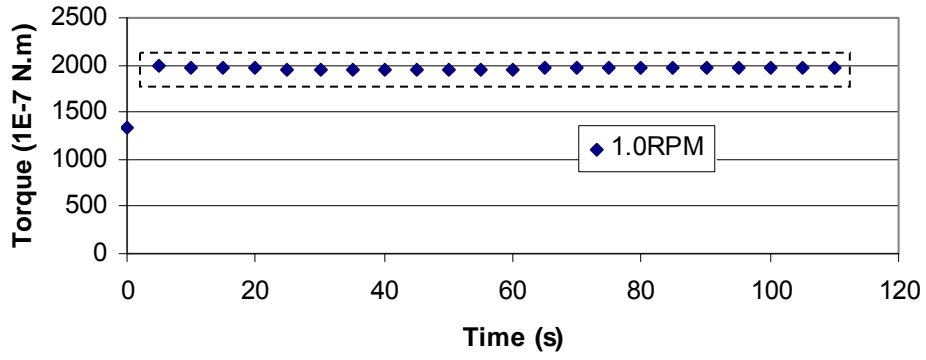
(i)



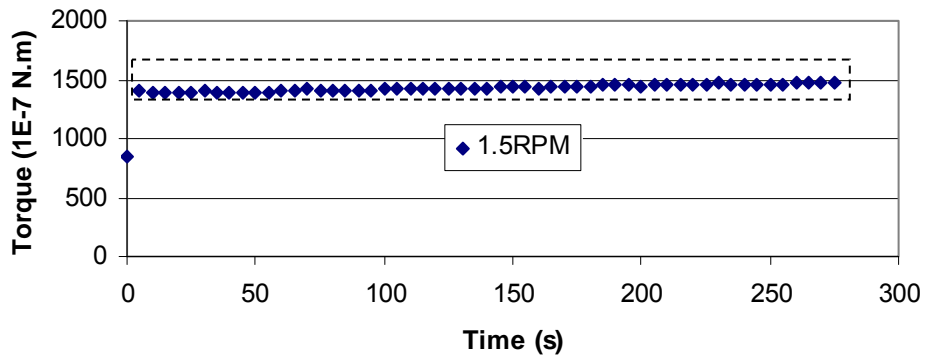
(j)



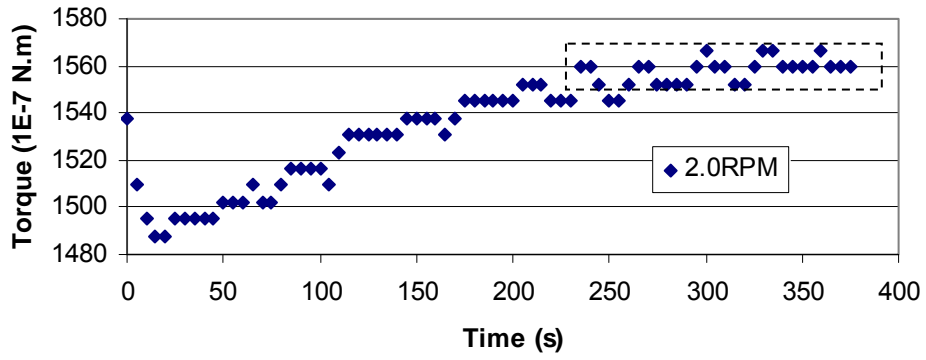
(k)



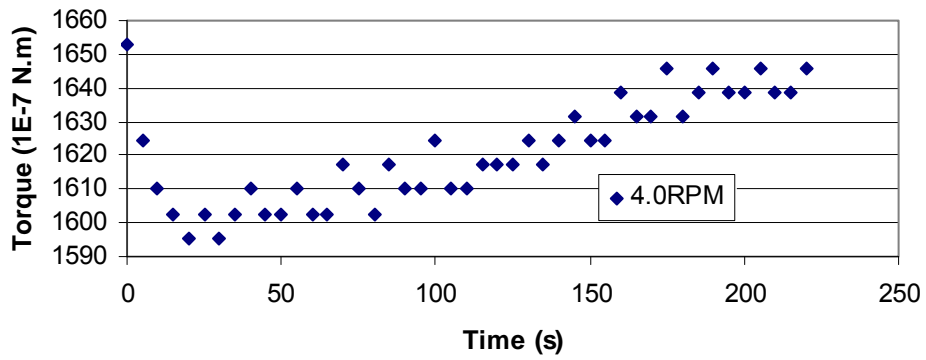
(l)



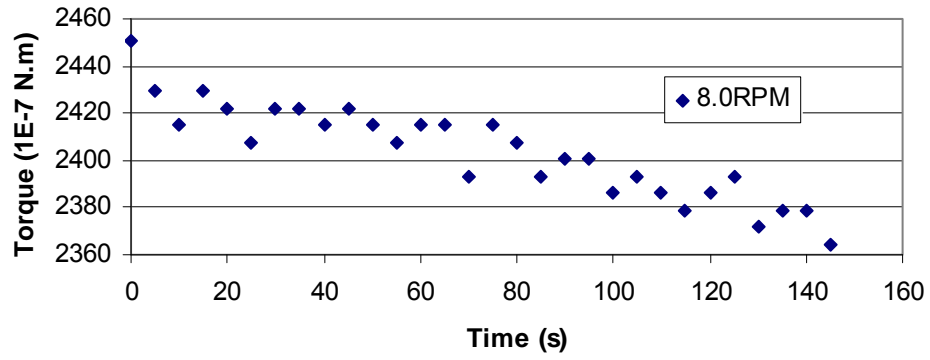
(m)



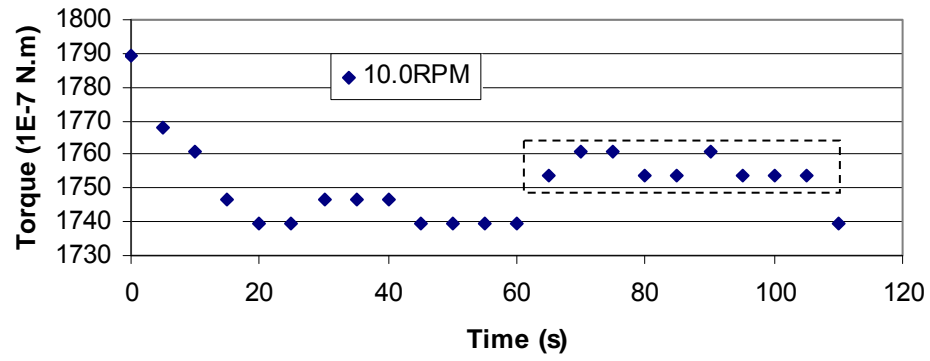
(n)



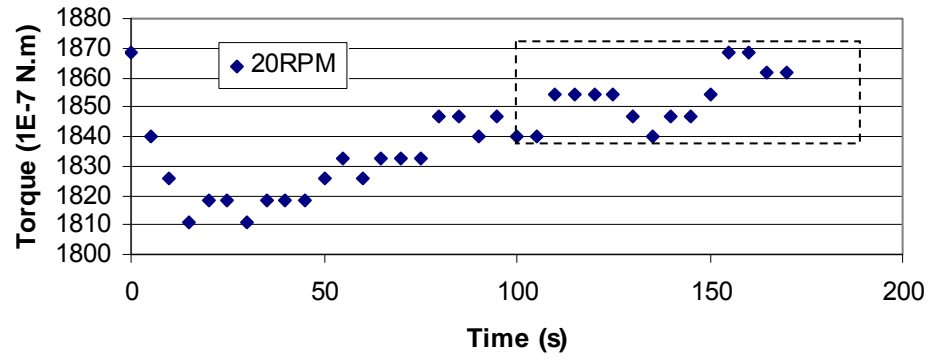
(o)



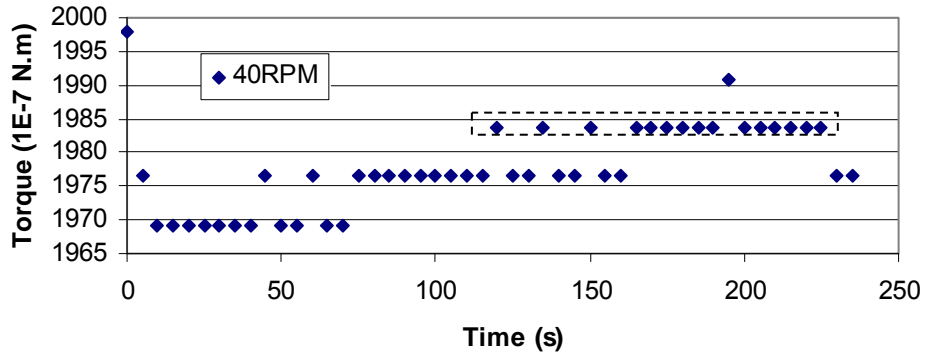
(p)



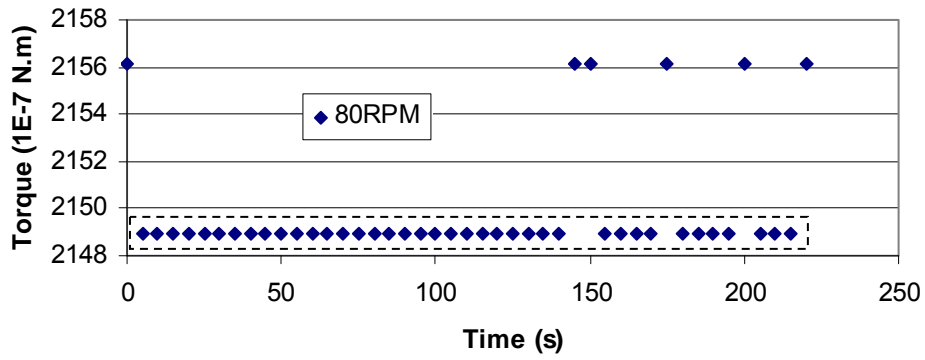
(q)



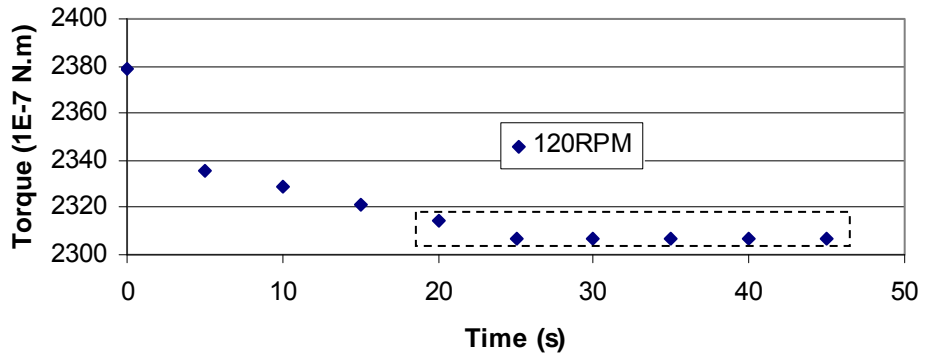
(s)



(t)

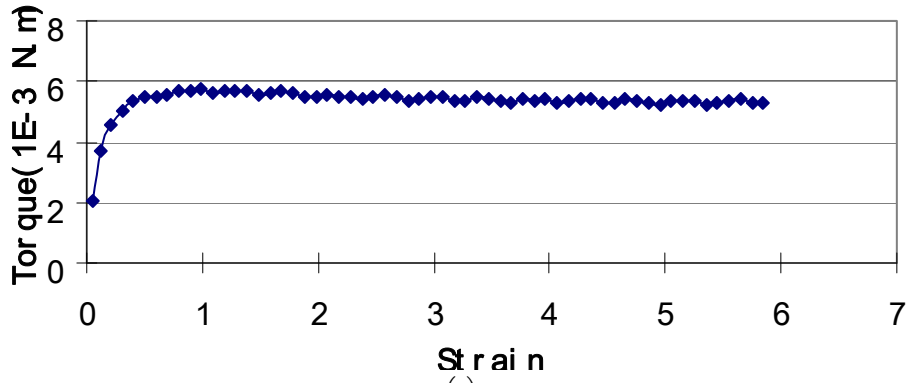


(u)

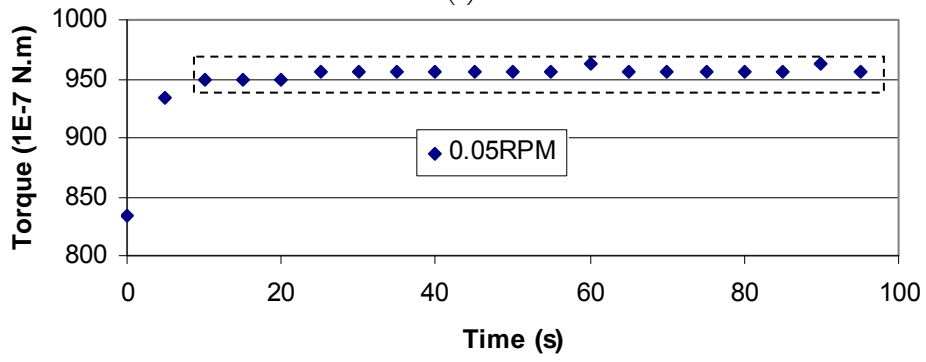


(v)

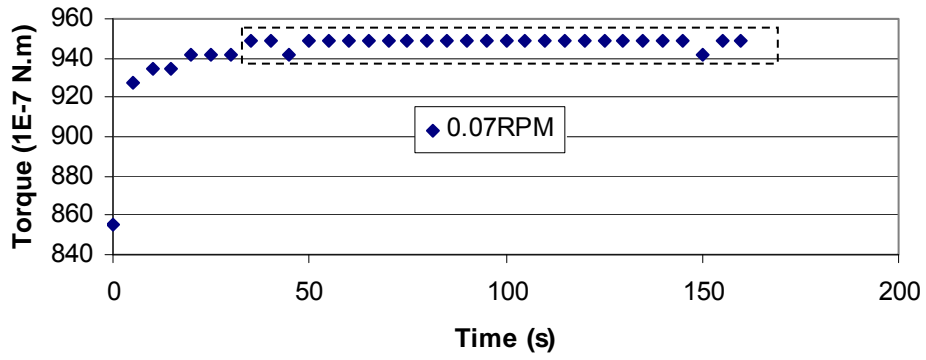
Figure A.4 Raw Data for Slurry with Solids Content of 52% and Fines Content of 60% (a: Plot of Torque vs. Shear Strain from Vane Shear Test; b-v: Plot of Torque vs. Time from Viscosity Measurements)



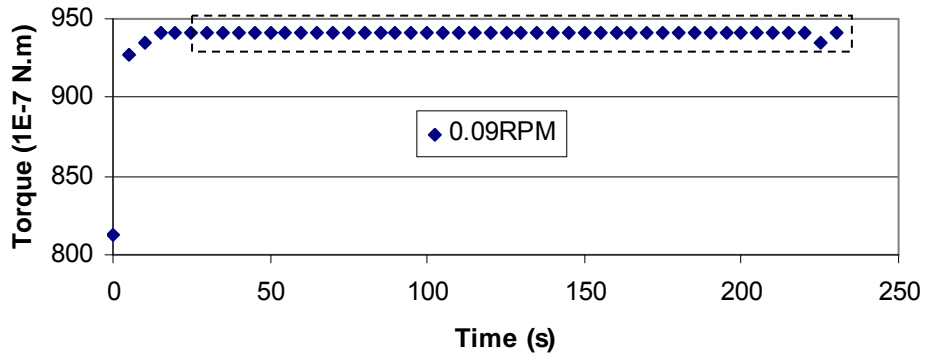
(a)



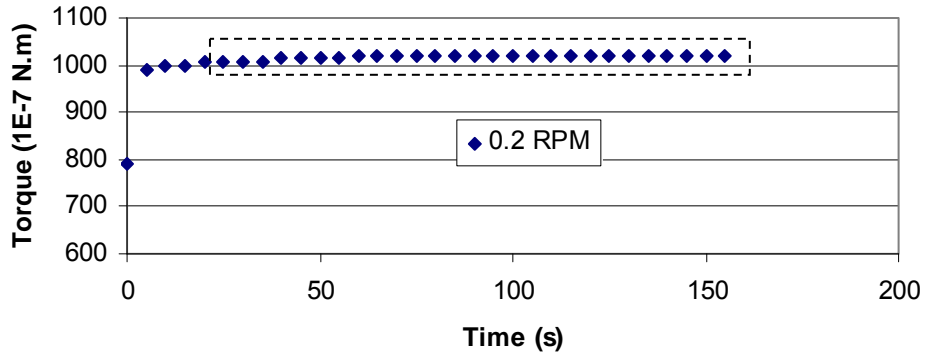
(b)



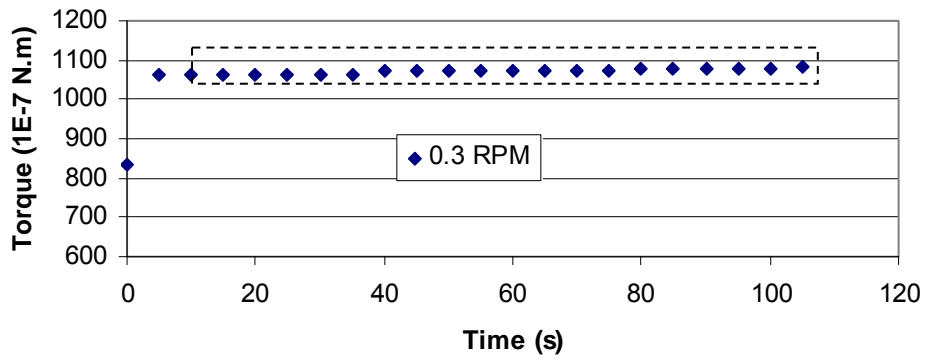
(c)



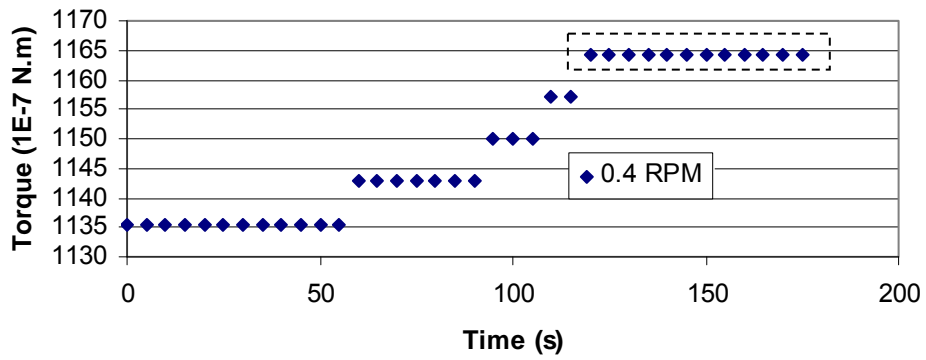
(d)



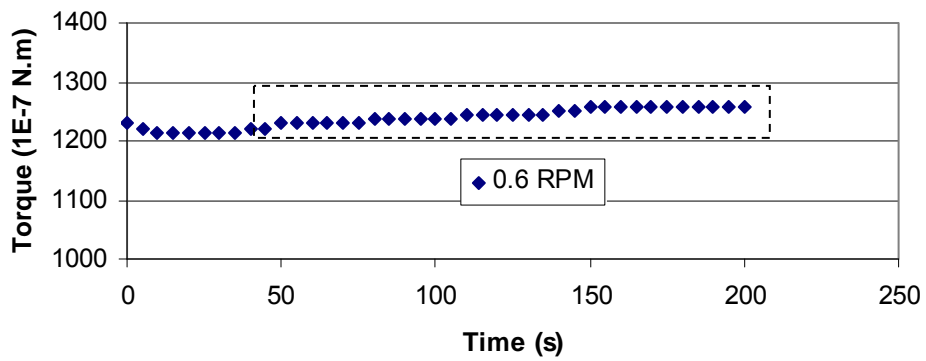
(e)



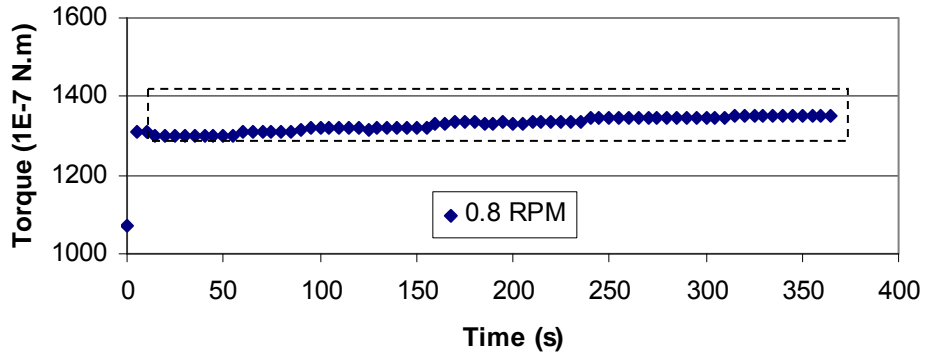
(f)



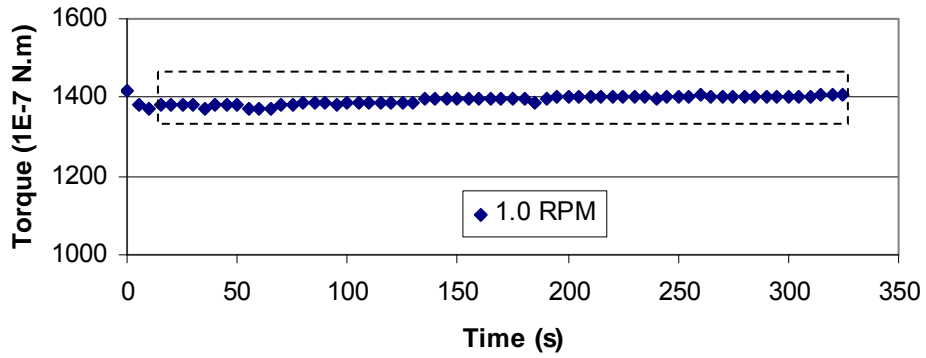
(g)



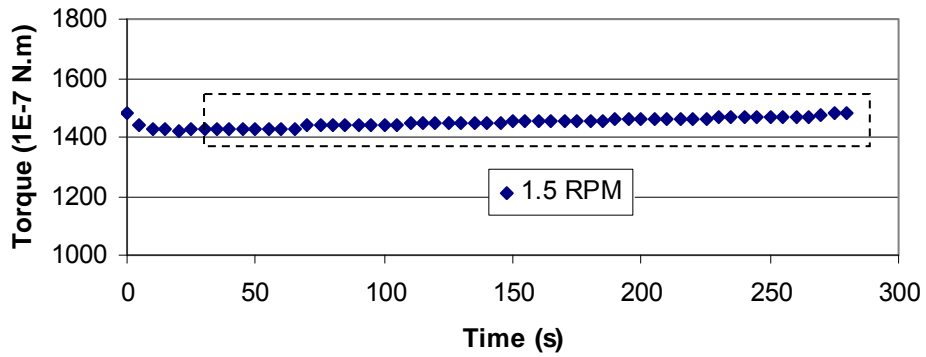
(h)



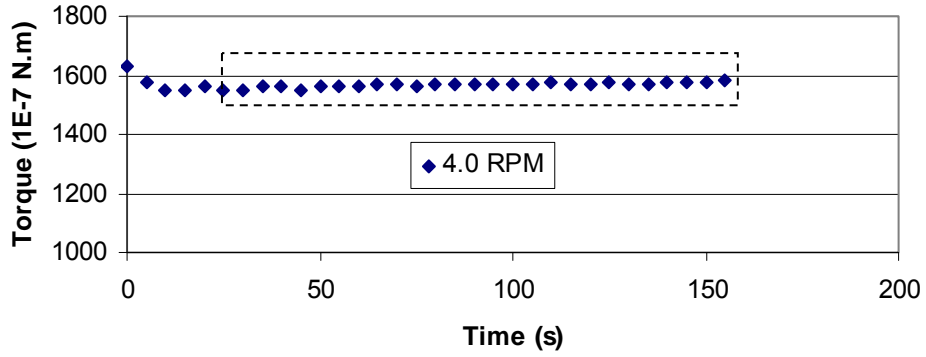
(i)



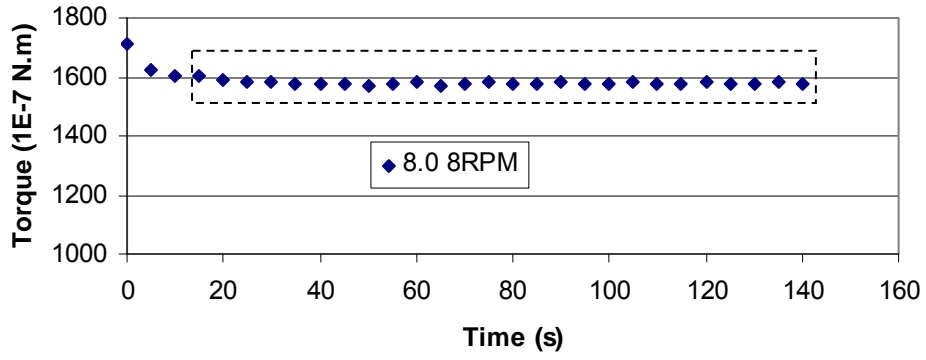
(j)



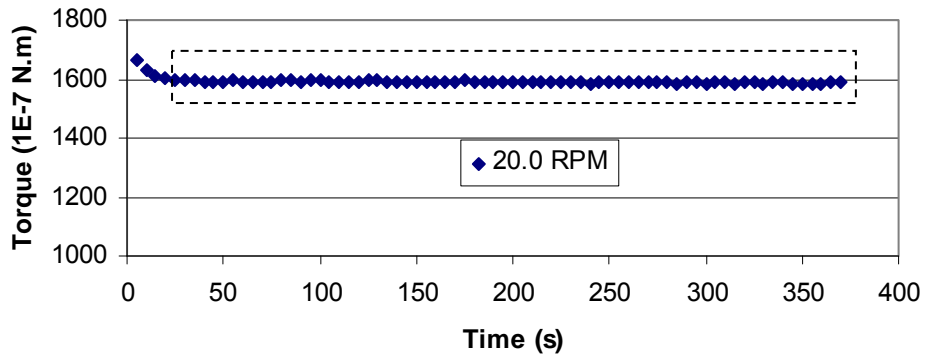
(k)



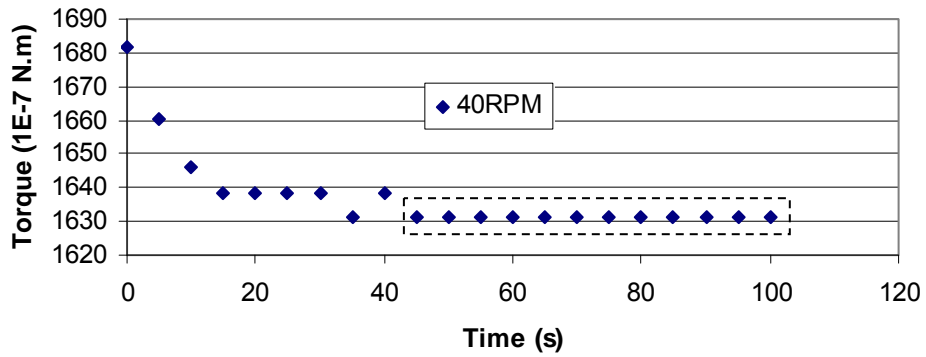
(l)



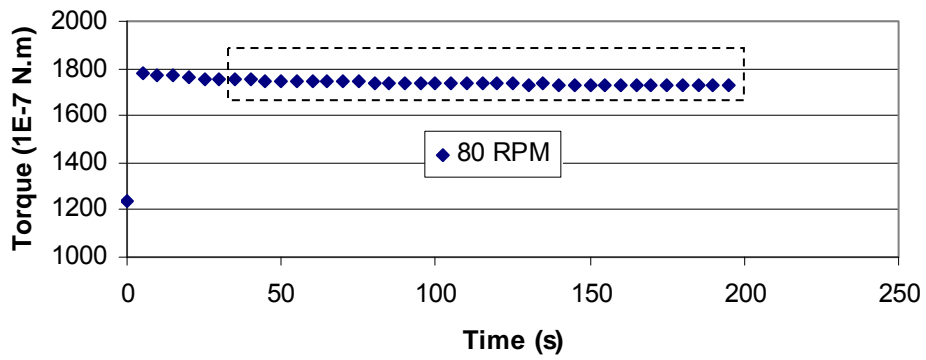
(m)



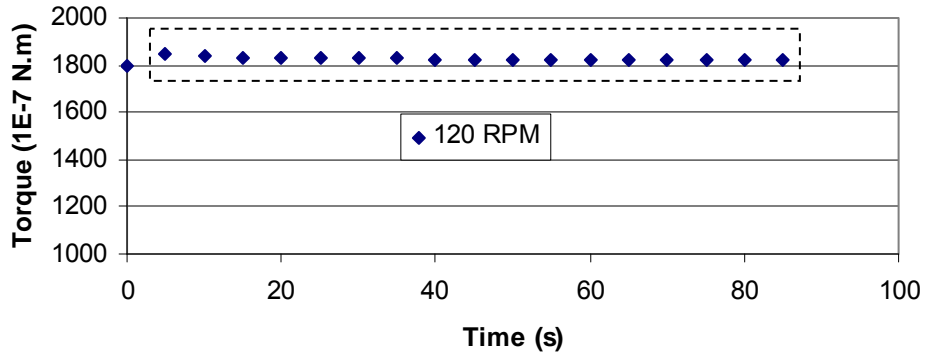
(n)



(o)

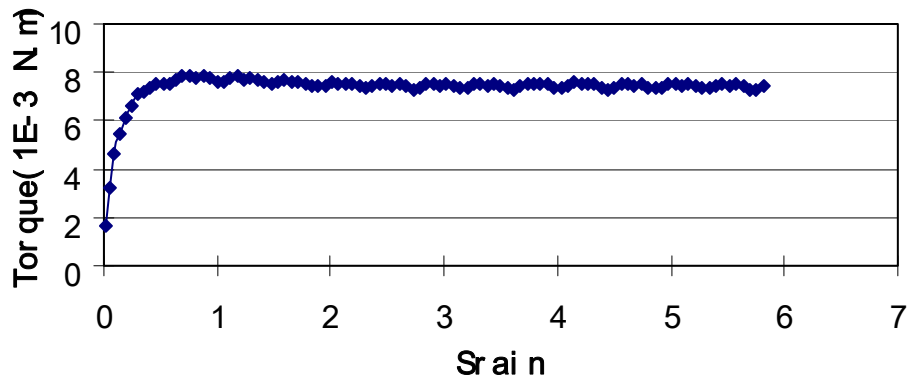


(p)

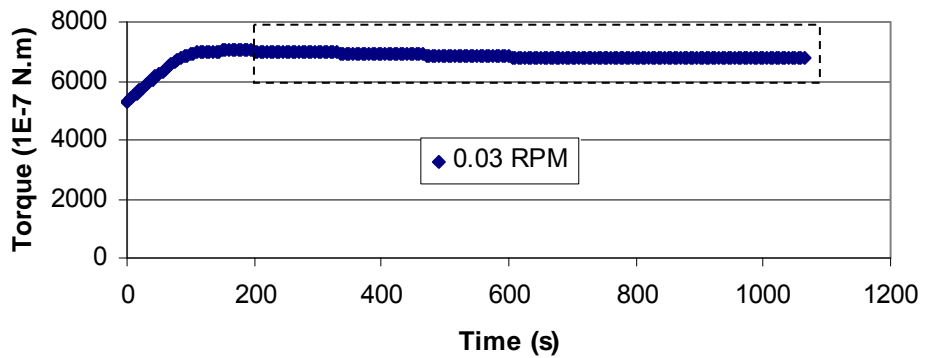


(q)

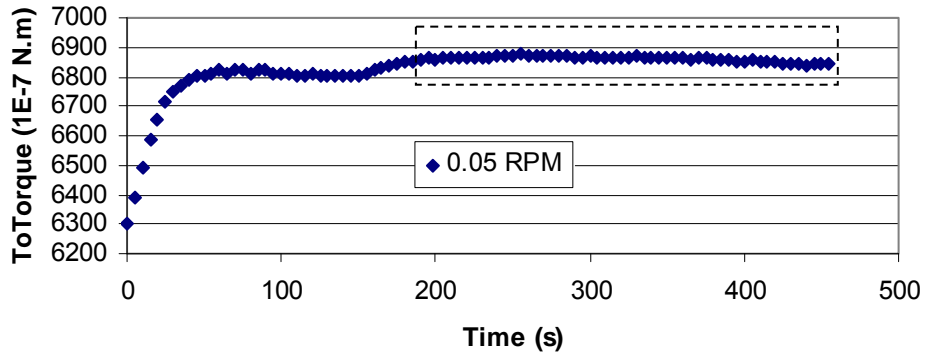
Figure A.5 Raw Data for Slurry with Solids Content of 40% and Fines Content of 94% (a: Plot of Torque vs. Shear Strain from Vane Shear Test; b-o: Plot of Torque vs. Time from Viscosity Measurements)



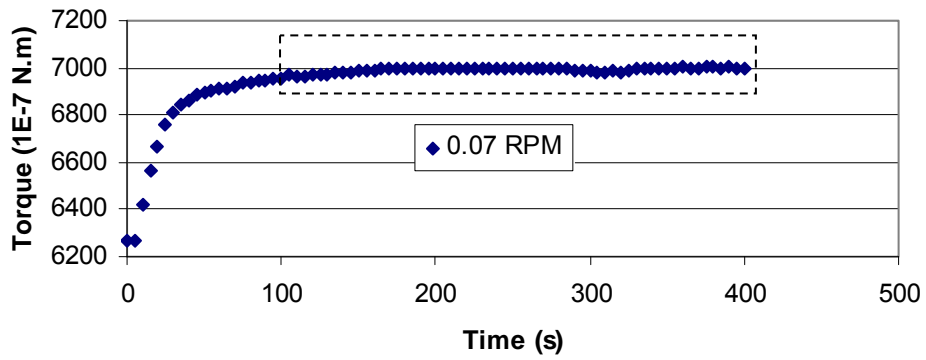
(a)



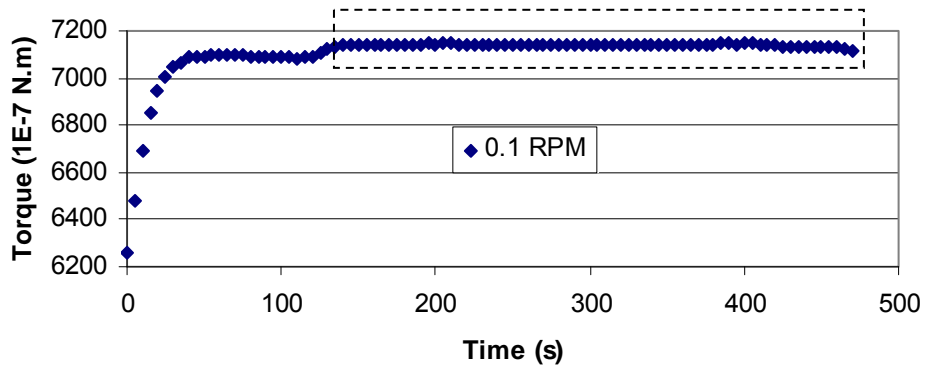
(b)



(c)

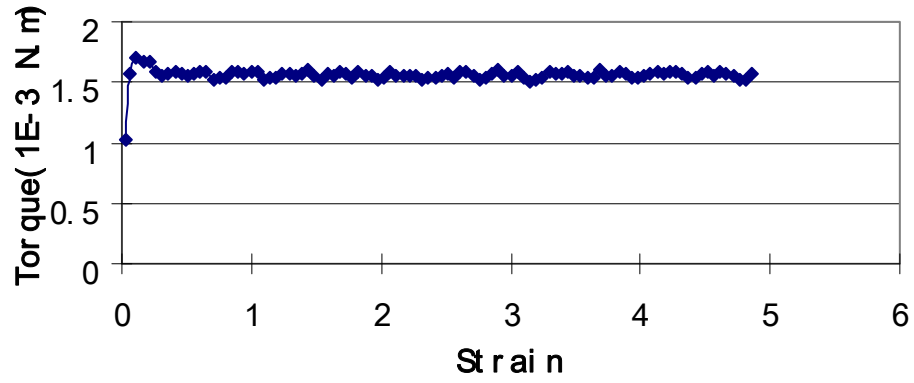


(d)

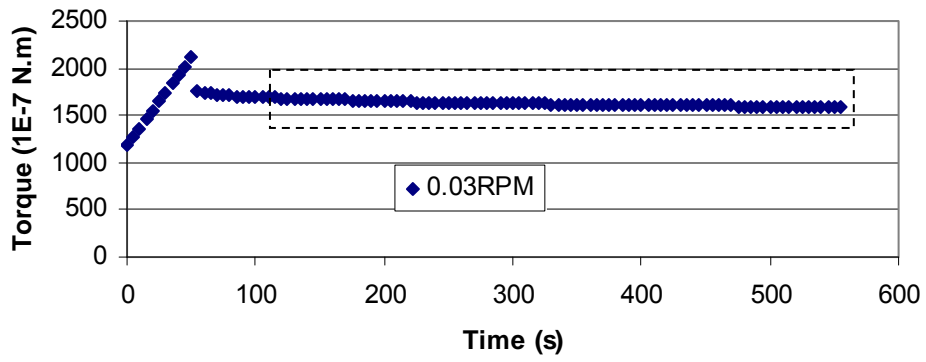


(e)

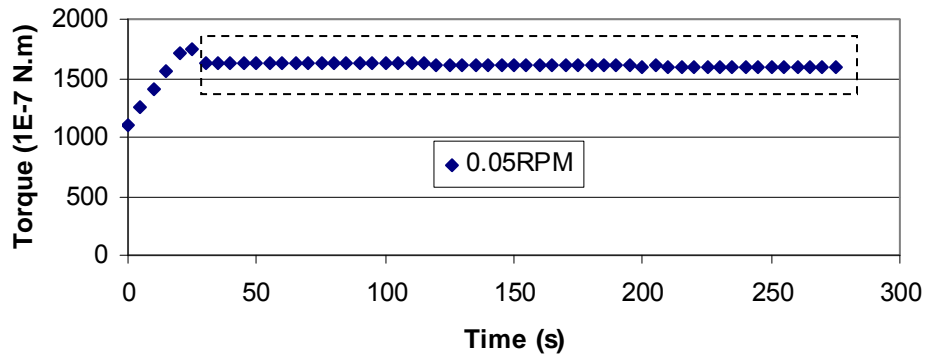
Figure A.6 Raw Data for Slurry with Solids Content of 61% and Fines Content of 95% (a: Plot of Torque vs. Shear Strain from Vane Shear Test; b-o: Plot of Torque vs. Time from Viscosity Measurements)



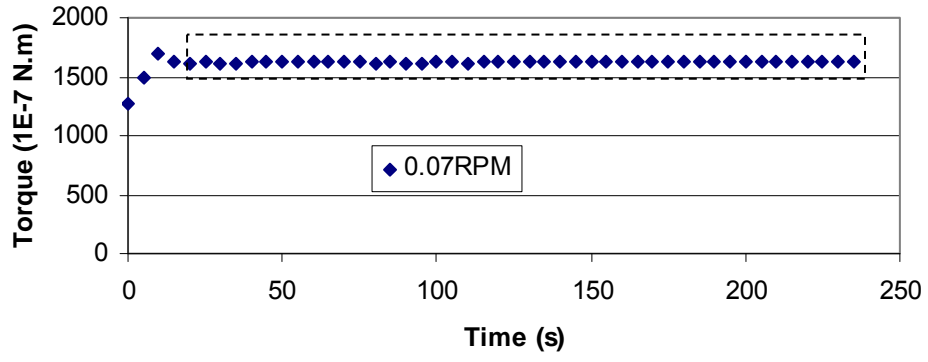
(a)



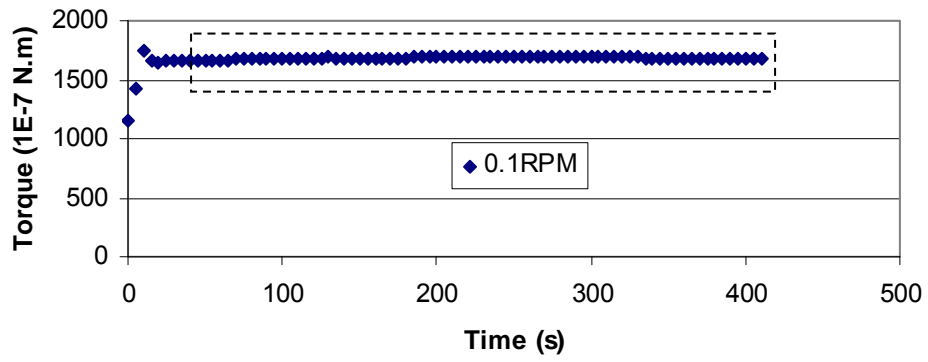
(b)



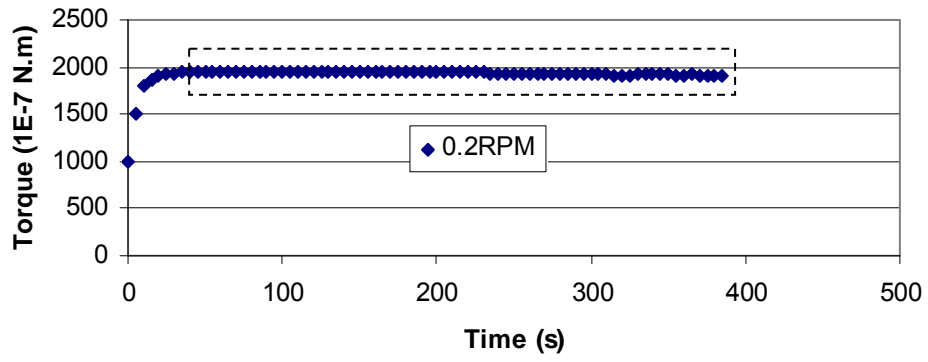
(c)



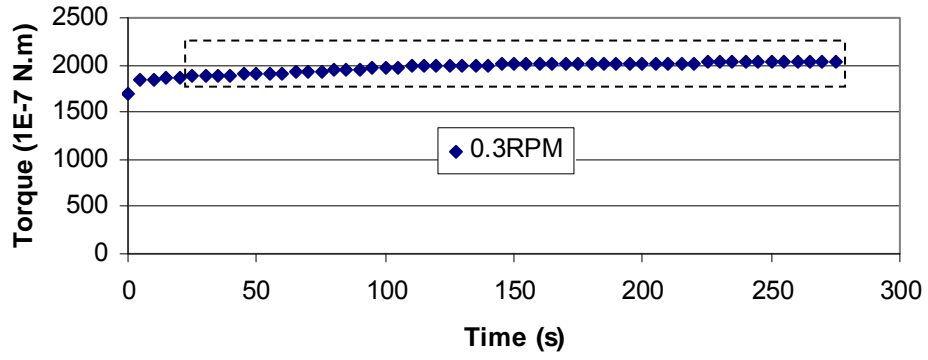
(d)



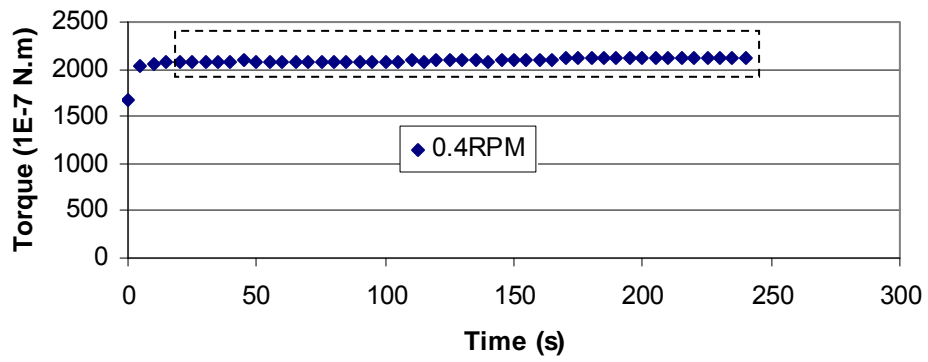
(e)



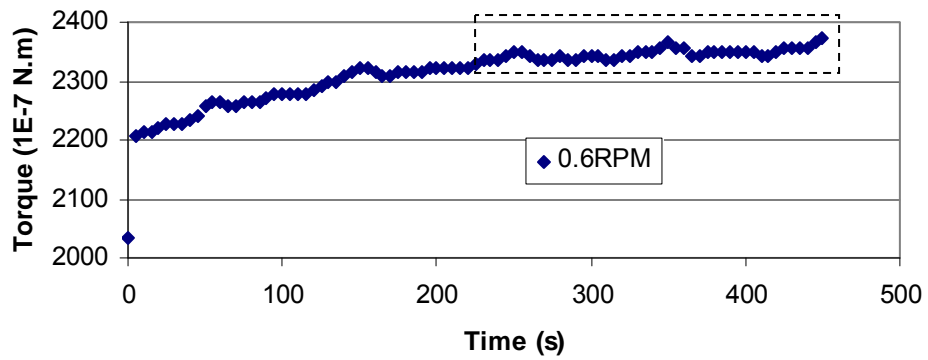
(f)



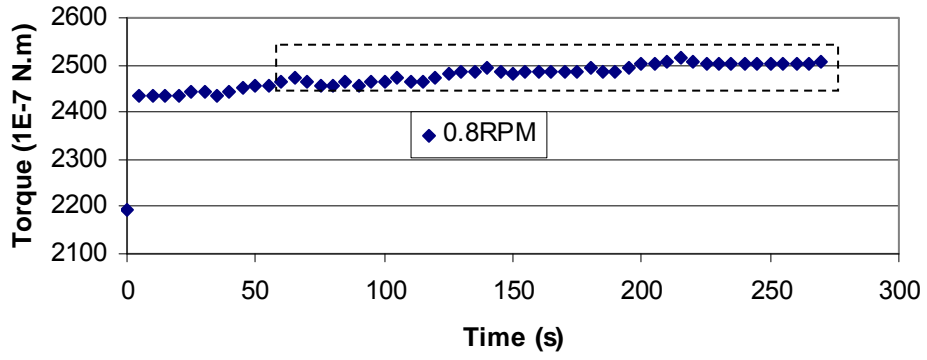
(g)



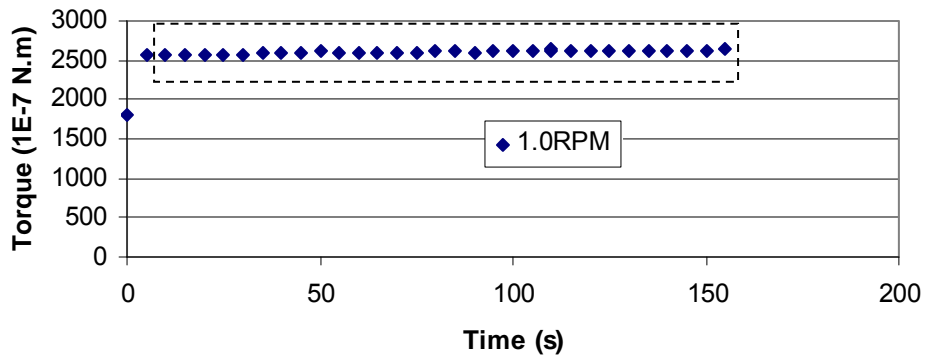
(h)



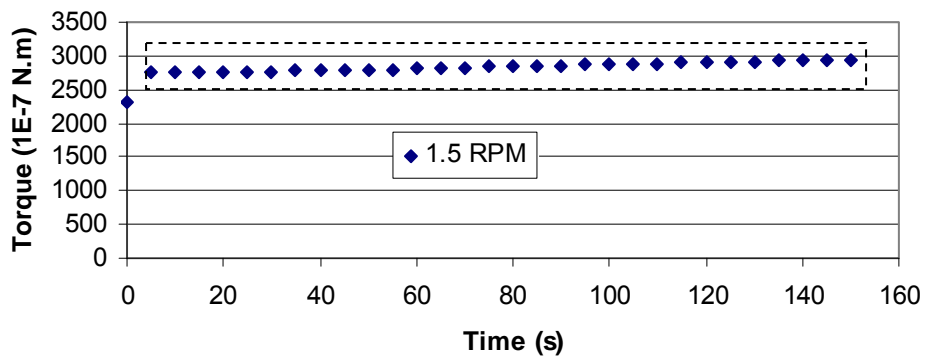
(i)



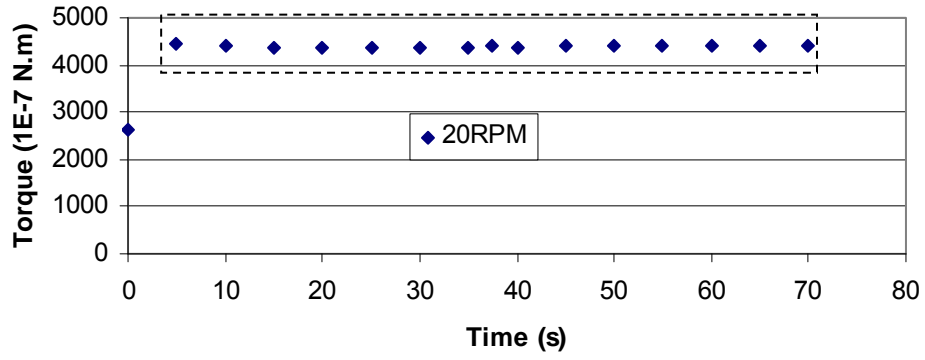
(j)



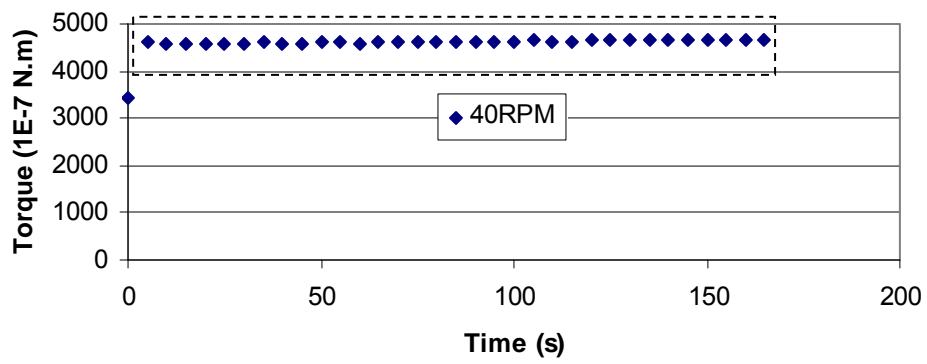
(k)



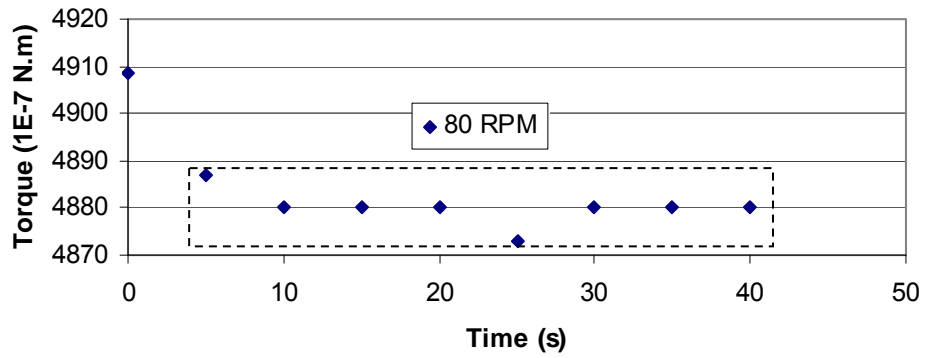
(l)



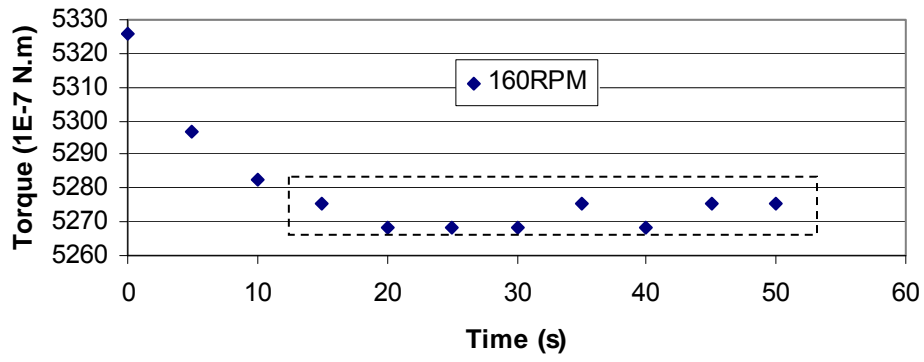
(m)



(n)

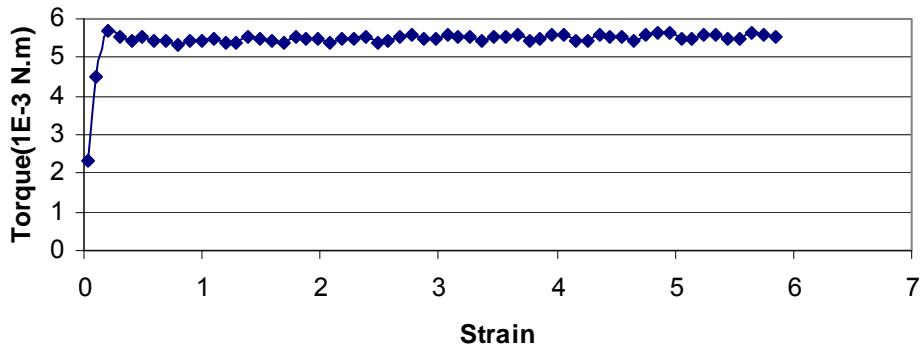


(o)

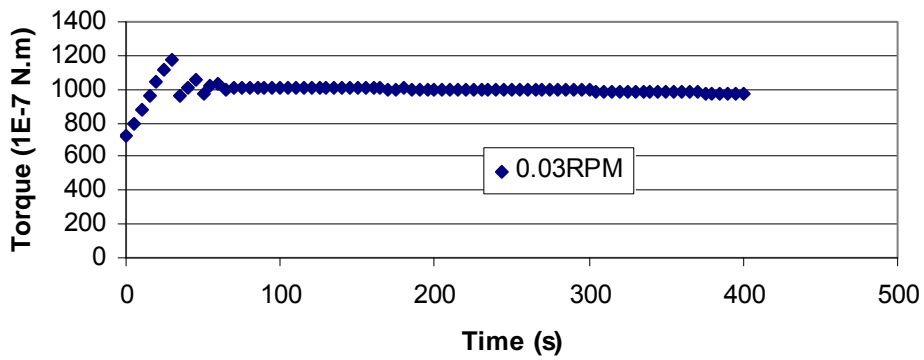


(p)

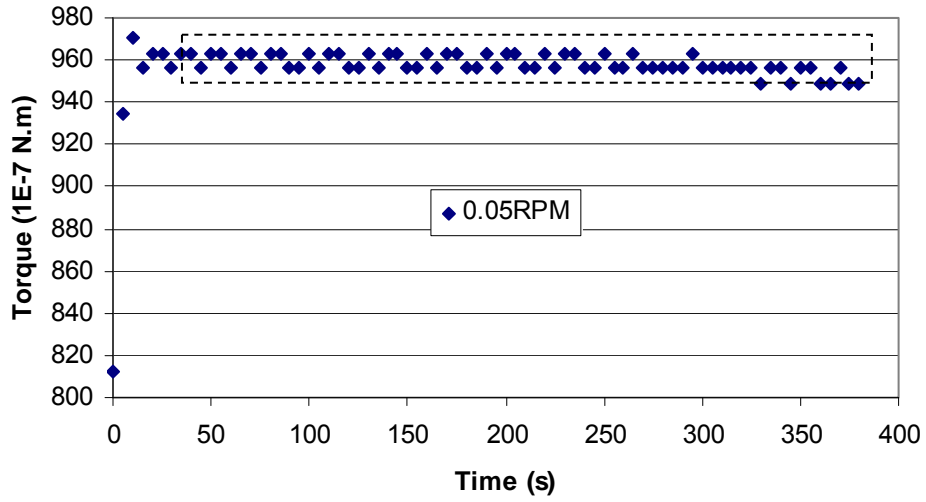
Figure A.7 Raw Data for Slurry with Solids Content of 50% and Fines Content of 95% (a: Plot of Torque vs. Shear Strain from Vane Shear Test; b-p: Plot of Torque vs. Time from Viscosity Measurements)



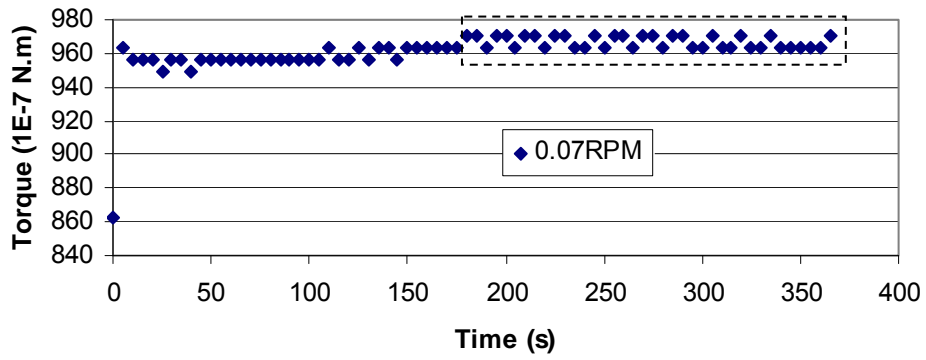
(a)



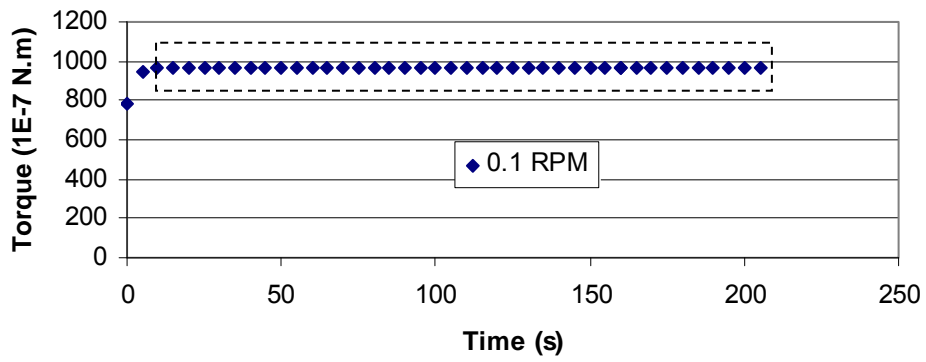
(b)



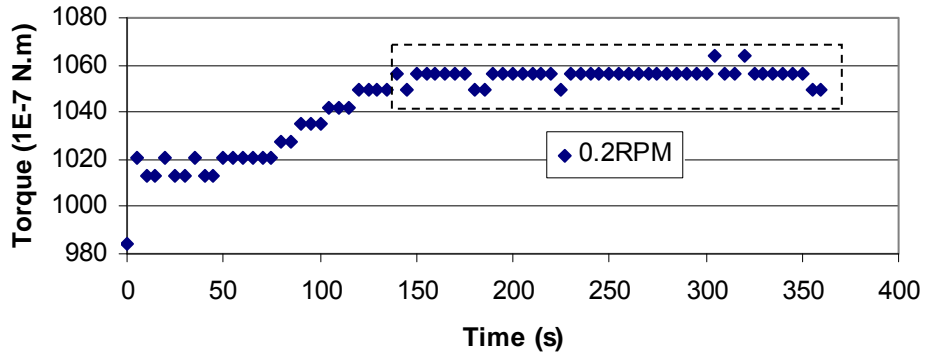
(c)



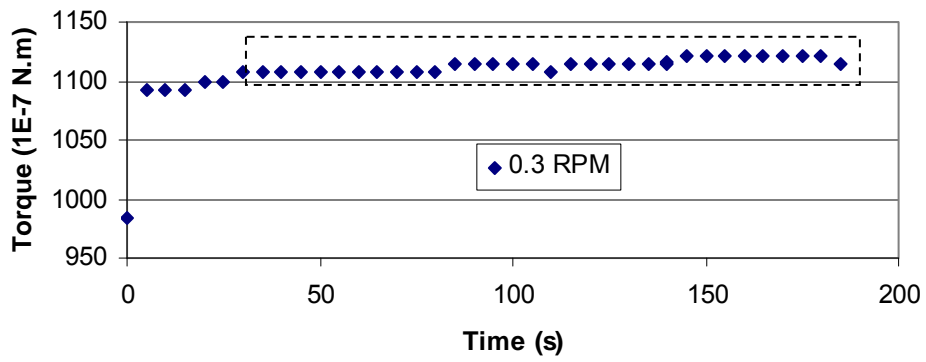
(d)



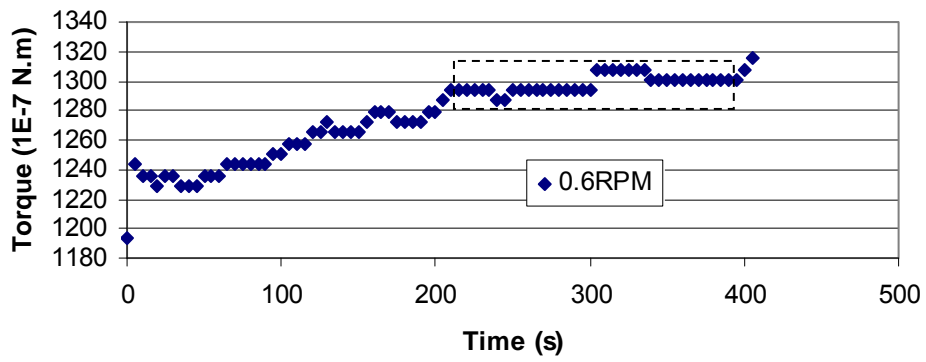
(e)



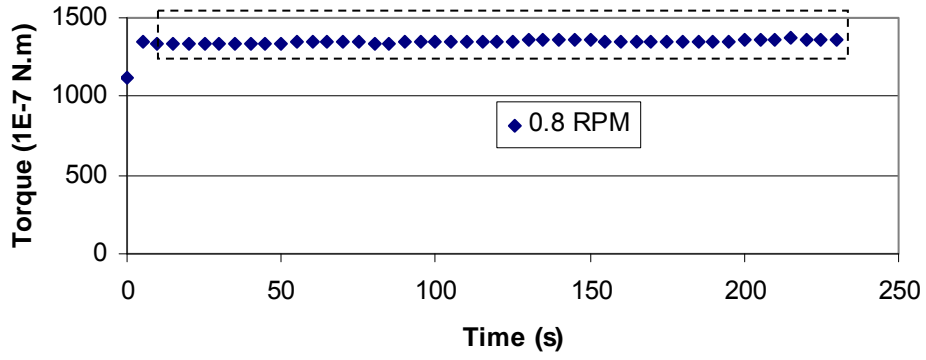
(f)



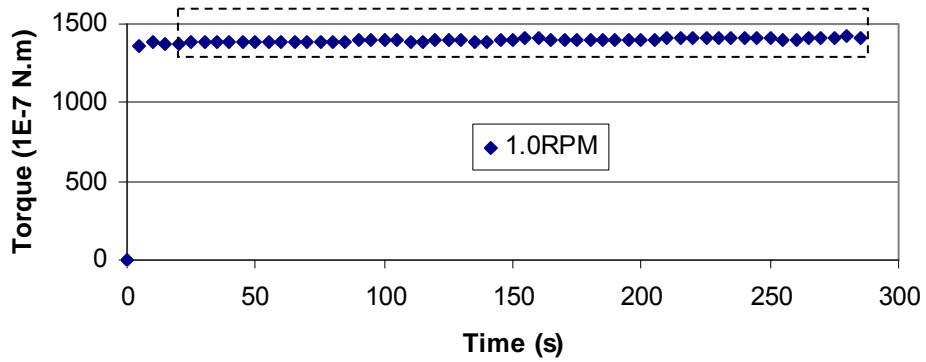
(g)



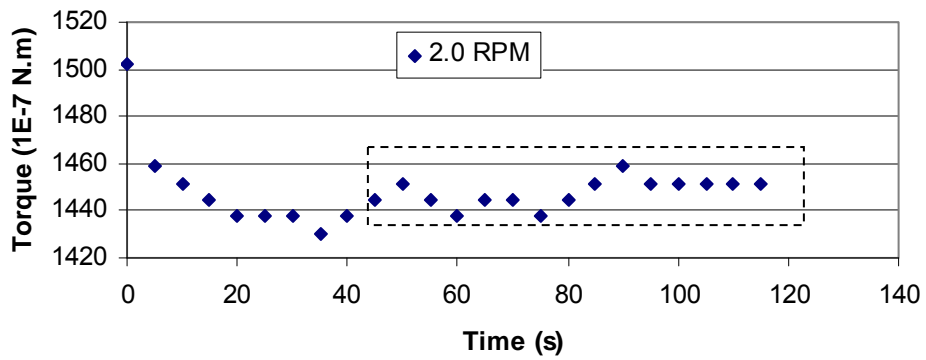
(h)



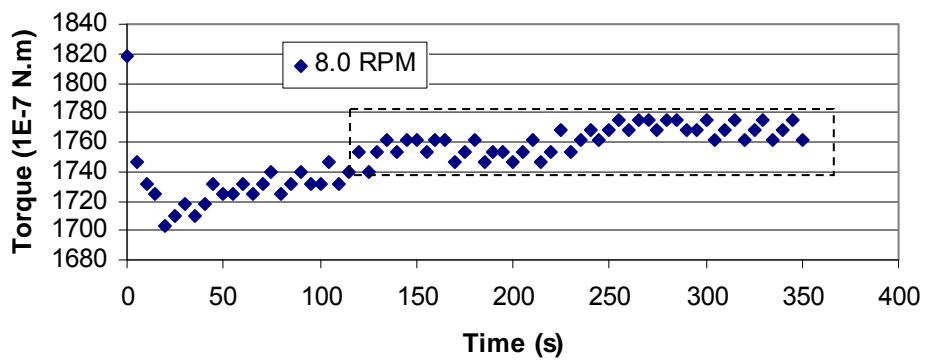
(i)

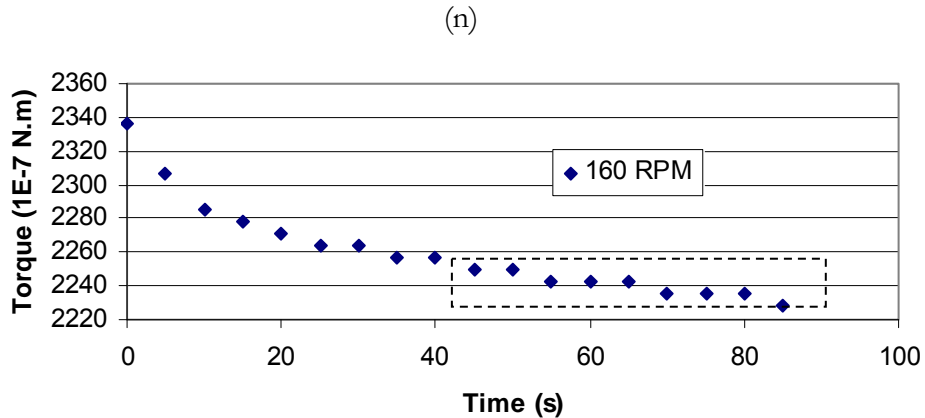
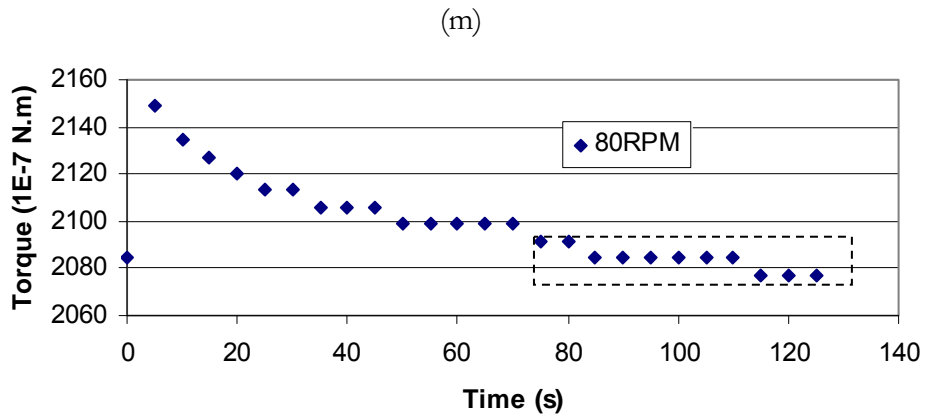
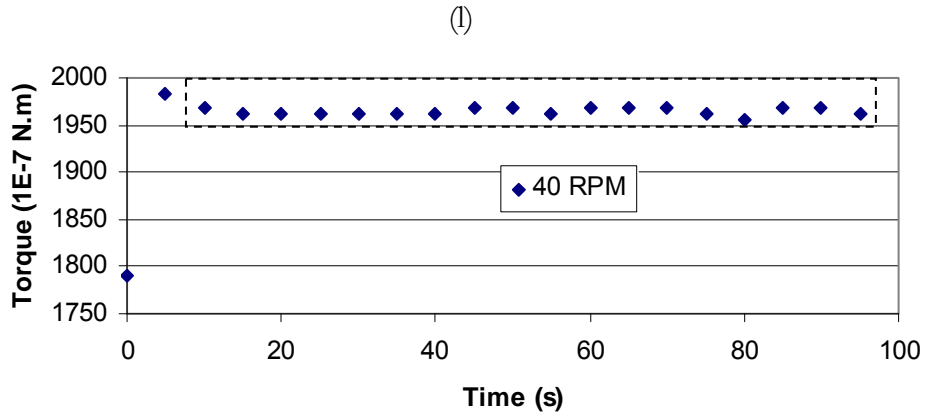


(j)



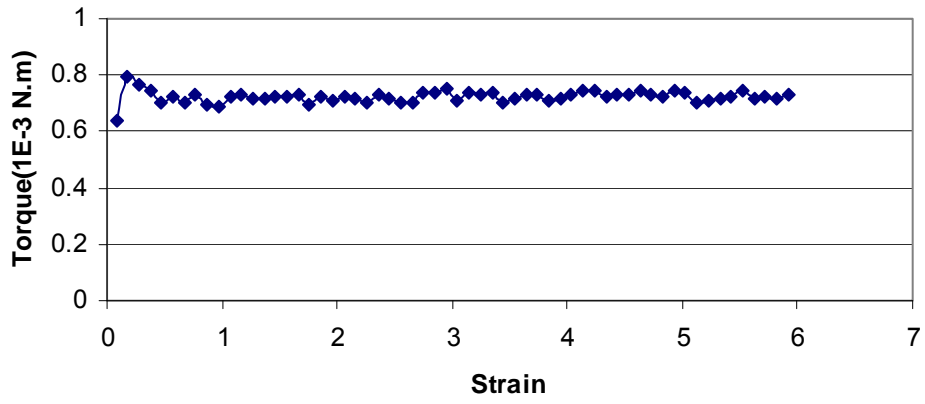
(k)



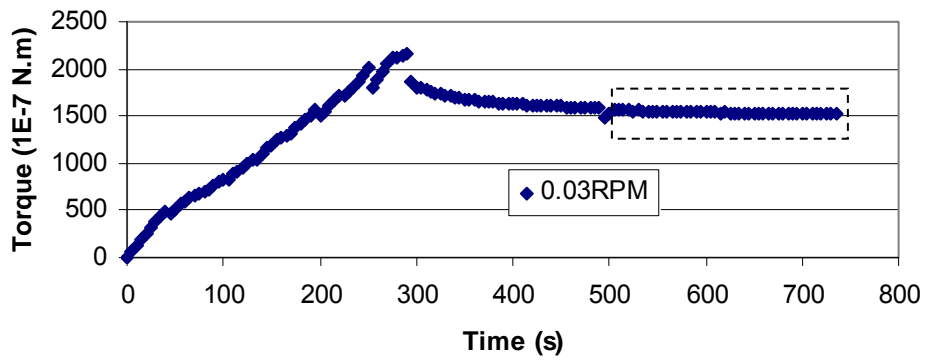


(o)

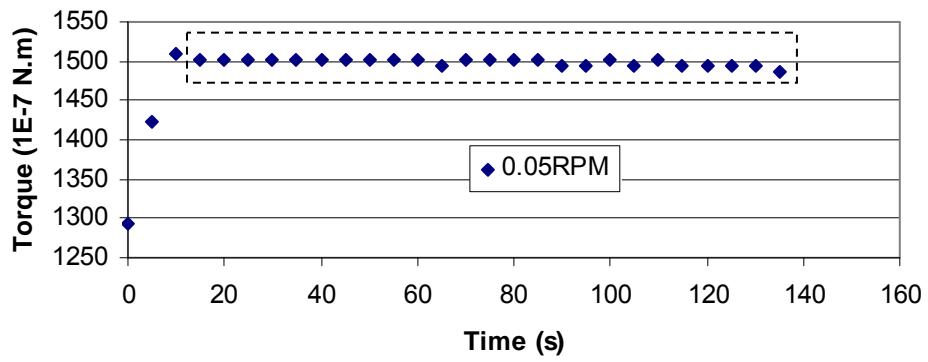
Figure A.8 Raw Data for Slurry with Solids Content of 49% and Fines Content of 68% (a: Plot of Torque vs. Shear Strain from Vane Shear Test; b-o: Plot of Torque vs. Time from Viscosity Measurements)



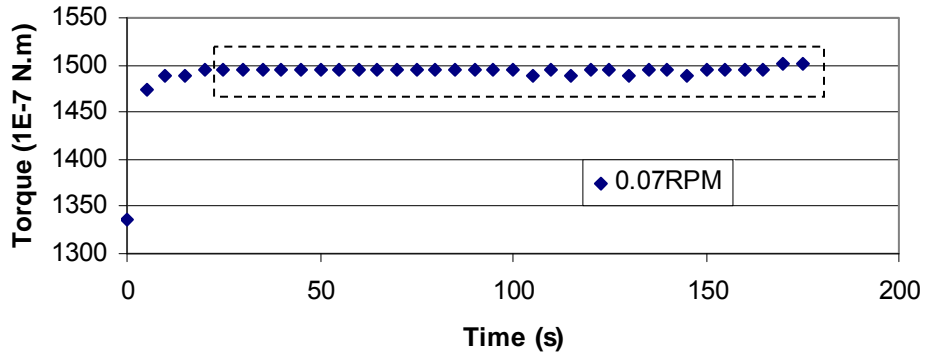
(a)



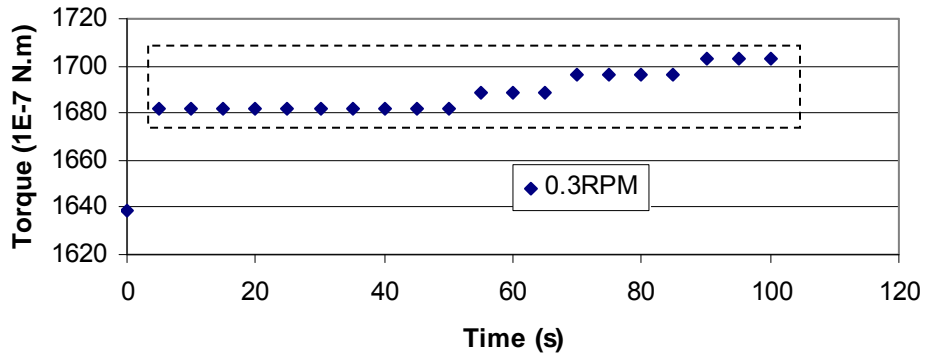
(b)



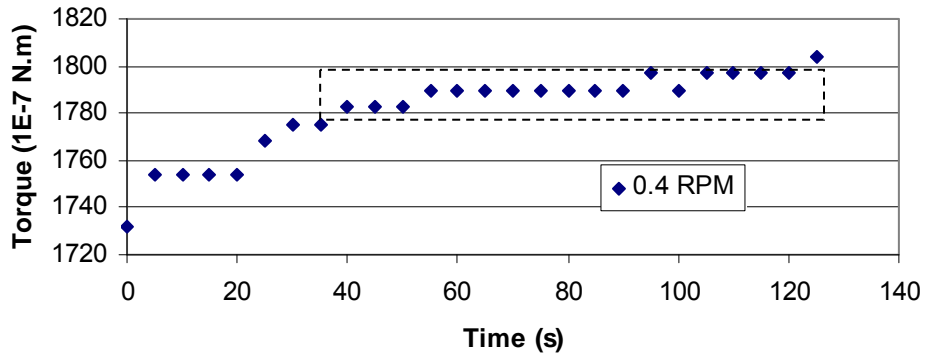
(c)



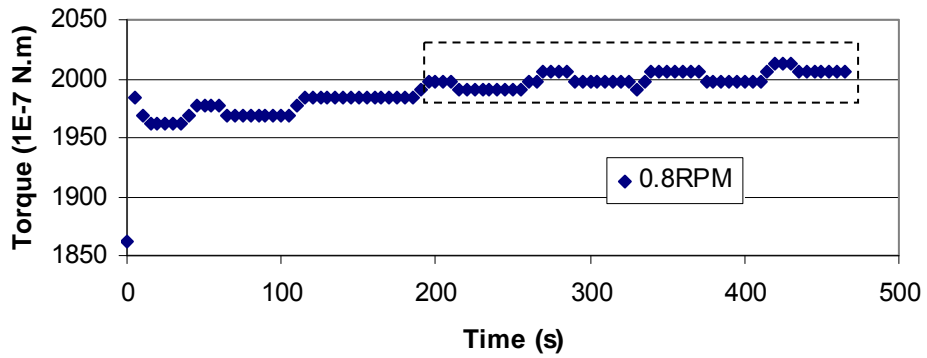
(d)



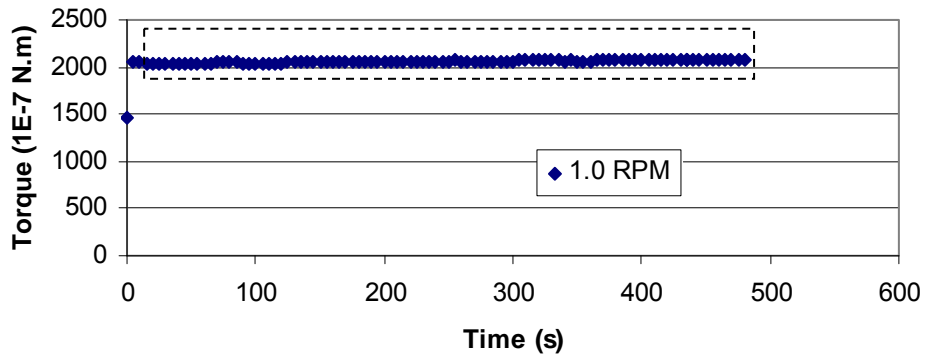
(e)



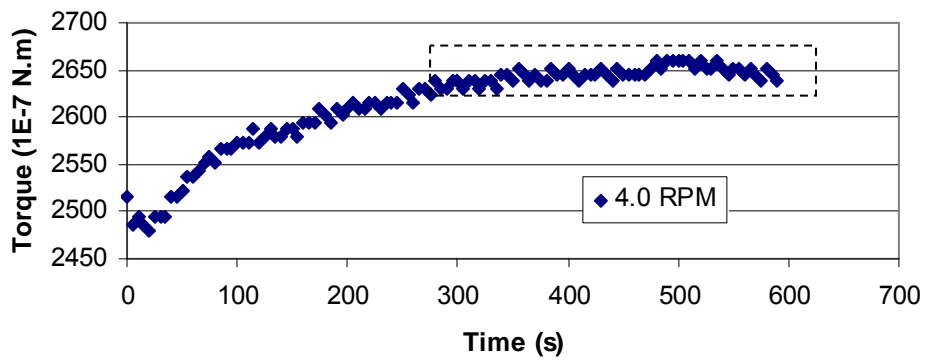
(f)



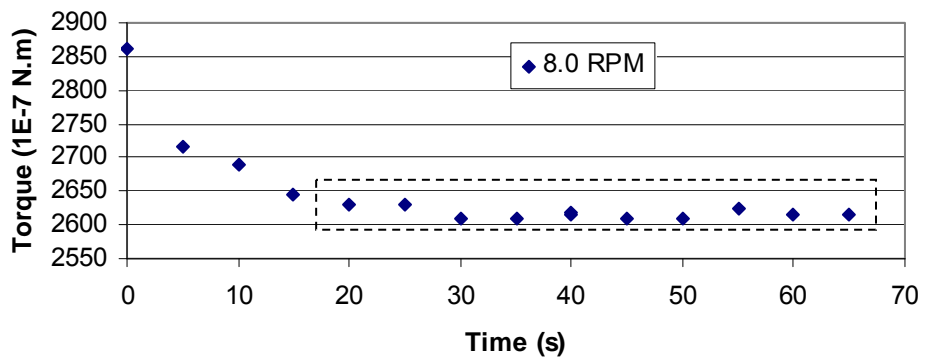
(g)



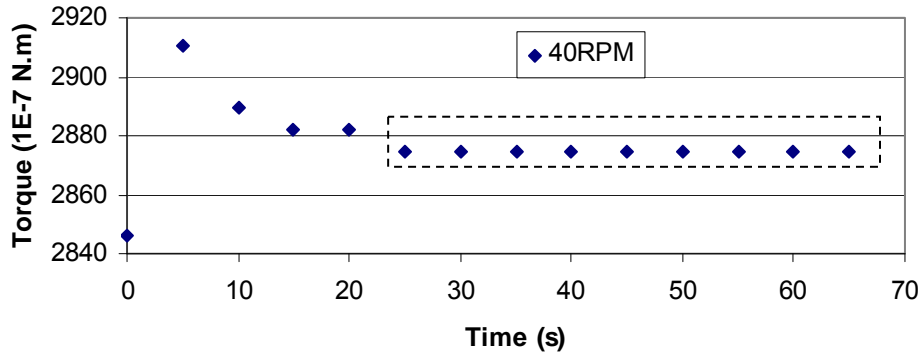
(h)



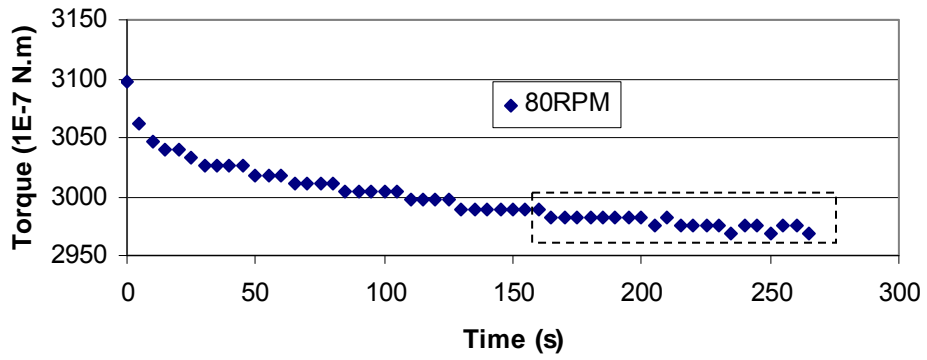
(i)



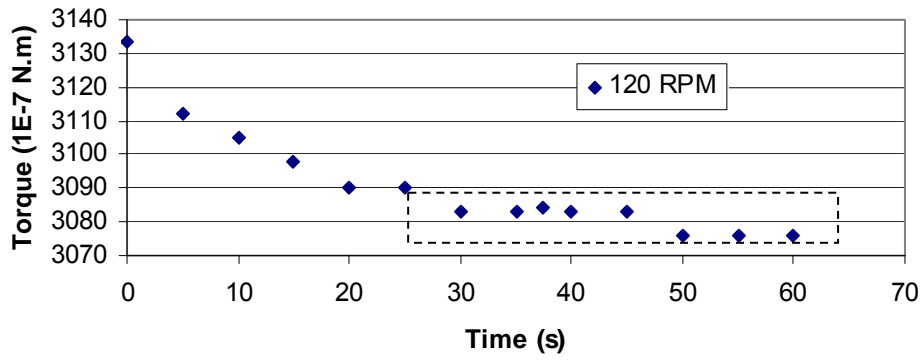
(j)



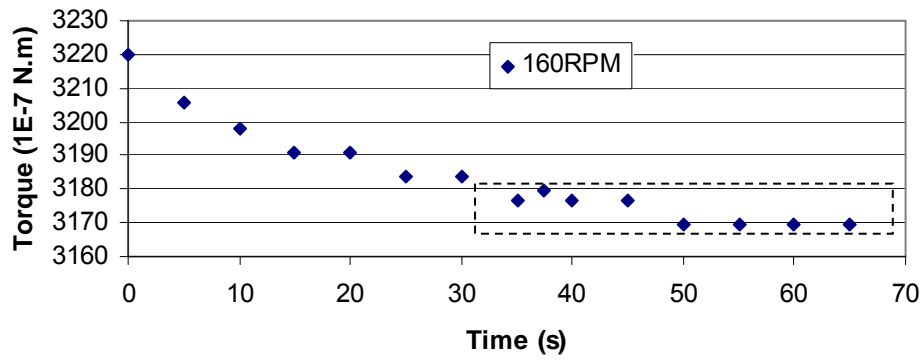
(k)



(l)

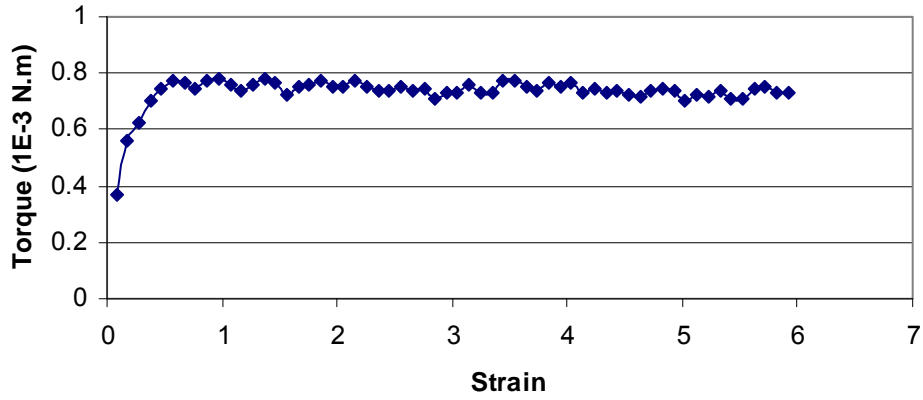


(m)

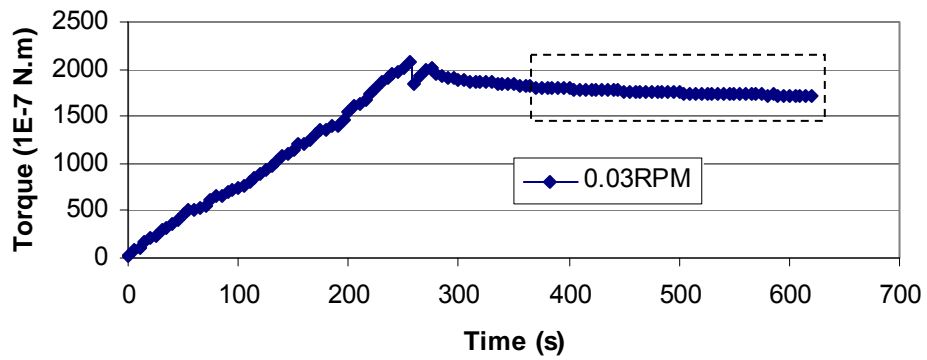


(n)

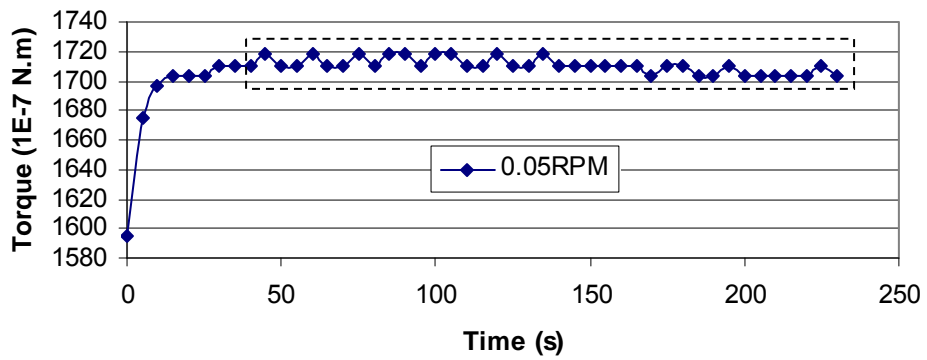
Figure A.9 Raw Data for Slurry with Solids Content of 51% and Fines Content of 78%  
(a: Plot of Torque vs. Shear Strain from Vane Shear Test; b-n: Plot of Torque vs. Time  
from Viscosity Measurements)



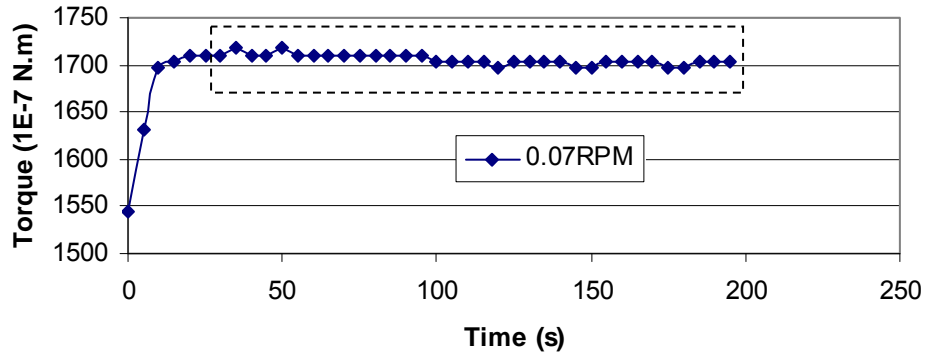
(a)



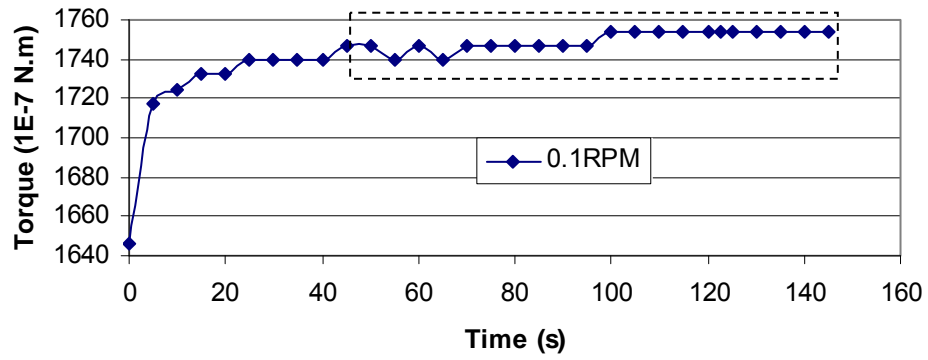
(b)



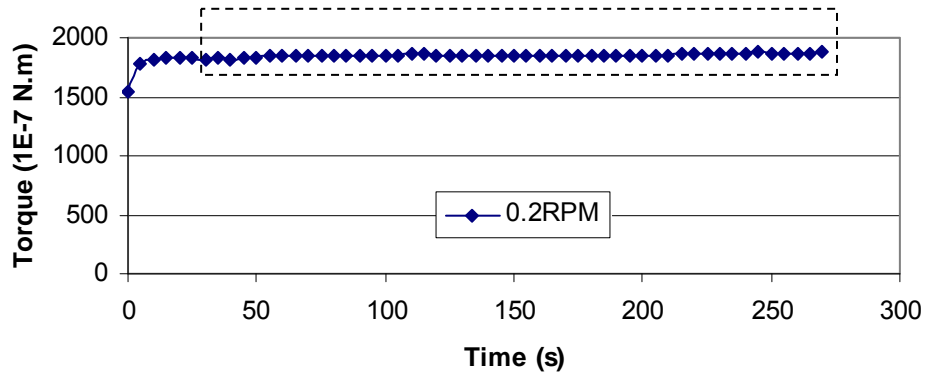
(c)



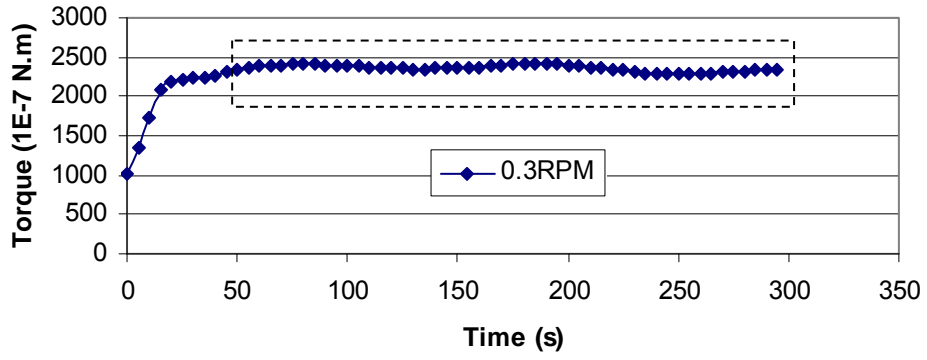
(d)



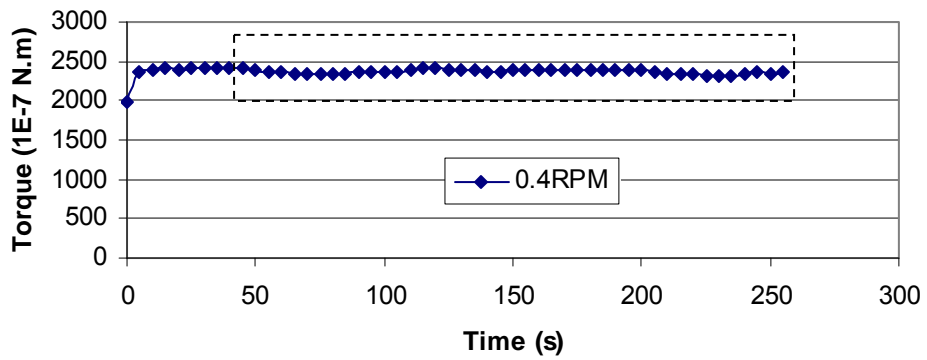
(e)



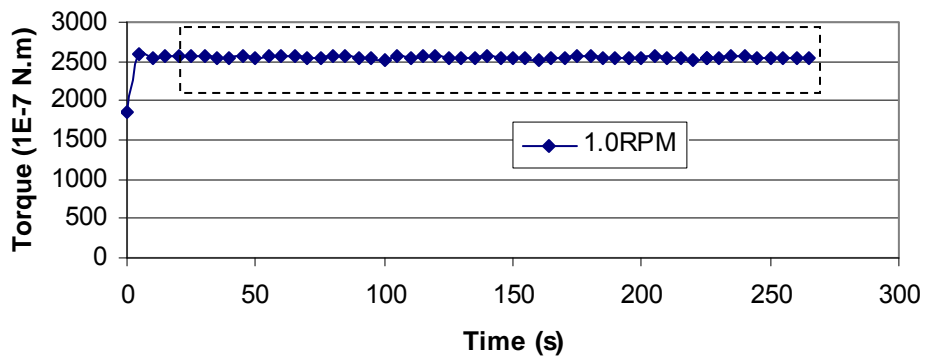
(f)



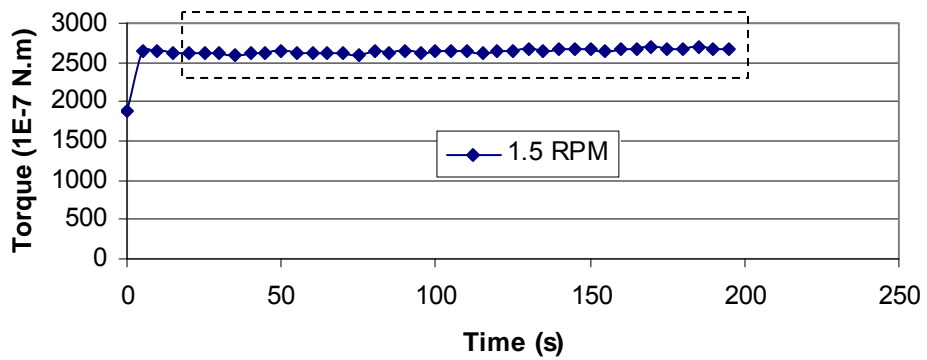
(g)



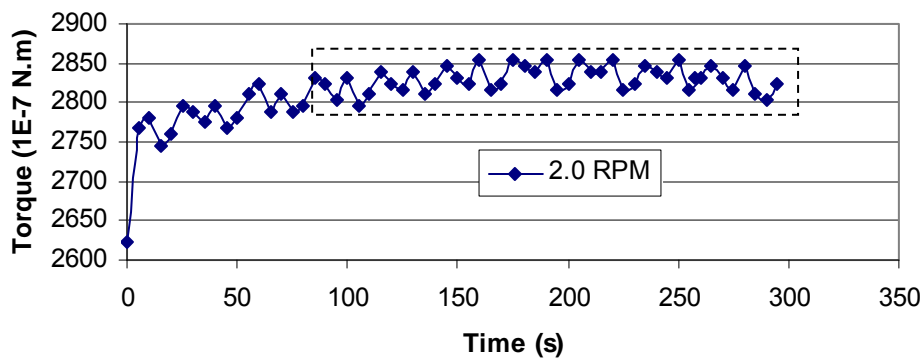
(h)



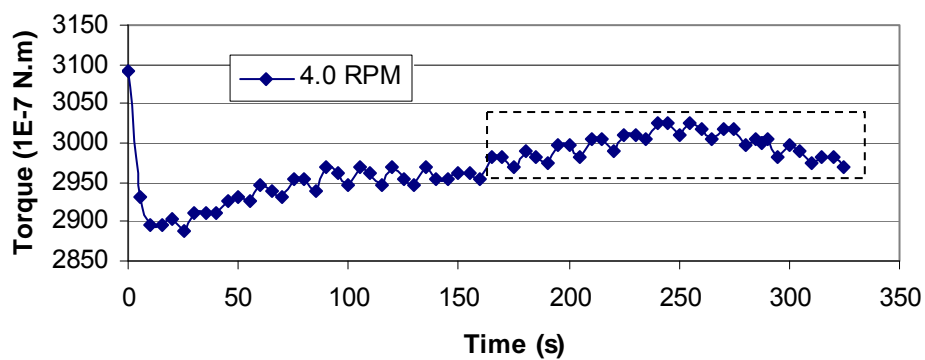
(i)



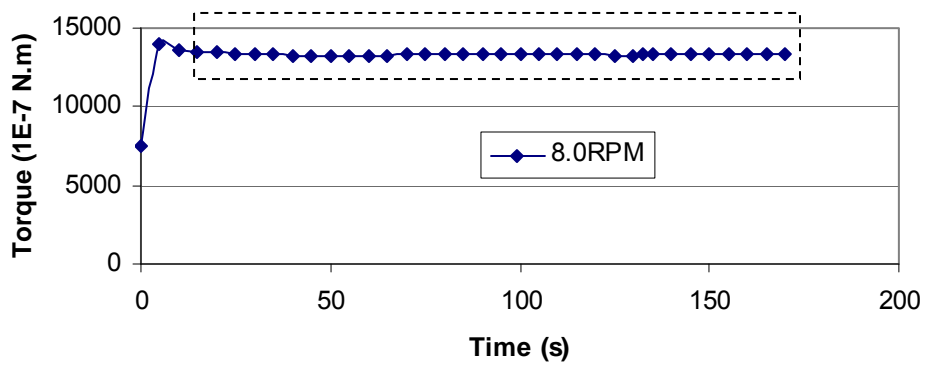
(j)



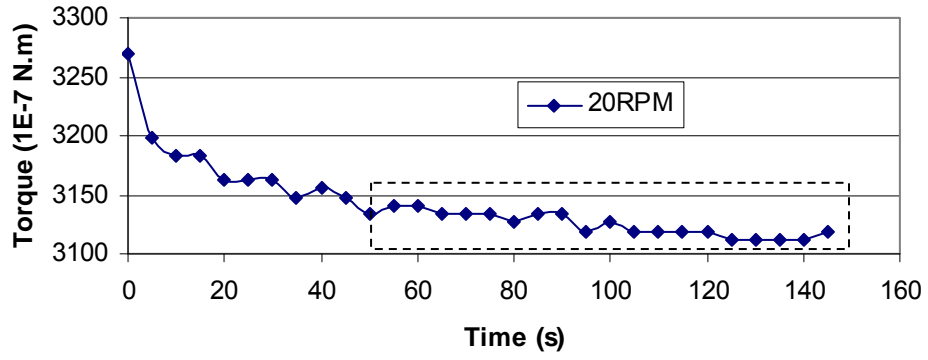
(k)



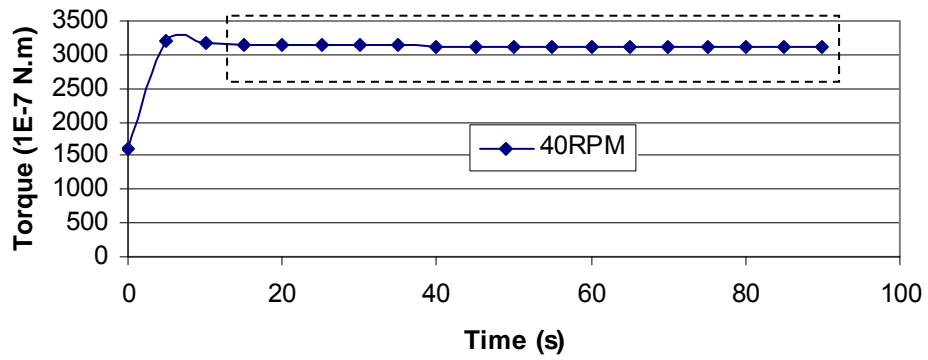
(l)



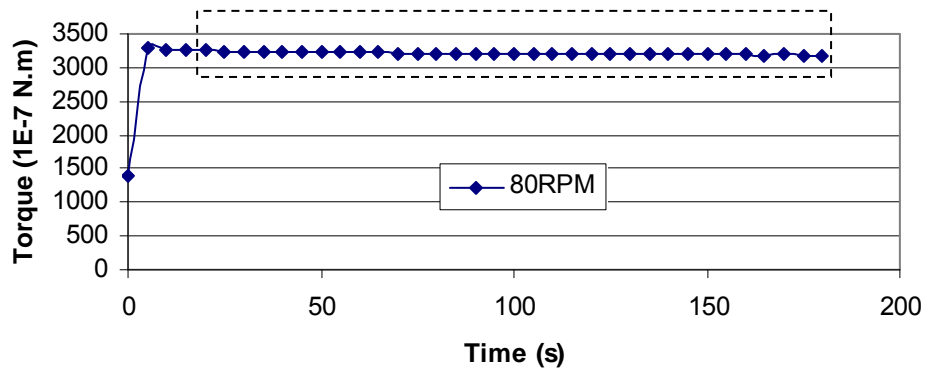
(m)



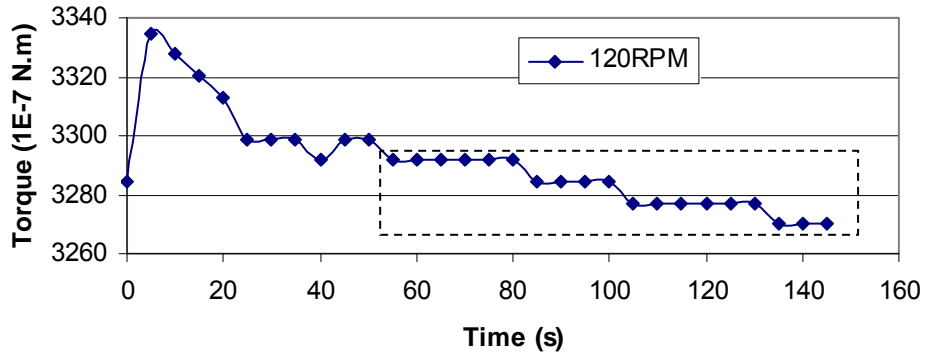
(o)



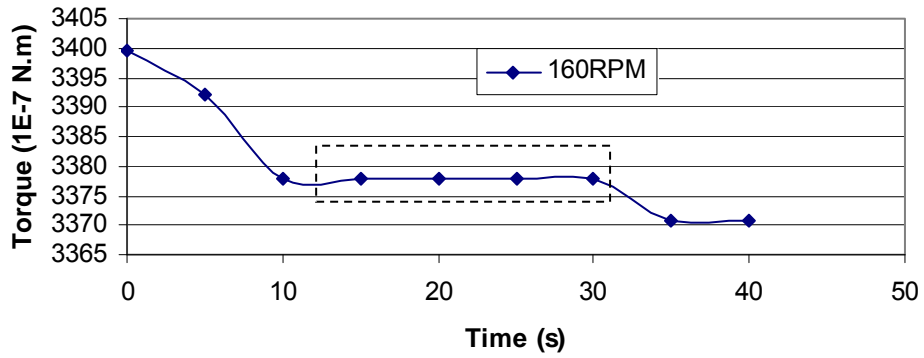
(p)



(q)

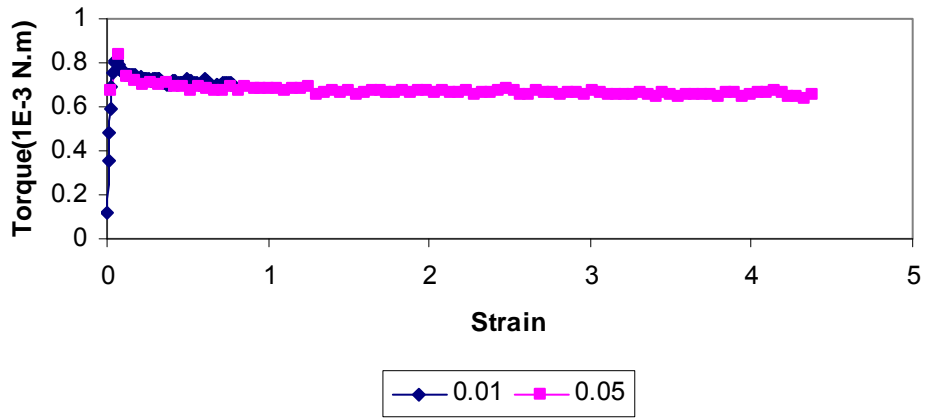


(r)

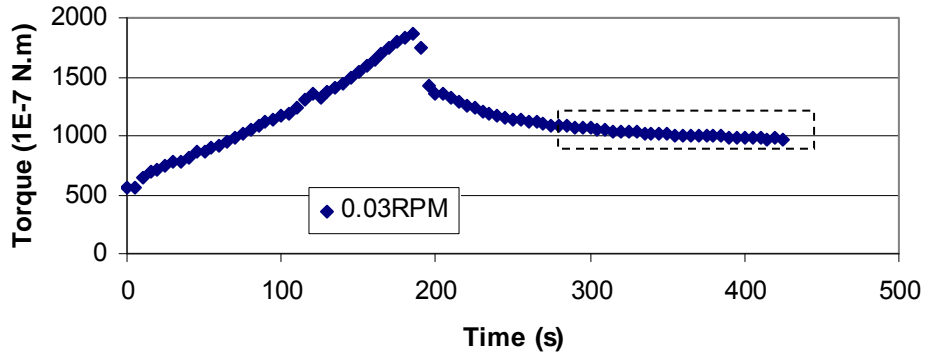


(s)

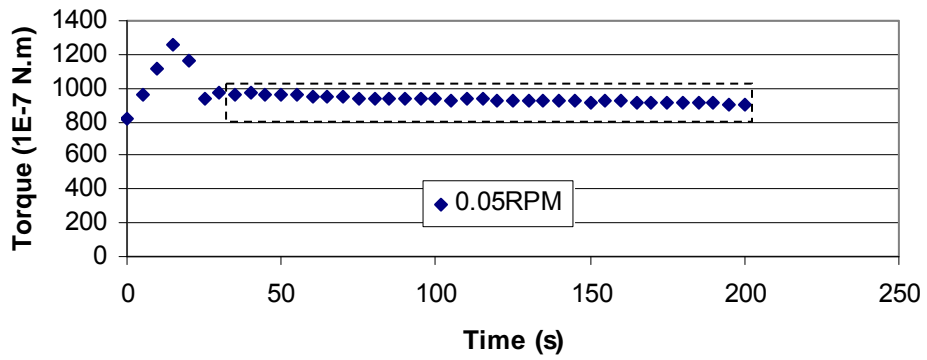
Figure A.10 Raw Data for Slurry with Solids Content of 49% and Fines Content of 86% (a: Plot of Torque vs. Shear Strain from Vane Shear Test; b-r: Plot of Torque vs. Time from Viscosity Measurements)



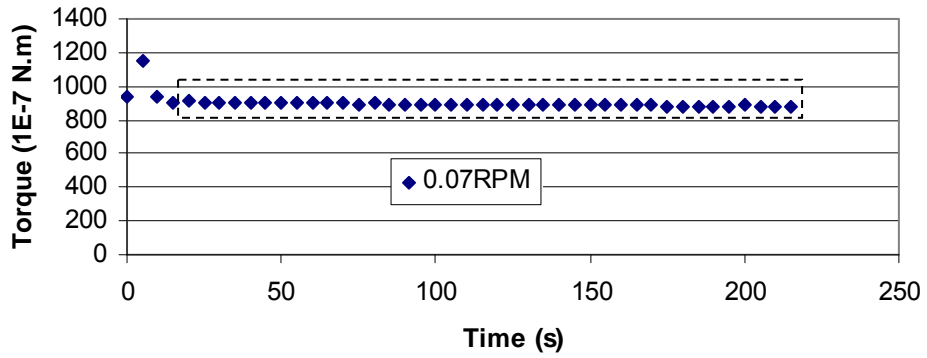
(a)



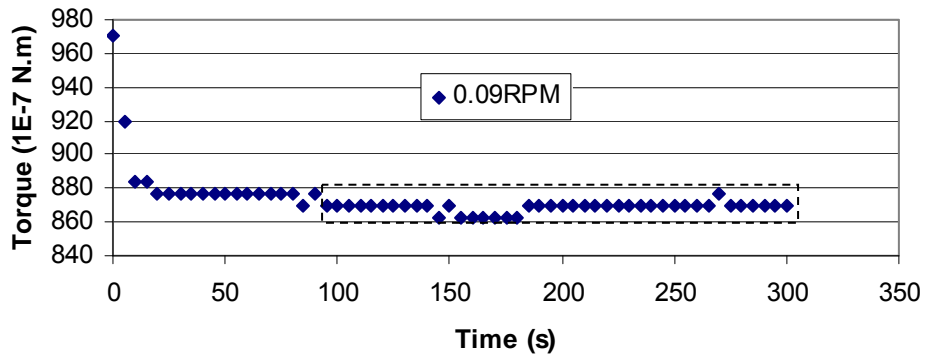
(b)



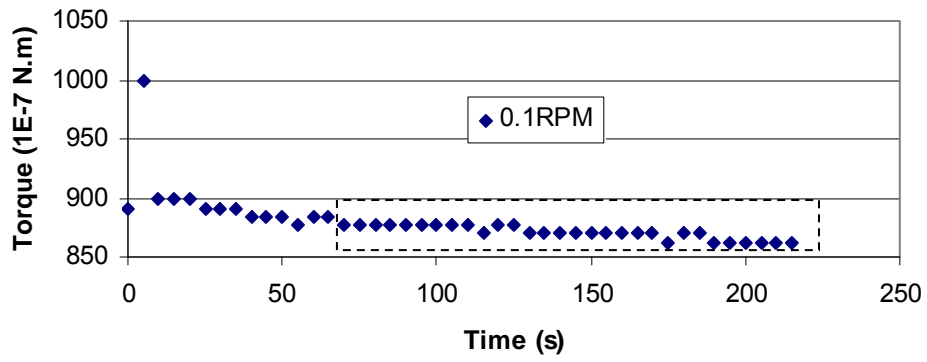
(c)



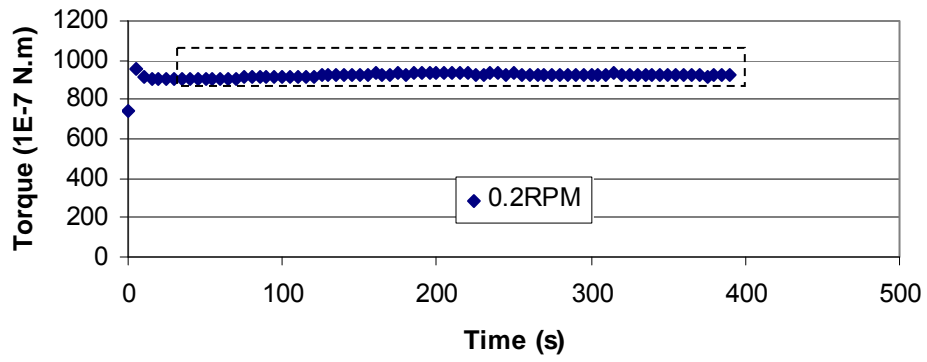
(d)



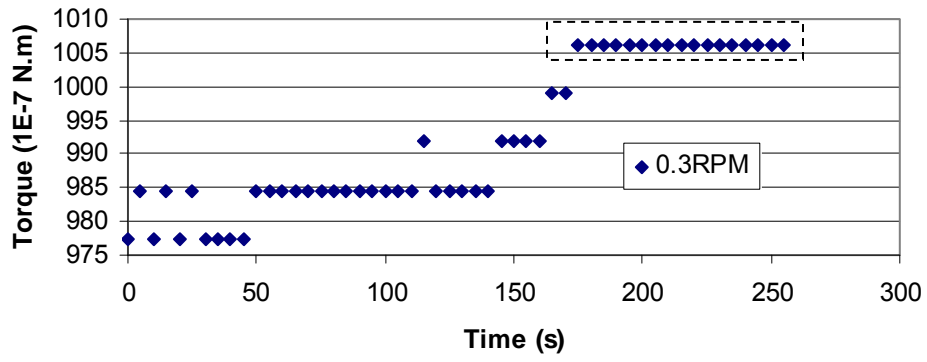
(e)



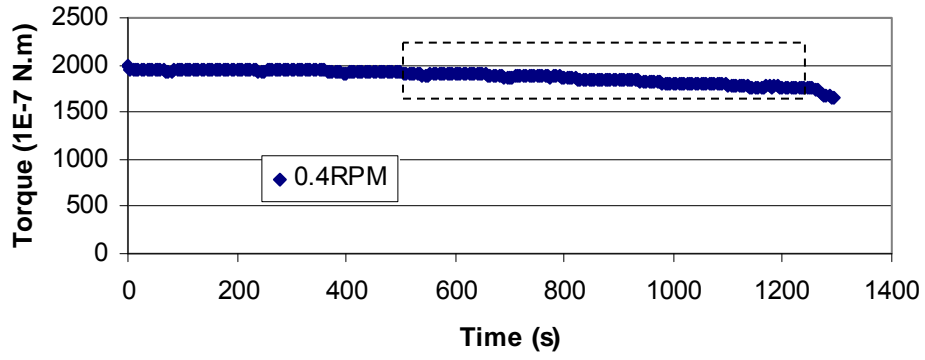
(f)



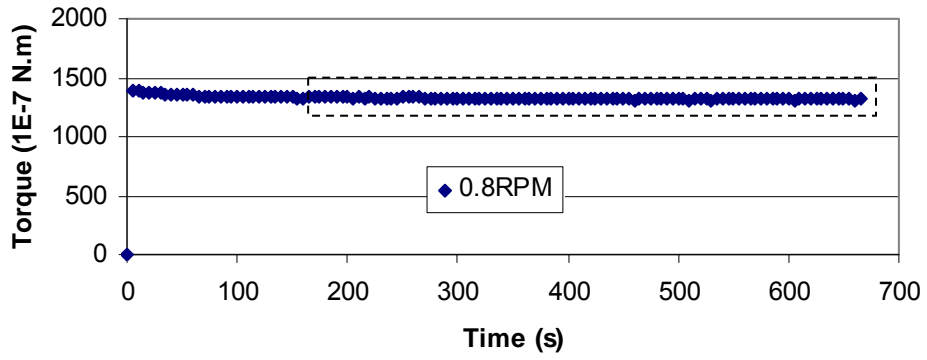
(g)



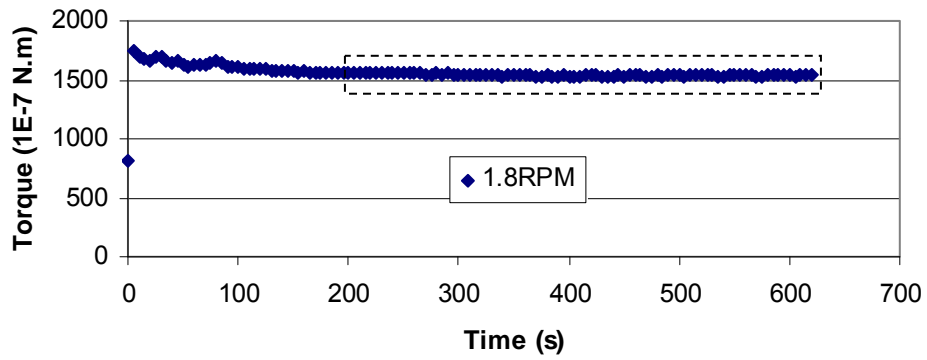
(h)



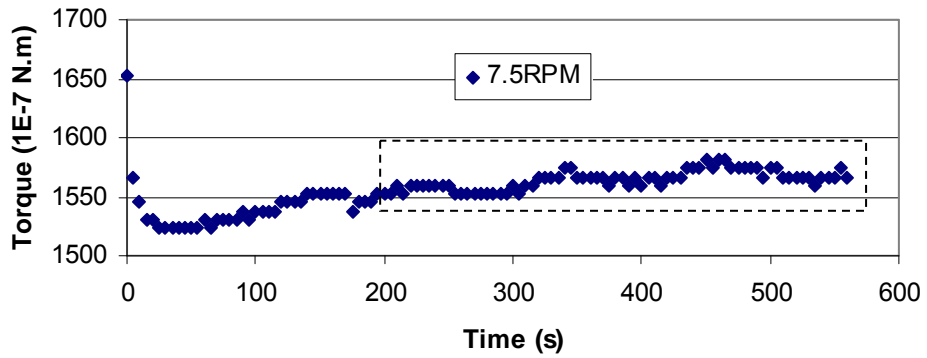
(i)



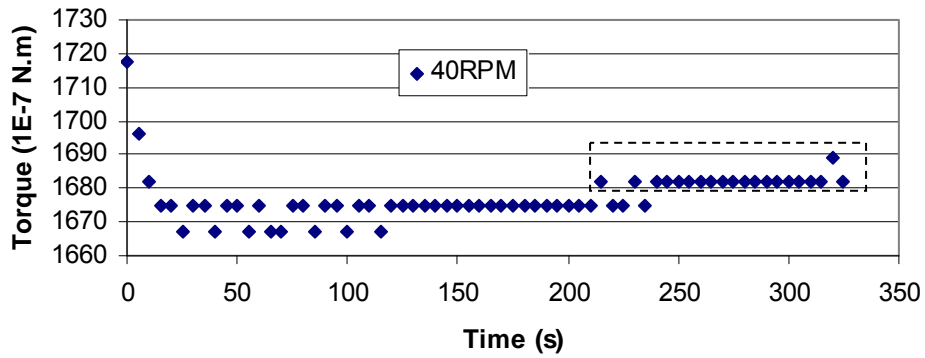
(j)



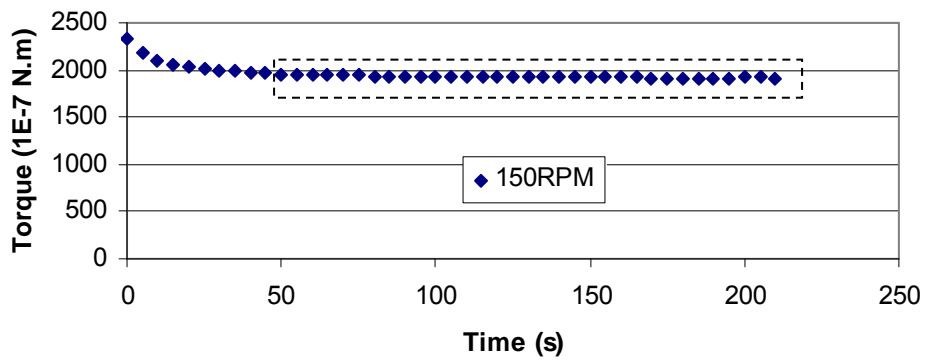
(k)



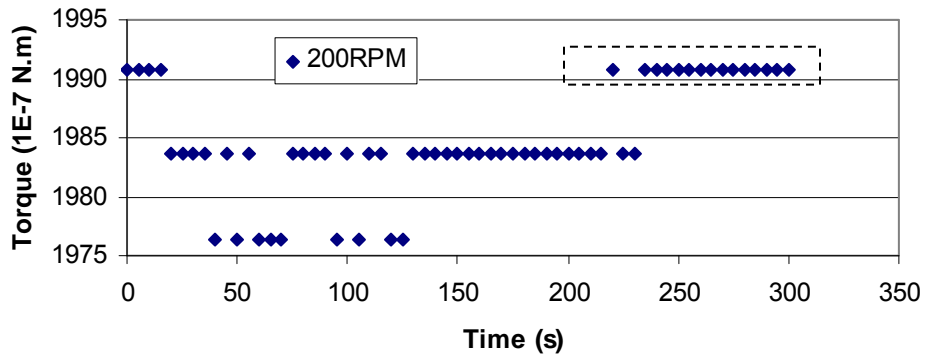
(k)



(l)

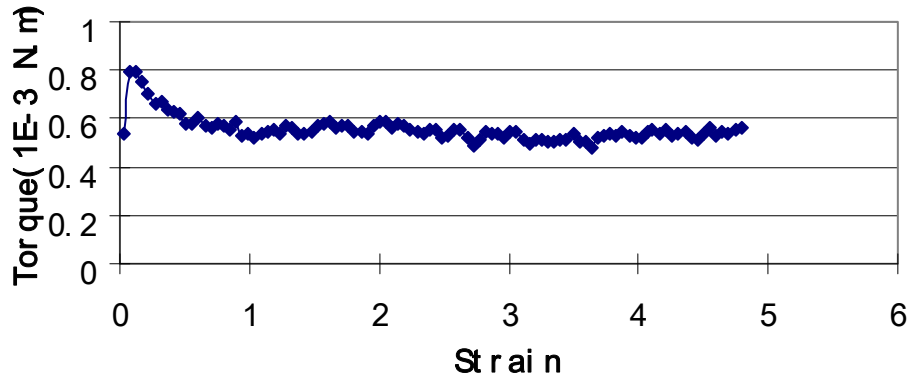


(m)



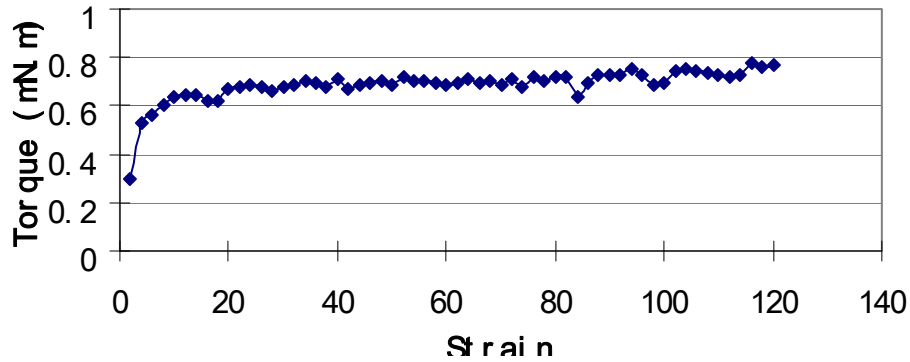
(o)

Figure A.11 Raw Data for Slurry with Solids Content of 41% and Fines Content of 95% (a: Plot of Torque vs. Shear Strain from Vane Shear Test; b-o: Plot of Torque vs. Time from Viscosity Measurements)



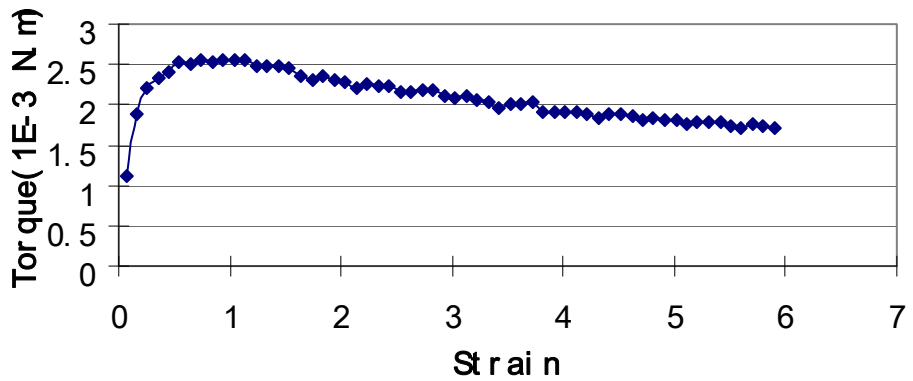
(a)

Figure A.12 Raw Data for Slurry with Solids Content of 19% and Fines Content of 24% (a: Plot of Torque vs. Shear Strain from Vane Shear Test)



(a)

Figure A.13 Raw Data for Slurry with Solids Content of 25% and Fines Content of 49% (a: Plot of Torque vs. Shear Strain from Vane Shear Test)



(a)

Figure A.14 Raw Data for Slurry with Solids Content of 27% and Fines Content of 94% (a: Plot of Torque vs. Shear Strain from Vane Shear Test)